IAEA TECDOC SERIES

Modelling of Water Cooled Fuel Including Design Basis and Severe Accidents

*Proceedings of a Technical Meeting
Held in Chengdu, China,
28 October–1 November 2013*

IAEA
International Atomic Energy Agency

EDITORIAL NOTE

This publication has been prepared from the original material as submitted by the contributors and has not been edited by the editorial staff of the IAEA. The views expressed remain the responsibility of the contributors and do not necessarily represent the views of the IAEA or its Member States.

Neither the IAEA nor its Member States assume any responsibility for consequences which may arise from the use of this publication. This publication does not address questions of responsibility, legal or otherwise, for acts or omissions on the part of any person.

The use of particular designations of countries or territories does not imply any judgement by the publisher, the IAEA, as to the legal status of such countries or territories, of their authorities and institutions or of the delimitation of their boundaries.

The mention of names of specific companies or products (whether or not indicated as registered) does not imply any intention to infringe proprietary rights, nor should it be construed as an endorsement or recommendation on the part of the IAEA.

The IAEA has no responsibility for the persistence or accuracy of URLs for external or their party Internet web sites referred to in this publication and does not guarantee that any content on such web sites is, or will remain, accurate or appropriate.

MODELLING OF WATER COOLED FUEL INCLUDING DESIGN BASIS AND SEVERE ACCIDENTS

The following States are Members of the International Atomic Energy Agency:

AFGHANISTAN
ALBANIA
ALGERIA
ANGOLA
ANTIGUA AND BARBUDA
ARGENTINA
ARMENIA
AUSTRALIA
AUSTRIA
AZERBAIJAN
BAHAMAS
BAHRAIN
BANGLADESH
BELARUS
BELGIUM
BELIZE
BENIN
BOLIVIA, PLURINATIONAL
  STATE OF
BOSNIA AND HERZEGOVINA
BOTSWANA
BRAZIL
BRUNEI DARUSSALAM
BULGARIA
BURKINA FASO
BURUNDI
CAMBODIA
CAMEROON
CANADA
CENTRAL AFRICAN
  REPUBLIC
CHAD
CHILE
CHINA
COLOMBIA
CONGO
COSTA RICA
CÔTE D'IVOIRE
CROATIA
CUBA
CYPRUS
CZECH REPUBLIC
DEMOCRATIC REPUBLIC
  OF THE CONGO
DENMARK
DJIBOUTI
DOMINICA
DOMINICAN REPUBLIC
ECUADOR
EGYPT
EL SALVADOR
ERITREA
ESTONIA
ETHIOPIA
FIJI
FINLAND
FRANCE
GABON
GEORGIA

GERMANY
GHANA
GREECE
GUATEMALA
GUYANA
HAITI
HOLY SEE
HONDURAS
HUNGARY
ICELAND
INDIA
INDONESIA
IRAN, ISLAMIC REPUBLIC OF
IRAQ
IRELAND
ISRAEL
ITALY
JAMAICA
JAPAN
JORDAN
KAZAKHSTAN
KENYA
KOREA, REPUBLIC OF
KUWAIT
KYRGYZSTAN
LAO PEOPLE'S DEMOCRATIC
  REPUBLIC
LATVIA
LEBANON
LESOTHO
LIBERIA
LIBYA
LIECHTENSTEIN
LITHUANIA
LUXEMBOURG
MADAGASCAR
MALAWI
MALAYSIA
MALI
MALTA
MARSHALL ISLANDS
MAURITANIA
MAURITIUS
MEXICO
MONACO
MONGOLIA
MONTENEGRO
MOROCCO
MOZAMBIQUE
MYANMAR
NAMIBIA
NEPAL
NETHERLANDS
NEW ZEALAND
NICARAGUA
NIGER
NIGERIA
NORWAY
OMAN

PAKISTAN
PALAU
PANAMA
PAPUA NEW GUINEA
PARAGUAY
PERU
PHILIPPINES
POLAND
PORTUGAL
QATAR
REPUBLIC OF MOLDOVA
ROMANIA
RUSSIAN FEDERATION
RWANDA
SAN MARINO
SAUDI ARABIA
SENEGAL
SERBIA
SEYCHELLES
SIERRA LEONE
SINGAPORE
SLOVAKIA
SLOVENIA
SOUTH AFRICA
SPAIN
SRI LANKA
SUDAN
SWAZILAND
SWEDEN
SWITZERLAND
SYRIAN ARAB REPUBLIC
TAJIKISTAN
THAILAND
THE FORMER YUGOSLAV
  REPUBLIC OF MACEDONIA
TOGO
TRINIDAD AND TOBAGO
TUNISIA
TURKEY
UGANDA
UKRAINE
UNITED ARAB EMIRATES
UNITED KINGDOM OF
  GREAT BRITAIN AND
  NORTHERN IRELAND
UNITED REPUBLIC
  OF TANZANIA
UNITED STATES OF AMERICA
URUGUAY
UZBEKISTAN
VANUATU
VENEZUELA, BOLIVARIAN
  REPUBLIC OF
VIET NAM
YEMEN
ZAMBIA
ZIMBABWE

The Agency's Statute was approved on 23 October 1956 by the Conference on the Statute of the IAEA held at United Nations Headquarters, New York; it entered into force on 29 July 1957. The Headquarters of the Agency are situated in Vienna. Its principal objective is "to accelerate and enlarge the contribution of atomic energy to peace, health and prosperity throughout the world".

IAEA-TECDOC-CD-1775

MODELLING OF WATER COOLED FUEL INCLUDING DESIGN BASIS AND SEVERE ACCIDENTS

PROCEEDINGS OF A TECHNICAL MEETING HELD IN CHENGDU, CHINA, 28 OCTOBER–1 NOVEMBER 2013

INTERNATIONAL ATOMIC ENERGY AGENCY
VIENNA, 2015

FOREWORD

The demands on nuclear fuel have recently been increasing, and include transient regimes, higher discharge burnup and longer fuel cycles. This has resulted in an increase of loads on fuel and core internals. In order to satisfy these demands while ensuring compliance with safety criteria, new national and international programmes have been launched and advanced modelling codes are being developed. The Fukushima Daiichi accident has particularly demonstrated the need for adequate analysis of all aspects of fuel performance to prevent a failure and also to predict fuel behaviour were an accident to occur.

This publication presents the Proceedings of the Technical Meeting on Modelling of Water Cooled Fuel Including Design Basis and Severe Accidents, which was hosted by the Nuclear Power Institute of China (NPIC) in Chengdu, China, following the recommendation made in 2013 at the IAEA Technical Working Group on Fuel Performance and Technology. This recommendation was in agreement with IAEA mid-term initiatives, linked to the post-Fukushima IAEA Nuclear Safety Action Plan, as well as the forthcoming Coordinated Research Project (CRP) on Fuel Modelling in Accident Conditions. At the technical meeting in Chengdu, major areas and physical phenomena, as well as types of code and experiment to be studied and used in the CRP, were discussed.

The technical meeting provided a forum for international experts to review the state of the art of code development for modelling fuel performance of nuclear fuel for water cooled reactors with regard to steady state and transient conditions, and for design basis and early phases of severe accidents, including experimental support for code validation. A round table discussion focused on the needs and perspectives on fuel modelling in accident conditions.

This meeting was the ninth in a series of IAEA meetings, which reflects Member States' continuing interest in nuclear fuel issues. The previous meetings were held in 1980 (jointly with OECD Nuclear Energy Agency in Helsinki, Finland), 1983 (Risø, Denmark), 1986 (Vienna, Austria), 1988 (Preston, United Kingdom), 1992 (Pembroke, Canada), 1995 (Dimitrovgrad, Russian Federation), 2001 (Halden, Norway) and 2011 (Mito, Japan). The 2011 meeting, in Japan, focused on fuel behaviour and modelling under design basis accidents. Such a short interval of two years between these last two technical meetings emphasizes the importance of the subject and the urgency to accelerate the process of accident related fuel behaviour code development and verification.

The meeting was attended by 30 specialists in fuel performance modelling and experimental support from 16 Member States, and the Joint Research Centre's Institute for Transuranium Elements. A total of 21 papers were presented at three sessions.

The IAEA wishes to thank all the participants for their contributions, in particular to the NPIC hosts for the excellent organization of the meeting, including the technical visit to NPIC testing facilities. The IAEA officer responsible for this publication was V. Inozemtsev of the Division of Nuclear Fuel Cycle and Waste Technology.

CONTENTS

SESSION 3: MODELLING OF SEVERE ACCIDENTS AND EXPERIMENTAL SUPPORT

SUMMARY

Session 1: Development of Codes for Modeling of Fuel Behaviour under Steady State and Transient Condition

Chairperson: R. Williamson

1.   BACKGROUND

The first session of this technical meeting was devoted to code development for modeling fuel behaviour under plant normal operation conditions and anticipated operational occurnaces. Later sessions focused on modeling of fuel behaviour under design basis accidents (DBA) and severe accidents, including experimental support.

Six papers were presented in this session and ranged from studies of improved models for individual phenomena (gap heat transfer and burnup) to code coupling (neutronics/thermal-hydraulics/fuel performance) to general overviews of legacy and developing fuel performance codes (BaCo/BISON/Peregrine).

2.   SUMMARIES AND COMMENTS

The presentation from the Atomic Energy National Commission of Argentina (CNEA) considered their legacy code BaCo, which was originally developed in the 70's to study fuel rod behaviour under irradiation and is presently being used to assist in design of advanced PHWR and innovative PWR fuel. Although the code is focused on PHWR fuel, it maintains compatibility with PWR, BWR, WWER, PHWR MOX and other advanced and experimental fuels. The presentation provided an overview of general code capabilities and included discussion of advanced features, such a 3D FEM submodeling, statistical analysis, and multirod (full core) batch type simulations. Developers and users of BaCo have enjoyed a long-term interest in the IAEA series of Coordinated Research Projects (CRP) on fuel behaviour modeling. Comparisons of BaCo to a few selected cases from FUMEX I, II and III were reviewed. The authors voiced support for a new CRP focused on severe accidents such as RIA and LOCA.

A presentation from the Nuclear and Radiation Safety Center (NRSC) of Armenia discussed the importance of coupling neutronic, thermal-hydraulic and fuel performance codes in order to take advantage of the strengths of each approach, while mitigating any drawbacks. An iterative approach was outlined that is planned for the coupling of PARCS (neutronics), PATHS (thermal-hydraulics) and TRANSURANUS (fuel performance). It was concluded that application of coupled codes will allow nuclear reactor safety margins to be quantified without unnecessary over-conservatism.

The Korea Atomic Energy Research Institute (KAERI) summarized efforts to develop an improved gap element for finite-element based gap conductance modeling. Traditional gap conductance models are highly nonlinear (the gap conductance increases rapidly during final gap closure) and strongly coupled (small changes in fuel or clad displacement lead to large local temperature variation) which can result in difficulties with numerical convergence. The authors reviewed traditional gap conductance models and described a linearized 1D gap conductance element applicable to multidimensional analysis. The linearized gap element was implemented in ANSYS and, for a 1D problem, compared against the general multidimensional thermal contact model in

ANSYS. Good temperature comparisons and improved convergence characteristics were shown. Further investigation of the linearized model on realistic multidimensional geometries, where significant relative fuel-clad motion occurs, is warranted.

A presentation from the State Scientific and Technical Centre for Nuclear and Radiation Safety (NRS-SSTC) in Ukraine described testing of the TRANSURANUS burnup model (TUBRNP) against HELIOS neutron transport code calculations for Gd-doped WWER-1000 fuel pins. A variety of different enrichment and initial Gd_2O_3 concentrations were considered. Both the standard and an optimized version of TRANSURANUS were used, with the optimized version including formulations to account for burnup and fuel radius dependencies of the gadolinium cross sections. Numerical test results demonstrated that the optimized version provides radial Gd and power distributions that are closer to HELIOS results. In further testing, it was shown that the Gd-optimization approach resulted in higher maximum fuel temperatures, approximately 10% higher in steady-state regimes and 30% higher during a control rod ejection transient.

The Idaho National Laboratory (INL) in the United States presented an overview of the BISON fuel performance code, which is a modern multi-physics, multi-dimensional finite-element based code that has been under development since 2009. A brief background was provided on the code's computational framework, governing equations, and material and behavioral models. Ongoing code verification and validation work was outlined, and comparative results were provided for several validation cases including a pellet clad mechanical interaction case from FUMEX-III. Recent applications were discussed, including specific description of two areas where 3D treatment is important, namely, fuel with a missing pellet surface and fuel pellet eccentricity. Future efforts with BISON will include a strong validation effort relying on prior FUMEX cases and collaborations with the Halden Reactor Project and the UK's National Nuclear Laboratory. Code development efforts will focus on improving contact and fuel fracture models and include a major emphasis on enhancing the code to model accident behavior. The INL has strong interest in participating in the proposed new FUMAC CRP.

A final presentation summarized fuel modeling activities within the US Consortium for Advanced Simulation of LWRs (CASL) program. Two codes were described, Peregrine, for engineering scale fuel performance analysis, and MAMBA, for multi-scale modeling of CRUD formation and growth. Peregrine is a derivative of the BISON code described above, and was created for specific use within CASL. The codes share a framework such that all non-CASL proprietary code is located in a library assessable by both codes, leading to substantial leveraging of development efforts. Recent validation of Peregrine against test reactor data and the industry standard code FALCON was reported with generally favorable comparisons. MAMBA combines heat transport, thermodynamics and chemical kinetics to predict cladding erosion and CRUD layer formation and distribution. An early qualitative validation study provided promising results, with more detailed studies underway. Coupling of Peregrine and MAMBA is planned. Future development and validation activities for both codes and for CASL in general, were outlined.

3.   PROBLEMS, CHALLENGES AND PERSPECTIVES

Nuclear fuel behavior is highly complex involving a wide variety of coupled physical phenomena (multiphysics) which operate over a wide range of spatial scales (multiscale) and which must be simulated over a broad range of time scales (steady operation to rapid transients and accidents). This complexity imposes challenging requirements for modeling and simulation,

requiring extensive data for adequate validation. As demonstrated in the recent FUMEX-III exercise, well-validated codes can provide reasonable predictions of fuel behavior, however, there are clearly areas where improved predictive capability is needed. Examples include fission gas release at high burnup, fuel swelling under transient conditions, accurate modeling of gap closure and frictional contact between pellets and clad [1].

Modern computational methods and computer hardware have recently enabled researchers to extend nuclear fuel modeling to 3D and provided opportunity to explore more mechanistic-based simulation of lower length and time scale processes. Numerous examples of this work are beginning to appear in the literature. Certainly additional experimental data are needed to validate these models.

Including more fundamental physical behavior in fuel performance modeling, for example phenomena that has traditionally been accounted for via boundary conditions, will lead to higher fidelity simulation. Accordingly, efforts are underway by several researchers to couple fuel performance codes to neutronics and thermal-hydraulic simulation, as well as couple to lower length scale predictions of microstructural evolution. These coupled tools should also provide higher fidelity simulation of accident behavior.

Modern computational tools which are more mechanistic based and less empirical offer promise for using computational modeling to explore and develop new materials and fuel designs (e.g., accident tolerant fuels) and provide predictions in regions where experimental data are lacking.

4.   RECOMMENDATIONS FOR FUTURE WORK

Even well-validated fuel performance codes have areas where improved predictive capability is needed including fission gas release at high burnup, fuel swelling under transient conditions, accurate modeling of gap closure and frictional contact between pellets and clad. Additional efforts in this area are needed.

Session 2: Modelling of fuel performance under design basis accidents

Chairperson: Jinzhao Zhang

1. BACKGROUND

An accurate and reliable simulation of fuel rod behaviours during normal and accident conditions is important for fuel rod design and safety analysis in nuclear power reactors. With regard to Ref [4], "design basis accident represents an accident causing accident conditions for which a facility is designed in accordance with established design criteria and conservative methodology, and for which releases of radioactive material are kept within acceptable limits". The fuel rod behaviours during the design basis accidents (DBA), such as the Loss of coolant accidents (LOCA) and reactivity initiated accidents (RIA), are of particular interests during the last 2 decades. Many LOCA and RIA tests have been performed with high burnup fuel rods in various test reactors (such as the LOCA tests in the Halden reactor, the RIA tests in the CABRI and NSRR reactors). Those tests have contributed to a better understanding of the complex physical phenomena, such as fuel fragmentation, relocation, dispersal, cladding ballooning, burst, oxidation and hydriding, and so on [3]–[4].

As a consequence, the nuclear safety authorities of various countries (like the USNRC and IRSN) are considering revisions to the current LOCA and RIA safety (or acceptance) criteria [1, 5], and the nuclear industry is improving their fuel rod codes and analysis methods to verify those safety criteria.

Several international benchmark exercises have been organized in the past 5 years, dealing with fuel modelling during accident conditions:

- IAEA FUMEX-III project [1];
- OECD fuel rod codes RIA [5];
- OECD LOCA benchmarks [6].

It is useful to have an overview of these benchmarks before proposing the new project on fuel modelling under accident conditions (FUMAC).

2. SUMMARIES OF THE SESSION PAPERS AND COMMENTS

Seven papers were presented in this session covering different aspects of nuclear fuel modelling at RIA and LOCA conditions.

The first paper of this session presented the Tractebel Engineering (GDF SUEZ, Belgium) approach to qualifying the FRAPCON/FRAPTRAN fuel rod codes for simulation of fuel behaviour during LOCA and RIA accidental conditions, and the application of the statistical uncertainty and sensitivity analysis methods to fuel behaviour modelling. The simulation and uncertainty analysis of an OECD fuel rod codes RIA benchmark case (CABRI RIA test CIP3-1) and an OECD LOCA benchmark case (Halden LOCA test IFA-650.5) are presented in details.

Those results showed the importance of realistic physical models and uncertainty analysis of the relevant input parameters and the key models in fuel modelling during LOCA and RIA. The perspectives for further model improvements and benchmarks are also discussed.

EC/JRC Institute for Trabsuranium Elements (Germany) presented the model adaptations to the TRANSURANUS fuel performance code, in order to be able to simulate design basis accident (DBA) conditions. The developments and associated validation work for LOCA conditions include modifications in the models for large strains, for the crystallographic phase transition in Zircaloy, and for burst release and large cladding deformations. The ongoing work for simulations of RIA conditions include the models for the plenum temperature, along with the separate effect studies and detailed model developments made in parallel by means of multi-scale and multi-physics tools for the high burnup structure.

It is concluded that there are needs for model developments and further verification and validation in the frame of international benchmark exercises dedicated to DBA simulations and the first phase of a severe accident, i.e. when the cylindrical fuel rod geometry is preserved.

CEN Cadarache (France) presented the 'multi design' new generation software environment called PLEIADES developed by the CEA in the framework of a research cooperative program with EDF and AREVA. In particular, he presented the general description of the PWR fuel performance simulation code ALCYONE in the PLEIADES environment (general computation algorithm,

advanced fission gas model for UO_2 and MOX fuels, 3D computation scheme), focusing on specific developments which have been done to simulate accidental conditions such as LOCA and fast transients for different dimensional models.

The multi-dimensional computation scheme of ALCYONE has been extended to accidental irradiation conditions representative of a fast transient or a LOCA transient. Thanks to these developments a set of 1D and 3D models is now available to simulate fuel rod behaviour from pellet cladding interaction up to cladding ballooning. Some developments are still in progress to improve this first version. First results devoted to the validation of the 3D model for the CABRI REP Na experiments or more recently to the interpretation of a LOCA experiment show that the PLEIADES platform can offer advanced simulation tools to improve the analyse of the local behaviour under accidental irradiation condition.

IRSN (France), JAEA (Japan) and OECD/NEA presented the OECD RIA fuel codes benchmark. Following the recommendations from the OECD/NEA/CSNI technical workshop on Nuclear Fuel Behaviour during Reactivity Initiated accidents in 2009, a benchmark of the RIA fuel codes was organized within the activities of the WGFS in 2010–2012. The final report of the first benchmark has been approved by the CSNI during its June 2013 meeting. The main conclusions of this benchmark are:

- With respect to the thermal behaviour, the differences in the evaluation of fuel temperatures remain limited, although significant in some cases. The situation is very different for the cladding temperatures that exhibited considerable scatter, in particular for the cases when water boiling occurs;
- With respect to mechanical behaviour, the parameter of largest interest is the cladding hoop strain because failure during RIA transient is resulting from the formation of longitudinal cracks. When compared to the (known) results of an experiment that involved only PCMI, the predictions from the different participants appeared acceptable even though there was a factor of 2 between the highest and the lowest calculations. The conclusion is not as favorable for a case for which both the experimental results are unknown and water boiling is predicted to appear. In this case, a factor of 10 on the hoop strain between the calculations was exhibited.
- Other mechanical results compared during the benchmark were fuel stack and cladding elongations. The scatter remains limited for the fuel stack elongation, but the cladding elongation was found much more difficult to evaluate;
- The fission gas release evaluations were also compared. The ratio of the maximum to the minimum values appears to be roughly 2, which is estimated to be relatively moderate given the complexity of fission gas release processes;
- Failure predictions that may appear as the ultimate goal of fuel code dedicated to the behaviour under RIA conditions were compared: it appears that the failure/no failure predictions are fairly consistent between the different codes and with experimental results. However, when assessing the code qualification, one should rather look at predictions in terms of enthalpy at failure because it is a parameter that may vary significantly between different predictions (and that is also of interest in practical reactor applications). In the frame of this benchmark the failure prediction levels among the different codes were within a +/- 50% range.

The recommendation from the first benchmark is to launch a second phase RIA fuel rod codes benchmark with the following specific attentions:

- The emphasis should be put on deeper understanding of the differences in modelling of the different codes; in particular, looking for simpler cases than those used in the first benchmark may be of interest.
- The clad to coolant heat transfer in case of water boiling under RIA conditions, and more specifically during the film boiling regime, is of particular interest because on the one hand large uncertainties exist on the models and on the other hand it makes large differences in the thermal as well as in the mechanical predictions.
- To identify and to assess the strengths and weaknesses of the physical models in the codes, the calculated results have to be compared with experimental data wherever it is possible. Thus, the selected new cases should provide a high amount of reliable measurements.
- It was also identified that a sensitivity study of the results to the input parameter is desirable in order to assess the impact of the initial state on the results of the transient.
- Due to the large scatter between the calculations that was shown in the first benchmark, it appears that an assessment of the uncertainty of the results should be performed for the different codes. This should be based on a well-established and shared methodology.

The OECD/CSNI/WGFS RIA Fuel Codes Benchmark Phase II is scheduled to begin early 2014 and to implement to above recommendations. So far, 23 organizations have already expressed their wish to participate.

Academy of Sciences, Centre for Energy Research (Hungary) presented the use of finite element codes to study phenomena caused by local characteristics of the fuel rods without statistical averaging as inherently included in the 1D or 1.5D fuel modelling codes (such as assumptions of uniformity, homogeneity and axisymmetry). With finite element codes, the basic assumptions on the homogeneity and uniformity of the cladding can be lifted: the effects of inhomogeneities and slight variations in thickness can be studied in e.g. LOCA conditions. The effect of cracks in the pellets with a mixture of bonded and not bonded cladding areas on PCMI can also be studied. Some qualitative examples are made by means of the finite element code MSC. Marc 2005 r[3]. The present study reveals that local characteristics (geometry, material properties, pellet-cladding bonding, etc.) have an essential influence on the outcome of experiments, usually resulting in asymmetric behaviour. This asymmetry can lead to either a more or a less favourable situation than homogeneous, symmetric, i.e. 'regular' setups.

Considering the data need for simulating phenomena depending on local characteristics of the fuel rod, the present work can be continued in two ways. One is to plan measurements according to sensitivity analyses carried out on the above or similar models, which would then yield more accurate constitutive relations for the mechanical properties of the materials involved in the experiments. The other is to simulate experiments with the (usually averaged) data provided and extend the model assuming inhomogeneities, imperfections, asymmetry, etc. to find out what caused the actual exact experimental outcome. It is believed that the PCMI modelling has to be extended to 3D and the models have to be refined to account for more details of the fuel element.

Nuclear Safety Research Center, JAEA (Japan) presented the JAEA's investigation on the effects of coolant subcooling, flow velocity, pressure, and cladding pre-irradiation on the heat transfer from fuel rod surface to coolant water during RIA boiling transient. The study was based on a computational analysis, with the RANNS code, on the transient data from RIA-simulating experiments in the nuclear safety research reactor (NSRR); boiling heat transfer coefficients were estimated by inverse-heat-conduction calculations using the histories of measured cladding temperature and estimated heat generation in pellets, and the effects of coolant condition were analyzed by a two-phase laminar boundary layer model for stable film boiling. The experimental data used in this study cover coolant conditions with subcoolings of ~10–80 K, flow velocities of 0–3 m/s, pressures of 0.1–16 MPa, and fuel burnups of 0–69 GWd/tU.

The analysis showed that the film boiling heat transfer coefficients during RIA boiling transient increase with coolant subcooling, flow velocity, and pressure as predicted by the model for stable film boiling. The estimated boiling heat transfer coefficients were significantly larger than those predicted by semi-empirical correlations for stable film boiling: about 1.5 times larger for stagnant water condition and 2–8 times larger for forced flow condition, respectively. The analysis also suggested that the heat transfers during both transition and film boiling phases are strongly enhanced by pre-irradiation of the cladding. The irradiation effect was clearly seen at large subcooling of ~80 K and atmospheric coolant pressure, and was rather moderate at small subcooling of ~10 K and coolant pressure of ~7 MPa. These behaviours of boiling heat transfer are incorporated into the RANNS code mainly as modified empirical correlations for boiling heat transfer coefficient.

This paper shows the importance of realistic boiling heat transfer models in the RIA fuel behaviour modelling.

Institute for Nuclear Research (Romania) presented the simulation of the behaviour of an instrumented, unirradiated, zircaloy-sheathed UO_2 fuel element assembly of CANDU type, subjected to a coolant depressurization transient in the X-2 pressurized water loop of the NRX reactor at the Chalk River Nuclear Laboratories. The high-temperature transient conditions are such as those associated with the onset of a loss of coolant accident (LOCA). The data and the information related to the experiment are those included in the OECD/NEA-IFPE Database. The TRANSURANUS fuel performance code was used, along with the corresponding fabrication and in-reactor operating conditions specific of the CANDU PHWR fuel. The simulated results were compared with the experimental ones. Further work is needed to improve the CANDU fuel behaviour modelling during LOCAs.

3. PROBLEMS, CHALLENGES AND PERSPECTIVES

The major problems and challenges for fuel behaviour modelling during design basis accidents like LOCA and RIA are:

- Significant differences in various fuel rod codes and analysis applications due to:
  - Different modelling approaches and simplifications (realistic vs conservative, empirical vs first principle, micro vs macro, 1/1.5D vs 2/3D, finite difference vs finite element…);
  - Different validation databases, material properties models and application scopes;
  - User effects (assumptions);
  - Lack of appropriate uncertainty and sensitivity analysis.

- Lack of well-instrumented separate effect tests to validate/calibrate the relevant physical models in the fuel rod codes:
    o the crystallographic phase transition in Zircaloy;
    o large cladding deformations (ballooning) and failures (PCMI, burst);
    o fuel fragmentation and relocation;
    o high burnup structure and burst release,
    o pleanum gas temperatures;
    o axial gas transportation;
    o transition and film boiling heat transfer during RIA;
    o blowdown and reflod heat transfer during LOCA.

In order to improve the fuel behaviour modelling during design basis accidents like LOCA and RIA, we need:

- well-designed and instrumented LOCA/RIA tests;
- well specified benchmark cases to really compare the performance of basic models (axial elongation, thermal expansion, FGR…);
- carefully examination of the models and assumptions used in simulations;
- to include uncertainty analysis by using a simple, transparant, robust and flexible statistcial uncertaitny analysis method (e.g., order statistics).

Note that some international experiments or code benchmarks are planned or ongoing, such as:

- OECD/NEA/CSNI/WGFS RIA fuel rod codes Benchmark;
- OECD CABRI International Program for RIA tests;
- JAEA NSRR RIA tests;
- OECD Halden Reactor Project LOCA tests;
- KIT QUENCH-LOCA program;
- OECD SCIP-III project for LOCA tests and simulation.

4. RECOMMENDATIONS FOR FUTURE WORK

In order not to duplicate the efforts of the ongoing OECD RIA fuel rod codes benchmark Phase II, it is recommended that the future work on FUMAC should focus on LOCA fuel behaviour modelling.

For this purpose, LOCA tests with detailed measurements and/or uncertainties estimation are needed. It is suggested to focus on a few, but well instrumented tests, such as the Halden or QUENCH-LOCA tests.

In addition, it is suggested to perform uncertainty and sensitivity analysis to quantify the impacts of uncertainties in fuel rod data, test conditions and models.

Last but not least, the thermal hydraulic model should be improved to better simulate the transient heat transfer conditions at the cladding surface during the LOCA/RIA transient. This may be resolved by coupling fuel rod codes with a qualified system or sub-channel thermal hydraulic code.

Session 3: Modelling of severe accidents and experimental support

Chairperson: J. Stuckert

1. BACKGROUND

Whereas the two first meeting sessions were devoted to the water-cooled fuel behaviour under normal and DBA (design basis accident) conditions, this session observed phenomena during the DBA and early phase of design extension conditions (DEC). The early used terminology "beyond design basis accidents, or BDBA" [7] is not more recommended by the IAEA, because the IAEA Safety Standards SSR/1-2 on Design of Nuclear Power Plants [2] introduced "design extension conditions" as "Postulated accident conditions that are not considered for design basis accidents, but that are considered in the design process of the facility in accordance with best estimate methodology, and for which releases of radioactive material are kept within acceptable limits. Design extension conditions could include conditions in events without significant fuel degradation and conditions with core melting".

Seven presentations give state of the art for investigations in field of the fuel rod behaviour at high temperatures, including physical-chemical effects inside claddings as well as in fuel pellets.

2. SUMMARIES AND COMMENTS

The presentation from Bulgarian Institute for Nuclear Research and Nuclear Energy (IRNE) gives brief description of a typical VVER-1000 reactor (V-320 model used for Kozloduy NPP) and adaptation of the MELCOR code (version 1.8.5) to description of a station black-out (SBO) accident with debris formation and core melting in about 10^4 s after accident beginning. The calculation results shows dependency of core degradation process on debris porosity. Larger porosity results in later relocation of corium to the bottom head and corresponding later failure of the reactor vessel. Injection of water into the reactor core by the high pressure pump at temperatures between 1200 and 1500 °C does not resulted in further generation of hydrogen and avoids significant destruction of the reactor core.

The Nuclear Power Institute of China (NPIC) has investigated the oxidation kinetics of the N18-Zirconium alloy (wt%: 1.0Sn, 0.27Nb, 0.38Fe, 0.07Cr, 0.07O) in steam at temperatures between 700 and 1200°C. Sheets of N18 and Zircaloy-4 with sizes 30x20x2 mm were oxidised in vertical tube furnace at temperatures 700°C, 800°C, 900°C, 1000°C, 1100°C and 1200°C during times between 5 and 250 min. Pre- and post-test weighing given values of weight gain. Transition of parabolic kinetics to linear one was observed at temperatures between 700°C and 1000°C at similar times for both alloys. The oxidation rates of N18 and Zry-4 alloys are quite similar excluding the linear part at 800°C. At this temperature the oxidation rate of N18 was noticeable higher. Metallographic investigations showed typical breakaway structure of oxide layers for both materials after long oxidation (more than 100 min) at temperatures between 700°C and 1000°C. Oxide structures for T > 1000°C have typical homogeneous columnar structure for both alloys. The phase transformation in N18 metal from alpha to alpha + beta and from alpha + beta to beta were indicated as 775°C and 938°C, correspondingly (for Zry-4 this values are 810°C and 980°C). Formation of hydrides inside of N18 metal was observed after oxidation at different temperatures.

The Czech Research Centre ÚJV Řež presented overview of modelling works covered a whole range of reactor operating conditions. The analysis of normal operation and anticipated operational occurrences is carried out with using of the TRANSURANUS code. Detailed modelling of fuel rod response during design basis accident is evaluated using the FRAPTRAN code to estimate the number of failed rods and to verify the fuel and cladding temperatures. In order to better understand the single effects, such as pellet-pellet contacts, cracks in pellets, pellet defects during normal operations or influence of azimuthal cladding temperature inhomogeneity during Loss of Coolant Accident (LOCA), the detailed 2D and 3D models are created on the basis of commercial Finite Element Model (FEM) systems COSMOS/M and ABAQUS. It was emphasized that a series of new models should be developed for description of the following phenomena: determination of the optimum power rise rates after the core reloads during normal operations, relocation of fragmented fuel into the ballooned cladding region and release of fission gas products during LOCA. Fuel behaviour under severe accident conditions was mainly studied with application of different versions of the integral code MELCOR, which was validated against results of the bundle tests QUENCH and PHEBUS-FP, and the integral LOFT LP-FP-2 test. Especially the QUENCH-12 test with a VVER test bundle was analysed in great detail. Some bundle tests were analysed with severe fuel damage (SFD) codes ICARE2 and SCDAP/RELAP.

VTT Technical Research Centre of Finland performed state of the art review of actual understanding of radionuclide release from high burn-up fuel. The review includes two parts: 1) description of nuclide inventory, known mechanisms of nuclide formation in fuel, migration and release depends on the fuel microstructure; 2) consideration of phenomena modelling. Nuclide release mechanisms depend firstly on their chemical nature: 1) Noble gases and volatile fission products, 2) Fission products forming metallic precipitates, 3) Forming oxide precipitates, 4) Dissolved as oxides in the fuel matrix. Other important parameters are fuel grain sizes, temperature, fuel oxidation, high burn-up structure (HBS) with rim layer at pellet periphery. Most of the computer codes include only modules for description of the noble gas releases under conditions of normal operations. These models should be enhanced to take into account the radial distribution of nuclides, HBS and higher temperatures for severe accidents.

The presentation from the Karlsruhe Institute of Technology (KIT) gives overview of out-of-pile experimental programs on severe and LOCA accidents at KIT during last twenty years. These programs include series of bundle experiments as well as separate effect tests. The CORA program was devoted to investigation of integral material behaviour inside of PWR, BWR and VVER test bundles. The results of the integral CORA tests allow the definition of three temperature regimes in which large quantities of liquid phases form which cause extended fuel rod bundle damage and accelerate damage progression: 1) 1500–1700 K: localised core damage; 2) 2100–2300 K: extended core damage; 3) 2900–3150 K: total core destruction. A temperature escalation due to the zirconium-steam reaction started in the upper, i.e. hotter bundle half at about 1400 K and propagated from there downwards and upwards. The cladding integrity can be lost far below the melting point of Zircaloy by eutectic interactions with stainless steel of absorber claddings or absorber materials themselves (e.g. B_4C), resulting in formation of liquid phases at temperatures as low as 1550 K. The CORA quench tests have demonstrated that quench did not result in an immediate decrease of the bundle temperature. In order to explicitly investigate the effect of reflood on bundle degradation the QUENCH program was initiated in 1996 and is still on-going. In eight from seventeen tests, reflooding of the bundle led to a temporary temperature excursion driven by runaway oxidation of

Zr-alloy components and resulting in release of a significant amount of hydrogen, typically two orders of magnitude greater than in those tests with "successful" quenching in which cool-down was rapidly achieved. Considerable formation, relocation, and oxidation of melt were observed in all tests with escalation. Following mechanisms were detected, which can accelerate temperature excursion and hydrogen release during injection of water into the overheated bundle: 1) low reflood flow rates < 1 g/s/rod; 2) breakaway effect with weakness and spallation of protective oxide layer; 3) steam starvation; 4) nitride formation by air ingress with formation of very porous oxide layer during following reflood; 5) high temperatures with melt relocation outside claddings and intensive melt oxidation; 6) eutectic interactions between B_4C, stainless steel and Zircaloy-4 leading to low melting point. The so-called secondary hydriding of claddings and its influence on the cladding mechanical properties will be investigated during the QUENCH-LOCA program at KIT.

The presentation of Mexican National Commission of Nuclear Safety and Safeguards describes the MELCOR modelling of two hypothetical Station Blackout (SBO) scenarios for the BWR reactor of the Laguna Verde NPP. Whereas first scenario includes no cooling water injection, the second scenario considers the reflood initiation after 36000 seconds. Both scenarios are the same until the reflood imitation on the end of the core dryout and shows that the core melt formation occurs on about 32000 s. Melt relocated to the reactor bottom head and interacted with the wall of reactor pressure vessel (RPV) with final vessel failure on 43200 s in the first case and on 68400 s in the second case. I. e. the water injection delayed the vessel failure in about 7 hrs. The late water injection, if 30% of core is already damaged, can cool only intact elements; the mass of the melt cannot be completely cooled and relocated to the RPV bottom. The total hydrogen production is about 20% less for the second scenario.

Nuclear Safety Institute of Russian Academy of Sciences (IBRAE) presented a new mechanistic SFPR (Single Fuel Rod Performance) code for modelling of single fuel rod behaviour under various regimes of LWR reactor operation (normal and off-normal, including severe accidents). The code is designed by coupling of two stand-alone mechanistic codes: 1) SVECHA/QUENCH (for modelling of Zr cladding thermo-mechanical and physical-chemical behaviour) and 2) MFPR (for modelling of irradiated UO_2 fuel behaviour and fission products release). In the numerical scheme of S/Q the cladding is considered as a cylindrical shell consisting of three layers: external oxide layer, α-Zr(O) and β-Zr layers. The layers growth is calculated by the oxidation model which is based on the solution of the oxygen diffusion problem across the multi-layered cladding structure and is tightly coupled with the hydrogen uptake and release model. The influence of oxide cracking on the oxidation kinetics is self-consistently simulated by the mechanical deformation module tightly coupled with the oxidation module. The MFPR code self-consistently describes evolution of fuel micro-structure (point defects, such as vacancies and interstitials, and extended defects, such as gas bubbles, sintering pores and dislocations), which strongly influences the intra- and intergranular diffusion transport of gas atoms in irradiated UO_2. The main outputs of the code are gas-bubble size and concentration (including intra- and intergranular bubbles and pores), chemical speciation of solid-phase FPs, point- and extended-defect characteristics, fuel oxygen potential, densification, swelling and FP release. The SFPR code was verified on the basis of the CONTACT (Grenoble) in-pile test results.

Presentation of Westinghouse Electric Company described properties of advanced pellet and cladding materials, developed to enhanced fuel behaviour under operational and accident conditions.

The concept of accident tolerant fuels (ATF) includes various combinations of fuel/cladding materials: UN/SiC, U_3Si_2/SiC, UN/Coated Zircaloy, and U_3Si_2/Coated Zircaloy. From the common physical point of view, the advantages of alternative to UO_2 fuel materials are higher density (economically more attractive) and high thermal conductivity (as result – significantly lower temperature in the pellet centreline, i.e. reduction of the melting risk). However, U_3Si_2 has quite low melting point (1665°C instead 2840°C for UO_2) and UN fuel requires enrichment on rare ^{15}N, to achieve an acceptable neutron economy, and a treatment to be oxidation resistant to reactor coolant. Due to higher fuel swelling rate under irradiation the pellet-cladding gap should be increased and probably filled with a liquid metal (instead helium) to enhance the heat transfer. The advantages of the SiC cladding material are high melting point (<2500°C instead 1825°C for Zircaloy) and very high resistivity to oxidation in steam (factor 100 in comparison to Zircaloy) with minimal generation of H_2 from the oxidation reaction. From the other hand, the mechanical properties of SiC are worse than for Zry (e.g. low crip) and the SiC thermal conductivity is with factor 4 lower. At the moment, coated Zr claddings, which provide significant improvement in fuel reliability during normal operations and moderate safety improvement during accidents, could be implemented faster in the current LWR fleet due to using the same cladding bulk material and geometry.

3. PROBLEMS, CHALLENGES AND PERSPECTIVES

Two of seven presentations in this session were devoted to application of integral code MELCOR to modeling of hypothetical station-black-out (SBO) accident at selected NPPs. The outcomes of many international benchmarks show that the results of such modeling depend strongly on user experience and the knowledge of different parameters of implemented empirical correlations. To reduce such kind of indeterminations the more precise mechanistic models should be used. Good example of self-consistent models gives the SFPR code. Nevertheless, each model should be based on well prepared single effect tests (e.g. oxidation of new cladding materials, or fission product release from high burnup fuel). Finally, each code should be verified by comparison with results of good instrumented integral tests. The series of versatile QUENCH tests provides very good basis for organization of corresponding benchmarks.

4. RECOMMENDATIONS FOR FUTURE WORK

Futher work to understand the pertinent complex physical-chemical phenomena, e.g. oxidation/hydriding of newly developed cladding materials and fission product release from high burnup fuel and others, is recommended. Different countries focused these efforts on development of miscellaneous computer codes or experimental investigations. International cooperation in the field of design basis and severe accidents could harmonize this work and should allow a significant enhancement of the code capabilities. The use of more precise mechanistic models is recommended.

REFERENCES

[1]   INTERNATIONAL ATOMIC ENERGY AGENCY, Improvement of Computer Codes used for Fuel Behaviour Simulation (FUMEX-III): Report of a coordinated research project 2008–2012, IAEA-TECDOC-1697, (2013).

[2]   INTERNATIONAL ATOMIC ENERGY AGENCY Safety Standards, Safety of Nuclear Power Plants: Design, Specific Safety Requirements No. SSR-2/1, IAEA, Vienna, 2012.

[3]   OECD, Nuclear Fuel Behaviour in Loss-of-Coolant Accident (LOCA) Conditions, State-of-the-art Report, NEA No. 6846, (2009).

[4]   OECD, Nuclear Fuel Behaviour under Reactivity-Initiated Accident (LOCA) Conditions, State-of-the-art Report, NEA No. 6847, NEA/CSNI/R(2010)1, (2010).

[5]   OECD, RIA Fuel Codes Benchmark, Volume 1 & 2, OECD/NEA CSNI report (to appear), (2013).

[6]   OECD, Benchmark calculations on HALDEN IFA-650 LOCA test results, NEA/CSNI/R (2010) 6, (2010).

[7]   INTERNATIONAL ATOMIC ENERGY AGENCY, IAEA Safety Glossary, Terminology Used in Nuclear Safety and Radiation Protection, 2007 Edition, IAEA, Vienna, (2007).

DEVELOPMENT OF CODES FOR MODELING OF FUEL BEHAVIOUR UNDER STEADY
STATE AND TRANSIENT CONDITIONS

(SESSION 1)

Chairperson

R. Williamson

USA

ASSESSMENT OF THE BACO CODE WITH THE PAST, PRESENT & FUTURE CRP FUMEX EXERCISES OF THE IAEA

A. C. MARINO
División Laboratorio de Simulación de Materiales y Combustibles (SiM³)
Gerencia Ciclo del Combustible Nuclear (GCCN)
Comisión Nacional de Energía Atómica (CNEA)
Centro Atómico Bariloche (CAB)
S. C. de Bariloche, Río Negro, Argentina
Email: marino@cab.cnea.gov.ar

Abstract. The BaCo code was developed to simulate the nuclear fuel rods behaviour under irradiation. BaCo is focussed in PHWR fuel and has good compatibility with PWR, BWR, WWER, among others type of fuels (commercial, experimental or prototypes). The code includes additional extensions for 3D calculations, statistical analysis, fuel design and a full core analysis. The main BaCo features and the BaCo code results of the most demanding cases included in the Coordinated Projects of the IAEA and an overview of the main findings of our participation of those code comparisons is presented. The main BaCo code features in the area of the most demanding exercises of the series of Coordinated Research Projects FUMEX (Fuel Modelling at Extended Burnup) of the IAEA and an overview of the main findings of our participation in those projects of code evaluation taking into account the accuracy of the calculations and the modelling of the nuclear fuel materials is presented. We used the last version of the code without major changes for these exercises in order to properly obtain the keys for the improvement of BaCo.

1. INTRODUCTION

The BaCo code (Barra Combustible, Spanish expression for fuel rod) was developed at the end of the 1970s in Atomic Energy National Commission of Argentina (CNEA) with the purpose of studying the fuel rod behaviour under irradiation conditions [1, 2]. BaCo currently gives the modelling support for the design of advanced PHWR -CARA fuel [3]- and innovative PWR fuels -as the fuel for the CAREM reactor [4]. The confidence in the results regarding the description of the fuel behaviour under irradiation enables the inclusion of the BaCo code in several international fuel code comparison programs as D-COM [5], CRP FUMEX I [6], II [7] and III. Although the development of BaCo was focused on PHWR fuels [8], as CANDU and Atucha ones, the code holds a full compatibility with commercial as PWR, BWR, WWER [9] and MOX [10], advanced, experimental, prototypes and/or unusual fuels. The BaCo code includes additional tools as the software package for finite elements 3D calculations [11] and the statistical analysis for advanced fuel designs by taking into account the as fabricated fuel rod parameters and their statistical uncertainties [12]. BaCo allows the calculation of a complete set of irradiations as for example the calculation of a full reactor core [13]. It is of crucial importance nowadays to develop a better experimental and theoretical knowledge of the processes related with the evolution of defects and the accumulation of fission products for modelling the fuel behaviour under different operating conditions and the evolution of a spent fuel over long period of time. The current experimental database could be enough to support empirical correlations and modelling for current fuels [14]. Nevertheless, new approaches are required if the actual fuel computer codes will be used to simulate new materials and extreme situations as ultra high burnup. The unavailable data needed for new fuels development will be obtained through a multiscale modelling (M^3), a methodology that will provide the theoretical approach to model the properties of materials through ab initio, molecular dynamics, kinetic Monte Carlo and finite elements calculations over the relevant length and time scales of each method [15, 16].

2. THE BACO CODE

The BaCo code was developed at CNEA for simulating nuclear fuel rods behaviour under irradiation [1, 2]. The development of BaCo is focused on PHWR fuels, as CANDU [8] and Atucha ones [13], under irradiation and during storage conditions [17-19] also, it keeps a good compatibility with advanced fuel materials, as for example uranium nitride and carbide at least for illustrative and comparative purpose.

The BaCo modelling of UO_2 pellets includes elastic deformation, thermal expansion, creep, swelling, densification, restructuring, relocation, cracks and fission gas release. For the Zry cladding, the code models elastic deformation, thermal expansion, anisotropic plastic deformation, creep and growth under irradiation. The modular structure of the code easily allows us to input different material properties. It can be used for any geometrical dimension of cylindrical fuel rods pellets (either compact or hollow, with or without dishing) and Zry cladding. A special feature of the BaCo code is its complete treatment of the fuel with or without mechanical contact to the pellet surface and the clad, at any irradiation stage.

Fuel rod power history and either cladding or coolant external temperatures must be given to the program. Rod performance is numerically simulated using finite time steps (finite differences scheme). The code automatically selects time steps according to physical criteria. Temperature profiles within pellet and cladding, main stresses at pellet and cladding, radial and axial crack pattern in the pellet, main strains and hot geometry of pellet and cladding, change in porosity, grain size and restructuring of the pellet, fission gas release to the free volume in the rod, trapped gas distribution in the fuel and in the UO_2 grain boundary, internal gas pressure and current composition of the internal gas and dishing shape evolution, are calculated. The output contains the distribution along the rod axis of these variables. The details of the mechanical and thermal treatment and the pellet, cladding and constitutive equations are available in reference [1] and an extended description of the code is included in reference [2].

BaCo assumes azimuthal bi-dimensional symmetry in cylindrical coordinates for the fuel rod (1). Although angular coordinates are not considered explicitly, angular dependent phenomenon, as well as radial cracking, are simulated through the angular averaging method (20). Also axial pellet cracking and relocation are included in BaCo. The hypotheses of axial symmetry and modified plane strains (constant axial strain) are used in the numerical modelling. The fuel rod is separated in axial sections in order to simulate its axial power profile dependence. Rod performance is numerically simulated using finite time steps (finite differential scheme). The modular structure of the code easily allows the description of phenomena observed in the UO_2 pellet and the Zry cladding behaviour. The current version of BaCo can be applied to any geometrical dimensions of cylindrical fuel rods mainly with UO_2 pellets (either compact or hollow, with or without dishing) and Zry cladding. However, the code allows us to calculate fuel rods with other materials for the pellets and the cladding as metallic uranium, uranium carbide, uranium nitride (for pellets) and silicium carbide (for cladding), at least for illustrative and comparative purpose, due to the simplicity of the modelling of these materials included in BaCo [15, 16].

3. ADVANCED FEATURES OF BACO

BaCo 3D tools [11], statistical analysis [12], full core calculations [13] and graphical data post-processing improve the code performance and the analysis of the calculations [2].

Although the BaCo code uses a quasi-two-dimensional approach, the use of several three dimensional (3D) finite element features allow a complementary analysis of 3D properties, as for example the stress-strain state at a specific period of time during the irradiation [11]. The BaCo code results were enhanced by using "ad hoc" tools developed at the MECOM and SiM³ Divisions (Bariloche Atomic Centre, CNEA) [20]. The temperature profile, the crack pattern and the boundary conditions (as the inner pressure, pellet stack weight, etc.), among others, are calculated with BaCo as the input data to the 3D stress-strain state and the deformations of the UO_2 pellet.

For a better understanding of the uncertainties and their consequences, the mechanistic approach must therefore be enhanced by the statistical analysis [12]. BaCo includes a probability analysis within their code structure covering uncertainties in fuel rod parameters, in the code parameters and/or into the fuel modelling taking into account their statistical distribution. As consequence, the influence of some typical fabrication parameters on the fuel cycles performance can be analyzed. It can also be applied in safety analyses and economics evaluation to define the operation conditions and to assess further developments. These tools are particularly valuable for the design of nuclear fuel elements since BaCo allows the calculation of a complete set of irradiations.

4. THE NEEDS OF SIMULATIONS AND EXPERIMENTAL DATA

Experimental data are the common need for fuel design, fuel performance analysis and fuel modelling. These experiments are very expensive and lengthy in time. Due to those reasons it was implemented the IFPE in order to share data of irradiation of nuclear fuels [7]. The simulation with computer codes is the key in order to close the bridge between the fuel design and the needs of experimental results.

The codes will provide a frame to define the power history and the parameters of the experiments after the analysis of similar irradiations and simulations. It is a useful tool to reduce the number of experiments which, together with the code results, will constitute the complete description of the fuel behaviour, in particular the PIE

5. COORDINATED RESEARCH PROJECT FUMEX I (1993–1996)

The first edition of the Coordinate Research Project on Fuel Modelling at Extended Burnup (CRP FUMEX) of the International Atomic Energy Agency (IAEA) was devoted to several blind tests by using experimental data provided for the OECD Halden Reactor Project (HRP) [6]. This CRP was originally focussed on thermal and mechanical calculations; finally the thermal affairs were mainly assessed. A set of instrumented fuels allowed following the evolution of some parameters (pellet centre temperature, inner pressure of the rod, cladding elongation, fission gas release and cladding diameter). The experiences include PIE analysis. The final burnup reached for the fuels were intermediate (25 MWd/kgU) and high (50 MWd/kgU). The main features of these exercises were the strong details of the experimental data of the HPR (see the Fig. 1 where a simplified power history of the case 1 is included). The comparisons among the calculations of the participants and the experimental results were focused in the thermal issues of the fuel behaviour. Case 1 looks similar than the expected behaviour of the CAREM fuel (4), a new reactor at present designed by CNEA.

The first step in the resolution of the exercises was the treatment of the experimental data due to its extreme length. The second step was the detection and fixing of bugs in the codes and in the analysis of the HPR data.
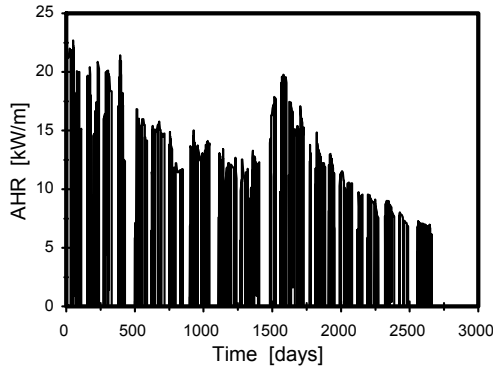
FIG. 1. Power history corresponding to the Case 1 of the CRP FUMEX I.
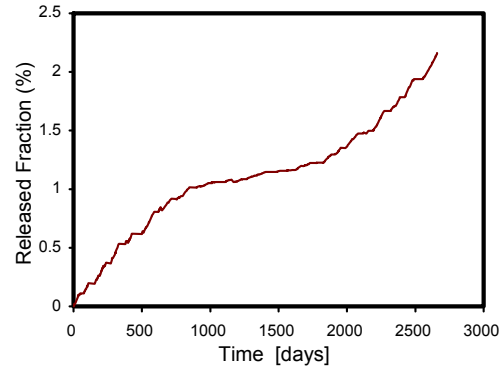
FIG. 2. BaCo calculation for Fraction of Fission Gas Release, case 1 of CRP FUMEX I. The experimental result at EOL (End of Life) was FGR = 1.8 %.

We found a good agreement between experimental and calculated data. As an example of the BaCo code performance see the Fig. 2 showing our answer for the fission gas release. The Fig. 3 includes the power history for the FUMEX case 2 and the Fig. 4 shows the BaCo output for inner pressure in the rod in the same case. This results emphasized the performance of BaCo due to the calculation of the inner gas pressure inside the fuel rod are taking into account the thermal calculation, the fission gas release and the evaluation of the free volume. The complete evaluation of the CRP FUMEX I was published in the final report of the IAEA [6].
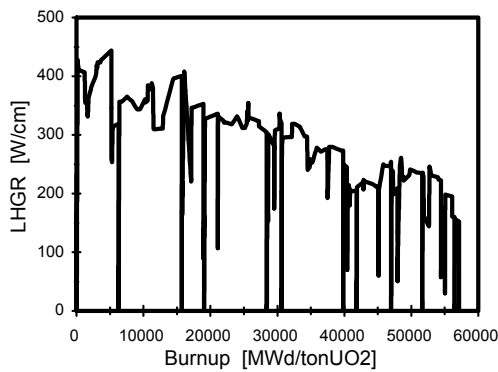
FIG. 3. Power history corresponding to the Case 2 of CRP FUMEX I.
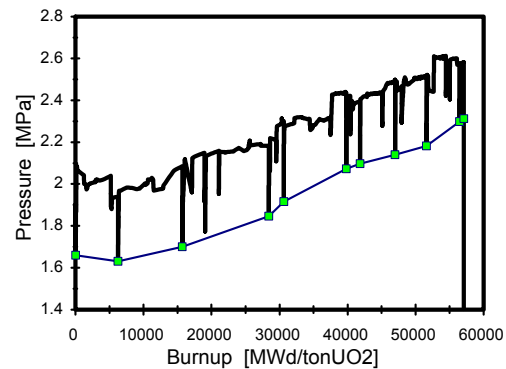
FIG. 4. Pressure in the rod vs. burnup for case 2 of CRP FUMEX I. The experimental data are the squared dots corresponding to the pressure at specific shutdowns.

5.1 A Fuel Failure in the CRP FUMEX I

Case number 4 of the first edition of the CRP FUMEX was a demanding exercise. It was a blind test as all the cases of FUMEX I. Two experimental fuel rods were instrumented and they were assembled in an unknown IFA of the HRP. One of them was filled with 3 bar He (rod A) and the

second one with 1 bar He (92%) and Xe (8%) (rod B). The Fig. 5 shows the power history of these fuel rods and the Fig. 6 shows the gas pressure of the rod A.
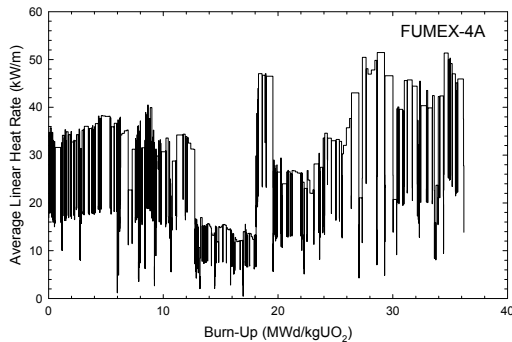
FIG. 5. Power history corresponding to the Case 4-A of CRP FUMEX I.
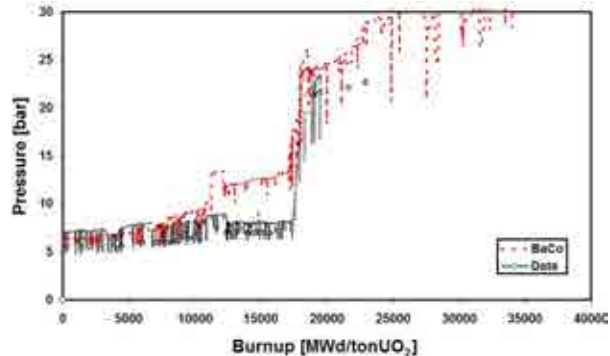
FIG. 6. Gas pressure inside the fuel rod 4-A. Experimental data and BaCo calculations.

A failure was attained in the fuel rod at the middle of the expected full irradiation. The event is not mentioned in the final TECDOC of IAEA [6] but it was commented by Dr. W. Wiesenack during the first Research Coordinated Meeting (RCM) in Halden, July 1993. The on-line measurement of the gas pressure was stopped due to a failure in the rod at the top of a power ramp. Nevertheless it was possible to continue the experiment. The calculations with the BaCo code were in good agreement with the experimental data (see Fig. 6). The coolant pressure was ~33.6 bar. The codes can continue after the event and it was calculated an overpressure into the fuel rod.

6. COORDINATE RESEARCH PROJECT FUMEX II (2001–2006)

The CRP FUMEX II was covered for 27 fuel performance database cases containing important fuel performance information such as fission gas release, fuel centreline temperature, rod internal pressure, clad creep and radial FP distribution measurement data. Those cases were included in the IFPE [7]. The second edition of the CRP FUMEX was not a blind test. The data of the cases included the results of the exercises. The major objective of the program was to improve the high burnup fuel performance code prediction capabilities. We selected the PWR Cases 15 and 16 of the program in order to illustrate the accuracy of the BaCo predictions and detailed information of these cases in order to assess the performance of our code.

This CRP included ideal power histories of CANDU fuels at very high power levels. It was found a high probability of failures at those levels of irradiation due to that the calculated gas pressure in the fuel rods were over the coolant pressure as it is explained in reference [21].
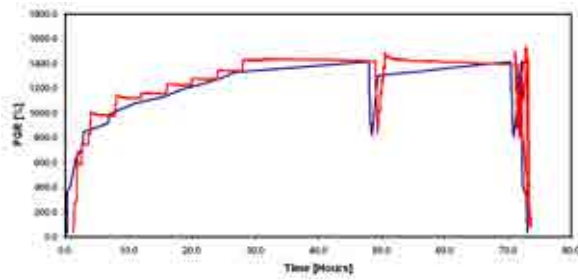
FIG. 7. Pellet centreline data and calculation during the bump test. Case 15 of CRP FUMEX II.
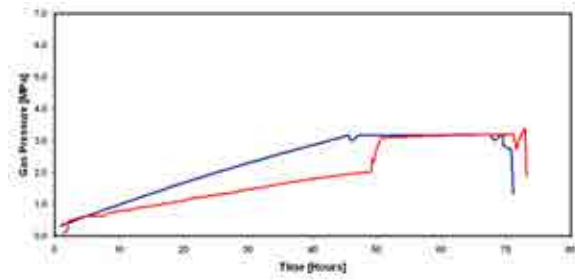
FIG. 8. Experimental data and calculation of the inner gas pressure during the bump test at EOL.

6.1 CRP FUMEX II -Case 15, RISØ Test

The Risø National Laboratory in Denmark have carried out three irradiation programs of slow ramp and hold tests, so called 'bump tests' to investigate fission gas release and fuel micro structural changes. The third and final project, which took place between 1986 and 1990, bump tested fuel re-instrumented with both pressure transducers and fuel centreline thermocouples. The data from the project were particularly valuable due to the in-pile data on fuel temperatures and pressures as well as extensive PIE [22]. This bump irradiation test, case 14 of the CRP FUMEX II, was carried out on 1988 in the test reactor DR3 at Risø under PWR conditions. A fuel rod was refabricated from a segment supplied by Advanced Fuels Corporation (ANC) and instrumented with pressure transducer and fuel centreline thermocouple. The fill gas was 14.66 bar helium. Figure 7 shows the pellet centre temperature calculated with BaCo and the experimental measurement.

Bump testing of AN4, case 15 of the CRP FUMEX II, was carried out in December 1987. The fuel rod was refilled with Xe during refabrication. This case is valuable for the comparison with the previous cases of fuel pins filled with He. Likewise the use of the Xe as filling gas reproduces the worst case of thermal conductivity in the gap pellet-cladding. Figure 8 shows the inner gas pressure calculation and data. The difference between data and BaCo at the first part of the experiment is done due to the position of the pressure transducer (at the top of the fuel), the shutdown after the first ramp and the axial power profile. The inner pressure at the bottom is higher than at the top of the fuel due to the power profile and PCI at the middle of the rod. As BaCo calculates an average gas pressure then we have that difference. Nevertheless we have a very good agreement between these experiments and the BaCo code results.

6.2 Coordinate Research Project FUMEX II -Case 16, HBEP Test

The High Burnup Effects Programme (HBEP) was an international group-sponsored program managed by Battelle Pacific Northwest Lab. (BNW). The principal objective of the HBEP was to obtain well characterized data on FGR for typical LWR fuel irradiated to high burnup levels [23]. The data set produced for the code simulation contains a full irradiation history with clad temperature and local power. The selected cases include annular pellets. The data are particularly valuable for the evaluation of the FGR at EOL and the fission products radial distribution. The measurements for the code comparison were: FGR at EOL, fission products and Pu distribution with a burnup ~51 and 67~69 MWd/kgUO$_2$. The main results are included in the Table 1.

TABLE 1. A COMPARISON BETWEEN THE BaCo CODE CALCULATIONS AND THE EXPERIMENTAL DATA FOR THE CASE 16 –HBEP TEST– OF THE CRP FUMEX II

Case 16 (rod 363)	Data	BaCo
Average Burnup at EOL [MWd/kgU]	66.7	69.0
FGR [%]	3.80	3.25
Hot Pressure [MPa]		3.29
Pressure STP [MPa]	2.06	2.84
Case 17 (rod 365)	Data	BaCo
Average Burnup at EOL [MWd/kgU]	69.4	65.7
FGR [%]	2.40	3.70
Hot Pressure [MPa]		6.55
Pressure STP [MPa]	3.38	5.52
Case 18 (rod 370)	Data	BaCo
Average Burnup at EOL [MWd/kgU]	50.9	52.0
FGR [%]	1.40	2.00
Hot Pressure [MPa]		6.31
Pressure STP [MPa]	3.28	4.62

Figure 9 shows the power history of the case 16 of CRP FUMEX II. The burnup was calculated with BaCo using the time as input data. We find a good agreement between the calculated burnup and the data (see the Chart 1). The Fission Gas Release (FGR) calculation is included in Fig. 10. The release is thermally activated due to the limitation of our FGR model where the so-called HBS is not included. Nevertheless, the empirical approach used in the FGR model includes high burnup fuel irradiation results in their parameterization (1). The FGR calculated agrees very well with the experimental result at EOL. Figure 11 shows the inner gas pressure calculated with the BaCo code. We find an acceptable correlation between our estimation and the data at EOL. The cases do not include the evaluation of pellet stack length data but we include that calculation with an illustrative purpose (see Fig. 12). Here we can identify a pellet densification up to a burnup of ~170 days; swelling is present after that date.
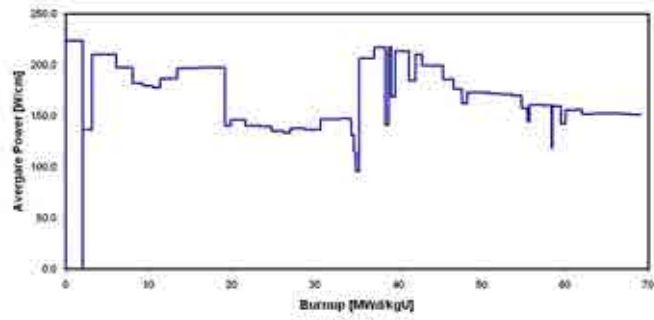
FIG. 9. Average linear power of the fuel rod 363 from the HBEP experiment (Case 16 of CRP FUMEX II). Burnup calculated with the BaCo code (time was the data).
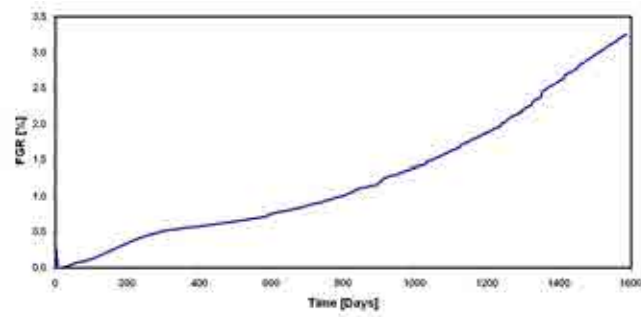
FIG. 10. Fission gas release calculated with the BaCo code (Case 16 of the CRP FUMEX II). FGR data at EOL was: 3.80%.
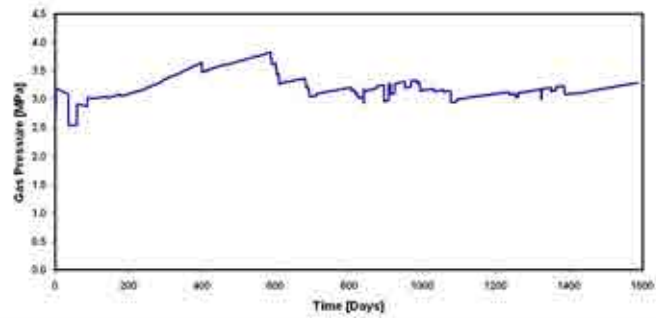
FIG. 11. Inner gas pressure of the fuel rod 363 from HBEP experiment (Case 16 of CRP FUMEX II -HBEP test-). Pressure data at EOL was 2.06 (STP) and 2.84 MPa (STP) was calculated for BaCo.
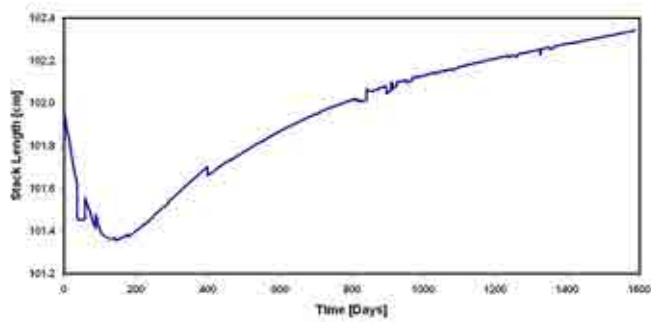
FIG. 12. Pellet stack length calculated with the BaCo code for the fuel rod 363 from HBEP experiment (Case 16 of CRP FUMEX II).

7. CRP FUMEX III (2008–2011)

The third edition of the CRP FUMEX III [24] is based on a big set of experiments of the OECD-IFPE [25]. A minor set of six irradiations were selected for the organizers as mandatory cases in order to produce a comparative evaluation of the codes.

The Risø cases of the CRP FUMEX II were repeated in the third edition due to its difficulties (see previous section with this case).

7.1 CRP FUMEX III (AREVA idealized case 2)

This case is an idealized irradiation based on measurements of three fuel rods operated for 3, 4 and 7 cycles in a commercial French PWR reactor. It was allows an empirical evaluation of the FGR of a single power history with a maximum burnup of about 81500 MWd/tonU and a FGR of about 9%. The Fig. 13 illustrates the BaCo calculations of FGR and the given FGR "data" including the uncertainties based on the measurements and the fabrication.

The participants of the CRP FUMEX III were pushing the limits of their codes in order to simulate this case due to the extreme burnup of discharge. BaCo found good agreement in the two first points in the area of the usual extended burnup. Nevertheless we obtain an under prediction of the third point due to the fault of the modelling of the influence of Hi-Bu microstructure (in particular its influence with the FGR).
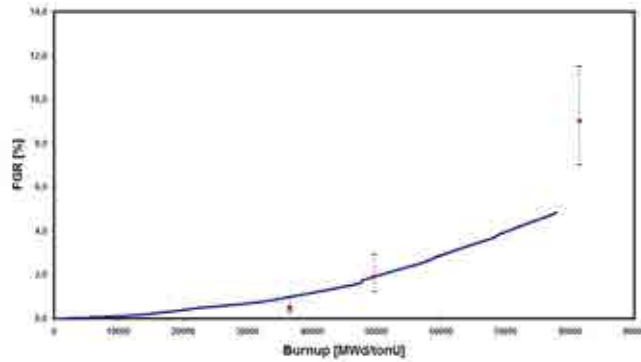
FIG. 13. BaCo code calculation of the Fission Gas Release (FGR) vs. Burnup (idealized case provided by AREVA).

7.2 CRP FUMEX III (AECL-JC-bundle)

A Prototype CANDU Fuel bundle for the Bruce reactor was irradiated in the NRU experimental reactor at Chalk River Laboratories in experimental loop facilities under typical CANDU reactor conditions. The bundle was a 37-element fuel assembly prototype, it was coated with graphite and it was not instrumented. Coolant for the test was pressurized light water under typical PHWR conditions of approximately 9 to 10.5 MPa and 300°C. The bundle was subjected to extensive post-irradiation examination [26]. The outer element burnup averaged was approximately 640 MWh/kgU at EOL (End of Life"). Outer element powers was varied between 57 kW/m near the beginning of life (BOL) and 23 kW/m at EOL
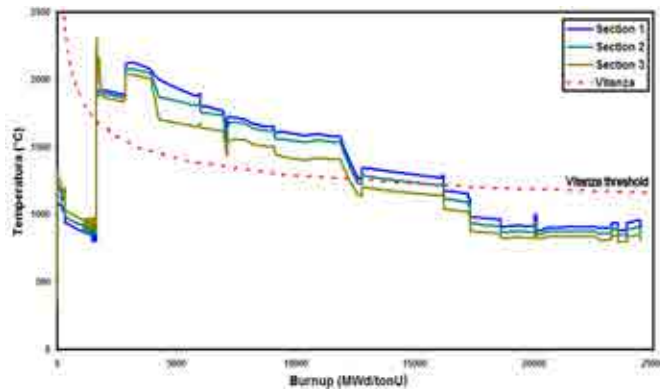
FIG. 14. Fuel pellet centre temperature calculated with the BaCo code. Outer fuel rod of the bundle AECL-JC.

The Fig. 14 shows the BaCo calculations of the fuel pellet centre temperature at three axial positions of the fuel. It was included the Vitanza threshold in order to take a first approach to the fission gas release (FGR). We find that the curves of temperature for the three axial segments are over the Vitanza threshold. The Fig. 15 includes the evolution of the central hole, the radius of the columnar grains, the equiaxed grains and the zone without restructuring. The heat transference during

irradiation is not optimized due to the use of a 90% of Ar as filling gas. The Fig. 16 shows the inner gas pressure of the fuel rod of the CANDU fuel rod under study and the coolant pressure included as a reference line. The pressure is under the coolant pressure during the entire irradiation as we expect from a conservative point of view.
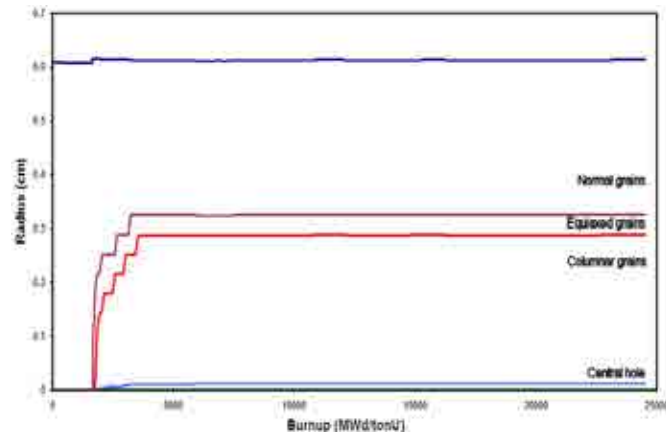
FIG. 15. Grain size evolution. Outer fuel rod of the bundle AECL-JC.
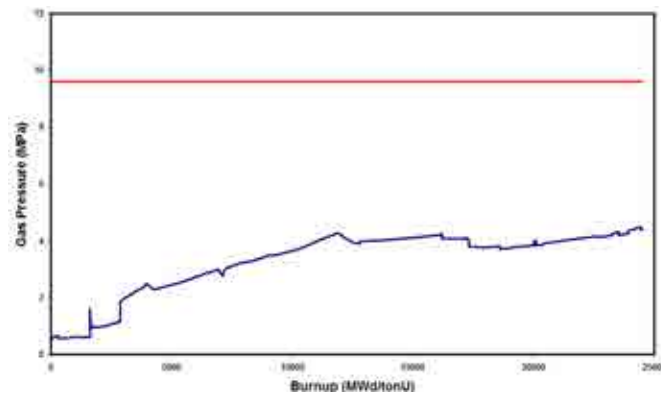
FIG. 16. Inner gas pressure of the fuel rod. Outer fuel rod of the bundle AECL-JC. Coolant pressure included as a reference line.
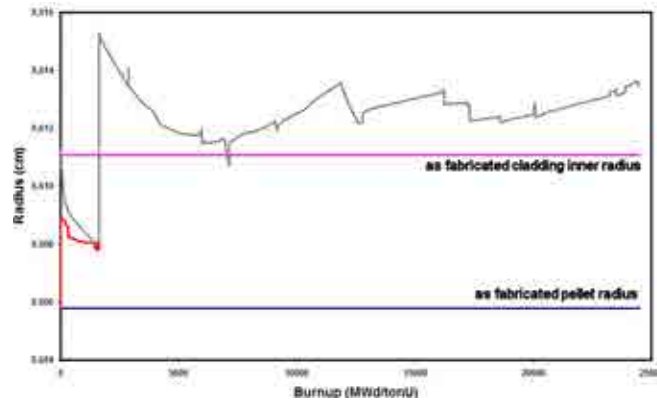
FIG. 17. Pellet and inner cladding radius evolution. Outer fuel rod of the Bundle AECL-JC.

The Fig. 17 shows the curves of the inner radius of the cladding and the radius of the pellet. We includes the lines of the as fabricated pellet radius and the as fabricated inner cladding radius as a reference. We do not obtain the closure of the gap at BOL like we expect for the CANDU fuels due to the extreme conditions of this experiments.

An example of the 3D tools used for the improvements of the normal BaCo output is included in the Fig. 18. The plots are: the 3D mesh used for the finite element post-processing, 3D radial displacement where the ridges are clearly shown, the hoop stress, the von Mises equivalent stress and the radial profile at the most demanding pellet during the irradiation of the bundle AECL-JC.

TABLE 2. A COMPARISON BETWEEN THE BaCo CODE CALCULATIONS AND THE EXPERIMENTAL DATA FOR A CANDU CASE –AECL-JC TEST– OF THE CRP FUMEX III

AECL bunde JC	Data	BaCo
Burnup(av) [MWd/tonU]	~26600	24500
FGR(av) [cm³]	~48–60	21 (5.3%)
Xe [%]	0.8595	0.784
Kr [%]	0.0753	0.138
He [%]	0.0413	0.0078
Ar [%]	0.0193	0.070
Diameter(av) [cm]		
up	~1.318	1.3215
middle	~1.319	1.3523
lower	~1.318	1.3335
Length change [mm]	~1.1	1.12
Grain size (fractional radius)		
Columnar grain growth	~0.47	~0.47
Equiaxed grain growth	~0.56–0.60	~0.53
Ridge heights [mm]	0,055–0.075	0.045
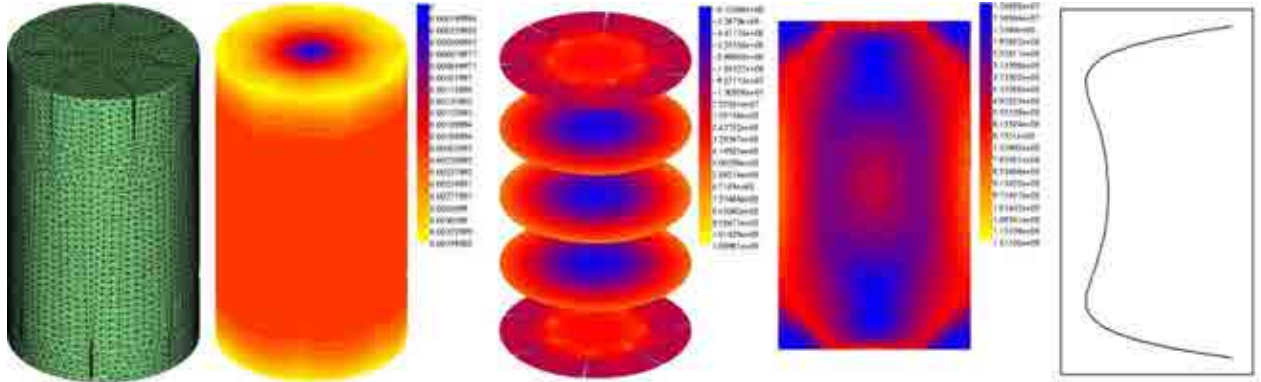
FIG. 18. 3D mesh for finite elements calculation, 3D radial displacement, hoop stress, von Mises equivalent stress and radial profile of the most demanding pellet during the irradiation of the bundle AECL-JC.
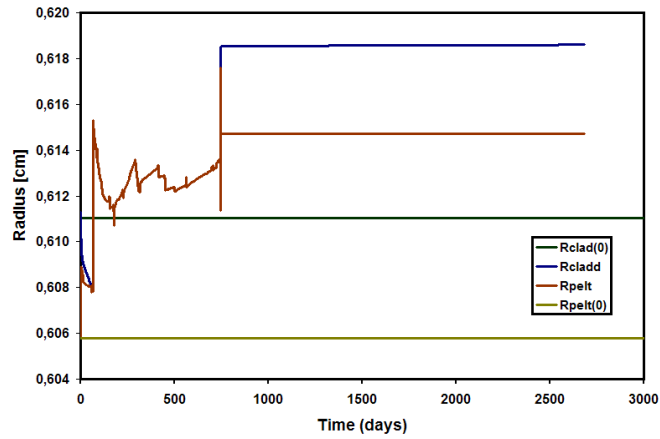
FIG. 19. Pellet and clad inner radius evolution during irradiation and at dry storage conditions. Bundle AECL-JC.

7.3 AECL-JC-bundle at dry storage conditions

The fuel element must not fail during the operation of the power plant. It is emphasized in this section that the fuel integrity must also be kept during the intermediate storage at pools or silos.

The simulation of the fuel behaviour under dry storage conditions can be calculated by using the BaCo code as an extension of the normal application of the analysis of nuclear fuel elements under irradiation. The safe conditions of storage, in particular the temperature of the dry storage system, were analysed and the results are presented in Figures 19 to 22.

The Fig. 19 shows the evolution of the pellet and cladding radius during irradiation and at the dry storage. We observed the opening of the pellet-cladding gap due to the change of the boundary conditions at EOL; the coolant pressure is present during irradiation and the ambient pressure during storage (approx. 3000 days).

29
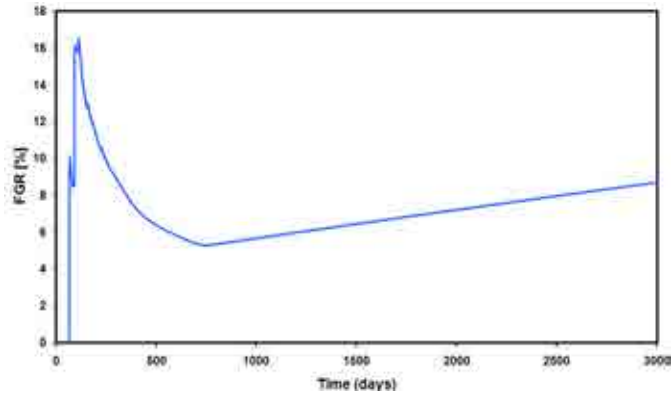
FIG. 20. Fission gas release during irradiation and at dry storage conditions. Bundle AECL-JC.
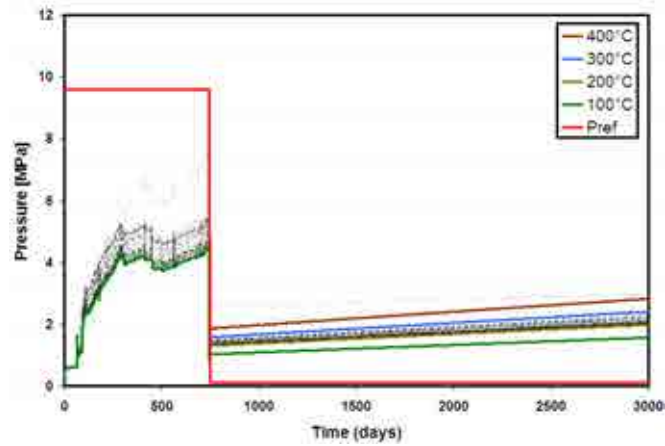
FIG. 21. Fuel rod inner gas pressure during irradiation and at dry storage conditions. Bundle AECL-JC.

The Fig. 20 shows the FGR at the same time of the previous plot; it is observed a small release of fission gasses thermally activated. The Fig. 21 shows a parametric analysis of the inner gas pressure at four different values of the temperature of the storage device; a statistical analysis is included. The Fig. 22 includes the same analysis for the hoop stress of the cladding of the Bundle AECL-JC.

We found that there is a small increment of stresses and gas pressure into the fuel rod due to a small fission gas release in the presence of the corrosive elements or compounds as I, Cs, CsI, etc. A stress corrosion cracking (SCC) failure could be achieved in the fuel due to the accumulated damage of the cladding during irradiation and the small but constant increment of FGR.
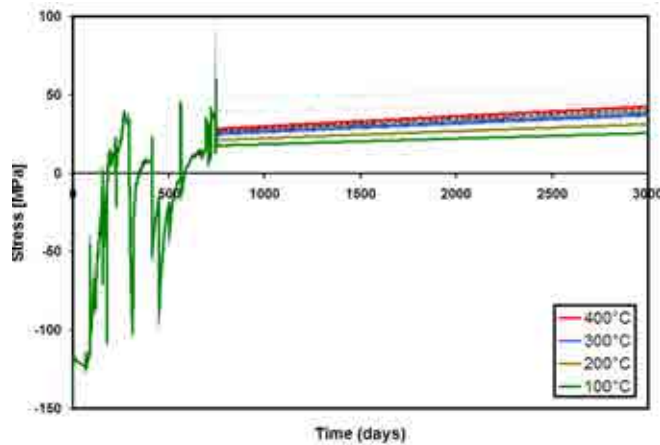
FIG. 22. Hoop stress during irradiation and at dry storage conditions. Bundle AECL-JC.

7.4 A Fuel Failure in the CRP FUMEX III

The irradiation of the first MOX nuclear fuel rods made in Argentina began in 1986. These experiences were made in the HFR Petten ("High Flux Reactor"), Holland. Six MOX fuel rods were fabricated in the α Facility (GCCN-CNEA-Argentina). The modelling support of the experiment was conducted with the BaCo code [10].

The power histories were defined from calculations performed with the BaCo code in 1986 in order to obtain a high burnup compatible with the 80's PHWR technology, to produce mechanical demanding conditions at the cladding and to define a high power ramp at EOL up to a value enough to induce a failure due to PCI-SCC. The final burnup of the most demanding fuel rod was 15000 MWd/ton(M). Ramping of that fuel rod was interrupted when an increase of coolant activity was detected. After discharge, a visual inspection of the rod showed the presence of a small circular hole in the cladding. Additional PIE showed that the hole was due to a SCC failure as it was predicted with BaCo.

These irradiations were included in the IFPE in 2000 and they were cases of the CRP FUMEX III. The name of the experiment is: IFPE/CNEA-MOX-RAMP.
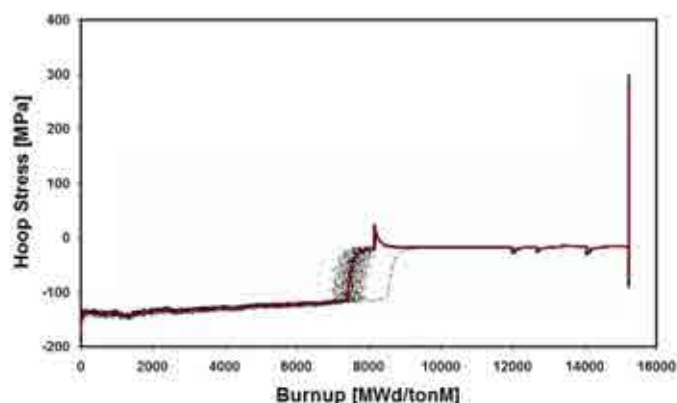
FIG. 23. Hoop stress (including a sensibility analysis) of the CNEA-MOX-RAMP case (CRP FUMEX III).

FIG. 24. SCC failure at the CNEA-MOX-RAMP case [10].

The Fig. 23 shows the BaCo calculations of the hoop stress at the cladding of the BU15 experiment. The Fig. 24 is the PIE of a part of the defective fuel rod showing a crack due to SCC. The calculated hoop stress at the cladding is over the PCI-SCC threshold of σ_{SCC}= 170 MPa for PHWR fuels.

8. A FEW APPOINTMENTS FOR A NEW COORDINATE RESEARCH PROJECT FUMEX

All the editions of the CRP FUMEX covered a complete scope of nuclear fuel behaviour including exercises for severe accidents but we remark that the first CRP FUMEX was focused mainly to thermal calculations, the second one to FGR issues and the last edition of the CRP to mechanical affairs. Each CRP was associated with several TCM of the IAEA.

The cases of severe accidents as RIA and LOCA were not taken into account for all the participants. A new project covering these technical issues could be welcome in particular for the area of nuclear regulatory affairs. Not all the participants were receptive to the simulation of severe accidents because the codes are working with the purpose to analyse the fuel performance, to assist the design and PIE of nuclear fuel elements.

There is a bridge between the nuclear fuel behaviour under normal conditions and under severe accidents. The bridge is the analysis and modelling of fuel failures in order to mitigate and prevent these minor accidents. It could be plausible a new CRP focused on the predictions of fuel failures, not only in accident conditions in order to properly continue with the previous three CRP.

9. CONCLUSIONS

This work describes briefly the main features of BaCo. The BaCo code capabilities were exposed with the simulation and the analysis of the fuel rod behaviour in three selected examples of the IAEA CRP FUMEX I, two cases of the 2nd edition of the CRP, and three cases of the CRP FUMEX III including some 3D outputs and the statistical analysis in the CANDU case of the CRP FUMEX III. We emphasize the value of the exercises by using the last case for its simulation under dry storage conditions after the irradiation.

An excellent agreement between data and BaCo outputs were found in both cases of the CRP FUMEX I. The goal of our participation in that project were the thermal improvements and the tools and new programming of the code required for the management of extensive and detailed data input as the ones provided for the HRP.

The first test of the CRP FUMEX III, the AREVA test, presented in this work was a computational experiment of commercial irradiation based on empirical observations up to an ultra high burnup (~81000 MWd/tonU). We found an excellent agreement between the BaCo calculations and the empirical data at normal and high burnup. An underprediction of the FGR was found at ultra high burnup (EOL) and it will be taking into account in order to improve the code.

One of the Risø cases of the CRP FUMEX II and III was analysed. Good results for the BaCo code were obtained. This bump test was one of the most demanding cases of the project.

We continue with an extensive calculation of one of the CANDU cases provided by AECL for the inclusion in the IFPE and in the CRP FUMEX III. It was included the 3D calculations by using the extension tools of the BaCo code and the parametric and probabilistic analysis of the dry storage of one of those CANDU advanced prototype fuel. That analysis shows the importance of the temperature of the storage device and its influence in a small but continuous increment of the gas pressure inside the fuel rod under the aggressive environment accumulated during the irradiation (17).

The D-COM and the CRP FUMEX I, II and III, including the blind exercises with CANDU fuels of India, were deeply focused in the performance of nuclear fuel rods under the point of view of the fuel modelling and code calculations. The feedback of those projects goes to fuel elements design and the prevention of fuel failures during operation. Nevertheless it were not included too much cases with fuel failures in order to detect those events with the codes.

CRP FUMEX II and III included a few cases of RIA and LOCA. The response of the participants to those cases was enough to conclude that there was no interest for a while for the qualification the codes for those accident conditions in particular because these are more related with questions of safety analysis and regulatory affairs more than the fuel rod behaviour.

Then it could be mandatory to continue with a forth edition of CRP FUMEX with accident conditions -the proposed CRP FUMAC of the IAEA-. Nevertheless, from the point of view of the nuclear fuel modelling, the mitigation of fuel failures, the improvement of the fuel production and its performance, it could be reasonable the delay of the CRP FUMAC and prepare a new CRP FUMEX IV with the focus in fuel failure detection and its mitigation including the dry storage of the fuel and not only during the front end of the fuel cycle.

REFERENCES

[1]   MARINO, A. C. et al., BaCo (BArra COmbustible) Code Version 2.20: a thermo-mechanical description of a nuclear fuel rod, Journal of Nuclear Materials, Vol. **229**, April II, p155–168 (1996).

[2]   MARINO, A.C., Starting Point, Keys and Milestones of a Computer Code for the Simulation of the Behaviour of a Nuclear Fuel Rod, Science and Technology of Nuclear Installations, Volume **2011**, Article ID 326948 (2011).

[3]   BRASNAROF, D. O. et al, A New Fuel Design for Two Different HW Type Reactors, Science and Technology of Nuclear Installations, Volume **2011**, Article ID 194650 (2011).

[4]   BOADO MAGAN H. et al, CAREM Projects Status", Science and Technology of Nuclear Installations, **2011**, Article ID 326948 (2011).

[5]   MISFELD, I., The D-COM blind problem on fission gas release, IAEA, International Working Group on Fuel Performance and Technology for Water Reactors, OECD-NEA-CSNI/IAEA Specialist's Meeting on Water Reactor Fuel Safety and Fission Products Release in Off-Normal and Accident Conditions, RISØ National Laboratory, IWGFTP/16 (1983).

[6]   INTERNATIONAL ATOMIC ENERGY AGENCY, Fuel modelling at extended burnup, Report of the Co-ordinated Research Programme on Fuel Modelling at Extended Burnup-FUMEX, IAEA-TECDOC-998, (1996).

[7]   KILLEEN, J. et al, Fuel modelling at extended burnup: IAEA coordinated research project FUMEX-II in Proceedings of the International LWR Fuel Performance Meeting (Top Fuel '06), Salamanca, Spain, (2006).

[8]   MARINO, A. C., Computer simulation of the behaviour and performance of a CANDU fuel rod, Proceedings of the 5th International Conference on CANDU Fuel, Toronto, Canada, September 1997.

[9]   MARINO, A. C., An approach to WWER fuels with BaCo, Proceedings of the 7th International Conference on WWER Fuel Performance, Modelling and Experimental Support, Albena, Bulgaria, (2007).

[10]   MARINO, A. C., ADELFANG, P. and PÉREZ, E. E., Irradiation of Argentine MOX fuels. Post-irradiation results and experimental analysis with the BACO code, Journal of Nuclear Materials, Vol. **229**, April II, p169–186 (1996).

[11]   DEMARCO, G. L. and MARINO, A. C., 3D Finite Elements Modelling for Design and Performance Analysis of UO_2 Pellets, Science and Technology of Nuclear Installations, Volume **2011**, Article ID 843491, (2011).

[12]   MARINO, A. C. et al, Sensitivity analysis applied to nuclear fuel performance related to fabrication parameters and experiments, Proceedings of the 14th International Conference on Structural Mechanics in Reactor Technology, Lyon, France, (1997).

[13]   MARINO, A. C. et al, High power ramping in commercial PHWR fuel at extended burnup, Nuclear Engineering & Design, vol. **236**, no. 13, pp. 1371–1383 (2006).

[14]   TURNBULL, J. A. et al, Experimental data on PCI and PCMI within the IFPE database, Proceedings of the International Seminar on Pellet-Clad Interaction in Water Reactor Fuels (PCI '04), Aix-en-Provence, France, (2004).

[15]   MARINO, A. C. et al, in Proceedings of the Present and Future Trends in PHWR Fuel Material Modelling with the BaCo code, 21st International Conference on Structural Mechanics in Reactor Technology, (SMiRT 21), November 6–11, 2011, New Delhi, India, (2011).

[16] MARINO, A. C., JAROSZEWICZ, S., LOSADA, E. L., MARTIN, V. E., MOSCA, H., and GARCÉS, J. E., Simulation of Nuclear Materials and Fuels by using the BaCo code and Multiscale Modelling of Materials (M³), Water Reactor Fuel Performance Conference (TopFuel 2012), September 2–6, 2012, Manchester, United Kingdom, (2012).

[17]   MARINO, A. C., PHWR fuel rod behaviour during dry storage, No. 2022, in Proceedings of the Water Reactor Fuel Performance Meeting (WRFPM 2009/Top Fuel), September 6–10, 2009, Paris, France, (2009).

[18]   MARINO, A. C., CANDU Fuel Rod Behaviour during Dry Storage, Proceedings of the 11th International Conference on CANDU Fuel, Niagara Falls, Ontario, Canada, October 17–20 2010, (2010).

34

[19] MARINO, A. C., An overview of the dry storage of nuclear fuels with the BaCo code, Proceedings of the 8th International Conference on WWER Fuel Performance, Modelling and Experimental Support, Helena Resort near Burgas, Bulgaria, September 26 –October 4, 2009, (2009).

[20] MARINO, A. C., Crack and dishing evolution models and PCI-SCC considerations for fuel pellets in a quasi-bidimensional environment, in Proceedings of the "Les Journées de Cadarache 2004, International Seminar on Pellet-Clad Interaction in Water Reactor Fuels", Aix en Provence, France, 9–11 March 2004, (2004).

[21] MARINO, A. C., CRP FUMEX PHWR cases a BaCo Code Point of View and Its Results, in Proceedings of the International IAEA Technical Meeting on Pressurized Heavy Water Reactor Fuel: Integrity, Performance and Advanced Concepts, 24–27 September 2012, Bucharest, Rumania, IAEA-TECDOC-CD-1751, IAEA, Vienna (2014).

[22] KNUDSEN, P. et al., Final Report on the Risø Fission Gas Project, RISOE-FGP-R17rev. (June 1983) NEA -1634/01 (http://www.nea.fr/abs/html/nea-1634.html).

[23] High Burnup Effects Programme Final Report, DOE/NE/34046-1 [HBEP-61(3P27)] NEA-1510/03 (http://www.nea.fr/abs/html/nea-1510.html).

[24] INTERNATIONA ATOMIC ENERGY AGENCY, Improvement of Computer Codes Used for Fuel Behaviour Simulation" (FUMEX-III), IAEA-TECDOC-1697, IAEA, Vienna (2013).

[25] OECD-NEA International Fuel Performance Experiments (IFPE) database (http://www.oecd-nea.org/science/wprs/fuel/ifpelst.html).

[26] OECD-NEA International Fuel Performance Experiments (IFPE) database (http://www.oecd-nea.org/tools/abstract/detail/nea-1596).

IMPORTANCE OF COUPLED NEUTRONICS AND FUEL PERFORMANCE CODES

S. BZNUNI, A. AMIRJANYAN
Nuclear and Radiation Safety Center,
Yerevan, Armenia
E-mail: s.bznuni@nrsc.am

T. DOWNAR, A.WARD
University of Michigan,
Ann Arbor, Michigan,
United States of America
E-mail: downar@umich.edu

Abstract. One of the important steps of nuclear reactor Deterministic Safety Analysis (DSA) is the estimation of radiological consequences under normal operation and accidental conditions. On one hand, the application of coupled system thermal-hydraulic/neutronics codes can estimate fuel failure rates or percentages based on the calculated Peak Clad Temperature (PCT) or other acceptance criteria which can introduce considerable uncertainty and potential overestimation of the actual fuel failure rates and conservatism in the predicted dose rates. On the other hand, the application of fuel performance codes could decrease the above mentioned uncertainties, however they currently use very modest neutronics and thermal-hydraulics models. Therefore, the coupling of the system thermal-hydraulics/neutronics and fuel performance codes make it possible to perform best estimate DSA and provide the potential to decrease the conservatism in radiological consequence analysis. The paper will propose the coupling of the US NRC PARCS and TRANSURANUS codes and their application to best estimate steady-state and transient analysis of a VVER.

1. INTRODUCTION

Coupling of the nodal core simulator codes like PARCS/PATHS [1] with the fuel performance codes like TRANSURANUS [2] will significantly improve consistency between neutronics and fuel mechanical predictions during quasi-static core depletion and accidental conditions. This will enhance the prediction of the neutronics performance by employing more accurate nodal fuel temperatures which takes into account changes in the gap conductance with burnup. Similarly, best-estimate prediction of fuel rod performance (temperature, cladding strains, corrosion/hydrogen pickup, etc.) can be improved by using more accurate channel fluid temperatures and pin power distributions in the fuel performance analysis. An important application of an improved code system for nuclear reactor core performance is to evaluate the sensitivity and uncertainty of the figures of merit (ex. dose rates, peaking factors, criticality, cladding strains) on the input parameters to the coupled system (ex. fuel rod geometry/materials, cross sections). This information is useful in quantifying the margins that exist within a particular core/fuel design and operating strategy. The following paper provides a preliminary overview of the proposed coupling methodology.

2. PROPOSED COUPLING METHODOLOGY

As part of the core neutronics simulation, nodal core simulators generally have methods embedded within them to calculate the coolant (and thus fuel) temperature distribution (required for cross section evaluation at a particular statepoint). The complexity of this thermal-hydraulic evaluation method varies from code to code; PARCS has a drift-flux-based thermal-hydraulic subcode called PATHS to calculate the temperature and fluid conditions for both PWRs and BWRs. Within the rest of this paper, when discussing the three classes of physics relevant to steady-state reactor core simulation, we will treat PATHS as a distinct thermal-hydraulics module; however,

currently PATHS is executed within PARCS. For accidental conditions complex thermal-hydraulics behavior is treated by coupling with system codes like RELAP, TRACE.

In its normal execution, the fuel performance code uses a user-input power history and axial power shape to model the behavior of an individual fuel rod. It uses as input the core inlet temperature and pressure and performs a rudimentary closed-channel thermal-hydraulics model to calculate the temperature distribution along the pin. This is then used as a boundary condition for the fuel temperature distribution calculation in the fuel pin. The gap conductance and fuel properties are permitted to vary with burnup to take into account the effects of irradiation damage, fission product build up, and dimensional changes.

In contrast, PARCS/PATHS utilizes input specified fuel thermal-physical properties (e.g. gap conductance, conductivity, etc) and fuel dimensions that are time invariant and that are used throughout the entire core during the fuel depletion. The power distribution is then calculated using the Doppler fuel temperature that results from these fixed properties. The effect of fuel burnup on the reactor core is captured in the cross section library, not in the fuel performance models. PARCS currently performs macroscopic depletion in which nuclide densities are homogenized together with the microscopic cross section data for each axial node in a fuel assembly. Several industry core simulators (e.g. SIMULATE-3) perform microscopic fuel depletion in which the Bateman equations are solved explicitly to compute the nuclide densities in each fuel node. However, in recent version of PARCS it is possible to "back out" the nuclide densities for each assembly using the data stored by the lattice physics code used to pre-compute the assembly homogenized cross sections. PARCS tracks the burnup and void/control rod history of each fuel node and an interpolation is performed using the lattice code output files. Work is ongoing at University of Michigan to utilize the existing pin power reconstruction methods in PARCS to extend this capability to provide detailed fuel pin isotopics. The detailed pin nuclide data could be used to inform the TRANSURANUS models which currently rely on empirical nuclide field information (e.g. fission gas release, conductivity, etc).

Another important aspect of proposed approach not only provides fuel performance code with nodal isotopics but their axial distributions parameterized by state variables using the lattice code output files.

In summary:
- Fuel Performance
  - Simple thermal-hydraulics;
  - User-input power shapes;
  - Detailed fuel models.
- PARCS
  - Detailed, burnup-dependent power distribution;
  - Nodal / pin isotopics (through additional scripts).
- PATHS
  - Detailed thermal-hydraulics;
  - Simple fuel models.

The overall coupling design is to take advantage of the things each code does well separately, while mitigating the drawbacks. Fig. 1 illustrates the exchange of information between the codes that we seek to achieve.
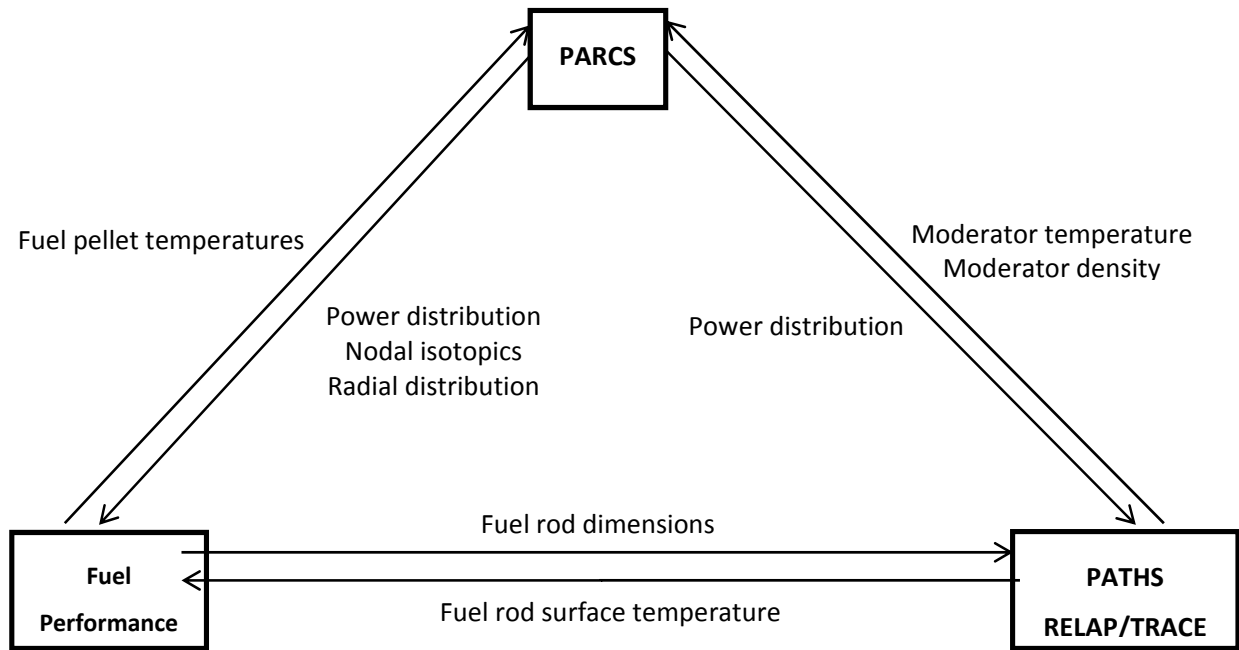
FIG. 1. Information exchange between TRANSURANUS and PARCS/PATHS during execution.

The overarching benefit of this coupling is to provide the core simulation with physics models that more faithfully represent the actual reactor. This will be achieved by improving the fidelity of the core depletion modeled in PARCS by providing a fuel/clad temperatures that takes into account the material changes within the fuel rods during burnup; and second, by improving the prediction of the fuel material changes and fuel rod behavior computed by the fuel performance code. This is achieved by providing the fuel performance code with a more accurate axial power distributions computed in PARCS that take into account the feedback between the fuel thermo-mechanical effects and the burnup history of the reactor core.

In order to achieve these benefits, we propose to employ the solution scheme described in Fig. 2. The basic idea is to iterate between the fuel temperatures and axial power shapes calculated by the fuel performance code and PARCS, respectively, within each burnup step until consistency is achieved; then, we advance to the next burnup step. Within each step, the information described in Fig. 1 will be passed between the codes. Since the changes from step to step are generally not large, each step should converge within a few iterations. Since the fuel performance code and PARCS are both fast running codes, this scheme should be tractable for core depletion on a PC.

The mechanics of the coupling are currently being investigated. The method proposed is to use a simple transparent method will be implemented which relies on a PERL script to control code execution and workflow.

```
                    ┌────────────────────────┐
                    │     Burnup step n      │
                    └────────────────────────┘
                                 │
                                 ▼
        ┌────────────────────────────────────────┐
        │  Compute power shape and coolant         │◄──────────────┐
        │  conditions using PARCS/PATHS            │               │
        │  with previous iterate fuel temperature  │               │
        └────────────────────────────────────────┘               │
                                 │                                 │
                                 ▼                                 │
        ┌────────────────────────────────────────┐               │
        │        Calculate fuel changes with       │               │
        │     TRANSURANUS (temperature,            │               │
        │  dimensional, chemical, FGR) using       │               │
        │    updated power shape and coolant       │               │
        │              conditions                  │               │
        └────────────────────────────────────────┘               │
                                 │                                 │
                                 ▼                                 │
                         ◇─────────────◇                          │
                        ╱               ╲          ┌──────┐        │
                       ╱  Temperature     ╲         │  No  │────────┘
                      ╱   and power        ╲───────▶└──────┘
                      ╲   shape             ╱
                       ╲  converged?       ╱
                        ╲               ╱
                         ◇─────────────◇
                                 │
                          ┌──────┐
                          │ Yes  │
                          └──────┘
                                 │
                                 ▼
                    ┌────────────────────────┐
                    │    Burnup step n+1     │
                    └────────────────────────┘
```
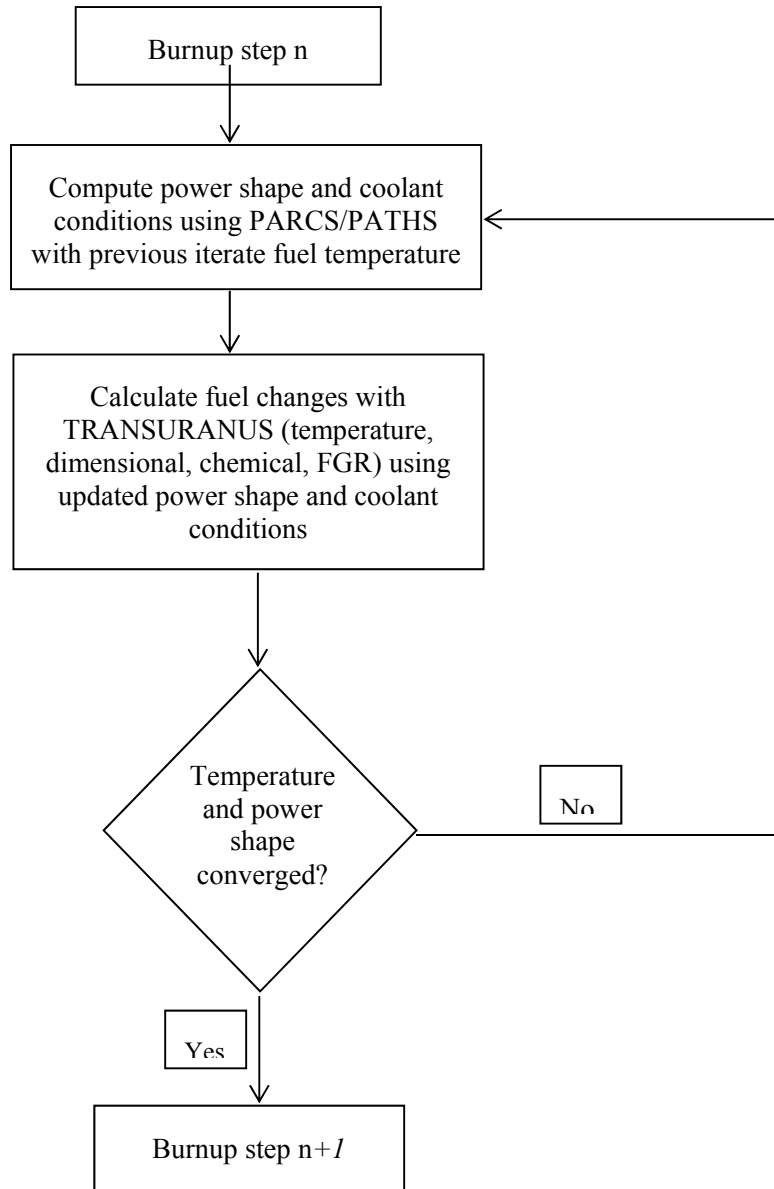
FIG. 2. Proposed TRANSURANUS/PARCS explicit coupling scheme.

Verification and validation efforts will be based on comparative analysis of standalone and coupled codes with relevant experimental data.

3. CONCLUSIONS

Advanced approach of coupling neutronics, T/H and fuel performance codes is suggested and discussed that in addition linear heat rate includes transfer of local isotopics and its radial distribution to fuel performance code. Application of coupled codes system will allow to quantify safety margins of nuclear reactor without unnecessary overconservatism.

REFERENCES

[1] T. DOWNAR, Y. XU V. SEKER, N. HUDSON, PARCS, U.S. NRC Core Neutronics Simulator, THEORY MANUAL, Department of Nuclear Engineering and Radiological Sciences University of Michigan (2012).

[2] K. LASSMANN, TRANSURANUS: a fuel rod analysis code ready for use, Journal of Nuclear Materials, 188 (1992) 295–302.

ADAPTIVE LINKED GAP ELEMENT FOR FE-BASED GAP CONDUCTANCE MODEL

H.C. Kim[a], Y.S. Yang[a], Y.H. Koo[a]
[a]LWR Fuel Technology Division, Korea Atomic Energy Research Institute,
1045 Daedeok-daero, Yuseong-gu, Daejeon,
Korea, Republic of
Email: hyochankim@kaeri.re.kr

Abstract. A light water reactor (LWR) fuel rod consists of a zirconium alloy cladding tube and uranium dioxide pellets with a slight gap between them. The modeling of the heat transfer across the gap between fuel pellets and the protective cladding is essential to understanding the fuel behavior under irradiated conditions. Based on the Ross and Stoute model, the gap conductance that specifies the temperature gradient within the gap is very sensitive to the gap thickness in a certain region. Many researchers have been being developing fuel performance codes based on a finite element method (FE) to calculate the temperature, stress, and strain for a multidimensional analysis. The gap conductance model for multi-dimension is a difficult issue in terms of convergence and nonlinearity because the gap conductance is a function of gap thickness which depends on the mechanical analysis at each iteration step. In this paper, an adaptive linked gap element (AGE) has been proposed to resolve the convergence issue and nonlinear characteristic of multidimensional gap conductance. The elements that link the node of a pellet surface with the node of the cladding surface virtually are generated, so as to transfer heat as a function of gap thickness at every iteration step. To evaluate the proposed methodology for the simulation of the gap conductance, a thermo-mechanical coupled FE model has been established using ANSYS Parametric Design Language (APDL). In terms of the calculation accuracy and convergence efficiency, the proposed model has been evaluated for variable cases.

1. INTRODUCTION

A light water reactor (LWR) fuel rod consists of zirconium alloy cladding and uranium dioxide pellets, with a slight gap between them. Therefore, the mechanical integrity of zirconium alloy cladding is one of the most critical issues in terms of safety because it is an important barrier for fission products released into the environment. To evaluate the stress and strain of the cladding during operation, fuel performance codes have simulated thermo-mechanical behavior since the 1970s.

A LWR fuel performance code should incorporate a thermo-mechanical model owing to the existence of the fuel-cladding gap. Generally, the gap that is filled with helium gas at the beginning of the burnup results in a temperature drop along the radius direction. The gap conductance that specifies the temperature gradient between the pellet and cladding is a function of gap thickness according to the Ross and Stoute model. In particular, gap conductance can be sensitive against the gap thickness once the gap size decreases within several micrometers. The accurate modeling of the heat transfer across the gap between fuel pellets and the protective cladding is essential to understand the fuel performance, including the cladding stress and behavior under irradiated conditions.

Therefore, an iterative thermo-mechanical coupled analysis is required in the fuel performance code to calculate the temperature distribution throughout the pellet and cladding. Recently, multidimensional fuel performance codes have been developed in advanced countries in order to understand the thermo-mechanical behaviors such as pellet-cladding mechanical interaction (PCMI) for normal conditions, DBA (design based accident), and even severe conditions using the Finite Element Method (FEM).

Most of the fuel performance codes that are able to simulate a multidimensional analysis are used to calculate the radial temperature distribution and perform a multidimensional mechanical analysis based on a one-dimensional (1D) temperature result. The FRAPCON-FRAPTRAN code

system incorporates a 1D thermal module and two-dimensional (2D) mechanical module [1, 2]. The FEXAXI-5 code also calculates the 1D temperature distribution and 2D mechanical analysis in same manner as the FRAPCON-FRAPTRAN code system [3]. In this method, the multidimensional gap conductance model is not required owing to a 1D temperature analysis.

On the other hand, a gap conductance model for a multi-dimension should be developed in the code to perform a multidimensional thermal analysis. ALCYONE introduces an equivalent heat convection coefficient that represents the multidimensional gap conductance as a function of gap thickness [4]. The BISON code employed a thermo-mechanical contact method that is specifically designed for tightly-coupled implicit solutions that employ Jacobian-free solution methods [5]. On the commercial finite element package (ANSYS), thermo-mechanical simulation in 2D and 3D states were carried out with a thermal contact coefficient (TCC), which is not varied as a function of the gap thickness [6].

In general, a thermal contact algorithm is a nonlinear calculation that is a highly expensive approach numerically. The gap conductance model for multiple dimensions is a challenging issue in terms of the convergence and nonlinearity because the gap conductance is a function of gap thickness, which depends on the mechanical analysis at each iteration step. Owing to the characteristics of a multiphysics calculation in the fuel performance code, the number of calling sequences of the thermo-mechanical module should be minimized, and the module should be converged efficiently in order to achieve convergence of the entire code system. Therefore, a linearized model for simulation of multidimensional gap conductance should be developed with valid assumptions that are specified for a fuel rod behavior.

In this paper, an adaptive linked gap element (AGE) has been proposed to simulate the multidimensional gap conductance of a fuel rod. Instead of thermal contact, it employs the linearized thermal gap element that functions as the gap thickness so as to resolve convergence issue and nonlinear characteristic of multidimensional gap conductance. The AGE can be regenerated in order to minimize the distortion of the temperature analysis when a thermal deformation occurs. Some assumptions for the linearized model are studied. To evaluate the proposed model, a thermo-mechanical coupled FE module using the AGE has been built using the commercial FE code system (ANSYS APDL). For an evaluation of the proposed model, temperature distribution calculated by the AGE model was compared with that calculated by thermal contact (TCC) model that simulates the gap model without any assumptions. The convergence studies demonstrate that the proposed model for a multidimensional gap model is efficient and valid.

2. MULTIDIMENSIONAL GAP CONDUCTANCE MODEL

2.1 Ross and Stoute model

The conductance across the interface between UO_2 and zircaloy can be considered as the sum of three terms: heat transfer across the gap by conduction through the gas, h_g; solid conductance across contact areas when the gap is closed, h_s; and a radiative heat transfer term, h_r [7].

$$h = h_g + h_s + h_r \tag{1}$$

According to the Ross and Stoute model, the radiative heat transfer term can be represented as eq. (2).

$$h_r = \frac{\lambda(T_{fs}^2 + T_{ci}^2)(T_{fs} + T_{ci})}{\dfrac{1}{\varepsilon_f} + \dfrac{r_{fs}}{r_{ci}}\left(1 - \dfrac{1}{\varepsilon_c}\right)} \tag{2}$$

where

λ is the Stefan-Boltzmann constant [$\mathrm{W \cdot m^{-2} K^{-4}}$];

T_{fs} is the temperature of the fuel surface [K];

T_{ci} is the temperature of the inner cladding surface [K];

r_{fs} is the fuel outer surface radius [m];

r_{ci} is the cladding inner surface radius [m];

ε_c is the emissivity of the cladding surface;

ε_f is the emissivity of the fuel surface.

Equations (3) and (4) show solid conductance that the mechanical contact induces and gas conductance that represent the heat transfer coefficient through gas in the gap, respectively.

$$h_s = a \cdot P_{rel} \cdot \frac{K_f K_c}{K_f + K_c} \frac{e^{(0.528\ln(R_2) - 5.738)}}{\sqrt{R_f^2 + R_c^2}} \tag{3}$$

where

a is a constant that depends on the interfacial pressure;

P_{rel} is the ratio of interfacial pressure to cladding Meyer hardness;

K_f is the fuel thermal conductivity [$\mathrm{W \cdot m^{-1} K^{-1}}$];

K_c is the cladding thermal conductivity [$\mathrm{W \cdot m^{-1} K^{-1}}$];

R_f is the roughness of the fuel surface [m];

R_c is the roughness of the inner cladding surface [m];

R_2 is the roughness of the rougher surface [m].

$$h_g = \frac{k_{gas}}{d + d_{min} + g_f + g_c} \tag{4}$$

where

k_{gas} is the gas thermal conductivity in the gap [W·m⁻¹K⁻¹];

d is the gap thickness [m];

d_{min} is the summation of the fuel roughness and inner cladding roughness [m];

g_f is the temperature jump distances at the fuel surface [m];

g_c is the temperature jump distances at the cladding surface [m].

In a steady-state operation, h_r is of little importance because the range of the surface temperature is below 1000 K. When the gap opens, h_s should be zero because the interfacial pressure is zero. During normal operation, the variation of h_s, h_r, and h_g calculated by FRAPCON-3.4 are shown in Fig. 1. The value of h_r is approximately 10^4 times smaller than that of h_g for the whole operation. While the gap opens, h_s is kept as zero because there is no mechanical interaction. After the gap closes, the value of h_s that depends on the interfacial pressure is 10^2 times smaller than that of h_g. At around 500 hours, 'soft contact' can be investigated. This means that two surfaces are still stuck together without interfacial pressure. The comparison demonstrates that h_g is the dominant factor among the three gap conductance components while the gap opens and even after the gap closes. In this work, the multidimensional gap conductance model is dealt with for only the gas gap conductance while the gap opens.
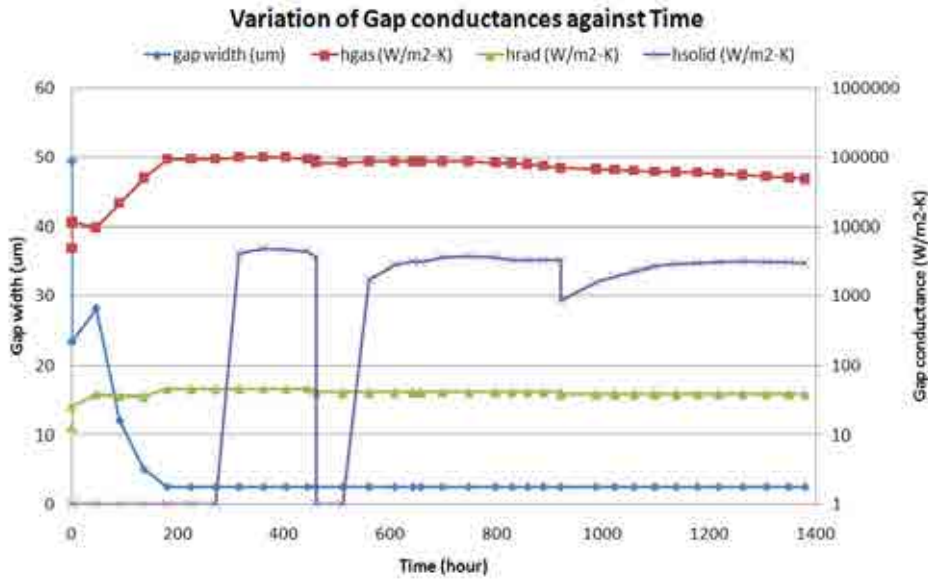
FIG. 1. Comparison of h_s, h_r and h_g during normal operation.

2.2 Adaptive linked gap element

To develop an effective multidimensional gap conductance model, an adaptive linked gap element (AGE) has been proposed instead of a thermal contact algorithm. The role of AGE is to transfer heat from the pellet to the cladding like a virtual thermal bridge. As shown in Fig. 2, the generated AGE links the i-node on the pellet surface and j-node on the cladding surface. Because the AGE does not exist in practice, it is applied for only a thermal analysis.
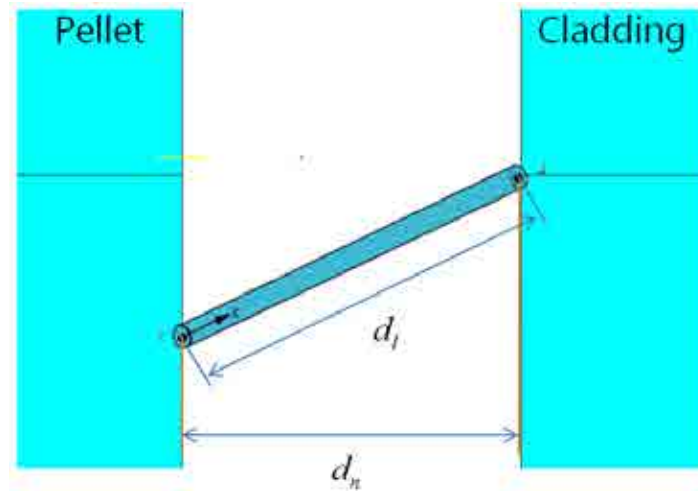
FIG. 2. Description of adaptive linked gap element.

The AGE should be characterized as a function of gap thickness to represent the characteristics of gas gap conductance in eq. (4). Therefore, the equivalent thermal conductivity of the AGE can be defined by following eq. (5) and eq. (6).

$$h_{g,ij}(T_{pellet,i} - T_{cladding,j}) = \frac{k_{eqv,ij}}{d_{l,ij}}(T_{pellet,i} - T_{cladding,j}) \tag{5}$$

where

$h_{g,ij}$ is the gas gap conductance of i-j AGE [W•m^{-2}·K^{-1}];

$T_{pellet,i}$ is the pellet temperature of the i-node [K];

$T_{cladding,j}$ is the inner cladding temperature of the j-node [K];

$k_{eqv,ij}$ is the equivalent thermal conductivity of i-j AGE [W·m^{-1}·K^{-1},];

$d_{l,ij}$ is the length of i-j AGE [m].

$$k^t_{eqv,ij} = \frac{k_{gas}}{d^t_{n,ij} + d_{min} + g_f + g_c} d^t_{l,ij} \tag{6}$$

where

$k^t_{eqv,ij}$ is the equivalent thermal conductivity of i-j AGE at the tth iteration step [W·m^{-1}·K^{-1},];

$d^t_{n,ij}$ is the normal distance of i-j AGE between the pellet and cladding at the tth iteration step [m];

$d^t_{l,ij}$ is the length of the i-j AGE at the tth iteration step [m].

45

The AGEs should be automatically regenerated at each iteration step when the thermal deformation of a pellet occurs. The algorithm for the regeneration of the AGEs is to search the node point on the cladding surface that is positioned in a minimum distance from the node point of the pellet surface. When the node on the pellet surface is linked to the searched node on the cladding surface, the AGE is generated and its equivalent thermal conductivity is also calculated.

The proposed AGE model for multidimensional gap conductance has two assumptions as follows:

- Only linked nodes through the AGE can transfer heat;

- The size of the gap thickness is determined as the radial distance between the AGE nodes.

When we look into the heat transfer mechanism in the gap, heat on the pellet surface affects the faced element and the vicinity of the elements in general. However, in the case of the fuel rod, the heat flux between the faced elements is dominant in comparison with the heat flux between the node on the pellet and the vicinity of the elements owing to the geometry characteristics. The first assumption can be valid because the heat flux between the node on the pellet and the vicinity of the elements can be ignored. The size of the gap thickness should be calculated along the normal direction of the element on the pellet. For the AGE model, the size of the gap thickness is defined as the radial distance between the AGE nodes.

2.3 Thermo-mechanical module using the AGE

Using ANSYS Parametric Design Language (APDL), which is a programmable language in ANSYS [8], we established the thermo-mechanical model using the AGE for an evaluation of the multidimensional gap conductance model.
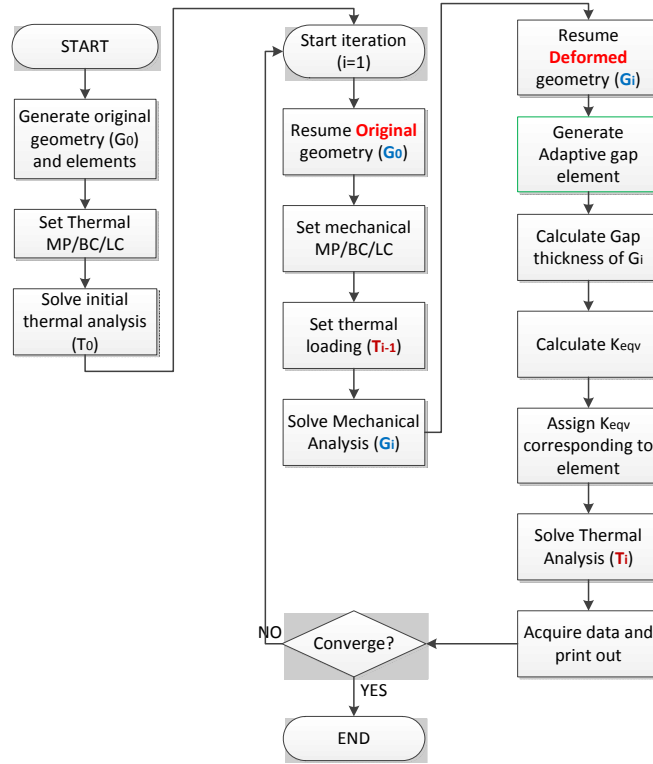
FIG. 3. Flowchart of thermo-mechanical module using AGE.

The iterative procedure of the thermo-mechanical calculation that employs the AGE is shown in Fig. 3. The initial thermal analysis with the given boundary and loading conditions was performed before the iteration starts. Based on the initial temperature result (T_0), the iterative thermo-mechanical analysis starts. In the $(i)^{th}$ mechanical analysis, the mechanical and thermal deformation are calculated based on the $(i-1)^{th}$ temperature result. For this mechanical analysis, the AGEs generated in the $(i-1)^{th}$ thermal analysis should be eliminated. Subsequently, the $(i)^{th}$ thermal analysis begins with the deformed geometry that comes from the $(i)^{th}$ mechanical analysis. The adaptive linked gap elements for the $(i)^{th}$ thermal analysis are generated at the deformed geometry. The target node on the inner cladding surface that is positioned at a minimum distance from the node on the pellet surface are searched and linked together. The equivalent heat conductivity of the linked element is also calculated with the normal distance between two nodes along the radial direction. Once the $(i)^{th}$ thermal analysis is completed, the temperature results of the $(i)^{th}$ thermal analysis are compared with those of the $(i-1)^{th}$ thermal analysis for the convergence check. Through the above iterative calculation, the mechanical results (stress, strain) and thermal results (temperature) can be converged [9, 10].

3. EVALUATION

To evaluate the proposed AGE model for a multidimensional gap conductance, the temperature distribution simulated with the AGE model is compared with that of the thermal contact coefficient (TCC) model that simulates the multidimensional gap conductance in general. The convergence trend of the thermo-mechanical model with the AGEs was also studied.

3.1 Evaluation of temperature calculation

To verify the temperature calculation using the AGEs, temperature results using the AGEs are compared with those using the TCC model for the first step. The TCC model that belongs to the ANSYS models can simulate the thermal contact and gap conductance model generally in spite of the nonlinear contact model. As it can be only applied to the non-deformed geometry that the thermal stress induces, thermal analyses of the two models are carried out with the undeformed geometry. The material properties are applied as follows: thermal conductivity of the fuel is 5.87 mW/mm·K, and the thermal conductivity of the cladding is 15.29 mW/mm·K. The loading condition has a constant heat generation of the fuel of 789.056 mW/mm^3. As boundary conditions, all surfaces are adiabatic except for the outer cladding surface. The temperature of the outer cladding surface is fixed at 623.15K.
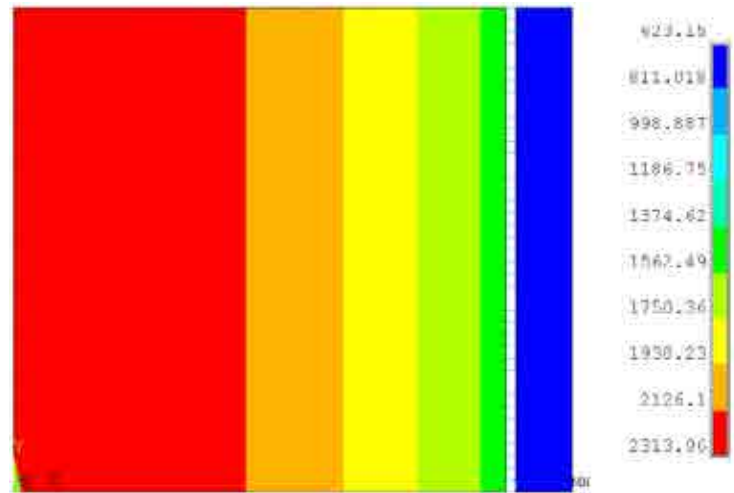
(a) Temperature distribution calculated with the AGEs.
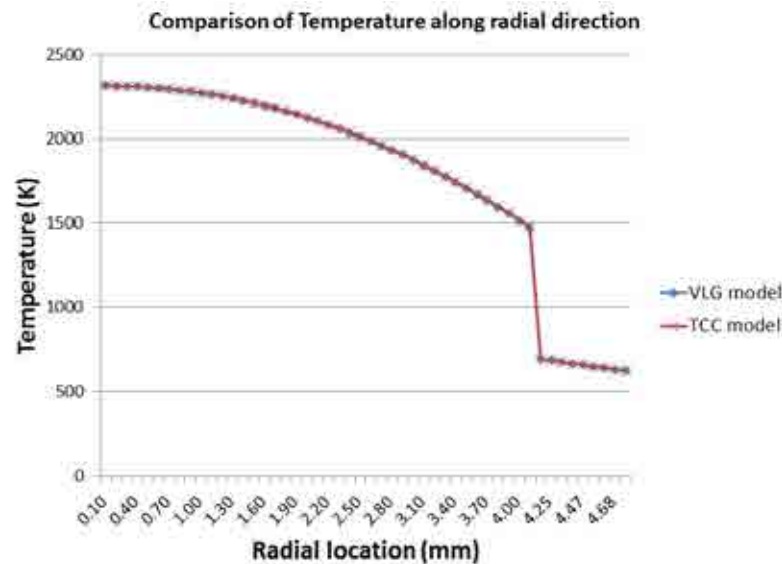
(b) Comparison of temperature simulated by TCC model and AGE model.

FIG. 4. Verification of the AGE model.

As shown in Fig. 4, the temperature results calculated with the AGEs show a good agreement against those of the TCC model. Therefore, the proposed AGE model is verified in terms of the calculation accuracy. To complete the verification of the proposed model, the temperature results should be compared with the TCC model after deformation induced by thermal stress occurs. A comparable TCC model does not exist.

3.2 Study of convergence trend

The calculation of the gap conductance requires an iterative thermo-mechanical procedure because the gap conductance depends on the gap thickness that is obtained by a mechanical analysis. Owing to the sensitivity of the gap conductance against the gap thickness, convergence of the iterative calculation for multidimensional gap conductance can be a challenging issue. Therefore, the convergence trend of the thermo-mechanical calculation using the AGE was studied.
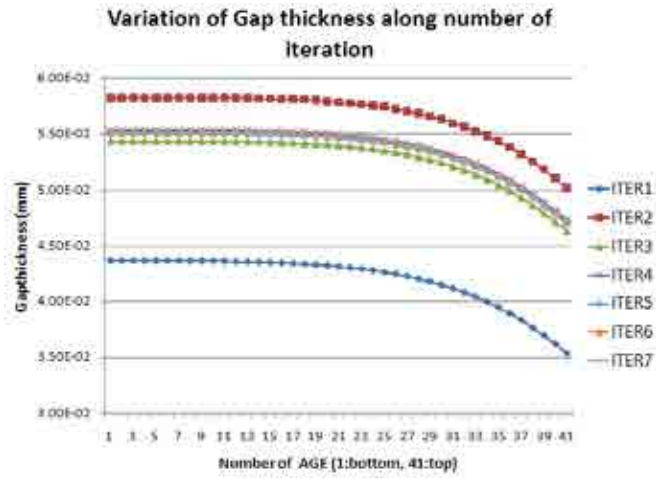
(a) Variation of gap thickness.
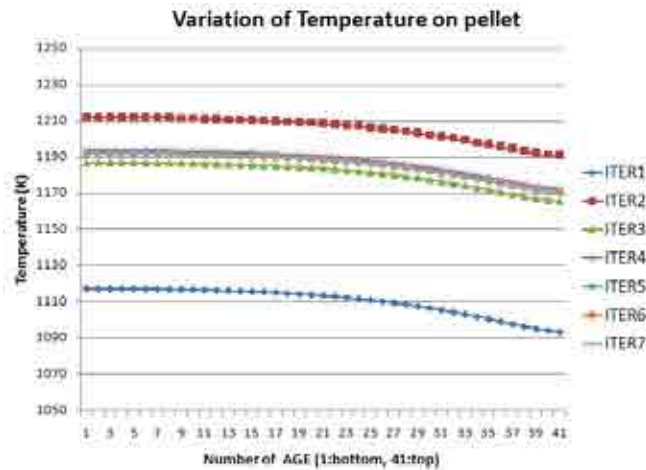
(b) Variation of pellet surface temperature.

FIG. 5.Convergence trend of the AGE model.

Figures 5(a) and 5(b) show the convergence trend of temperatures on the pellet nodes and gap thicknesses between the pellet and cladding surface against the number of iterations, respectively. The X axis represents the node number, where the bottom is '1' and the top is '41'. At the first iteration step (ITER1), the gap thicknesses are minimized because the thermal strains of the pellet elements are maximized on the basis of the initial high temperatures. Corresponding to the gap thickness, the high gap conductance leads to a relative low temperature on the pellet node. The temperature of the top node '41' is lower than that of the bottom due to the isotropic thermal expansion of the pellet. For the next step, the pellet temperature becomes high again as the gap sizes widen. The difference in the temperature variation between the current step and previous step declines gradually. The convergence trend of the AGE model demonstrates that the iterative thermo-mechanical calculation can be converged efficiently and the temperature trend of the nodes behaves in the same manner. As a result, the convergence condition of the multidimensional gap conductance can be defined as a function of temperature.

4. CONCLUSION

LWR fuel performance codes should incorporate an iterative thermo-mechanical calculation to resolve the gap conductance issues, iteratively. However, the gap conductance in a multidimensional model is a challenging issue owing to its nonlinearity and convergence characteristics. This works proposed an adaptive linked gap element (AGE) to develop the linearized multidimensional gap conductance model. To evaluate the proposed model, a thermo-mechanical module using the AGE has been built using a commercial FE code system (ANSYS APDL). For an evaluation of the temperature calculation, the temperature distribution of the AGE model was compared with that of thermal contact model. The temperature results of the AGE model show good agreement against that of the TCC model. The convergence studies demonstrate that the AGE model for a multidimensional gap model can be converged efficiently and the temperature trend of the nodes behaves in the same manner.

REFERENCES

[1] GEELHOOD, K.J., LUSCHER, W.G., BEYER, C.E., CUTA, J.M., FRAPTRAN 1.4: A Computer code for the Transient analysis of oxide fuel rods, NUREG/CR-7023, Vol. **1**, MD (2010).

[2] KNUUTILA, A., Improvements on FRAPCON3/FRAPTRAN mechanical modeling, VTT-R-11337-06, FINLAND (2006).

[3] SUZUKI, M., Light Water Reactor Fuel Analysis Code FEMAXI-V, JAERI-DATA/Code 2000-030, JAPAN (2000).

[4] MICHEL, B., SERCOMBE, J., NONON, C., FANDEUR, O., Modeling of Pellet Cladding Interaction, Comprehensive Nuclear materials, Elsevier Ltd., Amsterdam 682–691, (2012).

[5] HANSEN, G., A Jacobian-free Newton Krylov method for mortar-discretized thermo-mechanical contact problems, J. Computational Physics **230,** 6546, (2011).

[6]   KUZNETSOV, V.I., KRUPKIN, A.V., NOVIKOV, V.V., Crack Initiation and Growth in Fuel Pellets Modeling Using ANSYS Software, Proc. TopFuel 2013, Charlotte, North Carolina, 65–71,(2013).

[7]   BERNA, G.A., BEYER, C.E., DAVIS, K.L., LANNING, D.D., FRAPCON-3: A Computer Code for the Calculation of Steady-State, Thermal-Mechanical Behavior of Oxide Fuel Rods for High Burnup, NUREG/CR-6534, Vol. 2, MD (1997).

[8]   ANSYS®, Release 14.0, Help System, ANSYS Mechanical, ANSYS Inc.

[9]   KIM, H.C., YANG, Y.S., KIM, D.H., BANG, J.G., KIM, S.K. and KOO, Y.H., Study of Gap Conductance model for Thermo-mechanical fully coupled Finite Element model, Transactions of the Korean Nuclear Society Autumn Meeting, Gyeongju, (2012).

[10] KIM, H.C., YANG, Y.S., KOO, Y.H., "Development of FE-based gap conductance model using Adaptive link element", Proc. KSME for CAE and applied mechanics, Pusan, 303-304, (2013).

OPTIMIZATION OF THE TRASURANUS BURNUP MODEL FOR GD-DOPED WWER-1000 FUEL PINS BASED ON RESULTS OF HELIOS CODE

M. Ieremenko, I. Ovdiienko
State Scientific and Technical Centre for Nuclear and Radiation Safety
Kyiv, Ukraine
Email: ml_eremenko@sstc.kiev.ua

Abstract. This paper describes results of testing of the TRANSURANUS burn-up model (TUBRNP routine) for Gd-doped WWER-1000 fuel pin based on results of HELIOS code. The testing covers the analysis of different types of nuclear fuel rods from a neutronic point of view that one can encounter in the VVER-1000 reactor core. The HELIOS computations simulate the assembly geometry, and combine 4 different ^{235}U enrichment configurations with 4 different Gd_2O_3-concentrations. For each of these combinations the radial distribution of the concentrations of ^{155}Gd and ^{157}Gd compute in one Gd-doped rod. Based on these results the recommendations on using cross section of Gd in TRANSURANUS TUBRNP model were proposed.

1. INTRODUCTION

TRANSURANUS [1], [2] is a computer code for the thermal and mechanical analysis of cylindrical fuel rods in nuclear reactors. As part of the code, the TUBRNP model calculates the local concentrations of U, Pu and Nd as a function of the radial position across a fuel pellet (radial profiles). These local quantities are required for the determination of the local power density, the local burn-up, and the source term of fission products. In view of the primary importance of the relative radial power profile for the thermal and mechanical analysis of nuclear fuel, priority is given to relative rather than to absolute concentrations.

The present paper pursues our work by testing the TUBRNP model for Gd-doped WWER-1000 fuel. To this end, Gd-doped fuel rods in a WWER-1000 assembly were simulated by neutron transport calculations for different initial fuel compositions and different neutron spectra. The calculated local concentrations of ^{155}Gd, ^{157}Gd and radial power distribution were used for proposing of recommendations on using cross section of Gd in TRANSURANUS TUBRNP model.

2. GOAL OF TESTING

This testing was done in framework of Software Licensing Agreement No31796 signed by Institute of Transuranium Elements (ITU), Germany and State Scientific and Technical Centre for Nuclear and Radiation Safety (SSTC NRS), Ukraine. According this Agreement for testing following objects were chosen:

— TRANSURANUS version - v1m1j11;

— TUBRNP routine, describing the radial power profile in nuclear fuel rods of profiled bundles with Gd-doped UO_2 fuel;

— Fuel assembly (FA) for WWER-1000 reactors. Combine 4 different ^{235}U enrichment configurations with 4 different Gd_2O_3-concentrations. For each of these combinations the radial distribution of the concentrations of ^{155}Gd and ^{157}Gd compute in one Gd-doped rod.

3. INITIAL DATA FOR TESTING

All Initial data for testing were chosen according with Software Licensing Agreement, Ref [4] and with typical operational data for WWER-1000. On Fig. 1 configuration of a WWER-1000 fuel assembly is presented. This FA are different with last modification of FA with Gd-fuel pins used on Ukrainian Nuclear Power Plants (NPP) but this differences are not significant for testing TUBRNP routine. Various of ^{235}U- and Gd- enrichments, of Gd-pins places in FA covers all modern FAs and their neutron spectrum characteristic. In Tables 1÷3 initial ^{235}U enrichments, contents of Gd_2O_3 and main parameters applied for simulating are presented.
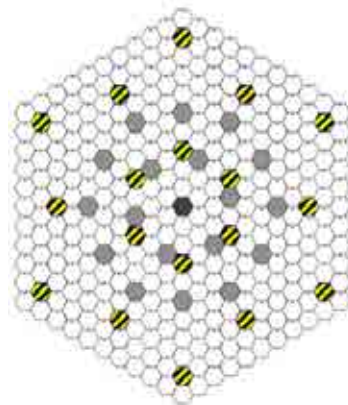
-Gd-doped WWER-1000 fuel pin

FIG. 1. Configuration of a WWER-1000 fuel assembly [4].

TABLE 1. INITIAL ^{235}U ENRICHMENTS FOR WWER-1000 FUEL RODS

^{235}U/^{tot}U, (wt.%)		
Gd-doped rods	Periphery rods	Remaining rods
2.4	2.4	3.0
3.3	4.0	4.0
3.6	3.6	4.0
3.6	4.4	4.95

TABLE 2. INITIAL CONTENTS OF GD$_2$O$_3$ FOR WWER-1000 FUEL RODS

Gd$_2$O$_3$/Fuel, (wt.%)
5.0
6.0
8.0
9.0

TABLE 3. MAIN PARAMETERS APPLIED FOR SIMULATING THE WWER-1000 FUEL RODS

Pellet inner radius (mm)	0.75
Pellet outer radius (mm)	3.785
Cladding inner radius (mm)	3.860
Cladding outer radius (mm)	4.55
Pin pitch (mm)	12.75
Mean fuel temperature (°C)	732
Mean moderator temperature (°C)	305
Moderator density (g/cm^3)	0.72
Boron concentration (g/kg H$_2$O)	3.0

4. HELIOS MODEL

A HELIOS code [3] for detailed neutronic transport as well as depletion calculations was used. FA was presented as 1/6 part of whole assembly with mirror boundary conditions. Gd-doped rods in HELIOS model was divided on 30 rings. Visualisation of HELIOS FA model is presented at this Technical Meeting (TM) in PowerPoint version of this paper and available as Ref [5].

5. RESULT OF STANDARD VERSION OF TRANSURANUS CODE

On Fig. 2 concentration of ^{155}Gd, ^{157}Gd calculated by HELIOS & TRANSURANUS codes at different burnup points is presented. On Fig. 3 radial power distribution calculated by HELIOS & TRANSURANUS codes at different burnup points is presented. As it is possible to see from figures, there are differences between results of two codes in the radial profile of power and of gadolinium concentration. The reason of difference and a proposal on optimisation of code TRANSURANUS are presented in following chapters of paper.
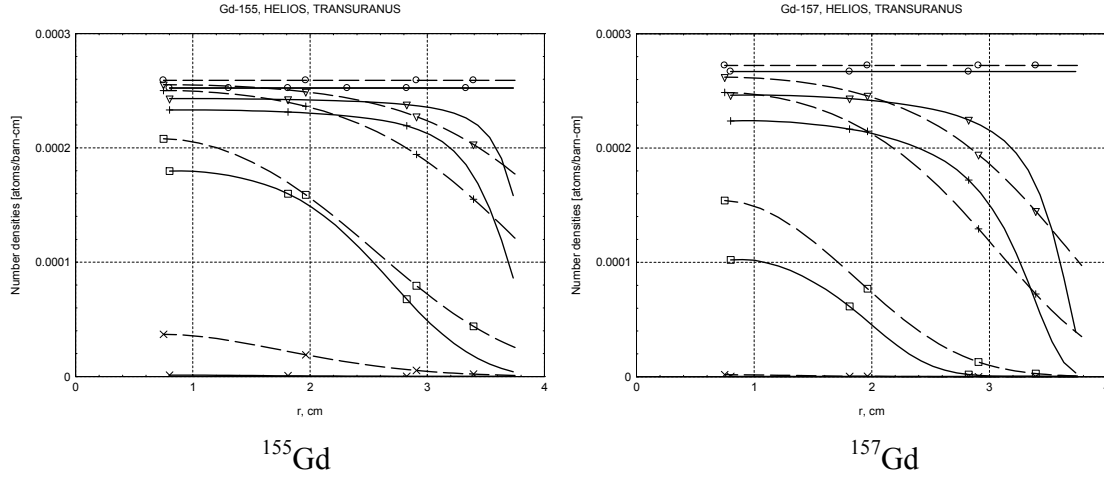
$$^{155}Gd \qquad\qquad ^{157}Gd$$

FIG. 2. Concentration of ^{155}Gd, ^{157}Gd. HELIOS (solid line) & TRANSURANUS (dashed line), Burnup=0, 0.4, 0.8, 3.1, 10 MW·d/kgU.
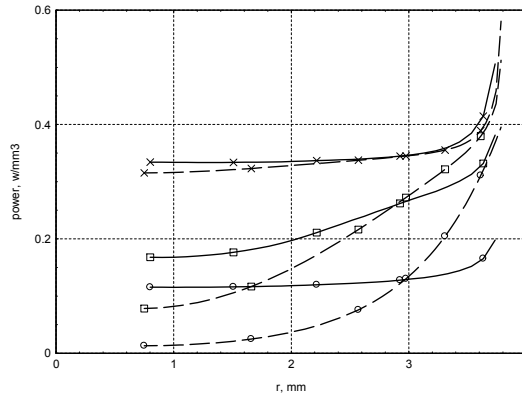
FIG. 3. Radial power distribution (W·mm^{-3}). HELIOS (solid line) & TRANSURANUS (dashed line), Burnup=0, 3.1, 10 MW·d/kgU.

6. PROPOSAL FOR OPTIMISATION OF TUBRNP ROUTINE

According to [1] in order to determine neutron flux distribution $\Phi(r)$, thermal flux diffusion theory can be applied as follows:

$$\nabla^2 \Phi - \kappa^2 \Phi = 0 \tag{1}$$

The inverse diffusion length:

$$\kappa = \sqrt{\frac{\Sigma_{a,tot}}{D}} \tag{2}$$

is derived from the macroscopic absorption cross sections:

$$\Sigma_{a,tot} \approx \sum_k \sigma_{a,th,k} N_k \tag{3}$$

The resulting solutions of the differential equation are based on the modified Bessel functions (of the first and the second order type) and the flux profile function of inverse diffusion length κ (2):

$$\Phi(r) = f(\kappa) \tag{4}$$

and κ is function of microscopic absorption of gadolinium

$$\kappa = f(\sigma_a) = f(\sigma_a^{155,157}) \tag{5}$$

Concentration of gadolinium is defining by following equations:

$$N_{155}(bu_{n+1}, r) = N_{155}(bu_n, r)e^{-\sigma_a^{155}A_{dbu}} , \ N_{157}(bu_{n+1}, r) = N_{157}(bu_n, r)e^{-\sigma_a^{157}A_{dbu}} \tag{6}$$

For calculation of neutron flux (power) distribution $\Phi(r)$ and concentration of gadolinium isotopes 155 and 157 the constant value of microscopic cross sections are used:

$$\Phi(r)\ldots \sigma_{a,therm}^{157} = 85000\ b , \ \sigma_{a,therm}^{155} = 19800\ b$$

$$N_{155,157}(r)\ldots \sigma_a^{157} = 3800\ b , \ \sigma_a^{155} = 1471b$$

But absorption microscopic cross sections of gadolinium isotopes 155 and 157 has a strong dependence form burnup (Fig. 4) and radial positions (Fig. 5).
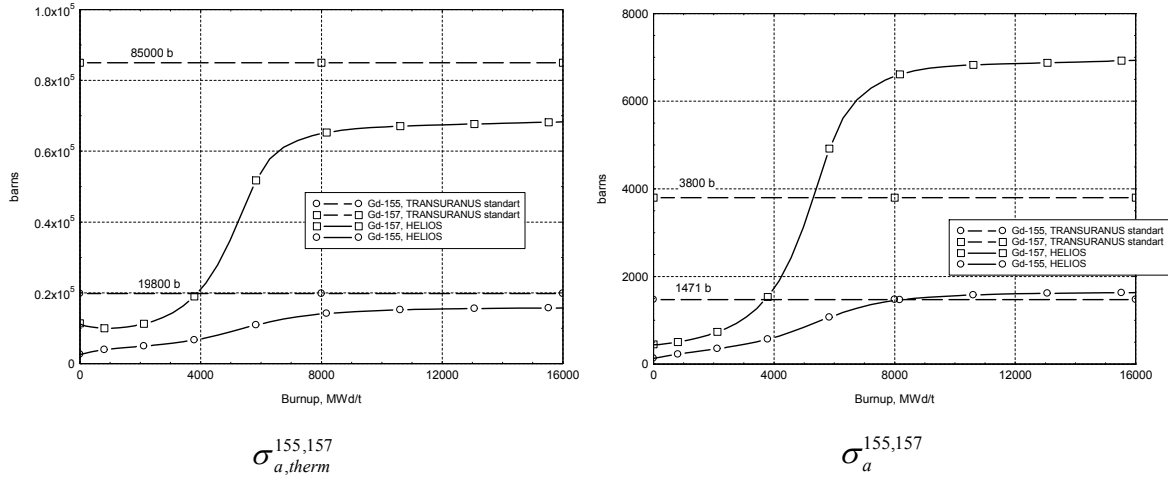
FIG. 4. Microscopic cross sections σ_a and $\sigma_{a,therm}$ of gadolinium isotopes at burnup.

$$\sigma_a^{155} \qquad\qquad\qquad\qquad \sigma_a^{157}$$
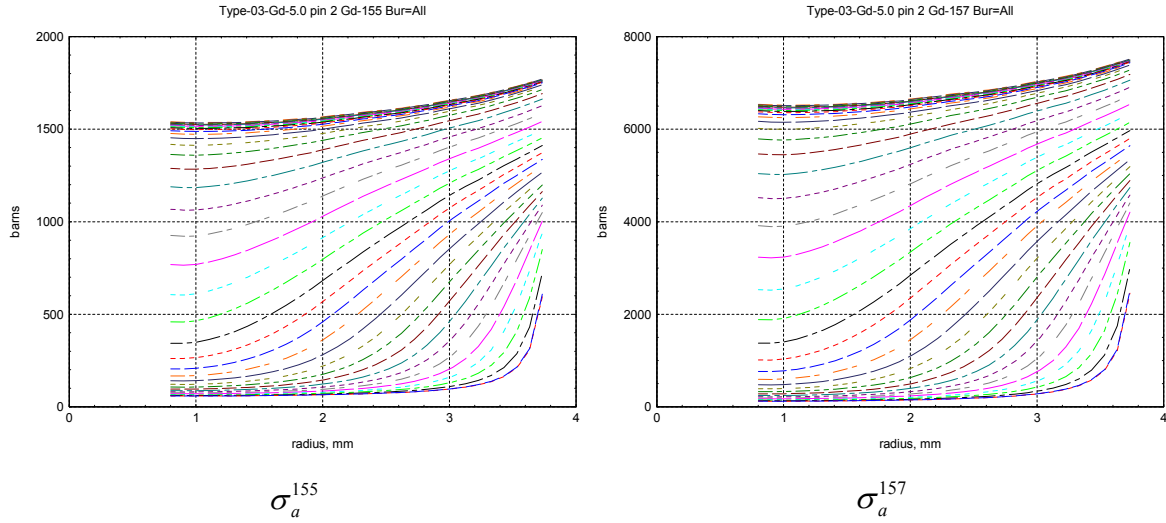
FIG. 5. Microscopic cross sections σ_a of gadolinium isotopes at radius. Bottom line – burnup =0, top line – burnup>10 MW·d/kgU.

For the account of this factor to replace constant values of gadolinium cross sections by dependences on burning and radius was offered:

$$\Phi(r),\ \sigma_{a,therm}^{155,157} = const\ \rightarrow\ \sigma_{a,therm}^{155,157} = f(bur)$$

$$N_{155,157}(r),\ \sigma_a^{155,157} = const\ \rightarrow\ \sigma_a^{155,157} = f(bur,r)$$

For this activity the gadolinium cross-sections in tables format was used. These tables of gadolinium cross-section were calculated by HELIOS code.

7. RESULT OF OPTIMISED VERSION OF TRANSURANUS CODE

Results of calculation with use of optimised version TRANSURANUS are presented on Figures 6 and 7 below. As it is possible to see from figures the distribution of gadolinium concentration and of power on pellet radius became closer to the results of code HELIOS. A difference of absolute value of gadolinium concentration is connected to differences with initial concentration of gadolinium for fresh fuel which directly define in HELIOS model and are calculated by TRANSURANUS from densities, enrichments etc.
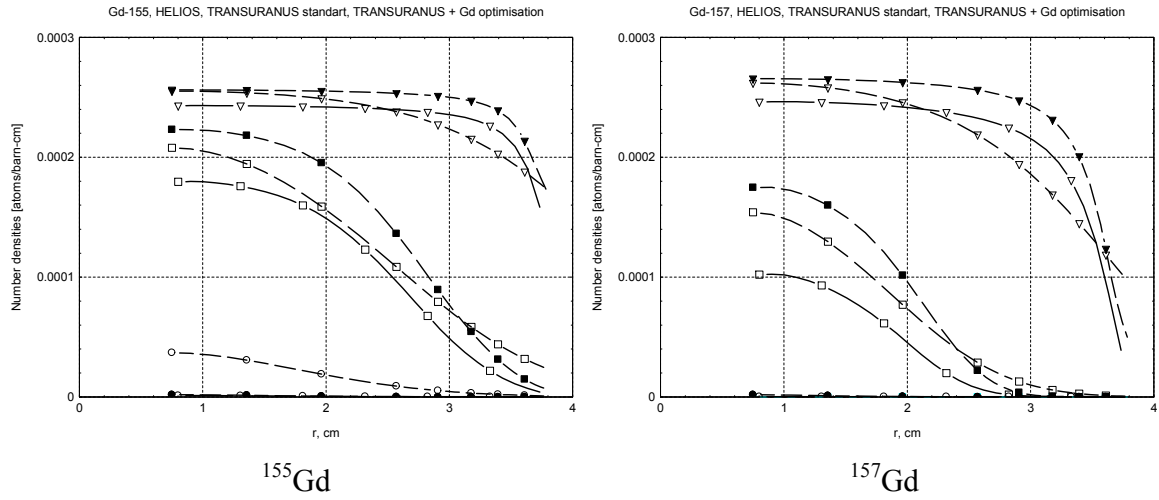
^{155}Gd

^{157}Gd

FIG. 6. Concentration of ^{155}Gd, ^{157}Gd. HELIOS (solid line) & TRANSURANUS (dashed line). Standard version of TRANSURANUS with empty marker, TRANSURANUS with Gd-optimisations with filled marker. Burnup=0.4, 3.1, 10 MW·d/kgU
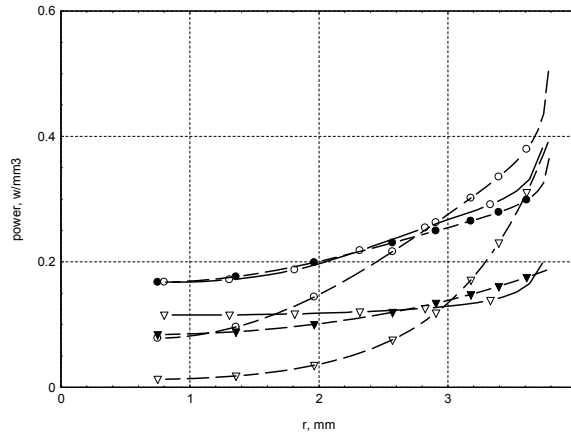
FIG. 7. Radial power distribution. HELIOS (solid line) & TRANSURANUS (dashed line). Standard version of TRANSURANUS with empty marker, TRANSURANUS with Gd-optimisations with filled marker. Burnup=0, 3.1 MW·d/kgU.

58

8. VARIATIONS OF INITIAL PARAMETERS AT CROSS-SECTION CALCULATIONS BY HELIOS

The definition of dependences sensitivity of gadolinium microscopic cross sections from a variation of initial data in   frameworks of WWER-1000 design characteristics (Table 4) was following step of our working on developing of the proposal on optimisation of code TRANSURANUS. At this stage it has been defined dependence of gadolinium microscopic cross sections from initial data, position of Gd-doped fuel pin in fuel assembly, enrichments of uranium and gadolinium. On the basis of the executed calculations (Fig. 8 and 9) it is possible to make a conclusion, that the greatest influence on gadolinium microscopic cross sections has the moderator density. Also it is necessary to calculate of gadolinium microscopic cross sections sets for each types of fuel. It is important to notice, that in calculations it was not considered changes of boric acid concentration in moderator.

TABLE 4. VARIATIONS OF PARAMETERS APPLIED FOR SIMULATING THE WWER-1000 FUEL RODS

	-	Stand.	+
Power (w/gHM)	29.74	42.49	55.23
Mean fuel temperature (K)	805	1005	1205
Mean moderator temperature (K)	558	578	598
Moderator density (g/cm^3)	0.688	0.720	0.753
T fuel radial profile		No/Yes	
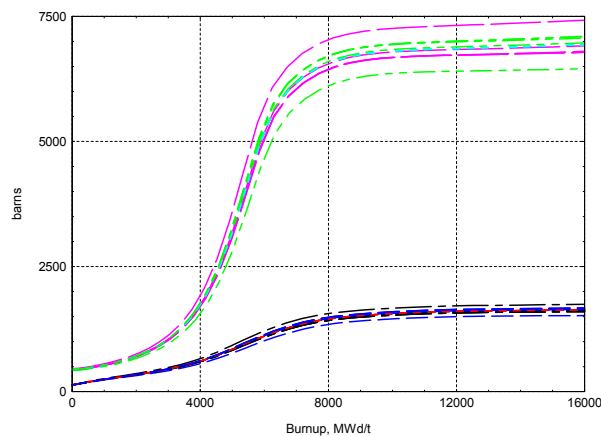
FIG. 8. Microscopic cross sections $\sigma_a^{155,157}$ of gadolinium isotopes at burnup. HELIOS. Variations of all parameters.
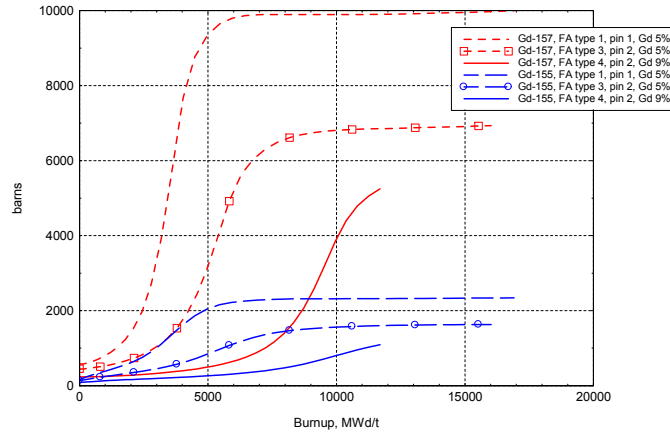
FIG. 9. Microscopic cross sections $\sigma_a^{155,157}$ of gadolinium isotopes at burnup. HELIOS. Variations of all FA types, Gd %.

9.   TESTING OF OPTIMISED VERSION OF TRANSURANUS CODE

For developing of recommendations about use of an optimised TRANSURANUS code the comparative calculations of WWER-1000 FA in basic operating modes with use of two versions of a code have been carried out. Standard version of TRANSURANUS code (v1m1j11, without changes) and Gd-optimised. Calculations are executed for a stationary mode of fuel burning and the transient - control rod ejection. The stationary mode was modelled with use of two histories of the FA power - constant power (similar accepted in calculations by HELIOS, FA burnup approximately 10 MW*d/kgU) and the real fuel power typical for core operation (FA burnup approximately to 60 MW*d/kgU). As transient the control rod ejection has been chosen. In a transitive mode the fresh fuel cartridge was considered. Below, in chapters 9.1 and 9.2, results of comparison of calculations for the chosen modes are presented (cross-code comparison).

9.1 Steady-state regime

For comparison of results of calculation by two versions of a code in a stationary mode following base characteristics are chosen:

 ⸺ Maximal temperature of fuel;

 ⸺ Maximal cladding temperature

 ⸺ Gap between fuel pellet and cladding;

 ⸺ Cladding inner pressure;

 ⸺ Cladding stresses.

On Fig. 10 the differences between two version of codes for a burning mode «HELIOS power» is presented. All results are presented in the form of "$X^{standart}$-$X^{Gd-optimised}$". The greatest difference is marked for maximal fuel temperature on an initial part of burning ($\approx$10%). Other consider characteristics change slightly (<3%). In view of good conditions of cooling the cladding temperature practically does not change.
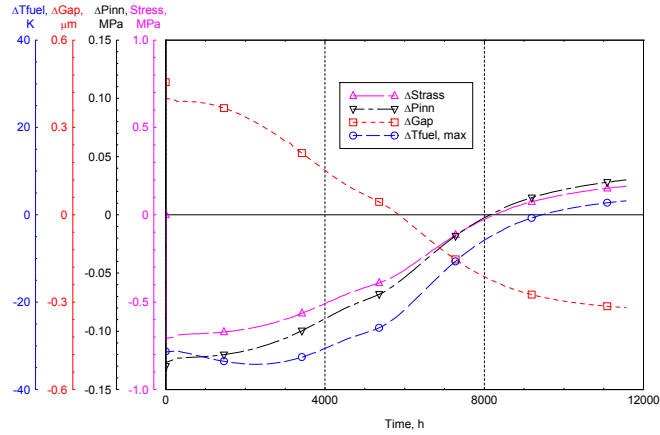
FIG. 10. Differences between two version of TRANSURANUS code: (Standart-Gd_optimised) for basic thermo-mechanical characteristics. Steady-state, HELIOS power.

On Fig. 11 the differences between two version of codes for a burning mode «real power» is presented. All results are presented in the form of "$X^{standart}$-$X^{Gd-optimised}$". The greatest difference is marked for maximal fuel temperature on an initial part of burning ($\approx$10%). Other consider characteristics change slightly (<3%). In view of good conditions of cooling the cladding temperature practically does not change.
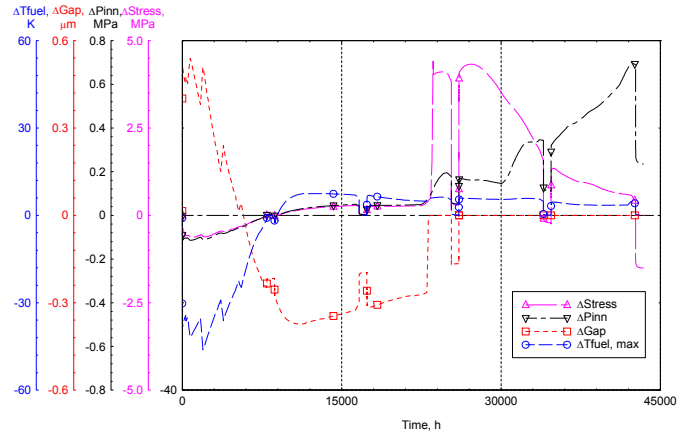
FIG. 11. Differences between two version of TRANSURANUS code: (Standart-Gd_optimised) for basic thermo-mechanical characteristics. Steady-state, real power.

9.2 Transient regime

For comparison of results of calculation by two versions of a code in a transient mode following base characteristics are chosen:

—Maximal temperature of fuel;

—Maximal temperature of cladding;

— Average enthalpy of the fuel.

On Fig. 12 the differences between two versions of codes for a transient mode is presented. All results are presented in the form of "$X^{standart}$-$X^{Gd\text{-}optimised}$". The greatest difference is marked for maximal fuel temperature ($\approx 30\%$). For average enthalpy of the fuel the difference is up to $\approx 10\%$. For cladding temperature the difference is up to $\approx 2\%$ but this event (control rod ejection) characterised by good conditions of cooling. For events with valuable worsening of heat exchange this difference (for cladding temperature) will be more significant (correspond to difference of fuel temperature).
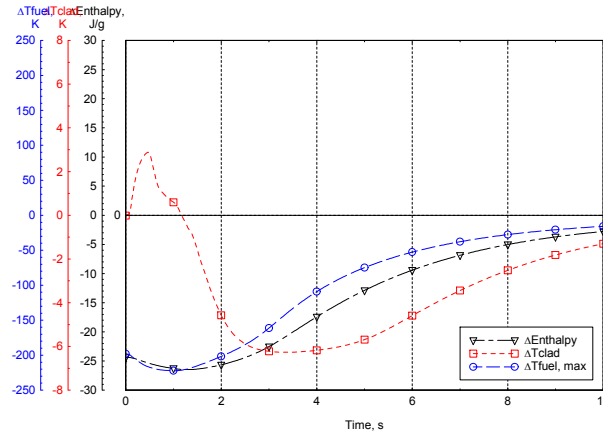
FIG. 12. Differences between two version of TRANSURANUS code: (Standart-Gd_optimised) for basic thermo-mechanical characteristics. Transient regime.

9.3 Conclusion

— Using gadolinium cross-sections in view of function of burnup and radius make TRANSURANUS results (Gd and power distribution) close to HELIOS.

— Gadolinium cross-sections can be present as approximation formula, direct table values and so on.

— Sets of gadolinium cross-sections can be calculated by spectral code.

— On the basis of the executed calculations it is possible to make a conclusion, that the greatest influence on gadolinium microscopic cross sections has the moderator density. Also it is necessary to calculate of gadolinium microscopic cross sections sets for each types of fuel.

— Using proposed Gd-optimisation for TRANURANUS code make the maximal fuel temperature higher up to $\approx 10\%$ in steady-state regimes. Other consider characteristics change slightly ($<3\%$). In view of good conditions of cooling the cladding temperature practically does not change.

— In transient regimes Gd-optimisation make the maximal fuel temperature higher up to $\approx 30\%$. For average enthalpy of the fuel the difference is up to $\approx 10\%$. For events with valuable worsening of heat exchange using proposed Gd-optimisation will be have more significant influence on cladding temperature (correspond to difference of fuel temperature).

REFERENCES

[1]   EUROPEAN COMMISSION, Transuranus handbook. Document Number Version 1 Modification 1 Year 2011 ('V1M1J11') January 2011, EC Join Research Centre Institute for Transuranium Elements.

[2]   LASSMANN, K., TRANSURANUS: a fuel rod analysis code ready for use, J. Nucl. Mater. **188** (1992) 295.

[3]   CASSEL, J.J. et al. HELIOS: Geometric Capabilities of a New Fuel-Assembly Program. Topical Meeting on Advances in Mathematics, Computations and Reactor Physics. Pittsburg, Pennsylvania, April 28 – May 2 1991, Vol.2, pp 10.2.1 1–13.

[4]   INTERNATIONAL ATOMIC ENERGY AGENCY, Characteristics and use of urania-gadolinia fuels, IAEA-TECDOC-844, November 1995, p.73.

[5]   IEREMENKO, M., OVDIENKO, I., Optimization of the TRANSURANUS burnup model for Gd-doped WWER-1000 fuel pins based on results of the HELIOS code, Power Point version, available from:
http://www.iaea.org/OurWork/ST/NE/NEFW/Technical_Areas/NFC/documents/fuel-engineering/TM-Chengdu-2013/Presentations/Session_1/1.4_Optimization_of_the_TRASURANUS_burnup_model_for_Gd-doped_WWER-1000_fuel_pins_based_on_results_of_HELIOS_code_(M._Ieremenko,_et._al.).pdf

OVERVIEW OF THE BISON MULTIDIMENSIONAL FUEL PERFORMANCE CODE

R. L. Williamson[1], J. D. Hales[a], S. R. Novascone[a], G. Pastore[a], D. M. Perez[a]
B. W. Spencer[a], R. C. Martineau[a]

Abstract. BISON is a modern multidimensional multiphysics finite-element based nuclear fuel performance code that has been under development at the Idaho National Laboratory (USA) since 2009. A brief background is provided on the code's computational framework (MOOSE), governing equations, and material and behavioral models. Ongoing code verification and validation work is outlined, and comparative results are provided for select validation cases. Recent applications are discussed, including specific description of two applications where 3D treatment is important. A summary of future code development and validation activities is given. Numerous references to published work are provided where interested readers can find more complete information.

1. INTRODUCTION

BISON is a modern finite-element based nuclear fuel performance code that has been under development at the Idaho National Laboratory (USA) since 2009 [1]. The code is applicable to both steady and transient fuel behavior and can be used to analyze 1D (spherically symmetric), 2D (axisymmetric and plane strain) or 3D geometries. BISON has been used to investigate a variety of fuel forms including LWR oxide fuel [1], TRISO coated-particle fuel [2], and metallic fuel in both rod [3] and plate geometries.

This overview paper provides a brief background on the code's computational framework, governing equations, and material and behavioral models. Ongoing code verification and validation efforts are outlined. Recent applications are discussed with specific description of two applications where a 3D treatment is important. A summary of planned code development and validation activities is given. Numerous references to published work are provided where interested readers can find more complete information.

2. BACKGROUND

BISON is built using the INL Multiphysics Object-Oriented Simulation Environment, or MOOSE [4]. MOOSE is a massively parallel, finite element-based framework to solve systems of coupled non-linear partial differential equations using the Jacobian-Free Newton Krylov (JFNK) method [5]. This enables investigation of computationally large problems, for example a full stack of discrete pellets in a LWR fuel rod, or every rod in a full reactor core. MOOSE supports the use of complex two and three-dimensional meshes and uses implicit time integration, important for the widely varied time scales in nuclear fuel simulation. An object-oriented architecture is employed which greatly minimizes the programming effort required to add new material and behavioral models.

---

[1] Fuel Modeling and Simulation Department, Idaho National Laboratory, Idaho Falls, Idaho, USA

The BISON governing relations currently consist of fully-coupled partial differential equations for energy, species, and momentum conservation. Users can select a subset of these equations (e.g., energy and momentum for thermomechanics analysis) within the input file. The code employs both nonlinear kinematics, which accounts for large deformation, and nonlinear material behavior. A detailed description of the nonlinear kinematics is provided in [1]. For nonlinear plasticity and creep, strains are calculated implicitly utilizing the radial return method; the specific procedure is outlined in [6].

Focusing principally on UO_2 fuel, models are included in BISON to describe temperature and burnup dependent thermal properties, solid and gaseous fission product swelling, densification, thermal and irradiation creep, fracture via relocation or smeared cracking, and fission gas production, generation, and release [1]. For TRISO coated-particle fuel, an empirical model is included to compute CO production, which can be added to released fission gas to affect particle pressure [2].

Recently an improved fission gas release model was implemented in BISON, based on the work of Pastore et al. [7]. While retaining a physics-based description of the relevant mechanisms, the model is characterized by a level of complexity suitable for application to engineering-scale nuclear fuel analysis and consistent with the uncertainties pertaining to some parameters. The treatment includes the fundamental features of fission gas behavior, among which are gas diffusion and precipitation in fuel grains, growth and coalescence of gas bubbles at grain faces, grain growth and grain boundary sweeping effects, thermal, athermal, and transient gas release. This model, as implemented in BISON, was recently compared to a variety of experiments from the FUMEX-II [8] and FUMEX-III [9] International Atomic Energy Agency (IAEA) Coordinated Research Projects (CRP) [10]. Comparison of results with available experimental data up to moderate burn-up, demonstrated an encouraging predictive accuracy, without any fitting applied to the model parameters.

Focusing initially on Zircaloy as a clad material, models are available for instantaneous plasticity, thermal and irradiation creep, and irradiation growth. The plasticity and creep models can be applied simultaneously, in cases where both phenomena are active.

Gap heat transfer is modeled in the traditional manner with the total conductance across the gap computed as a sum of the gas conductance, the increased conductance due to solid-solid contact, and the conductance due to radiant heat transfer [1]. This model is typically applied between the fuel and clad, but can also be used to simulate heat transfer between individual pellets, between a pellet and end cap, or between fracture surfaces.

Mechanical contact between materials is implemented through the use of node/face constraints, which prevent nodes on one side of an interface from penetrating faces on the other side of the interface. This is accomplished in a manner similar to that detailed by Heinstein and Laursen [11] and discussed in greater detail in [12]. Finite element contact is notoriously difficult to make efficient and robust in three dimensions and continuous effort is underway to improve the mechanical contact algorithms in BISON.

For LWR fuel, the pressure in the gap and plenum is computed assuming a single cavity volume and using the ideal gas law. The moles of gas, the temperature, and the cavity volume are free to change with time. The moles of gas at any time is computed as the original amount of gas (computed based on original pressure, temperature, and volume) plus the amount in the cavity due to fission gas released. The gas temperature is computed as a weighted average of the pellet exterior and cladding interior surfaces, with weighting based on an approximation of the volume of gas contained between

the solid surfaces. The cavity volume is computed as needed based on the evolving pellet and clad geometry.

A variety of other material models have been implemented in BISON, often by users needing a specific model not available in the material library. These include thermal models for MOX and U_3Si_2 fuel, thermal and mechanical models for HT9 stainless steel cladding, irradiation-induced strain and creep models for pyrolitic carbon, and an irradiation creep model for SiC. These models are described in more detail in the BISON theory manual [13]. As mentioned above, the object-oriented architecture employed in MOOSE/BISON significantly minimizes the programming required to add new material and behavior models.

3. VERIFICATION AND VALIDATION

From the beginning, the development of BISON has been accompanied by the creation of numerous verification tests in which specific features of the code are tested to see if they compute the correct analytical or known solution. There are currently over 800 regression tests in the MOOSE/BISON framework. During code development, these regression tests are run frequently on a variety of computer platforms, and the results are checked against trusted solutions.

An effort is also underway to assess BISON's capability to predict real fuel behavior, principally by comparison to data from a variety of instrumented LWR fuel rods. This assessment effort has been invaluable, leading to the discovery of development oversights and errors not apparent from the simpler regression tests. Additionally it has led to improved confidence in BISON's ability to predict nuclear fuel behavior.

To date, 21 assessment cases have been simulated with BISON, as summarized in Table 1. Indicated in the table are the measured quantities for comparison, namely fuel centerline temperature (FCT) at beginning of life (BOL), throughout life (TL) and during power ramps (Ramps), fission gas release (FGR), cladding elongation (Clad-Elong), and cladding outer diameter following pellet clad mechanical interaction (PCMI). Many of these assessment cases grew out of participation in the IAEA sponsored FUMEX-III Coordinated Research Project [9] and are priority cases from either FUMEX-II [8] or FUMEX-III. Other cases were chosen based on recommendations from nuclear fuel experts. This section summarizes comparisons for a selected set of the cases in Table 1, as identified with an asterisk, to give an overview of the BISON validation effort. A more detailed description of this activity is given in [14] and a comprehensive assessment paper is in preparation.

3.1 Beginning of Life Fuel Centerline Temperature

The IFA-431 and IFA-432 fuel assemblies were irradiated in the Halden Boiling Water Reactor from 1975 to 1977 and 1975 to 1984, respectively. Each assembly contained six instrumented rods, with centerline temperature instrumentation in the top and bottom ends of the fuel pellet stack. The test rods initially contained fresh UO_2 fuel. Three of the six rods (1, 2, and 3) from each experiment were used for Beginning of Life (BOL) temperature comparisons. All six rods were meshed using 2D-RZ axisymmetric quadratic (quad-8) elements. For simplicity, the pellet stack was modeled as a smeared column containing thermocouple holes at the top and bottom, to best represent the actual fuel geometry.

Fuel cracking occurs during the first rise to power, increasing the effective fuel volume and decreasing the gap width. The gap width and thus cracking have a strong influence on fuel

temperature. Cracking is modeled in BISON using either a simple empirical relocation model or a more mechanistic smeared cracking model. For the BOL comparisons shown here, the empirical relocation model was used. Calibration of this model to a variety of experiments was considered in conjunction with this study, as described in Swiler et al. [15]. A relocation activation energy of 5 kW/m was used here based on this study.

Temperature comparisons during the first rise to power are significant since they isolate several important aspects of fuel rod behavior before complexities associated with higher burnups are encountered. For example, proper prediction of BOL centerline temperatures requires accurate models for the fuel and clad thermal conductivity, gap heat transfer, thermal expansion of both the fuel and the clad materials (to predict an accurate gap width), and fuel relocation.
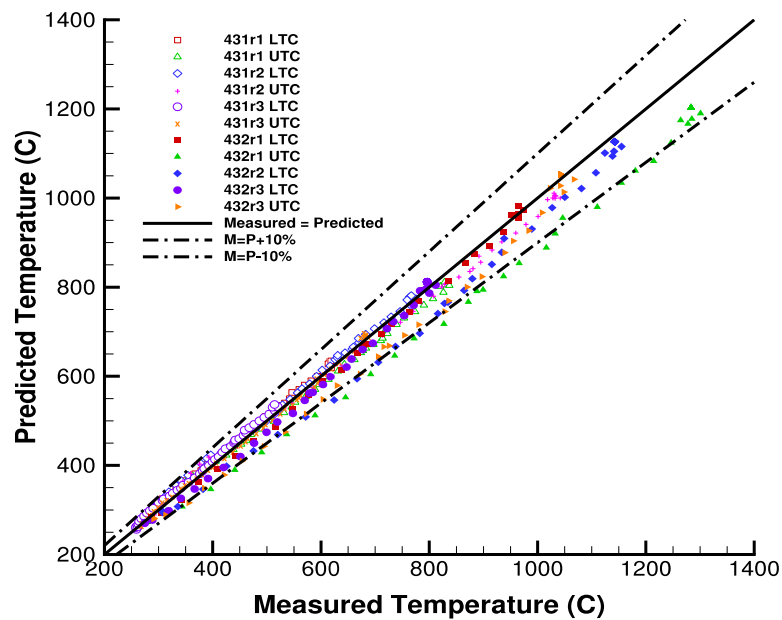
FIG. 1. Measured vs. predicted fuel centerline temperature for rods 1, 2, and 3 in IFA-431 and IFA-432. LTC and UTC stand for lower and upper thermocouples respectively.

TABLE 1. SUMMARY OF BISON LWR ASSESSMENT

Experiment	Rod	FCT BOL	FCT TL	FCT Ramps	FGR	Clad-Elong	Clad-Dia (PCMI)
IFA-431*	1	X					
IFA-431*	2	X					
IFA-431*	3	X					
IFA-432*	1	X					
IFA-432*	2	X					
IFA-432*	3	X					
IFA-513	1	X	X				
IFA-513	6	X	X				
IFA-515.10	A1	X	X				
IFA-597.3	7			X		X	
IFA-597.3	8			X			
Risø-3*	AN3			X	X		
Risø-3	AN4			X	X		
FUMEX-II	27(1)				X		
FUMEX-II	27(2a)				X		
FUMEX-II	27(2b)				X		
FUMEX-II	27(2c)				X		
Risø-3*	GE7						X
OSIRIS	J12						X
REGATE							X
IFA-431 (3D)	4	X					

Figure 1 compares measured and predicted BOL fuel centerline temperature for all six rods. Note that for IFA-432 Rod 2, only lower thermocouple comparisons are possible since the gamma thermometer in the upper rod location failed to operate. The overall agreement is excellent, with only one rod falling outside of the +/-10% error band.

3.2 Fuel Temperature and Fission Gas Release during Ramp Testing

The Risø AN3 experiment was one of the FUMEX-II priority cases [8] and was conducted at the Risø DR3 water-cooled HP1 rig. This experiment utilized a re-fabricated fuel rod from a PWR fuel pin irradiated over four cycles. The re-fabricated rod was shortened and fitted with a fuel centerline thermocouple and pressure transducer. The re-fabricated (shortened) rod geometry was assumed for both the base irradiation and ramp test. The pellet stack was modeled as two smeared fuel blocks, with an annular block at the top to account for the thermocouple hole. The fuel and clad were modeled using a 2D-RZ axisymmetric quad-8 mesh.

Figure 2 compares the fuel centerline temperature and fission gas release to both experimental data and predictions from the well-known and validated codes TRANSURANUS and ENIGMA. Data for code comparisons were digitized from plots provided in the FUMEX-II final report [16]. In

view of the uncertainties involved in FGR modeling, the predictions are very reasonable, both in terms of FGR value at the end of life and kinetics of the phenomenon. Fuel centerline temperature comparisons are excellent. The more accurate prediction of fission gas release observed with BISON leads to better fuel centerline temperature comparisons as gas release and fuel temperature are strongly coupled. Obviously this single rod comparison does not permit any general comparisons between BISON and other fuel performance codes.
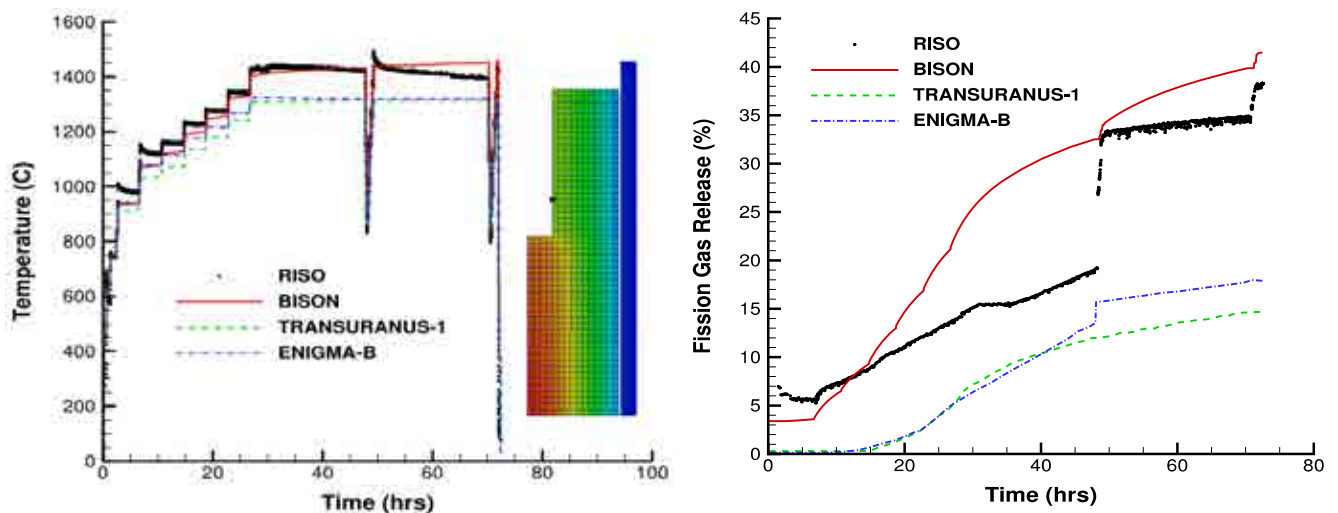
FIG. 2. Fuel centerline temperature and fission gas release comparisons during the Risø AN3 power ramp. Comparisons are included to experimental data and other code predictions. The contour plot shows a typical drilled fuel mesh (magnified 5X in the radial direction) with the dot indicating the comparison location.

3.3 Pellet Clad Mechanical Interaction

The Risø GE7 test was one of the FUMEX-III priority cases [9] also conducted at the HP1 rig under BWR conditions. This experiment utilized a fuel pin segment that was base irradiated over four reactor cycles and then bump tested. The segment was neither punctured nor opened for re-fabrication for the bump test. Although the axial power distribution during base irradiation was relatively flat, there was a significant axial power profile, weighted heavily to the bottom of the fuel segment, during the bump test. The rod segment contained 72 fuel pellets and was modeled assuming 2D-RZ axisymmetry with each pellet considered separately (discrete pellet mesh). Quadratic quadrilateral finite elements were used.

Comparison of the predicted and measured clad final outer diameter, as a function of rod length, is shown in Fig. 3. BISON over-predicts the clad creep-down during base irradiation, resulting in a rod diameter approximately 10 μm less than measured values. The prediction, however, is very reasonable. Permanent clad deformation during the bump test is observed over roughly the bottom two-thirds of the rod. BISON predicts the shape of this deformation nicely. The high frequency oscillation in the BISON curve is a result of ridges formed in the cladding at pellet-pellet interfaces due to the hourglass shape of the pellets. Note that the amplitude of the ridges compare very well with that observed experimentally. The commonly observed ``bamboo'' profile along the clad length

is obvious in a contour plot included in the figure, which shows the radial displacement on a short section of the deformed clad. Each displacement peak (red zone) corresponds to one of the peaks in the BISON predicted rod diameter curve. Also included in Fig. 3 are results from ENIGMA as provided by personnel at the National Nuclear Lab. BISON compares well with ENIGMA, which also over predicts the fuel creep-down resulting in an under prediction of the final fuel diameter.

3.4 TRISO Coated-particle Fuel

Note th   rticle fuel, based on code
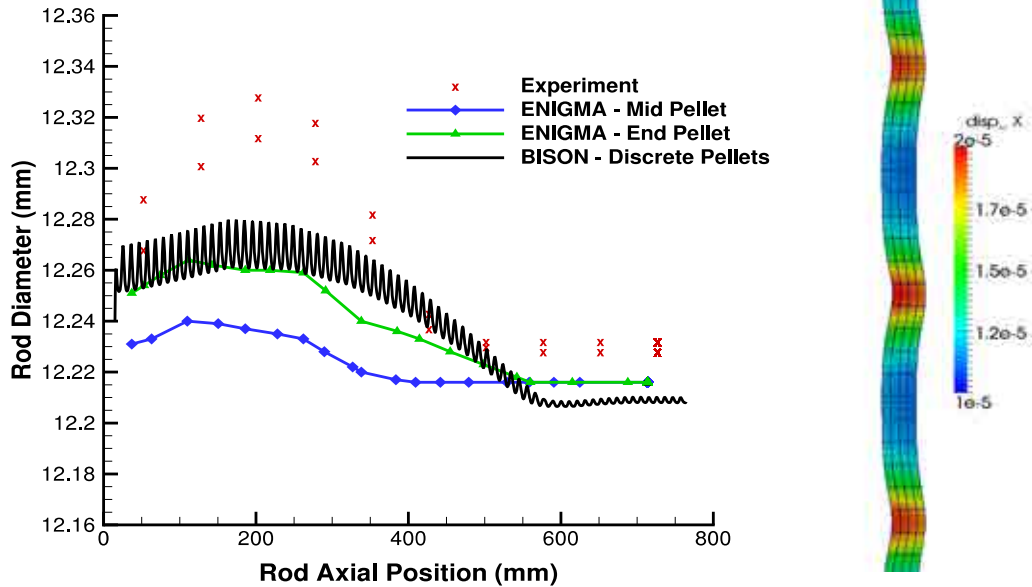
FIG. 3. BISON post-bump rod diameter predictions compared to measurements and ENIGMA calculations. Also shown are radial displacement contours for a short section of cladding. The radial mesh is scaled 2X and the displacements magnified 30x to improve visualization.

comparisons to numerous benchmark cases from an IAEA CRP [17], was recently completed and is documented in [2].

4. APPLICATIONS

BISON has been applied to a variety of LWR fuel rods using both smeared and discrete pellet meshing, and assuming both axisymmetric and 3D behavior (see [1, 14]). Additionally, the code has been applied to TRISO coated-particle fuel [2], fast oxide fuel, and metal fuel in both rod and plate form [3]. In this section, two LWR applications are described, in both cases where 3D analysis is important. The first considers fuel with a missing pellet surface and the second investigates the effect of fuel pellet eccentricity.

4.1 Simulation of Missing Pellet Surface Defects

4.1.1 *Problem and Model Description*

Local geometric irregularities in fuel pellets caused by manufacturing defects known as missing pellet surfaces (MPS) can in some circumstances lead to elevated cladding stresses that are sufficiently high to cause cladding failure [18, 19]. Accurate modeling of these defects can help understand and possibly prevent these types of failures.

To study the influence of MPS defects on the cladding, results from 1.5D or 2D fuel performance analyses are typically mapped to thermo-mechanical models that consist of a 2D plane-strain slice or a full 3D representation of the geometry of the pellet and clad in the region of the defect [20, 21]. There are three main potential sources of error due to mapping results from global fuel rod simulations to local 2D or 3D models of the defect. The first of these is that errors can be introduced in mapping results from a fuel rod model to provide the boundary conditions for a local model of the defect region. Secondly, the fuel/cladding system is influenced by multiple coupled physics, all of which influence both the global behavior of that system as well as the behavior in the region of a defect. These physics and behavior models are typically included in a fuel rod simulation, but may not necessarily be included in a local model of the region near the defect. Finally, the geometry of the MPS defect is inherently 3D. Problems can arise due to the use of reduced dimensionality models of the defect region.

To address the sources of error outlined above, BISON has been used to model short segments of fuel rods that include a pellet with a defect. A single 3D model is used to model both the global fuel performance and the local effects of the defect, so there is no need to map results between two models. The complete set of coupled physics and behavior models used in the fuel rod simulation is also used to model the region of the defect, and because the model is in 3D, its dimensionality is appropriate for the phenomena it is used to simulate. Note that this investigation is only summarized here and is described in greater detail in [22].

Figure 4 shows two finite element meshes of rod segments with imperfections used in this work. A constant-depth missing surface extends over the full depth of a pellet at the center of the five-pellet segment in each of these models. One case has a 0.25 mm deep defect, and the other has a 0.5 mm deep defect. Both of these models are run under the same conditions to study the effect of varying the imperfection depth. The models take advantage of a symmetry plane passing through the center of the defect, and boundary conditions are applied to enforce symmetry conditions. Both models have 106589 nodes and 22578 20-noded quadratic elements. Quadratic elements are used for both the fuel and the cladding because they smoothly represent 3D curved geometry for thermal and mechanical contact.
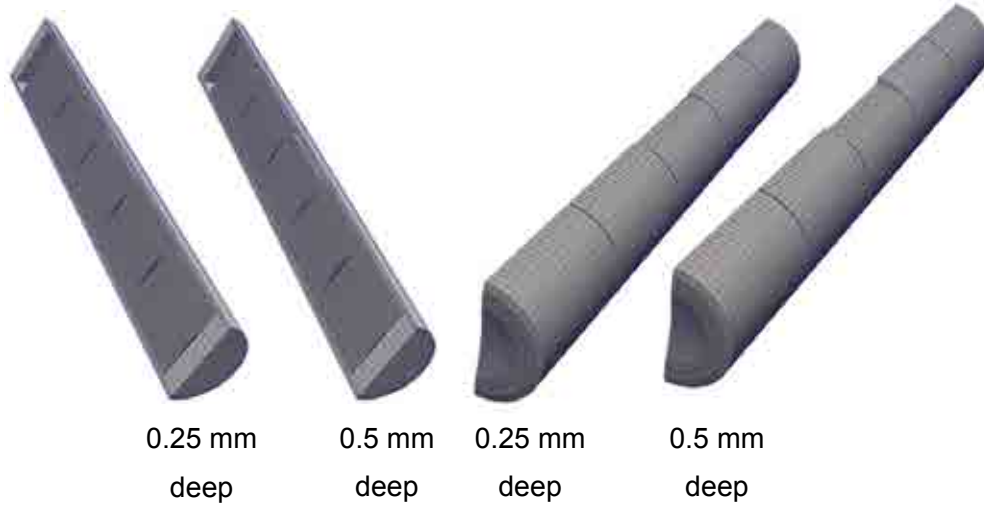
FIG. 4. Computational meshes of rod segments with a defective pellet.
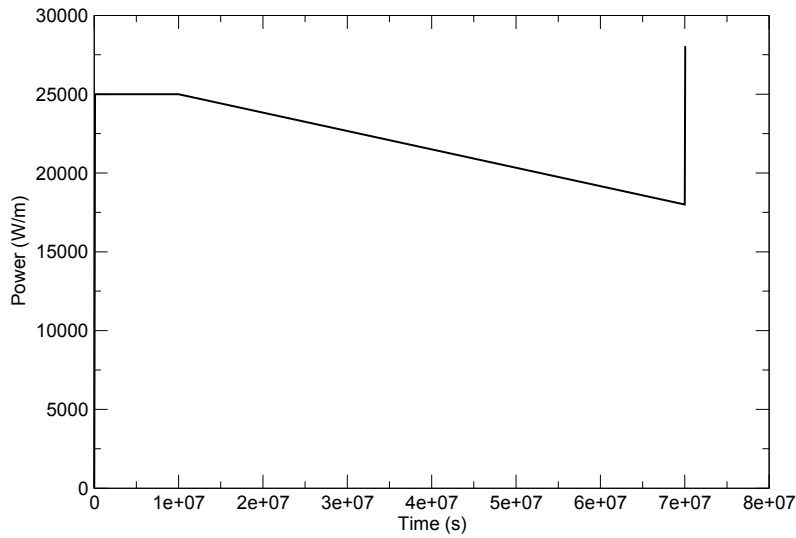
FIG.5. Idealized power history for the MPS/analyses.

Coupled heat conduction and solid mechanics equations are solved. The pellets have temperature and burnup-dependent conductivity and swelling, and are modeled as linear elastic with thermal expansion. The cladding material has constant thermal conductivity and a combined creep and plasticity model is used for the mechanical constitutive behavior. Cladding creep is dependent on both temperature and fast neutron flux. Fission provides a volumetric heat source to the fuel. Thermal conductance across the fuel/cladding gap is based on distance, roughness, gas composition, and surface emissivity. A flux boundary condition is used to model heat transfer from the cladding to the coolant. This boundary condition employs a constant convection coefficient to calculate the

flux between the cladding surface, which has a calculated temperature, and the fluid, which has a prescribed temperature.

The fission rate is uniformly distributed both axially and radially. The idealized power history shown in Fig. 5 is applied to both models and includes an initial power-up, base irradiation that includes holding the power constant for a time and then slowly ramping it down, and then a power ramp after 7e+7 seconds. The power ramp is expected to cause elevated stress and strain in the region of the defect due to pellet-clad mechanical interaction.

4.1.2   Results

The MPS defect causes elevated temperature at the center of the pellet and in the region of the pellet adjacent to the defect due to decreased conductance across the gap at the defect. The clad temperature is reduced in the area immediately across from the defect, and is elevated in neighboring areas. These effects can be seen in Fig. 6(a), which shows the pellet and clad temperature at the end of the ramp, and in Fig. 6(b), which shows just the clad, with displacements magnified 15x. As expected, the effects of the MPS defect are more pronounced with the deeper defect.

| 0.25 mm | 0.5 mm | | 0.25 mm | 0.5 mm |
| deep defect | deep defect | | deep defect | deep defect |

(a) pellets and cladding

(b) only cladding shown
(deformations magnified 15x)
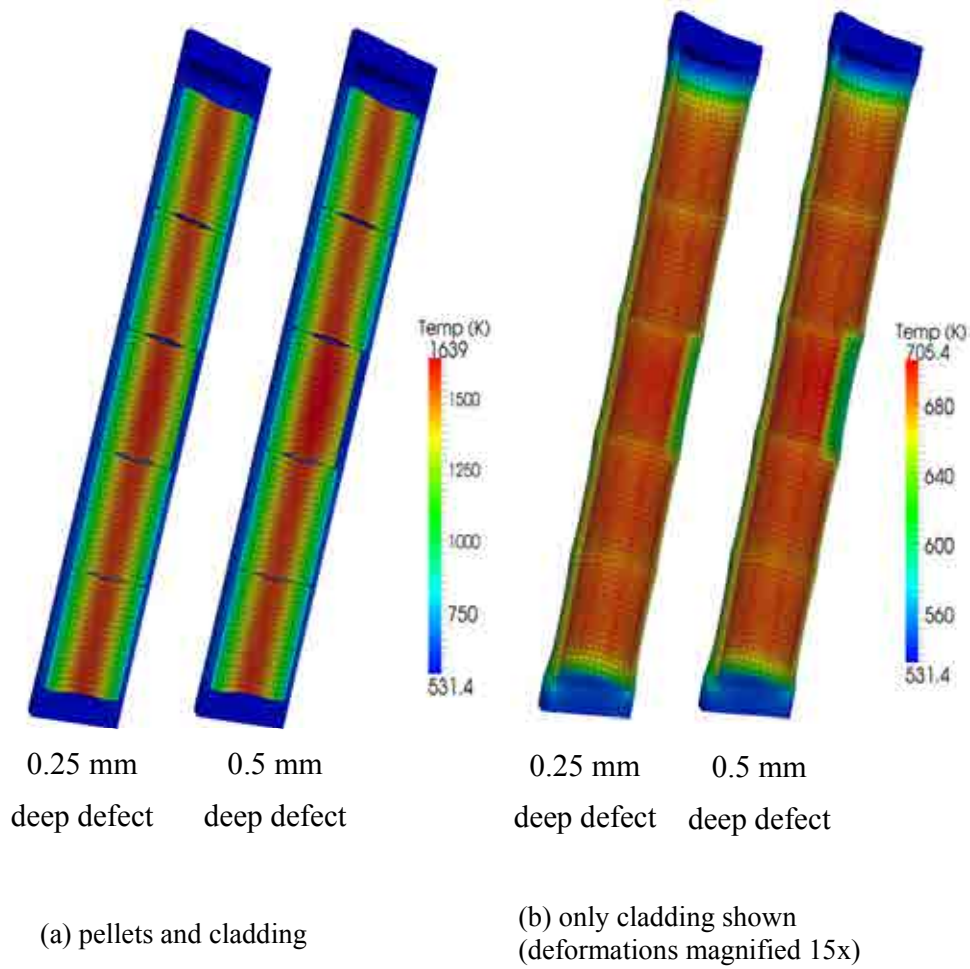
FIG. 6. Predicted temperature at end of power ramp.

The distance between the pellet and the clad is much greater adjacent to the MPS defect than it is for undamaged pellets. This causes a dramatic decrease in the conductance across the gap and a corresponding decrease in heat transfer between the pellet and clad adjacent to the defect. The temperature is thus elevated in the fuel near the surface with the defect. Because of the higher fuel temperature, the cladding temperature is elevated around the boundaries of the defect, where the gap conductance is unaffected by the defect. Immediately adjacent to the defect, the cladding temperature is significantly decreased because of the lower gap conductance.

The mechanical effects of the MPS defect are evident in contour plots of the von Mises stress and effective creep strain in the cladding, shown in Fig. 7 and Fig. 8 respectively. These are shown with displacements magnified 15x at the end of the power ramp for the two different defect depths. For both cases, there are pronounced pellet-clad mechanical interaction (PCMI) effects. The clad across from the defect bends inward due to the coolant pressure, and is supported around the boundaries of the defect in the pellet containing the defect and on the rims of the pellets above and below the defect. These regions have high contact pressures and elevated stresses in the cladding. This region exhibits classical plate bending behavior, with high tensile stresses in the interior of the cladding and high compressive stresses on the exterior of the cladding at the center of the defect.

Around the boundaries of the defect, the stresses are reversed, with high compressive stresses on the cladding interior and high tensile stresses on the cladding exterior.

0.25 mm 0.5 mm

deep defect deep defect Zoomed-in view of 0.5 mm deep defect
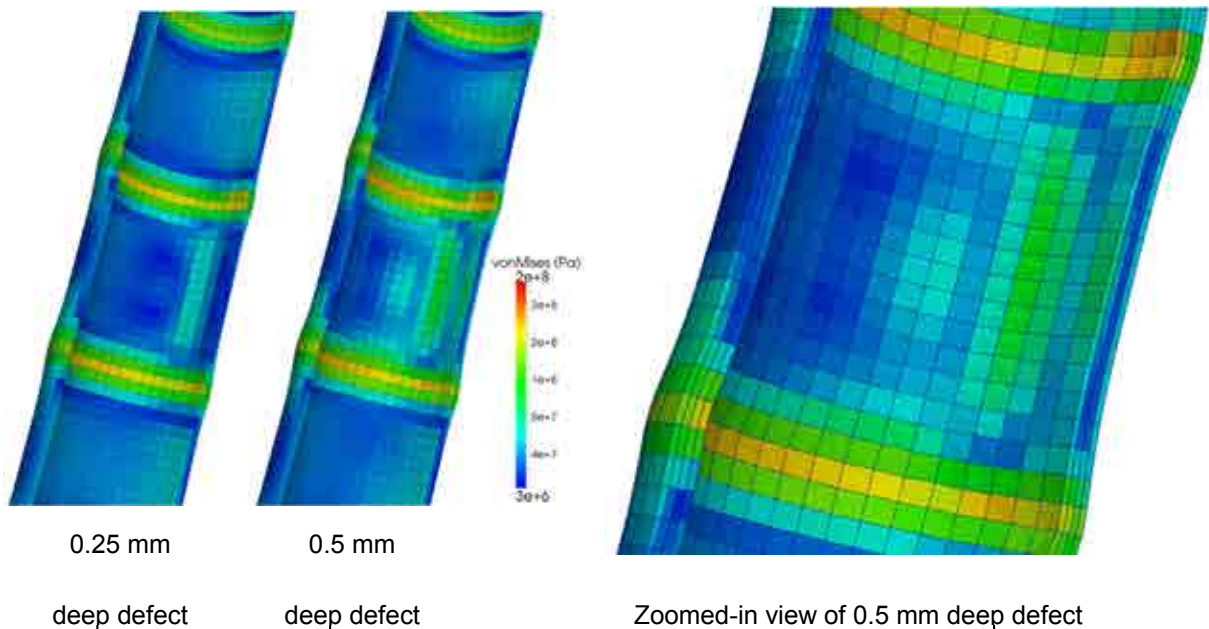
FIG. 7. Predicted von Mises stress at end of power ramp. Displacements are magnified 15x.

Cladding creep has a significant effect in relaxing stresses, both during the base irradiation and during the power ramp. As shown in Fig. 8, the creep strains are low adjacent to the defect, but high around the boundary of the defect. This is largely due to the fact that temperatures are lower adjacent to the defect and higher around its edges.

Contact friction between the fuel and cladding is another effect that significantly influences cladding mechanical behavior near the defect. BISON currently models 3D frictionless and glued contact, but not frictional contact. Frictionless contact was used in the models presented here. The 0.5 mm deep defect model was also run with the baseline set of parameters, but with glued contact, which allows no tangential slip once mechanical contact is established. A comparison of the hoop stresses at the end of the power ramp for the frictionless and glued contact cases is shown in Fig. 9. The increased constraint around the boundaries of the defect due to glued contact result in significantly higher tensile stresses on the cladding interior at the center of the defect. The actual result is likely bounded by the results obtained using the frictionless and glued contact models and clearly demonstrates the need for a frictional contact model. Work is currently underway to enable 3D frictional contact in BISON.

MPS defects clearly have a significant effect on the mechanical response in the cladding in the region of the defect. As shown in the analyses presented here, larger defects result in elevated stresses in the cladding. Stresses also increase with increased friction between the pellet and clad.

0.25 mm
deep defect

0.5 mm
deep defect

Zoomed-in view of 0.5 mm deep defect
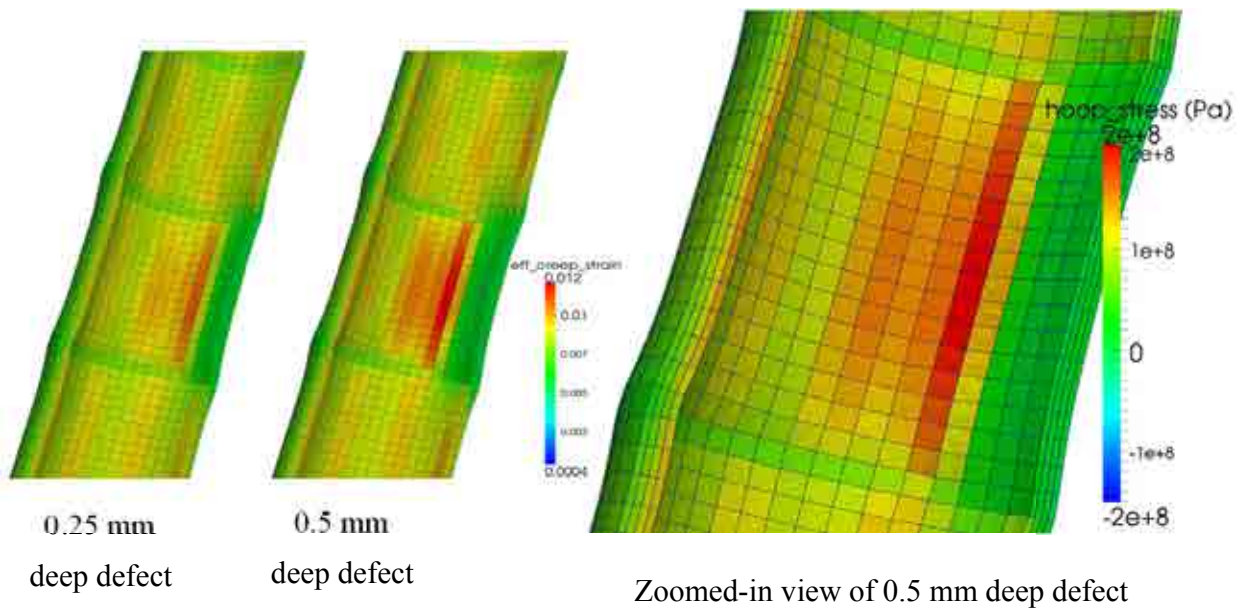
FIG. 8. Predicted effective creep strain at end of power ramp. Displacements are magnified 15x.

Frictionless
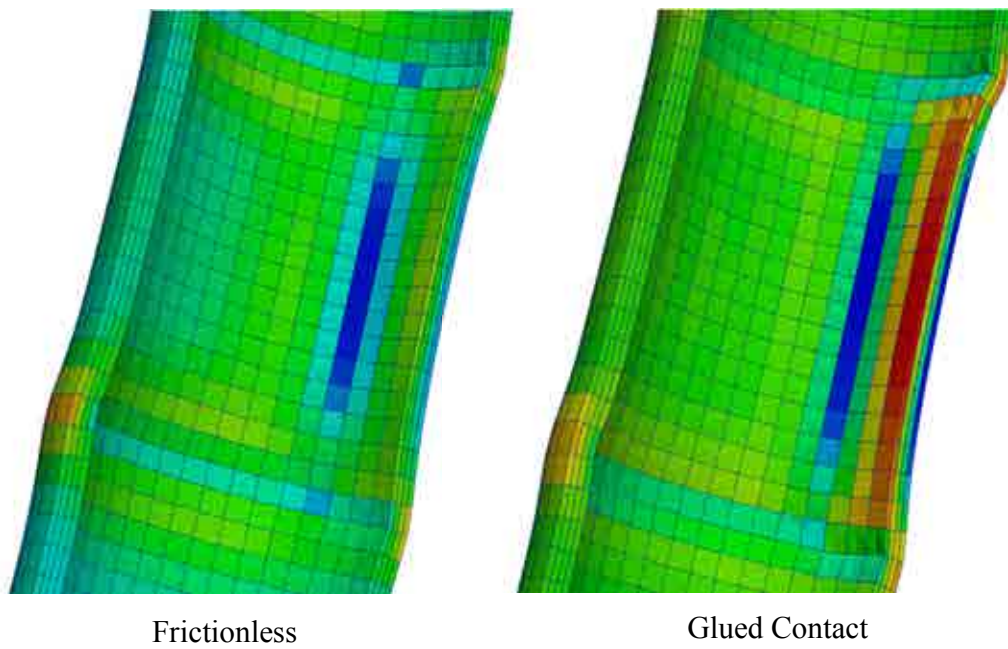
Glued Contact

FIG. 9. Effect of frictionless versus glued contact on predicted hoop stress. Displacements are magnified 15x.

76

4.2 Simulation of pellet eccentricity effects

4.2.1 Problem and model description

The Halden IFA-431 experimental assembly was briefly described in Section 3.1. Rod 4 of this series was designed to analyse the effects of xenon-filled gaps and pellet eccentricity. As shown schematically in Fig. 10, the top and bottom of the fuel column were mechanically constrained with oversized pellets and molybdenum rods to ensure concentricity of the test pellets at the top of the fuel column and eccentricity of the test pellets at the bottom of the fuel column [23]. Due to the non-axisymmetric geometry of this experiment, it is not a viable candidate for analysis using most fuel performance codes, which are limited to, at most, 2D analysis. This experiment was recommended by Halden researchers as one that could benefit from 3D analysis using BISON. The objective was to gain insight into the cause of differences between the measured temperature in concentric and eccentric rods. Note that this investigation is only summarized here and is described in greater detail in [24].
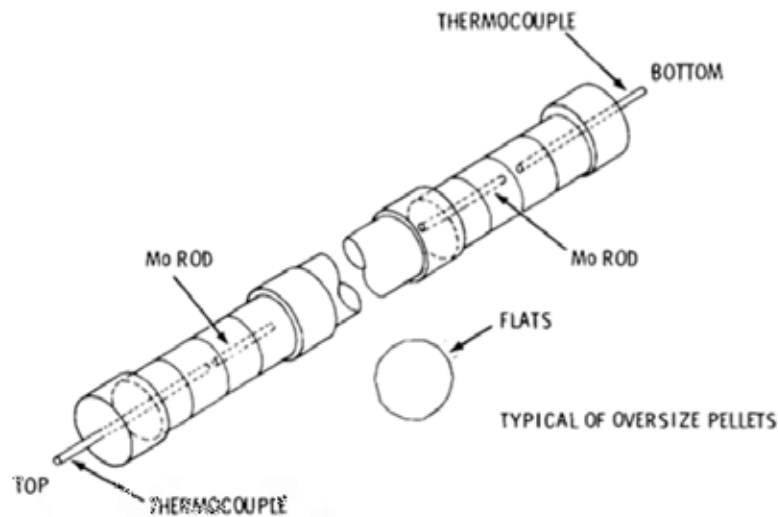
FIG. 10. IFA-431 Rod 4 fuel column schematic [23].

To simplify analysis, the top and bottom of the fuel column were modelled as two separate shortened rods. The 3D models of these rod sections used hex-20 elements, represented the fuel as a smeared column, and employed a symmetry plane passing through the fuel centreline. Figure 11 shows the concentric (left) and eccentric (right) meshes used for this comparison. A simplified power history was assumed, with the power ramped from 0 to 20 kW/m over a 90,000 second time period.

4.2.2 Results

Initial predictions indicated that BISON was over-predicting the fuel centreline temperature for both the concentric and eccentric comparisons. It was observed that the relocation model, with its default activation point of 19.7 kW/m, was not affecting the gap size except at the highest power

levels in the study. Experimental observations such as [25], however, indicate that fuel cracking (and thus the onset of relocation) occurs at much lower power, on the order of 5 kW/m. This served as motivation for a study of the effects of the relocation activation power. The results of this parametric study, shown in Fig. 12, concur that the relocation model should be activated at a power of roughly 5 kW/m, much lower than the default value. A recently reported more rigorous parametric study reached a similar conclusion [15].
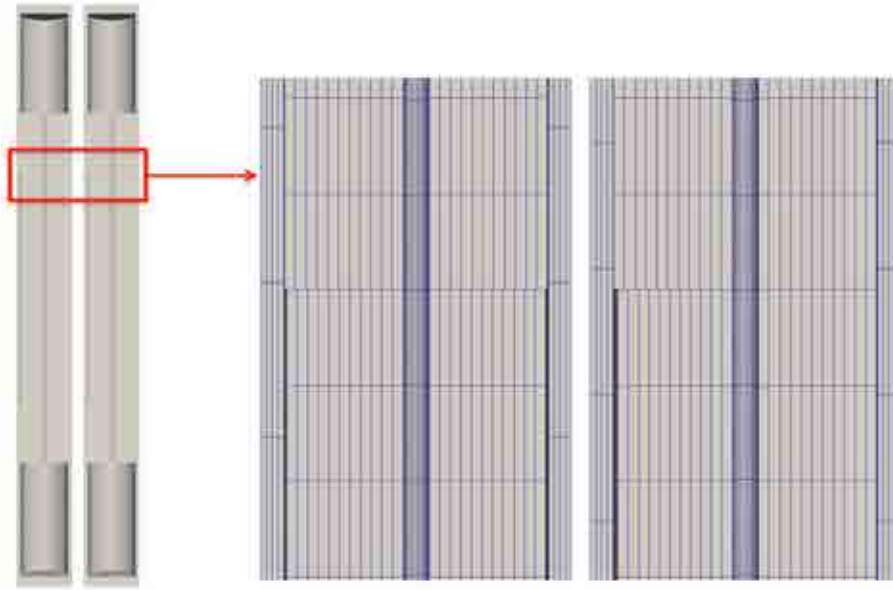
FIG. 11. IFA-431 Rod 4 3D half symmetry meshes for concentric (left) and eccentric (right) sections.
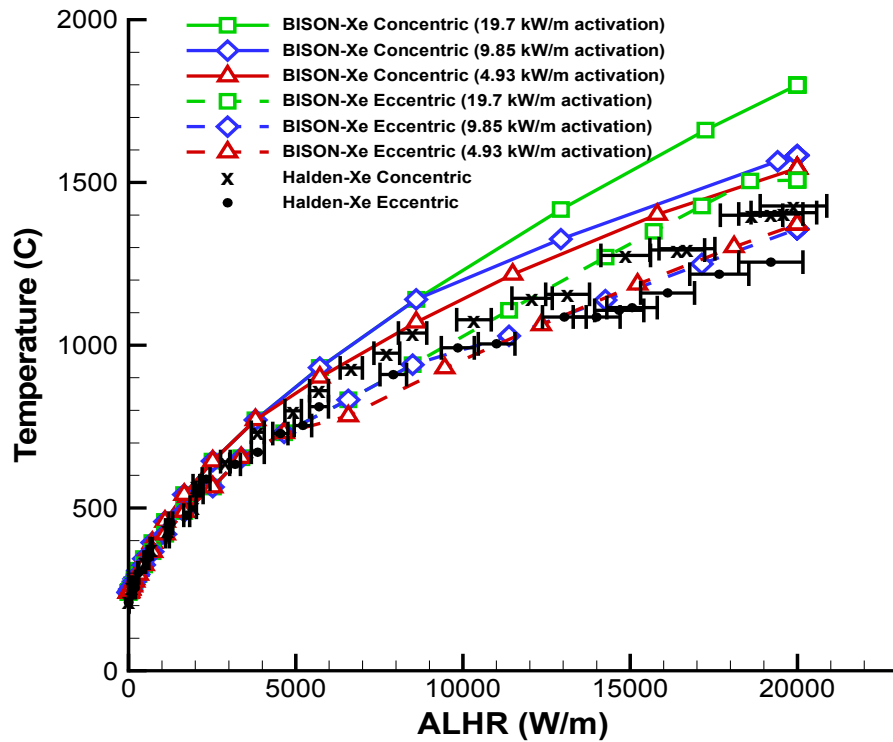
FIG. 12. Fuel centreline temperature comparisons for concentric (solid lines) and eccentric (dashed lines) pellets with varying relocation activation threshold power. Error bars are +/- 5% power uncertainty, ALHR-average linear heat rate.

Both the experimental and analysis results indicate that the fuel centreline temperature measured is lower in the eccentric pellets than the concentric pellets. This raises the question of whether this is because fuel temperatures in the eccentric pellets are lower, or because the thermocouple is located away from the hottest location in the fuel. Figure 13 shows a side-by-side comparison of the concentric and eccentric pellets, accompanied by a plot of the fuel temperature along the cross-section of the pellets at the mid-plane of the fuel. It can be seen that the concentric test pellets are indeed hotter, and also that the thermocouple is not at the hottest location in the eccentric pellets, which is offset from the centreline due to pellet eccentricity. The peak fuel temperature of the concentric pellets occurs, as expected, at the fuel centre (TC location) and is ~2074 K. The peak temperature for the eccentric pellets occurs at 1.412 mm to the left of the TC location (refer to Fig. 13) and is ~1884 K.

The comparison confirms with modern 3D analysis tools that the measured temperature difference between concentric and eccentric pellets is not an artefact and provides a quantitative explanation for the difference. The comparison further demonstrates that, although an old experiment, IFA-431 Rod 4 is clearly still of value since it provides a rare opportunity to validate 3D behavior in a fuel performance code.
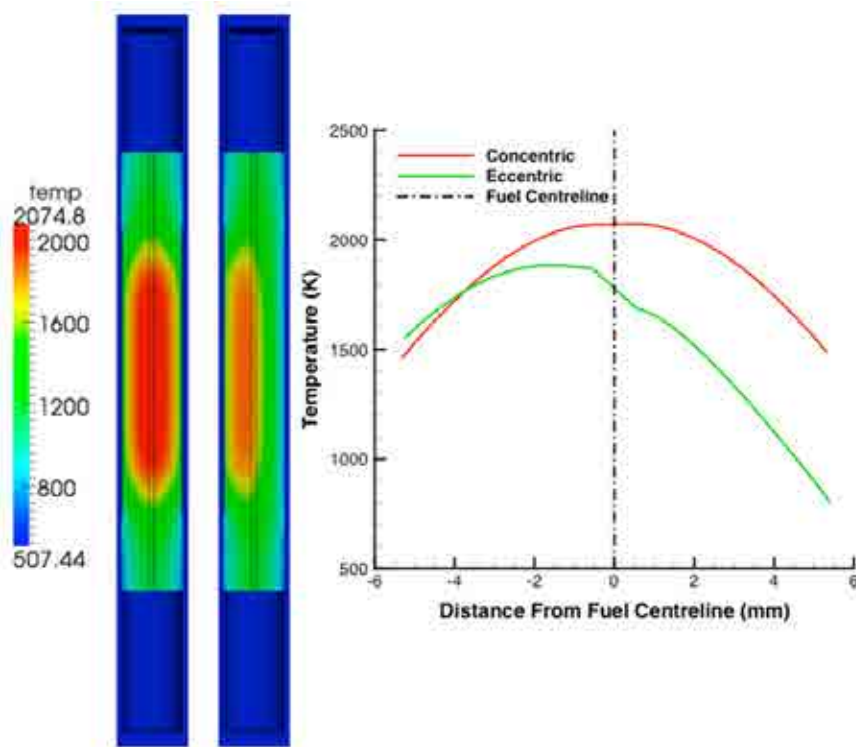
FIG. 13. Temperature contour plot of the concentric (left) and eccentric (right) pellets and fuel temperature along the cross-section of the pellets, at the fuel mid-plane.

5. SUMMARY OF FUTURE EFFORTS

5.1 Verification, Validation and Uncertainty Quantification

Although significant verification and validation work has been completed, much work remains. Enlarging the validation base will be a major focus going forward, with continuing work on cases from the FUMEX-II and FUMEX-III CRPs. Collaborations have been developed with the Halden Reactor Project and the National Nuclear Laboratory to enlarge and hasten this effort. Because BISON is under active development, a system is being developed to frequently run all assessment cases and compare results to those from prior code versions. Sensitivity and uncertainty quantification analyses will continue.

5.2 Code Development

Active capability development also continues with BISON. For general fuel behavior analysis, priorities include a more robust and efficient thermomechanical contact model, improved fracture capabilities (both smeared and discrete) and development of a more extensive set of material models.

Efforts are also underway to enhance BISON to model accident behavior. Much of the necessary capability is inherent in the code, including transient operators with adaptive time stepping, arbitrary geometry with large deformation mechanics, and fully-coupled physics with implicit numerics. Development will continue on improved fission gas modeling, specifically coupling gas release to fuel swelling and implementing a burst release model. With regards to cladding behavior, models will be included for temperature and strain rate dependent plasticity, high temperature creep, hydrogen diffusion and embrittlement prediction, and rapid steam oxidation including a moving material interface.

ACKNOWLEDGEMENTS

REFERENCES

[1] WILLIAMSON, R. L., HALES, J. D., NOVASCONE, S. R., TONKS, M. R., GASTON, D. R., PERMANN, C. J., ANDERS, D., MARTINEAU, R. C., Multidimensional multiphysics simulation of nuclear fuel behavior, Journal of Nuclear Materials, **423** (2012) p. 149–163.

[2] HALES, J. D., WILLIAMSON, R. L., NOVASCONE, S. R., PEREZ, D. M., SPENCER, B. W., PASTORE, G., Multidimensional multiphysics simulation of TRISO particle fuel, Journal of Nuclear Materials, **443**, (2013) p. 531–543.

[3] MEDVEDEV, P., Fuel performance modeling results for representative FCRD irradiation experiments: Projected deformation in the annular AFC-3A U-10Zr fuel pins and comparison to alternative designs. Technical Report INL/EXT-12-27183 Revision 1, Idaho National Laboratory, (2012).

[4] GASTON, D., NEWMAN, C., HANSEN, G., LEBRUN-GRANDIE´ D., MOOSE: A parallel computational framework for coupled systems of nonlinear equations, Nuclear Engineering and Design, **239**, (2009) p. 1768–1778.

[5] KNOLL, D. A., KEYES, D. E., Jacobian-free Newton-Krylov methods: A survey of approaches and applications, Journal of Computational Physics, **193(2)**, (2004) p. 357– 397.

[6] HALES, J. D., NOVASCONE, S. R., WILLIAMSON, R. L., GASTON, D. R., TONKS, M. R, Solving nonlinear solid mechanics problems with the Jacobian-free Newton Krylov method. CMES: Computational Modeling in Engineering &. Science, **84(2)** (2012) p. 123–154.

[7] PASTORE, G., LUZZI, L., DI MARCELLO, V., VAN UFFELEN, P. Physics-based modelling of fission gas swelling and release in UO_2 applied to integral fuel rod analysis, Nuclear Engineering and Design, **256** (2013) p. 75–86.

[8] KILLEEN, J. C., TURNBULL, J. A., SARTORI, E., Fuel modelling at extended burnup: IAEA coordinated research project FUMEX-II, Proceedings of the 2007 International LWR Fuel Performance Meeting, San Francisco, California, Paper 1102, Sept. 30–Oct. 3 (2007).

[9] INTERNATIONAL ATOMIC ENERGY AGENCY, Improvement of Computer Codes Used for Fuel Behavior Simulation (FUMEX-III), Report of a Coordinated Research Project 2008– 2012, IAEA-TECDOC-1697, International Atomic Energy Agency, Vienna (2013).

[10] PASTORE, G., HALES, J. D., NOVASCONE, S. R., PEREZ, D. M., SPENCER, B. W., WILLIAMSON, R. L., Analysis of fission gas release in LWR fuel using the BISON code, 2013 LWR Fuel Performance Meeting – TopFuel, Charlotte, NC, September 15–19 (2013).

[11] HEINSTEIN, M., LAURSEN, T., An algorithm for the matrix-free solution of quasistatic frictional contact problems, International Journal of Numerical Methods in Engineering, **44** (1999) p. 1205–1226.

[12] HALES, J. D., ANDRS, D., GASTON, D. R., Algorithms for thermal and mechanical contact in nuclear fuel performance analysis, Proceedings of the International Conference on Mathematics and Computational Methods Applied to Nuclear Science and Engineering, Sun Valley, Idaho, May 5–9 (2013).

[13] HALES, J. D., NOVASCONE, S. R., PASTORE, G., PEREZ, D. M., SPENCER, B. W., WILLIAMSON, R. L., BISON theory manual: The equations behind nuclear fuel analysis, Technical Report, Idaho National Laboratory (2013).

[14] PEREZ, D. M., WILLIAMSON, R. L., NOVASCONE, S. R., LARSON, T. K., HALES, J. D., SPENCER B. W., PASTORE G., An evaluation of the nuclear fuel performance code BISON, Proceedings of the International Conference on Mathematics and Computational Methods Applied to Nuclear Science and Engineering, Sun Valley, Idaho, May 5–9 (2013).

[15] SWILER, L. P., WILLIAMSON, R. L., PEREZ, D. M., Calibration of a fuel relocation model in BISON, Proceedings of the International Conference on Mathematics and Computational Methods Applied to Nuclear Science and Engineering, Sun Valley, Idaho, May 5–9 (2013).

[16] INTERNATIONAL ATOMIC ENERGY AGENCY, Fuel modeling at extended burnup (FUMEX-II), Report of a Coordinated Research Project 2002–2007, IAEA-TECDOC-1687, Vienna (2012).

[17] Advances in high temperature gas cooled reactor fuel technology, IAEA-TECDOC-1674, International Atomic Energy Agency, Vienna (2012).

[18] ALESHIN, Y., BEARD, C., MANGHAM, G., MITCHELL, D., MALEK, E., YOUNG, M., The effect of pellet and local power variations on PCI margin, Proceedings of Top Fuel 2010, Orlando, FL, USA, September (2010).

[19] GROESCHE,L F., BART, G., MONTGOMERY, R., YAGNIK, S. K., Failure Root Cause of a

PCI Suspect Liner Fuel Rod, IAEA Technical Meeting on Fuel Failure in Water Reactors: Causes and Mitigation, Bratislava, Slovakia, June 17–21 (2002).

[20] LEE, J.S., YOO, J.S., KIM, H.K., The Mechanical Behavior of Pellet-Cladding with the Missing Chip under PCMI Loadings during Power Ramp, Proceedings of the 2007 International LWR Fuel Performance Meeting, Paper 1022, San Francisco, CA, Sept. 30–Oct. 3 (2007).

[21] KHVOSTOV, G., LYON, W., ZIMMERMAN, M. A., Application of the FALCON code to PCI induced cladding failure and the effects of missing pellet surface, Annals of Nuclear Energy, **62** (2013) p. 398–412.

[22] SPENCER, B. W., HALES, J. D., NOVASCONE, S. R., WILLIAMSON, R. L., 3D Simulation of Missing Pellet Surface Defects in Light Water Reactor Fuel Rods, Proceedings of Top Fuel 2012, Manchester, United Kingdom, September 2–6 (2012).

[23] WILLIFORD, R. E., HANN, C. R., Effects of Fill Gas Composition and Pellet Eccentricity, Technical Report BNWL-2285/NRC-1&3 (1977).

[24] HALES, J. D., PEREZ, D. M., WILLIAMSON, R. L., NOVASCONE, S. R., SPENCER, B. W., MARTINEAU, R. C., Validation of the BISON 3D fuel performance code: Temperature comparisons for concentrically and eccentrically located fuel pellets, Enlarged Halden Programme Group Meeting: Proceedings of the Fuels and Materials Sessions, Volume HPR-378, Storefjell Resort Hotel, Norway, March 10–15 (2013).

[25] OGUMA, M., Cracking and relocation behaviour of nuclear fuel pellets during rise to power, Nuclear Engineering and Design, **76** (1983) 35–45.

US DOE CASL PROGRAM FUEL PERFORMANCE MODELING FOR STEADY STATE AND TRANSIENT ANALYSIS OF LWR FUEL

Robert Montgomery[1*], C. Stanek[2], W. Liu[3], and B. Kendrick[2]
[1]Pacific Northwest National Laboratory, Richland, WA 99352, USA
[2]Los Alamos National Laboratory, Los Alamos, NM 87545, USA
[3]ANATECH Corp, San Diego, CA 92121, USA

Abstract. The US DOE's Consortium for Advanced Simulation of LWRs (CASL) program has undertaken an effort to enhance and develop modeling and simulation tools for a virtual reactor application, including high fidelity neutronics, fluid flow/thermal hydraulics, and fuel and material behavior. An important goal of this effort is to provide methods for multi-physics coupling, including full core modeling of neutronics, coolant channel flow, and fuel behavior. The fuel performance analysis efforts in the CASL program aim to provide 3-dimensional capabilities for single and multiple rods to assess safety margins and the impact of plant operation and fuel rod design on the fuel thermo-mechanical-chemical behavior, including Pellet-Cladding Interaction (PCI) failures, CRUD-induced Power Shift (CIPS) and CRUD-Induced Localized Corrosion (CILC) failures in PWRs. These capabilities will accurately calculate the thermal, mechanical, and chemical conditions throughout a single fuel rod during operation in a LWR reactor. To this end, two engineering scale codes have been developed by the CASL efforts to date: the Peregrine fuel rod performance code and the MAMBA CRUD formation and boron deposition code. Each of these codes address the multi-physics material behavior aspects of the phenomena being represented, provide the interface to the neutronics and thermal-hydraulics tools, and establish a framework for employing microscale models through a variety of methods, including direct use, improved mechanistic or empirical models, or limited parameter response surfaces. Recent activities to demonstrate the capabilities of Peregrine and MAMBA for LWR fuel performance modeling have successfully shown that these codes are approaching or exceed the capabilities of industry standards, such as the EPRI Falcon and BOA codes. MAMBA and Peregrine are able to reliably calculate CRUD distributions, cladding and fuel temperatures, cladding deformations, and fission gas release as a function of the environmental conditions defined by power, fast fluence, and coolant flow and chemistry. The focus of this paper will be an overview of the important fuel rod modeling requirements for reactivity initiated accidents (RIA), and outline the corresponding plan to extend the multi-scale, multi-physics fuel modeling tools developed by CASL that will enable consideration of RIA.

1. INTRODUCTION

Within the US DOE's CASL Program, there are ongoing efforts to develop an advanced nuclear fuel rod thermo-mechanical modeling and simulation capability for steady state and transient conditions in Light Water Reactors (LWRs) [1, 2]. The focus of this paper will be an overview of the important fuel rod modeling requirements for reactivity initiated accidents (RIA), the plan to develop these capabilities within the CASL multi-scale, multi-physics fuel modeling tools, and a current status of the fuel modeling development activities. Lastly, the paper will discuss the recent efforts to demonstrate the fuel modeling capabilities for steady-state fuel performance calculations and how the fuel performance modeling framework will be adapted for use in transient and design basis accident analyses.

---

[*] Corresponding Author: 902 Battelle Blvd. P.O. Box 999, MSIN K9-69, Richland, WA 99352,

robert.montgomery@pnnl.gov

1.1 CASL Overview

The US DOE's Consortium for Advanced Simulation of LWRs (CASL) program has undertaken an effort since 2010 to develop advanced modeling and simulation tools for a virtual reactor simulation application, including advanced neutronics, thermal hydraulics, computational fluid dynamics, coolant chemistry, and fuel and material behavior [2]. An important goal of this effort is to provide methods for multi-physics coupling, including full core modeling of neutronics, coolant channel flow, and fuel thermo-mechanical response. The fuel performance analysis efforts in the CASL program aim to provide 3-dimensional capabilities for single and multiple rods to assess safety margins and the impact of plant operation and fuel rod design on the fuel thermo-mechanical-chemical behavior, including Pellet-Cladding Interaction (PCI) failures, CRUD-induced Power Shift (CIPS) and CRUD-Induced Localized Corrosion (CILC) failures in PWRs [1- 5]. To this end, two engineering scale codes have been developed by CASL to date: the Peregrine fuel rod performance code [1] and the MAMBA CRUD formation and boron deposition code [5]. Each of these codes address the multi-physics material behavior aspects of the phenomena being represented, provide the interface to the neutronics (neutron flux, fission density, power) and thermal-hydraulics tools (coolant temperature, pressure, flow rate, and chemistry) and establish a framework for employing microscale models through a variety of methods, including direct use, improved mechanistic or empirical models, or limited parameter response surfaces.

The fuel performance code, Peregrine, is an engineering scale finite element method (FEM) code that is built upon the MOOSE/ELK/FOX structure/architecture, which is also common to BISON [6, 7]. Peregrine uses both 2-D and 3-D geometric fuel rod representations and contains a materials properties and fuel behavior model library for the UO_2 and Zircaloy system common to PWR fuel derived from on both open literature sources and the FALCON code [8-9]. The primary purpose of Peregrine is to accurately calculate the thermal, mechanical, and chemical processes active throughout a single fuel rod during operation in a reactor, for both steady state and off-normal conditions. MAMBA (MPO Advanced Model for Boron Analysis) is a FORTRAN based computer code built on the ChemPac chemical kinetics package, which simulates three-dimensional crud growth and boron deposition along the outer surface of a single fuel rod [5]. The code also determines the local chemistry conditions occurring within the CRUD deposits. MAMBA represents many of the primary coupled physics and chemistry domains associated with CRUD formation and boron deposition, including non-uniform heat generation and transfer within a porous medium, material deposits due to precipitation and chemical reaction, and mass transport of soluble species within the CRUD layer and boiling chimneys due to concentration and fluid flow gradients.

Complementary to the development of higher fidelity engineering scale modeling capabilities, CASL has a mission to explore and develop microscale modeling of important material behavior such as irradiation and microstructural effects on cladding creep and growth, hydrogen absorption, hydride formation, pellet cracking and fragmentation, and fission gas release kinetics. The goals of the lower length scale (microscale) modeling are to provide or inform more mechanistically-based material and behavior models for use at the engineering scale, with the desired outcome of improved modeling uncertainties and higher confidence in predictive methods. For example, CASL is developing a crystallographic texture aware plastic deformation model that is based on the so-called visco-plastic self-consistent (VPSC) model pioneered by Lebensohn and Tome [10]. This approach assumes that each grain can be treated as an inhomogeneity embedded in a homogeneous medium

(i.e. the polycrystal). An interaction equation for the grain can be formulated that relates the stress and strain rate of the grain to the effective medium. VPSC has recently been integrated in to Peregrine and can be used to assess anisotropic creep and growth, grid-rod gap development as well as severe plastic deformation during an RIA. Currently, studies are being performed to determine a strategy for using VPSC rather than existing empirical models, as the computational expense is significant.

During the first three years of the CASL program, the majority of activities have centered around the development of advanced modeling capabilities by either 1) enhancing existing computational tools, such as the COBRA-TF thermal-hydraulics code and the HYDRA-TH computational fluid dynamics code [11,12] or 2) building new tools such as the MAMBA PWR CRUD thermochemistry and material deposition code and the Peregrine fuel performance code [1, 5]. The initial focus has been on specific challenge problems associated with normal plant operation, such as CRUD-induced power shift (CIPS), CRUD-induced localized corrosion (CILC), and pellet-cladding interaction (PCI). To date, the major outcomes have been the demonstration of higher fidelity representation of neutron flux and fission density distribution, single phase flow distributions around spacer grids, CRUD deposition patterns, and fuel rod behavior modeling. An important activity has been the active coupling of different physics to have improved representation of the key phenomena. This has included the coupling of the neutronics, thermal-hydraulics, and CRUD deposition codes into a single solution for calculating 3-D CRUD patterns that incorporate the impact of the spacer grids [13, 14].

With the development activities for advanced modeling and simulation tools for normal operation well underway, and with several key milestones completed, the CASL effort is now expanding the challenge problem suite to include reactor accident modeling, starting with the reactivity-initiated accident (RIA) and the loss of coolant accident (LOCA). These complex accident scenarios require modeling and simulation tools to represent both the larger scale reactor and coolant system neutronics/fluid dynamics responses to external events as well as the detailed fuel rod and assembly thermal/mechanical/chemical behavioral response. In both cases, the interaction of irradiation-induced changes in material behavior with the rapidly changing neutron flux or fission rate, temperature, and thermal-hydraulic conditions requires detailed modeling of the fuel pellet and cladding to evaluate the potential for cladding failure, release of fission products, fuel pellet fragmentation and relocation, and flow blockage [15, 16]. This paper will primarily discuss the current plan to address the fuel behavior modeling requirements for the RIA event, however, some commonalities with the fuel behavior during a LOCA event will be noted where appropriate.

1.2 Importance of fuel modeling in accidents

The recognition that fuel behavior modeling is important for transient and accident evaluations goes back to the early days of reactor and fuel accident testing. In 1975, Thompson, et al. developed and used the fuel behavior code FRAP-T developed by the US NRC to identify the important fuel rod variables that impact the maximum cladding surface temperature during an RIA event [17]. Parameters that were evaluated included the initial reactor coolant conditions (temperature and pressure), the energy deposition during the event, and fuel rod design parameters. By comparing to experimental data from RIA tests performed in SPERT, Thompson, et al. were able to identify deficiencies in the models used in FRAP-T and highlight the key experimental parameters that

impact maximum cladding temperature. Building on this experience, Burchill, et al. prepared an overview of the design basis accidents used to license LWRs that can adversely impact the performance and integrity of the cladding and defined the important fuel and cladding characteristics to be represented in fuel behavior modeling [18].

Fuel behavior modeling for transient and accident conditions has become even more significant following the simulated RIA and LOCA testing of high burnup fuel at the CABRI facility in France, at the Japanese Atomic Energy Agency (JAEA) [15], and the Halden reactor [16]. The unexpected behavior exhibited by several high burnup fuel rods required extensive analytical modeling to interpret the in-pile and post-test examination results [19-24]. Isolating the individual effects of burnup accumulation in the pellet, irradiation damage in the cladding, and non-prototypical testing conditions required detailed fuel behavior modeling that included advanced depiction of the active thermal, mechanical, and chemical processes. The insights gained from fuel behavior modeling assisted in understanding the experimental data and observations obtained from integral fuel rod experiments or post-irradiation examinations and provided methods to translate the results of non-prototypical testing conditions to those applicable to commercial reactor conditions. These efforts were necessary to ensure that the conclusions derived from the testing of high burnup fuel are used properly to modify regulatory acceptance criteria applied in the safety evaluations of LWRs.

While the importance of fuel modeling under accident conditions has been acknowledged for many years, only recently have the capabilities become available to move from simplified geometric representation (2-D axisymmetric or planar) and empirical material models to 3-D geometric representation with non-uniformities and more mechanistic behavior models. Recently, Hursin, et al. performed an assessment using improved neutron kinetics methods to illustrate the effects of local pellet power distribution on the cladding mechanical response, as defined by the cladding Strain Energy Density (SED) calculated by the fuel performance code FALCON, during a realistic, full core RIA scenario [25]. A high-fidelity neutronic analysis was performed using the transient solution scheme in DeCART for a realistic PWR full core model with explicit representation of individual fuel rods and surrounding coolant channels [26]. The DeCART calculation allowed for local perturbations in power (axial and azimuthal) during the RIA due to water rod effects. In addition, the PARCs neutron kinetics code was used to perform an analysis representative of industry methods, which uses assembly-level geometry and cross-section homogenization [27]. The nodal calculation performed in PARCS used homogenized two group cross-section constants and kinetics data, together with standard pin power reconstruction methods to determine pin-wise power factors. The approach used in PARCs does not capture the local fuel rod power variations due to proximity to coolant channels.

The results of this analysis led to the following observations:

- The differences in the kinetic parameters used in PARCS and DeCART had the largest impact on the cladding mechanical response;
- The modeling of fuel rod exposure in the current industry methodologies results in lower fuel rod energy deposition and calculated cladding SED during an RIA fuel rod analysis.
- The effect of azimuthal power variation within a given fuel rod had at least a 10% impact on the SED and these effects should be taken into consideration during RIA analysis, especially for high exposure fuel.

This review highlights the importance of higher fidelity modeling on the fuel rod response during RIA events and the role fuel rod modeling can have on defining the margin to fuel rod failure or loss of rod geometry due to high temperature effects.

2. IMPORTANT ASPECTS OF LWR FUEL BEHAVIOR DURING RIA EVENTS

Two state-of-the-art reports prepared by the Nuclear Energy Agency (NEA) within the Organization for Economic Co-operation and Development (OECD) describe the current understanding of LWR fuel behavior during RIA and LOCA events [15, 16]. Each of these reports provide a detailed summary of typical accident event sequences in BWRs and PWRs, the regulatory acceptance criteria for fuel safety, the database of experiments available to understand fuel behavior, and the requirements for future modeling and testing of fuel. The following is a short summary of the important material properties, behavioral responses, and processes important to LWR fuel rod behavior during RIA events. This understanding will guide the prioritization of model development for advancing the state-of-the-art in transient fuel behavior modeling.

The fuel and cladding characteristics that influence the rod behavior during transients can be separated into those material properties or responses that are affected by the pre-transient irradiation environment and those that are activated by the imposed off-normal conditions. During normal operation, persistent changes in the microstructure, chemistry, and geometry of the pellet and cladding occur in response to thermal processes, chemical reactions, fission or irradiation damage, and mechanical forces. These changes can have an important impact on the behavior of a fuel rod during an LWR accident, as demonstrated in the transient fuel testing results obtained on highly irradiated fuel rods over the last twenty years. Some examples of pre-transient irradiation effects on transient fuel behavior include; 1) cladding corrosion during operation can result in hydrogen pickup into the cladding and the formation of zirconium hydrides (ZrH_2) that, when combined with irradiation-induced damage can reduce the plastic strain capability of the cladding, 2) buildup and redistribution of fission gas atoms into grain boundary bubbles combined with rapid heating can lead to excessive fission gas swelling, pellet fragmentation, and release, and 3) hydrogen pickup in the cladding during corrosion can lead to enhanced oxygen diffusion and changes in oxygen solubility during high temperature oxidation and material embrittlement following thermal quench.

It can be concluded that the fuel behavior exhibited during transient power or cooling conditions is influenced by the pre-irradiated material state. This highlights the importance of consistency between the models and methods used to calculate the fuel rod changes caused by normal operation and the fuel behavior expected during a transient. This point is highlighted further in the next section using the reactivity insertion accident as an example.

3. RIA FUEL ROD BEHAVIOR DATABASE

The RIA event is a hypothetical design basis accident caused by an unplanned reactivity insertion into the core due to a failure in the reactivity control system. At sufficiently high reactivity insertion values, the reactor experiences a prompt-critical power event that is terminated by temperature feedback and reactor safety system actuation. Prompt energy deposition occurs over a time period between 2 to 100 milliseconds, producing a near-adiabatic heat up of the fuel pellet that can lead to fuel and clad melting and rapid fuel-coolant interactions. RIA events have led to the

destruction of more than one reactor core since the inception of nuclear power. As a result, the core design process places restrictions on the amount of reactivity worth for individual control rods or control blades in order to meet fuel rod failure and core coolability requirements. Understanding how the effects of fuel design and operation influences fuel behavior during a RIA event ensures that reactor designers, operators, and regulatory authorities maintain sufficient safety margins in the unlikely event of an RIA.

Jernvisk, et al. have summarized the database of integral rod experiments, separate effects tests, and material property tests on RIA fuel behavior [15]. More than 1000 integral rod tests have been performed in the US, France, Japan, and Russia to evaluate the impact of rapid energy deposition on the fuel rod response and failure modes expected following an RIA. This database provides several key insights into the fuel behavior and expected failure modes during a hypothetical event in a LWR. EPRI performed an extensive review of this database beginning in 1994 and were able to develop an important understanding of the fuel behavior as a function of burnup [19, 23, and 28]. A key observation from the EPRI evaluations is that burnup or prior irradiation history has an important impact on the fuel rod behavior during and following a power pulse and the fuel rod failure mechanisms. The RIA fuel behavior evolution with burnup is shown schematically in Fig. 1, which depicts the changes in pellet-cladding gap thickness with irradiation caused by pellet relocation, pellet swelling, and cladding creep and the evolution of the cladding ductility induced by outer surface corrosion and hydrogen absorption effects [28].
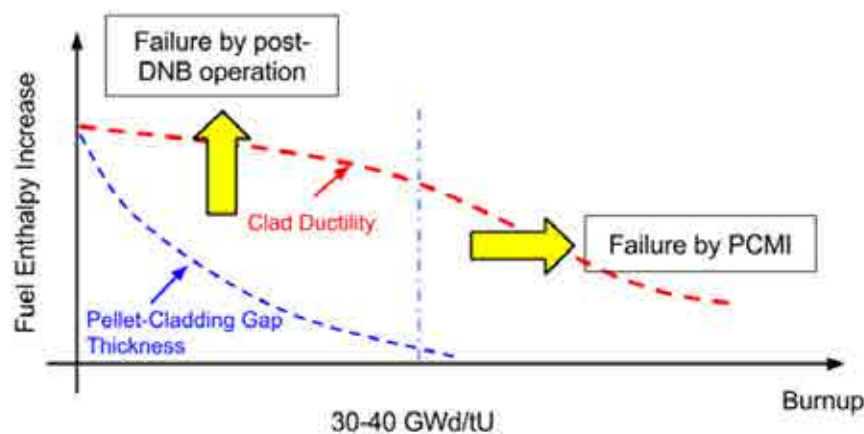
FIG 1. Evolution of RIA fuel failure mechanisms as a function burnup, and impact on key fuel rod characteristics[28].

3.1 Key fuel behavior characteristics for RIA

The partitioning of fuel rod characteristics and behavior responses throughout the spectrum of normal operation to accident conditions for an RIA is shown in Table 1. The information presented in Table 1 follows the progression of fuel behavior during an RIA as outlined by Sunderland, et. al., who developed this perspective on the evolution of fuel rod behavior from analytical evaluations of more than 40 RIA simulation tests conducted around the world [23]. This evaluation clearly

identified the synergistic effects between the pellet and cladding on the evolution of the thermal and mechanical states leading to cladding deformations and ultimately, cladding failure. In this context, the results of their evaluation found that fuel behavior during a RIA power pulse can be divided into two phases as shown in Fig. 2.

Phase 1 in RIA fuel behavior occurs during the prompt energy deposition of the power transient, which is about 60 to 95% of the power pulse, depending on the pulse width, amount of energy deposition, and pellet-cladding gap size. The pellet heat-up due to the energy deposition during Phase 1 takes place under near adiabatic conditions with only a small amount of heat conduction to the cladding. As a consequence, the pellet behavior response is governed by the cracked pellet thermal expansion, pellet-cladding mechanical interaction, and high compressive stress confinement of fission gas bubbles. The cladding behavior is affected by high strain rate loading, outer surface oxide and CRUD cracking and spallation, and cladding embrittlement by irradiation damage and hydriding. Cracking of the cladding may happen depending on the ability of the tube to accommodate the hoop and axial mechanical strains imposed by the pellet thermal expansion.
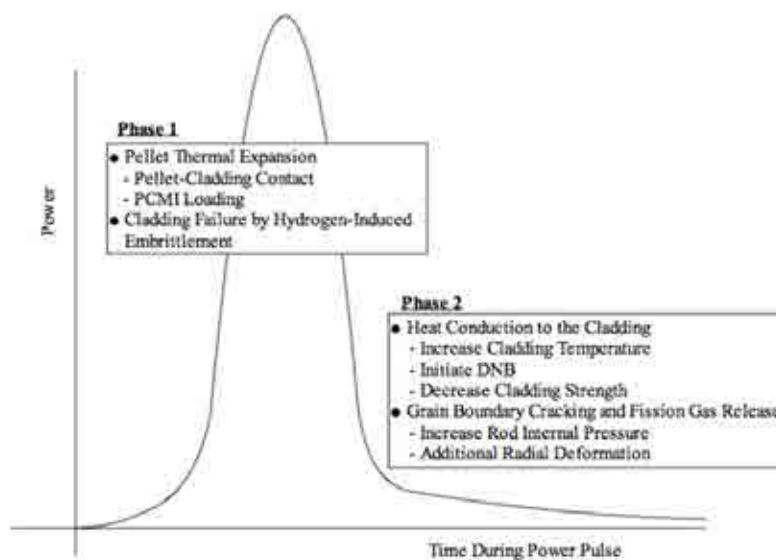
FIG 2. Schematic of Phases 1 and 2 of the clad loading process during an RIA power pulse [23].

Phase 2 is the delayed energy deposition portion of the power transient, where heat conduction becomes a dominant mechanism. Heat conduction from the fuel to the cladding in Phase 2 causes an increase in the cladding temperature, which improves the cladding ductility and decreases the cladding yield strength. Depending on the coolant conditions, the heat flux can exceed a critical value and initiate departure from nucleate boiling (DNB) at the cladding outer surface. Depending on the amount of energy deposition or the occurrence of DNB, cladding temperatures can exceed 600°C. The fuel rod response during the later portion of the power pulse is controlled generally by cladding thermal creep and plastic flow, oxidation reactions and oxygen diffusion in the cladding, fission gas release kinetics, and clad-to-coolant heat transfer. At higher temperatures, cladding deformations above those from PCMI can develop and lead to large local cladding strains, if the local internal pressure exceeds the external coolant pressure. This behavior is similar to clad ballooning

during a LOCA event. Finally, at energy deposition levels above 180 cal/gm, high temperature cladding oxidation is initiated because temperatures can exceed 1000°C. The wall-thinning and oxygen uptake at these temperatures can lead to cladding embrittlement sufficient to crack the cladding once liquid coolant rewets the rod surface. Thermal shock fracture is the primary mode of cladding failure for high energy deposition tests on low to intermediate burnup fuel rods that survive the Phase 1 conditions.

TABLE 1. FUEL ROD CHARACTERISTICS IMPORTANT TO FUEL ROD INTEGRITY DURING AN REACTIVITY-INITIATED ACCIDENT (RIA)

Fuel rod initial conditions	RIA Phase 1 Near-Adiabatic Energy Deposition	RIA Phase 2 Energy Deposition with Heat Transfer
Residual pellet-cladding gap thickness/fuel-clad bonding	Thermal expansion of cracked pellet structure (crack volume closure rates)	Fission gas behavior in both grain boundary and intragranular bubbles
Cracked pellet state/fragment distribution	Gap mechanical contact and thermal conductance	Transient fission gas release kinetics
Fission gas distribution in pellet: grain boundaries and grain concentrations	Fuel fragmentation and dispersal kinetics after cladding fracture	Axial gas transport kinetics within/adjacent to fuel column (localized pressurization)
Fission gas release into the gap and plenum	Fuel fragment coolant interaction and pressure generation	Fuel fragmentation and dispersal kinetics
Fissile isotope/burnup distribution		Effective fuel thermal conductivity
Cladding corrosion and CRUD layer build up	Cladding fast strain rate behavior/plasticity	Cladding thermal annealing/plastic behavior recovery

Fuel rod initial conditions	RIA Phase 1	RIA Phase 2
	Near-Adiabatic Energy Deposition	**Energy Deposition with Heat Transfer**
Cladding hydrogen uptake/content, distribution of hydrides, etc.	Fracture and spallation of oxide and crud layer	Thermal creep and creep rupture
Cladding creep deformations	Cladding crack formation and growth (displacement controlled deformation)	High temperature oxidation (Oxygen uptake and diffusion in cladding)
Cladding Irradiation damage (dislocation densities, second phase particle amorphization, etc.)		Thermal shock stress distributions in cladding during quench/rewetting
Boron deposition/Coolant chemistry		Material mechanical behavior as function of phase (ZrO2, high O alpha, and prior beta)
		Post-Departure from Nucleate (DNB) clad-to-coolant heat transfer

4. CASL FUEL BEHAVIOR MODELING APPROACH

Simulation of the processes leading to cladding failure during normal operation (e.g. PCI) and during transient conditions (e.g. RIA and LOCA) requires a modeling approach that considers the coupled thermo-mechanical-chemical behavior on-going in a fuel rod during the operating life-time, operational transients, and accident events. The fuel modeling capabilities in CASL are being designed to calculate the behavior of a single fuel rod to establish the conditions of temperature, pellet and cladding deformations, fission products distributions, and cladding-coolant reaction surfaces prior to an operational power maneuver, transient power excursion, or abnormal thermal hydraulic event, and then the evolution of these conditions during the operational or abnormal event

to understand the margin to fuel rod failure and loss of geometry. To accomplish these goals requires using a computational framework that has 1) the flexibility to consider the local geometry conditions within a fuel rod, 2) the ability to represent the multiple, coupled physics active within a fuel rod, 3) the capabilities to consider the wide variety of material property and behavior models (fission gas release, swelling, corrosion) needed to simulate the changing conditions within the fuel rod, and 4) the ability to time march the numerical solution throughout the long-term operating history prior to an event, as well as, the short-term transient conditions, in a computationally efficient manner. Previous efforts to construct fuel behavior modeling codes have varied from analytically-based solutions for simplified sets of equations to multi-dimensional finite element formulations [29], [30]. Each type of approach has various advantages and disadvantages; however, most of these approaches have proved useful in simulating selected aspects of fuel rod behavior during normal operation and off-normal events.

CASL is developing advanced modeling and simulation for LWR fuel behavior using a multi-scale, multi-physics approach that applies engineering scale methods to identify the conditions and important fundamental mechanisms that influence material performance or behavior response. Based on this information, microscale modeling approaches are being used to construct improved representations for key material properties such as xenon diffusion within UO_2 matrix, cladding irradiation-induced growth and creep, zirconium alloy reactions with water, hydrogen uptake, iodine reactions with zirconium, and coolant chemistry-rod interactions. This approach is being applied to model and understand both cladding failure by PCI and the CRUD-induced fuel performance problems; CIPS and CILC. Each of these fuel performance challenges are inherently multi-physics and multi-scale, with coupled thermal, mechanical, and chemical components that are functions of material characteristics, physical chemistry, temperature gradients, stress fields, and irradiation-induced damage.

4.1 Multiscale, multi-physics modeling approach for CRUD

The formation of CRUD on the fuel rod outer surface can play an important role on reactor safety during normal operation, i.e. CIPS, accident behavior, i.e. LOCA Peak Cladding Temperature (PCT), and fuel reliability, i.e. CILC [3, 31]. In pressurized water reactors (PWRs), the primary CRUD source is corrosion of the steam generator tubing. These corrosion particulates circulate the primary loop and deposit on the fuel rod outer surfaces. CRUD deposits are composed mostly of nickel ferrite ($NiFe_2O_4$), nickel oxide, and nickel metal with other nickel-iron-chrome spinels [3]. The boron concentration within the CRUD layer increases with increasing CRUD thickness due to the higher cladding temperatures and increased internal boiling within the CRUD layer. The internal boiling occurs within "chimneys" that develop in the CRUD, as shown in Fig. 3. The coolant and its soluble species, such as boric acid and lithium, are drawn in. As the coolant vaporizes, the soluble species are left behind and concentrate along the cladding surface. The subsequent precipitation of lithium tetraborate (Li_2B4O_7) is governed by equilibrium thermodynamics. It is a function of temperature and determined experimentally.

The presence of boron deposition in the CRUD influences local neutron flux and power generation due to localized absorption of neutrons, changing the cladding surface heat flux. Fluctuations in local power further complicate the chemical and thermal-hydraulic conditions due to changes in local temperature, thermal gradients, and boiling. The interaction of the local solid state

and liquid chemistry, thermal hydraulic conditions, and fuel rod power make CRUD formation and boron deposition a tightly coupled multi-physics, multi-scale phenomenon that requires advanced modeling simulation tools.

Using a multi-scale, multi-physics approach, the CRUD formation and boron deposition model development activities include three different length scales: (1) the macroscopic length scale represented by a 2D/3D finite difference computational cell (MAMBA), (2) the microscopic length scale to capture the microstructure and chemical kinetics within the CRUD layer, and (3) the atomistic length scale. The resulting modeling capabilities have a much higher resolution model than that used by industry today to calculate CRUD formation and boron deposition [32]. Higher resolution modeling capabilities are needed in order to account for the large thermal variations along the fuel rod surfaces (due to variations in coolant flow patterns), power levels, and to more accurately assess CIPS and CILC risk.
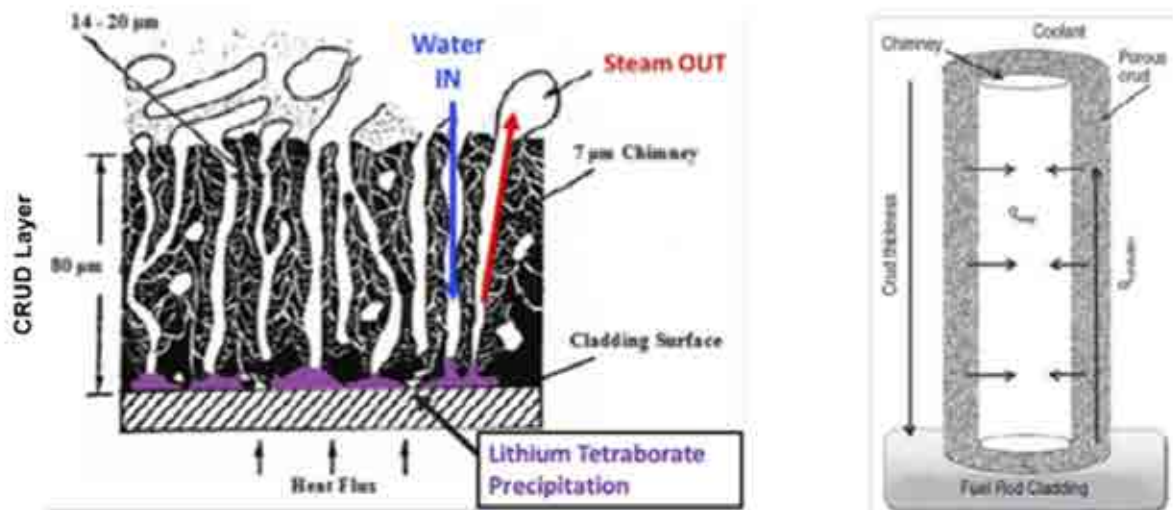
FIG 3. Sample CRUD layer showing in-flow of water and out-flow of steam in chimneys leading to $Li_2B_4O_7$ precipitation (left) [33], and the heat transfer within a chimney (right) [3].

The engineering scale code MAMBA has been built to simulate, in 3-dimensions, CRUD growth along the surface of a single fuel rod [13, 14]. The primary physics and chemistry associated with CRUD formation currently treated in MAMBA include: (1) solving a general non-linear 3D heat transport equation for the CRUD layer including localized heat sinks due to internal boiling within the CRUD layer, (2) an adaptive grid which grows in time as mass deposits on the surface of the CRUD, (3) time evolving microstructure (porosity) of the CRUD layer due to localized deposition and precipitation of $NiFe_2O_4$ and $Li_2B_4O_7$ within the pores of the CRUD, (4) time evolving lithium and boric acid coolant chemistry both at the CRUD surface and inside the pores of the CRUD, (5) mass transport of various soluble coolant species into the interior of the CRUD due to boiling induced Darcy flow, (6) diffusion of various soluble species inside the CRUD due to the flow induced concentration gradients within the CRUD layer, and (7) mass evaporation in the form of

steam vapor due to the localized boiling inside the CRUD layer. This is described schematically in Fig. 4 from reference [3]. The crud surface deposition rate is governed by two rate parameters, one for boiling regions that is multiplied by the local mass evaporation rate (i.e., the steaming flux leaving the boiling chimneys), and one for non-boiling regions. In boiling regions, the crud growth rate is enhanced due to the boiling induced flow of coolant into the crud's surface, which increases the flux of particulates onto the crud's surface. The crud surface deposition rate also includes a user selectable option for including an erosion (loss) term. The coolant chemistry is supplied by the user or an "ex-core" model and consists of the standard inputs: (1) boron concentration (ppm), (2) lithium concentration (ppm), (3) H_2 concentration (cc/Kg), (4) soluble Ni (ppb), (5) soluble Fe (ppb), and (6) particulate $NiFe_2O_4$ concentration (ppb).
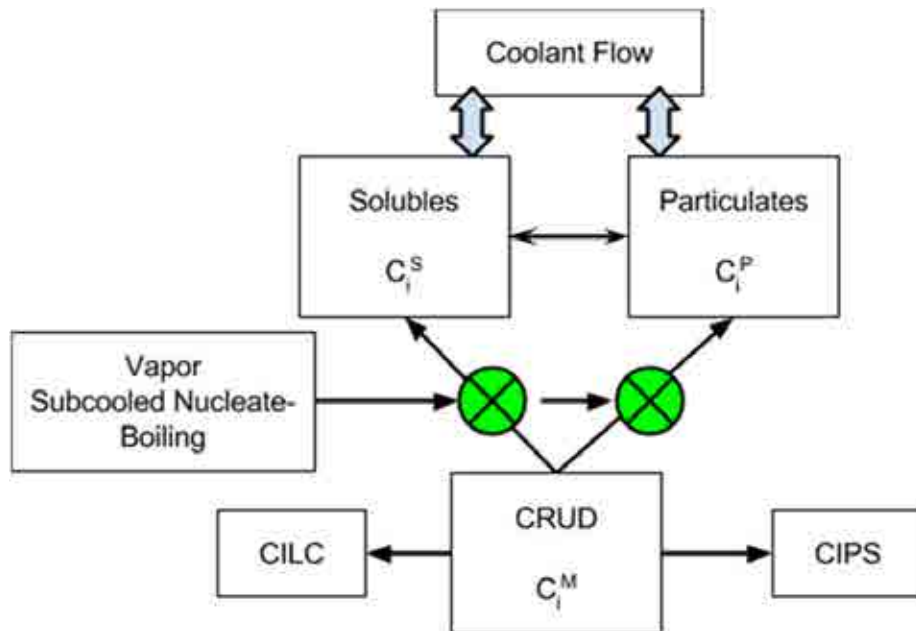
FIG 4. Flowchart of the MAMBA crud model showing the relationship between the different phases, interfaces, and sub-models. The C_i represent the concentrations of the various elemental species in each phase where i= Ni, Fe, B, Li, Zn, Zr, Cr, Co [3].

To address the issues of required physics-based modeling that would be too computationally intense for MAMBA to calculate on-the-fly, a sub-model called MAMBA-BDM (Boron Deposition Model) has been developed [34]. The goal of MAMBA-BDM is to compute very precise parameters upon request by MAMBA, to use in its engineering-scale calculations, and to pass data up to fuel performance codes. The main parameters output by MAMBA-BDM are the overall CRUD temperature, the surface CRUD temperature, the peak cladding temperature, the boron mass loading (either mass, mole fraction, or number density), and the total fraction of heat flux due to wick or nucleate boiling. MAMBA-BDM is a first-principles, physics based model with no fitting factors. Highly detailed models for temperature, pressure, and species concentration distributions, along with highly coupled materials models, form the basis of its calculations. No openly published CRUD models to date have employed this degree of coupling between physical distributions and material

properties. MAMBA-BDM currently has the capability to run its physics models on any geometry and is implemented in INL's MOOSE framework, a massively parallel object oriented simulation environment developed by Gaston et al. [6].

Furthermore, modeling CRUD deposition requires information on the axial and azimuthal distributions of power and cladding temperature, as well as the modeling of the flow swirling induced by the grid spacers. As a result, MAMBA requires input or coupling with neutronics and thermal-hydraulics modeling tools to ensure proper feedback between the physics controlling CRUD formation and boron deposition and the external factors arising from reactor operation.

4.2 Multiscale, multi-physics modeling approach for PCI

PCI is a natural outcome of the UO_2/Zr-alloy cylindrical design with ceramic pellets that crack, a small interference gap between the pellet and cladding tube, high operating temperatures, and volatile fission products. Figure 5 is a representation of a cracked pellet impinging on the cladding as a consequence of thermal expansion of the pellet [35]. The tangential and shear forces applied to the cladding by the pellet are a function of the equilibrium pellet and cladding condition (i.e. gap size or residual contact force) at the start of the power increase, the power level at gap closure, the interfacial friction conditions, and the maximum local power. Above a certain level of localized cladding stress and fuel temperature, the volatile fission products released from the hotter central part of the pellet begin to react with the zirconium alloy cladding inner surface, causing crack initiation and then crack propagation. As highlighted in Fig. 5, the circumstances that lead to PCI are a complex interplay of thermal, mechanical, and chemical processes active in the fuel rod.
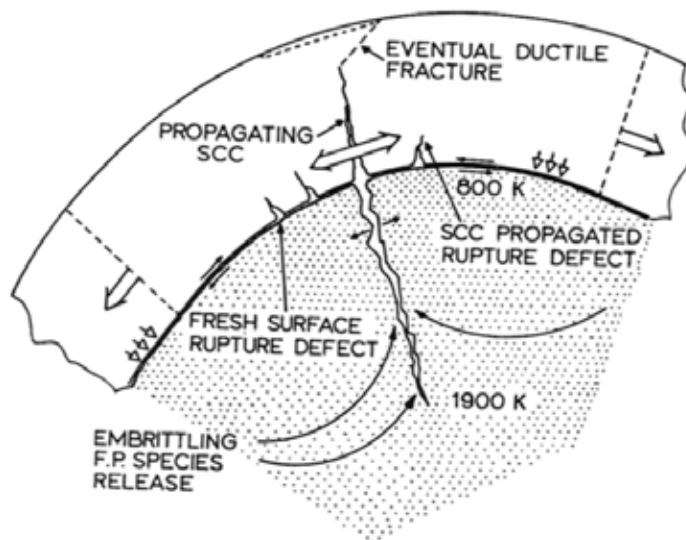
FIG 5. Schematic of the Pellet-Cladding Interaction Mechanisms (reproduced from [35]).

Similar to MAMBA CRUD modeling, the focus of the Peregrine develop activities has been to utilize a modern computational framework based on the finite element method to represent the geometric domains of a single nuclear fuel rod composed of UO_2 ceramic pellets contained within a Zircaloy tube [1]. This framework is interfaced with material and behavior models that represent

specific thermal, mechanical, or chemical material characteristics. The fuel behavior model development for the PCI challenge problem consists of three different length and time scales: (1) the engineering scale 2D/3D finite element fuel behavior code to capture integral fuel rod behavior, (2) microscope length scale model development to account for the texture, microstructure, alloy contents, and lattice damage network on cladding creep and growth, clad hydride formation, and waterside corrosion, and (3) atomistic length scale modeling to provide improved understanding of diffusion coefficients and chemical reaction kinetics associated with fission gas release, fission product attack of the cladding, and corrosion.

The Peregrine framework consists of a numerical representation of the heat conduction and the equilibrium mechanics equations, which are coupled via the temperature and displacement variables. Peregrine is built upon the MOOSE/ELK/FOX structure/architecture, which is also common to the BISON code [7]. This code architecture uses the finite element method for geometric representation and MOOSE uses a Jacobian-free, Newton-Krylov (JFNK) scheme to solve systems of partial differential equations [6]. The ability to employ massively parallel computational capabilities is one of many advantages to utilizing the MOOSE/ELK/FOX foundation. Peregrine is being constructed within a framework that supports or contains the following capabilities:

- Statics with elasticity, plasticity with strain hardening, creep, large strains, large displacements, and smeared plus explicit cracking;
- Unsteady (transient) heat transfer including conduction, convection and radiation with time and spatial (axially, radially and potentially azimuthally in a cylindrical fuel element) dependent internal heat generation;
- 2D axisymmetric, plane strain, and plane stress representations, including contact and friction interactions between pellets and between the pellet and cladding;
- 3D statics with contact and friction, and heat transfer;
- Mixed dimensional coupling (via multipoint constraint equations, etc.), e.g., combined 2D and 3D numerical representations for coupled global (2D) and local effects (3D) modeling; and
- Utilizes high performance computing platforms to achieve the massively parallel performance and scalability required to perform coupled multi-physics simulations of full-length 3D representations of the fuel rod components.

Figure 6 provides an overview of the major components in Peregrine and some of the functionality included in each component. There are six major components within Peregrine that together provide the functionality to perform fuel performance calculations. The computational framework in MOOSE provides four of the components: Problem Setup, Physics Solution, Global Parameters Integration, and Results Output as native elements that can serve as building blocks for Peregrine. This has simplified the development time for Peregrine and allowed the rapid advancement of multi-dimensional finite element representation of a fuel rod and detailed analyses using existing material property models from Falcon.

In addition to the computational framework from MOOSE, Peregrine contains material property and constitutive model library that allows for thermal, mechanical, and chemical property models and irradiation effects models, such as fission product-induced swelling, irradiation creep, fission gas release, and pellet cracking. A key focus of the CASL material modeling effort is to

develop more in-depth physics-based models for zirconium alloy and UO_2 ceramic materials. These models include irradiation creep and growth, thermal creep, outer cladding surface corrosion, inner surface cladding corrosion, fission product release and transport, and ceramic material fracture behavior. Since Peregrine development is underway in parallel with this activity, simplified models for key behaviours and properties have been initially incorporated into the code from several sources, including open literature empirical models, MATPRO data routines from the DOE and NRC [36], and select models from the EPRI fuel performance code, Falcon [37], [38].

Problem Setup
- Power Density
- Burnup Distribution
- Fast/Thermal Flux Dist
- Thermal B/C
- Mechanical B/C

Material Properties (e.g.)
- Specific Heat
- Density
- Conductivity
- Elastic/Plastic Behavior
- Creep Rate

Behavior Models (e.g.)
- Swelling/Densification/Cracking
- Irradiation Creep/Growth
- Grain Growth
- Fission Gas Release
- Corrosion

Physics Solution
- Thermal Transport
- Mechanical Forces
- Chemical Transport

Global Parameters Integration
- Rod Pressure
- Fission Gas Composition
- Linear Power

Result Output
- Write global variables
- Shift Internal State Variables

FIG 6. Schematic of Peregrine Code Structure.

The empirical/semi-empirical material and behavior models currently incorporated into Peregrine provide the ability to replicate the existing fuel modeling capabilities in established codes such as FRAPCON [39] and Falcon [37], [38]. This provides an excellent starting point for identifying areas for improvement in key material property or behavior models using advanced modeling and simulation capabilities, such as density functional theory, molecular dynamics, or phase-field approaches [40]–[42]. The use of these methods in computational material science to elicit details into the fundamental physics of irradiated material behavior may offer the engineering scale methods the opportunity to improve the semi-empirical models currently used in Falcon or MATPRO with improved parameters or additional terms to account for expanded representation of the relevant physics.

4.3 Coupling material performance, neutronics, and thermal-hydraulics

Fuel rod performance and reactor system performance are coupled through a complex network of both tight and loose physics variables, and the importance of these interconnected relationships depends on the operational scenarios and conditions. As such, developing standalone fuel performance modeling tools focused on a specific behavioural aspect is incomplete because of the assumptions required to impose certain boundary conditions, initial conditions, and forcing functions.

CASL realizes the importance of coupling the fuel performance modeling codes with the tools required to provide the high fidelity information on fission density and fast neutron flux, and coolant flow, pressure, and chemistry conditions. Both Peregrine and MAMBA have been actively coupled to neutronics and thermal-hydraulics or computational fluid dynamics codes to supply the necessary feedback between fuel temperature, chemistry, and geometry on fission density and coolant flow. The implementation of automated coupling of material performance, neutronics, and thermal-hydraulics is an active area for CASL. These efforts are using and developing advanced computational methods and exercising high performance computers to overcome limitations in complex solution algorithms and address the inherent problems of information exchange.

4.4 Important considerations for RIA modeling

As described by Jernvisk, most RIA fuel behavior modeling to date has been focused on the thermo-mechanical conditions important to Phase 1, with a keen interest on capturing the effect of prior irradiation on the pellet-cladding mechanical interaction phenomena. The goals of these efforts have been to understand the cladding failure conditions observed in the RIA-simulation experiments and translate this knowledge to fuel rod behavior during hypothetical LWR events and the fuel failure criteria used to demonstrate that the reactor will remain in a safe configuration after the event. These evaluations have used 2-D axisymmetric geometric representations, simplified cladding to coolant heat transfer modeling, and generally ignored the presence of non-uniformities in corrosion layer thickness, material properties, and azimuthal power distribution. By disregarding these 3-D effects or the complexities of high temperature behavior, the current efforts to determine the fuel rod failure and post-failure consequences have left several important questions unanswered, and as a result, potentially restrictive failure or core coolability criteria have been established to ensure that the margin to safety is maintained.

Improved multi-physics and multi-scale modeling methods are necessary to begin to answer such questions as: the impact of non-uniform power deposition, the consequences of cracking and spalling of the corrosion layer thickness under rapid loading conditions, and the important role of cladding to coolant heat transfer and high temperature behavior during the Phase 2 period of an RIA. This is in addition to the mostly empirical nature of the material models currently used in the methods to evaluate RIA events. As newer fuel and cladding materials are introduced, advanced modeling tools can be used to estimate their performance during hypothetical RIA events to reduce the number of expensive irradiation experiments in test reactors, provided these tools have the ability to capture the influence of material characteristics on the overall fuel rod behavior. Such an effort will require a multi-dimensional fuel rod behavior analysis code that can consider the 3-D effects caused by non-uniform power deposition, variations in material properties cause by local effects (cracks, interfaces, porosity, etc.), the microstructural and alloy effect on material behavior, and

advanced high temperature mechanical and chemical material models. Additionally, detailed information will be needed on the prior irradiation conditions within the fuel rod, as summarized in Table 1, the ability to couple with advanced neutron kinetics methods to capture non-uniform power deposition, and an interface with an advanced thermal-hydraulics code to obtain the proper rod to coolant heat transfer from single phase fluid flow to post-DNB film boiling conditions.

Several activities either on-going or planned within CASL will begin to address the needed capabilities for advanced modeling of RIA events. This includes development of a more mechanistic cladding deformation model using the visco-plastic self-consistent modeling approach, coupling Peregrine and MAMBA to provide a more accurate distribution of cladding corrosion and CRUD layer distribution, and improved fission gas diffusion kinetics needed to define intragranular and intergranular bubble distributions.

As previously mentioned, we have started an effort to resolve the cladding deformations due to PCMI as well as due to ballooning by using the VPSC approach. Specifically, an enhanced version of VPSC where the constitutive framework is based on dislocation density (based on the seminal work of Beyerlein and Tome [43]), which attempts to account for the vacancy and interstitial loops in the cladding created by irradiation, and their interaction with mobile dislocations, which ultimately lead to increased strain hardening and embrittlement. This approach was recently used to perform proof of principle calculations for incorporation of the effect of irradiation dose on the flow stress for Zircaloy-4, where the effect of irradiation on flow stress is captured by modifying the critical resolved shear stress using a dislocation based strain-hardening equation that accounts for the interaction of mobile network dislocations with the irradiation loops. The densities of irradiation loops are determined by a microstructure based irradiation growth formulation. The ultimate goal is that the model will be able to predict the stress state for a given loading condition, burn-up and transient time during a reactor operation.

It is also necessary to ultimately couple MAMBA and Peregrine in order to establish the initial fuel rod conditions, i.e. corrosion layer and CRUD thickness, prior to a transient event. For example, non-uniform oxide spallation was observed in CABRI experiments and advanced modeling can have an important role in understanding the effect of corrosion layer constituents, pulse width, coolant conditions, etc. on transient spallation behavior [44]. In addition, CRUD will play a role during Phase 2 of an RIA event when heat conduction becomes dominant, post-DNB heat transfer is critical, large cladding deformation are possible, and HT oxidation is active.

5. STATUS OF FUEL BEHAVIOR MODELING IN CASL

The fuel behavior modeling capability development within CASL has reached a level of maturity where both the MAMBA and Peregrine codes have begun benchmarking and validation activities using data from separate effects tests, integral fuel rod evaluations, and comparison to commercial reactor irradiation observations. CASL as recently completed an initial validation and benchmark activities for Peregrine using test rod irradiation data from the Halden, RISØ, and Studsvik test reactors and comparisons to the Falcon fuel performance code. Similarly, demonstration cases have been performed with MAMBA coupled to neutronics and thermal-hydraulics/CFD codes to qualitatively understand the impact of higher fidelity physics and geometric modeling can have on CRUD layer calculations.

5.1 Validation and Benchmarking of MAMBA for PWR CRUD Growth

Validation of MAMBA calculations is inherently difficult. One reason for this difficulty is that the resolution of MAMBA is generally higher than typical experimental characterization. Also, an ideal validation scenario would involve high resolution experimental data collected in situ during operation. Addressing these challenges will require advanced diagnostics and characterization methodologies, and it is envisioned that computational predictions may accelerate the development and eventual deployment of advanced techniques. However, until advanced techniques are developed, there is much to be learned about CRUD behavior from a qualitative comparison between high-resolution calculations and a combination of plant data. For example, MAMBA results such as those shown in Fig. 7 contain information about CRUD thickness, composition and temperature. These can be qualitatively compared to, for example, oxide thickness data collected on fuel rods that experienced CRUD. Although oxide thickness is not a measure of CRUD thickness, it is expected that there will be some correlation. Also and importantly, the azimuthal variation of oxide thickness data has been collected for certain plants, which can be valuably compared to MAMBA calculations that have been coupled to computational fluid dynamics, see e.g. [13]. In addition to plant data, MAMBA results can also be more directly compared to experimental data collected at facilities that grow artificial CRUD, e.g. Westinghouse's so-called WALT loop [45], [46]. An advantage of this approach is that a number of variables can be adjusted in the loop experiments in order to compare to MAMBA results. There is also the opportunity for more in situ characterization than in core.
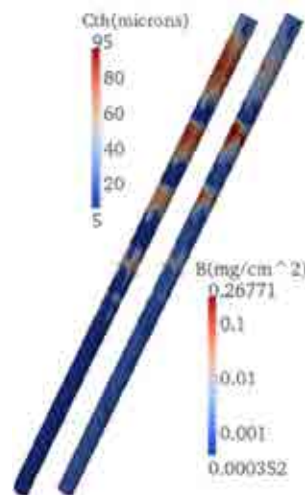
FIG. 7. CRUD thickness (left) and boron concentration (right) for a representative MAMBA calculation coupled to computational fluid dynamics simulation [13].

5.2 Steady State Fuel Performance Modeling Using Peregrine

The fuel performance modeling efforts in CASL have recently completed a benchmarking and validation exercise of the Peregrine steady state modeling capabilities using in-reactor measurements of temperature, fuel rod dimensional changes, and fission product release obtained from a variety of experimental programs on irradiated fuel. These efforts have successfully shown that Peregrine is

approaching the abilities of industrial nuclear fuel modeling programs to reliably calculate the fuel temperatures, cladding deformations, and fission gas release in an operating fuel rod as a function of the environmental conditions within a nuclear reactor.

The benchmarking and validation of Peregrine is currently based on the results from fourteen (14) fuel rods selected from the Instrumented Fuel Assembly (IFA) test programs in Halden, the RISØ Fission Gas Project 3 program, and the Studsvik Super-Ramp program. These rods have been analyzed with both Peregrine and Falcon using axisymmetric 2-D geometric representations of the fuel column and cladding as shown in Fig. 8. These 14 fuel rods experienced irradiation conditions ranging from beginning of life to those typical of high burnup.

Comparisons between the Peregrine and Falcon calculations have been made with the measured data, e.g. fuel temperatures, cladding elongation, etc.; in addition to code to code comparisons for the pellet-cladding gap thickness and gap thermal conductance, which are critically important to fuel performance, but for which there is limited or non-existent data. A comparison of Peregrine to fuel centerline temperatures from more than 550 measurements is shown in Fig. 9, along with a comparison to the industry fuel performance modeling software package, Falcon. The square (red) symbols represent the Peregrine results and the triangle (green) symbols indicate the Falcon results for the same set of rods. The results are scattered about the perfect agreement line, with both codes showing about a ±50 K (90°F) variation. The general trend is for Peregrine to calculate a slightly lower temperature, while Falcon calculates a slightly higher the temperature compared to the measurements.
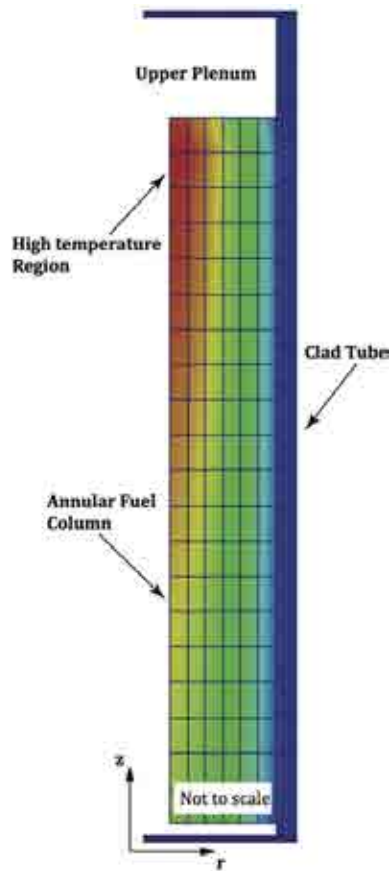
FIG. 8. 2-D Axisymmetric geometric representation of a test rod containing central hole for a thermocouple. A contour of the temperature is superimposed on the finite element mesh.
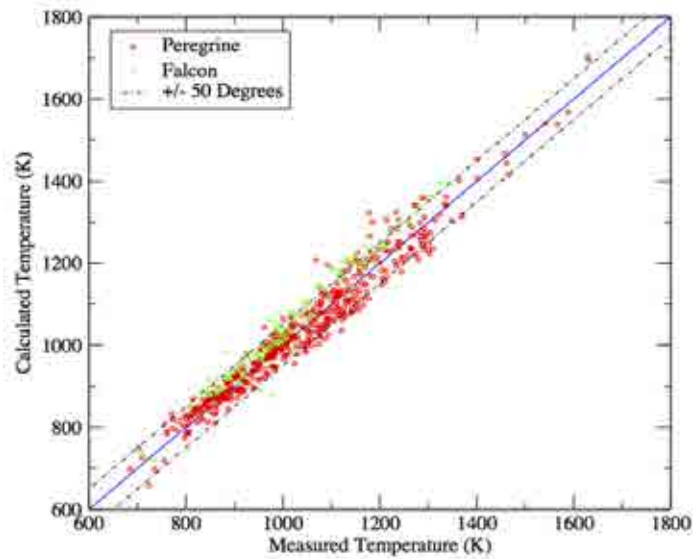
FIG 9. Calculated versus measured fuel centerline temperature from Peregrine (red symbols) and Falcon (green symbols) for over 550 measurements in Halden tests rods.

Similar comparisons have been conducted between mechanical deformation and fission gas release data obtained from in-pile measurements and post-irradiation examinations. For the mechanical calculations, the agreement between code calculations and measurements are reasonable for the cladding deformations prior to strong pellet-cladding mechanical interaction, i.e. below 25 kW/m or for ramps to high power. These types of irradiation conditions highlight the deficiency of the mechanical modeling capability for strong frictional contact between fuel and cladding and modeling of gaseous swelling effects, which could have pronounced effects during high power ramps.

In the case of fission gas release, calculations have been performed using two different fission gas release models; a classical implementation of the Forsberg-Massih approach [47] and a more recent extension of the Forsberg-Massih model by Pastore, et al. to consider the influence of grain boundary bubble growth and interlinkage [48]. Overall, the preliminary fission gas release calculations for nine of the test cases covering a number of operating conditions have shown that Peregrine has the general capability of modeling fission gas release. Comparisons of Peregrine calculations using both the classical Forsberg-Massih model and the Pastore model to the measured data find that the extensions proposed by Pastore improve the representation of the high temperature fission gas release during rapid power maneuvers as shown in Fig. 10. However, modeling of fission gas release has been a challenging part in nuclear fuel performance codes; existing models in fuel performance codes generally do not provide a versatile capability of calculating fission gas release, which is strongly influenced by local characteristics of the fuel material and the physical processes active at various operating and accident conditions.
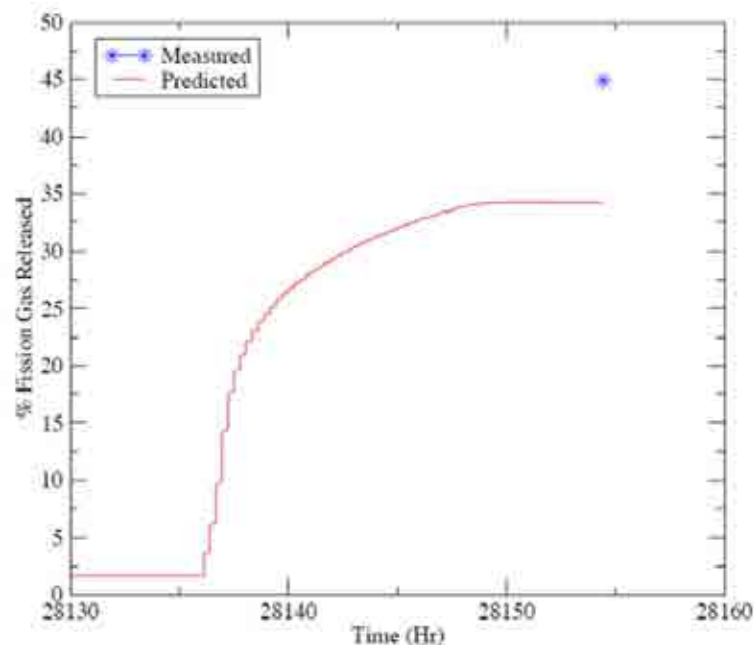
FIG 10. Calculated Fission Gas Release Fraction for PK2-3 Test Rod during the Power Ramp using Pastore Model [[48]] and the Post-ramp Measurement for Comparison.

Improved understanding of the spatial distribution of fission gas (i.e. intragranular vs. intergranular) is critical to enhancing the semi-empirical models currently used in engineering scale

fuel performance codes. As such, Fig. 11 describes a multiscale approach to address the role of microstructure in fission-gas behavior for nuclear fuel [49]. First in Fig. 11a, DFT is employed to determine the diffusivity and diffusion mechanism of Xe in UO_2 [50]. Then, atomistic pair potentials are used in molecular dynamics/atomic-scale methodologies to determine the interactions between fission-gas atoms and grain boundaries [51], [52], dislocations [53], and other extended defects (Fig. 11b). Then, mesoscale models can be developed from the atomic results, and can subsequently be used to determine the role of more realistic microstructures on fission-gas behavior as shown in Fig. 11c. The ultimate goal, of course, is to develop a compositionally and microstructurally aware model of fission-gas retention and release to be used by a fuel performance code.

| (a) | (b) | (c) |
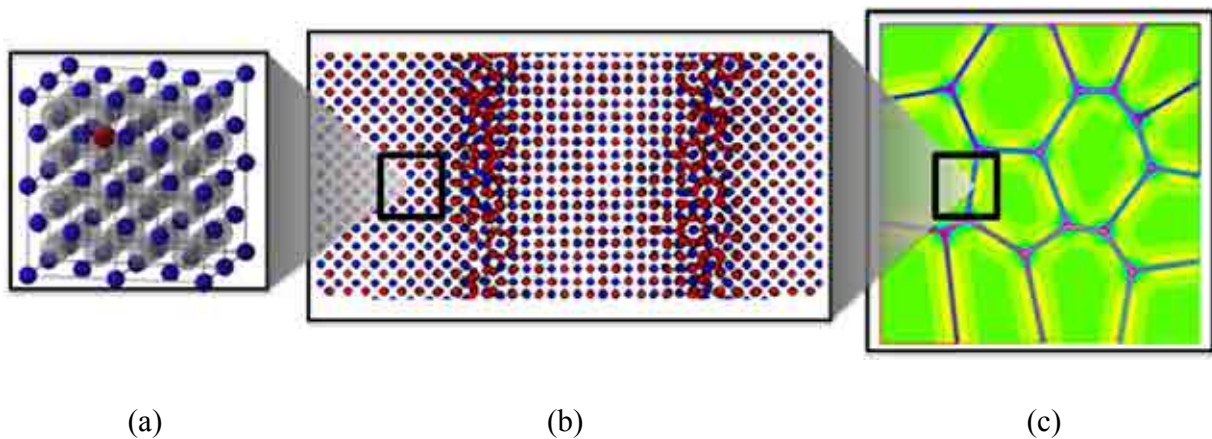
FIG. 11. A schematic example of multiscale (atomistic to mesoscale) modeling for fission gas atom behavior in UO_2 [[49]].

5.3 Application to Transient Conditions - RIA

In preparation for extending the fuel modeling efforts to transients, the fuel performance code Peregrine has been used to calculate the fuel behavior during Phase 1 of an RIA event. The objective of this analysis was to exercise the current capabilities within Peregrine and identify the areas that are lacking or require modification. The demonstration case consisted of a ~30 millisecond power pulse initiated at hot-zero power conditions. The maximum deposited energy reached about 120 cal/gm (~500 J/gm), with the rod average linear power exceeding 4000 kW/m. A chopped cosine axial power distribution was applied in the model. Constant cladding to coolant heat transfer conditions are assumed throughout the analysis time. The fuel pellet and cladding material properties and the pellet cladding gap thickness were initialized at conditions representative of a 70 GWd/tU peak burnup rod. At this burnup level, the build-up of fissile isotopes at the pellet periphery leads to a highly non-linear radial power profile, with a power occurring that the pellet rim region that is more than 3 times the pellet average value.

The diagram below in Fig. 12 highlights the thermo-mechanical results achieved to date on modeling RIA fuel behavior with Peregrine. Presented are the fuel rod temperature contour (central

image) and mid-height radial temperature profile at 0.5 seconds, the cladding stress and strain response up to 0.5 seconds, the radial power distribution across the pellet at the start of the event, and the rod average linear power time history. This time corresponds to the end of the energy deposition from the prompt power pulse, as shown in the diagram. The results highlight the capabilities of Peregrine to capture the near-adiabatic heatup of the pellet during the energy deposition in Phase 1 of the event. Peak pellet temperatures approaching 1800 K near the pellet periphery are calculated as a result of the rapid energy deposition and radial power distribution. Using a mechanical constitutive law representative of Zircaloy-4 material, the cladding stress-strain response calculated by Peregrine indicates yielding and plastic deformation during the later portion of the energy deposition. Lastly, the pellet-cladding closure and contact algorithm used in MOOSE does a good job of capture the rapid contact forces and increase in contact conductance due arising from pellet thermal expansion. It should be noted that linear finite element representation was used for the fuel column in this demonstration. This type of element does not capture well the non-linear heat conduction and generation for present during rapid RIA events. As a result, the numerical approach causes some artificial heat conduction (or numerical drift) that will be addressed in the future by using quadratic elements for these applications.
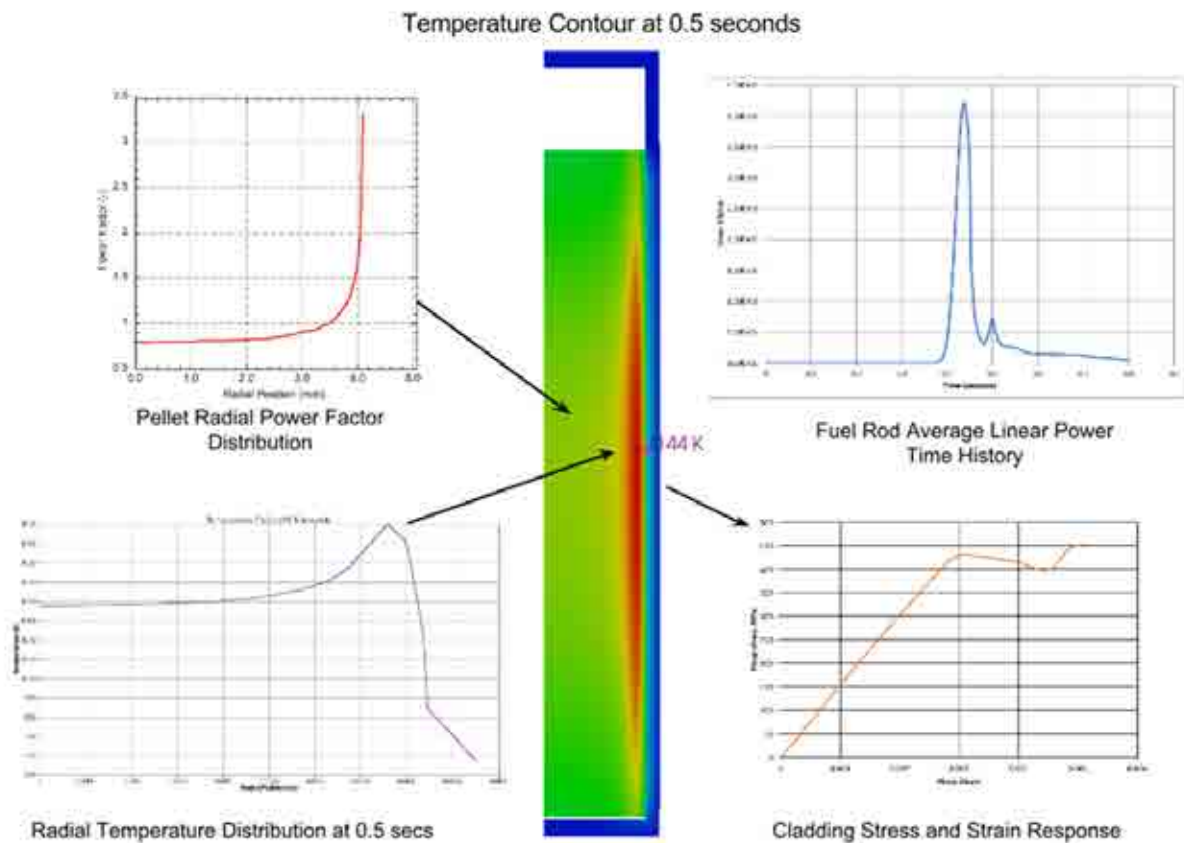

FIG. 12. Initial results from Peregrine calculations of Phase 1 fuel behavior during a 30 millisecond power pulse. Shown is a temperature contour at 0.5 seconds from the start of the transient.

6. SUMMARY

While the importance of fuel modeling under accident conditions has been acknowledged for many years, only recently have the capabilities become available to move from simplified geometric representation (2-D axisymmetric or planar) and empirical material models to 3-D geometric representation with non-uniformities and more mechanistic behavior models. CASL is developing advanced modeling and simulation capabilities for LWR fuel behavior using a multi-scale, multi-physics approach that applies engineering scale methods to identify the conditions and important fundamental mechanisms that influence material performance or behavior response. Based on this information, microscale modeling approaches are being used to construct improved representations for key material properties such as xenon diffusion within the UO_2 matrix, cladding irradiation-induced growth and creep, zirconium alloy reactions with water, hydrogen uptake, iodine reactions with zirconium, and coolant chemistry-rod interactions.

Currently, this approach is being applied to model and understand both cladding failure by PCI and the CRUD-induced fuel performance problems; CIPS and CILC, important fuel performance limiting conditions for steady state operation. However, several activities either on-going or planned within CASL will begin to address the needed capabilities for advanced fuel behavior modeling for off-normal conditions, particularly RIA and LOCA. This includes development of a more mechanistic cladding deformation model using the visco-plastic self-consistent modeling approach, coupling Peregrine and MAMBA to provide a more accurate distribution of cladding corrosion and CRUD layer distribution, and improved fission gas diffusion kinetics needed to define intragranular and intergranular fission gas bubble distributions. These upcoming enhancements center around establishing the initial fuel rod conditions prior to an accident, and focus is also needed in modeling the fuel behavior during an accident. Improved multi-physics and multi-scale modeling methods are necessary within the transient regime to begin answering important questions such as; 1) the impact of non-uniform power deposition within the pellet, 2) the consequences of cracking and spalling of the corrosion layer thickness under rapid loading conditions, 3) the important role of cladding to coolant heat transfer and 4) high temperature mechanical and chemical reaction behavior.

Peregrine and MAMBA benchmarking and validation activities provide confidence in the development of the fuel performance modeling capabilities within CASL, but also highlight the challenges in accurately modeling the complex thermal and mechanical behavior inherent in nuclear fuel performance. A number of improvements in the material and behavior models have been identified, and future development activities will focus on enhancing and implementing these models into Peregrine and MAMBA. In particular, improvements to the representation of pellet cracking and relocation, fission gas retention and release, gap thermal conductance, pellet-clad mechanical contact (including improved advanced creep and growth models) and cladding oxidation and hydride formation and growth are needed. These advancements will expand the fidelity of Peregrine and provide the ability to accurately model three-dimensional aspects of fuel performance, such as pellet-clad interaction with missing pellet surfaces. In some cases, advanced models for these topics are being developed within the Materials Performance and Optimization (MPO) focus area and will be implemented in Peregrine and MAMBA to enhance code capabilities.

REFERENCES

[1] MONTGOMERY, R. O., Peregrine: Advanced Modeling of Pellet-Cladding Interaction (PCI) Failure in LWRs, Proceedings of the TopFuel 2012 Reactor Fuel Performance Meeting, Manchester, U.K., Sep. 2–6, (2012).

[2] Energy Innovation Hubs, U.S. Department of Energy, 1000 Independence Avenue, SW, Washington, D.C. 20585; www.energy.gov/hubs/index.htm.

[3] DESHON, J., HUSSEY, D., KENDRICK, B., et al., "PWR Fuel CRUD and Corrosion Modeling", Advanced Fuel Performance: Modeling and Simulation, JOM Vol. 63 No. 8, 2011.

[4] SECKER, J. R. et. al, CASL Multi-physics PWR modeling including Crud Induced Power Shift (CIPS) and Crud Induced Localized Corrosion (CILC), Proceedings of the TopFuel 2012 Reactor Fuel Performance Meeting, Manchester, Manchester, U.K., Sep. 2–6, (2012).

[5] KENDRICK, B. K., "CASL Multiphysics Modeling of Crud Deposition in PWRs," Proceedings of the 2013 LWR Fuel Performance Meeting, Charlotte, NC. September 15–19, (2013).

[6] GASTON, D., NEWMAN, C., HANSEN, G., AND LEBRUN-GRANDIE´, D., MOOSE: A parallel computational framework for coupled systems of nonlinear equations. Nucl. Eng. Design, **239**, p. 1768–1778, (2009).

[7] WILLIAMSON, R., HALES, J., NOVASCONE, S., TONKS, M., GASTON, D., PERMANN, C., ANDRS, D., AND MARTINEAU, R., "Multidimensional multiphysics simulation of nuclear fuel behavior," Journal of Nuclear Materials 423(2012) 149–163.

[8] MONTGOMERY, R. O., LYON, W. F., JAHINGIR, M. N., AND YAGNIK, S., Capabilities of the FALCON Steady State and Transient Fuel Performance Code, Proceedings of the the 2004 International Meeting on LWR Fuel Performance, Orlando FL, September 19–22, (2004).

[9] Fuel Analysis and Licensing Code: Falcon MOD01: Volume 1: Theoretical and Numerical Bases, EPRI, Palo Alto, CA: 2004. 1011307.

[10] LEBENSOHN, R. A., TOMÉ, C. N., A Self-Consistent Anisotropic Approach for the Simulation of Plastic Deformation and Texture Development of Polycrystals: Application to Zirconium Alloys, Acta Metall,. Mater. Vol. **41**, No. 9, pp. 2611–2624, (1993).

[11] THURGOOD, M. J. et al. COBRA/TRAC - A Thermal-Hydraulics Code for Transient Analysis of Nuclear Reactor Vessels and Primary Coolant Systems, NUREG/CR-3046, Pacific Northwest Laboratory, (1983).

[12] BAKOSI, J., CHRISTON, M.A., LOWRIE, R.B., PRITCHETT-SHEATS, L.A., NOURGALIEV, R.R., Large-eddy simulations of turbulent flow for grid-to-rod fretting in nuclear reactors, Nuclear Engineering and Design, Volume **262**, September 2013, Pages 544–561.

[13] WALTER, D. et al., High-Fidelity Simulation of CRUD Deposition on a PWR Fuel Pin With Grid Spacers: A Proof-Of-Principle Using The Fully-Coupled MAMBA/DeCART/Star-CCM+ Code, Proceedings of the 15th International Topical Meeting on Nuclear Reactor Thermalhydraulics, NURETH-15, Pisa, Italy, May 12–15, 2013.

[14] PETROV, V., et al., "Impact of 3D Spatial Variations In Fluid Flow On The Prediction of CRUD Deposition in a 4x4 PWR Sub-Assembly," Proceedings of the 15th International Topical Meeting on Nuclear Reactor Thermalhydraulics, NURETH-15, Pisa, Italy, May 12–15, 2013.

[15] OECD/NEA, Nuclear Fuel Behavior Under Reactivity-Initiated Accident (RIA) Conditions: State-of-the-art Report, NEA/CSNI/R(2010)1, NEA No. 6847, ISBN 978-92-64-99113-2.

[16] OECD/NEA, Nuclear Fuel Behavior Under Loss-of-Coolant Accidents (LOCA) Conditions: State-of-the-art Report, NEA/CSNI/R(2009)15, NEA No. 6846, ISBN 978-92-64-99091-3.

[17] THOMPSON, L.B., TOLMAN, E.L. and MACDONALD, P.E. Analysis of fuel behavior during reactivity initiated accidents, CONF-750360-1, OSTI-4158752, presented at the Enlarged Halden Programme Group Meeting, Geilo, Norway, 16–21 March 1975.

[18] BURCHILL, W. E., Requirements for Analysis of Transient Fuel Rod Behavior during Design Basis Events, EPRI NP-1022, June (1978).

[19] MONTGOMERY, R.O., RASHID, Y.R., OZER, O. and YANG, R.L., Assessment of RIA-Simulation Experiments on Intermediate- and High Burnup Test Rods, Nuclear Safety, Vol. 37, No. 4, Nuclear Regulatory Commission, Bethesda, Maryland, October-December, 1996, pp. 372–386.

[20] YANG, R. ET AL., Topical Report on Reactivity Initiated Accident: Bases for RIA Fuel and Core Coolability Criteria, EPRI 1002865, Palo Alto, USA (2002).

[21] YANG, R., MONTGOMERY, R., and WAECKEL, N., Revised Reactivity Initiated Accident Acceptance Criteria for High Burnup Fuel, Proceedings of the European Nuclear Society ENS TopFuel 2003 Conference, Wurzburg, Germany, March 16–19, 2003.

[22] PAPIN, J., CAZALIS, B., FRIZONNET, J.M., FÉDÉRICI, E., LEMOINE, F., SYNTHESIS of CABRI-RIA Tests Interpretation, Eurosafe Forum 2003, Paris, November 2003.

[23] SUNDERLAND, D.J., MONTGOMERY, R.O., AND OZER, O., Evaluation of Recent RIA-Simulation Experiments with the FALCON Fuel Performance Code, Proc. of the 2004 International Meeting on LWR Fuel Performance, Orlando, Florida, September 19–22, 2004.

[24] MONTGOMERY, R.O., JAHINGIR, M.N., ALVIS, J. M., AND OZER, O., Analysis of Fuel Behavior During LOCA Tests Using FALCON MOD01, Proceedings of the 2005 Water Reactor Fuel Performance Meeting, Kyoto, Japan, October 2005.

[25] HURSIN, M., DOWNAR. T.J., MONTGOMERY, R., Impact of improved neutronic methodology on the cladding response during a PWR reactivity initiated accident, Nuclear Engineering and Design, Volume 262, September 2013, Pages 180–188, ISSN 0029-5493, http://dx.doi.org/10.1016/j.nucengdes.2013.04.023.

[26] JOO, H., et al., Methods and performance of a three-dimensional whole-core transport code DeCART, Proceedings of the PHYSOR 2004, pp. 21–24, 2004.

[27] DOWNAR, T., XU, Y. PARCS: A Multi-Dimensional Two-Group Reactor Kinetics Code Based on the Nonlinear Analytic Nodal Method, PUNE-98-26, Purdue University, 2004.

[28] MONTGOMERY, R.O., Analysis of Reactivity Initiated Accident-Simulation Tests Conducted at the CABRI and NSRR Facilities in France and Japan, EPRI, Palo Alto, CA 2003. 1002863.

[29] LASSMANN, K. The structure of fuel element codes, Nucl. Engrg. Des. 57 (1980) 17–39.

[30] BILLONE, M., MONTGOMERY, R., RASHID, Y.R., and HEAD, J., Advancements in the behavioral modeling of fuel elements and related structures, Nucl. Engrg. Des. 134, (1992), 23–36.

[31] WALKER, S.P., et al., The Mechanisms for Heat Transfer in CRUD-Coated Light Water Reactor Fuel, and Their Consequences, Water Chemistry and Clad Corrosion/Deposition Including Fuel Failures, Proceedings of a Technical Meeting held in Kiev Ukraine, IAEA-TECDOC-CD-1692, (2010).

[32] Modeling PWR Fuel Corrosion Product Deposition and Growth Processes, EPRI, Palo Alto, CA: 2004. 1009734.

[33] Materials and Chemistry Report, (Palo Alto, CA: EPRI, 2009), 1018580.

[34] SHORT, M.P., HUSSEY, D., KENDRICK, B.K., BESMANN, T.M., STANEK, C.R., YIP, S., Multiphysics modeling of porous CRUD deposits in nuclear reactors, Journal of Nuclear Materials, Volume 443, Issues 1–3, November 2013.

[35] ROBERTS, J.T.A., Structural materials in nuclear power systems, Plenum Press, 1981, pp. 53–60.

[36] HAGRMAN D.L. ET AL., MATPRO – Version 11 (Revision 2) A Handbook of Materials Properties for Use in the Analysis of Light Water Reactor Fuel Rod Behavior, NUREG/CR-0479, TREE-1280, Nuclear Regulatory Commission and EG&G (1981).

[37] MONTGOMERY, R.O., LYON, W.F., JAHINGIR, M.N., AND YAGNIK, S., Capabilities of the FALCON Steady State and Transient Fuel Performance Code, Proceedings of the 2004 International Meeting on LWR Fuel Performance, Orlando FL, September 19–22, 2004.

[38] Fuel Analysis and Licensing Code: FALCON MOD01: Volume 1: Theoretical and Numerical Bases, EPRI, Palo Alto, CA: 2004. 1011307.

[39] K. J. Geelhood, et al., FRAPCON-3.4: A Computer Code for the Calculation of Steady-State, Thermal-Mechanical Behavior of Oxide Fuel Rods for High Burnup, NUREG/CR-7022, PNNL-19418, March 2011.

[40] Li, Y., et al., Phase-field simulations of intragranular fission gas bubble evolution in UO_2 under post-irradiation thermal annealing, Nuclear Instruments and Methods in Physics Research Section B: Beam Interactions with Materials and Atoms, Vol. **303**, pp. 62–67, 2013,

[41] Liu X.Y., Andersson, D.A., Uberuaga, B.P., "First-principles DFT modeling of nuclear fuel materials," J. Mater. Sci., **47**, pp. 7367–7384, 2012.

[42] Li, Y., et al., "Mesoscale Benchmark Demonstration Problem 1: Mesoscale Simulations of Intra-granular Fission Gas Bubbles in UO_2 under Post-Irradiation Thermal Annealing," FCR&D-MDSM-2012-000098, April 2012.

[43] BEYERLEIN, I.J., TOMÉ, C.N., A dislocation-based constitutive law for pure Zr including temperature effects, International Journal of Plasticity, Volume **24**, Issue 5, May 2008, Pages 867–895.

[44] Georgenthum, V., Desquines, J., Arnaud, R., Study and modelling of zirconia cracking and spalling in high burnup PWR fuel claddings submitted to RIA transients, Proceedings of the 2005 Water Reactor Fuel Performance Meeting, Kyoto, Japan, October 2005.

[45] WANG, G., et al., Methods to reduce CIPS/CILC risk for the zero fuel failure by 2010 initiative, 18th International Conference on Nuclear Engineering (ICONE 18), Xian China, (2010).

[46] WANG, G., et al., "Westinghouse Advanced Loop Tester (WALT) Update", 16th International Conference on Nuclear Engineering, Session 10–17, ICONE16-48480, May 2008.

[47] FORSBERG, K., and MASSIH, A.R., Diffusion Theory of Fission Gas Migration in Irradiated Nuclear Fuel UO_2, Journal of Nuclear Materials, **135**, pg. 140–148, 1985.

[48] PASTORE, G., LUZZI, VALENTINO DI MARCELLO, L., VAN UFFELEN, P., Physics-based modelling of fission gas swelling and release in UO_2 applied to integral fuel rod analysis, Nuclear Engineering and Design, Volume **256**, March 2013, Pages 75–86, ISSN 0029-5493.

[49] STANEK, C.R., GRIMES, R.W., UNAL, C., MALOY, S.A. AND SCOTT S.C., Chapter 13: Nuclear Energy - Current and Future Schemes, in Materials for Energy and Environmental Sustainability, D. Ginley and D Cahen, Ed., Cambridge University Press (2011).

[50] ANDERSSON, D. A., UBERUAGA, B.P., NERIKAR, P.V., UNAL, C., and STANEK, C.R., 2011, Xe and U transport in $UO_{2\pm x}$: density functional theory calculations, Phys. Rev. B. **84** (2011) 054105.

[51] NERIKAR, P.V., RUDMAN, K., DESAI, T.G., BYLER, D., UNAL, C., MCCLELLAN, K.J., PHILLPOT, S.R., SINNOTT, S.B., PERALTA, P., UBERUAGA, B.P. , and STANEK, C.R., Grain boundaries in uranium dioxide: scanning electron microscopy experiments and atomistic simulations, J. Am. Ceram. Soc. **94[6]** (2011) 1893.

[52] NERIKAR, P.V., PARFITT, D.C., ANDERSSON, D.A., UNAL, C., SINNOTT, S.B., GRIMES, R.W., UBERUAGA, B.P. and STANEK, C.R., Xenon segregation to dislocations and grain boundaries in uranium dioxide, Phys. Rev. B **84** (2011) 174105.

[53] PARFITT, D., BISHOP, C.L., WENMAN, M.R. and GRIMES, R.W., Strain fields and line energies of dislocations in uranium dioxide, J. Phys. – Condens. Matter, **22** (2010) 175004.

MODELLING OF FUEL PERFORMANCE UNDER DESIGN BASIS ACCIDENTS

(Session 2)

Chairperson

J. Zhang

Belgium

SIMULATION OF FUEL BEHAVIOURS UNDER LOCA AND RIA USING FRAPTRAN AND UNCERTAINTY ANALYSIS WITH DAKOTA

J. ZHANG, Z. UMIDOVA, A. DETHIOUX
Tractebel Engineering (GDF SUEZ)
Avenue Ariane 7, B-1200 Brussels, Belgium
Phone: 32.2.773.9843, Fax: 32.2.773.8900
E-mail: jinzhao.zhang@gdfsuez.com

Abstract. The Tractebel Engineering's approach to qualifying the FRAPCON/FRAPTRAN fuel codes for simulation of fuel behaviour during LOCA and RIA accidental conditions is first described, followed by the simulation and uncertainty analysis of an OECD fuel rod codes RIA benchmark case (CABRI RIA test CIP3-1) and an OECD LOCA benchmark case (Halden LOCA test IFA-650.5). Those results showed the importance of the uncertainty analysis of the input parameters and the key models. The perspectives for further model improvements and benchmarks are also discussed.

1. INTRODUCTION

An accurate and reliable simulation of fuel rod behaviors during normal and accidental conditions is important for fuel rod design and safety analysis in nuclear power reactors.

The fuel rod behaviors during the design basis accidents, such as the Loss-Of-Coolant Accidents (LOCA) and Reactivity Initiated Accidents (RIA), are of particular interests during the last 2 decades. Many LOCA and RIA tests have been performed with high burnup fuel rods in various test reactors (such as the LOCA tests in the Halden reactor, the RIA tests in the CABRI and NSRR reactors). Those tests have contributed to a better understanding of the complex physical phenomena, such as fuel fragmentation, relocation, dispersal, cladding ballooning, burst, oxidation and hydriding, and so on [1], [2].

As a consequence, the nuclear safety authorities of various countries (like the USNRC and IRSN) are considering revisions to the current LOCA and RIA safety (or acceptance) criteria [3], [4], and the nuclear industry is improving their fuel rod codes and analysis methods to verify those safety criteria.

As the Owner's Engineer of the Belgian utility Electrabel, Tractebel Engineering (TE) has been working since 2010 on qualification of the fuel rod codes FRAPCON and FRAPTRAN [5-8] for the following intended applications [9]:

- Independent verification of fuel rod design provided by fuel vendors;
- Independent verification of vendors' LOCA/RIA safety analysis and reloads fuel safety evaluation;
- Generation of fuel rod input data for neutronics code;
- Feasibility studies for power uprate, burn-up extension and power modulation;
- Operational and licensing support.

This has been achieved partly by performing selected benchmark exercises in the IAEA FUMEX-III project [10], the OECD fuel rod codes RIA [11]–[12] and LOCA benchmarks [13]–[14] using FRAPCON and FRAPTRAN codes and by sharing expertise and information with other participants.

In addition, TE is also developing an approach to analyzing the uncertainties in multi-physics modelling and safety analyses, including fuel behavior simulation [15].

In this paper, the Tractebel Engineering's approach to qualifying the FRAPCON/FRAPTRAN fuel codes is first described, followed by the uncertainty analysis method. The FRAPTRAN simulation of the OECD RIA benchmark case CIP3-1 and the Halden LOCA test IFA-650.5, as well as uncertainty analysis are then presented. The results showed the importance of realistic physical modelling and the uncertainty analysis of input parameters and key models. Finally, the perspectives for further model improvements and benchmarks are discussed.

2. FRAPCON/FRAPTRAN FUEL ROD CODES

The FRAPCON3.4 [5] and FRAPTRAN1.4 [6] fuel rod performance and transient analysis codes have been developed in the framework of reactor safety research program conducted for the U.S. Nuclear Regulatory Commission (NRC) by Pacific Northwest National Laboratory (PNNL).

FRAPCON is developed for analysing the thermal-mechanical behaviour of LWR fuel rods under steady-state and power ramp operating conditions. FRAPTRAN code is developed for analysing the thermal-mechanical behaviour of LWR fuel rods under transient and accident conditions including LOCA and RIA.

Experimental data were used for assessing the FRAPCON and FRAPTRAN capabilities. The worldwide community also contributes to the development, testing and assessment of models [8].

2.1 Major models and capability

FRAPCON and FRAPTRAN are the analytical tools which use a common set of material properties documented in the material properties handbook to define the thermal and mechanical properties of the fuel and cladding at temperatures ranging from room temperature to melting.

Different types of fuels ((U, $Pu)O_2$, $UO_2Gd_2O_3$ and UO_2 with ZrB_2 coatings) and different types of claddings (Zircalloy-2, Zircalloy-4, ZIRLO and M5) can be modelled in FRAPCON and FRAPTRAN codes. The models and correlations for fuel, cladding and gas, as well as the water properties are embedded within FRAPCON and FRAPTRAN.

FRAPCON and FRAPTRAN include the following major models:
- Fuel thermal models including thermal conductivity degradation;
- Mechanical models, including the default FRACAS-I model and Finite Element Analysis (FEA) model;
- Fission gas release (FGR), rod internal pressure and void volumes models (default Massih model and FRAPFGR model);
- Cladding oxidation and hydrogen content models.

A simplified thermal-hydraulic model is included in FRAPCON code. The boundary conditions in FRAPCON code consist in definition of coolant pressure, inlet temperature and mass flow as function of time. FRAPCON also generates the initialization file for FRAPTRAN transient calculations.

The FRAPTRAN thermal-hydraulic model is a simplified model with static heat transfer correlations in various heat transfer modes. The thermal-hydraulic boundary conditions in FRAPTRAN code consist in four options. In case of LOCA and RIA applications, two of these options "Coolant" and "Heat" are often used: "Coolant" option for specifying thermal-hydraulic boundary condition (i.e., calculated heat transfer coefficients and cladding temperature) and "Heat" option for thermal-mechanical boundary condition (i.e., imposed heat transfer coefficients and cladding temperature).

2.2 Developmental verification and validation

The purpose of the developmental code assessment is to assess the code against a limited set of well-qualified data that span the range of limiting operational conditions for commercial light-water reactors (LWRs) to verify that the code adequately predicts the integral test data. The integral test data of interest are fuel temperatures, FGR, corrosion, void volumes, and cladding deformation.

The primary FRAPCON3.4 code assessment database (used also for benchmarking the thermal and FGR models) consists of 133 fuel rods. These include 88 fuel rods with steady-state power operation covering a wide range of burnups and 45 fuel rods with steady-state irradiations followed by an end-of-life (EOL) power ramp [5].

The cases used for FRAPTRAN1.4 code assessment were selected on the criteria of having well-characterized design and operational data and spanning the ranges of interest for both design and operating conditions [2]. Two principal sets of data were used: data from RIA test programs and data from LOCA test programs. The code assessment database consists of 43 integral assessment cases [6].

The extensive developmental code verification and validation ensure a wide range of applicability of both codes. In addition, the bias and sensitivity in both codes have been assessed [7].

3. INDEPENDENT VALIDATION OF FRAPCON AND FRAPTRAN

3.1 The approach

The strategy for code qualification at TE consists in using a code with extensive verification and validation performed by the code developer and the international users on the one hand, and performing selected independent validation on the other hand, with the following objectives:
- Mastering the code use;
- Assessing the applicability to specific applications.

This qualification is based on a through review of the FRAPCON and FRAPTRAN code description documents, the extensive development assessment performed by the code developer (PNNL), and some benchmarks with the vendor's fuel rod codes. In addition, TE has performed selected benchmark exercises in the IAEA FUMEX-III project and the OECD fuel rod codes LOCA and RIA benchmarks using FRAPCON and FRAPTRAN codes.

3.2 Contribution to the IAEA FUMEX III

The Fuel Modelling at Extended burnup program (FUMEX) is a series of Coordinated Research Projects (CRP) organized by the International Atomic Energy Agency (IAEA). The objective is to improve the predictive capabilities of codes used in fuel behaviour modelling for extended burn-up.

For FUMEX III (2009–2011) [10], several cases were identified for different fuel types (PWR, BWR and VVER) at high burnups at normal operating, power ramp and accidental conditions. The selected cases focused on the following topics at extended burnup above 50 MWd/kg:

- Fission gas release (FGR);
- Pellet to Clad Interaction (PCI) or Pellet to Clad Mechanical Interaction (PCMI).

TE has analysed the following cases:

- Studsvik Super-ramp cases (PK1, PK2, PK4, PK6, PW3 and PW5);
- NSRR BWR RIA fuel rods FK1-3;
- AREVA Idealised case (normal operation fission gas analysis).

The results are presented in the FUMEX III final report [10].

3.3 Contribution to the OECD fuel rod codes RIA benchmark

The RIA fuel codes benchmark is organised in the frame of the activities of the Working Group on Fuel Safety (WGFS) of the OECD/NEA. The objective is to assess the capability and accuracy of the existing fuel rod codes to simulate fuel behaviours and evaluate the proposed safety criteria for the design basis RIA.

The selected cases are 4 RIA experiments that were or will be conducted on very similar rods in both CABRI and NSRR test reactors.

TE participated in this benchmark using the FRAPCON/FRAPTRAN codes. The results are presented in an OECD report [11] and are summarized in [12]. In particular, TE has performed a preliminary uncertainty and sensitivity analysis [21], [22].

3.4 Simulation of the OECD LOCA benchmark

The OECD LOCA benchmark is also organised in the frame of the activities of the Working Group on Fuel Safety (WGFS). The objective is to check the ability of the fuel rod codes to predict or reproduce the measurements and to identify the improvements to be made in the codes. It was focused on the thermal and mechanical responses of fuel and cladding during the Halden LOCA tests (IFA-650.3–5). The results are presented in an OECD report [14].

TE did not participate in this benchmark, but simulated, in a later stage, the same Halden LOCA tests using the FRAPCON/FRAPTRAN codes [23] and performed uncertainty analyses [24].
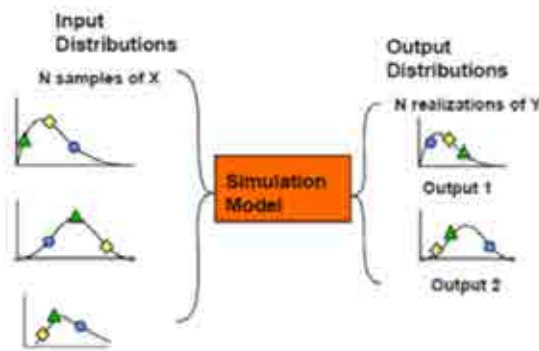
4. UNCERTAINTY ANALYSIS METHOD

4.1 The non-parametric order statistics method

Uncertainty analysis is becoming a regulatory requirement and industrial standard for fuel behaviour modelling and safety analyses [15]. Among all the available uncertainty analysis methods, the non-parametric order statistics method is so-far the most widely used in the nuclear safety analysis.

In this method, the thermal-hydraulic, neutronic and thermal mechanic computer codes are treated as "black boxes", and the input uncertainties are propagated to the simulation model output uncertainties via the code calculations with sampled input data from the known distributions, as shown in Fig. 1.

FIG. 1. The uncertainty analysis method by propagation of input uncertainties [20].

The statistical uncertainty analysis method consists in the following 5 major steps:

1) All relevant uncertain parameters for the codes, plant modelling schemes, and plant operating conditions are identified;

2) Any dependencies between uncertain parameters are quantified or defined, and the variation ranges and/or probabilistic distribution functions (PDFs) for each uncertain parameter are quantified or defined, based on engineering judgment and experience feedback from code applications to separate and integral effect tests and to full plants simulation.

3) The uncertainty ranges of input parameters are randomly and simultaneously sampled N times by a simple Monte Carlo simulation, according to the combined subjective probability distribution of the uncertain parameters.

4) Code calculations are performed using the sampled N sets of parameters as inputs. By performing code calculations using variations of the values of the uncertain input parameters, and consequently calculating results dependent on these variations, the uncertainties are propagated through the calculations, and the calculated results include the total uncertainty at the defined probability content (quantile or percentile) and confidence level.

5) The calculation results are ranked by order and a certain rank is selected as the estimator of the output of interest (i.e., selected key safety variables or figures of merits, such as peak-

cladding temperature or PCT in a LOCA) at the defined probability content and confidence level. Statistical evaluations are also performed to determine the sensitivity of input parameter uncertainties on the uncertainties of key results (parameter-importance analysis).

The order statistics method needs to select a reasonable number of input uncertainty parameters and associated range of variations and possible distribution functions for each one. Selection of parameters and their distribution must be justified.

The number of code calculations (N) is determined by the requirement to estimate the probability content or tolerance (quantile)-confidence level interval for the calculation output results of interest. It is currently a common practice to rely on the non-parametric tolerance limits procedure to determine the minimum sample size. The so-called Wilks' formula [16] is used to determine the minimum number of calculations needed for deriving the one-sided tolerance limits (with top rank as the upper limit):

$$1 - \gamma^N = \beta \tag{1}$$

or the two-sided tolerance limits (with top rank as the upper limit, and lowest rank as the lower limit):

$$1 - \gamma^N - N\,(1-\gamma)\,\gamma^{N-1} = \beta \tag{2}$$

Where $\beta \times 100$ is the confidence level (%) that the maximum code result will not be exceeded with the probability $\gamma \times 100$ (%) (quantile) of the corresponding output distribution, which is to be compared to the acceptance criterion. A more general formulation was given by Guba and Makai [17].

The confidence level is specified to account for the possible influence of the sampling error due to the fact that the statements are obtained from a random sample of limited size. N is representing the number of calculations such that the maximum calculated value in the sample is an upper-bound statistical tolerance limit. As an example, for a 95th/95th percentile ($\gamma = \beta = 0.95$), a minimum number of N=59 calculations should be performed for the single-sided, and 93 for the double-sided tolerance limit.

The non-parametric tolerance limits are used since nothing should be known about the distribution of the random variable except that it is assumed continuous. Moreover, the number N of code runs is independent of the number of the selected input uncertain parameters, but only depending on the tolerance limit quantile and on the desired confidence-level. The number of code runs for deriving sensitivity measures is also independent of the number of input parameters.

This method is very robust and simple to implement, which makes it extremely interesting for licensing applications to nuclear safety analyses. However, it has been shown that this method may lead to rather conservative results (in particular when using the first rank) and variability (e.g., outliers). One way to improve the method is to increase the number of code calculations, and take higher ranks as the estimators for the given probability content (quantile) and confidence level. This may be limited by the requested large calculation efforts in case of complex coupled code systems.

Due to its simplicity, robustness and transparency, this method will be implemented for most of the TE intended applications [15]. However, an optimised number of calculations will be determined to improve the accuracy.

4.2 The sensitivity and uncertainty analysis tool

The DAKOTA (Design Analysis Kit for Optimization and Terascale Applications) code has been developed by the Sandia National Laboratory [18]. As shown in Fig. 2, it provides a flexible, extensible interface between simulation codes and iterative analysis methods, via DAKOTA input files and executable. Among others, DAKOTA contains algorithms for uncertainty quantification (UQ) with sampling (Monte-Carlo or Latin Hypercube), epistemic uncertainty methods, and sensitivity analysis. These capabilities may be used on their own or as components within advanced strategies.
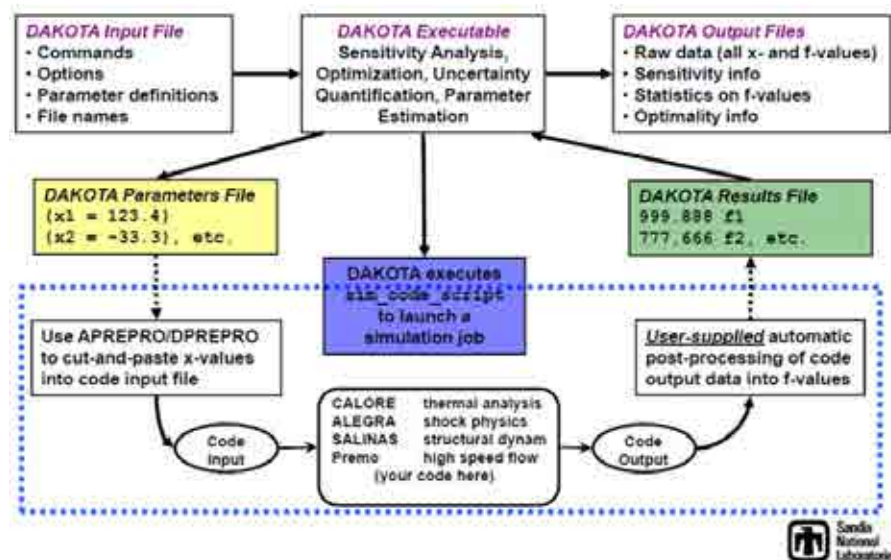
FIG. 2. The DAKOTA uncertainty/sensitivity analysis process [19].

For the applications presented in this paper, the input uncertainty parameter ranges and distributions, as well as the uncertainty analysis method and number of samples are defined in the *DAKOTA Input File*. Based on the sampled or assigned input uncertainty parameters in the *DAKOTA Parameter File*, various scripts have been developed to create the code input files, to execute the simulation jobs, and to collect the code calculation output data into the *DAKOTA Results File*. The *DAKOTA Executable* will then perform the requested statistical uncertainty and sensitivity analysis, and provide the information in the *DAKOTA Output Files*.

5. FRAPTRAN SIMULATION AND UNCERTAINTY ANALYSIS OF THE OECD RIA BENCHMARK CASE CIP3-1

5.1 The OECD RIA benchmark case CIP3-1

Since 1990's, a series of RIA tests have been performed at the Nuclear Safety Research Reactor (NSRR) and CABRI test reactor with highly irradiated fuels and highly corroded claddings. Those

tests have indicated that cladding failure at high burnups may occur at lower fuel enthalpy levels than the current regulatory limits.

The CIP3-1 is a RIA test that will be performed in the CABRI test reactor with pressurised water loop, at a pressure of 155 bars, an inlet temperature of 280 °C, and an inlet velocity of 4m/s. The channel has a diameter of 15 mm. The CABRI core power during the irradiation of CIP3-1 is assumed to be a 10 ms pulse.

The rodlet used for this experiment is refabricated from a ENUSA fuel rod standard PWR 17x17 UO2 rods cladded with ZIRLO that was irradiated for five cycles in the Vandellós 2 PWR nuclear power plant, up to a maximum local burnup close to 75 GWd/t. The rodlet has a length of about 702 mm, with a plenum of about 2 cm^3, and a He filling pressure of 20.5 bar.

This is a blind pre-test calculation; the anticipated maximum injected energy at peak power node is 115 cal/g and the pulse width at half maximum is expected to be about 8.8 ms. The objective of this test, together with other planned RIA tests, is to check if the coolant conditions (in particular the coolant temperature), pulse width and other experimental parameters in the test reactor prevent the cladding from heating up and deforming as might be expected in a commercial light water reactor.

5.2 FRAPCON/FRAPTRAN modelling and assumptions

FRAPCON3.4 code is used to simulate the base irradiation of the fuel rod, based on the specifications. The base irradiation for the test rodlet is then performed with some adjustment in the input parameters such as power history, inlet temperature and plenum length. The calculation results (burnup, corrosion thickness) are compared with the available measured data, in order to validate the FRAPCON input model and assumptions.

FRAPTRAN1.4 is used to calculate the transient behaviour of the fuel rodlet during the RIA test, using the base irradiation obtained with FRAPCON3.4. The filled gas after refabrication and the number of moles in the plenum are adapted.

The default model options are used. In particular, the "Coolant" option is used for the thermal hydraulic boundary conditions.

5.3 Uncertainty analysis

The uncertainty and sensitivity analysis method based on the Wilks' formula is then applied to this test rod (CIP3-1). The objective is to test the applicability of the uncertainty analysis method to fuel rod behaviour calculations, and to determine the optimal number of calculations to obtain an acceptable accuracy of the Wilks' estimator.

Following the approach presented in §4.1, all input parameters (test conditions, rod fabrication data) and the models that may be subject to uncertainties are first chosen based on the engineering judgement. Some sensitivity analyses are then performed on the individual input parameters of the code in order to determine the most influential ones.

For each of the identified key uncertainty input parameters, a mean value, a standard deviation and a range of variation (lower and upper limit values) as well as the distribution type must be defined, as summarized in Table 1.

For the current application, a normal distribution has been assigned to all the considered input parameters. For the geometrical parameters, this is justified by the fact that a lot of measurements

have been done during the fabrication. Their standard deviation has been taken as the half of the maximum of the absolute value of the difference between their nominal value and their upper or lower bound.

The coolant inlet temperature as well as the power history (for both the base irradiation and the pulse) is measured values. They are thus dependent on great number of independent random variables (i.e. the factors influencing a measure are numerous and random) and the central limit theorem shows that a variable which is dependent on great number of independent random variable also has a normal behaviour. Their mean has been taken as the value provided in the specification and their standard deviation has been taken as the standard measurement error considered in a nuclear power station.

TABLE 1. INPUT UNCERTAINTY PARAMETERS FOR STATISTICAL UNCERTAINTY ANALYSIS OF CIP3-1 FRAPCON/FRAPTRAN SIMULATION.

Input uncertainty parameter	Mean	Standard deviation	Lower bound	Upper bound	Distribution
Thermal conductivity model	0	1	-2	2	Normal
Thermal expansion model	0	1	-2	2	Normal
Fission gas release model	0	1	-2	2	Normal
Fuel swelling model	0	1	-2	2	Normal
Cladding creep model	0	1	-2	2	Normal
Cladding corrosion model	0	1	-2	2	Normal
Cladding hydrogen uptake model	0	1	-2	2	Normal
Multiplicative factor on the temperature history during base irradiation	1	0,00355	0,9929	1,0071	Normal
Multiplicative factor on the power history during base irradiation	1	0,02	0,96	1,04	Normal
Multiplicative factor on the power pulse	0,92976	0,0186	0,89257	0,96695	Normal
Coolant inlet enthalpy (J/kg) during the transient	1232080	5080	1221920	1242240	Normal
Cladding outside diameter (m)	0,0095	0,000019	0,009462	0,009538	Normal
Cladding inside diameter (m)	0,008357	0,000019	0,008319	0,008395	Normal
Dish radius (m)	0,002475	0,0000625	0,00235	0,0026	Normal
Fuel density (%)	95,5	0,75	94	96,5	Normal
Pellet diameter (m)	0,008192	0,000006	0,00818	0,008204	Normal
Cladding roughness (μm)	0,6355	0,31725	0,001	1,27	Normal
Fuel roughness (μm)	1,6005	0,79975	0,001	3,2	Normal
Cold plenum length during base irradiation (m)	0,029531	0,000884	0,0278	0,0301	Normal

Finally the parameters on the models in FRAPCON have also been chosen as normal for the same reasons as for the coolant temperature and power history. Since they bias the model to the number of standard deviation corresponding to the number assigned to them, their mean is zero and their standard deviation 1. The range of all these variables has been chosen as being their means plus or minus two times their standard deviations. The impact of the number of calculations and distributions of the input uncertainty parameters are also studied.

5.4 Results and discussion

5.4.1 Base case

A base case with nominal values for all input parameters is defined, and the default models in both FRAPCON/FRAPTRAN codes are chosen in the calculations. The "best estimate" calculation results will be compared with those made by other organizations using various fuel rod codes, in order to identify their differences and to propose improvements in the modelling. Figures 3–5 illustrate some results for the FRAPTRAN simulation of CIP3-1 base case.
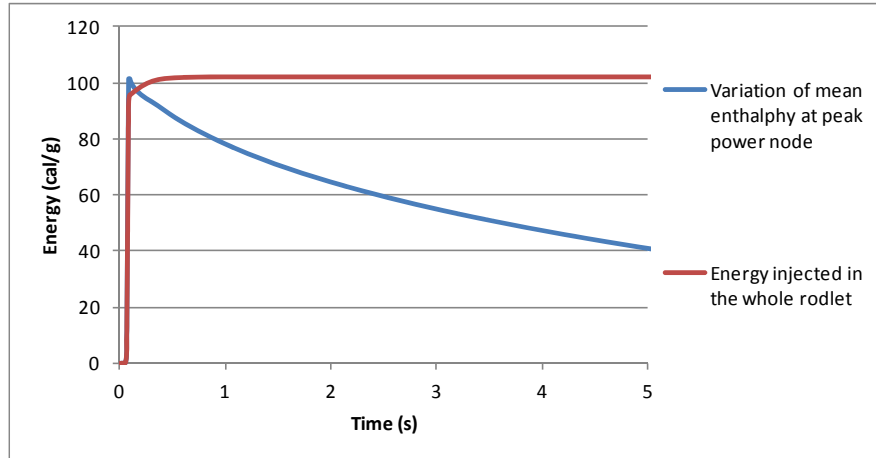
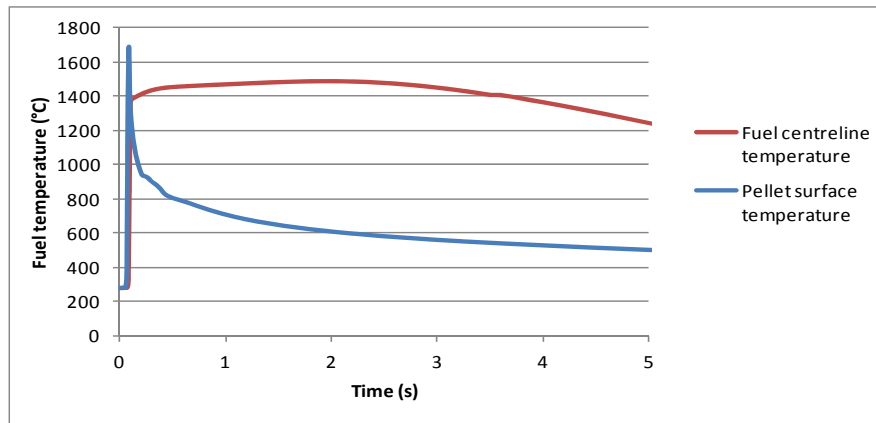*FIG. 3. Energy injected and the enthalpy at peak power node (CIP3-1).*

FIG. 4. Fuel centreline and pellet surface temperatures at peak power node (CIP3-1).
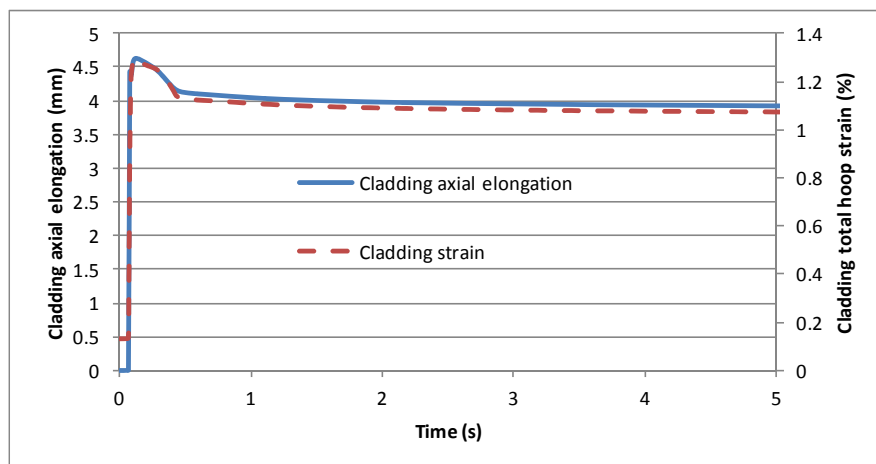

FIG. 5. Cladding axial elongation and total hoop strain at peak power node (CIP3-1).

Comparison of the results with other codes indicates that the fuel thermal-mechanical behaviours (fuel temperature, variation of enthalpy and deposited energy) are well predicted by FRAPTRAN, so is the time of fuel failure.

However, a correct prediction of cladding temperature is rather difficult due to the inadequacy of the FRAPTRAN thermal hydraulic models for the test capsule.

5.4.2 Uncertainty analysis

For the benchmark purpose, the double-sided tolerance limit is used in order to define the lower and upper bound of the calculated output values for the whole RIA transient. The objective is to demonstrate if the experimental data or the calculated mean values are well bounded by them.

From Eq. 2, for a probability of 95% at a confidence level of 95%, the minimum number of simulations is determined as N=93, if we take the top rank as the upper bound and the lowest rank as the lower bound. The so-defined lower and upper bound values, as well as the best estimate values for the enthalpy increase after steady-state at peak power node (PPN) are shown in Fig. 6. The calculated best estimate value is well bounded by both lower and upper limits.

The impact of the input parameters distributions is also studied by changing all the distributions in Table 1 from normal to uniform distribution with the same variation range. As shown in Fig. 6, the uniform distribution for all input uncertainty parameters tends to give larger differences between the lower and upper limits.

The impacts of distributions and the number of samples on the maximum mass fuel enthalpy increase are shown in Fig. 7. It can be observed that both the Wilks' quantile and the empirical quantile increase when uniform distribution is used for the input uncertainty parameters. This is what was expected since the uniform distribution favours the sampling of extreme values of the input uncertainty parameters, which is equivalent to increase the uncertainties on the input parameters, and hence leads to higher quantiles which are the uncertainties on the output parameters. The impact of the input parameter distributions is thus important. Their distributions should therefore be chosen carefully and more study is needed to determine them precisely (at least for the consequent input uncertainty parameters).
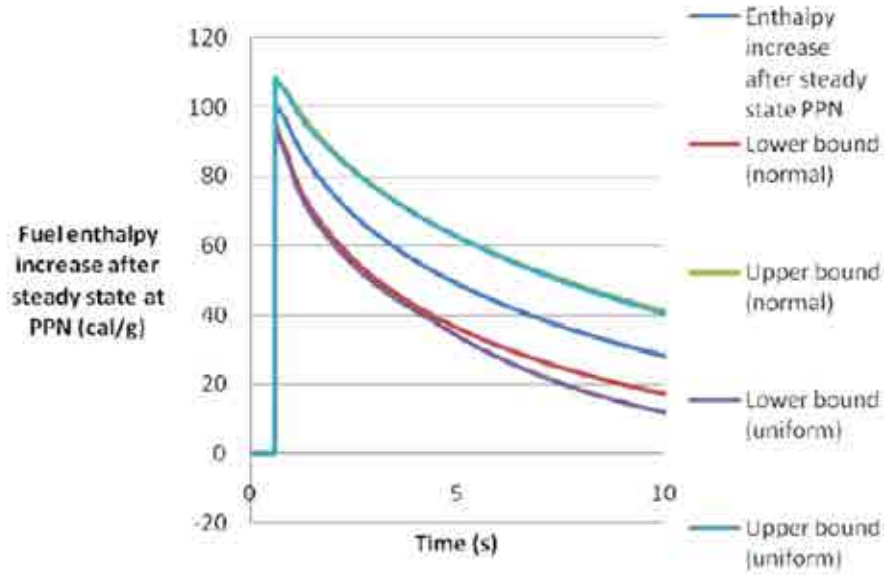
FIG. 6. The statistical uncertainty analysis results for CIP3-1 simulation [21].
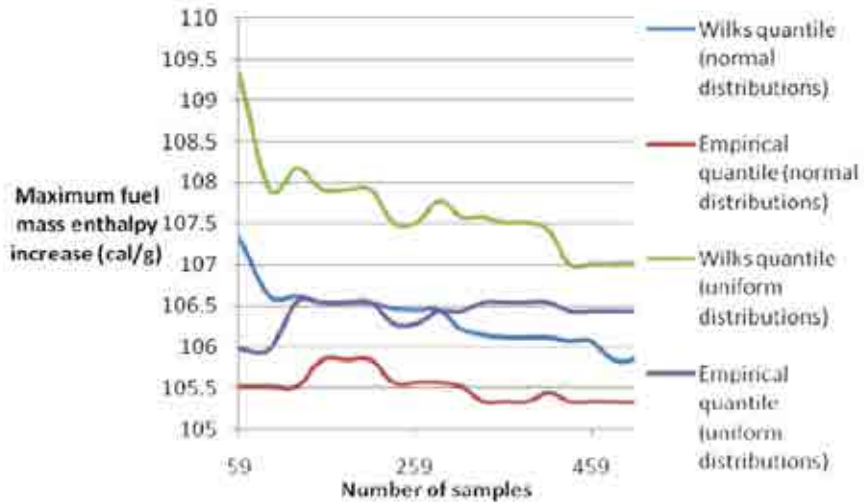
FIG. 7. Impact of input uncertainty parameters distribution for CIP3-1 simulation [21].

On the other hand, for both distributions, the Wilks' quantile and the empirical quantile tend to converge as the number of samples increases. This indicates that the accuracy of the predicted lower or upper bounds with higher order increases with the number of samples. However, this improvement may be limited by the needed computational efforts. A balance should be made when choosing the number of samples in the practical applications.

The DAKOTA code calculates also the Pearson's correlation between the input and output parameters. This correlation is used to determine the correlation coefficient not between the parameters themselves but rather between the ranks of the parameters allowing determining if there is a monotone relation between them. The input uncertainty parameters having a strong Pearson's

correlation (typically higher than 0.75) should be carefully defined due to their importance. The input uncertainty parameters having a weak Pearson's correlation (typically less than 0.25) with every output parameter can be eliminated (or simply keep at best estimate), after verification on the scatter plots that there is not another type of relation between the considered input uncertainty parameters and the output parameters (such as a sinusoidal relation).

The scatter plot in Fig. 8 below shows that the calculated energy input in the fuel has a strong relation with the sampled multiplicative factor on the power pulse (Pearson's correlation coefficient is approximately equal to 0.94).
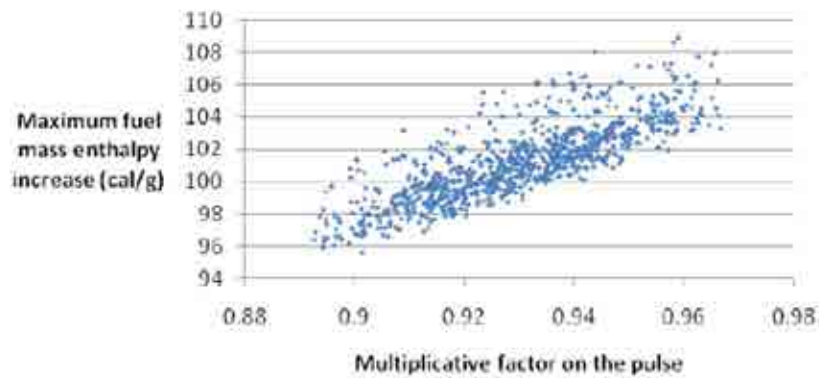
FIG. 8. Impact of the power pulse multiplier on CIP3-1 simulation uncertainty [21].

However, the scatter plot in Fig. 9 shows that there is effectively no dependency between the fuel enthalpy increase and the cold plenum length during base irradiation (Pearson's correlation coefficient is approximately equal to -0.04). It can thus be considered as having a weak influence, and hence can be eliminated as one input uncertainty parameter.
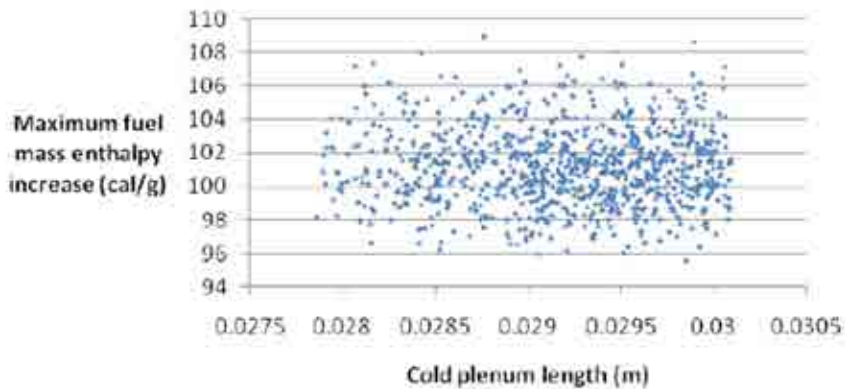
FIG. 9. Impact of the cold plenum length on CIP3-1 simulation uncertainty [21].

The above results show that the DAKOTA sensitivity analysis by Monte Carlo sampling is a simple and powerful tool to determine the importance of the input parameters in statistical uncertainty analysis.

It has been also shown that the prediction of the failure of fuel rod is sensitive to the following initial states and the following parameters or models:
- Initial gap thickness;
- Initial cladding spallation;
- Void volume;
- Fission gas release.

5.5 FRAPTRAN Simulation and Uncertainty Analysis of the Halden LOCA test IFA-650.5

5.5.1 The Halden LOCA test IFA-650.5

The OECD Halden Reactor Project (HRP) has performed many well-instrumented fuel rod in-pile experiments in the Halden Boiling Water Reactor, a heavy water cooled and moderated research reactor in Norway.

The objective of the Halden LOCA tests IFA-650 is to study fuel behaviours such as fuel fragmentation and relocation, cladding ballooning, burst (rupture) and oxidation during typical LOCA transient for PWR, BWR and VVER high burnup fuels [13]. In this paper, we present only the FRAPTRAN simulation of the Halden LOCA test IFA-650.5, which is one of the OECD LOCA benchmark cases [14].

The entire fuel rods with high burnup provided by Framatome ANP have been cut into pieces and then one rodlet was selected and re-fabricated for the LOCA test. The UO_2 fuel pellet has an initial enrichment of 3.5%, and has been irradiated in reactors for 2064 EFPD, reaching a burnup of 83 GWd/t. The cladding is DX ELS0.8b SRA (similar to Zr-4) type with a liner, having an average oxidation layer of 65 μm and hydrogen content of 650 ppm. The rodlet is about 500 mm, with an initial fill gas pressure of 40 bar.

A single fuel rodlet was located in a high-pressure flask connected to the heavy water loop 13 of the Halden reactor. The fuel power was controlled by reactor power. Nuclear power generation in the fuel rodlet is used to simulate decay heat, whereas the electrical heater surrounding the rod is simulating the heat from surrounding rods.

As shown in the following Fig. 10, the rig and rod instrumentations consisted of three cladding thermocouples at the bottom (TCC1) and upper (TCC2 & 3) part of the rod, three heater thermocouples at different axial elevations (TCH1 at bottom, TCH2 at mid and TCH3 at top), a cladding extensometer (EC2) and a rod pressure sensor (PF1), rig coolant thermocouples (two at rig inlet, TI, and two at outlet, TO), three axially distributed vanadium neutron detectors (ND) to measure axial power distribution and two fast response cobalt NDs to monitor rapid flux and power changes.

The IFA650.5 test was conducted on October 23rd, 2006. The test was initiated by letting the coolant out from the bottom of the rig. About 5 min after the rod burst, the test was terminated by reactor scram. The measured fuel total linear heat rate after calibration was ~25 W/cm. The heater power was adjusted to 17 W/cm. The axial power profile was nearly symmetric, with an axial peak to average power factor of ~1.05. The instrumentation worked well, the target peak cladding temperature of 1100 °C was achieved, and cladding burst occurred at 750 °C. The measured cladding and heater temperatures and heater power are shown in Fig. 11.
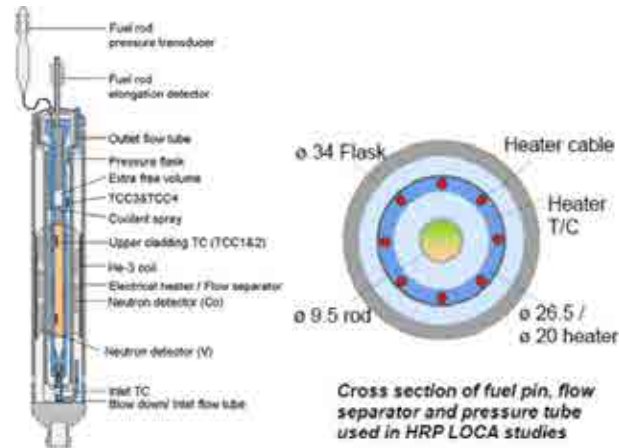
FIG. 10. Schematic of Halden LOCA Rig IFA-650 [13].
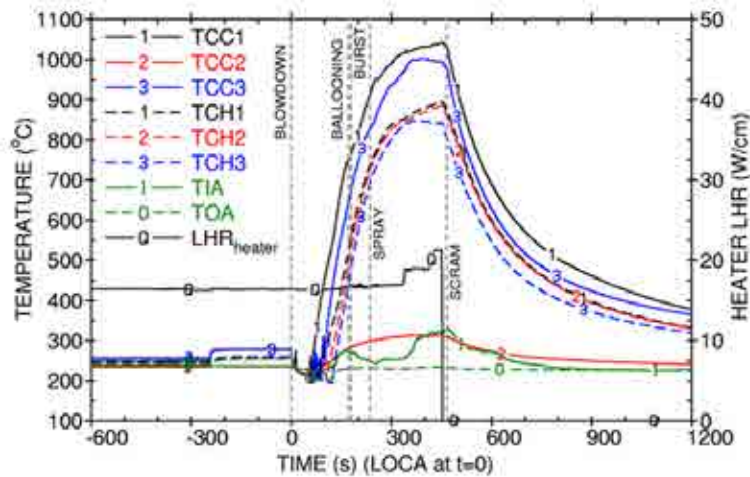
FIG. 11. Cladding (TCC), heater (TCH), coolant inlet/outlet (TIA/TOA) temperatures, and heater power during IFA-650.5 [14].

A temperature maximum of 1040°C was measured with TCC1 at the bottom of the rod just prior to the scram. If the axial power profile is used for estimation of a peak temperature, a PCT value (about 1080°C) close to the target is obtained. The cladding thermocouples showed temperature increase throughout the test until scram, only the increase rate decreased slightly after the burst. Note that one of the thermal couples at the upper part (TCC2) of the cladding fails, indicating appraently the coolant temperarure (close to TIA).

The indications of cladding burst are shown in Fig. 12. Cladding burst was detected ~178 s after the start of blowdown. The rod pressure starts to drop at 178 s. At the same time a step-like response is seen in the elongation signal. TCC1 also reacts to the cladding burst with a small step. Also the gamma monitor on the blowdown line reacts to the burst ca. 15 s later.
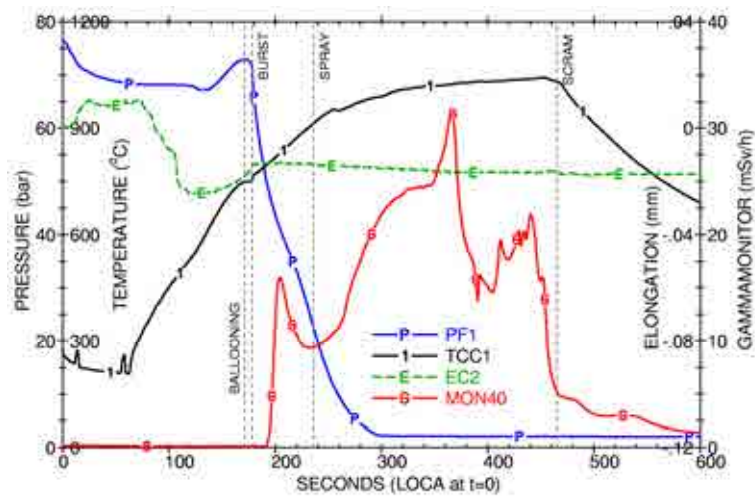
FIG.12. Cladding burst indication in IFA-650.5 [14]

The measured cladding temperatures at the time of burst were about 750 ºC at the bottom of the rod (TCC1) and about 670 °C at the top (TCC3). Temperature increase rate at the bottom of the rod during heat up was 5.5 ºC/s to 0.4 ºC/s, slowing down towards the end. The temperature increase rate at TCC1 decreased prior to the burst, probably due to ballooning. At TCC3 the ballooning and burst had no significant effect on the temperature increase rate.

The measured maximum pressure prior to ballooning and burst was 72.9 bar, which (with ~4 bar rig pressure) corresponds to a hoop stress of about 48 MPa. The pressure maximum was measured ~171 s after LOCA, i.e. ballooning probably started this time, just 8 s before burst.

The rod pressure dropped very slowly after the burst. This is probably caused by a small crack in the cladding, instead of a large burst opening. This is in agreement with the relatively short time between the start of clad deformation and burst.

5.5.2   FRAPCON/FRAPTRAN modelling assumptions

The objective of the work is to verify the FRAPTRAN's capability for simulating the fuel thermal and mechanical responses (such as rod internal pressure, fuel temperature, clad elongation, clad strain, clad burst) during LOCA transient.

We have simulated LOCA fuel behaviours based on Halden LOCA test series (IFA-650.3-5) using fuel rod computer codes FRAPCON and FRAPTRAN. This paper will present only the results for IFA-650.5.

In order to simulate the fuel rod conditions before the LOCA tests, FRAPCON input models have to be built to generate initial conditions for FRAPTRAN analysis. The father fuel rod and the re-fabricated rodlet have the same number of nodalization: 17 for radial nodes and 9 for axial nodes.

In both FRAPCON and FRAPTRAN input models, most of the data are set according to the specifications of IFA-650.5 test or the code manual recommended values. The refabricated rodlet FRAPCON3.4 input model has been validated by comparing with available measured data. The refabricated rodlet FRAPTRAN1.4 initialization file is the output of FRAPCON-3.4 input model which contains gas data from the initial father rod and subsequent Fission Gas Release (FGR) history data. The number of moles of new gas mixture and the relative amount of each gas species in the

refabricated rodlet has been adapted to match the calculated and measured initial rod internal pressure.

Due to the lack of verification of the "Coolant" model for LOCA conditions, the two set of measured cladding temperature data (TCC1 & TCC3) and a fixed very high coolant-cladding heat transfer coefficient are imposed as thermal-hydraulic boundary conditions (using the "Heat" option) in the FRAPTRAN1.4 input model for the rodlet. The imposed cladding temperatures are shown in Fig. 13. Note that for the FRAPTRAN simulation, a steady state period of 100 s is imposed; the LOCA transient is assume to occur at 100 seconds and end at the scram time (about 580 s).
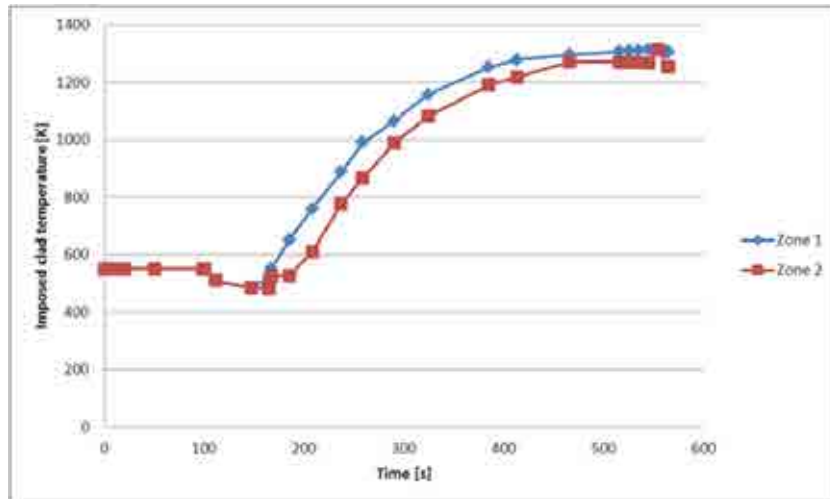
FIG. 13. The imposed cladding temperature for IFA-650.5.

The default models in FRAPTRAN are selected for most of the models, namely:
- the FRACAS-I rigid pellet model (finite difference model) for fuel rod mechanical response;
- the default BALON2 high temperature clad failure model based on empirical strain and stress limits for the burst;
- the Massih model for fission gas release;
- the Cathcart-Pawel model for high temperature oxidation.

As the default plenum gas temperature model predicts unrealistic internal fuel rod internal pressure, due to the use of the "Heat" option in FRAPTRAN1.4, modifications to the code have been made to allow specification of an external plenum volume held at a defined constant gas temperature. An arbitrary value of 127°C is chosen in this simulation.

Note that this assumption presents the major source of uncertainties, as the plenum gas temperature varies with time. It is possible to further improve the code by either imposing an evolution of plenum gas temperature during transient (if measured or calculated by other codes), or improving the FRAPTRAN gas plenum temperature model to calculate the plenum gas temperature.

5.5.3   Uncertainty analysis

The objectives of the uncertainty analysis on the FRAPTRAN simulation of IFA-650.5 are:
- To identify the most important input parameters influencing the result of interest;

- To evaluate the impact of the uncertainties on the uncertainties of the calculation results.

Based on a Phenomena Identification and Ranking Table (PIRT) analysis and previous analyses [23], the uncertainty parameters that influence the LOCA fuel behaviours simulation are identified in three categories:
- Fuel rod fabrication data
- Models
- Operation or test boundary conditions.

The selected uncertainty parameters are given in Table 2. Some parameters are added for confirmation of their importance, while material properties are not included. The distributions and ranges are taken as usually used in literature.

TABLE 2. INPUT UNCERTAINTY PARAMETERS FOR STATISTICAL UNCERTAINTY ANALYSIS OF IFA-650.5 FRAPCON/FRAPTRAN SIMULATION

Parameter	Unit	Distribution	Mean	Sigma	Lower	Upper
Fabrication						
Clad inner diameter	[mm]	Normal	9.3	0.02	9.26	9.34
Pellet outer diameter	[mm]	Normal	9.13	0.0065	9.117	9.143
Resintering	[kg/m³]	Normal	100	22.222	55.556	144.444
Cladding roughness	[μm]	Normal	0.50	0.15	0.20	0.80
Models						
Fuel thermal conductivity	[σ]	Normal	0	1	-2	2
FGR model	[σ]	Uniform	0		-2	2
Fuel thermal expansion	[σ]	Uniform	0		-2	2
Corrosion model	[σ]	Uniform	0		-2	2
Boundary conditions						
Plenum temperature	[K]	Uniform	558.25		528.25	588.25
Cladding temperature	[#]	Uniform	1		0.975	1.025
Relative power during base irradiation	[#]	Normal	1	0.01	0.98	1.02
Relative power during transient	[#]	Normal	1	0.033	0.934	1.066

σ and # - deviations

With the DAKOTA code, Monte-Carlo simple random sampling of all parameters is performed, leading to 93 FRAPCON/FRAPTRAN runs. After executing these runs, DAKOTA collects the interested output parameters. By using the first order statistics, the minimum and maximum values of each interested output parameter are the corresponding lower and upper bounds (5/95 and 95/95, double-sided). In addition, sensitivity analyses also performed with DAKOTA on the individual input parameter of the code, and the Pearson's correlation coefficients are used to determine the most influential input parameters. This process is shown in Fig. 14.
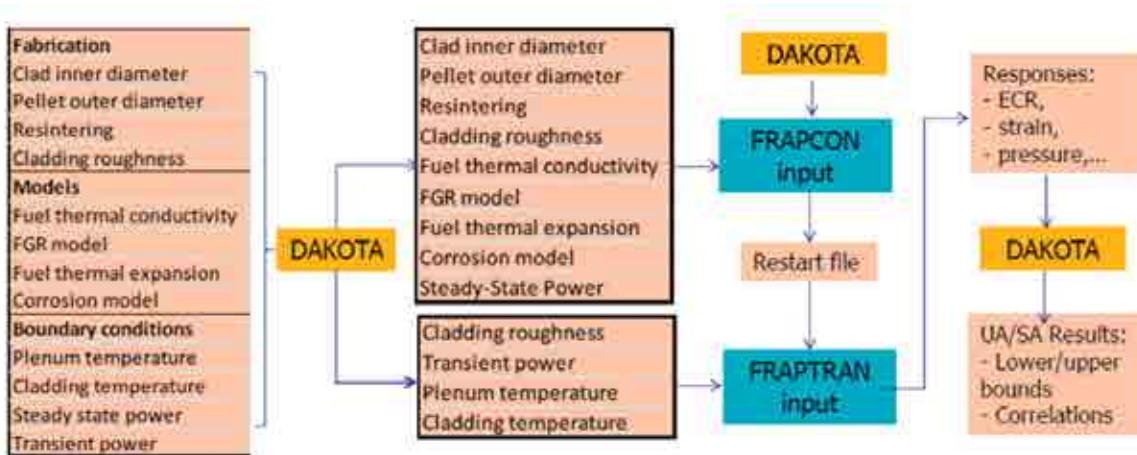
FIG. 14. The uncertainty and sensitivity analysis process.

5.5.4 Results and discussion

5.5.4.1 Base case

The calculated nominal rod internal pressure of IFA-650.5 with the modified FRAPTRAN1.4 is compared with the experimental data is shown in Fig. 15.
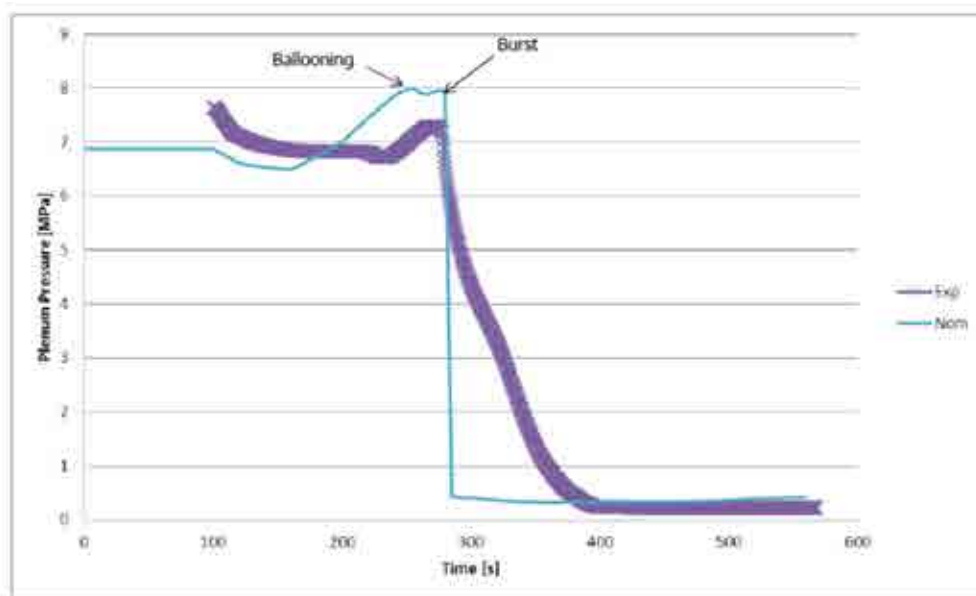
FIG. 15. Comparison of the calculated and measured rod internal pressure for IFA-650.5.

After the end of the blowdown phase at about 155 s, the rod internal pressure increases as the fuel rod starts to heap up, until ballooning occurs at about 258 s, followed by burst at about 285 s. The burst time is nearly the same as measured. The peak pressure reaches about 80 bar at burst, and reduces rapidly after the break. The slower pressure reduction as found in the test is due to fuel clad gap closure which restricts gas flow, which cannot be modelled by most fuel rod codes [14].

5.5.4.2 Uncertainty analysis

Both the calculated upper and lower bounds for rod internal pressure are showed together with the nominal and experimental data in Fig. 16.
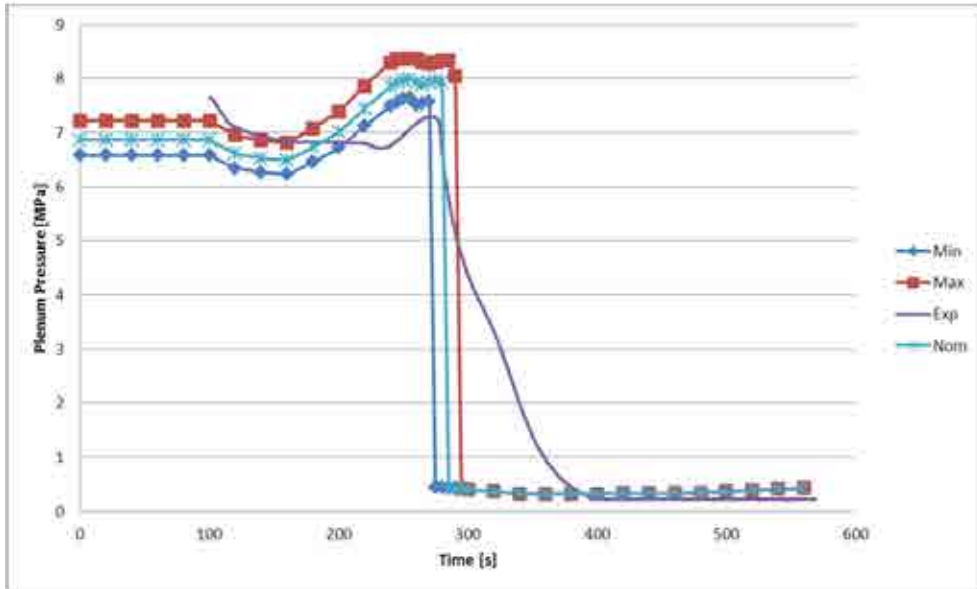
FIG. 16. Comparison of the calculated nominal, upper and lower bounds and measured rod internal pressure for IFA-650.5.

The uncertainty bounds are rather uniform before and during the burst, but are not able to cover the experimental data, indicting the inability of the code to predict the transient rod internal pressure. This is not surprising because of the larger uncertainties in the gas plenum pressure model and the lack of axial gas transportation model.

The calculated nominal, upper and lower bounds for fuel average temperature; cladding elongation and radial strain are shown in Fig. 17–19.

During the heatup phase after blowdown, the fuel average temperature increases until scram, consistent with the imposed cladding temperatures, and the uncertainty bounds are rather uniform (Fig. 16). However, the uncertainty bounds of both cladding axial elongation and radial strain show strong variations after the ballooning and burst (Fig. 17–18), indicating strong and possibly non-linear impacts of various input parameters.

134
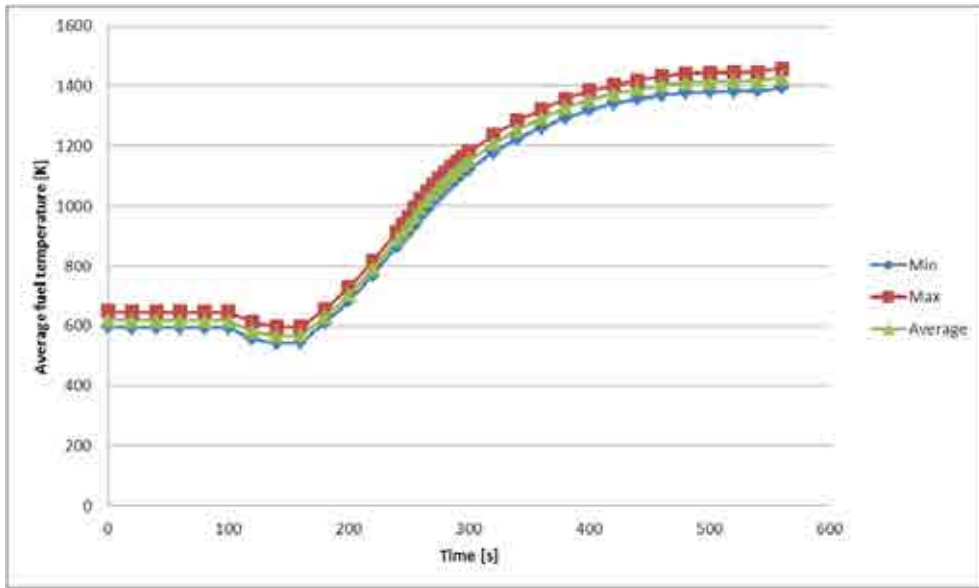
FIG. 17. Calculated fuel average temperature for IFA-650.5.
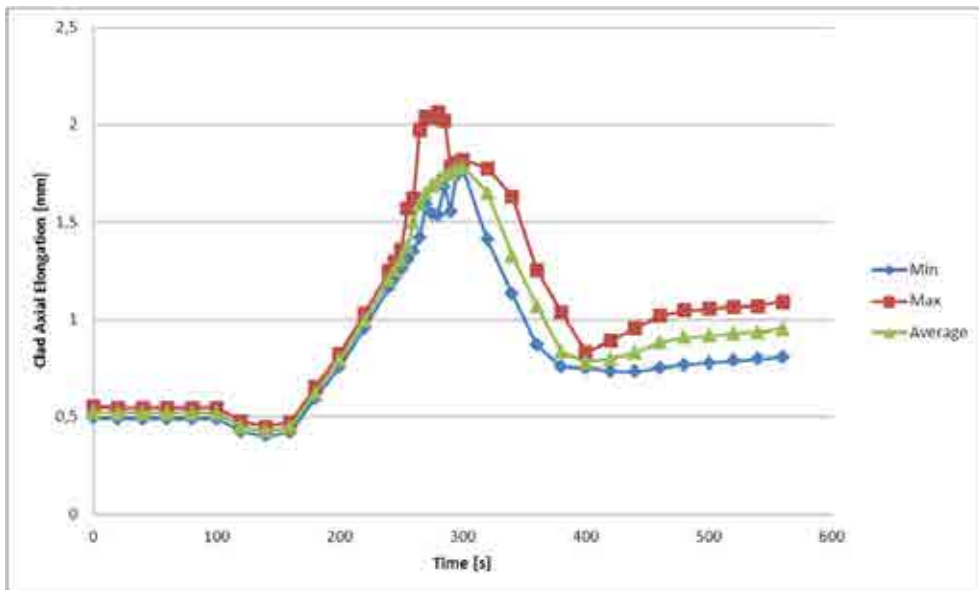
FIG. 18. Calculated cladding axial elongation for IFA-650.5.
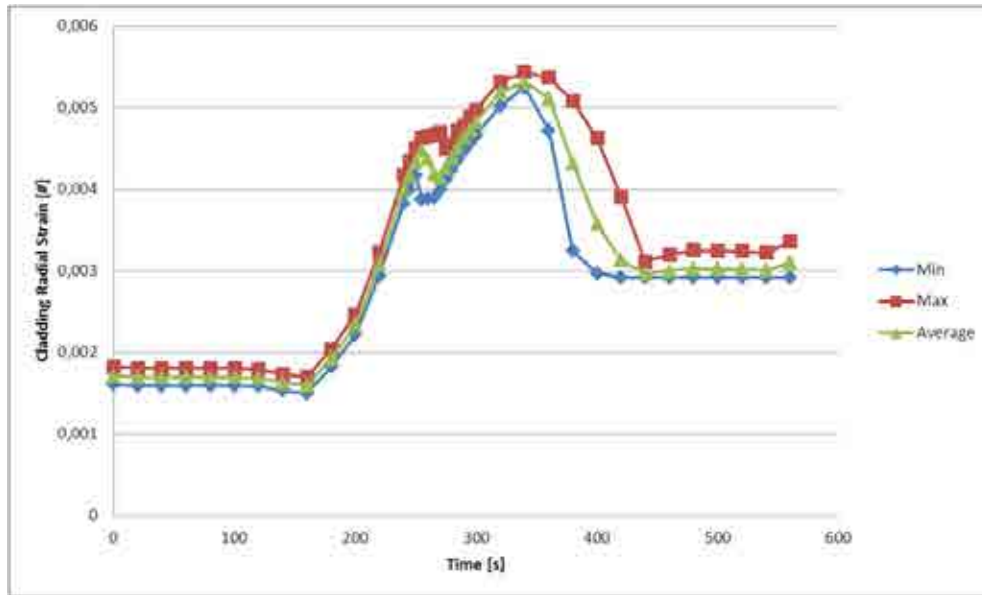
FIG. 19. Calculated cladding radial strain for IFA-650.5.

The calculated nominal, upper and lower bounds for total equivalent cladding reacted (ECR) with Cathcart-Pawel (C-P) model are shown in Fig. 20. The uncertainty bounds at steady state are rather uniform and wider, and the transient oxidation occurs only at high cladding temperature (after 300 s).

In order to identify the most influential input parameters on each output parameter of interest, the Pearson's correlation coefficients from the DAKOTA sensitivity analyses are used. Pearson's linear correlation coefficients designate the linear correlation between one input parameter and one output parameter:

•   Absolute values less than 0.25 indicate week correlation (in yellow);

•   Absolute values between 0.25 and 0.75 indicate moderate correlation;

•   Absolute values above 0.75 indicate strong correlation (in green).

For example, Table 3 shows that the fuel temperature before the burst at the node 6 (close to burst) is significantly impacted by the cladding diameter, power, fuel thermal conductivity, steady state corrosion, and cladding temperature, but is less impacted by the cladding roughness and plenum gas temperature.
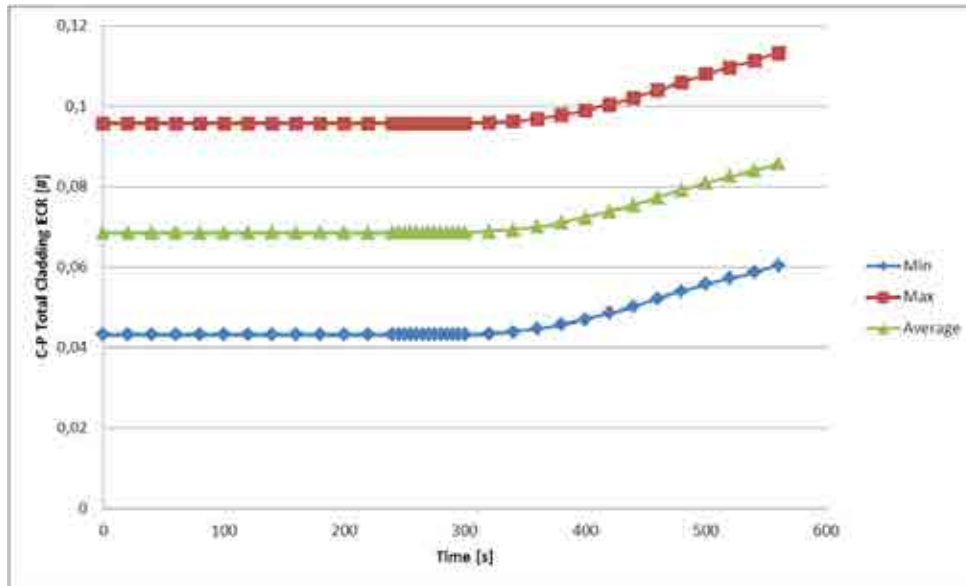
FIG. 20. Calculated Cathcart-Pawel total ECR for IFA-650.5.

TABLE 3. PEARSON'S CORRELATION COEFFICIENTS FOR FRAPTRAN SIMULATION OF FUEL TEMPERATURE FOR IFA-650.5.

Instant = 180 s, node 6	Av. Fuel T.	Center T.
Clad inner diameter	0,88	0,89
Pellet outer diameter	-0,71	-0,73
Resintering	0,42	0,43
Cladding roughness	0,10	0,09
Fuel thermal conductivity	-0,97	-0,98
Relative power during transient	0,94	0,96
Relative power during base irradiation	0,89	0,91
FGR model	0,54	0,57
Fuel thermal expansion	0,99	0,99
Steady state corrosion model	0,80	0,82
Plenum temperature	0,17	0,18
Cladding temperature	1,00	0,99

The rod internal pressure/burst time before burst at node 6 (close to burst position) are impacted significantly by the plenum gas temperature and cladding temperature, and RIP is also impacted by fuel thermal expansion model (Table 4). On the contrary, the cladding axial elongation and radial strain are impacted by more parameters and models, which explain the strong variations after the ballooning and burst (Fig. 17–18).

TABLE 4. PEARSON'S CORRELATION COEFFICIENTS FOR FRAPTRAN SIMULATION OF FUEL TEMPERATURE FOR IFA-650.5.

Instant = 180 s, node 6	Internal P.	Elongation	R. strain	Burst time
Clad inner diameter	-0,34	0,93	0,85	-0,32
Pellet outer diameter	0,22	-0,26	0,01	-0,11
Resintering	-0,02	-0,01	-0,04	-0,05
Cladding roughness	-0,24	-0,23	-0,20	0,16
Fuel thermal conductivity	0,72	0,49	0,59	0,00
Relative power during transient	0,31	0,98	0,75	-0,17
Relative power during base irradiation	-0,35	0,89	0,81	0,06
FGR model	-0,04	0,14	0,13	-0,07
Fuel thermal expansion	-0,91	-0,80	-0,85	0,10
Steady state corrosion model	-0,38	1,00	1,00	0,19
Plenum temperature	1,00	1,00	1,00	-0,99
Cladding temperature	1,00	1,00	1,00	-1,00

Finally, the cladding oxidation at node 6 (close to burst position) is impacted only by cladding diameter, initial power and steady-state corrosion model before transient (ECR650.5 in Table 5), but is impacted also by cladding transient temperature only before the end transient (ECR650.5e).

138

TABLE 5. PEARSON'S CORRELATION COEFFICIENTS FOR FRAPTRAN SIMULATION OF ECR FOR IFA-650.5.

Node 6	ECR 650.5	ECR 650.5 e
Clad inner diameter	-0,99	-0,81
Pellet outer diameter	-0,57	0,00
Resintering	0,05	0,09
Cladding roughness	-0,05	0,00
Fuel thermal conductivity	0,06	-0,11
Relative power during transient	0,02	0,08
Relative power during base irradiation	1,00	0,99
FGR model	-0,10	-0,25
Fuel thermal expansion	-0,05	-0,01
Steady state corrosion model	1,00	1,00
Plenum temperature	-0,13	0,29
Cladding temperature	0,10	1,00

This shows again that the DAKOTA sensitivity analysis is a powerful tool for determining the most influential input parameters. Indeed, it is much easier and more efficient than the sequential single-parameter sensitivity studies performed to define the important input uncertainty parameters.

CONCLUSIONS

In order to perform an independent verification of vendors' LOCA/RIA safety analysis and reloads fuel safety evaluation, Tractebel Engineering has been working on the qualification of the fuel rod codes FRAPCON and FRAPTRAN for fuel behaviour modelling. This is partly achieved by participation in the IAEA and OECD fuel rod codes benchmarks.

At the same time, Tractebel Engineering is working on applications of the statistical uncertainty and sensitivity analysis methods based on the DOKOTA code to fuel behaviour modelling.

Based on the simulation and uncertainty analysis of the OECD fuel rods RIA benchmark case CIP3-1 using FRAPCON and FRAPTRAN and comparison with other codes, it can be concluded that:

- FRAPCON & FRAPTRAN predict quite well the fuel thermal behaviour during RIA (by comparing with other codes), and hence are adequate for design/safety criteria verification;
- FRAPCON & FRAPTRAN mechanical and thermal hydraulic models need to be improved to well predict the cladding temperature and deformation, as well as PCMI failures during RIA;
- The failure of fuel rod is sensitive to the initial conditions and the following parameters/models:
  o Initial gap thickness;
  o Initial cladding spallation;

- o Void volume;
- o Fission gas release.
- Uncertainty and sensitivity analysis is needed to quantify their impacts.

Based on the simulation and uncertainty analysis of the OECD Halden LOCA benchmark case IFA-650.5, it can be concluded that:

- With the measured cladding temperatures and imposed plenum gas temperature as boundary conditions, FRAPCON and FRAPTRAN are able to simulate the Halden LOCA tests IFA-650, in particular:
  - o Fuel pellet temperature;
  - o Rod internal pressure;
  - o The ballooning and burst time.
- FRAPCON & FRAPTRAN plenum gas temperature, mechanical and thermal hydraulic models need to be improved to well predict the cladding temperature and deformation, as well as fuel relocation and dispersal during LOCA;
- The important parameters influencing the calculation results of interests during LOCA are identified:
  - o Plenum gas temperature;
  - o Cladding temperature;
  - o Cladding inner diameter;
  - o Initial power and steady-state corrosion for oxidation.
- Uncertainty and sensitivity analysis is needed to quantify their impacts.

It has been also shown that the accurate simulation of relevant physical phenomena during LOCA/RIA is essential for further uncertainty and sensitivity analysis. In particular, the following models should be improved or implemented in FRAPCON and FRAPTRAN:

- FGR;
- plenum gas temperature;
- axial gas transportation;
- cladding ballooning and burst;
- fuel relocation and dispersal.

For validation of the models, LOCA/RIA tests with detailed measurements and/or uncertainties estimation are needed. Therefore, it is suggested, in the future IAEA FUMAC project, to focus on a few, but well instrumented tests, such as the Halden LOCA tests. In addition, it is suggested to perform uncertainty and sensitivity analysis to quantify the impacts of uncertainties in fuel rod data, test conditions and models.

Last but not least, the thermal hydraulic model should be improved to better simulate the transient heat transfer conditions at the cladding surface during the LOCA/RIA transient. The measured cladding temperatures have been imposed as a boundary condition in the previous benchmarks, however, it is essential to predict the cladding temperature for verification of the safety criteria in the LOCA/RIA safety analysis. This may be resolved by coupling FRAPTRAN with a qualified system or sub-channel thermal hydraulic code like RELAP5.

REFERENCES

[1] NUCLEAR ENERGY AGENCY ORGANIZATION FOR ECONOMIC CO-OPERATION AND DEVELOPMENT (NEA/OECD), Nuclear Fuel Behaviour in Loss-of-Coolant Accident (LOCA) Conditions, State-of-the-art Report, NEA No. **6846**, (2009).

[2] NUCLEAR ENERGY AGENCY ORGANIZATION FOR ECONOMIC CO-OPERATION AND DEVELOPMENT (NEA/OECD), Nuclear Fuel Behaviour under Reactivity-Initiated Accident (RIA) Conditions, State-of-the-art Report, NEA No. **6847**, NEA/CSNI/R(2010)1, (2010).

[3] CLIFFORD, P. and FLANAGAN, M. E., Proposed Modification of Cladding Embrittlement Criteria, Proceedings of the TOPFUEL 2009, Paris, France, September 7–9, 2009.

[4] CLIFFORD, P.M., The U. S. Nuclear Regulatory Commission's Strategy For Revising The RIA Acceptance Criteria, Proceedings of the 2012 Top Fuel Reactor Fuel Performance Meeting, Manchester, United Kingdom, September 2–6, 2012.

[5] GEELHOOD, K.J., LUSCHER, W.G., and BEYER, C.E., FRAPCON-3.4: A Computer Code for the Calculation of Steady-State, Thermal-Mechanical Behavior of Oxide Fuel Rods for High Burnup, NUREG/CR-7022, Vol. **1** & Vol. **2**, US NRC, (2010).

[6] GEELHOOD, K.J., LUSCHER, W.G., BEYER, C.E., and CUTA, J.M., FRAPTRAN 1.4: A Computer Code for the Transient Analysis of Oxide Fuel Rods, NUREG/CR-7023, Vol. 1 & Vol. 2, US NRC, 2010.

[7] GEELHOOD, K.J., LUSCHER, W.G., BEYER, C.E., SENOR, D.J., CUNNINGHAM, M.E., LANNING, D.D., and ADKINS, H.E., Predictive Bias and Sensitivity in NRC Fuel Performance Codes, NUREG/CR-7001, PNNL-17644, Pacific Northwest National Laboratory, Richland, WA, USA, (2009).

[8] K. GEELHOOD, Recent Updates to NRC Fuel Performance Codes and Plans for Future Improvements, J. Nuclear Engineering and Technology, Vol. **43** NO.6 December 2011.

[9] UMIDOVA, Z., DETHIOUX, A., ZHANG, J., Qualification of FRAPCON/FRAPTRAN Codes for Fuel Rod Design Verification and Fuel Safety Evaluation, Proceedings of the 2012 Top Fuel Reactor Fuel Performance Meeting, Manchester, United Kingdom, September 2–6, 2012.

[10] INTERNATIONAL ATOMIC ENERGY AGENCY, Improvement of Computer Codes used for Fuel Behaviour Simulation (FUMEX-III): Report of a coordinated research project 2008–2012, IAEA-TECDOC-1697, (2013).

[11] OECD/NEA, RIA Fuel Codes Benchmark, Volume **1** & **2**, CSNI report (to appear), (2013).

[12] PETIT, M. et al, The OECD/CSNI/WGFS Benchmark on Reactivity Initiated Accident Fuel Codes, presented at IAEA Technical Meeting On Modelling Of Water-Cooled Fuel Including Design Basis And Severe Accidents, Chengdu, China, 28 October – 1 November 2013.

[13] KOLSTAD, E., WIESENACK, W., OBERLÄNDER, B., TVERBERG, T., High burn-up fuel behaviour under LOCA conditions as observed in Halden experiments, IAEA Technical Meeting on Fuel Behaviour and Modelling under Severe Transient and LOCA Conditions, Mito, Japan, 18–21 October, 2011.

[14] OECD, Benchmark calculations on HALDEN IFA-650 LOCA test results, NEA/CSNI/R (2010) 6, 15 November 2010.

[15] ZHANG, J., SEGURADO, J. and SCHNEIDESCH, C., Towards an Industrial Application of Statistical Uncertainty Analysis Methods to Multi-physical Modelling and Safety Analyses, Proc. OECD/CSNI Workshop on Best Estimate Methods and Uncertainty Evaluations, Barcelona, Spain, 16–18 November 2011.

[16] WILKS, S.S., Determination of Sample Sizes for Setting Tolerance Limits, The Annals of Mathematical Statistics, Vol. **12**, pp. 91–96, 1941.

[17] GUBA, A., MAKAI, M., and P´AL, L., Statistical aspects of best estimate method—I, Reliability Engineering and System Safety, vol. **80**, no. 3, pp. 217–232, 2003.

[18] ADAMS, B., et al., DAKOTA, A Multilevel Parallel Object-Oriented Framework for Design Optimization, Parameter Estimation, Uncertainty Quantification, and Sensitivity Analysis: Version 5.2 User's Manual, Sandia Technical Report SAND2010–2183, December 2011. (http://www.cs.sandia.gov/dakota)

[19] ADAMS, B., DAKOTA 5.0 and JAGUAR 2.0 Capability Overview, SAND 2008-7901P, Sandia National Labs. (2008).

[20] SANDIA NATIONAL LABORATORIES, DAKOTA Uncertainty Quantification, SAND 2009-0511P, 2009.

[21] HELMAN, T., Application of the statistical uncertainty analysis method to simulation of Reactivity Insertion Accidents with FRAPCON3.4/FRAPTRAN1.4, Master Thesis, Free University of Brussels, Belgium, September 2011.

[22] ZHANG, J., HELMAN, T., UMIDOVA, Z. and DETHIOUX, A., Statistical Uncertainty Analysis of CIP3-1 Simulation with FRAPCON/FRAPTRAN - Preliminary Results and Suggestions, presented at the OECD/WGFS 1st Seminar on RIA fuel rod codes benchmark, Paris, 19–20 September, 2011.

[23] DOU, D., Assessment of Fuel Behaviour during LOCA Using FRAPCON/FRAPTRAN," Master thesis, INSTN, CEA, France, Sep. 2012.

[24] DETHIOUX, A., UMIDOVA, Z. and ZHANG, J., Uncertainty analysis on FRAPTRAN simulation of the Halden LOCA tests IFA-650.4&5, HPG Workshop on Data Uncertainties, Halden, Norway, September 4–5, 2013.

142

MODELLING OF NUCLEAR FUEL UNDER ACCIDENT CONDITIONS BY MEANS OF TRANSURANUS

P. VAN UFFELEN[1], J. VAN DE LAAR[1], A. SCHUBERT[1], V. DI MARCELLO[1], L. VLAHOVIC[1], L. HOLT[2,3]
[1]European Commission, Joint Research Centre, Institute for Transuranium Elements
Hermann-von-Helmholtz-Platz 1, D-76344 Eggenstein-Leopoldshafen, Germany
[2]Helmholtz-Zentrum Dresden - Rossendorf, Bautzner Landstrasse 400, 01328 Dresden, Germany
[3]Technical University Munich, Germany

Abstract. The TRANSURANUS fuel performance code, which is developed at the JRC-ITU and in collaboration with many partner institutes since more than three decades, has been adapted in order to be able to simulate design basis accident (DBA) conditions. In a first step, the developments and associated validation work will be summarised for LOCA conditions.

This part includes modifications in the model for large strains, for the crystallographic phase transition in Zircaloy, and for burst release and large cladding deformations. In a second step, the ongoing work for simulations of RIA conditions will be outlined that include the model for the plenum temperature, along with the separate effect studies and detailed model developments made in parallel by means of multi-scale and multi-physics tools for the high burnup structure.

Finally, the perspectives of model developments and needs for further verification and validation in the frame of international benchmark exercises dedicated to DBA simulations and the first phase of a severe accident, i.e. when the cylindrical fuel rod geometry is preserved, will be presented for discussion.

6. INTRODUCTION

The safe and economic operation of nuclear fuel rods requires predicting their behaviour and to verify compliance with safety criteria under both normal operation and postulated accidents. The accurate description of the fuel rod's behaviour, involves various disciplines such as nuclear and solid state physics, metallurgy, ceramics, applied mechanics and the thermal heat transfer. The strong interrelationship of these disciplines calls for the development of computer codes describing the general fuel behaviour, such as the TRANSURANUS code [1]. Fuel designers and safety authorities rely heavily on this type of codes. Nevertheless, two types of fuel performance codes are generally being applied, corresponding to the normal operating and the design basis accident conditions (e.g. LOCA and RIA) respectively. In order to simplify the code management by limiting the number of programs and in order to take advantage of the hardware improvements, one should generate a single fuel performance code that can cope with the different conditions.

On the one hand, extending the application range of a fuel performance code originally developed for steady-state conditions to accident conditions requires modifications to the basic equations in the thermal-mechanical description of the fuel rod behaviour [2], stable numerical algorithms and a proper time-step control, in addition to the implementation of specific models dealing with the high temperature behaviour of cladding such as observed under LOCA conditions [3]. For dealing with RIA events, one should check carefully the thermal expansion model because of the edge-peaked power distribution, as well as the other models affecting the effective cold gap width [4], and the model for thermal heat transfer in the plenum. On the other hand, for fuel performance codes developed to simulate some aspects of the nuclear fuel behaviour under accident conditions, such as TESPA [5] or MFPR [6], either the thermo-mechanical behaviour of the fuel must be incorporated and/or the extension of models to normal operating conditions is necessary to consider burnup dependent phenomena such as thermal conductivity degradation, fission gas release and swelling as

well as cladding corrosion. Such a posteriori modifications of the fuel performance code may entail difficulties in terms of convergence and calculation time.

Thanks to a clearly defined mechanical and mathematical framework as well as a consistent modelling, the TRANSURANUS fuel performance code has been able to cope with normal, off-normal and accidental operating conditions right from the beginning in 1973. Despite the fact that the numerical solution techniques enable handling of non-steady-state conditions and provide an ideal framework for a code to handle all conditions, some of the phenomena important for design basis accidents (DBA) were not incorporated.

In the second part of this paper a short overview will be made of the code and model developments aiming at the simulation of a LOCA. The third section will summarise the equivalent work carried out for RIA simulations. The final part of the paper will outline the future developments, and in particular describe the need for benchmarking that is expected in the frame of the FUMAC co-ordinated research project that is being prepared by the IAEA.

7. MODEL DEVELOPMENTS FOR LOCA

As a first step, the EXTRA project was launched in order to extend the TRANSURANUS code capabilities to LOCA conditions [7]. This project focused on the simulation of the Zr1%Nb cladding performance under LOCA conditions via the incorporation of newly developed correlations for off-normal conditions for (1) the cladding steam reaction rate, (2) the phase transition between the alpha (α) phase and the beta (β) phase, (3) the clad deformation rate (ballooning) model and (4) the cladding failure criteria. In parallel to this project, similar models for Western type PWRs have been implemented and tested as well [8]. In a follow-up project, the hydrogen uptake of Zr1%Nb cladding and its effect on the oxidation and mechanical strength were addressed [9]. All these developments have been reported previously and are therefore not repeated here.

More recently, an experimental study has been carried out to analyse the dynamic phase transition in the Nb containing alloy E110. The primary purpose of that analysis was to provide experimental data in order to harmonize the modelling of the phase transition in the conventional cladding materials of both Western and Russian type reactors, based on a modified Johnson-Mehl-Avrami model in line with Forgeron's approach [10]:

$$\beta_{eq} = 1 - \exp\left[-\left(K \left(T_{eq} - T_0 \right) \right)^n \right] \tag{1}$$

where $K = (T_{63.2\%} - T_0)^{-1}$, and $T_{63.2\%}$ is the equilibrium temperature corresponding to 63.2% of the β-phase, $T_0 = (^oC)$ is the so-called incubation (onset) temperature and n is a dimensionless constant. Based on the linear extrapolation of the experimental data obtained by means of the differential scanning calorimeter (DSC) with E110 samples to a zero heating rate, one could obtain an alternative equilibrium curve for the $\alpha \leftrightarrow \beta$ phase change of the E110 material being analysed. The set of extrapolated points has been fitted with the function as above, leading to $T_{63.2\%} = 1157.92$ K (885°C), $K = (T_{63.2\%} - T_0)^{-1} = 8.28 \ 10^{-3}$, $T_0 = 1037.15$ K (764°C) and $n = 2.94$. The resulting model is compared with the experimental curves corresponding to equilibrium and heating rates of 3 and 20 K/min in Fig. 1. These values are very close to those obtained by Forgeron et al. for the M5 alloy: $T_{63,2\%} = 1141.2$ K (868°C), $K = 8.4 \ 10^{-3}$, $T_0 = 1022.15$ K (749°C) and $n = 2.9$. The results thus confirm the retarding effect due to Nb diffusion during the crystallographic phase change in the range of heating rates applied, and are in accordance with the experimental data in the literature for heating of M5,

and Zry4 alloys. The new proposed equilibrium curve for E110 is different from that presently implemented in the TRANSURANUS code, which was developed in the frame of the EXTRA project [7].
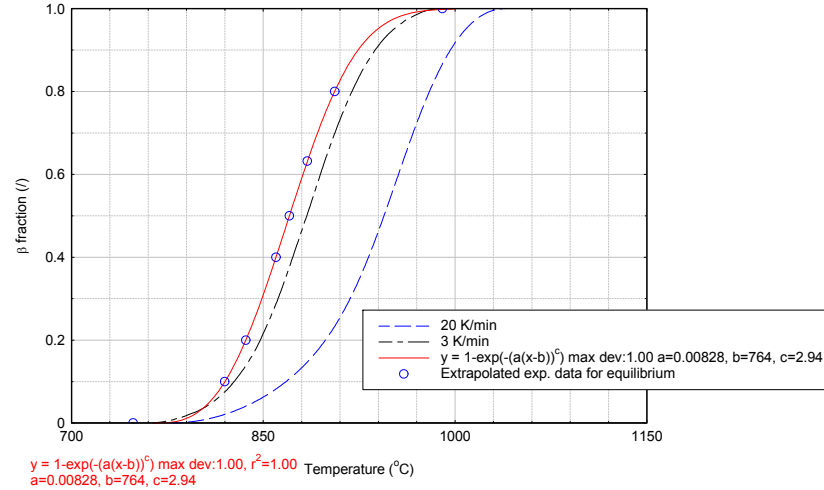
FIG. 1. Fraction of the β phase as a function of temperature in E110 samples. The red line between the experimental points corresponds to the equilibrium temperature. The two other lines correspond to the fraction of the β phase measured at a temperature increase rate of 3 and 20 K·min⁻¹.

When fitting the five parameters of the Forgeron's model for the dynamic phase change, one obtains $c_1 = -8.64$, $c_2 = -3.096 \times 10^{-3}$, $T_0 = 480$, $K = 2.44 \cdot 10^{-3}$, and $n = 11.4$, where

$$\frac{d\beta}{dt} = K(T) \cdot \beta \cdot (1 - \beta) \qquad \cdot (2)$$

where $K(T)$ is an empirical formula of the temperature:

$$K = \pm \left| T - T_{eq} \right| \cdot \exp \left(c_1 + c_2 \cdot \left| T - T_{eq} \right| \right) \qquad (3)$$

The comparison with the experimental data is shown in Fig. 2.

When considering the curves for the transition in the above-mentioned figure, one could also represent this by means of an error function. This is equivalent with representing the DSC signal, when corrected with the linear background during the phase change, by means of a Gaussian distribution. Such a distribution is characterized by a mean value (μ) and a standard deviation (σ), which are equivalent to the two fitting constants in the empirical function proposed by Forgeron et al. [10]. However, when considering the shift of μ and σ as a function of the heating rate, one can obtain one and the same formulation for both the static model as well as the dynamic model for the $\alpha \leftrightarrow \beta$ phase transition:

145

$$\beta = \frac{1}{2}\left[1 + erf\left(\frac{T-\mu}{\sqrt{2}\sigma}\right)\right] \qquad (4)$$

where

$$\mu = \mu_0 + \mu_1 \cdot \frac{dT}{dt} \qquad (5)$$

$$\sigma = \sigma_0 + \sigma_1 \cdot \frac{dT}{dt} \qquad (6)$$
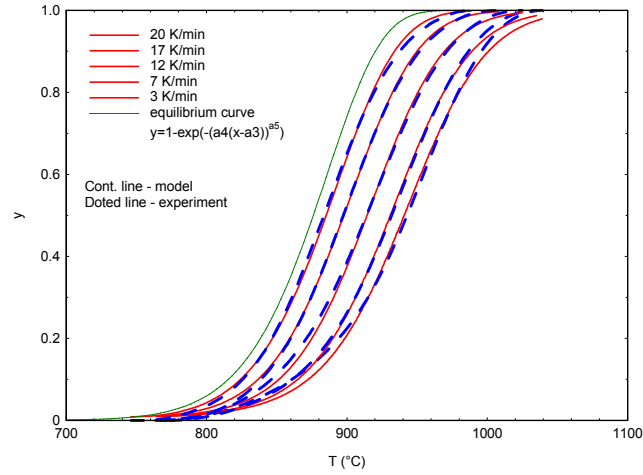
FIG. 2. Comparison of the measured fraction of the β phase as a function of temperature in E110 samples at heating rates between 3 and 20 K·min^{-1} with the predicted values according to the model of Forgeron [10] fitted on those data.

Accordingly, we have fitted the experimental curve by means of the Gaussian distribution:

$$\frac{d\beta}{dt} = \frac{1}{\sqrt{2\pi}\sigma}\exp\left[-\frac{1}{2}\left(\frac{T-\mu}{\sigma}\right)^2\right] \qquad (7)$$

When plotting the values for μ and σ as a function of the heating rate one can derive the values for μ_0, μ_1, σ_0 and σ_1:

$$\mu = 870,03 + 3,8599 \cdot \frac{dT}{dt}$$

$$\sigma = 42,237 + 0,2203 \cdot \frac{dT}{dt} \cong 45$$

<div style="text-align: right">(8)</div>

The value obtained for μ_0 coincides with the equilibrium temperature at which the β-fraction is 50 % derived from the extrapolated lines in our previous report, i.e. the temperature obtained with Eq. (1) when β = 50%. When comparing the values for μ_1 and σ_1, it appears that the shift of the transition curve, which is attributed to the diffusivity of Nb atoms in the Zr1%Nb matrix, is much more affected by the heating rate in comparison with the width of the transition curve, within the range of heating and cooling rates analysed (± 0.3 K·s^{-1}), Fig. 3. This model will be implemented in the TRANSURANUS code for testing its impact on the simulation of separate effect burst tests.
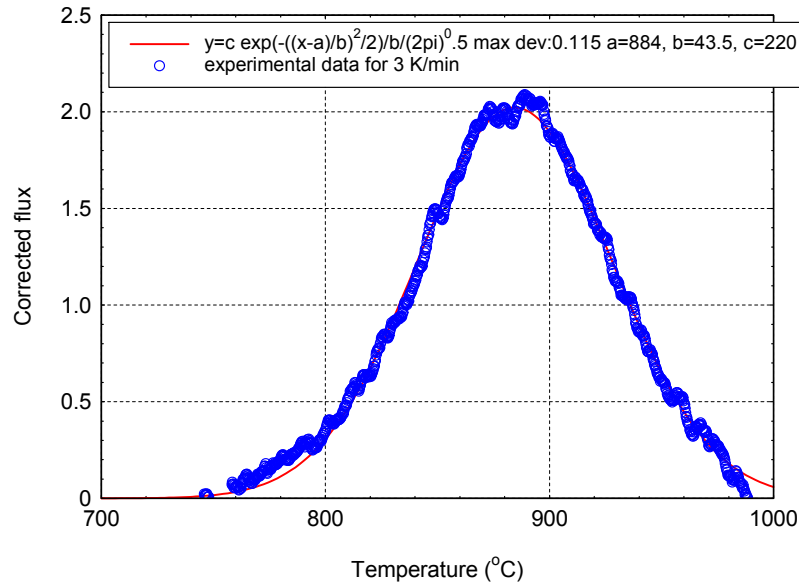
FIG. 3. Corrected flux of the DSC measured during heating up the Zr1%Nb (E110) sample at a heating rate of 3 K/m.

In parallel with the model development for the phase change in E110 cladding, an updated set of models and correlations for the cladding behaviour during LOCA conditions have been developed for taking into account the hydrogen content [11]. More precisely, new models were developed for the TRANSURANUS code to describe the influence of the hydrogen content on the creep behavior of Zircaloy-4 cladding tubes. The creep model was calibrated on isothermal burst experiments performed for hydrided and non-hydrided specimens. For that purpose Norton creep parameters (structure parameter, stress exponent) were adopted in each crystallographic phase domain. In addition, Large-Break-LOCA calculations were performed for a quarter core of a German PWR to determine the extent of damage. On the basis of the new Zircaloy-4 models, correlations for other cladding tube materials that take into account the influence of hydrogen can be implemented easily. Both model developments for E110 and Zircaloy-4 have to be merged in the latest version of the TRANSURANUS code for further distribution to the network of users.

Apart from the research described above, the TRANSURANUS code was extended in order to take into account large creep strains for the simulation of clad ballooning occurring during a LOCA. While the first order theory gives very good results for small strains below approx. 5%, reaching large strains values imply numerical instabilities due to the violation of the volume balances.

For the code extension for large cladding deformations, use was made of both the COMSOL numerical solution as well as an analytic solution. The creep problem was analyzed adopting the well-known Norton's law considering both inward and outward creep behaviour. A sensitivity analysis was carried out in order to address the effect of geometry, the effect of using different flow laws and the effect of the strain-displacement relation. The effect of change in geometry due to deformations was identified to be important thanks to the comparison between COMSOL and TRANSURANUS solutions for the first order theory. A proposal for an extended flow law was made in order to take into account that the geometry is significantly changing during large creep strains. The effect of adopting different flow laws was also addressed showing a significant impact on the solution, either with small or large strain approximations. The inadequacy of the first order theory for large strains was quantified showing that this simplified approach is leading to a violation of the volume balance.

Finally, the effect of different strain-displacement relations was investigated analysing separately its influence in order to assess the validity of the large strains approximation. This was verified by comparison with the analytic solution. In particular, thanks to the COMSOL software flexibility, it was possible to simulate the conditions under which the analytic solution is valid in order get rid of the possible differences introduced by other approximations/assumptions such as the applied flow law. As a result, it was shown that the large strains approximation to mechanics is in a very good agreement with the analytic solution. Discrepancies can become important in the case of internal pressurized tubes above 35–40% strain (50–60% Lagrangian strain). Moreover, extrapolation of the first order theory to large strain analysis in fuel performance code applications must be avoided because it is not conservative for the prediction of the mechanical behaviour. These results have been presented and discussed in detail elsewhere [12]. Nevertheless, the overall impact of the large strain analysis has been assessed on the basis of the integral LOCA test IFA-650.2 that was part of the FUMEX-III co-ordinated research project of the IAEA, and on the basis of the separate clad ballooning tests that have been included in the IFPE database. Some of the results are shown in Fig. 4 and Fig. 5, wherein we compare the effect of the small and large strain analysis in combination with the effect of different cladding failure criteria.
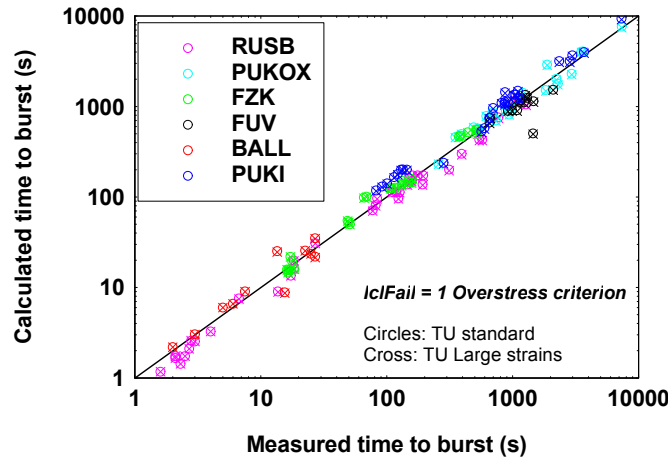
FIG. 4. Calculated and measured time-to-burst comparison for the overall EXTRA project database. The overstress criterion (Iclfail=1) has been applied for determining the time of burst.

In terms of the predicted time-to-burst, the results of the large strain analysis are similar to those obtained with the standard TRANSURANUS algorithm. The similarity of the computed time-to-burst is mainly because of the fact that when ballooning occurs with subsequent burst, the deformation is very rapid even when the stress remains moderately low during LOCA (maximum burst pressure of 17 MPa among the EXTRA project tests), when compared to stresses during pellet-mechanical interaction during normal operation conditions. However, the predicted time-to-burst obtained with the large strain mechanical algorithm is slightly reduced, because higher stresses are calculated, indicating that the standard algorithm may not be on the safe side for LOCA analysis.
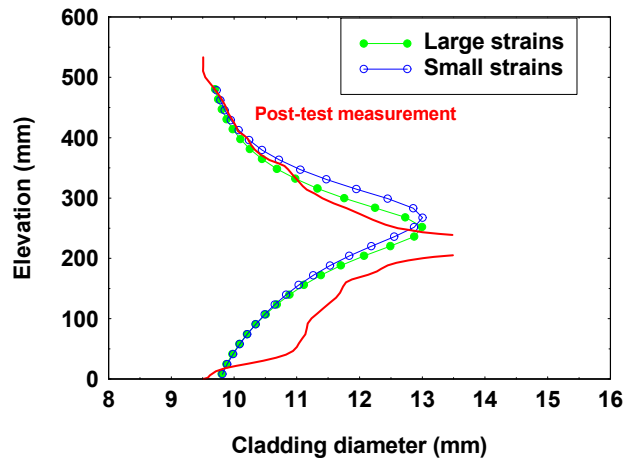
FIG. 5. Measured and calculated axial profile of the cladding outer diameter of the IFA650.2 Halden case in the FUMEX-III CRP of the IAEA.

The integrity of fuel rod claddings during a LOCA is usually assessed by comparing calculated stresses or strains with the corresponding failure thresholds. Sauer [13] has proposed an alternative

149

and stand-alone algorithm, whereby the cladding integrity is evaluated on the basis of the time elapsed since the LOCA onset. This criterion relies on the relationship between failure time and cladding loading that must be known. The relationship can be established computationally by monitoring the cladding inner and outer radii during the high temperature creep process. The cladding is defined to be defective when the predicted inner radius equals or exceeds the anticipated outer radius. With the proposed method it is straightforward to compute the cladding burst times on the basis of creep correlations. These correlations can be developed on the basis of creep properties in uniaxial tests. Expensive experiments with cladding tubes in special test equipment would therefore be redundant, which appears as the main advantage of the proposed simple algorithm. Nevertheless, implementation of this additional algorithm in the standard TRANSURANUS code still requires extensive independent testing on the basis of experimental data for burst tests in the open literature.

In addition to the model developments for the cladding under LOCA conditions, there is currently a development for modelling the transient release from the high burnup structure (HBS) during a LOCA. As a first step a new model has been developed for the establishment of the HBS as a function of the local temperature and effective burnup. This approach accounts for the fact that at higher temperatures defect annealing occurs, which can prevent the HBS formation, and will be published separately (see also section on RIA modelling below). In a second step, a new empirical model for fission gas release during a LOCA has been developed, implemented and tested in the TRANSURANUS version of Westinghouse [14]. The model considers fragmentation, caused by over-pressurisation of inter-granular bubbles due to a sudden temperature increase in the HBS and relief of PCMI, formation of micro-cracks at the brittle grain boundaries as well as in the HBS zone. In this way, it constitutes a logical extension of the ramp release model due to micro-cracking at grain boundaries developed for the TRANSURANUS code as a result of the FUMEX-II CRP [15].

The empirical gas release model for LOCA conditions considers the volume of the HBS zone in the fuel, the amount of fragmented fuel, and the fraction of FGR from the fragmented region. The latter is dependent on both the temperature and its rate of change, whereas the previous model for grain boundary cracking was dependent on the local burnup, the temperature and the power rate. The new empirical fission gas release model is being validated on the basis of integral LOCA tests. If it is considered appropriate for distribution to other TRANSURANUS users, it will first have to be consolidated with the existing fission gas release and swelling models of the standard version of the code.

8. MODEL DEVELOPMENTS FOR RIA

Preliminary assessments of RIA simulations by means of TRANSURANUS have been carried out by partner institutes. The most recent of which were in the frame of the FUMEX-III CRP [16] of the IAEA and the RIA fuel codes benchmark of the OECD-NEA [17]. The corresponding code improvements have only been launched in the wake of these analyses. The first model improvement for RIA concerned the burst release associated with caused by grain boundary cracking and was presented in the frame of FUMEX-II.

The second development is on-going and deals with the plenum temperature model. These models in fuel performance codes often neglect the axial temperature gradients of the structural elements, although the axial heat conduction can have an important effect under accident conditions. For this purpose, a new analytical model based on a 2D heat transport equation has been incorporated in a test

version of the TRANSURANUS code [18]. The model is based on a finite volume solution of the Fourier heat conduction equation and provides an advanced method for the analysis of the plenum gas temperature distribution under transient conditions. However, it is still prone to limitations: it assumes stagnant gas conditions, neglects the heat transport between the plenum gas and the structural components (spring and cladding) by natural convection, neglects the heat transport between the structural components by radiation and also neglects the gamma heating of the structural components. The test version of the TRANSURANUS code with this plenum temperature model has been applied to LOCA simulations without any problems. Therefore the new 2D plenum gas temperature model provides a more sophisticated approach to define the plenum gas temperatures in comparison with the simplified point models of the standard TRANSURANUS code. Hence, the model gives the possibility of a more precise evaluation of the rod internal pressure, increasing this way the credibility of the TRANSURANUS code in safety analyses. However, the overall validation of the model through benchmarks against experimental data and results of FEM (Finite Element Method) code analyses is necessary.

For this purpose a simplified two-dimensional finite element model is under development. Heat convection and conduction in a typical upper plenum are considered with reference to a 17x17 PWR fuel rod design, and also the power generated by the spring due to gamma heating is taking into account. The governing equations (i.e., heat balance and Navier-Stokes equations) are solved by means of the FEM commercial software COMSOL Multiphysics. At present only the steady-state solution has been tested. Further analyses are:

1. parametric analyses by varying boundary conditions (normal operating conditions, LOCA, RIA), power levels and radial power distribution (parabolic, or a profile corresponding to that during a RIA in a high burnup fuel), geometry, etc.;

2. analysis of contribution from gamma heating during a RIA;

3. analysis of the contribution from radiative heat transfer in the plenum.

The simulation of the plenum temperature during a RIA like the FK1 case of FUMEX-III is underway.

A third development builds on the new model for the HBS formation. The HBS has an important potential effect on fuel behaviour during DBA such as a RIA. The RIA stress state and the related cladding response depend strongly on the fuel burn-up, e.g. the fission gas release during DBA conditions [19]. The new model should improve the above-mentioned empirical model for gas release from the HBS during LOCA, based on separate effect studies relying on disc irradiations. For that purpose, new experimental results for Xe depletion from the High Burnup Rim Project (HBRP) have been analysed. The discs with a ^{235}U enrichment of around 25% were irradiated and submitted to post irradiation examination such as electron probe microanalysis. The influence of the burn-up and temperature on Xe concentration was investigated using a multi-physics approach involving various simulation tools: FEM analysis of the temperature by means of the MARC code, a coupled and detailed neutronic and burnout analysis by means of SERPENT, and a macroscopic simulation by means of a model for the HBS in the TRANSURANUS code. The temperature influence was modelled by means of the temperature dependent effective burn-up:

$$\Delta bu_{eff} = \begin{cases} \Delta bu, T \leq T_{thres} \\ 0, T > T_{thres} \end{cases} \qquad (9)$$

where T is the local fuel temperature expressed in °C, Δbu is the considered burn-up increment, T_{thres} is the temperature threshold in °C for healing of defects and T is the local fuel temperature in °C.

Good agreement was found between the modelled temperature threshold of the effective burn-up and the experimental temperature threshold between un- and restructured fuel in the HBRP. However, a systematic difference was observed between the onset burn-up derived from the Xe measurements in highly enriched discs such as those of HBRP and the corresponding values derived from irradiated Light Water Reactor (LWR) fuel rods and reported in the open literature. A sensitivity study identified the neutron flux spectrum and the fission product yields as main reasons for the observed differences.

Based on the new model for the HBS formation that is presented in detail elsewhere [20], a new model for the release from this structure under DBA is being developed, which depends on the local temperature levels, the effective burnup and should account for any constraint effect. It relies on local experimental data obtained from HBS samples in a Knudsen Cell coupled with a mass spectrometer, as well as on the basis of integral results observed in fuel rod segments, Fig. 6.
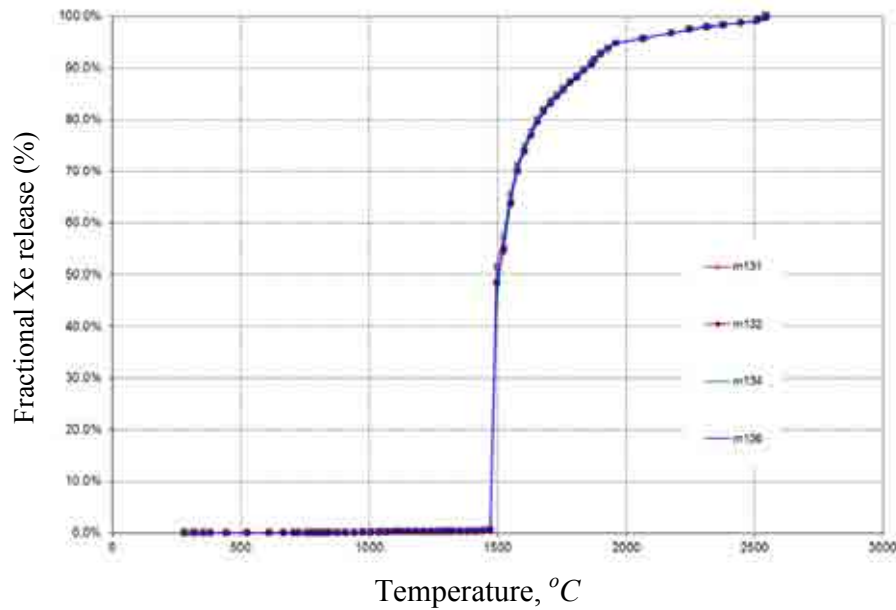
FIG. 6. Example of fractional Xe release (%) as a function of temperature (°Celcius) in an high burnup fuel sample by means of heating in the Knudsen Cell at JRC-ITU.

Finally, a general interface is presented for coupling the TRANSURANUS fuel performance code with thermal hydraulics system codes, sub-channel codes or reactor dynamics codes [21]. As first application the reactor dynamics code DYN3D was coupled in order to describe the fuel rod behavior

in a more detailed way. More precisely, the influence of the high burn-up structure formation, geometry changes and the fission gas release are included. In the coupling, DYN3D provides only the time-dependent rod power and thermal hydraulics conditions to TRANSURANUS, which in turn transfers parameters like fuel temperature and cladding temperature back to DYN3D, Fig. 7.

A control rod ejection transient was analyzed by both the DYN3D standalone approach and the coupled code complex DYN3D-TRANSURANUS. Due to space-dependent effects in the neutron kinetics on the one hand, and due to the mixed composition of the core containing fresh, low, medium and high burn-up fuel assemblies, the impact of the local fuel rod behavior is relevant. Altogether, the maximum of the total reactor power was almost 85 MW higher for DYN3D-TRANSURANUS in comparison to DYN3D.

The results in Fig. 8 for instance reveal that the detailed fuel rod behavior modeling influences the neutronics due to the Doppler reactivity effect of the fuel temperature. In particular, for high burn-up fuel, DYN3D-TRANSURANUS calculates values for the node centerline fuel temperature up to more than 150 K higher than DYN3D. The main reasons of the differences seem to be the UO_2 properties (e.g. thermal conductivity), and the radial power density profile over the fuel pellet radius, and the geometry changes (e.g. gap width). The coupled code system has therefore a potential to improve the assessment of safety criteria, at a reasonable computational cost, and could be applied for generalised platforms aiming at integrated accidents simulations such as considered in the frame of the NURESIM project [22], NURISP project and ongoing NURESAFE project of Euratom.
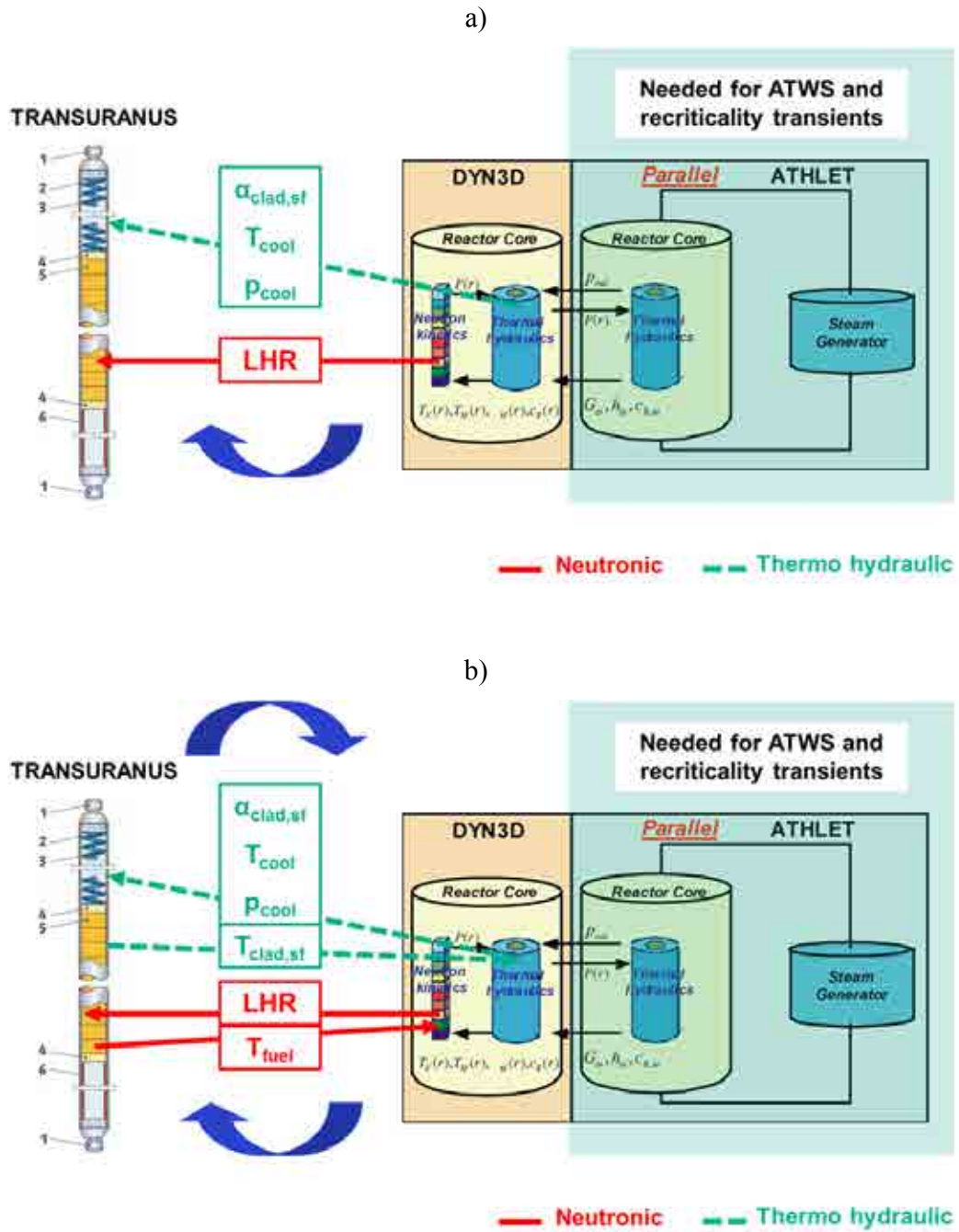
FIG. 7. Data transfer between the reactor dynamic code DYN3D on the one side and the general TRANSURANUS coupling interface and TRANSURANUS on the other side for a) one-way coupling and b) two-way coupling. For ATWS and re-criticality transients, the code system DYN3D-TRANSURANUS will be combined with the already used code system DYN3D-ATHLET in the future.
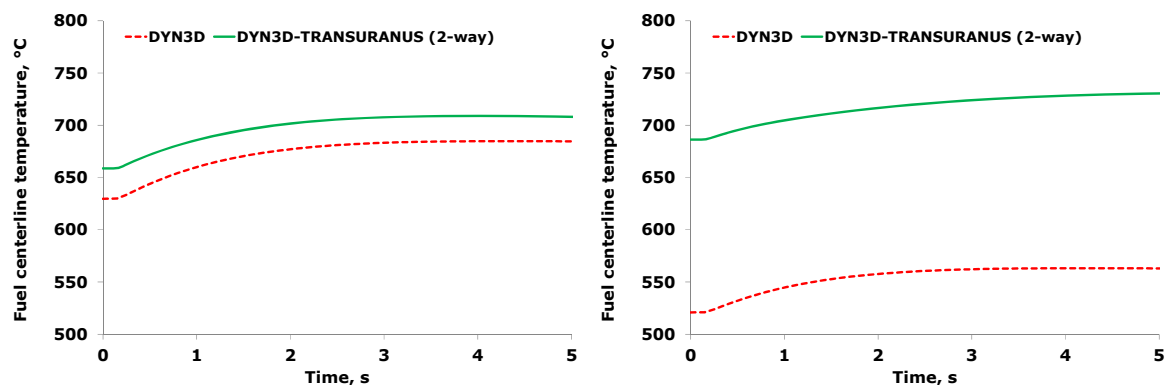
FIG. 8. Node fuel centerline temperature of fresh fuel (left) and high burn-up fuel (right) during the control rod ejection transient.

9. SUMMARY AND CONCLUSIONS

In order to simplify the code management and the interface between the codes, and to take advantage of the hardware progress it is necessary to generate a code that can cope with both normal operating and design basis accident conditions. Thanks to a clearly defined mechanical-mathematical framework and a consistent modelling, the TRANSURANUS fuel performance code was designed from its inception to be able to cope with normal, off-normal and accidental operating conditions. Nevertheless, the extension of the application range of the code to design basis accident conditions such as LOCA and RIA required specific models to be developed and implemented. In a first step, models for dealing with a LOCA have been implemented and tested. They include new Zry-4– and Zr1%Nb-specific models for the high temperature oxidation, the $\alpha{\rightarrow}\beta$ phase transformation, the plastic deformation and the failure of the fuel cladding under LOCA conditions. New correlations were developed for the Zr1%Nb cladding alloy considering the interference between cladding oxidation, strain rate and mechanical strength, and analysing the dynamic phase change in order to account for the effect of the heating or cooling rates, as well as for the hydrogen content. Also a new mechanical model for the large cladding strains has been developed and compared with finite element calculations as well as experimental data from the IFPE database. The merging and harmonisation of these LOCA-specific models in the different test versions of the TRANSURANUS code are underway.

More recently the model capabilities for simulation of RIA conditions have been launched. In particular, models covering the burst release from the HBS, the thermal heat transfer in the plenum and the coupling of the fuel performance code with reactor dynamics code such as DYN3D are under development and provide promising results. The validation of these new models and multi-physics tools will be continued with the upcoming RIA integral tests of the CABRI Water Loop Project of the OECD-NEA. The new experimental data are expected to provide a better understanding of the fuel behaviour under RIA because former RIA integral tests were conducted under non-typical light water reactor conditions, e.g. sodium as coolant in the CABRI experiments or stagnant water in the NSRR experiments. In the future the model development for RIA will be completed by the implementation of a fuel rod failure model for RIA as it was done already for LOCA.

Furthermore, properly defined benchmarks, for instance in the frame of FUMAC from the IAEA and the second RIA fuel codes benchmark of the OECD-NEA, would be very welcome in view of the further validation of the new code developments for design basis accidents. For the sake of

complementarity with the RIA benchmark of the NEA, the FUMAC CRP should focus on the LOCA specific issues such as clad oxidation, deformation, rupture and embrittlement at high temperature as well as fission gas release and fragmentation from the fuel at high burnup. Some data for this purpose are already available in the IFPE database. For example the separate effect studies on cladding (oxidation, ballooning, compression, etc.) cover tests with fresh and irradiated materials from different reactor types. As far as integral LOCA tests data are concerned, there is the IFA-650.2 case as well as the MT4 and MT6 cases. Nevertheless, new data are needed in order to cover higher burnup fuels and corresponding modern cladding types, or from different reactor types. A new case from the IFA-650 series in Halden (e.g. IFA-650.6 with a VVER rod irradiated to a discharge burnup of approximately 56 MWd/kgU), a case from the ALPS program in Japan, or the QUENCH-LOCA tests being conducted at KIT or a selection from the LOCA tests conducted by the US NRC in Studsvik and Argonne can provide additional information for code validation in terms of hydrogen content profile in the cladding for instance. In this respect the simulation of the Paks incident may also be considered, although this has already been analysed by a specialist group of the NEA.

Whichever integral cases will be selected, the first RIA fuel codes benchmark of the NEA and the LOCA case analysis in the frame of FUMEX-III revealed the need to specify the boundary conditions in order to focus on the fuel and cladding performance, rather than on the uncertainties related to the thermal-hydraulic analysis.

In order to complete discussions about each case, they should be extended with an appropriate sensitivity study, for example varying the cladding outer temperature. The code-to-code comparison also requires a well specified set of parameters to be pre-defined as for example was done in FUMEX-III.

Finally, it should be underlined that the separate effect tests and integral LOCA tests mentioned above can not only be used for the comparison of the conventional fuel performance codes describing the fuel behaviour in a so-called one-and-half dimension, but also for the multi-dimensional codes that are currently under development. In addition, is should be pointed out that these tests cover the initiating phase of severe accidents, i.e. as long as the fuel rod cylindrical geometry prevails. Later phases of severe accidents are considered in a separate benchmark of the OECD-NEA for accident tolerant fuels, wherein some results from the Fukushima accident will be simulated by means of severe accident codes.

ACKNOWLEDGEMENT

REFERENCES

[1]   LASSMANN, K., TRANSURANUS: a fuel rod analysis code ready for use. Journal of Nuclear Materials, 1992. **188**: p. 295–302.
[2]   LASSMANN, K. and P. VAN UFFELEN, The Structure of Fuel Rod Codes, in Publications Office, JRC Publications. 2004, European Commission.

[3]   VAN UFFELEN, P., et al. Status and Perspectives of Fuel Performance Modelling at the Institute for Transuranium Elements. in 6th International Conference on WWER Fuel Performance, Modelling and Experimental Support. 2005. Albena, Bulgaria.

[4]   MEYER, R.O. The U.S. Nuclear Regulatory Commission's research on fuel behaviour under accident conditions. in Int. Meet. on LWR Fuel Performance, "Nuclear fuel: addressing the future", Topfuel. 2006. Salamanca, Spain.

[5]   SONNENBURG, H.G. Study of fuel rod criteria for LOCA condition in the light of recent experimental data. in Int. Meet. on LWR Fuel Performance, "Nuclear fuel: addressing the future", Topfuel. 2006. Salamanca, Spain.

[6]   VESHCHUNOV, M.S., et al., Development of mechanistic code MFPR for modelling fission product release from irradiated UO_2 fuel. Nuclear Engineering and Design, 2006. **236**(2): p. 179–200.

[7]   CS. GYŐRI, et al. Extension of TRANSURANUS Code Applicability with Niobium Containing Cladding Models (EXTRA). in EU Research in Reactor Safety, Conclusion Symposium on Shared-Cost and Concerted Actions (FISA-2003). 2003. Luxembourg: Proceedings - EUR 21026.

[8]   SPYKMAN, G., et al. Implementation of a Cladding Failure Model for a Loss of Coolant Accident (LOCA)-Analysis in Transuranus. in Enlarged Halden Programme Group Meeting on High Burn-up Fuel Performance, Safety and Reliability. 2004. Sandefjord, Norway.

[9]   VAN UFFELEN, P., et al., Extending the application range of a fuel performance code from normal operating to design basis accident conditions. Journal of Nuclear Materials, 2008. **383**: p. 137–143.

[10]   FORGERON, T., et al. Experiment and Modelling of Advanced Fuel Rod Cladding Behaviour under LOCA Conditions: Alpha-Beta Phase Transformation Kinetics and EDGAR Methodology. in 12th. Int. Symposium: Zirconium in the Nuclear Industry. 2000. West Conshohocken.

[11]   DACKERMANN, U., Influence of Hydrogen on the Burst Behavior during Large Break Loss of Coolant Accidents of Zirconium Alloy Fuel Rod Claddings, in Lehrstuhl für Nukleartechnik. 2011, Technische Universtät München: München. p. 133.

[12]   DI MARCELLO, V., et al. Simulation of large clad creep strains with the TRANSURANUS fuel performance code for LOCA (F1.5). in EHPG Meeting. 2013. Storefjell, Norway.

[13]   SAUER, G., Algorithmic determination of fuel rod cladding burst time at elevated temperatures. Kerntechnik, 2010. **75**: p. 1–2.

[14]   CS. GYŐRI and P. BLAIR, An empirical model for fuel fragmentation and fission gas release under LOCA conditions, in International workshop "Towards nuclear fuel modelling in the various reactor types across Europe". 2011: Hannover, Germany.

[15]   VAN UFFELEN, P., et al. Development of a transient fission gas release model for TRANSURANUS. in Water Reactor Fuel Performance Meeting. 2008. Seoul, Korea.

[16]   PASTORE, G. 2013, Email on 31.01.2013.

[17]   OECD-NEA, RIA Fuel Codes Benchmark 2013, Paris, France.

[18]   GYŐRI, C., A 2D Numerical Method to Simulate Transient Heat Conduction in the Plenum Gas of LWR Fuel Rods, in International Workshop "Towards nuclear fuel modelling in the various reactor types across Europe", P.V. Uffelen, Editor. 2013: Karlsruhe, Germany.

[19]   OECD-NEA, Nuclear fuel behaviour under reactivity-iniated accident (RIA) conditions. 2010, Paris, France.

[20]   HOLT, L., et al., Sensitivity study of Xe depletion in the high burn-up structure of UO_2. Journal of Nuclear Materials (in preparation), 2013.

[21]   HOLT, L., et al. Development of a general coupling interface for the fuel performance code TRANSURANUS tested with the reactor dynamic code DYN3D. in 10th International conference on WWER fuel performance, modelling and experimental support. 2013. Sandanski, Bulgaria: Bulgarian Academy of Sciences.

[22]   NURESIM, FINAL ACTIVITY REPORT, in European Commission, Community Research Report. 2008.

158

ADVANCED SIMULATION OF FUEL BEHAVIOR UNDER IRRADIATION IN THE PLEIADES SOFTWARE ENVIRONMENT

V. MARELLE, B. MICHEL, J. SERCOMBE, P. GOLDBRONN, C. STRUZIK, A. BOULORE
CEA, DEN, DEC,
Centre de Cadarache,
13108 Saint Paul lez Durance,
France

Abstract. A "multi design" new generation software environment called PLEIADES has been developed by the CEA in the framework of a research cooperative program with EDF and AREVA. In this general software environment, ALCYONE is the PWR fuel performance simulation code.

It is a multi-dimensional simulation software (1D, 2D and 3D), with applications for normal, transient and accidental conditions. It also has several levels of modelling, from industrial models to mechanistic ones depending on the amount of multi-scale details expected in the results of the simulation. The different dimensional schemes share the same thermo-mechanical Finite Element Method code CAST3M.

The 1D scheme describes the behaviour of the whole rod and gives access to integral values such as rod fission gas release, clad profilometry and elongation. The 3D scheme allows a local study of Pellet Clad Mechanical Interaction (PCMI) by modelling the thermo-mechanical behaviour of one or several pellet fragments and overlying cladding. The 2D scheme is a compromise between calculation time and the accuracy of the local fuel description. Recently the 3D approach has been extended to a short fuel rod model in order to simulate the ballooning phenomenon during accidental transients.

In this paper, we will present the general description of the ALCYONE simulation code in the PLEIADES environment (general computation algorithm, advanced fission gas model for UO_2 and MOX fuels, 3D computation scheme). A focus will be presented on specific developments which have already been done to simulate accidental conditions such as LOCA and fast transients for different dimensional models.

1. INTRODUCTION

In the general framework of nuclear fuel behaviour simulation, CEA has developed a "multi design" new generation simulation framework called PLEIADES. In this general framework, ALCYONE is the PWR fuel performance simulation application. It is a multi-dimensional simulation software (1D, 2D and 3D), with applications for normal, transient and accidental conditions. In this paper, we will present the general description of the ALCYONE simulation code in the PLEIADES environment (general computation algorithm, advanced fission gas model for UO_2 and MOX fuels, 3D computation scheme). A focus will be presented on specific developments which have already been done to simulate accidental conditions representative of a fast transient or a LOCA transient.

2. THE PLEIADES FUEL SOFTWARE ENVIRONMENT

The PLEIADES project [1] has been built to create a new simulation platform for the study of any reactor concept fuels behaviour. The three main parts of the PLEIADES environment are described in Fig. 1. The architecture provides generic tools for multi-physic algorithms, data exchange (based on the SALOME http://www.salome-platform.org standard) and the link with fuel data bases. It provides also SALOME tools for pre and post processing with friendly user interfaces. The second part of the PLEIADES platform is a physical component library for fuel simulation embedded in C++ classes in a unified software environment. The third and last part consists in a

generic computation algorithm, built with the architecture and the physical component library, with a user interface dedicated to each fuel concept. At the present time there are height computations schemes under operation in the PLEIADES platform. Six of them are dedicated to specific fuel concept studies and provide a large validation data base shared between CEA, EDF and AREVA. The V.E.R computation scheme is devoted to simulation at the volume element scale for generic fuel microstructure analyses. The LICOS computation scheme is used for preliminary fuel design studies on non-standard geometry concept. PCI modelling studies are achieved with the ALCYONE computation scheme which provides a multi-dimensional approach for PWR fuel rod concept.
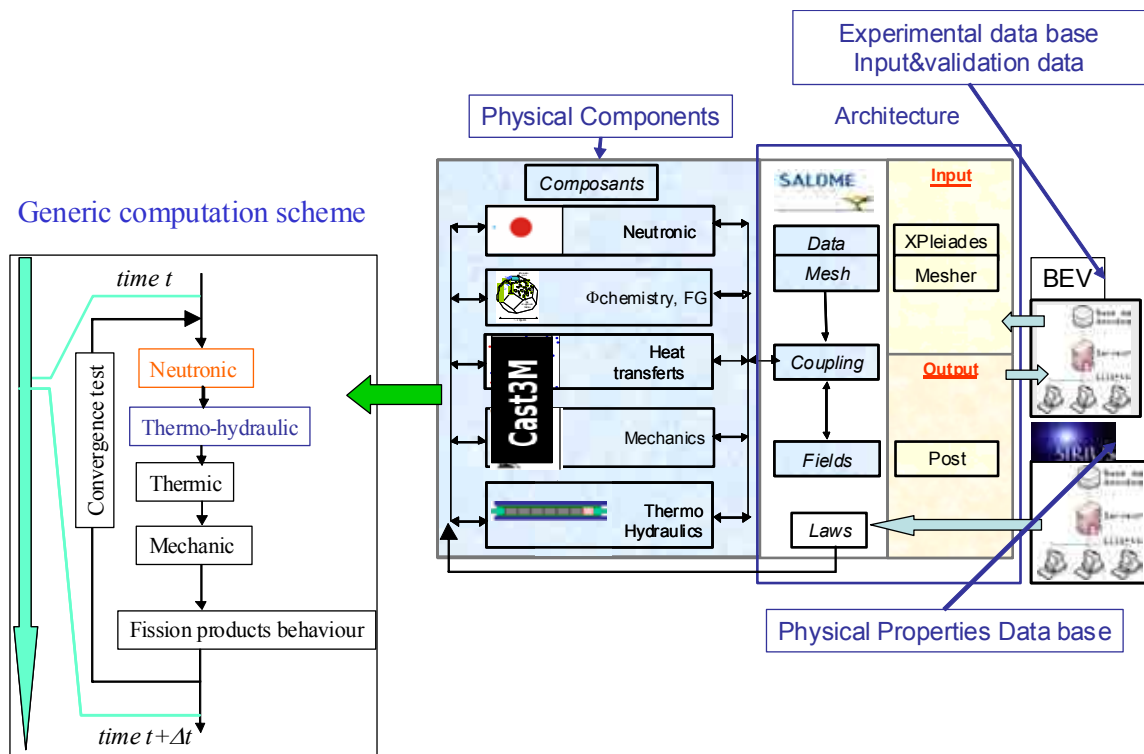
FIG. 1. PLEIADES fuel software environnement.

3. FUEL SIMULATION ALGORITHM

The main phenomena involved in fuel behaviour modelling under irradiation are presented in Fig. 1 [2]. These phenomena can be separated in two: on one side, neutronic and thermal-hydraulic problem, and on the other side, a non-linear multi-physic problem for fuel element behaviour under irradiation. The first problem is devoted to compute nuclear power deposition in the fuel and power evacuation from the fuel element toward the energy conversion system. The second problem is devoted to the computation of the temperature distribution in the fuel element, mechanical fields and structural material changes due to irradiation effects. Neutronic and thermo-hydraulic problems are strongly linked to computations at the scale of fuel assembly or reactor core. Thermal and mechanical computations are more relevant of the fuel element scale commonly used for structural

integrity assessment, when physico-chemical computation is mainly linked to mechanisms at an atomistic scale (densification and solid swelling processes, gaseous fission products behaviour).

4. FUEL MODELS FOR IRRADIATION UNDER NORMAL STEADY STATE AND TRANSIENT CONDITIONS

For normal steady state and transient conditions, simulation can be performed with the multidimensional computation scheme, and each scheme (1D, 2D and 3D) is based on the same fuel models.

4.1 Local power density computation

The power density distribution through the pellet is computed with a simplified approach coming from the first generation fuel performance code METEOR [3]. This approach is based on the one dimensional axisymmetric assumption first proposed by Palmer in the RADAR model [4] where the solution of the coupling BOLTZMANN and BATEMAN constitutive equations is given by (1).

$$P_V^{local} \infty \Phi(r).\sum_{pf} \overline{\sigma}_{pf}.C_{pf}(r).E_{pf} \tag{1}$$

Where $\Phi(r)$ is the neutron flux, $\overline{\sigma}_{pf}$ is the mean value of the one-group fission cross-section of each fissile atom (subscript pf) and $C_{pf}(r).E_{pf}$ the concentration of each fissile atom multiplied by its corresponding fission energy.

The shape factor of the neutron flux $\Phi(r)$ is derived from the simple one group diffusion theory, and the mean value is fitted in order to have a total power per unit length of fuel equal to the prescribed value. The mean value of the one-group fission cross section is fitted, as a function of the burn-up, with the results of the BOLTZMANN transport equation computation at the core scale. Fissile atom concentration is derived from the PRODHEL model [5] which computes also non fissile atom concentration and will replace in the PLEIADES platform the extended version of the RADAR model previously used in METEOR.

4.2 Thermal-hydraulic model

The thermal-hydraulic computation is devoted to assess the temperature of the heat transfer fluid and the wall exchange coefficient of the fuel element cladding. This temperature is then used as a boundary condition of the thermal problem in the fuel element (see section 3.1.3). Under normal irradiation conditions the thermal-hydraulic model used for Light Water Reactor's fuel rod takes into account a homogeneous two-phase flow either in permanent or low transient stages. This model requires a boundary condition coming from the measured temperature at the bottom of the fuel rod.

4.3 Thermal computation

Temperature distribution through the fuel element is computed according to the conservation energy principle given by equation (2).

$$\rho.c_p.\frac{dT}{dt} = div\lambda gradT + p_V^{local} \tag{2}$$

Power evacuation to the heat transfer fluid is taken into account with a flux boundary condition given by equation (3), where h is the wall exchange coefficient and T_∞ heat transfer fluid temperature computed in the thermo-hydraulic model. λ is the thermal conductivity of the irradiated material.

$$\Phi = h.(T_{wall} - T_\infty) \tag{3}$$

Concerning the thermal flux through the pellet cladding interface, an equivalent convection exchange coefficient is used in order to take into account conduction and radiation when gap is opened, or thermal contact resistance when gap is closed.

4.4 Mechanical computation

Mechanical state of the fuel element is computed with the static equilibrium equation (4) integrated according a weak formulation with the Finite Element method.

$$div\overline{\overline{\sigma}} = 0 \tag{4}$$

In addition to this equilibrium principle non-linear behaviour of the fuel element is taken into account through several mechanical models with the following constitutive equations for the pellet, cladding and pellet-cladding interface, as discussed below.

4.4.1 Pellet

Uncompressible viscoplastic behaviour under irradiation is taken into account in the pellet (5), where fission density rate leads to an induced creep effect (second term of equation (5)) with a low level of thermal activation energy (Q_{ic}), and an enhancement of the thermal creep (parameter   ). Material evolution due to irradiation is introduced in the model by the dependency of material parameters on the burn-up level and porosity of the fuel pellet. Then, for the mechanical properties of the fuel pellet, the impact of porosity on the elastic and creep parameters is taken into account. In this respect, a poro-viscoplastic compressible formulation for creep has been developed [6].

$$\frac{d\varepsilon_{creep}}{dt} = Max\left[A_i(p,D_G).\left(J_2(\overline{\overline{\sigma}})\right)^{n_i}.e^{-\frac{Q_i}{R.T}}\right].(1+\alpha.\frac{dF}{dt}) + B.\left(J_2(\overline{\overline{\sigma}})\right)\frac{dF}{dt}.e^{-\frac{Q_{ic}}{R.T}} \tag{5}$$

In equation (5) $d\varepsilon_{creep}/dt$ is the total creep strain rate, $J_2(\overline{\overline{\sigma}})$ the second invariant of the deviatoric stress tensor, t the time, T the temperature, p the porosity, D_G the fuel grain size, (A_i, n_i, Q_i, B,   , Q_{ic}) are material parameters, subscript i is equal to 1 and 2 for each thermal creep stage, dF/dt is the fission density rate and R is the universal gas constant.

Fuel cracking during irradiation and its coupling to visco-plastic behaviour is taken into account through a non-unified formulation. Constitutive equations of the fuel cracking model and its validation are detailed in references [7, 8]. In order to represent fuel cracking in the pellet fragment a continuum approach has been chosen. The development of micro-cracking, once the yield stress is reached and till the complete rupture of the material elementary volume, is represented by an instantaneous linear softening equation.

162

4.4.2 Cladding

The non-linear behaviour of the cladding under irradiation is taken into account by a non-unified formulation coupling a creep law (6) and a plasticity model like the example presented in equation (7).

$$\frac{d\varepsilon_v}{dt} = A.\left(J_2(\overline{\overline{\sigma}})\right)^{n_p}.e^{-\frac{Q_p}{R.T}}.e^{-B.t} + C.\left(J_2(\overline{\overline{\sigma}})\right)^{n_s}.e^{-\frac{Q_s}{R.T}}.\Phi^p \tag{6}$$

$$J_2(\overline{\overline{\sigma}} - \overline{\overline{X}}) - R_0 \leq 0 \text{ and } \overline{\overline{X}} = \frac{2}{3}.h.\overline{\overline{\varepsilon}}_p \tag{7}$$

In equation (6) $d\varepsilon_v/dt$ is the creep strain rate, the fast neutron flux, $(A, n_p, Q_p, B, C, n_s, Q_s, p)$ are material parameters and R is the universal gas constant. In equation (7), $\overline{\overline{X}}$ is the internal stress associated to kinematics hardening, R_0 the yield stress, h the hardening modulus and $\overline{\overline{\varepsilon}}_p$ the plastic strain.

Creep rate enhancement due to the effect of the fast neutron flux (E>1MeV) on the material is taken into account in the second term of equation (6) which models stationary creep. The irradiation-induced hardening of the material is introduced in the first term of equation (6) which models primary creep and by the dependency of the material parameters on neutron fluence. To account for the material behaviour on the whole loading range, two different sets of material parameters are used for creep at low stress level (base irradiation) and creep at high stress level (ramp test). The anisotropic behaviour of the cladding, particularly important for some alloys, can also be taken into account by using Hill's equivalent stress [9] instead of the Von Mises equivalent stress (J_2) in equation (6) and (7).

4.4.3 Pellet-cladding interface

Friction is of primary importance with respect to stress or strain concentration in the cladding [10, 11] and regarding fuel cracking [12, 13]. Measures of the friction coefficient between non-irradiated fuel materials and Zircaloy materials are usually within 0.4–0.7, and almost independent of the contact pressure, temperature and oxide thickness. Irradiation can enhance friction [12] and even lead to chemical bonding between the pellet and the cladding [13] at high burn-up. In 2D and 3D descriptions of the ALCYONE computation scheme fuel pellet – cladding system unilateral contact is assessed by the lagrangian multiplier method of the CAST3M Finite Element code, and a "Coulomb" model is introduced to take into account friction-slip or adherence, according to equation (8):

$$v_t = \begin{cases} 0 & if \quad \|F_t\| \leq \mu\|F_n\| \\ -cF_t & if \quad \|F_t\| = \mu\|F_n\| \end{cases} \tag{8}$$

with v_t the slip rate, F_n and F_t the normal and tangential forces, μ the friction coefficient and c a positive number.

4.4.4 *Chemical physical behaviour of fuel pellet*

4.4.4.1 Solid swelling and densification

Volume variation due to solid swelling and densification is computed with equation (9), where the strain rate is computed with the unit tensor and a function of the pellet burn up. Solid swelling is linked to solid fission products which tend to modify the crystallographic dimensions of uranium dioxide [3]. Densification process is the result of the annihilation of small porosities caused by the activation energy of fission peaks [14].

$$\dot{\bar{\bar{\varepsilon}}}_{SS\_D} = f(BU,...)\bar{\bar{I}} \tag{9}$$

4.4.4.2 Behaviour of gaseous fission products

The behaviour of gaseous fission products is modelled by different approaches:

1. A semi-empirical model for the simulation of integral tests [15],
2. Advanced models for detailed interpretation of laboratory results [16].

The constitutive equations presented in this paper give the main principles of the local coupling formulation between gaseous swelling and mechanical behaviour as it is computed in the advanced fission gas models used in the PLEIADES platform [17].

Gaseous swelling is derived from a non-linear time differential system composed of the following equations:

Balance equation for fission gas products transfer

$$f_i\left(C_{res}, \dot{C}_{res}, C_{b_j}, \dot{C}_{b_j}, G_{b_j}, \dot{G}_{b_j}, C_{ird_k}, \dot{C}_{ird_k}\right) = 0 \tag{11}$$

Gas state equations

$$gfpse\left(\sigma^{b_j}_{\text{interface}}, r_{b_j}, \frac{G_{b_j}}{C_{b_j}}, T\right) = 0 \tag{12}$$

Constitutive equations for pressurized cavities behaviour in solid medium

$$gs(\sigma^{b_j}_{\text{interface}}, \bar{\bar{\sigma}}_M, \frac{dr_{b_j}}{dt}, T,...) = 0 \tag{13}$$

The unknown functions of the differential equation system (11) are internal state variables describing material changes and gaseous fission product transfer under irradiation (see Table 1). The fission products gas state equation (12) and the pressurized cavities behaviour constitutive equation give an assessment of the bubble mechanical state.

TABLE 1. NOMENCLATURE OF INTERNAL STATE VARIABLES FOR PELLET CHEMICAL PHYSIC BEHAVIOR

C_{res}	Gas concentration per unit volume of fuel (mol/m^3) located in UO$_2$ atomic network
C_{b_j}	Bubble concentration per unit volume of fuel, subscript j describes the bubble type and size.
G_{b_j}	Gas concentration per unit volume of fuel (mol/m^3) located in bubble of type and size j
C_{ird_k}	Default (void, interstitial, dislocation) concentration per unit volume of fuel
$\sigma_{\text{interface}}^{b_j}$	Normal stress at the gas-solid interface for bubble type and size j
r_{b_j}	Radius of bubble type and size j
T	Local gas temperature
$\overline{\overline{\sigma}}_M$	Effective Cauchy stress tensor in the bulk material

4.4.5 Coupling of gaseous swelling and mechanical behaviour at fuel rod scale

The coupling problem between mechanical behaviour and gaseous fission products behaviour at time t can be decomposed as following:

1. Mechanical equilibrium equations

$$\begin{cases} div\,\overline{\overline{\sigma}}_M = 0 \text{ on } \Omega \\ \overline{\overline{\sigma}}_M.\vec{n} = \vec{\phi}_{BC} \text{ on } \partial\Omega_\phi \\ \vec{u} = \vec{u}_{BC} \text{ on } \partial\Omega_u \end{cases} \tag{14}$$

2. Mechanical non-linear behaviour

$$\frac{d\overline{\overline{\sigma}}_M}{dt} = \underline{\underline{E}} : \left(\frac{d\overline{\overline{\varepsilon}}_t}{dt} - \frac{d\overline{\overline{\varepsilon}}_{crack}}{dt} - \frac{d\overline{\overline{\varepsilon}}_{creep}}{dt} - \frac{d\overline{\overline{\varepsilon}}_{GS}}{dt} \right) \tag{15}$$

3. Gaseous fission products behaviour

$$\frac{d\overline{\overline{\varepsilon}}_{GS}}{dt} = f_{GS}(\overline{\overline{\sigma}}_M) \tag{16}$$

From a practical point of view the time integration of the multi-physics problem is derived from an incremental formulation, between times t and t+Δt, along irradiation loading time history.

Due to the fact that the constitutive gaseous swelling equations $f_{GS}(\overline{\overline{\sigma}})$ cannot be easily introduced in equation (15), an external iteration process as to be achieved between the mechanical problem (14),(15) and the gaseous swelling problem (16). This iteration process is based on the fixed point method where the coupling variables are the effective stress in the bulk material and the gaseous swelling strain variation during time step Δt. In this approach we assume that the gaseous swelling strain rate in equation (15) is constant and can be computed as:

$$\frac{d\overline{\overline{\varepsilon}}_{GS}}{dt} = \frac{\int_{t}^{t+\Delta t} f_{GS}(\overline{\overline{\sigma}}).dt}{\Delta t} \tag{17}$$

TABLE 2. NOMENCLATURE FOR THE COUPLING APPROACH BETWEEN GASEOUS SWELLING AND MECHANICAL BEHAVIOUR

Ω	Domain used to described the fuel element geometry
$\partial\Omega_{\phi}$	Frontier with force boundary conditions $\vec{\phi}_{BC}$
$\vec{n}$	Normal vector to $\partial\Omega_{\phi}$
$\partial\Omega_{u}$	Frontier with displacement boundary condition $\vec{u}_{BC}$
$\overline{\overline{\varepsilon}}_{t}$	Total strain
$\overline{\overline{\varepsilon}}_{crack}$	Crack strain
$\overline{\overline{\varepsilon}}_{creep}$	Creep strain
$\overline{\overline{\varepsilon}}_{GS}$	Gaseous swelling strain
$f_{GS}(\overline{\overline{\sigma}})$	Differential equation system for gaseous fission product behaviour equation (11) to (13)

5. FUEL MODELS FOR IRRADIATION UNDER ACCIDENTAL TRANSIENT CONDITIONS

In the case of the accidental transient conditions, the same multidimensional computation scheme is available, each dimensional scheme (1D, 2D or 3D) being based on the same models for fuel and cladding.

But in addition to the 'classical' multidimensional computation scheme, to calculate the cladding ballooning effect observed in some accidental conditions, the 3D scheme has been extended to the simulation of a stack of fuel pellets and their associated piece of cladding (Fig. 2), the ballooning effect being observed on several pellets [18]. The simulation of the ballooning needs a precise description of the coupling between thermal-mechanical modelling and fission gas behaviour model

(which calculates the swelling and the fission gas release of the fuel). The 3D multi-pellet scheme computes a precise evaluation of the voids in the vicinity of the cladding (cracks, chamfer, dishing…). The ballooning results of an equilibrium between the local pressure and the deformation of the cladding, which relaxes this pressure [19].
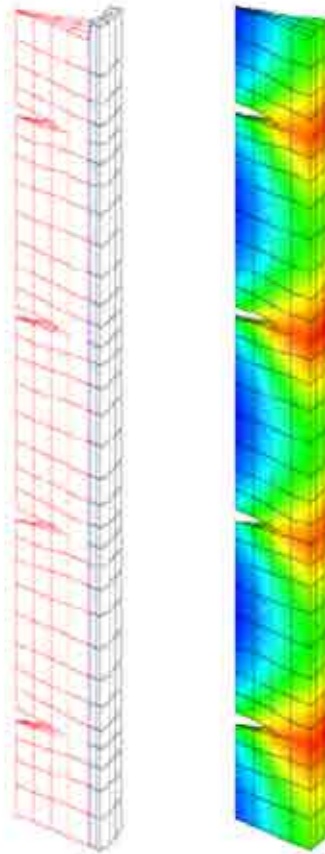
FIG. 2. 3D simulation of several pellets.

In accidental conditions, most of the models used in the ALCYONE application are the same as the ones in normal conditions, and in the following sections of this chapter, only the specific models dedicated to accidental transients are presented.

5.1 Thermal-hydraulic model

In order to simulate high power rate transient experiment a transient thermal-hydraulic coupling formulation between coolant and fuel rod has been introduced in ALCYONE. A first formulation has been developed for sodium coolant to simulate CABRI REP-Na experiments [20]. Recently a thermal-hydraulic model for PWR conditions has been implemented.

This model is based on the same approach than the one used in the SCANAIR code [21, 22], where the insulating of the steam blanket is simulated with the critical heat flux correlation. Figure 3

shows the evolution of the heat flux between the cladding and the coolant as a function of the surface temperature of the cladding.
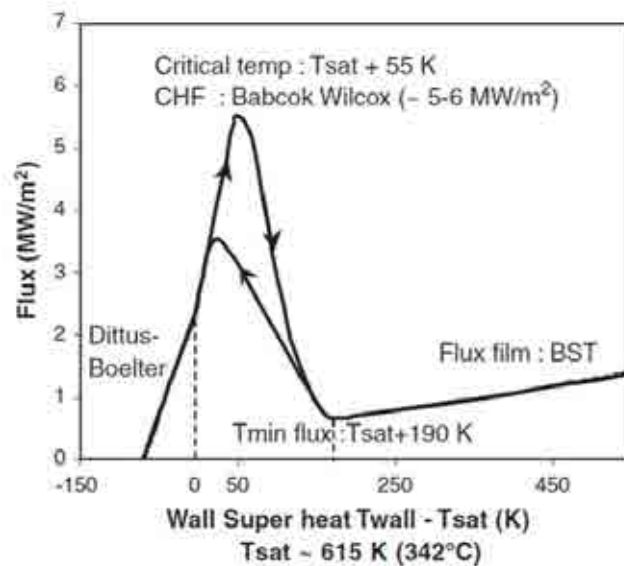

FIG. 3. Heat flux between cladding and coolant [22].

5.2 Mechanical behaviour of the cladding

In the case of fast transients, the behaviour of the cladding is considered to be anisotropic and viscoplastic without threshold [23].

For a transient representative of a LOCA accident the mechanical behaviour of the cladding also takes into account [24, 25]:

1. the alpha-beta phase transformation of zirconium alloy with the characteristic of temperature ramp rate $(T, \dot{T})$;
2. the associated modifications of the mechanical properties (creep law, more particularly);
3. the failure prediction of the cladding.

5.3 Numerical simulation of fuel element behaviour under Irradiation

5.3.1 Base irradiation

During the first power increase, the thermal gradient associated to the fuel fragmentation is at the origin of the hourglass shape of the pellet. The consequence is a reduction of the gap at the inter-pellet plane (see Fig. 4a) [26]. Then, during the power hold period the fuel element dimensions will change due to the following phenomena:

- Densification and solid swelling in the pellet
- Cladding creep under a compressive stress state.

The competition between these geometrical changes leads to a gap decrease with mainly two steps of PCI:

- Low interaction stage with a gap partially closed in the vicinity of the inter pellet plane,
- Strong interaction stage with a gap entirely closed and a significant contact pressure level (see Fig. 4b).

During the interaction period the pellet hourglass shape is printed in the cladding because of its inelastic strains due to material creep under external pressure loading. Moreover, the cladding diameter decrease can also tend to reduce the extent of pellet hourglass magnitude, thanks to stress relaxation due to irradiation induced creep in the pellet fragment. Through this analysis, it appears that the magnitude of clad primary ridges at the end of base irradiation is the result of the competition between cladding and pellet creep. The development of a high-burn up structure in the pellets with pronounced gas-swelling can smooth the radial deformation of the cladding after base irradiation, as shown in reference [27] for BWR fuel rods.
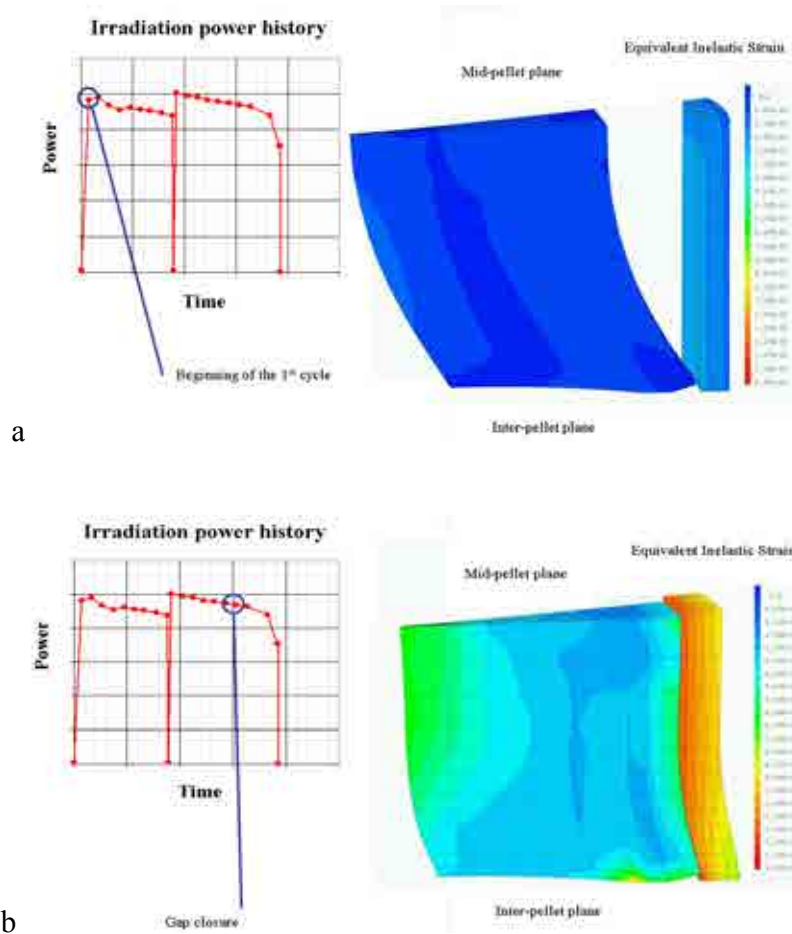
FIG. 4. Pellet-cladding gap closure and cladding ridging mechanisms under base irradiation.

5.3.2   Power ramp test

The behaviour of fuel rods during ramp testing depends on many factors: the geometry of the fuel pellet (height/diameter ratio of the pellet, dish volume, chamfer dimensions, …), the power history (maximum power, increase of power, power rate, duration of holding period, …), the thermo-mechanical behaviour of fuel and cladding (burn-up of the pellet, thermal expansion of the fuel

pellet, cladding creep and plasticity, fuel creep, …) and fission gas swelling in the fuel pellet [26, 28].

The diameter increase of the cladding during power ramp is driven by the thermal expansion of the pellet and by fission gas swelling if the temperature of the pellet is high enough. The contribution of gas swelling can be important particularly if the holding period is long (> 15–30 minutes) or if the fuel rod has a high burn up.

Cladding expansion during ramp testing is first induced at Inter-Pellet (IP) level due to the hourglass of the pellet resulting from the thermal gradient (see Fig. 5a) but soon it is compensated by dish filling due to creep and fission gas swelling of UO_2. If the height/diameter ratio of the pellet is large (> 1.5), the impact of creep on the Mid-Pellet (MP) plane will be small. Radial expansion will therefore be maximum at MP level since dish filling will limit radial expansion at IP level (see Fig. 5b). This is the reason why the MP ridges observed in the database can reach significant values (30 microns) and often exceed their IP counterparts by a factor 2 or 3, see Fig. 6. This is not the case with pellets of smaller height/diameter ratio (< 1) as was shown with ALCYONE 3D in reference [27] since dish filling has in this case consequences on the deformation of the mid-pellet plane due to axial creep. Hourglass induced strains remain therefore predominant in this configuration leading mainly to IP ridges.

The kinetics of Mid-Pellet ridge development strongly depend on the maximum power and temperature reached during ramp testing since radial expansion of the pellet and dish filling depend on these 2 parameters. Figure 7 gives the MP diameter increase of the pellet during the transient part of the ramp test due to the total swelling of the fuel pellet, in function of the maximum temperature of the pellet. Also plotted is the calculated dish filling in function of the maximum temperature.

As can be seen, when the pellet maximum temperature is greater than 1800°C fission gas swelling effect is significant at the fuel element scale. A threshold temperature can also be defined for complete filling up of the dishing (>70%) in the 3D simulations. It is close to 1700°C and hence of the same order than the 1800°C for fission gas swelling activation. Simulation results indicate furthermore that 100% dish filling is usually reached within a few minutes during the holding period if power is sufficient.

This interpretation of experimental results has been derived mainly from the 3D model of a single pellet fragment. Based on 3D simulations, a simplified pellet hourglassing model [29] with partial reversibility in case of power drop has also been developed for the generalized plane strain approach of the 1D axisymmetric representation or the 2D r-θ representation. Thanks to this simplified model, the pellet temperature can be assessed with a reasonable accuracy in the generalized plane strain approach.
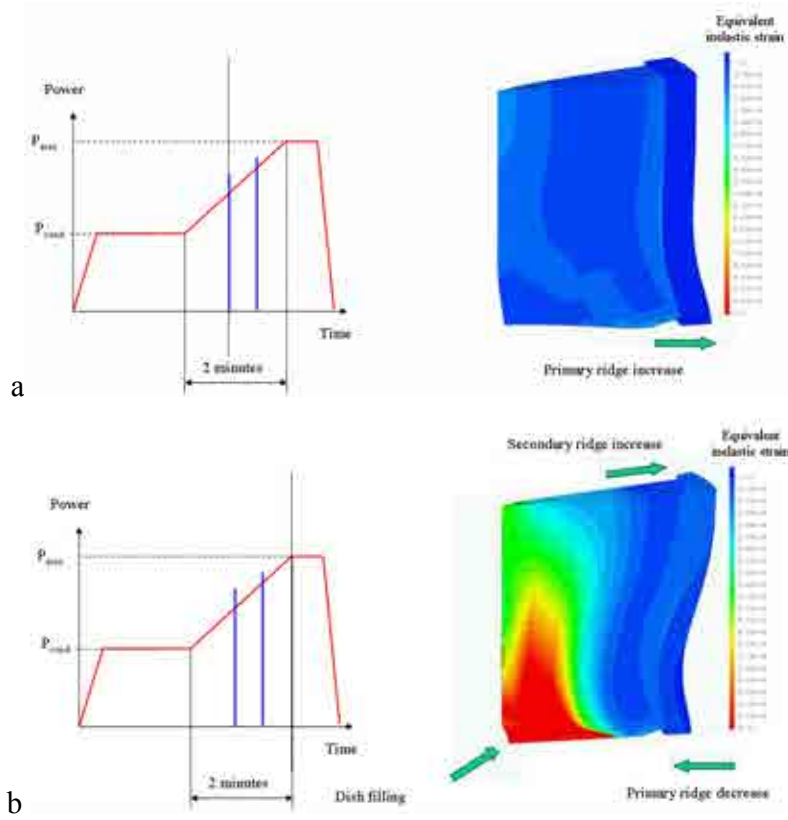
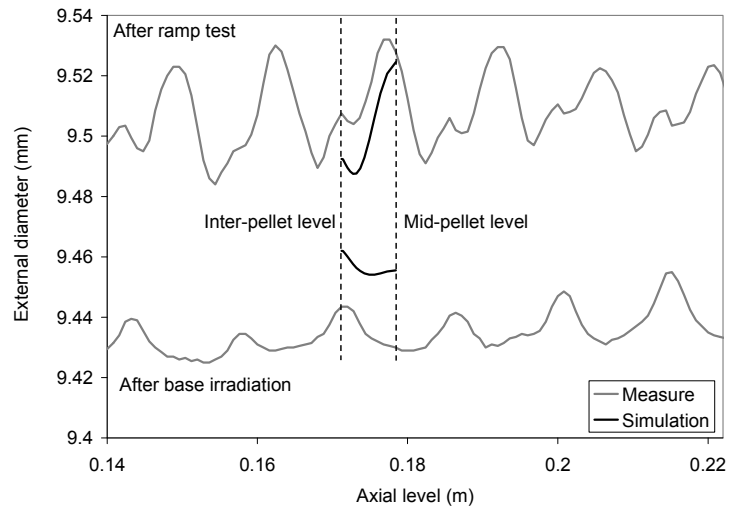*FIG. 5. Pellet viscoplasticity and cladding ridging mechanisms under power ramp test.*

FIG. 6. 3D calculated and measured ridges after base irradiation and ramp testing showing the important development of the mid-pellet ridge during ramp testing.
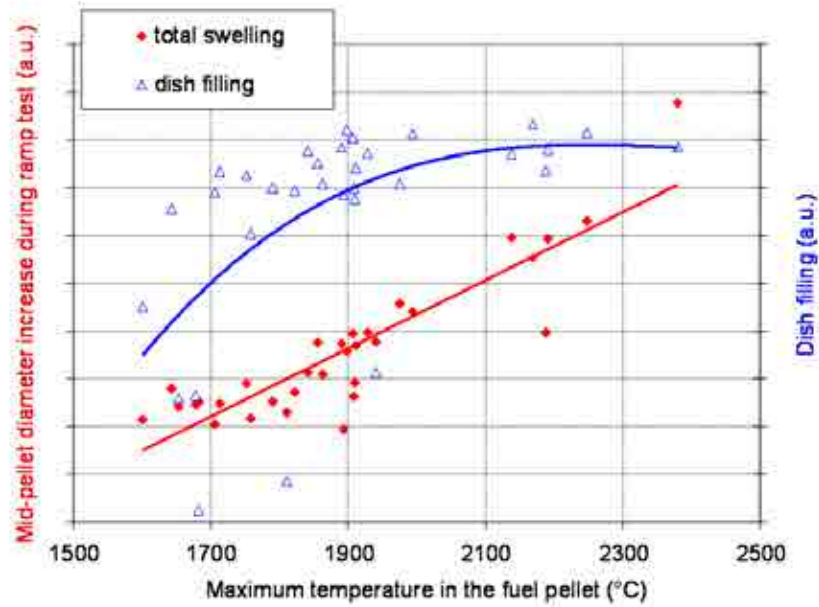
FIG. 7. Pellet diameter increase and dish filling during a power ramp test.

Fuel pellet fragmentation occurring at an early stage of irradiation and due to thermal stresses is taken into account through a 3D finite element model and its boundary conditions in the ALCYONE computation scheme. For secondary cracks occurring inside the pellet fragment a continuum damage model is used according to the constitutive equations given in reference [7]. Simulation results for secondary crack pattern assessment during a power ramp test are summarized in Fig. 8.

The latter shows that an axial crack (perpendicular to the axial direction) located at the mid pellet plane appears at the end of base irradiation. This crack is initiated in the simulation because of a tensile residual axial stress at the fragment centre after shutdown. In the power ramp test, at the beginning of the holding period at the maximum power level, this axial crack is closed, because of the thermal gradient which leads to compressive stresses around the fragment central axis. New axial and circumferential cracks have been initiated on the fragment outer part submitted to biaxial tensile stresses. After the ramp test, axial cracks initiated at the maximum power level in the outer part of the fragment are closed, the axial crack initiated at the end of base irradiation is re-opened in the fragment centre with new axial cracks initiated during reverse loading at the end of the power ramp test. Residual opening of the circumferential cracks initiated at the maximum power level is reduced after shutdown of the power ramp test, and radial cracks (perpendicular to the radial direction) are initiated on the outer part and at an intermediate radius. The latter is approximately the same than the radius reach by the circumferential cracks initiated from the pellet outer part.

172

$$\varepsilon_{zz}^{fis}$$

End of base irradiation

$$\varepsilon_{zz}^{fis} \qquad \varepsilon_{\theta\theta}^{fis}$$

Maximum power level of the ramp test

$$\varepsilon_{\theta\theta}^{fis}$$

$$\varepsilon_{rr}^{fis}$$

$$\varepsilon_{zz}^{fis}$$
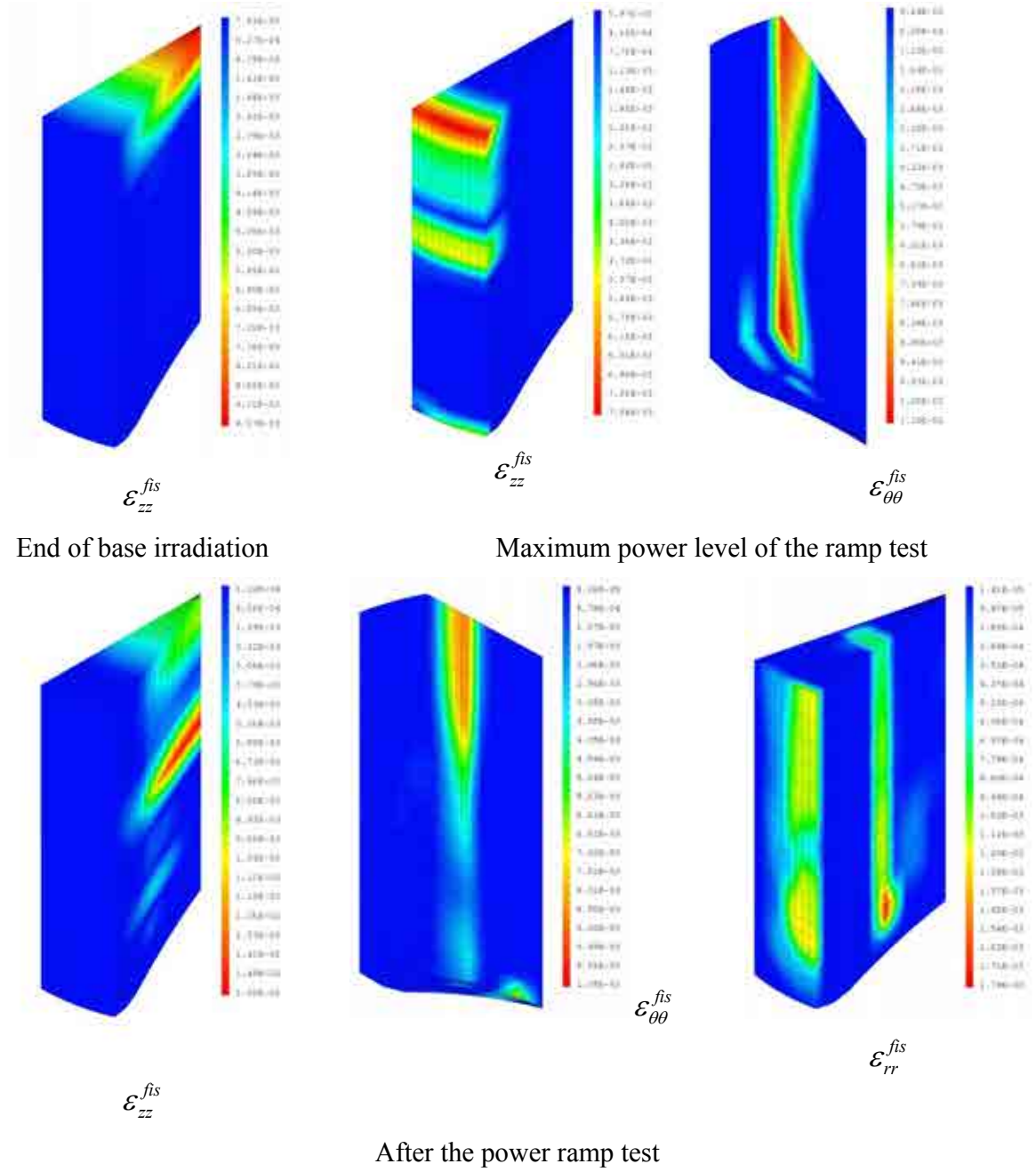
After the power ramp test

FIG. 8. Secondary crack pattern assessment during a power ramp test.

6. PRELIMINARY RESULTS OF SIMULATION IN ACCIDENTAL CONDITIONS

6.1 High power rate transient

In 2010 a first study has been achieved to simulate CABRI-REP Na experiments [20] in order to demonstrate the capacity of the ALCYONE 3D model for a detailed analyse of the PCMI stage. As

shown in reference [20] 3D simulations have been able to reproduce the measured increase of inter pellet ridge height (see Fig. 9) and dish filling with energy deposition. The time-scale of ridge formation has been analysed in more details and showed the progressive shift from a barrel-controlled diameter increase during the transient part of the pulse to an hourglass-controlled diameter increase during the next few seconds. Some works are still in progress to validate the ALCYONE multi-dimensional approach for high power rate transient in PWR conditions where a post stage of departure of nucleated boiling is reached.
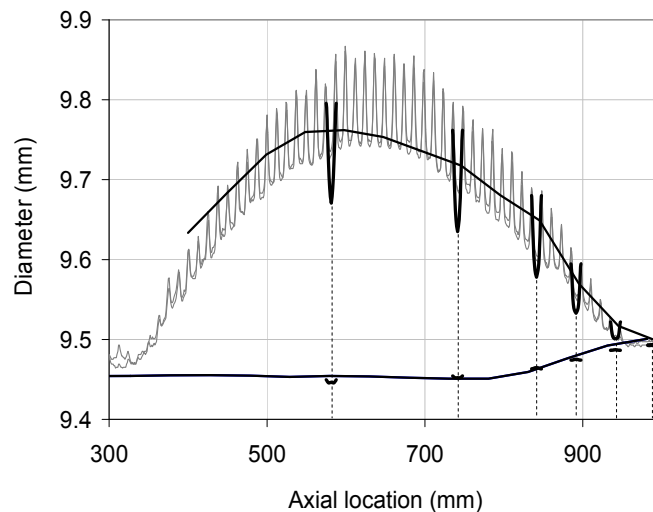
FIG. 9. Calculated (black lines: 1D and 3D) and measured (grey lines) residual clad diameter after the REP-Na2 pulse test [20].

6.2 LOCA transient

ALCYONE developments, to describe the fuel rod behaviour in loss of flow conditions, are in progress.

A recent study has been achieved to reproduce a LOCA experiment (internal pressure, free volume evolution, cladding failure), if the cladding temperature evolution is considered as input data. According these results the 1D computation scheme of ALCYONE can predict the rupture and the internal pressure drop as it is illustrated for the STUDSVIK 192 test [30] on Fig. 10. In the latter the computed rupture temperature is about 720°C to compare to an experimental value around 700°C. On the Fig. 11 a comparison between computed and experimental cladding axial profile is also illustrated for the STUDSVIK 192 test [30].

The modelling of possible fuel fragmentation for very high burn up fuel is still in progress. Nevertheless, the accuracy of the fission gas description should allow the discrimination between different fuels or rods taken into account their base irradiation history.
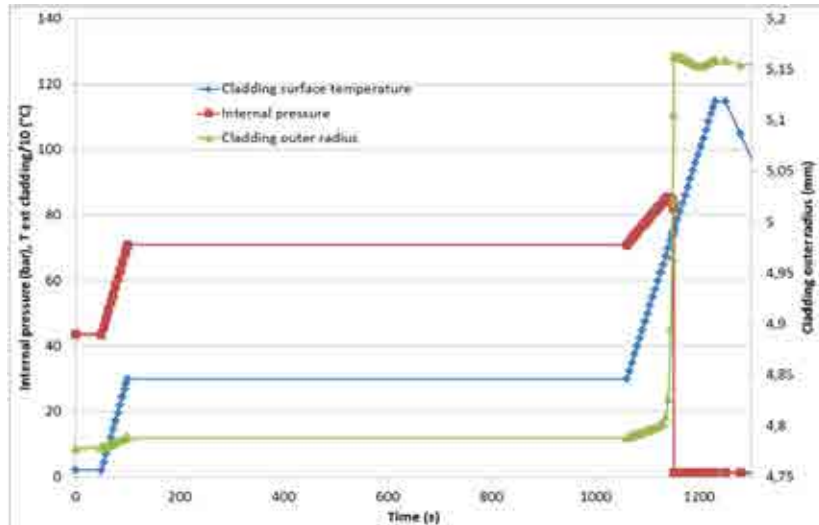
FIG. 10. Simulation of the Studsvik test 192 with ALCYONE.
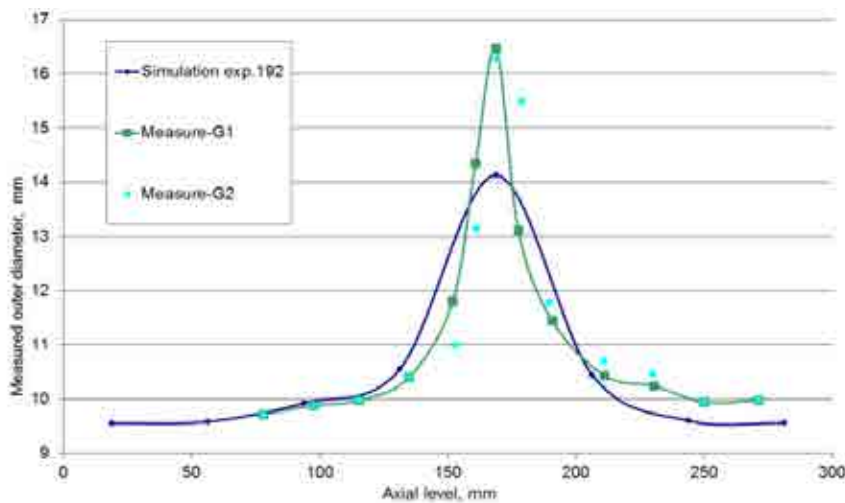
FIG. 11. Axial profile of cladding diameter after Studsvik test 192 (calculated and measure).

7. CONCLUSIONS

The PLEIADES fuel performance software environment has been developed for ten years. CEA's fuel physical models and performance codes have been fully implemented in the PLEIADES platform application. The PLEIADES platform applications are the reference for fuel R&D at CEA and in the framework of EDF-CEA-AREVA partnership.

PCI modelling can be validated and improved thanks to the multi-dimensional PWR PLEIADES application ALCYONE. The latter provides a multi-dimensional computation scheme which gives a detail analysis of fuel element behaviour and enables validation though the comparison with post irradiation examination (cladding residual diameter and ridges, dishing filling, pellet cracking,…). Stress and strain concentration involves in SCC can be computed with the 3D finite element solver

175

(CAST3M) of the PLEIADES platform. For local approach of SCC cladding failure a new mesh refinement method (multi-grid technique) is under development and a new component for fission products chemical recombination assessment will be implemented in the PLEIADES platform [31].

The multi-dimensional computation scheme of ALCYONE has been extended to accidental irradiation conditions representative of a fast transient or a LOCA transient. Thanks to these developments a set of 1D and 3D models is now available to simulate fuel rod behaviour from pellet cladding interaction up to cladding ballooning. Some developments are in still progress to improve this first version. First results devoted to the validation of the 3D model for the CABRI REP Na experiments or more recently to the interpretation of a LOCA experiment show that the PLEIADES platform can offer advanced simulation tools to improve the analyse of the local behaviour under accidental irradiation condition.

<div align="center">

REFERENCES

</div>

[1]   PLANCQ, D. et al., A unified environment for multi-dimensional fuel performance modelling, Proc. of the International Meeting on LWR Fuel Performance, Orlando, USA (2004).

[2]   STRUZIK, C., MARELLE, V., Validation of fuel performance CEA code ALCYONE, scheme 1D, on extensive data base., Transactions TopFuel2012 conference, Manchester (UK), Sept. 2012.

[3]   STRUZIK, C., MOYNE, M., PIRON, J.P. High burn up modelling of UO2 and MOX fuel with METEOR/TRANSURANUS version 1.5, in: Proceedings of ANS Conference, Portland, Oregon, 1997, pp. 126–132.

[4]   I. M. PALMER, K. W. HESKETH, and P. A. JACKSON, A Model for Predicting the Radial Power Profile in a Fuel Pin, Proc. Specialists' Mtg. Water Reactor Fuel Element Performance Computer Modelling, Preston, United Kingdom, International Atomic Energy Agency ~1992

[5]   LEMOINE, F., BERNARD, D., FEDERICI, E., Validation assessment of neutron calculations for radial and azimuthal distributions of actinides and fission products in PWR rods, 2011 Water Reactor Fuel Performance Meeting, China, (2011).

[6]   MONNERIE, Y., GATT, J.M., Overall viscoplastic behaviour of non-irradiated porous nuclear ceramics, Mechannics of Materials 38 (2006), 608–619.

[7]   MICHEL, B. et al., 3D fuel cracking modelling in pellet cladding mechanical interaction, Engineering Fracture Mechanics 75 (2008) 3581–3598.

[8]   MICHEL, B. et al., A new phenomenological criterion for Pellet Cladding Interaction rupture, Nucl. Eng. Des. 238 (2008) 1612–1628.

[9]   SONIAK, A. et al., Irradiation creep behaviour of Zr-base alloys, Zirconium in the Nuclear Industry: 13th International Symposium, ASTM TP 1423, G.D. Moan and P. Rudling, Eds., ASTM International, West Conshohocken, PA, 2002, 837–862.

[10]   ROBERTS, G., The concentration of stress in cladding produced by the expansion of cracked fuel pellets, Nuclear Engineering and Design, 47, 257–266 (1978).

[11]   BROCHARD, J. et al., Modelling of Pellet Cladding Interaction in PWR fuel, Transactions of SMIRT 16, Washington DC (2001).

[12]   SMITH, E., The fuel-cladding interfacial friction coefficient in water-cooled reactor fuel rods, Transactions, SMIRT 5, 1979.

[13]   WOOD, J.C., SURETTE, B.A., AITCHISON, I., Pellet cladding interaction − Evaluation of lubrification by graphite, Journal of Nuclear Materials, 88, 81–94 (1980).

[14] BOULORE, A., Étude et modélisation de la densification en pile des oxydes nucléaires UO2 et MOX, thèse de l'ENSMSE et de l'INPG, 2001.

[15] GARCIA, P., STRUZIK, C., AGARD, M., The effect of Fission Gas Swelling on Cladding Strains During Power Ramp Tests, Proceedings IAEA Conf. on Fuel Chemistry and Pellet Cladding Interaction Related to High Burn-up Fuel, Sweden, IAEA TECDOC 1179, 1998.

[16] NOIROT L., MARGARET, An advanced mechanistic model of fission gas behaviour in nuclear fuel, in: Proceedings of the 2005 Water Reactor Fuel Performance Meeting, Kyoto, Japan, 2–6 October 2005, Paper 1067.

[17] NOIROT L., MARGARET: A comprehensive code for the description of fission gas behavior, Nuclear Engineering and Design 241 (2011) 2099–2118.

[18] FUKETA, T., SASAJIMA, H., SUGIYAMA, T., Behaviour of high burnup PWR fuels with low-tin zircaloy 4 cladding under RIA conditions, Nuclear Technology 133 (2001) 50–62.

[19] GOLDBRONN, P., SERCOMBE, J., MICHEL, B., Avancées de la simulation du comportement du combustible nucléaire en 3D et en transitoire rapide. 21ème Congrès Français de Mécanique, Bordeaux (2013).

[20] SERCOMBE, J. et al., 1D and 3D modeling of PCMI during a RIA with ALCYONE V1.1, Proceedings of 2010 LWR Fuel Performance/TopFuel/WRFPM, Orlando, Florida, USA, September 26–29, 2010.

[21] MOAL, A., Advanced models for the simulation of post-DNB phenomena during RIA with SCANAIR, Proc. International conference TopFuel 2010, Orlando, Sept. 2010.

[22] BESSIRON, V., Modelling of Clad to coolant heat transfer for RIA applications, J. Nucl. Science and Technology, 44 (2006) 211–221.

[23] LE SAUX, M., Comportement et rupture de gaines en zircaloy4 détendu vierges, hudrurées ou irradiées en situation accidentelle de type RIA, PhD thesis CEA-R-6248 (2008).

[24] FORGERON, T. et al., Experiment and Modeling of Advanced Fuel Rod Cladding Behaviour Under LOCA Conditions: Alpha-Beta Phase Transformation Kinetics and EDGAR Methodology, Zirconium in the Nuclear Industry, 12. Int. Symposium, ASTM STP 1354, American Society for Testing and Materials, pp. 256–278, West Conshohocken, PA, 2000

[25] BRACHET, J.C. et al., Influence of the hydrogen content on the α/β phase transformation temperatures and on the thermal mechanical behaviour of Zy 4, M4, and M5 Alloys during the first phase of LOCA transient, Zirconium in the Nuclear Industry, 13th. Int. Symposium, ASTM STP 1423, American Society for Testing and Materials, pp. 673–701, West Conshohocken, PA, 2002

[26] MICHEL, B., PCMI assessment using 3D modelling, Transaction of the 18th Int. Conference SMIRT, Beijing, 2005.

[27] SERCOMBE, J., et al., 1D and 3D analyses of the Zy2 SCIP BWR ramp tests with the fuel codes METEOR and ALCYONE", Nuclear Engineering and Technology, Vol. 41, No. 2, March 2009.

[28] SERCOMBE, J. et al., Multi-dimensional modelling of PCMI during base irradiation and ramp testing with ALCYONE V1.1, Proceedings Top Fuel 2009, Paris, September 2009.

[29] GARCIA, P., STRUZIK, C., AGARD, M. and LOUCHE, V., Mono-dimensional mechanical modelling of fuel rods under normal and off-normal operating conditions, Nuclear Engineering and Design, Volume 216, Issues 1–3, July 2002, Pages 183–201.

[30] FLANAGAN, M., NUREG 2119: Mechanical Behaviour of Ballooned and Ruptured Cladding, February 2012.

[31] BARBIE, L. et al., AMR Methods in solids mechanics for pellet-cladding interaction modelling, ECCOMAS Conference, ADMOS 2011, Paris.

THE OECD/CSNI/WGFS BENCHMARK ON REACTIVITY INITIATED ACCIDENT FUEL CODES

M. Petit[1], O. Marchand[1], Y. Udagawa[2], and R. Rehacek[3]

[1]-IRSN/PSN/SEMIA Cadarache BP 3 13115 Saint-lez-Durance Cedex France
Email: marc.petit@irsn.fr, tel.-+33 4 4219 9646
[2]-JAEA/NSRC Tokai-mura Ibaraki-ken 319-1195 Japan
[3]-OECD/NEA Paris 12 boulevard des Iles 92130 Issy-les-Moulineaux France

Abstract. Reactivity-initiated accident (RIA) fuel rod codes have been developed for a significant period of time and they all have shown their ability to reproduce some experimental results with a certain degree of adequacy. However, they sometimes rely on different specific modeling assumptions the influence of which on the final results of the calculations is difficult to evaluate.

In order to contribute to the assessment of these codes, the Working Group on Fuel Safety (WGFS) of the OECD/NEA organized a benchmark. This exercise was based on a consistent set of four experiments on very similar highly irradiated fuel rods tested under different experimental conditions in the NSRR and CABRI test reactors.

The participation to the benchmark has been very important: 17 organizations representing 14 countries provided solutions for some or all the cases that were defined. In terms of computer codes used, the spectrum was also large as solutions were provided with FALCON, FEMAXI, FRAPTRAN, RANNS, RAPTA, SCANAIR, TESPAROD and TRANSURANUS.

This paper describes the main conclusions drawn from this benchmark.

1. INTRODUCTION

Reactivity-initiated accident (RIA) fuel rod codes have been developed for a significant period of time and they all have shown their ability to reproduce some experimental results with a certain degree of adequacy. However, they sometimes rely on different specific modeling assumptions the influence of which on the final results of the calculations is difficult to evaluate.

An Organisation for Economic Co-operation and Development (OECD)/Nuclear Energy Agency (NEA)/Committee on the Safety of Nuclear Installations (CSNI) technical workshop on "Nuclear Fuel Behavior during Reactivity Initiated Accidents" was held in September 2009 [1]. A conclusion from the session devoted to RIA safety criteria was that RIA fuel rod codes are now heavily used, within the industry as well as the technical safety organizations (TSOs), in the process of setting up and assessing revised safety criteria for the RIA design basis accident.

It is then very important to master the use of such codes for reactor accident studies, particularly those involving safety analyses. It is essential to identify and understand real accident conditions that deviate from those of experiments.

As a conclusion of the workshop, it was recommended that a benchmark between these codes be organized in order to give a sound basis for their comparison and assessment.

The benchmark started mid-2010 and was conducted over a period of three years. To begin with, a detailed and complete benchmark specification was prepared in order to assure as much as possible the comparability of the calculation results submitted. Then during the course of the exercise, three technical seminars were organized to compare and discuss the results obtained among the participants.

This paper summarizes the final results of the benchmark [2].

2. EXPERIMENTS AND CASES STUDIED

The cases to be computed are four experiments that were or will be conducted on nearly identical rods. These rods, fabricated by ENUSA, are standard PWR 17x17 UO_2 rods cladded with ZIRLO^{TM} that were irradiated in the Vandellos-2 reactor up to a maximum local burn-up close to 75 GWd/t.

The four experiments are CIP0-1, CIP3-1, VA-1 and VA-3:

- The CIP0-1 experiment was performed in the CABRI sodium loop facility [3], at 280°C and low pressure (~3 bars); the maximum injected energy at peak power node was equal to 99 cal/g and the pulse width at half maximum was 32.4 ms; there was no failure of the fuel rod during this experiment;

- The CIP3-1 experiment will be performed in the CABRI water loop facility, at 280°C and 155 bars; this will be a blind calculation; the anticipated maximum injected energy at peak power node is 115 cal/g and the pulse width at half maximum is expected to be about 8.8 ms;

- The VA-1 experiment was conducted in the NSRR reactor [4] [5], at room temperature and pressure; the maximum injected energy at peak power node was 140 cal/g (evaluated from specification data by integration of injected power between 0 and 0.5 s) and the pulse width at half maximum was 4.4 ms; the fuel rod failed during this experiment at injected energy of 66 cal/g (evaluated from specification data by integration of injected power between 0 and the rupture time);

- The VA-3 experiment was performed in the NSRR reactor [4], [5], at ~280°C and 70 bars; the maximum injected energy at peak power node was 115 cal/g (evaluated from specification data by integration of injected power between 0 and 0.5 s) and the pulse width at half maximum was 4.4 ms; the fuel rod failed during this experiment at injected energy of 86 cal/g (evaluated from specification data by integration of injected power between 0 and the rupture time).

Neither the CABRI facility in France, for experiments performed in the sodium loop, nor the Nuclear Safety Research Reactor (NSRR) in Japan provide test conditions identical to a commercial light water reactor during the hypothetical reactivity-initiated accident. It is generally believed that among the most significant differences is the cladding temperature effect. That is, do the coolant conditions, pulse width and other experimental parameters in the test reactor prevent the cladding from heating up and deforming as might be expected in a commercial light water reactor. Thus, the four experiments were selected as an ultimate benchmark exercise – to resolve the cladding temperature effect.

One of the main difficulties in the calculation of cladding temperature is the possible onset of boiling in experiments performed with water as the coolant. In order to ease the comparison between the codes and the determination of areas of agreement/disagreement of the models, it was proposed that an additional, hypothetical case with boiling inhibited be computed for experiments with water.

It was also proposed to run a calculation in which the cladding outer temperature is prescribed. The temperature trace to be used is issued from a SCANAIR calculation in which boiling is predicted. Thus, the cases to be computed are summarized in the following Table 1.

TABLE 1. CASES TO BE COMPUTED

Case #	Rod	Specific conditions
1	CIP0-1	Test in sodium, no boiling
2	CIP3-1	Hypothetical - Test in water, but boiling must be inhibited in the models
3	CIP3-1	Hypothetical – Test in water, but prescribe the clad outer temperature and use a flat axial power profile in CABRI
4	CIP3-1	Test in water, boiling possible
5	VA-1	Hypothetical - Test in water, but boiling must be inhibited in the models
6	VA-1	Test in water, boiling possible
7	VA-3	Hypothetical - Test in water, but boiling must be inhibited in the models
8	VA-3	Test in water, boiling possible

3. PARTICIPANTS AND CODES

The participation to the benchmark has been very important because 17 organizations provided solutions for some or all the cases that were defined. The participants originated from 14 countries. They are TRACTEBEL from Belgium, NRI from the Czech Republic, VTT from Finland, IRSN from France, HZDR, TÜV and GRS from Germany, MTA EK from Hungary, UNIPI from Italy, JAEA and JNES from Japan, KINS from Korea, VNIINM from Russia, CIEMAT and CSN from Spain, SSM represented by Quantum Technologies from Sweden, PSI from Switzerland, NRC and PNNL from the United States.

As it can be seen, research institutions, utilities, technical support organizations as well as safety authorities are all represented within the participants.

In terms of computer codes used, the spectrum was also large as solutions were provided with FALCON [5], FEMAXI [6] coupled to TRACE, FRAPTRAN [7] standalone or coupled to TRACE or TRABCO, RANNS [8], RAPTA, SCANAIR [9], TESPAROD and TRANSURANUS [10] standalone or coupled to RELAP5.

It is to be noted that all these codes are 1.5 D codes, with the notable exception of FALCON, which uses a 2D representation.

The following Table 2 presents the codes used by the different institutions. Also mentioned in this Table 2 are the steady state irradiation codes that were used to generate the initial state of the transient calculations.

TABLE 2. STEADY STATE IRRADIATION CODES

Contributor	Code	
	Steady State	Transient
SSM	Frapcon3.3	Scanair3.2
	Frapcon3.3	Scanair7.1
VTT	Enigma	Scanair6.6
IRSN	Frapcon3.4a	Scanair7.2
CIEMAT	Frapcon3.4a	Scanair7.1
	Frapcon3.4a	Fraptran1.4
NRC	Frapcon3.4a	Fraptran1.4
KINS	Frapcon3.4	Fraptran1.4/Trace
TRACTEBEL	Frapcon3.4a	Fraptran1.4
MTA EK	Furom	Fraptran1.3/Trabco
UNIPI	Transuranus	Transuranus/Relap
HZDR	Transuranus	Transuranus
TUV	Transuranus	Transuranus
JAEA	Femaxi	Ranns
JNES	Femaxi	Femaxi/Trace
PSI	Falcon-PSI	Falcon-PSI
GRS	Frapcon3.3	Tesparod
BOCHVAR	Rapta5.2	Rapta5.2
NRI	Transuranus	Fraptran1.4
	Transuranus	Transuranus

4. MAIN RESULTS OF THE BENCHMARK

This chapter provides a general discussion of the results obtained during the benchmark to identify the main conclusions that can be drawn. The following aspects are discussed: the use of input data, the thermal behavior, the mechanical behavior, the fission gas release, the failure prediction and the global effect of temperature.

4.1 Use of input data

The first lessons learned from the benchmark are on input data and the way they are used in the different codes.

There are two groups of input data that are necessary for performing a RIA calculation.

The first one is related to the initial state of the fuel before the transient. It is usually estimated with the use of a fuel performance code. In general, the influence of the initial state of the fuel on the behavior during RIA is difficult to assess. This would require a specific exercise (for example to use the results of different irradiation codes as input to a single transient code) that was out of the scope of this benchmark.
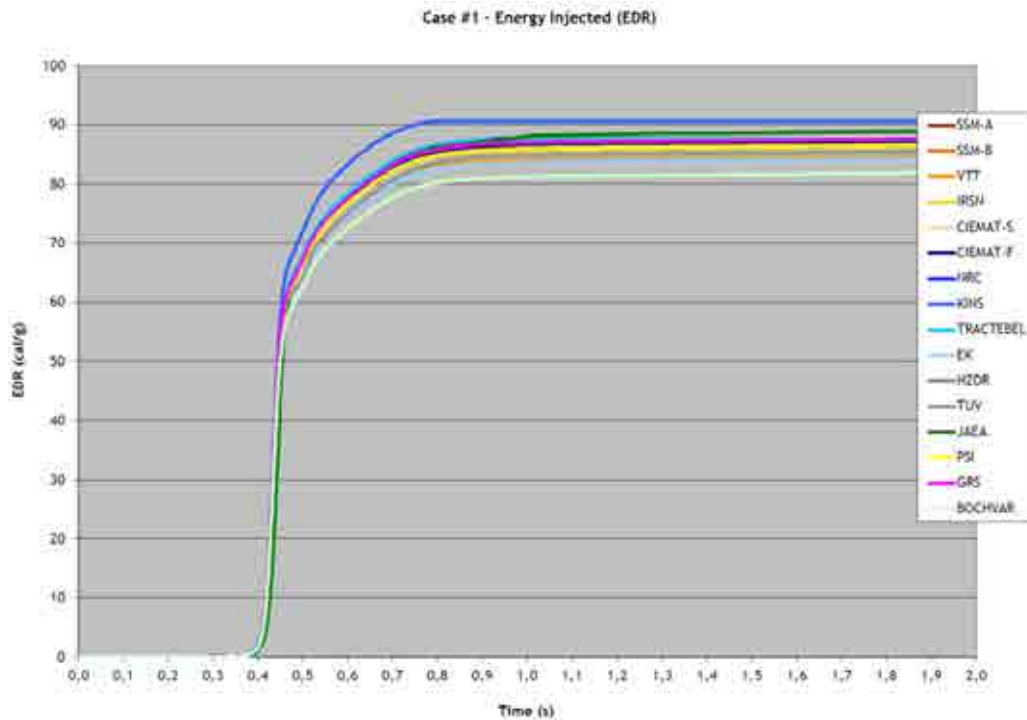

FIG. 1. Energy injected versus time for Case #1.

The second input data used for the transient calculation is the power pulse definition. It defines the energy injected in the fuel rod. Although the power pulses were precisely defined, it unexpectedly appeared that the different codes interpret them differently. This is shown for example in Fig. 1 that presents the injected energy as a function of time for case #1.

In this case, it appears that there is a difference of about 10% between the minimum and the maximum values in the different codes. In the case of short pulses, it was found that apart from the scatter also the shape of curve may be different.

It is recommended that the code developers carefully examine the way the input data are used because this source of difference, that appeared to be significant, should be completely removed.

4.2 Thermal behavior

The thermal behavior was evaluated by examining different parameters, mainly the enthalpy variation, the fuel centerline temperature, the fuel maximum temperature and the cladding temperature.

The comparison of the enthalpy variation as a function of time for case #6 is shown in Fig 2.
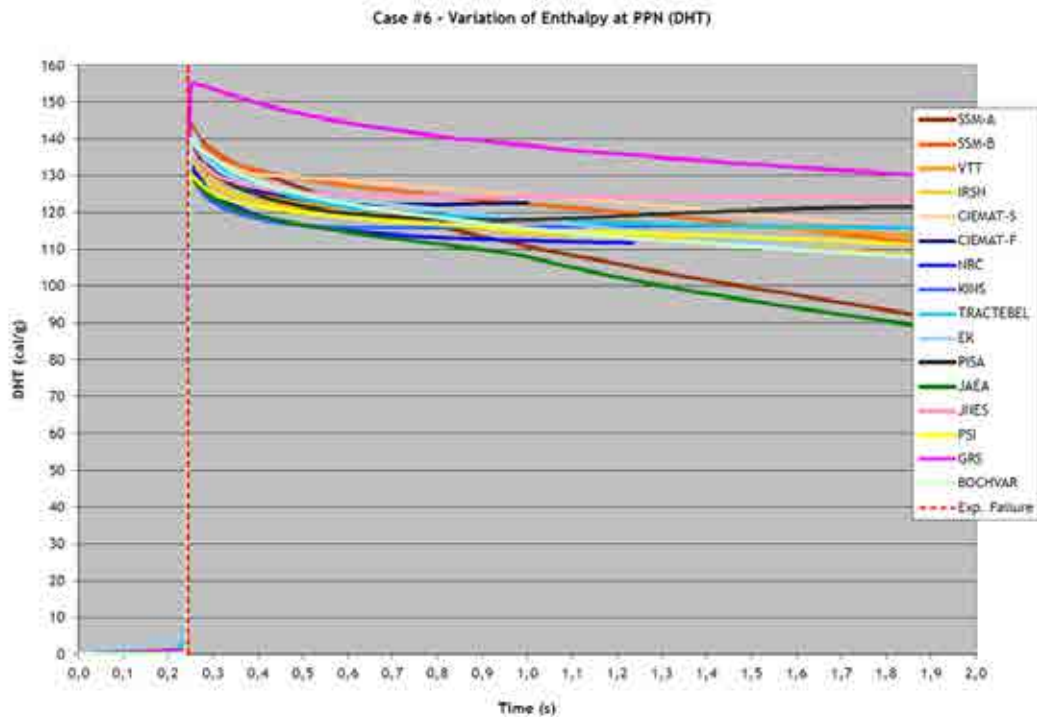
183

FIG. 2. Variation of Enthalpy at PPN versus time for Case #6.

In terms of maximum values, it appears that the differences mostly result from the differences in the input data (power pulse, see above) rather than from differences in the modeling. On the longer term, the slopes of the curves may differ, as a result of the different models of heat exchanges. In case #6, this is amplified by the fact that boiling is reached, resulting in specific models with additional uncertainties to be activated. When boiling was deactivated, as in case #5, the differences are of course less pronounced.

A comparison in terms of fuel centerline temperature is shown in Fig. 3. Again, the comparison appears quite satisfactory and the differences are essentially due to the differences in the use of the input data.

With regard to the cladding temperature predictions, it is interesting to distinguish the cases where coolant boiling occurs or not. In the latter case, it was found when analyzing case #5 that most of the solutions provided showed the same trend. However, even in this case, there is a large scatter in the values computed, with a maximum temperature ranging from about 350°C to about 900°C.

Results from the same case but allowing boiling of the coolant (as in the reality of the experiment) are shown in Fig. 4. This figure clearly shows considerable differences in the predicted cladding temperatures.

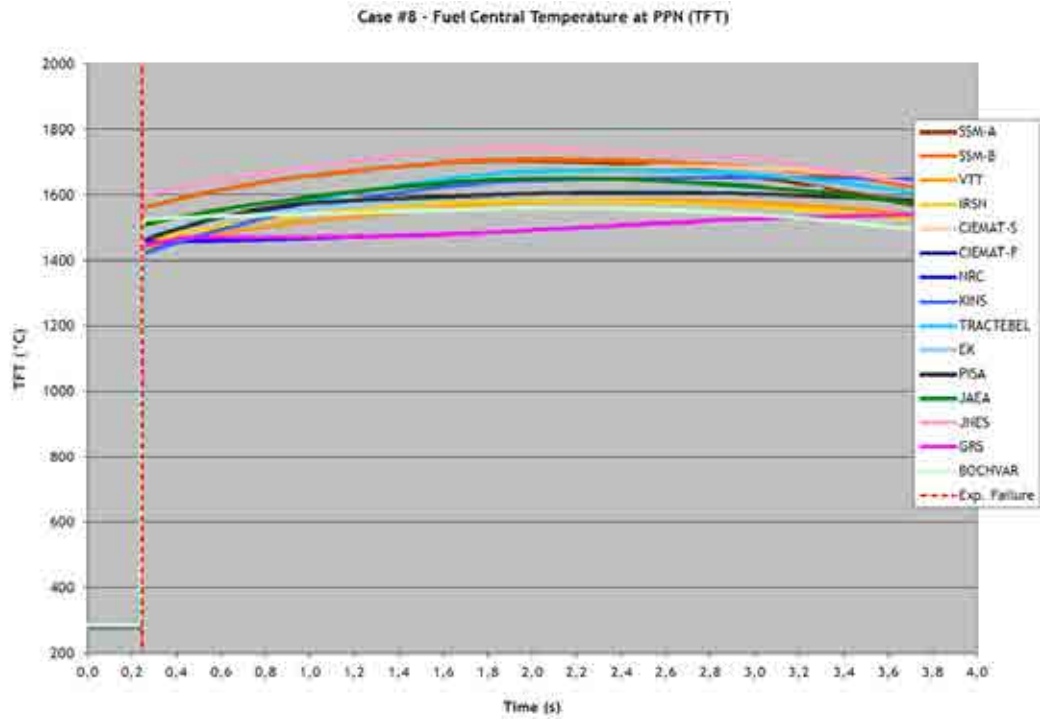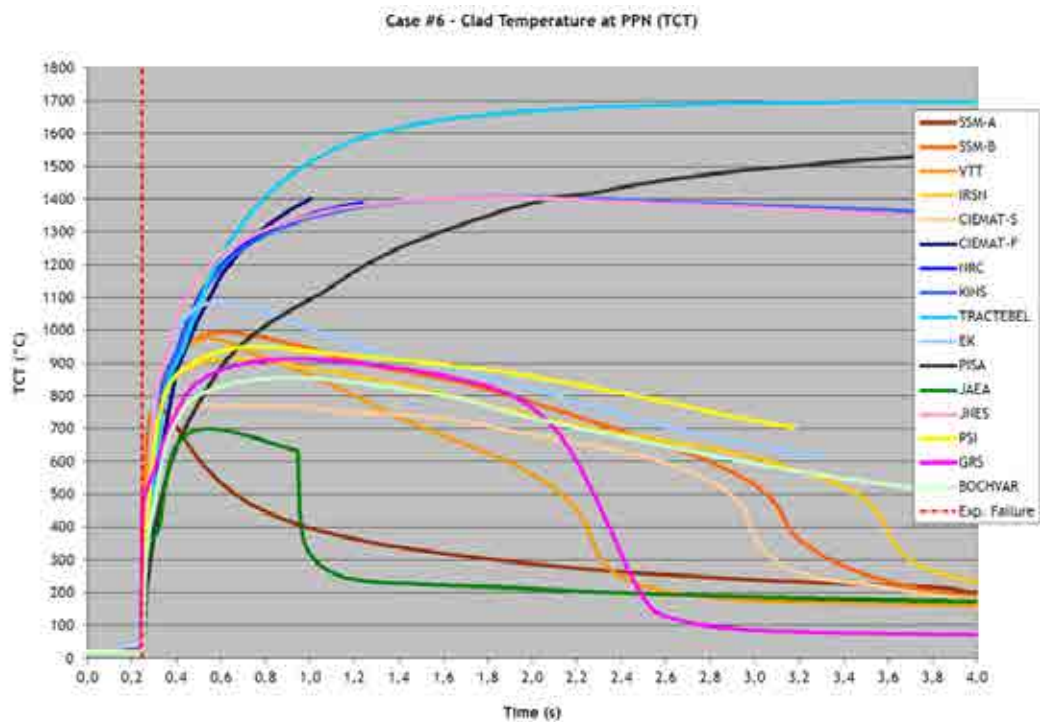*FIG. 3. Fuel Central Temperature at PPN versus time for Case #8.*

FIG. 4. Clad Temperature at PPN versus time for Case #6.

In Fig. 4, one can see that there are in fact two groups of predictions. In the first group, temperatures remain below 1100°C, they decrease relatively rapidly after 0.6s and most of them show rewetting; however, rewetting is predicted at different points in time. In the second group,

temperatures above 1100°C are predicted and they show no or only little decrease during the time period studied. As it was shown in [27] and [28], the second group is typical of codes that assume that the steady state correlations are applicable to transient. Indeed, boiling under fast transient conditions is nowadays known to be significantly different than under steady state conditions. The major effect shown here is that of the heat exchange in film boiling.

In general, models for boiling under fast transient conditions lack validation and the comparison shown above justifies that the subject of clad to coolant heat transfer during RIA deserve more attention in the future, in particular in terms of modeling.

4.3 Mechanical behavior

With respect to the assessment of the mechanical behavior, case #1 had a special interest because there were experimental results to compare to. More specifically, Fig. 5 shows the comparison between calculated and measured permanent hoop strain after the test as a function of height in the rodlet. Given the scatter in the experimental results that is due to the fact that oxide spalling occurred during the test, all the calculations appear to compare well to the measurements, with one being at the very lower bound.
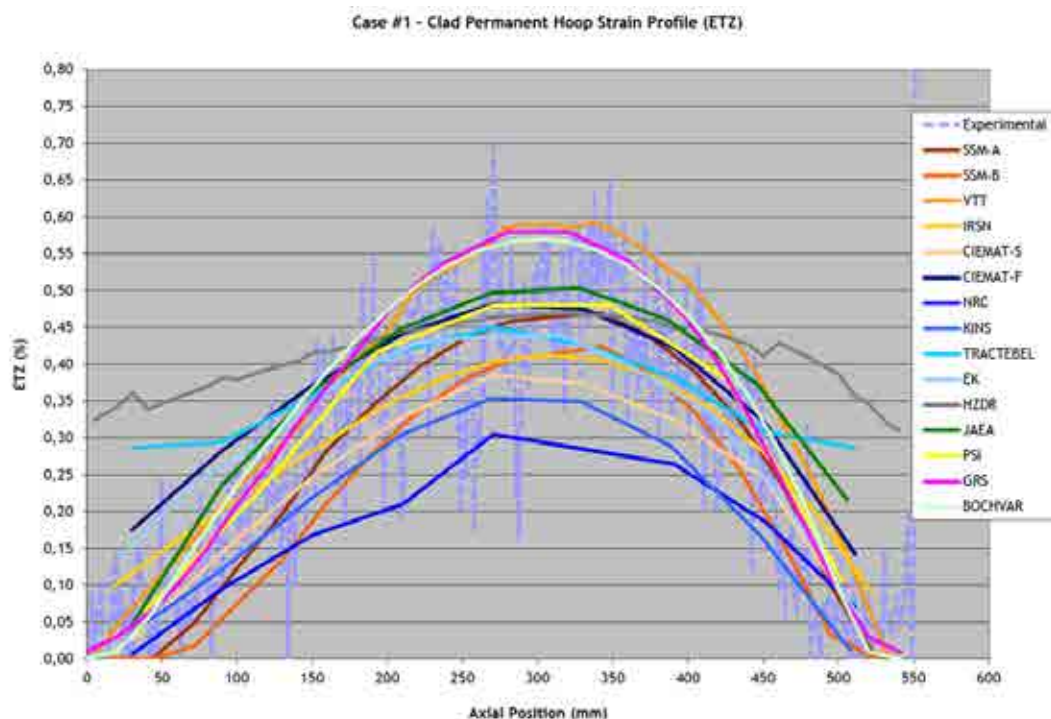
FIG. 5. Clad Permanent Hoop Strain Profile for Case #1.

The same plot is shown for case #4 in Fig. 6. As there is no experimental result in this case (the experiment not yet being performed), this case can be considered as a blind calculation. The scatter is here very large because apart from one calculation that predicts virtually no deformation, the maximum value varies in the proportion from 1 to 10. This is interpreted to be mostly due to the differences in the calculated cladding temperatures as shown in Fig 4. This would have a considerable impact on failure predictions for models that rely on a limit strain or on a limit strain energy density. For models based on a fracture mechanics approach, the influence is difficult to

predict because a higher temperature means a higher toughness which reduces the failure risk but at a same time a higher strain which on the contrary increases the failure risk.

The other parameters characterizing the mechanical behavior examined during the benchmark are the fuel stack elongation and the cladding elongation.

Results for the fuel stack elongation were generally found be relatively close to each other. The cladding axial elongation results appear more scattered as it can be seen in Fig. 7. The cladding elongation is a more difficult parameter to compute because it depends on a number of other values: the clad temperature, the gap closure instant, the assumptions for describing the contact between fuel and cladding (sliding, friction, sticking). In Fig. 7 calculated values are compared to measurements. Although calculations generally give the good order of magnitude, it is obvious that the computed values should be used cautiously and should be associated with a proper uncertainty.
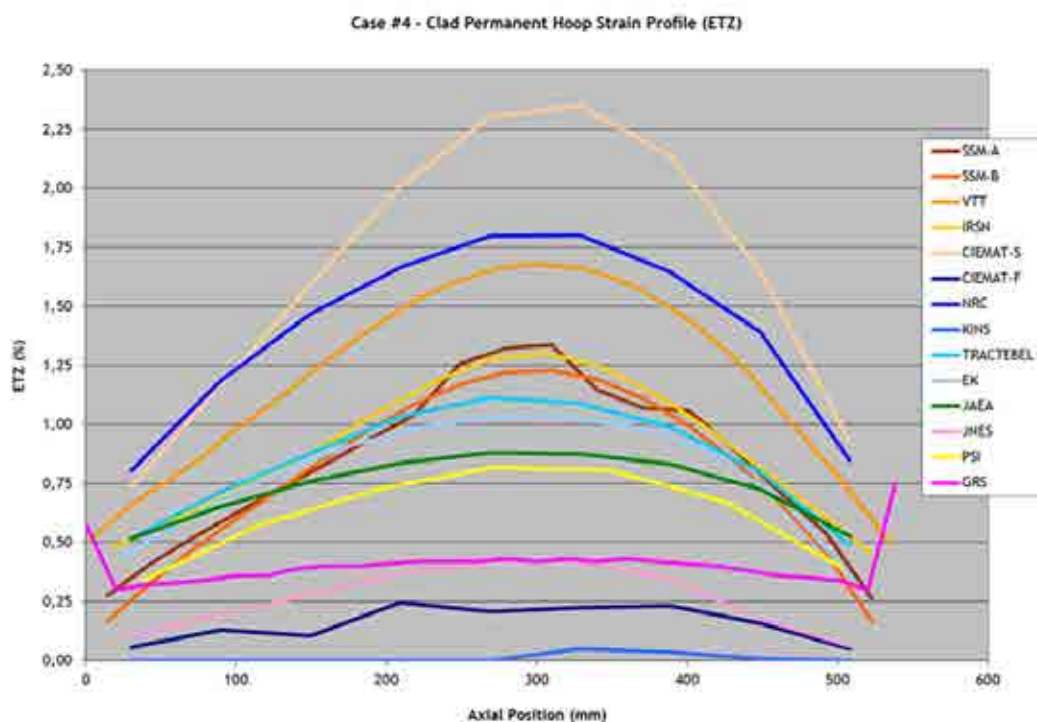
FIG. 6. Clad Permanent Hoop Strain Profile for Case #4.
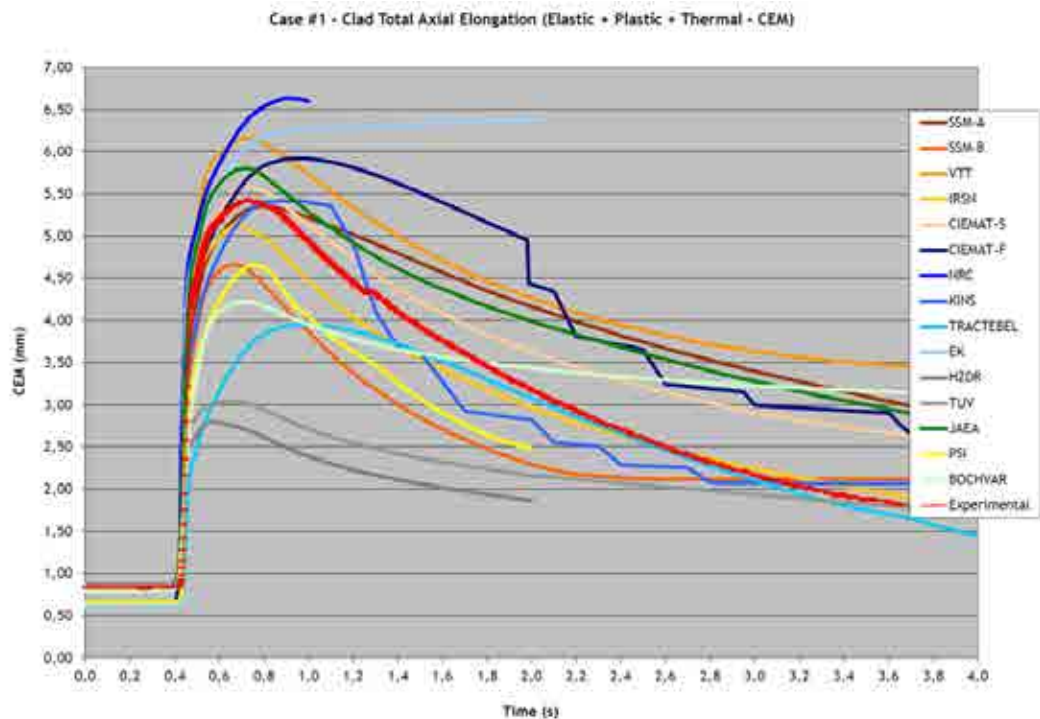
FIG. 7. Clad Total Axial Elongation versus time for Case #1.

4.4 Fission gas release

Typical fission gas release results are illustrated in Fig. 8. This graph shows that schematically there are two groups of results: the lower values are given by RANNS, RAPTA, SCANAIR and TRANSURANUS and higher values are given by FRAPTRAN and TESPAROD. FALCON appears to give intermediate results. With respect to the complexity of phenomena that govern the fission gas release during transients and to the relatively limited number of experimental data, the scatter in the results appears however not to be very high.

188

FIG. 8. Fission Gas Volume Release for Case #3.

4.5 Failure prediction

The failure (or non-failure) prediction may appear as the ultimate goal of fuel code dedicated to the behavior under RIA conditions. For this purpose, three parameters where defined in the benchmark to be able to compare the predictions of the different codes. Those values are:

C, a multiplier to be applied to the power pulse in order to reach failure (when it equals 1 then failure is predicted with the given pulse);

TAF, the time at failure (in ms);
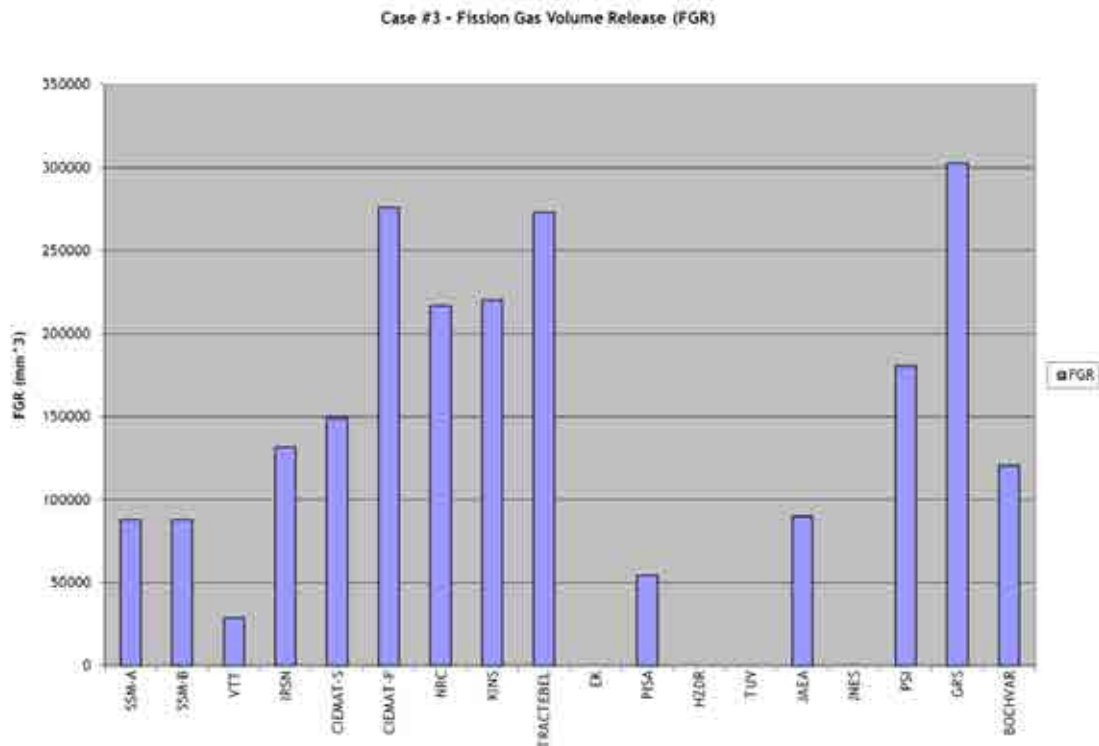
DHF, the enthalpy variation at failure (in cal/g).

During the benchmark, it was found that for the non-rupture case, all solutions provided also predicted non failure. In this case, the scatter was limited, with the C coefficient estimated to be between 1.1 and 1.5 and the enthalpy variation at failure between about 82 and 128 cal/g.

Also for the cases with failure, all the predictions are consistent with the experimental result, i.e. failure happens with the given conditions. There was also a very good agreement for the predicted time of failure between the codes and with the experimental value. However, the predicted enthalpy variation at failure was more scattered in this case, for example ranging from about 47 to 121 cal/g for case #6. This shows that for experiments with narrow pulses, the time of failure is not a good indication of the precision of the calculation and should not be used when looking at code validation.

To explain the range of the predicted enthalpy variation at failure, one should keep in mind that some of the most important parameters in PCMI failures during RIA simulating experiment are the

concentration and morphology of hydrides in the cladding. Even for rods that appear to have similar irradiation conditions, post-irradiation examinations show some variation in the cladding hydrogen content. Also, in case of a PCMI failure, the instant of pellet-cladding gap closure is important because it determines the time at which cladding stresses start to increase. In this benchmark it was determined that the difference in terms of gap closure between the codes was typically about 30 cal/g. Finally, it should be kept in mind that due to the fact that the considered experiments are very fast transients, the uncertainty on the experimental determination of the failure enthalpy is relatively important. In the present case, it was estimated to be in the order of +/- 10 cal/g.
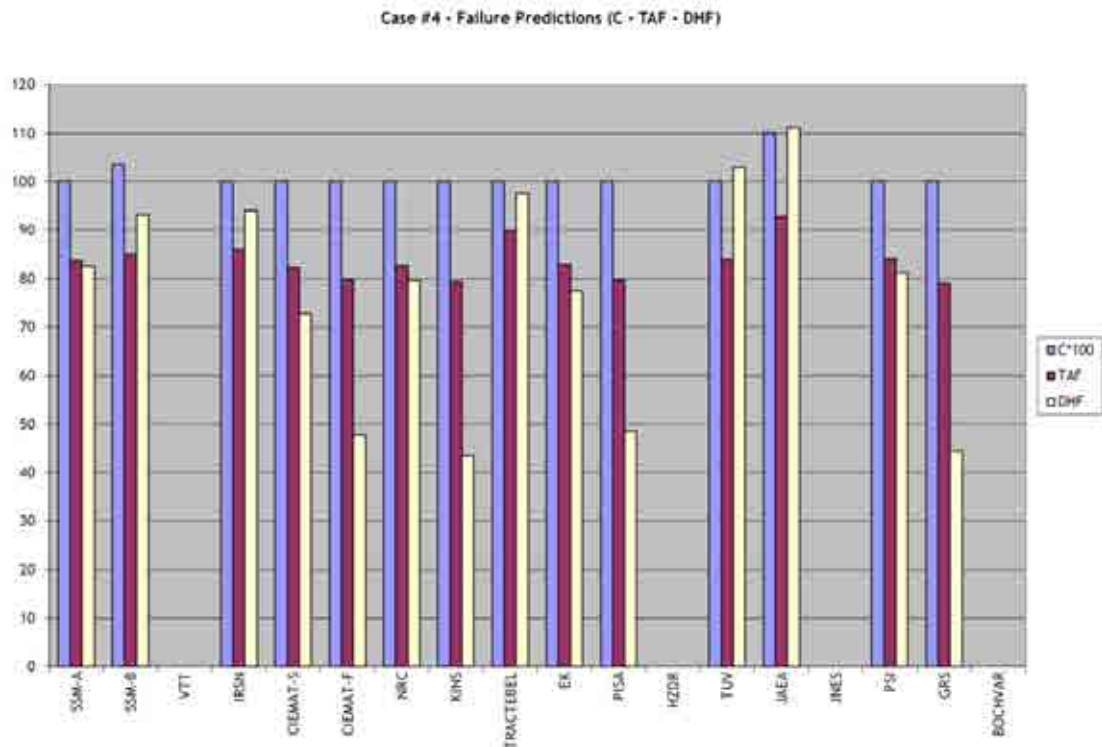
FIG. 9. Failure Predictions for Case #4.

Final case is the one for which the results is not known because the corresponding experiment is not yet performed. Results presented in Fig. 9 show that in this case some predict failure with the given conditions and some not. However, the C values reported are between 1 and 1.1, showing that if failure is not achieved, it should be very close to. Again predictions of time of failure do not vary very much. The enthalpy variation at failure predictions exhibit a scatter consistent with that of the previous case, between 42 and 111 cal/g.

4.6 Temperature effect

An objective of the benchmark was to assess the possibility of evaluating the "temperature effect". The question to be assessed is the ability of the RIA fuel codes to transpose results, in particular enthalpy at failure, from experiments performed at low temperature to experiments at high temperature or even to typical reactor conditions.

Given the scatter on predicted failure levels discussed above, it appears interesting to "normalize" the code predictions and to look at the way the codes predict failure in case #8 relative to the prediction of case #6. This is the purpose of Fig. 10. In this figure, one can see that whereas in

the experiment the enthalpy variation increases by 30%, the codes predict variations between -13 and +50%.

The main reason of the differences here is the failure criterion used and its input parameters. Indeed, different approaches are used to evaluate failure: a limit strain approach, elastic plastic fracture mechanics, a limit strain energy density. It is obvious that all those approaches do not capture the effect of temperature the same way. Moreover, even using the same code and the same approach, it appears that different users have different predictions because the failure criterion is used with different parameters.
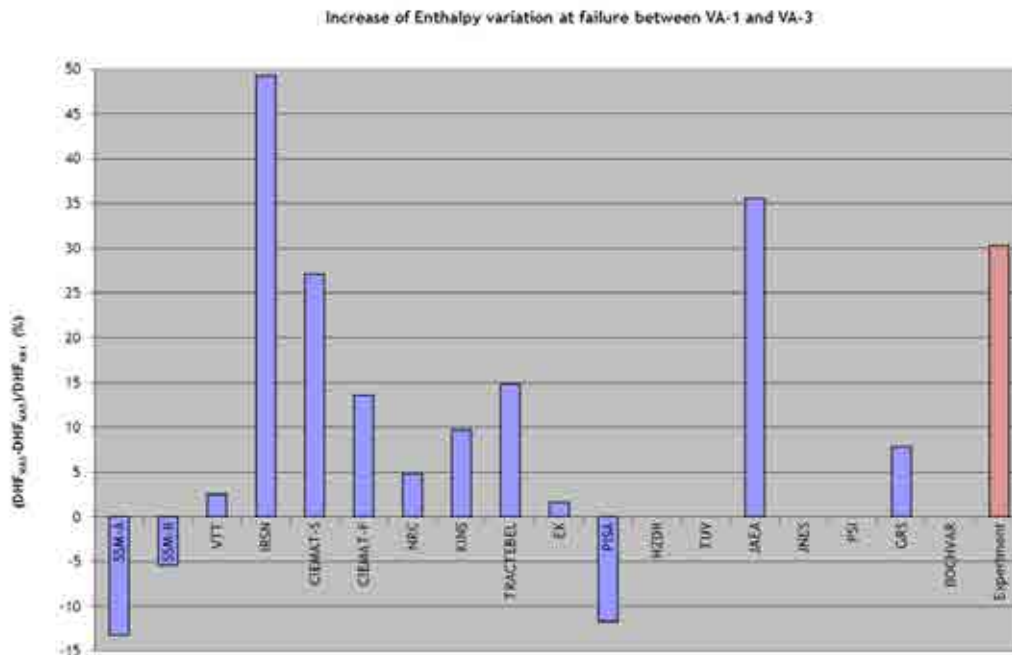

FIG. 10. Relative change of the enthalpy variation at failure between VA-1 and VA-3.

5. CONCLUSIONS

The first noticeable fact is that, nearly all the participants used code that rely on simplified geometrical representation usually referred to as 1.5D codes. Although some 3D calculations may be done (one example was shown by one participant), it appears that given the conclusions below, the detailed geometrical description is not a priority. Rather, it looks more important at this stage to put the efforts and continue working on physical modeling.

During the benchmark, one source of differences between the results of the participants was identified to be due to the way input data, in particular the power pulse, are interpreted within the different codes. It is recommended that the code developers carefully examine the way the input data are used because this source of difference, that appeared to be significant, should be completely removed.

It was not possible during this benchmark to assess the influence of the initial state (resulting from base irradiation) of the fuel on the behavior during RIA. Indeed it was not in the initial objectives of the action. Nevertheless, this would be an important thing to do in order to evaluate how much it accounts for on the scatter of the results. It appears not practical for any participant to be able to use the results of different irradiation codes as input to a single transient code and thus make

this assessment rigorously. An approximate way to do it would be to perform sensitivity analysis to input parameters and this is recommended for a possible follow-up action.

With respect to the thermal behavior, the general conclusion is that the differences in the evaluation of fuel temperatures remain limited, although significant in some cases. The situation is very different for the cladding temperatures that exhibited considerable scatter, in particular for the cases when water boiling occurs. This is easily understood because the thermal inertia of the cladding is very low compared to that of the fuel. Thus, even limited differences in the heat transfer conditions have a large impact on the cladding temperatures whereas they are hardly noticeable on the fuel temperatures. In particular, the film boiling heat transfer model was responsible for large differences between the calculations.

With respect to mechanical behavior, the parameter of largest interest is the cladding hoop strain because failure during RIA transient is resulting from the formation of longitudinal cracks. When compared to the (known) results of an experiment that involved only PCMI, the predictions from the different participants appeared acceptable even though there was a factor of 2 between the highest and the lowest calculations. In fact, due to the scatter in the experimental results, it is not possible to conclude that one of the calculations or one of the codes is much better than the others.

The conclusion is not as favorable for a case for which both the experimental results are unknown and water boiling is predicted to appear. In this case, a factor of 10 on the hoop strain between the calculations was exhibited. This is of course due for a large part to the differences on the cladding temperatures discussed above.

In this benchmark, the fission gas release evaluations were also compared. The ratio of the maximum to the minimum values appears to be roughly 2, which is estimated to be relatively moderate given the complexity of fission gas release processes.

Finally, failure predictions that may appear as the ultimate goal of fuel code dedicated to the behavior under RIA conditions were compared. As a conclusion, it appears that the failure/no failure predictions are fairly consistent between the different codes and with experimental results. However, when assessing the code validation, one should rather look at predictions in terms of enthalpy at failure because it is a parameter that may vary significantly between different predictions (and that is also of interest in practical reactor applications). In the frame of this benchmark the failure prediction levels among the different codes were within a +/- 50% range. Although major causes of the differences were identified, it is recommended to perform more systematic sensitivity and uncertainty analyses in a new phase of the benchmark to further assess the significance of the results produced.

A broader objective of the benchmark was to assess the possibility of evaluating the "temperature effect" that can be stated as: is it realistic to use the RIA fuel codes to transpose results, in particular enthalpy at failure, from experiments performed at low temperature to typical reactor conditions? Based on the conclusions formulated above, it appears obvious that it should be done with caution given the scatter that exists between the predictions of the different codes mainly due to the different approaches used to assess the rod failure level. In other words, if one makes such a transposition with two different codes, one may end up with two results that differ significantly.

DOSTÁL (NRI, Czech Republic), K. GEELHOOD (PNNL, United States), V. GEORGENTHUM (IRSN, France), A. GORZEL (ENSI, Switzerland), L. HOLT (HZDR, Germany), L.O. JERNKVIST (Quantum Technologies, Sweden), G. KHVOSTOV (PSI, Switzerland), J. KLOUZAL (NRI, Czech Republic), D. MÄRTENS (TÜV NORD, Germany), F. NAGASE (JAEA, Japan), T. NAKAJIMA (JNES, Japan), O. NECHAEVA (VNIINM, Russian Federation), I. PANKA (MTA EK, Hungary), J.M. REY GAYO (CSN, Spain), I.C. SAGRADO GARCIA (CIEMAT, Spain), A.D. SHIN (KINS, Republic of Korea), H.G. SONNENBURG (GRS, Germany), G. SPYKMAN (TÜV NORD, Germany), T. SUGIYAMA (JAEA, Japan).

REFERENCES

[1]   NUCLEAR ENERGY AGENCY/ COMMITTEE ON THE SAFETY OF NUCLEAR INSTALLATIONS, Proceedings of the workshop on Nuclear Fuel Behaviour during Reactivity Initiated Accidents, NEA/CSNI/R(2010)7.

[2]   NUCLEAR ENERGY AGENCY/ COMMITTEE ON THE SAFETY OF NUCLEAR INSTALLATIONS, RIA Fuel Codes Benchmark, NEA/CSNI/R(2013)7.

[3]   PETIT, M., GEORGENTHUM, V., SUGIYAMA, T., QUECEDO, M., DESQUINES, J., A Comparative Analysis of CABRI CIP0-1 and NSRR VA-2 Reactivity Initiated Accident tests – EUROSAFE 2007, Berlin (2007).

[4]   SUZUKI, T., UMEDA, M., Development of High Temperature Capsule for RIA-Simulating Experiment with High Burnup Fuel - IGORR 2007, Lyon (2007).

[5]   SUGIYAMA, T., UDAGAWA, Y., SUZUKI, M., NAGASE, F., Influence of Coolant Temperature and Power Pulse width on Fuel Failure Limit under Reactivity-Initiated Accident Conditions - Water Reactor Fuel Performance Meeting 2011, Chengdu (2011).

[6]   ELECTRIC POWER RESEARCH INSTITUTE, Fuel Analysis and licensing Code: FALCON MOD01: Volume 1: Theoretical and Numerical Bases, EPRI, Palo Alto, CA: 2004. 1011307.

[7]   SUZUKI, M., SAITOU, H., UDAGAWA, Y., Light water reactor fuel analysis code FEMAXI-7; model and structure [in Japanese], JAEA-Data/Code 2010-035 (2010).

[8]   CUNNINGHAM, M.E., BEYER, C.E., MEDVEDEV, P.G., BERNA, G.A., FRAPTRAN: A Computer Code for the Transient Analysis of Oxide Fuel Rods - NUREG/CR-6739, PNNL-13576, Pacific Northwest National Laboratory, Richland, WA.

[9]   SUZUKI, M., SAITOU, H., FUKETA, T., Analysis on pellet-clad mechanical interaction process of high burnup PWR fuel rods by RANNS code in reactivity-initiated accident conditions, Nuclear Technology, Vol. 155, pp. 282-292(2006).

[10]   MOAL, A., Advanced Models for the Simulation of Post-DNB Phenomena during Reactivity Initiated Accidents with SCANAIR, LWR Fuel Performance/TopFuel/WRFPM, Orlando (2010).

[11]   LASSMANN, K.,TRANSURANUS: a fuel rod analysis code ready for use, Journal of Nuclear Materials, Vol. 188 pp. 295-302 (1992).

[12]   BESSIRON, V., SUGIYAMA, T. and FUKETA, T. - Clad-to-Coolant Heat Transfer in NSRR Experiments, Journal of Nuclear Science and technology, Vol. 44, pp. 723-732 (2007).

[13]   BESSIRON, V., Modelling of Clad-to-Coolant Heat Transfer for RIA Applications, Journal of Nuclear Science and technology, Vol. 44, pp. 211-221 (2007).

FINITE ELEMENT MODELLING USED TO CLARIFY SEPARATE EFFECTS

K. KULACSY. D. ANTÓK, T. FEKETE, L. TATÁR
Hungarian Academy of Sciences Centre for Energy Research
Budapest, Hungary
E-mail: katalin.kulacsy@energia.mta.hu

Abstract. 1D and 1.5D fuel behaviour codes include either mechanistic or empirical models for the physical phenomena occurring in the fuel rods. Since it is in the nature of integral tests and of real-life situations (e.g. licensing) not to provide detailed, local pre-characterisation of the rods, some sort of statistical averaging is inherently included in the modelling of the processes. Often applied averaging leads to assumptions of e.g.

- uniformity,
- homogeneity,
- axisymmetry.

Finite element codes make it possible to account for 3D and local phenomena, e.g.

- PCMI including the effect of cracks in the pellets,
- PCI with a mixture of boded cladding areas.

Moreover, the basic assumption on the homogeneity and uniformity of the cladding can be lifted and the effect of inhomogeneities and slight variation in thickness can be studied in e.g. LOCA conditions.

MTA EK has started research to study such local phenomena in order to better understand and reproduce experimental data. The results are promising: the stress distribution in a cladding with bonded and unbonded areas differs significantly from the azimuthally symmetric case. The shape of the ballooned area of a fuel rod subjected to LOCA can only be reproduced if the above averaging assumptions are lifted, which leads to a new, second order approach.

1. BALLOONING

Ballooning experiments at KFKI AEKI (predecessor of MTA EK, [1]) were made with 50 mm long E110 cladding tube sections. The samples were oxidised to different extents and Zry-4 end plugs were welded onto them. Gas was conducted into the samples through a thin tube going through one of the end plugs in order to regulate the pressure inside the cladding. The samples were placed into a furnace, heated, and when the required constant temperature (between 650°C and 1200°C) was reached pressure was gradually increased until the samples burst. Depending on the corrosion state and the temperature of the cladding and on the pressure increase rate, various shapes could be observed (Fig. 1). Temperature and pressure values were recorded.
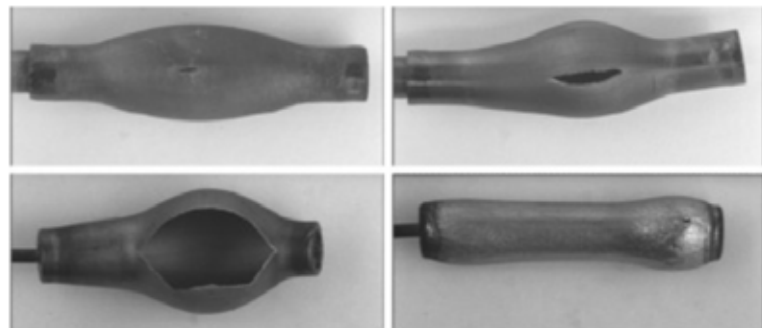
FIG. 1. Samples after burst tests [1].
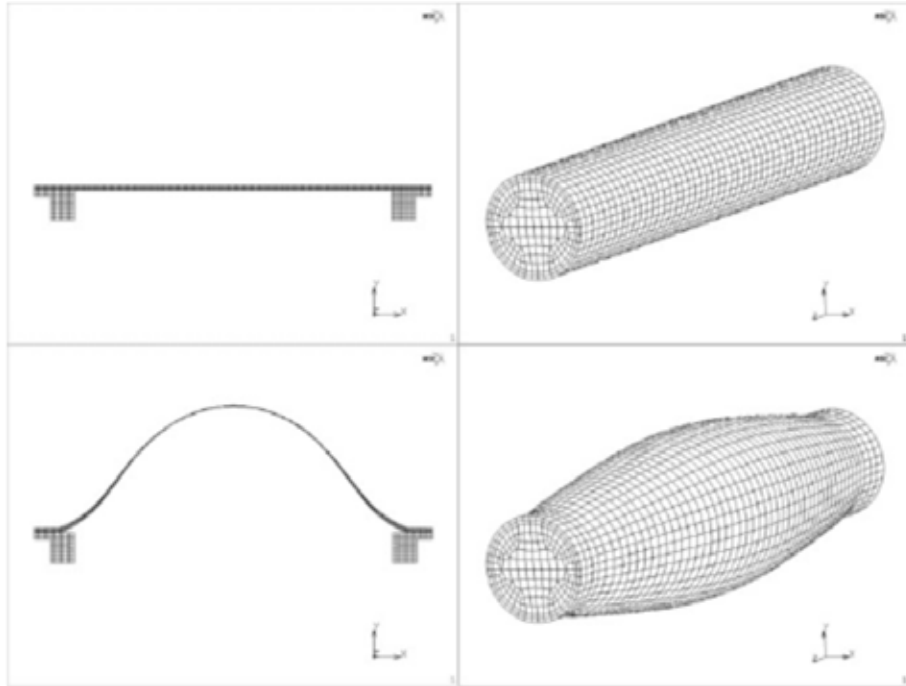
FIG. 2. 2D (left) and 3D (right) axisymmetric finite element models of a sample [2].

Axisymmetric finite element simulations [2] of the experiments necessarily yield deformations that display axial and planar symmetry (the latter with respect to the plane perpendicular to the symmetry axis and crossing the middle of the specimen), as shown in Fig. 2. However, no real sample exhibited such a shape after ballooning.

The shapes presented in Fig. 1 may be due either to material inhomogeneities or to geometric imperfections (deviations from the ideal shape or size). Simulations involving material inhomogeneities are presented in Figs 3–4.

Figure 3 presents the model of a sample where welding is supposed to have softened the material in rings parallel to the end plugs. (Light green bands have a yield stress 5%, white bands 10% lower than the bulk material.) Similar dumbbell shapes occurred in some experiments; see the bottom right picture in Fig. 1. Here axial symmetry is still maintained.
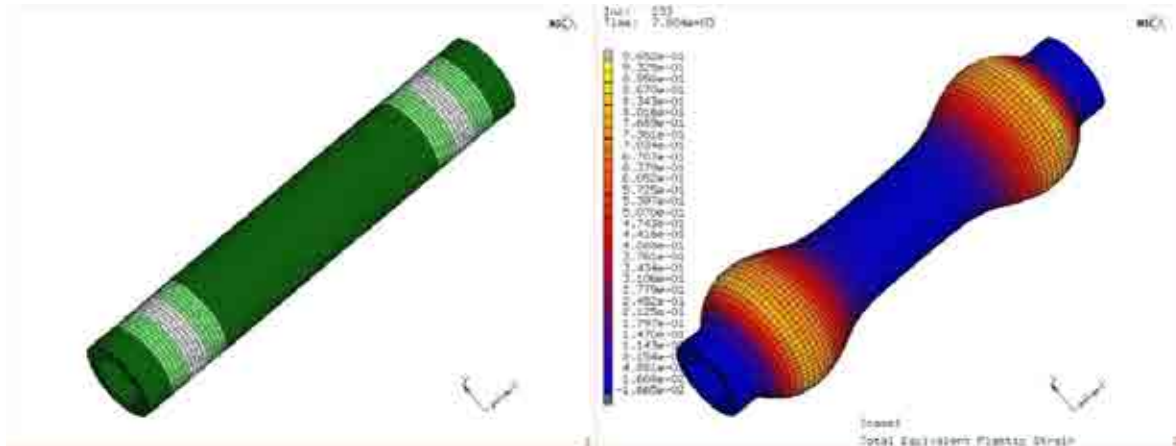
FIG. 3. Ballooning in inhomogeneous sample (softer rings, lighter colours) [2].
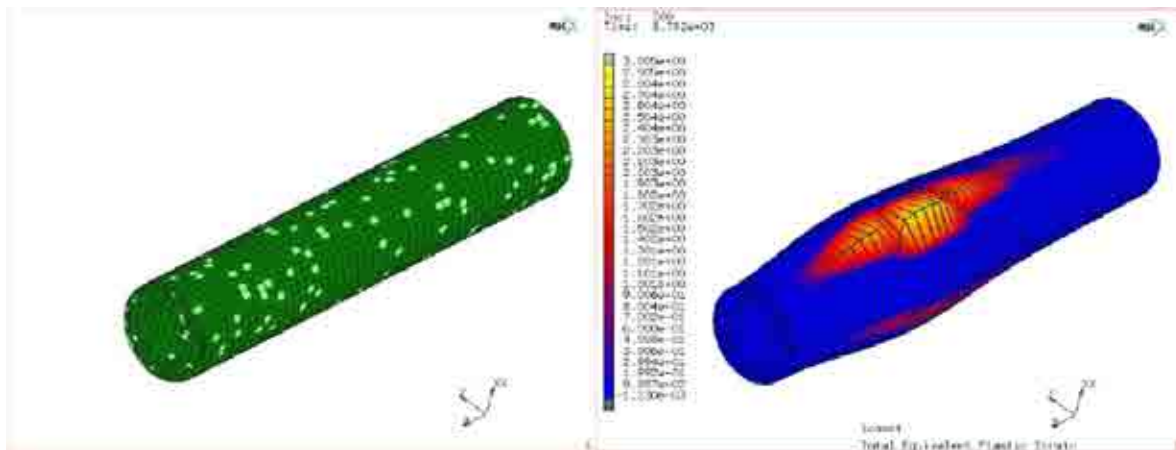
FIG. 4. Ballooning in inhomogeneous sample (random softer spots, light green) [2].

Figure 4 presents a model where 10% of the elements of the 3D model had a yield stress 3% lower than the bulk material and these softer spots (light green) were distributed randomly in the cladding. The simulation yielded a longitudinal burst, asymmetric in all respects, which closely resembles real ballooned samples.

The above LOCA simulations demonstrate that real life samples are rarely perfect either from the geometry or from the homogeneity point of view. In order to provide suitable data for the detailed simulation of the behaviour of fuel rods, material properties should be measured locally all along the samples.

Another series of simulations included a sensitivity analysis to see the effect of geometrical imperfections (cladding thickness) on simulation results. Ring compression tests made with E110 cladding were simulated ([2], not presented here). The manufacturing inner diameter of the cladding is $7.73^{+0.06}_{-0.03}$ mm, the outer is $9.1^{+0.10}_{-0.05}$, which means a 1% uncertainty in the diameter, but a 10% uncertainty in the thickness. This yields a 30% difference between the simulated force – displacement curves of the thickest and the thinnest cladding. In conclusion, the clad thickness needs

196

to be known at least with an accuracy of 10 μm, measured locally on the entire specimen to allow accurate simulation of the processes.

2. PELLET-CLADDING MECHANICAL INTERACTION

Finite element modelling is suitable for studying the effects of cracks in the pellet and friction or even bonding between pellet and cladding. As PIE's often reveal that the pellet fragments (formed during normal operation) are bonded to the cladding in some places, while they can move freely or with some friction in others, a qualitative 2D model has been built to see what this arrangement causes in terms of cladding stress.

A cracked pellet was modelled as shown in Fig. 5. Two cases were studied: the first where the pellet was bonded everywhere to the cladding and the second where the fragment below the crack moved freely, while that above the crack was bonded to the cladding. Axial symmetry was assumed with respect to the x and y axes. The pellet conserved its state during the simulation, i.e. no further crack opening was assumed. The aim of the simulation was to see the difference in the stress distribution in the cladding. However, the locations of maximum stress in the pellet revealed the weak points where further cracking was to be expected in the given geometry.

The fuel element was subjected to the ramp shown in Fig. 5.
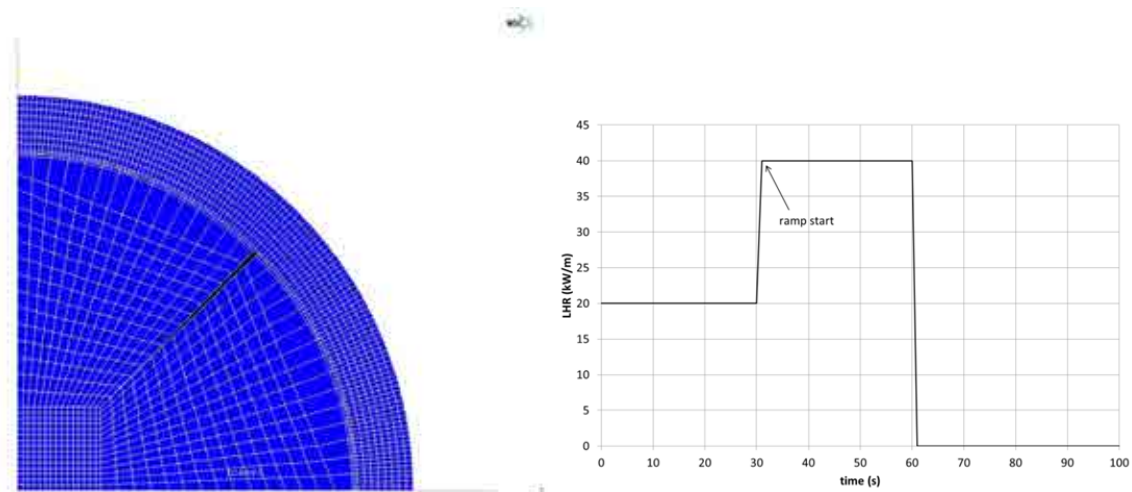
FIG. 5. Finite element model of a cracked pellet (left), sequence of ramp (right).

In the first case the stress distribution was obviously symmetrical, while in the second it showed strong asymmetry (Figs. 6–7).

When the pellet was bonded everywhere to the cladding, the cladding was subjected to tensile stress in all its cross-section and the maximum stress appeared on its inner surface in front of the crack tip. Also, the highest stress could be seen at the corner of the pellet.

When part of the pellet could move freely along the cladding, the entire inner surface of the cladding was compressed and the maximum stress appeared at some distance from the cladding inner surface, in front of the edge of the bonded pellet fragment. The stress levels in both the cladding and the pellet were lower. The entire arrangement became slightly elongated along the y axis.

3. CONCLUSIONS

The present study reveals that local characteristics (geometry, material properties, pellet-cladding bonding, etc.) have an essential influence on the outcome of experiments, usually resulting in asymmetric behaviour. This asymmetry can lead to either a more or a less favourable situation than homogeneous, symmetric, i.e. 'regular' setups.

4. FURTHER WORK

Considering the data need for simulating phenomena depending on local characteristics of the fuel rod, the present work can be continued in two ways. One is to plan measurements according to sensitivity analyses carried out on the above or similar models, which would then yield more accurate constitutive relations for the mechanical properties of the materials involved in the experiments. The other is to simulate experiments with the (usually averaged) data provided and extend the model assuming inhomogeneities, imperfections, asymmetry, etc. to find out what caused the actual exact experimental outcome. In any case the PCMI modelling has to be extended to 3D and the models have to be refined to account for more details of the fuel element.

FIG. 6. Stress distribution with completely bonded cladding (left) and cladding bonded only to the top pellet fragment (right).

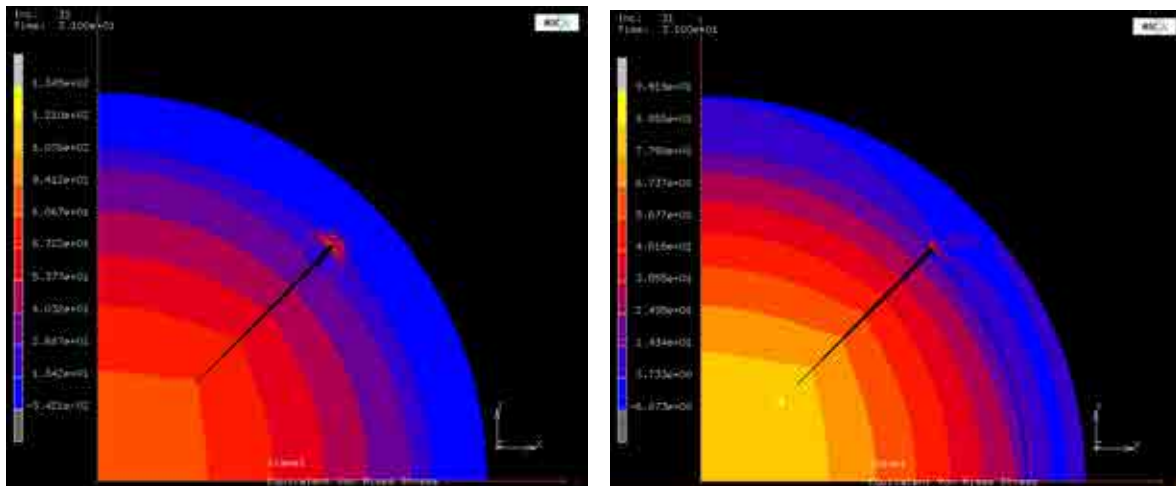*FIG. 7. Blow-up of the pellet crack tip: stress distribution with completely bonded cladding (left) and cladding bonded only to the top pellet fragment (right).*

REFERENCES

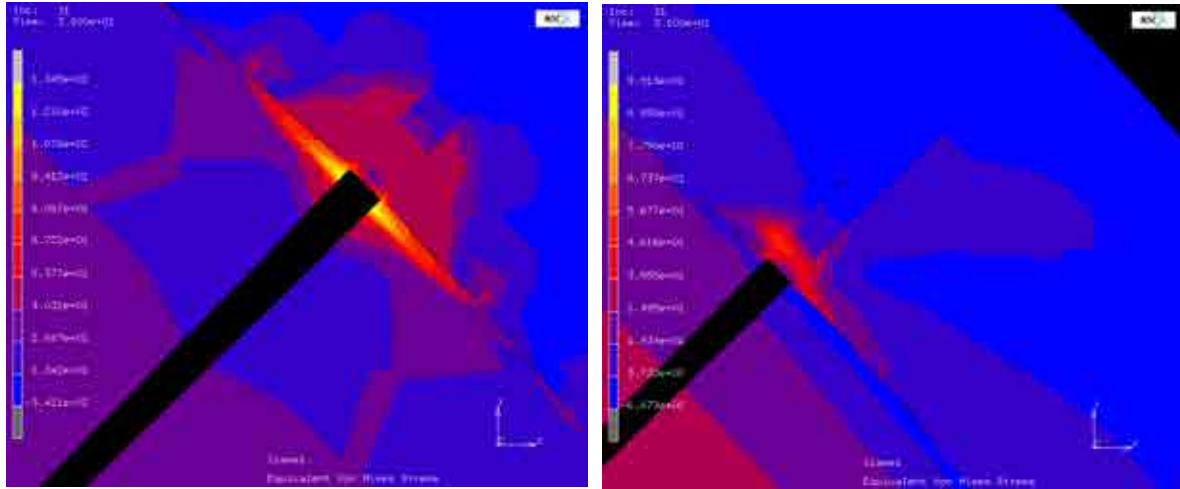[1]   PEREZ-FERÓ, E. et al., Experimental database of E110 claddings under accident conditions, IFPE Database, 2007.
[2]   ANTÓK, D. et al., Simulation of ring compression and ballooning tests performed on E110 cladding, Nukleon III (2010) 64 (in Hungarian).

EXPERIMENTAL ANALYSIS WITH RANNS CODE ON BOILING HEAT TRANSFER FROM FUEL ROD SURFACE TO COOLANT WATER UNDER REACTIVITY-INITIATED ACCIDENT CONDITIONS

Y. UDAGAWA, T. SUGIYAMA, M. SUZUKI, M. AMAYA
Fuel Safety Research Group, Nuclear Safety Research Center
Japan Atomic Energy Agency
Tokai-Mura, Ibaraki-Ken
Japan

Abstract. In order to promote a better understanding of the temperature evolution of fuel rod under reactivity-initiated accident (RIA) conditions, we have investigated the effects of coolant subcooling, flow velocity, pressure, and cladding pre-irradiation on the heat transfer from fuel rod surface to coolant water during RIA boiling transient. The study was based on a computational analysis, with the RANNS code, on the transient data from RIA-simulating experiments in the nuclear safety research reactor (NSRR); boiling heat transfer coefficients were estimated by inverse-heat-conduction calculations using the histories of measured cladding temperature and estimated heat generation in pellets, and the effects of coolant condition were analyzed by a two-phase laminar boundary layer model for stable film boiling. The experimental data used in this study cover coolant conditions with subcoolings of ~10–80 K, flow velocities of 0 to ~3 m/s, pressures of 0.1 to ~16 MPa, and fuel burnups of 0–69 GWd/tU. The analysis showed that the film boiling heat transfer coefficients during RIA boiling transient increase with coolant subcooling, flow velocity, and pressure as predicted by the model for stable film boiling. The estimated boiling heat transfer coefficients were significantly larger than those predicted by semi-empirical correlations for stable film boiling: about 1.5 times larger for stagnant water condition and 2–8 times larger for forced flow condition, respectively. The analysis also suggested that the heat transfers during both transition and film boiling phases are strongly enhanced by pre-irradiation of the cladding. The irradiation effect was clearly seen at large subcooling of ~80 K and atmospheric coolant pressure, and was rather moderate at small subcooling of ~10 K and coolant pressure of ~7 MPa. These behaviors of boiling heat transfer are incorporated into the RANNS code mainly as modified empirical correlations for boiling heat transfer coefficient.

1. INTRODUCTION

The temperature evolution of fuel cladding during a reactivity-initiated accident (RIA) involves rapid changes in the mechanical properties of the cladding tube and is believed to play the primary role in fuel behaviors such as deformation and failure. Cladding-temperature behavior accompanied by boiling of coolant water, which is the case of an RIA in light-water reactors and known as "Departure from Nucleate Boiling (DNB)", is influenced by coolant conditions such as subcooling, pressure, and flow velocity. To study the effects of the coolant conditions on the boiling heat transfer from the fuel rod surface to the coolant water has been therefore one of the main purposes of RIA research programs of Japan Atomic Energy Agency (JAEA), and so RIA-simulating experiments with fresh fuels had been conducted in the nuclear safety research reactor (NSRR) under a wide range of coolant conditions: subcoolings of ~10–80 K, flow velocities of 0–3 $\mathrm{m \cdot s^{-1}}$, and pressures of ~0.1–16 MPa [1]. Also pre-irradiated fuels had been subjected to the NSRR experiments under coolant conditions with subcoolings of ~10–80 K, stagnant water, and pressures of ~0.1–7 MPa [2–7].

Ohnishi et al. proposed an empirical model for the boiling heat transfer during an RIA on the basis of their investigation on a part of the results of the aforementioned NSRR experiments [8]. But their model was not well validated for the forced flow coolant conditions, since the corresponding data from the NSRR experiments were not fully available at that time. The present authors recently published a report providing an open access to the NSRR experiment data including the fuel specifications, test conditions, and transient records during pulse operations, since a considerable part

of the data had remained undisclosed [1]. The report also summarized characteristic values of the transient records such as cladding peak temperature, film boiling time, and surface superheat at quench, and showed that the effects of coolant conditions and pre-irradiation on the heat transfer from the fuel rod surface to the coolant water are significant in the RIA-simulating experiments. It was confirmed that, on the whole, the heat transfer is enhanced with increasing coolant subcooling, pressure, and flow velocity and with pre-irradiation of a fuel rod. Up to the present time none of existing computer codes for transient fuel behavior has not been verified with the temperature data measured under the varied conditions of coolant and fuel rods, to our knowledge.

The purpose of the present study is to promote development and validation of the DNB model for RIA transients to the extent covered by the current NSRR experiment database. Boiling heat transfer coefficients at the fuel rod surface during the experiments were estimated by inverse-heat-conduction calculations using the histories of measured cladding temperature and estimated heat generation in fuel pellets, and the effects of the coolant conditions were analyzed by two-phase laminar boundary layer models for stable film boiling [9,10]. The effect of pre-irradiation under the varied coolant conditions was discussed too. These behaviors of boiling heat transfer were tentatively incorporated into the RANNS code [11], mainly as modified empirical correlations for boiling heat transfer coefficient, and verified with the experimental data.
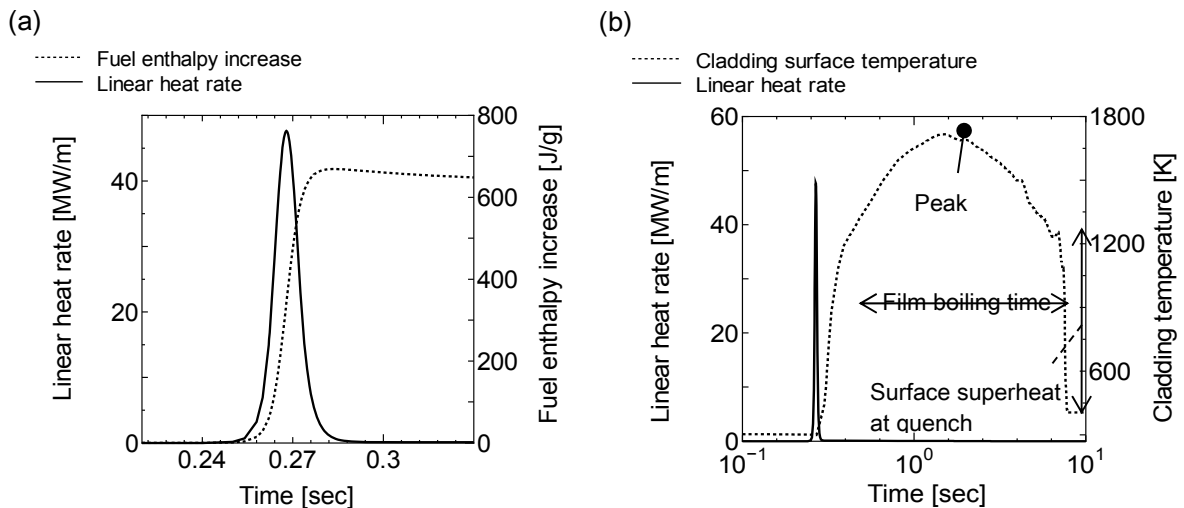
FIG. 1. Histories of (a-left) linear heat rate and enthalpy increase and (b- right) linear heat rate and cladding surface temperature of a test fuel rod fabricated with unirradiated 10%-enriched UO_2 pellets during an NSRR pulse irradiation with reactivity insertion of 2.6 dollars.

2. SUMMARY OF NSRR TEST CONDITIONS AND RESULTS

The NSRR is a modified TRIGA annular core pulse reactor which can safely produce high power and short pulses to simulate a power excursion in a RIA. This Section summarizes the NSRR test conditions and the results of temperature measurements that were analyzed in the present work. All the analyzed tests were previously reported, and the detailed descriptions of the tests are given in [1–7].

For the tests with fresh fuels, short test fuel rods were fabricated with unirradiated enriched UO_2

pellets and Zircaloy-4 cladding tubes. For the tests with pre-irradiated fuels, fuel segments cut from fuel rods irradiated in power reactors or in the "Japan Materials Testing Reactor (JMTR)" were refabricated into short test fuel rods. The test fuel rod was contained within a test capsule filled with coolant water for a stagnant coolant condition test, or placed at a test Section of water loop for a forced flow condition test. The test fuel rod was then subjected to pulse irradiation, which rapidly deposits energy in the pellets of test fuel rod. The temperature at the fuel rod surface was measured with bare-wire type R (Pt/Pt–13%Rh) intrinsic thermocouples of 0.2–0.3 mm diameter that were spot-welded to the cladding surface near the midheight of the pellet stack and at different axial positions.
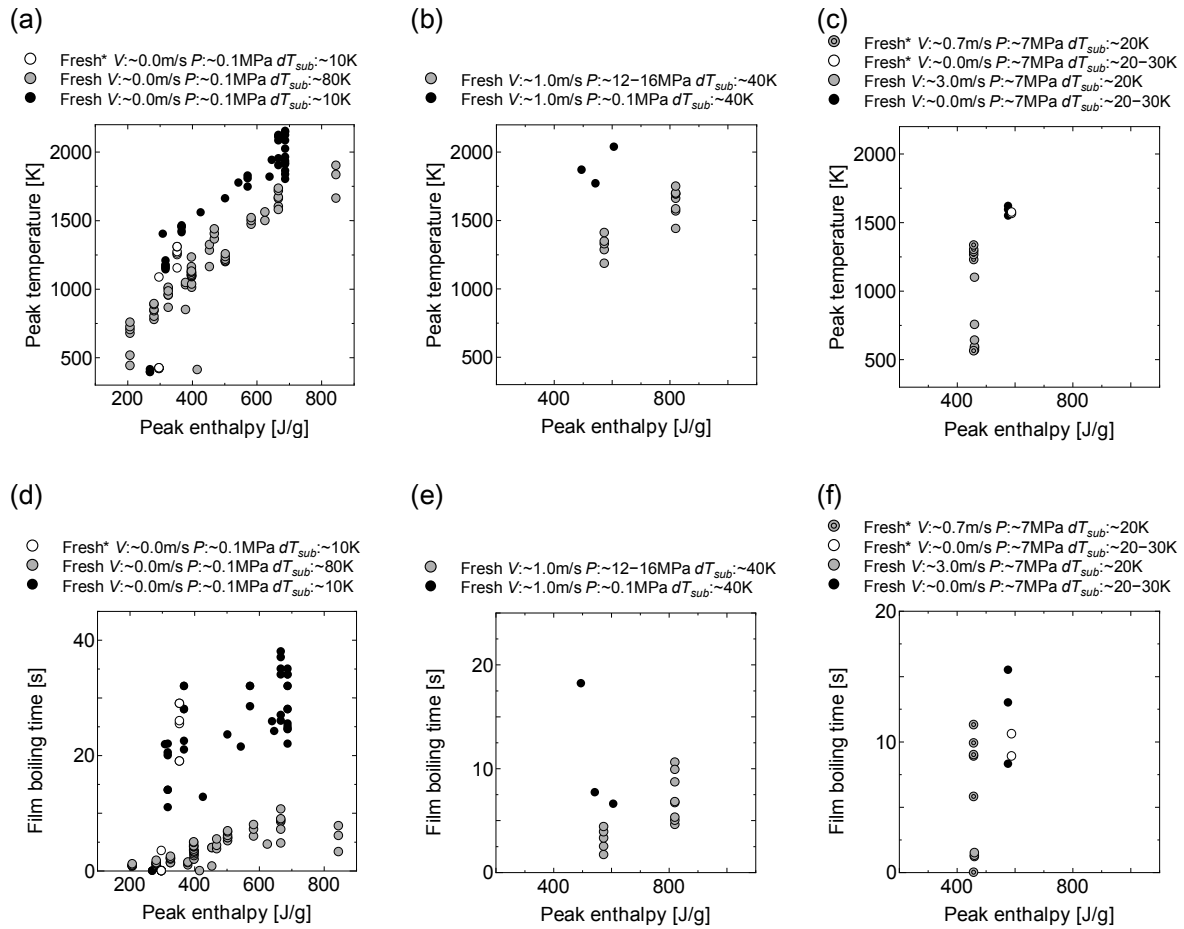
FIG. 2. Peak temperatures at fuel rod surface ((a)–(c)) and film boiling times ((d) – (f)) for test cases with fresh fuels conducted under the conditions of (a)(d) stagnant coolant, atmospheric coolant pressure, and varied coolant subcoolings, (b)(e) coolant flow velocity of ~1.0 m·s−1, coolant subcooling of ~40 K, and varied coolant pressures, and (c)(f) coolant pressure of ~7 MPa, coolant subcoolings of ~20–30 K, and varied coolant flow velocities. Legends with an asterisk like "Fresh*" denotes the result of the 2nd, 3rd, or the latter pulse irradiation in an iterative pulse-irradiation experiment in which a series of pulse-irradiations had been conducted on an identical test fuel rod.

Figure 1(a) shows typical histories of linear heat rate and enthalpy increase of a test fuel rod during an NSRR pulse irradiation test: an example case that a test fuel rod fabricated with

unirradiated 10%-enriched UO_2 pellets and Zircaloy-4 cladding tube was subjected to a pulse irradiation with reactivity insertion of 2.6 dollars. The linear heat rate is evaluated based on the NSRR power histories measured with neutron detectors and coupling factor, the ratio of the energy generated in unit mass of a test fuel to the total reactor power of the NSRR. The fuel enthalpy of the test rod quickly increases during the high power and decreases when cooling becomes dominant. The peak value of fuel-enthalpy increase is the main parameter in the NSRR experiment.

Figure 1(b) shows one of the cladding temperature histories measured in the identical case, with the linear heat rate. The designated characteristic values in the figure, peak temperature, film boiling time, and surface superheat at quench, were extracted from the temperature history and summarized in the previous report [1]. Figures 2(a)–(d) show a part of the summarized NSRR experiment results as functions of peak fuel enthalpy. In can be seen that the peak temperature and film boiling time decrease with increasing coolant subcooling ((a) and (d)), coolant pressure ((b) and (e)), and coolant flow velocity ((c) and (f)). In other words, the heat transfer from the fuel rod surface to the coolant water is enhanced with increasing coolant subcooling, coolant pressure, and coolant flow velocity. The coolant subcooling appears an effective parameter on the heat transfer regardless of the other coolant conditions, namely coolant pressure and flow velocity, while the effectiveness of the coolant pressure seems dependent on the other coolant conditions, and so does the coolant flow velocity [1]. The next Section gives a description of the method for analyzing these experiments to estimate the boiling heat transfer coefficients under the varied test conditions.

3. ALYTICAL METHOD

3.1 RANNS code

The RANNS code was used for simulating the fuel behavior during the pulse irradiation experiment, analyzing the transient record of the temperature at the fuel rod surface, and computing heat flux and heat transfer coefficient at the fuel rod surface [11]. The code analyzes thermal and mechanical behaviors of a single fuel rod under accident conditions. The basic framework and a major part of the modules are shared with the FEMAXI-7 code, the fuel behavior analysis code developed for normal operation conditions [12]. A coupled calculation of thermal analysis by solving one-dimensional heat conduction equation in the radial direction and quasi two-dimensional mechanical analysis in the radial and axial directions by finite-element method is conducted at every time step. The present analysis was conducted with solely one axial segment, since the pellet stack has an almost uniform linear power distribution in the axial direction in the NSRR tests. The pellet stack in one axial segment consists of 36 equal-volume ring elements. The cladding tube consists of eight equal-thickness ring elements and two outer oxide-layer elements.

The outer surface of the pellet stack and the inner surface of the cladding tube are thermally connected by pellet-cladding gap conductance model: modified Ross and Stoute model for fresh fuels and FEMAXI bonding model for irradiated fuels, respectively [13,12]. The model parameters R1 and R2, surface roughnesses of fuel pellets and cladding, for the modified Ross and Stoute model were set 0.2 μm in accordance with the validation study of the gap conductance model by Fujishiro [14]. These parameters give high gap conductance which is comparable to perfect thermal contact condition, for the case that fuel enthalpy is high and pellet-cladding gap is closed. Other thermal and mechanical properties adopted are the same with those adopted in the author's recent work [15].

3.2 Inverse-heat-conduction calculation

For estimating the film boiling heat transfer coefficient at the fuel rod surface from the experiment data, we performed inverse-heat-conduction calculations, by the use of the RANNS code, which took the cladding surface temperature at time t, $T_c(t)$, as the boundary condition of thermal calculation, in addition to the normal inputs such as fuel specifications and linear heat rate history during the pulse-irradiation. It should be noted that $T_c(t)$ is not the direct temperature reading of the thermocouples, attached to the cladding surface. In the case of film boiling duration in the NSRR experiment, the thermocouple reading for the cladding surface temperature shows a lower value than the actual one. This underestimation is due to the fin-cooling effect of the thermocouples: temperature drop caused by the TC wires attached to the cladding surface and known to be not negligible [16]. Hence, $T_c(t)$ was determined by $T_c(t) = T_{TC}(t) + \Delta T(t)$, where $T_{TC}(t)$ is the direct thermocouple reading and $\Delta T(t)$ is the temperature drop by the fin effect. The value of $\Delta T(t)$ was estimated in conformity with the Tsuruta's model, which had been validated against cladding temperatures determined by metallographic examination of the cladding and ZrO_2 layer thickness [16]. The estimated temperature drop $\Delta T(t)$ ranged from ~0–250 K, depending on the cladding surface temperature, coolant subcooling, coolant pressure, and the diameter of thermocouple wire. It should be again noted that the same procedure for correcting the fin effect has been applied also to all the temperature data referred to in the present study.

(a)

(b)

(c)
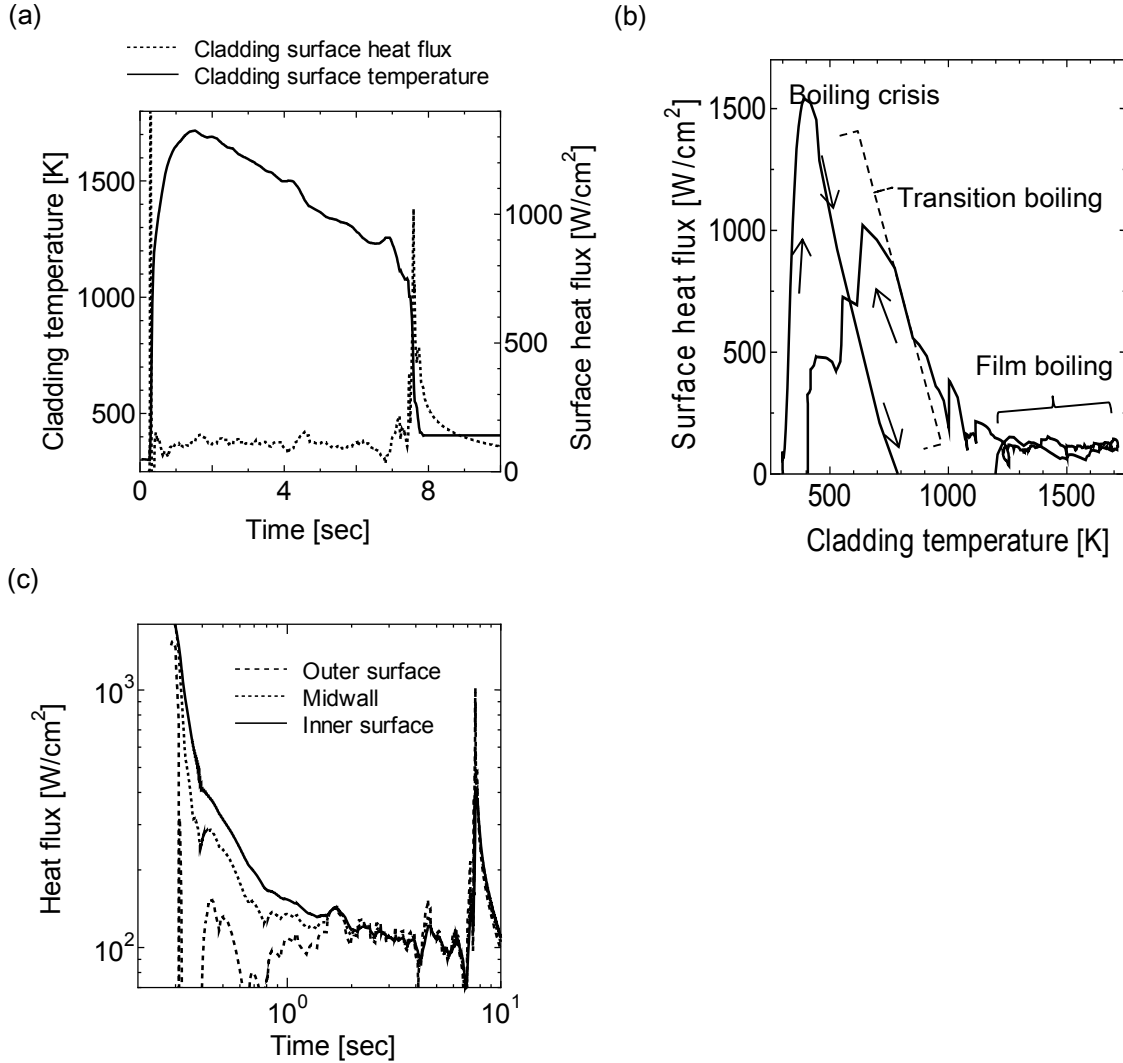
FIG. 3. *Inverse-heat-conduction calculation results for a test case with fresh fuel, stagnant coolant, atmospheric coolant pressure, and coolant subcooling of ~80 K: (a) histories of cladding temperature used as input and computed surface heat flux, (b) computed boiling curve, and (c) histories of computed heat fluxes at different radial positions in cladding thickness.*

The heat transfer coefficient at the fuel rod surface, $h_{surf}(t)$, is determined by

$$h_{surf}(t) = \frac{q(t,R_o)}{T_c(t) - T_{cool}(t)} = - \frac{k(t,R_o) \cdot \left(\frac{\partial T(t,r)}{\partial r}\right)_{r=R_o}}{T_c(t) - T_{cool}(t)} \quad (1)$$

where

$q(t,R_o)$ is the heat flux at the fuel rod surface [W·m^{-2}];

$T(t,r)$ is the cladding temperature [K];

$T_{cool}(t)$ is the coolant temperature [K];

$k(t,R_o)$ is the thermal conductivity at the fuel rod surface [W·m^{-1}·K^{-1}];

R_o is the outer radius of the cladding tube [m].

The heat transfer coefficient without radiation contribution, $h_{surf,cool}(t)$, is determined by

$$h_{surf,cool}(t) = h_{surf}(t) - h_{surf,rad}(t) \qquad (2)$$

where $h_{surf,rad}(t)$ is the radiation contribution computed in accordance with the Sakurai's correlation given in [10].

Figure 3(a) shows an example of heat-flux history at the cladding surface computed by the inverse-heat-conduction calculation, with the cladding-temperature history used as input. Two different boiling regimes, transition boiling and film boiling, can be identified in the boiling curve as shown in Fig. 3(b). The computed heat flux at a given temperature in the transition boiling regime was found to be quite sensitive to the input cladding temperature and scatter significantly even among inverse-calculation results for different thermocouples attached to an identical test fuel rod. Moreover, unrealistic minus heat flux often appeared as shown in the temperature range from 800–1200 K in Fig. 3(b), suggesting the difficulty in determining the transition boiling heat transfer coefficient directly from the computed boiling curve. Hence, the analysis focuses on estimating the film boiling heat transfer coefficients for a given test condition based on the inverse calculation results.

The following criteria were introduced to distinguish a data point of heat flux computed in the film boiling regime from that computed in the transition boiling regime, for processing numerous inverse calculation results in a consistent manner:

$$T_c(t) > T_{quench}(t) + 100 \qquad (3)$$

$$\left| \frac{q(t,R_i) - q(t,R_o)}{q(t,R_o)} \right| < \varepsilon \qquad (4)$$

$$\left| \frac{q(t,R_m) - q(t,R_o)}{q(t,R_o)} \right| < \varepsilon \qquad (5)$$

where

$T_{quench}(t)$ is the quenching temperature [K];

R_i is the inner radus of the cladding tube [m];

R_m is the midwall radius of the cladding tube [m];

ε is 3%.

The quenching temperature $T_{quench}(t)$ is determined by the following correlation, fitted to the previously reported quenching temperature data [1], as

$$T_{quench}(t) = T_{sat}(t) + dT_{quench}(t) \qquad (6)$$

$$dT_{quench}(t) = 550 \times \left(1 + \frac{0.002 \times dT_{sub}(t)}{P(t)} \right)$$
$$\cdot (1 - 0.04 \times P(t)^{1.1} V(t)^{0.2}) \cdot (0.1 \times P(t))^{0.15} \qquad (7)$$

$T_{sat}(t)$ is the saturation temperature of coolant water [K];

$dT_{quench}(t)$ is the fuel-rod-surface superheat at quench [K];

$dT_{sub}(t)$ is the coolant subcooling [K];

$P(t)$ is the coolant pressure [MPa];

$V(t)$ is the coolant flow velocity [m·s^{-1}].

    Figure 3(c) compares $q(t,R_o)$, $q(t,R_m)$, and $q(t,R_i)$ for the example case and show that computed heat flux values from t = ~1.5–7 second are similar to one another and appear to satisfy the criteria regarding $q(t,R_o)$. A data point of computed heat flux which satisfies all the criteria was extracted from the calculation output, and used for calculating the film boiling heat transfer coefficient by Eq. (1). Table 1 shows the number of the NSRR test cases for each test condition which were analyzed in the present work by the inverse-heat-conduction calculation.

TABLE 1. NUMBER OF TEST CASES THAT INVERSE-HEAT-CONDUCTION CALCULATION WAS PERFORMED

| | Test condition | | | |
| Test fuel | Coolant flow velocity | Coolant pressure | Coolant subcooling | Number of target test cases of inverse-heat-conduction calculation |
Fresh / Irradiated	m·s^{-1}	MPa	K	
Fresh	0.0	0.1	~10	6
Fresh	0.0	0.1	~80	5
Fresh	0.6	0.1	~20	1
Fresh	1.8	0.1	~20	1
Fresh	1.8	0.1	~40	1
Fresh	1.8	0.1	~80	1
Fresh	3.0	0.1	~80	1
Fresh	3.0	1	~80	1
Fresh	4.0	1	~80	1
Fresh	0.0	7	~10	4
Fresh	0.0	7	~20–30	2
Fresh	0.0	7	~50	1
Fresh	0.0	7	~80	1
Fresh	0.6	7	~10	1
Fresh	0.7	7	~20	1
Fresh	1.0	7	~10	2

(Table 1 continued)

| Test fuel | Test condition | | | Number of target test cases of inverse-heat-conduction calculation |
| | Coolant flow velocity | C oolant pressure | Coolant subcooling | |
Fresh / Irradiated	m·s^{-1}	MPa	K	calculation
Fresh	1.0	7	~60	1
Fresh	1.0	7	~100	1
Fresh	3.0	7	~10	2
Fresh	3.0	7	~20	1
Fresh	1.0	12	~40	1
Fresh	0.0	13–15	~20	2
Fresh	0.0	16	~50	1
Fresh	1.0	16	~40	1
Fresh	1.0	16	~50	1
Irradiated	0.0	0.1	~80	1
Irradiated	0.0	7	~10	1

4. RESULTS AND DISCUSSION

4.1 Inverse-heat-conduction calculations on fresh-fuel tests

Figures 4(a)–(d) compare the computed heat transfer coefficients at the fuel rod surface between the test groups with fresh fuel, different coolant subcoolings, and similar coolant pressures and flow velocities; the figures show that the separate effect of coolant subcooling on film boiling heat transfer in each figure. One data point plotted in the figures corresponds to a heat transfer coefficient $h_{surf,cool}$ computed at a time point in an inverse-heat-conduction calculation, so many points are plotted for one test condition, even for the test condition that consists of only one test case (see Table 1). Large scatter is seen in every case despite the effort that was made for sampling the data points selectively from quasi-stable film boiling regime as described in the previous Section. In addition some cases with high coolant pressure conditions show significant discrepancies in the $h_{surf,cool}$ values even between very similar test conditions: the ~10 K subcooling case in Fig. 4(c) and in the ~60 K subcooling case in Fig. 4(d). No reasonable explanation has not been given and regarded as brought by some errors in the measurement processes. But the effect of coolant subcooling is clear on average; the heat transfer coefficient for a given surface superheat increases with coolant subcooling. The effect of coolant subcooling appears to be enhanced with increasing coolant flow velocity.

FIG. 4. *Effect of coolant subcooling on film boiling heat transfer coefficient for test cases with fresh fuels conducted under the conditions of (a) stagnant coolant and atmospheric coolant pressure, (b) coolant flow velocity of ~1.8 m·s−1 and atmospheric coolant pressure, (c) stagnant coolant and coolant pressure of ~7 MPa, and (d) coolant flow velocity of ~1.0 m·s−1 and coolant pressure of ~7 MPa.*

(a)

○ Fresh V:~0.0m/s P:~7MPa dT_{sub}:~10K
● Fresh V:~0.0m/s P:~0.1MPa dT_{sub}:~10K

(b)

○ Fresh V:~0.0m/s P:~13–15MPa dT_{sub}:~20K
● Fresh V:~0.0m/s P:~7MPa dT_{sub}:~20–30K

(c)

○ Fresh V:~0.7m/s P:~7MPa dT_{sub}:~20K
● Fresh V:~0.6m/s P:~0.1MPa dT_{sub}:~20K

(d)

○ Fresh V:~1.0m/s P:~16MPa dT_{sub}:~50K
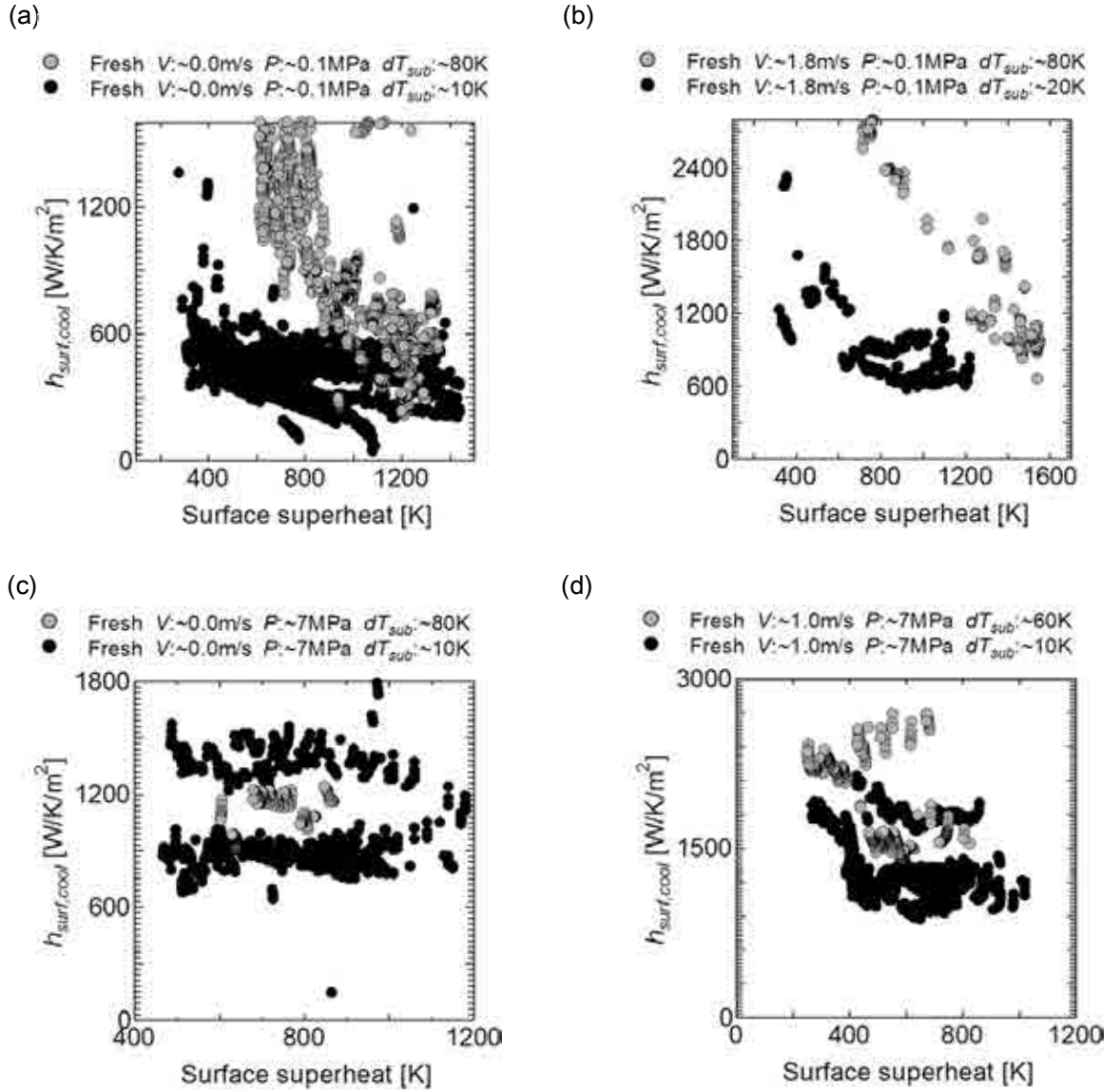● Fresh V:~1.0m/s P:~7MPa dT_{sub}:~60K

FIG. 5. Effect of coolant pressure on film boiling heat transfer coefficient for test cases with fresh fuels conducted under the conditions of (a) stagnant coolant and coolant subcooling of ~10 K, (b) stagnant coolant and coolant subcoolings of ~20–30 K, (c) coolant flow velocities of ~0.6–0.7 m·s−1 and coolant subcooling of ~20 K, and (d) coolant flow velocity of ~1.0 m·s−1 and coolant subcoolings of ~50–60 K.

Figures 5(a)–(d) compare the computed heat transfer coefficients at the fuel rod surface between the test groups with fresh fuel, different coolant pressures, and similar coolant subcoolings and flow velocities; the figures show the separate effect of coolant pressure on film boiling heat transfer in each figure. The heat transfer coefficient for a given surface superheat increases with coolant pressure. Neither the influence of coolant flow velocity nor coolant subcooling on the degree of the effect of coolant pressure is clearly seen.

(a)

Fresh V:~1.8m/s P:~0.1MPa dT_{sub}:~20K
Fresh V:~0.6m/s P:~0.1MPa dT_{sub}:~20K

(b)

Fresh V:~3.2m/s P:~0.1MPa dT_{sub}:~80K
Fresh V:~1.8m/s P:~0.1MPa dT_{sub}:~80K
Fresh V:~0.0m/s P:~0.1MPa dT_{sub}:~80K

(c)

Fresh V:~3.0m/s P:~7MPa dT_{sub}:~10K
Fresh V:~1.0m/s P:~7MPa dT_{sub}:~10K
Fresh V:~0.0m/s P:~7MPa dT_{sub}:~10K

(d)

Fresh V:~3.0m/s P:~7MPa dT_{sub}:~20K
Fresh V:~0.7m/s P:~7MPa dT_{sub}:~20K
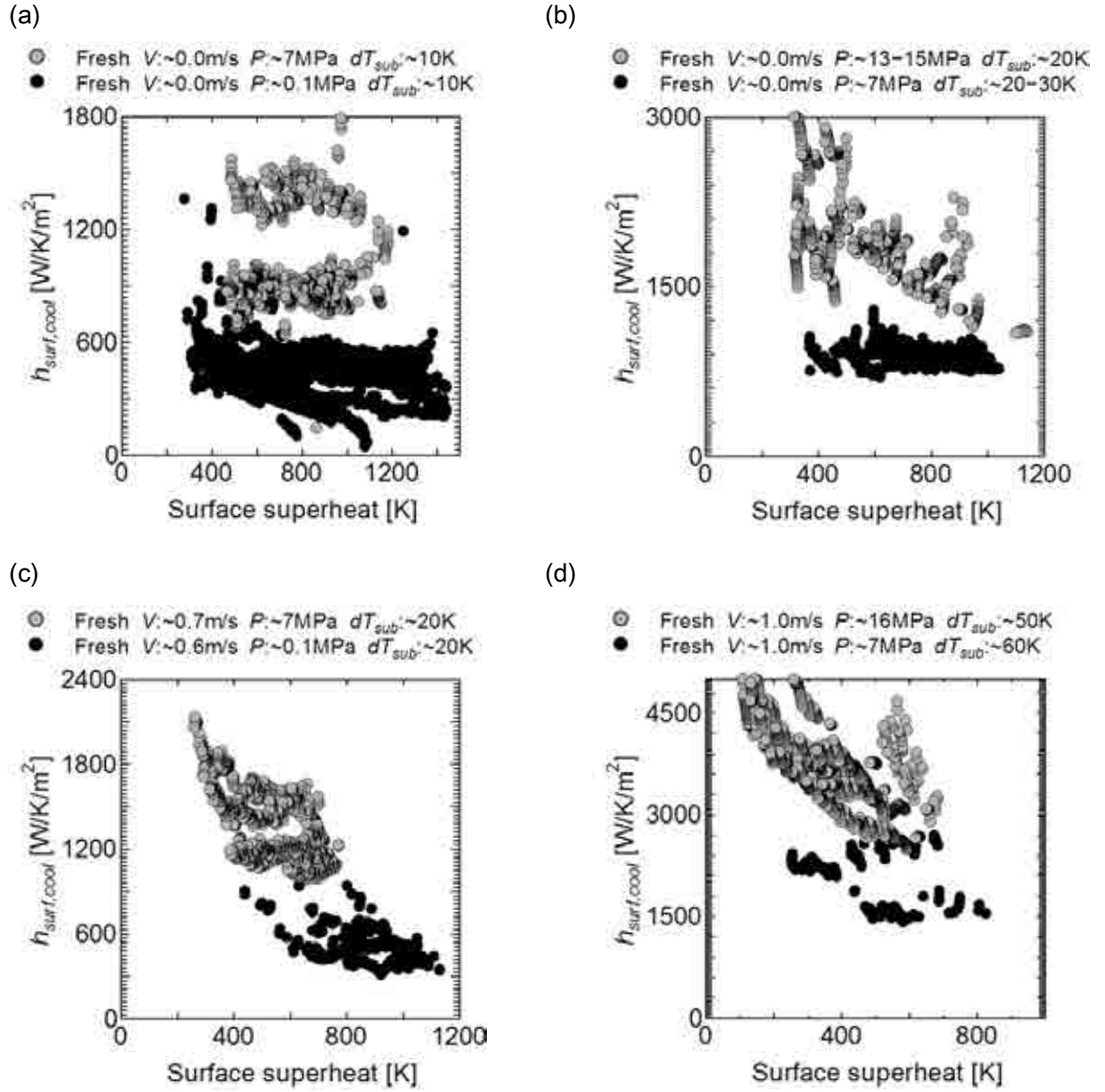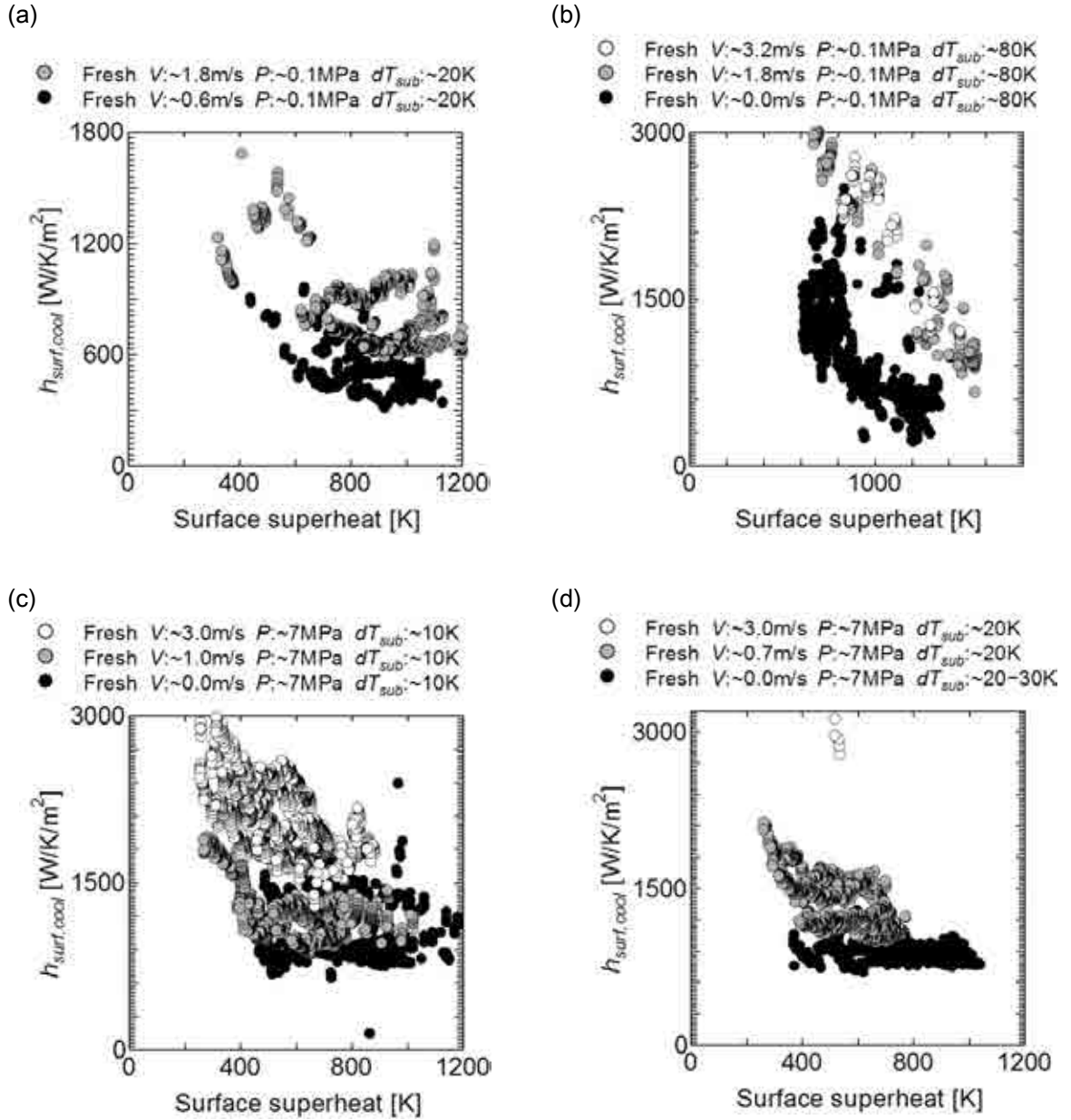Fresh V:~0.0m/s P:~7MPa dT_{sub}:~20–30K

FIG. 6. Effect of coolant flow velocity on film boiling heat transfer coefficient for test cases with fresh fuels conducted under the conditions of (a) atmospheric coolant pressure and coolant subcooling of ~20 K, (b) atmospheric coolant pressure and coolant subcooling of ~80 K, (c) coolant pressure of ~7 MPa and coolant subcooling of ~10 K, and (d) coolant pressure of ~7 MPa and coolant subcoolings of ~20–30 K.

Figures 6(a)–(d) compare the estimated heat transfer coefficients at the fuel rod surface between the test groups with fresh fuel, different coolant flow velocities, and similar coolant subcoolings and pressures; the figures show the separate effect of coolant flow velocity on film boiling heat transfer in each figure. The heat transfer coefficient for a given surface superheat increases with coolant flow velocity. The effect of coolant flow velocity appears to be enhanced with increasing coolant

211

subcooling and pressure.

4.2 Inverse-heat-conduction calculations on pre-irradiated fuel tests

It is known that the DNB threshold for the pre-irradiated fuel rods is higher than that for the fresh fuel rods. Film boiling over 1 second was scarcely observed in the NSRR experiments for the pre-irradiated fuel rods [17]. Figure 7(a) shows the history of the measured cladding temperature in the test TK-6 [4], in which the longest film boiling time was observed in the tests with prer-irradiated fuels, stagnant coolant, atmospheric pressure, and coolant subcooling of ~80 K. Even in this case the film boiling time is so short as ~1.5 sec, and the temperature gradient in cladding thickness did not become flat enough during the film boiling (see Fig. 7(b)) in the inverse-heat-conduction calculation. As a result, only a few points of computed $h_{surf,cool}$ (around 1.5 second in Fig. 7(a)) satisfied the criteria given by Equations (4) and (5) with $\varepsilon = 3\%$ as shown in Fig. 8(a). The figure shows the result of the case that $\varepsilon = 10\%$ was applied to the sampling criterion, for comparison. The threshold $\varepsilon = 10\%$ yielded more data points than $\varepsilon = 3\%$, but the value of $h_{surf,cool}$ shows a sharp variation in the narrow range of surface superheat 600–700 K, which is the case of this test condition alone in all the analyzed cases shown in Table 1. It is then considered to be difficult to determine a single boiling curve for this condition, at least from the available experimental data. Such a behavior is attributable to possible extension of the temperature range of the transition boiling regime due to the wettability enhancement [18], which is known to occur at gamma-irradiated oxidized-zircaloy surface [17, 19].
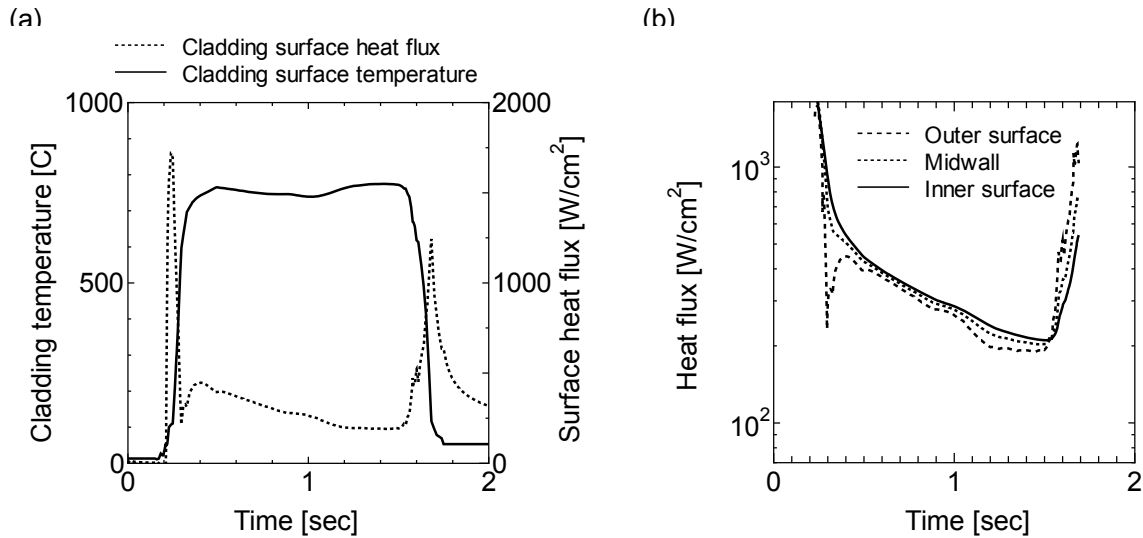

FIG. 7. Inverse-heat-conduction calculation results for the test TK-6, a test case with irradiated fuel, stagnant coolant, atmospheric coolant pressure, and coolant subcooling of ~80 K: (a) histories of cladding temperature used as input and computed surface heat flux and (b) histories of computed heat fluxes at different radial positions in cladding thickness.
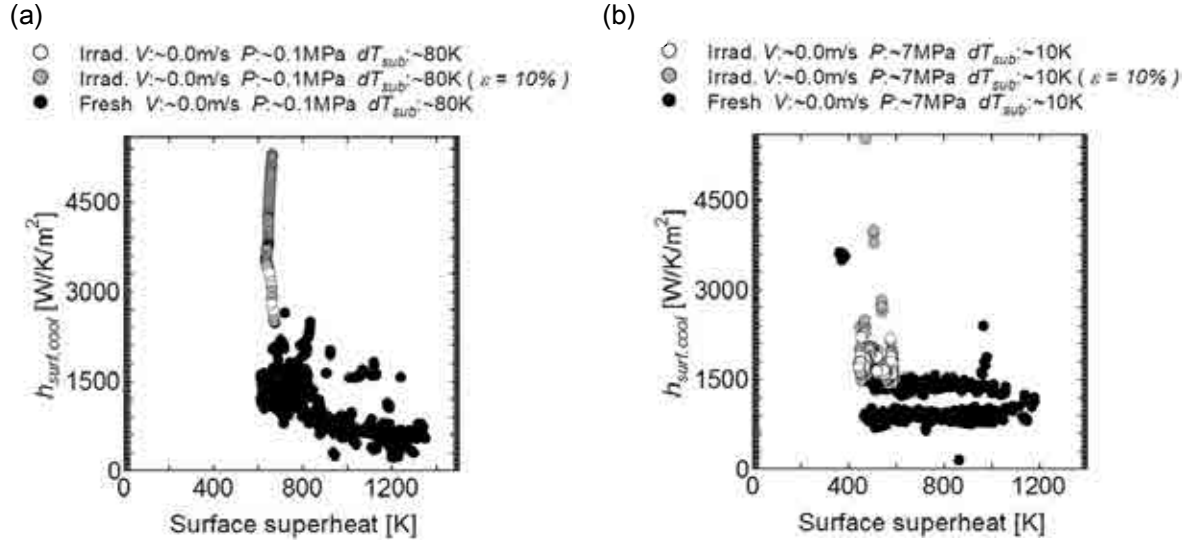
FIG. 8. Effect of pre-irradiation on film boiling heat transfer coefficient for test cases with irradiated fuels conducted under the conditions of (a) stagnant coolant, atmospheric coolant pressure, and coolant subcooling of ~80 K and (b) stagnant coolant, coolant pressure of ~7 MPa, and coolant subcooling of ~10 K.

The effect of pre-irradiation itself is clearly seen in the test case with stagnant coolant, atmospheric coolant pressure, and coolant subcooling of ~80 K shown in Fig.8(a); the boiling heat transfer at a given surface superheat is at least doubled or more compared to the fresh-fuel test cases. The effect of pre-irradiation to enhance the boiling heat transfer is clear also in the test case with stagnant coolant, coolant pressure of ~7 MPa, and coolant subcooling of ~10 K shown in Fig.8(b), but it appears rather moderate compared to the case of ~80 K coolant subcooling.

213

FIG. 9. *Comparisons of inverse-heat-conduction calculation results with correlations by Sakurai and Shiotsu for (a) stagnant water condition and (b) forced flow condition, respectively.*
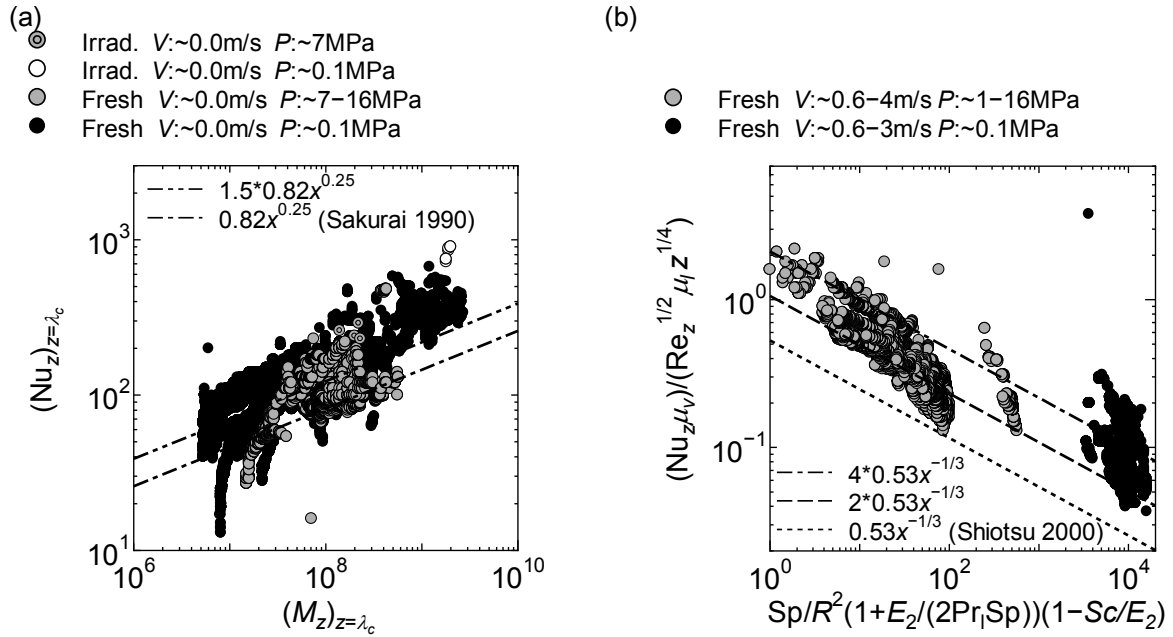
4.3 Analysis by a two-phase laminar boundary layer model for stable film boiling

We further analyzed the results of the present inverse-heat-conduction calculation in order to reduce the observed effects of coolant conditions to a set of numerical models which are available in the RANNS code, by using the two semi-empirical correlations proposed by Sakurai for pool film boiling heat transfer and proposed by Shiotsu for forced convection film boiling heat transfer, derived based on their solutions for two-phase laminar boundary layer film boiling models [9, 10]. The correlations provide comprehensive expressions of the effects of all the coolant conditions discussed here, namely subcooling, pressure, and flow velocity.

Figures 9(a) and (b) compare the inverse-heat-conduction calculation results with the correlations by Sakurai and Shiotsu for stagnant water condition and forced flow condition, respectively. One data point plotted in the figures corresponds to a computed heat transfer coefficient $h_{surf,cool}$ at a time point in an inverse-heat-conduction calculation. The horizontal axes are nondimensional parameters calculated from bulk coolant condition and surface superheat at each time point [10]. The vertical axes are Nusselt number and a parameter calculated from Nusselt number [10], and so proportional to the computed heat transfer coefficient $h_{surf,cool}$. The critical wavelength of Taylor instability was substituted for z, the distance from leading edge of a vertical cylinder, in Sakurai's correlation. The active length of the test fuel rod in each case was substituted for z in Shiotsu's correlation. It can be seen that both Sakurai's and Shiotsu's correlations reasonably reduce the complex effects of the coolant conditions on the film boiling heat transfer to the simple functions of the nondimensional parameters, despite the differences in the test conditions from theirs.
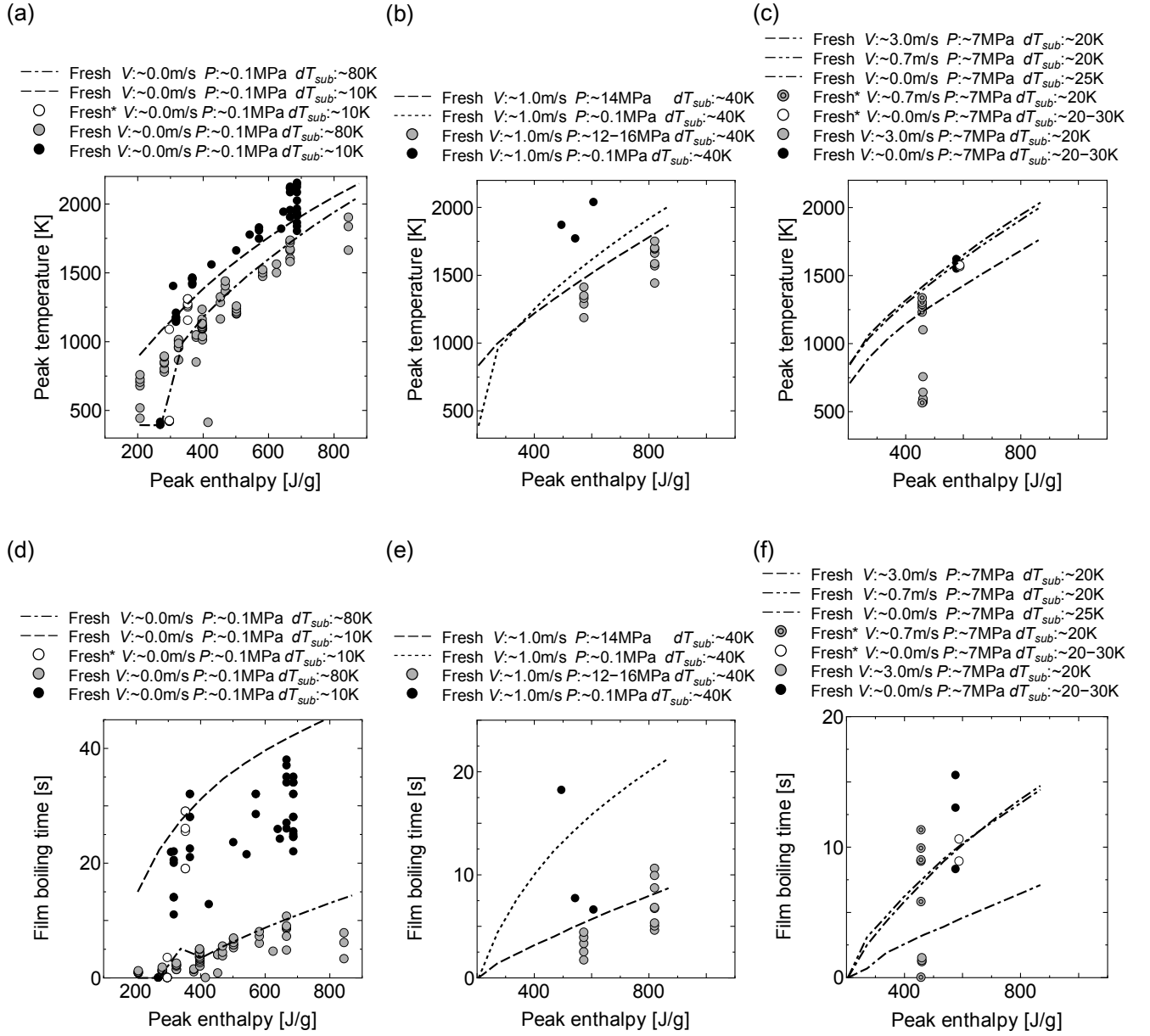
FIG. 10. Comparisons between calculations and measurements for peak temperatures at fuel rod surface ((a)–(c)) and film boiling times ((d)–(f)). Points and curves correspond to the experiments and the RANNS calculations, respectively. Legends with an asterisk like "Fresh*" denotes the result of the 2nd, 3rd, or the latter pulse irradiation in an iterative pulse-irradiation experiment in which a series of pulse-irradiations had been conducted on an identical test fuel rod.

The computed heat transfer coefficients $h_{surf,cool}$ are on average higher than those given by the their original correlations: about 1.5 times larger for stagnant water condition and 2–8 times larger for forced flow condition, respectively. For forced flow condition, the discrepancy is relatively large

in the atmospheric-pressure cases. Also the tendency of $h_{surf,cool}$ for decreasing with increasing surface superheat appears stronger than that predicted by the original correlations in some cases. The cause of these differences may be attributed to the fact that the analyzed temperature data are not of fully developed and stable film boiling state which was assumed in the derivation of their correlations. Regarding the relatively low values of $h_{surf,cool}$ at large surface superheats, heat generation by the chemical reaction of Zircaloy cladding with water could have played a role, which was not considered in the present inverse analysis.

4.4 Modified correlations for film boiling heat transfer coefficients incorporated into RANNS code

The correlations used in a RIA analysis with the RANNS code to compute the film boiling heat transfer coefficient without radiation contribution, $h_{surf,cool}(t)$, have been updated by

$$h_{surf,cool}(t) = h_{Sakurai,cool}(t) \cdot F_{pool} \cdot F_{irr} \qquad \text{(pool)} \qquad (8)$$

$$h_{surf,cool}(t) = h_{Shiotsu,cool}(t) \cdot F_{flow} \cdot F_{irr} \qquad \text{(forced convection)} \qquad (9)$$

$$F_{pool} = 1.5 \qquad (10)$$

$$F_{flow} = 2.5 - 0.15 \times \arctan(1.5 \times P(t) - 4.0) \qquad (11)$$

$$F_{irr} = 1.0 + 0.67 \times (1.0 - \exp(-\Phi/10^{24})) \qquad (12)$$

Where

$h_{Sakurai,cool}$ is the original correlation for stable film boiling given by Equation (1) ref. [10];

$h_{Shiotsu,cool}$ is the original correlation for stable film boiling given by Equation (32) in ref. [10];

F_{pool} is the model parameter for pool boiling;

F_{flow} is the model parameter for forced convection boiling;

F_{irr} is the model parameter for irradiated fuels;

Φ is the cladding fast fluence in $[m^{-2}]$.

The parameters F_{pool} and F_{flow} were introduced to improve global agreement of the predicted $h_{surf,cool}$ values with the experimental data summarized in Figs 9(a)(b). The parameter F_{irr} is to take into account the effect of pre-irradiation on the film boiling heat transfer which appeared in Figs 8(a)(b).

A set of RANNS calculations was then performed to verify the updated heat transfer models. Onset of DNB was predicted based on a threshold value of the thickness of vaporized liquid film layer at the fuel-rod surface, in accordance with the model proposed by Bessiron et al. [20]. Figures 10(a)–(f) compare the results of RANNS calculations, using the modified correlations, for the fresh-fuel tests.

It was found that introducing the parameter Firr is not enough to describe the effect of pre-irradiation, namely the strongly enhanced heat transfer; the calculations still overestimated the measured cladding temperatures significantly. Modification on the modeling of the transition boiling regime is thus being made and now under test for improving the simulation capability. Figures 11(a),

(b) compare tentative RANNS calculation results with the experimental data for the pre-irradiated fuel tests, together with the fresh-fuel test cases with similar coolant conditions. The calculation results for the pre-irradiated fuel cases, reproducing the lower peak temperatures than those in the fresh-fuel cases, were obtained by introducing additional dependencies of the boiling curves on the cladding fast fluence, coolant subcooling, and critical heat flux. Further investigation is required on the mechanism of the pre-irradiation effect on transition boiling, possibly as enhanced surface wettability, for developing a reliable model which is applicable to varied coolant and fuel conditions.
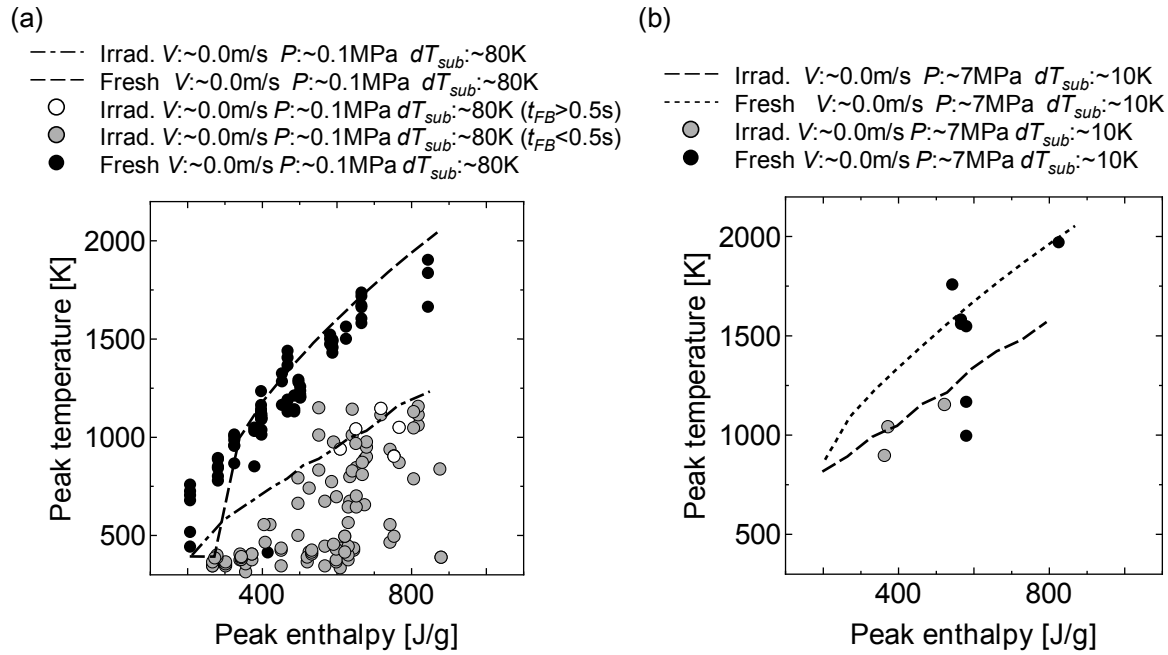

FIG. 11. *Comparisons between calculations and measurements for peak temperatures at fuel rod surface: fresh and pre-irradiated fuel test cases with (a) stagnant coolant, atmospheric coolant pressure, and coolant subcooling of ~80 K, and (b) stagnant coolant, coolant pressure of ~7 MPa, and coolant subcooling of ~10 K. Points and curves correspond to the experiments and the RANNS calculations, respectively. The legend tFB in Figure (a) denotes film boiling time.*

5. CONCLUSIONS

Inverse-heat-conduction calculations on the transient temperature data from RIA-simulating experiments were conducted with the RANNS code for estimating boiling heat transfer coefficients from the fuel rod surface to the coolant water, and the effects of coolant conditions and fuel-rod pre-irradiation were investigated. The present analysis indicated that the film boiling heat transfer coefficients during RIA boiling transient increase with coolant subcooling, flow velocity, and pressure, as predicted by the two-phase laminar boundary layer model for stable film boiling. The estimated boiling heat transfer coefficients were on average larger than those predicted by the semi-empirical correlations: about 1.5 times larger for stagnant water condition and 2–8 times larger for forced flow condition, respectively. This information was used for updating the correlations for the

film boiling heat transfer coefficient in the RANNS code. The analysis confirmed the effect of pre-irradiation to enhance the boiling heat transfer, which appeared very strong at large subcooling of ~80 K and rather moderate at small subcooling of ~10 K, and also suggested the difficulty of reducing the inverse calculation results for the pre-irradiated fuel cases to a single boiling curve for a given coolant condition. Further investigation is required on the mechanism of the pre-irradiation effect, possibly as enhanced surface wettability, for developing a reliable heat transfer model for pre-irradiated fuels.

ACKNOWLEDGEMENTS

REFERENCES

[1] UDAGAWA, Y., et al., Heat Transfer from Fuel Rod Surface under Reactivity-initiated Accident Conditions -NSRR Experiments under Varied Cooling Conditions-, JAEA-Data/Code 2013-021, Japan Atomic Energy Agency, Tokai (2014).

[2] FUKETA, T., et al., Behavior of LWR/MOX Fuels under reactivity-initiated accident conditions, Proc. Top Fuel 2009, Paris, France, September 6–10, 2009, pp.465–472 (2009).

[3] FUKETA, T., et al., Behavior of PWR and BWR fuels during reactivity-initiated-accident conditions, Proc. Int. Topical Mtg. LWR Fuel Performance, Park city, Utah, U.S.A., Apr. 10–13, 2000 (2000).

[4] FUKETA, T., et al., Behavior of high-burnup PWR fuels with low-tin Zircaloy-4 cladding under reactivity-initiated-accident conditions, Nucl. Technol. **133** 1 (2001) 50.

[5] SUGIYAMA, T., et al., Evaluation of initial temperature effect on transient fuel behavior under simulated reactivity-initiated accident conditions, J. Nucl. Sci. Technol. **47** 5 (2010) 439.

[6] NAKAMURA, T., et al., Boiling water reactor fuel behavior under reactivity-initiated-accident conditions at burnup of 41 to 45 GWd/tonne U, Nucl. Technol. **129** (2000) 141.

[7] FUKETA, T., et al., Behavior of pre-irradiated fuel under a simulated RIA condition (results of NSRR test JM-4), JAERI-Research 95–013, Japan Atomic Energy Agency, Tokai (1995).

[8] OHNISHI, N., et al., A study of subcooled film-boiling heat transfer under reactivity-initiated accident conditions in light water reactor, Nucl., Sci., Eng. **88** (1984) 331.

[9] SAKURAI, A., et al., Correlations for subcooled pool film boiling heat transfer from large surfaces with different configurations, Nucl. Eng. Design **120** (1990) 271.

[10] SHIOTSU, M., et al., Film boiling heat transfer from a vertical cylinder in forced flow of liquids under saturated and subcooled conditions at pressures, Nucl. Eng. Design **200** (2000) 23.

[11] SUZUKI, M., Present status of the verifications and model development of FEMAXI and RANNS codes in JAEA, IAEA-TECDOC-CD-1709, Vienna (2013).

[12] SUZUKI, M., et al., Light water reactor fuel analysis code FEMAXI-7; model and structure, JAEA-Data/Code 2010–035, Japan Atomic Energy Agency, Tokai (2010).

[13] ROSS, A., M., et al., Heat transfer coefficient between UO_2 and Zircaloy-2, CRFD-1075, Atomic Energy Comission of Canada Limited, Ontario(Canada), (1962).

[14] FUJISIRHO, T., A study on gap heat transfer of LWR fuel rods under reactivity initiated accident conditions, JAERI-M 84-063, Japan Atomic Energy Agency, Tokai (1984).

[15] UDAGAWA, Y., et al., Stress biaxiality in high-burnup PWR fuel cladding under reactivity-initiated accident conditions, J. Nucl. Sci. Technol. **50** 6 (2013) 645.

[16] TSURUTA, T., et al., Evalulation of thermocouple fin effect in cladding surface temperature measurement during film boiling, J. Nucl. Sci. Technol. **21** (1984) 515.

[17] SUGIYAMA, T., et al., Effect of cladding surface pre-oxidation on rod coolability under reactivity initiated accident conditions, J. Nucl. Sci. Technol. **41** (2004) 1083.

[18] HA, S., J., et al., A dry-spot model of critical heat flux in pool and forced convection boiling, Int. J. Heat Mass Trans. **41** (1998) 303.

[19] TAKAMASA, T., et al., Surface wettability caused by radiation induced surface activation, Thermal Sci. Eng. **12** (2004).

[20] BESSIRON, V., et al., Clad-to-coolant heat transfer in NSRR experiments, J. Nucl. Sci. Technol. **44** (2007) 723.

SIMULATION OF CANDU FUEL BEHAVIOUR INTO IN-REACTOR LOCA TESTS

A. PARASCHIV, G. OLTEANU, D.V. IONESCU, R.M. ROMAN
Institute for Nuclear Research,
Pitesti, Romania
Email: adrieana.paraschiv@gmail.com

Abstract. The purpose of this work is to simulate the behaviour of an instrumented, unirradiated, zircaloy-sheathed UO_2 fuel element assembly of CANDU type, subjected to a coolant depressurization transient in the X-2 pressurized water loop of the NRX reactor at the Chalk River Nuclear Laboratories in 1983. The high-temperature transient conditions are such as those associated with the onset of a loss of coolant accident (LOCA). The data and the information related to the experiment are those included in the OECD/NEA-IFPE Database (IFPE/CANDU-FIO-131 NEA-1783/01). As tool for this simulation is used the TRANSURANUS fuel performance code, developed at ITU, Germany, along with the corresponding fabrication and in-reactor operating conditions specific of the CANDU PHWR fuel. The results, analyzed versus the experimental ones, are encouraging and perfectible.

1. INTRODUCTION – LOCA OVERVIEW

It is known that the fuel performance in normal and in accident (Loss-Of-Coolant Accident (LOCA) and Reactivity-Initiated Accident or Reactivity-Insertion Accident (RIA)) conditions was and still is one of the most important issues for the international nuclear industry. Many international research programmes cover a large number of activities to address these issues. The LOCA as a Design-Basis Accident (DBA) is a central element in the design and licensing basis for the nuclear power plants. It is especially used for the design of the safety injection systems and the limitation of the reactor power at the hottest point in the core during normal operation.

LOCA's are hypothetical accidents that would result from the loss of reactor coolant, at a rate in excess of the capability of the reactor coolant makeup system, from breaks in pipes in the reactor coolant system [1]. As a result, a depressurization of the primary coolant system with power decrease to its residual level occurs. In such situation the fuel element cladding will be exposed to steam at elevated temperatures for few minutes until the Emergency Core Cooling System (ECCS) is set working and water quenches the fuel bundle [2]. The consequences for the fuel element in their evolutional order are [2–5]:

- the temperature increases and cladding dries-out;

- the transfer of the stored energy from the fuel to the cladding occurs;

- the cladding is possibly to overheat and in conjunction with high internal gas pressure and low coolant pressure may sustain extreme mechanical loading which leads to large plastic deformations (ballooning), so that a contact with the neighbouring elements will be possible;

- at around $800^{\circ}C$ cladding temperature, ballooning and burst occur;

- the ballooning can potentially be detrimental to cooling of the fuel assemblies, and the burst of an element also leads to cladding oxidation from the inside;

- the fuel fragments relocate either inside the ballooned zone or outside the element through the burst opening;

- the large exothermic heat generated during oxidation of the cladding cannot be adequately dissipated by cooling, eventually leading to run-away oxidation;

- the further heat-up leads to a severe oxidation of cladding at high temperature (metal-water reaction) with hydrogen generation and significant embrittlement of cladding;

- finally, the quenching due to reflooding water of the safety injection systems happens and the fuel element supports a thermal shock.

In a CANDU reactor, the fuel is loaded into horizontal pressure tubes, and is cooled by the flow of pressurized heavy water. In broad terms, a LOCA in a CANDU reactor follows a sequence similar to a PWR one. A break in the primary heat transport system initiates reactor shut down. There is an initial period of blowdown as the pressurized coolant vents from the system. As the coolant pressure drops, cooling is degraded and the fuel under goes a temperature transient. During this period, there is the possibility of fuel damage and release of fission products to containment. Initiation of the ECCS re-floods the reactor core, cooling the fuel and terminating the accident [5].

Despite these similarities with the PWR LOCA sequence, the horizontal pressure tube design and heavy water moderator mean that the details of the accident progression are quite different. However, the aspects related to the fuel element behaviour in a LOCA are the same with the already described.

For the accident conditions, there are acceptance criteria which must be fulfilled. So, the most fundamental acceptance criterion for DBA's is typically that there should be no or at most very limited radiological consequences to the public. In order to fulfill this criterion it is necessary to prevent the fuel melting and to avoid excessive fuel dispersal. It was thus necessary to design the ECCS's so that the fuel could be cooled efficiently during all phases of the DBA. This requirement naturally led to a criterion that the fuel must maintain a coolable core configuration through the whole LOCA sequence and that the structural but not necessarily the hermetical integrity of the fuel elements should be maintained [5]. Relating to the fuel element, the safety requirements demand to ensure the resistance of the fuel elements upon-quench and post-quench loads and to maintain a coolable geometry in the core.

These requirements are developed in safety criteria, associated with limit values, mainly expressed in terms of a maximum cladding temperature (PCT) and an equivalent cladding reacted ratio (ECR) with the aim of ensuring a residual ductility of the cladding to prevent fragmentation of the fuel elements that would impair the core coolability [4].

The LOCA criteria are based mostly on the data obtained with unirradiated cladding. On the other hand, the economical requirement to increase the fuel burnup at its discharge from reactor has imposed a revision of the data related to the safety criteria in LOCA conditions. With burnup increasing the corrosion, the hydrogen pickup and the neutrons irradiation effects become important and lead to the degradation of the mechanical properties of the cladding. Therefore, considerable experimental and analytical work has been performed in the nuclear world, in order to obtain a broader and deeper understanding of LOCA-related phenomena. Also, fully integrated tests were performed to provide valid data base for understanding fuel behaviour in the bundle geometry under more realistic LOCA conditions and validation of computer codes in this category [6].

This work joins in this last issue by simulating the behaviour of a fuel element of CANDU type, subjected to LOCA conditions in the Canadian FIO-131 experiment [7] using as tool of simulation the TRANSURANUS fuel performance code [8], developed at ITU, Karlsruhe, Germany, along with

the corresponding fabrication and in-reactor operating conditions specific of the CANDU PHWR fuel. The code version used is v1m1j09.

2. TREATMENT OF THE FUEL ELEMENT UNDER LOCA CONDITIONS WITH TRANSURANUS CODE

It is well known that TRANSURANUS [8] is a fuel performance code developed at the European Institute for TransUranium Elements to be used for many nuclear fuel designs (LWR, PWR, BWR, HWR, FBR and more recent VVER). In Romania, the Cernavoda NPP is one of CANDU type. By this reason in our Institute activities and studies dedicated to the assimilation of this code were developed in order to apply it to the CANDU type fuel behaviour analyses [9]. The results were presented in the framework of some editions of TRANSURANUS Users Meeting [10–12]. In the present work the capability of the TRANSURANUS code to simulate the CANDU fuel behaviour in the LOCA conditions is emphasized.

Generally, a LOCA safety analysis involves determining of the boundary conditions (coolant temperature, coolant pressure, sheath-to-coolant heat transfer coefficient) with a thermo-hydraulic code, the behaviour of the fuel element in normal operating conditions prior the onset of the accident with a fuel performance code followed by the fuel element analysis during LOCA conditions with a specialized code. The objective of this last analysis is to predict the potential for cladding failure during accident conditions.

The TRANSURANUS code uses a method that provides the unique possibility of the consistent simulation of fuel element behaviour under normal operation and accident conditions. The LOCA analysis is carried out in an automatic restart run, which allows the initiation of the LOCA-specific models either for fresh fuel elements (only LOCA simulation) or fuel elements with specific burnup (simulation of normal operation and LOCA). The model and material property options for the LOCA analysis are defined in a separated block of the input. The appropriate boundary conditions for the accident analysis (decay power, coolant pressure, coolant temperature and heat transfer coefficient) are also specified in the input block. The transition from normal to LOCA-specific models and operating conditions occurs at a time point defined by the user that corresponds to the time of the LOCA initiation.

On the basis of the defined boundary conditions the code calculates the temperature distribution and the fission gas release inside the fuel element, the corresponding inner pressure, the ZrO_2 thickness growth on the outer surface, the equivalent oxidation (ECR) and the large plastic deformation (ballooning) of the cladding. Fuel element burst is checked through appropriate failure criteria.

However, it must specify that the simulation of post-LOCA events is limited by the validity range of the applied correlations and material property functions. Generally, the present LOCA-specific models are validated up to 1200°C [8].

2.1 Outer cladding corrosion

In the TRANSURANUS code the outer cladding corrosion (water oxidation) during normal operation can be or not taken into account upon the user option. There are implemented in code more models to evaluate this corrosion depending on the fuel type. Also, the consideration of the corrosion

effect on the cladding behaviour, either only thermal, or along with the mechanical one (the weakening of the cladding) can be selected.

In order to simulate the zirconium-steam reaction during LOCA conditions, in the TRANSURANUS code the ZrO_2 layer thickness and the oxygen mass gain are calculated through a simple recursive formula which is appropriate for transient (varying temperature) conditions, assuming an isothermal oxidation process only during one time step interval. The evolution of the oxidation in one time step is dominated by the actual value of the temperature-dependent reaction rate constant. In addition to the temperature, the cumulative extent of the oxidation (oxide layer thickness or oxygen mass gain) depends on its initial value at the beginning of the time step and on the time step length, as well. The reaction rate constant is described by an empirical Arrhenius-type correlation. At present there are three optional sets of parameters in the steam oxidation model applicable for zircaloy: the Cathcart-Pawel [13], the Leistikow [13] and the Baker-Just [14] correlations. The high temperature cladding oxidation model is called only at temperature above 673 K (400°C) and if the cladding temperature was below this value the MATPRO corrosion model is applied automatically. The conservative Baker-Just correlation is applicable up to the range of the zircaloy melting.

The oxidation effect is the continuous thinning of the cladding (metal) wall. This affects both thermal and mechanical treatment of the cladding. The thinning of the cladding wall results in larger effective stress and consequently larger strain rate. The wall thinning is proportional to the ZrO_2 thickness calculated and the proportionality factor corresponds to the Pilling-Bedworth ratio for the Zr-ZrO_2 system [8]. The oxidation effect is taken into consideration in the mechanical analysis optionally.

2.2 Crystallographic phase transition

The volumetric fraction of the β-phase in zircaloy is calculated in the TRANSURANUS code by two approaches based on Forgeron´s methodology [15], selected correspondingly in the input options. The first is a static model in which the β-phase fraction is a simple function of the temperature assuming thermal equilibrium. The second is a dynamic model considering the hysteresis effect of the heating and cooling rates.

The effect of the α – β phase transition on the cladding deformation rate is simulated through the weighted superposition of the effective strain rates defined separately for the zirconium based alloys having HCP (hexagonal closed pack) and BCC (body centred cubic) crystal structures (α and respectively β phase). The weights are calculated in a subprogram as corresponding volumetric fractions of the two different phases.

2.3 Rate of cladding deformation

In order to describe the effective strain rate as a function of the effective stress and temperature, in the TRANSURANUS code are used specific correlations for the cladding alloy in the form of Norton-type equations. Because at high temperature peculiar to LOCA (600– 1200°C) both the crystallographic phase transition and the extensive oxidation of the zirconium influence the strength and the deformation of the cladding to a large extent, these phenomena are taken into account, as

well. The effective strain rate of zircaloy-4 under LOCA conditions is calculated on the basis of the correlations from ref. [16].

2.4 True tangential stress at the cladding rupture

The true tangential stress at the rupture of the cladding as a function of the cladding temperature and the oxygen concentration is defined by the corresponding correlations from the ref. [16] for α phase, β phase and respectively $\alpha - \beta$ phase. This stress is applied as a threshold value in the cladding failure model.

2.5 Rupture of the fuel cladding

Under LOCA conditions the cladding of the fuel element is possibly overheated and may sustain extreme mechanical loading which leads to large plastic deformations (ballooning) and finally to the burst of the tube. This large plastic deformation of the cladding is calculated incrementally in time in conformity with the treatment of non-elastic strains. However, the application of a proper strain rate relation is not sufficient to predict the cladding deformation at burst. The calculated maximum residual strain also depends on the applied cladding failure criterion. At present there are three basic principles implemented in the code in order to assess the cladding burst.

The first principle is a classic stress assessment comparing the calculated true tangential stress with a distinct failure limit in each time step. The failure threshold of the specific cladding alloy is calculated as a function of the actual temperature and oxidation as it was shown in the previous paragraph. This is the so called overstress criterion.

The second principle represents a plastic instability criterion based on the simultaneous assessment of the effective true strain and the effective strain rate and the comparison with the threshold values defined by the user in the input data.

The third principle is an overstrain criterion: the true tangential plastic strain is limited to the maximum of 50%.

These last two criteria, the plastic instability and overstrain, were introduced particularly for LOCA analyses and are always applied concurrently: if plastic instability is not indicated than the overstrain criterion is checked automatically.

In the code there are three possible options to select the appropriate failure criterion: the overstress criterion, the plastic instability with overstrain assessment criterion and, as an additional option, these three criteria can be checked concurrently.

The cladding is assumed burst when one of the selected criteria is fulfilled. Then the rod internal pressure is set equal to the coolant pressure and a cladding failure message concerning the axial location and the time of failure appears in the code output.

3. THE FIO-131 EXPERIMENT (AECL, CHALK RIVER LABORATORIES)

The FIO-131 experiment [7, 17] was performed in the NRX (National Research Experimental) reactor at the Chalk River Laboratories, Canada in 1983, as part of an experimental program on fuel performance under high temperature transient conditions such as those associated with the onset of a LOCA, with the aim to provide quantitative code verification data. The following outline of the experiment is based on the ref. [7].

An instrumented, unirradiated, zircaloy-sheathed UO$_2$ fuel element assembly was subjected to a coolant depressurization (blowdown) transient in the X-2 pressurized water loop of the NRX reactor. An image of the complex instrumentation of the experimental fuel element can be seen in Fig. 1, which is taken from ref. [7].

Fabrication parameters for the experimental fuel element do not correspond to the CANDU standard fuel, mainly due to the problems imposed by the instrumentation process.
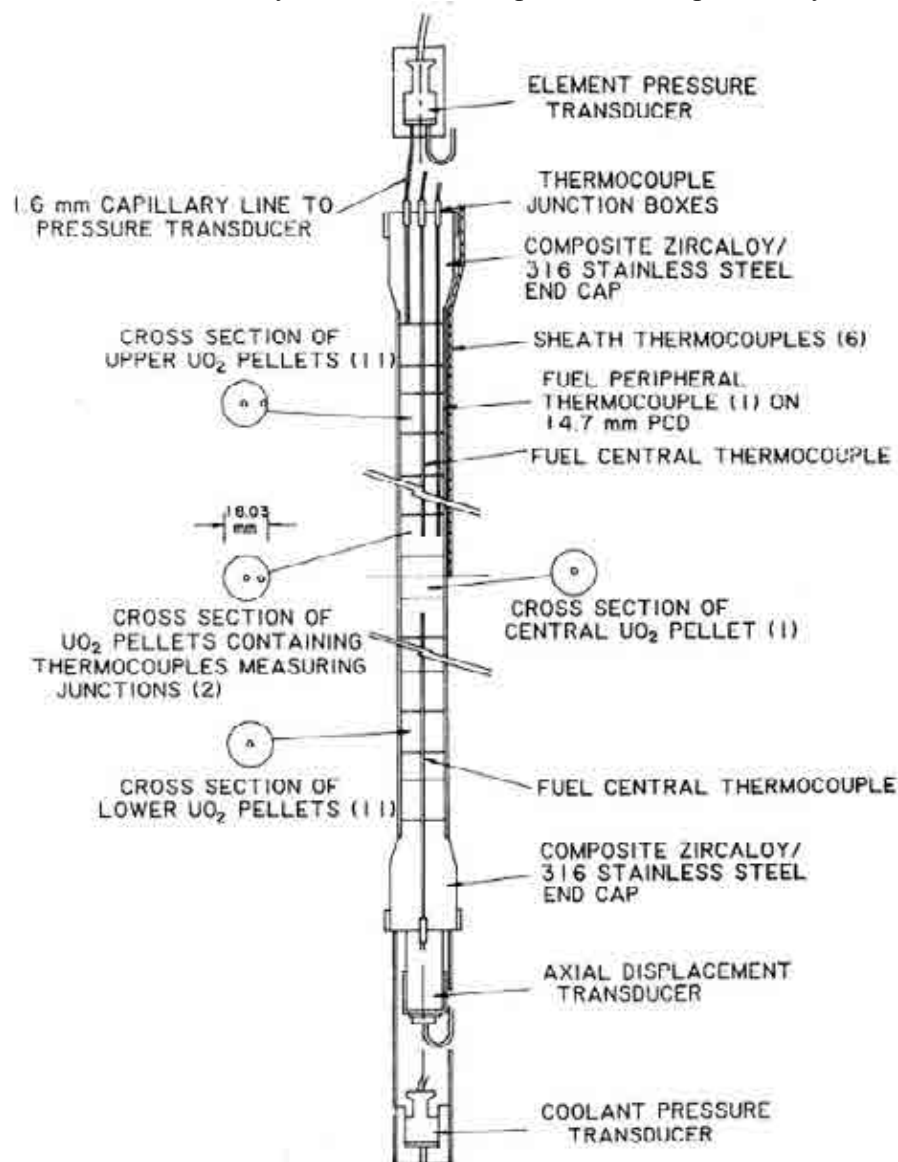

FIG.1. Instrumented fuel element in FIO-131 experiment [7].

So, all pellets contain a central hole (with two different diameter of the hole) and some of them have in addition, a peripheral hole and/or grooves to accommodate centreline and peripheral

thermocouples. For this reason, the fuel pellet diameter is larger than in the standard case. The pellets have single dishes. In order to reduce the neutron flux at the ends of fuel stack, the two end pellets contain natural uranium while the rest of pellets contain UO_2 enriched with 1.38wt% U-235. Also, the wall thickness of the cladding is about two times larger than the standard value and a capillary line connects the element internal volume to an eddy current pressure transducer. All these result in an internal volume about three times larger than that of CANDU fuel. In this situation, although the element contained gas at a pressure similar to high-burnup CANDU fuel, the cladding strain was not expected to contribute to internal pressure reduction as would smaller-diameter CANDU fuel.

In the FIO-131 experiment the experimental fuel element was pressurized in-situ prior to the blowdown, so that the internal element pressure was predetermined and set at the start of the transient. The internal pressure of the experimental element was artificially set, while operating in-situ just prior to the transient, to 8–9 MPa in order to simulate the amount of fission gas pressure expected in high-burnup CANDU fuel.

The fuel element and fuel assembly were instrumented to measure fuel, cladding and coolant temperatures during the entire testing irradiation. In addition, pressure transducers were provided for measuring the internal element gas pressure and coolant pressure during the blowdown transient. Fuel centreline temperature was measured by thermocouples at the top and bottom of the fuel stack. One thermocouple measured the fuel peripheral temperature at the element mid-point. Six thermocouples were laser-welded (semi-buried) to the cladding in pairs at top/middle/bottom locations. Thermocouples were located above and below the element to record coolant temperatures and buried in the flow tube to measure wall temperature. Experimental data were recorded by data acquisition systems.

The experimental fuel power was calculated from calorimetric data based on three separate inlet/outlet differential coolant temperature measurements. The best values were obtained from the thermocouples mounted on the flow tube.

During FIO-131 irradiation test the experimental fuel element supported two blowndown transients.
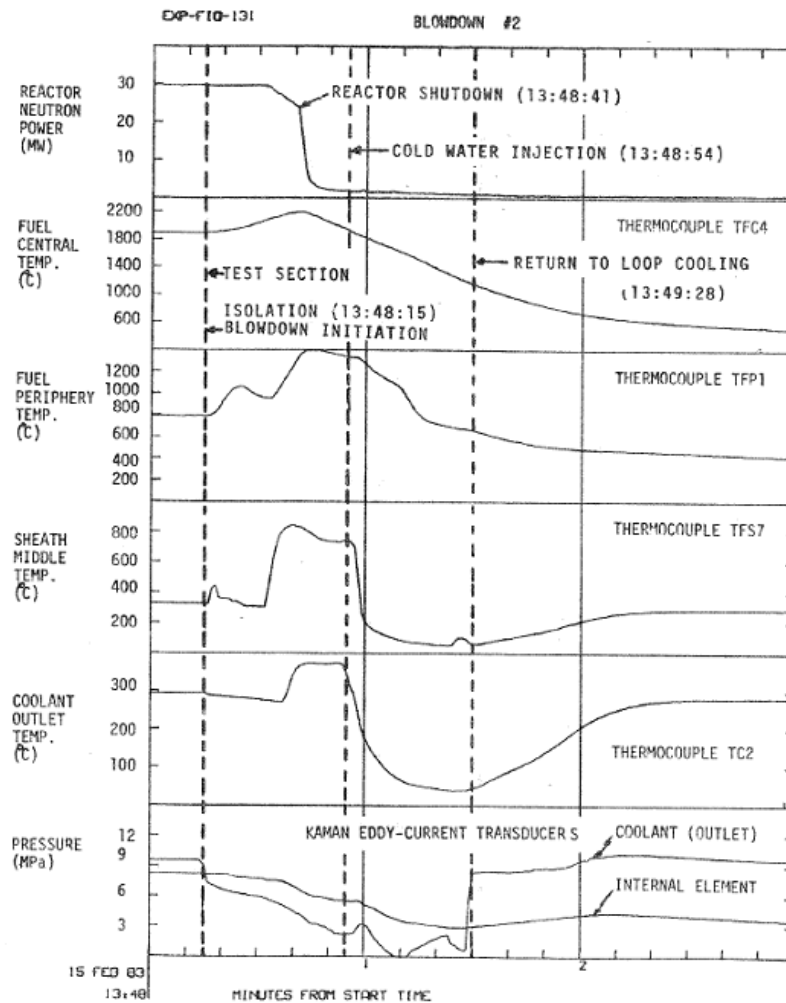
FIG.2. Second blowdown transient data in FIO-131 experiment [7].

The first transient was performed at low fuel temperatures to check reactor and loop systems and the data acquisition computer prior to the second transient who was performed at high-temperature to study the performance of a CANDU fuel element during LOCA and to provide documented data for validation. In the present work only the second transient is simulated. The sequence and timing of events during the second transient are plotted in Fig. 2.

The high-temperature transient was initiated with the fuel operating at a linear power rating of 65–68 kW/m. The fuel element internal pressure was raised to 8.14 MPa just before the transient. After isolation, the test section was blown down from the top and bottom simultaneously. Voiding of the test section to achieve the blowdown resulted in a fuel power increase of about 10%. The blowdown was initiated with the reactor at full power (30 MW). About 17 seconds into the transient, the reactor power was lowered to 23.8 MW and then was reduced to zero about 26 seconds after blowdown initiation. The transient was terminated by rewet injection 39 seconds into the transient. On blowdown, the coolant depressurized rapidly to near saturation pressure.

227

With blowdown, the clad went momentarily into dry-out, then rewet, as entrapped water above the element cooled the clad. The element then went into cladding dry-out for a second time starting from the bottom and propagating upwards about 17 seconds into the transient. The maximum clad temperatures ranged from 875°C at the bottom to 689°C at the top. The maximum fuel centreline temperature was 2200°C compared to a maximum fuel peripheral temperature of 1398°C.

The internal element pressure exceeded the coolant pressure for almost the entire transient. The experimental data as heat-up and quench rates for the fuel and clad, time at temperature, differential pressure across the cladding, the stored energy in the fuel, the recorded temperature and pressure data as well as the relative power history for the second transient, based on changes in the reactor neutron power and corrected for decay heat and for increased reactivity due to voiding of the coolant from the testing loop are given in ref. [7].

The fuel element survived the LOCA transient intact. Post-irradiation examination of the experimental fuel element included visual examination and profilometry performed in hot-cells, neutron radiography, and metallography.

The profilometry measurements revealed the presence of distinct ridges at pellet-interface locations, generally uniform in height, indicating that strong pellet-cladding mechanical interaction had occurred.

Neutron radiography results revealed both circumferential and longitudinal cracks in the fuel pellets. In the bottom half of the fuel stack the pellets was more severe cracked and a severe fuel fragmentation was also observed.

The fuel grain size measurements showed significant grain growth at the centre of the pellets, particularly at the bottom end of the element where pre-transient power and transient cladding temperatures were both at maximum values.

Metallographic examination of the cladding transverse sections showed that cladding deformation was circumferentially uniform. A white oxide layer was observed on the outside of the cladding with a varied thickness along its length from about 2 to 8 microns (on the hotter, bottom end), consistent with the measured axial temperature gradients.

4. RESULTS AND DISCUSSIONS

This work is a first application of the TRANSURANUS code to the simulation of the CANDU fuel element behaviour in the normal conditions of operation followed by the high-temperature transient conditions such as those associated with the onset of a LOCA. The experiment selected for simulation, FIO-131, is described in the former paragraph.

4.1 Details of modelling

A geometric model for the experimental fuel element was sketched to be used for simulation with the TRANSURANUS code. The model takes into account the fabrication constructive particularities of the experimental fuel element (different enrichment of the fuel pellets, two values for the central hole of the pellets) but also the axial distribution of the operating parameters (the neutron flux, the linear power, the temperature and pressure of the coolant). So, the geometric model, shown in Fig. 3, consists in 9 axial segments, each of them having their distinct data (above

mentioned) in the code input. In radial direction the fuel is divided in 20 concentric rings with 5 nodes each.
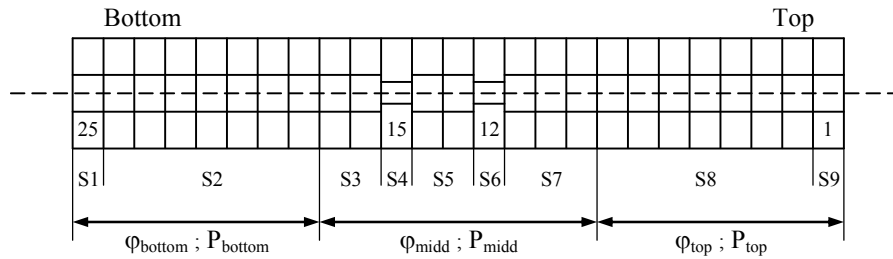

FIG.3. Fuel element geometric model used for simulation with TRANSURANUS code.

It has to mention that not all constructive details of the experimental fuel element were considered in the experiment simulation. As for example, among all holes and groves in the fuel pellets designed for the instrumentation only the central hole was taken into account. From the void volume point of view these holes were filled with the materials used for instrumentation in a large proportion and their contribution to the total void volume of the element can by neglect. But, the lack of material it is supposed to be considered in the calculus of the element power from the calorimetric experimental data while the model used in the code simulation skip this aspect. This means that the linear power used in the code would be corrected (increased) to avoid this situation that would lead to the under prediction of the fuel temperature.

The internal gas pressure in the fuel element was initially 0.101325 MPa and it was raised to 8.14 MPa with a in-situ pressurization system, just before the transient, to simulate the fission gas pressure expected in high-burnup CANDU fuel. In order to obtain with the code a value close to 8.14 MPa for the internal pressure at the end of the short steady-state irradiation period, the initial value of the internal pressure was set artificially at 2.4 MPa obtaining a calculated value of 8.14 MPa. It must be mentioned that, in fact, the TRANSURANUS code can solve a problem as the in-situ pressurization by using the restart option, but in the present case a restart option is already automatically used by the option for the LOCA analysis. Although the TRANSURANUS code accepts also multiple restarts, this possibility was not explored in this work.

As regard the operating conditions, in the experiment documentation [7, 17] the neutron flux and linear power data are supplied at times that are not in concordance with the times for the coolant condition (temperature and pressure) so that a supplementary processing of the data was necessarily. Also, the fast neutron flux requested as input data is not specified in refs [7, 17]. To skip this lack, a specific correlation for CANDU reactor was used:

*Fast neutron flux (n/cm^2 s) = 7.6 10^{10} *linear power (kW/m)*

However, a valid value is desired because the fast neutron flux affects the cladding material properties and these are important in the cladding deformation calculus.

In order to calculate the temperature at the outer surface of the cladding it must supply in the input data the coolant temperature and cladding-coolant heat transfer coefficient history. The last is mentioned in the test documentation [7] only for the short period of steady-state irradiation. For this reason the cladding-coolant heat transfer coefficient was calculated from the coolant temperature history assuming a constant temperature drop of 75°C in the coolant film. Again, this approach

affects all thermal calculus of the code and it is important to find a solution of this problem in the future for a correct simulation.

Concerning the options of model, for the steady-state irradiation were selected the models applicable to the CANDU type fuel as them were established in [9, IR-8964]. For the LOCA analysis the specific models and parameters, outlined in this work are as follows:

- the static model for the $\alpha - \beta$ crystallographic phase transition;

- all the three sets of parameters in the steam oxidation model applicable for zircaloy, taking into account the thinning of the cladding wall both in thermal and mechanical analysis were distinctly analyzed;

- the cladding outer surface corrosion in the steady-state irradiation was firstly avoided but, because the ZrO_2 thickness is dependent of the initial oxide thickness, a corresponding steady-state model was considered (EPRI/C-E/KWU [8]) with effect on both thermal and mechanical calculations;

- the cladding failure selected criterion is the one which checks concurrently the overstress criterion and the plastic instability criterion with overstrain assessment;

- the effective creep rate for the cladding plastic instability was the default value of 2%;

- the effective strain rate limit for cladding plastic instability was also the default value of 100 1/h;

- the limit value for the true tangential plastic strain is of 50%.

4.2 Results and comments

With the observations already discussed on the input options and on the fabrication and operating data, analysis of the FIO-131 experiment was performed with the TRANSURANUS code. Some aspects must be specified before to discuss the code results (Figs 4–6 and Table 1) against the experimental results.

So, only the first 64 seconds from the blowdown onset were simulated and in the graphic representations this is marked by a vertical dotted line named "End input data". For the remaining time up to 150 seconds, the simulations were made in the conditions of reactor normal shutdown in the last time step.

For comparison measured – calculated temperatures, the TRANSURANUS code results for the axial segment S4, which corresponds to the bottom centreline thermocouple position were used.

The evolution of the internal pressure during the second blowdown from the FIO-131 experiment, both measured and calculated with TRANSURANUS code, along with experimental values of the coolant pressure are shown in the Fig. 4. At the beginning of the depressurization (accident initiation), the calculus shows an increase of the internal pressure that is in contrast with the experimental observation.

A possible explanation of this situation can be the following: The internal pressure of the experimental fuel element was artificially increased, while operating in-situ just prior to the transient, to 8.14 MPa, by new gas injection. The temperature of the gas injected in the element to simulate the amount of fission gas pressure expected in high-burnup CANDU fuel is not specified in the test documentation but, it is more probable that it would be smaller than the gas temperature in the fuel

element gap during operation, what explain the experimental comportment. On the contrary, in the code simulation, in this point of the irradiation history, the gas from the internal void volume has a higher temperature than in the real case. This behaviour affects of course the fuel temperature calculus as it can see in the Figs. 5a and 5b.

Returning to the internal pressure, in Fig. 4 one can see that the aspect of the two curves (calculated and measured) is similar enough for the time period considered for the simulation. A remedy for the problem above pointed would be the use of the TRANSURANUS code feature for multiple restarts.

The temperature and pressure of the coolant are presented in the two Figs. 4 and 5 in order to emphasize on the one hand, the correctness of the input data, and on the other hand, the time period taken into consideration in the code simulation.

Regarding the temperature evaluation at the outer surface of cladding, as it was already mentioned, it is important to have valid values of the cladding-coolant heat transfer coefficient. In the prior paragraph it was sketched the manner of calculation of this coefficient when it is not given by the experimentalist. For the short period of steady-state irradiation from the beginning of the test, the values of this coefficient are known and the temperatures calculated for the cladding outer surface overlap on the experimental ones (Fig. 5c). Further, the calculated and measured curves for the outer surface temperature of the cladding have only a similar aspect.
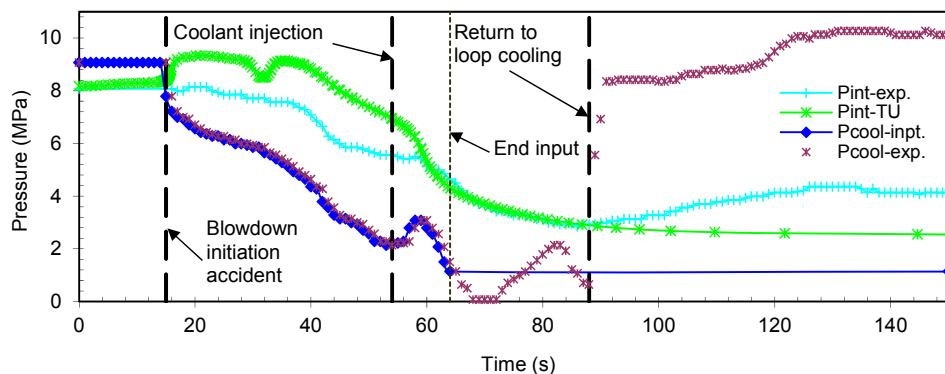

FIG. 4. Internal gas pressure and coolant pressure in the second blowdown in FIO-131 experiment.

The lack of the valid value of the coolant heat transfer coefficient can be avoided in the TRANSURANUS code if it is known in exchange, the evolution of the cladding outer surface temperature. This remedy would be applied in a further assessment.

For the fuel surface temperature there are not values properly measured in this location because the peripheral fuel thermocouples record the fuel temperature at a depth under the fuel outer surface, while the code furnishes exactly the fuel surface temperature. In this situation it is to be expected that the experimental values to be situated above the code results (Fig. 5b), due to the temperature gradient in this place of the fuel. Of course, the effective difference between the two curves is affected also by the difference between the temperatures on the outer surface of cladding, measured and calculated.
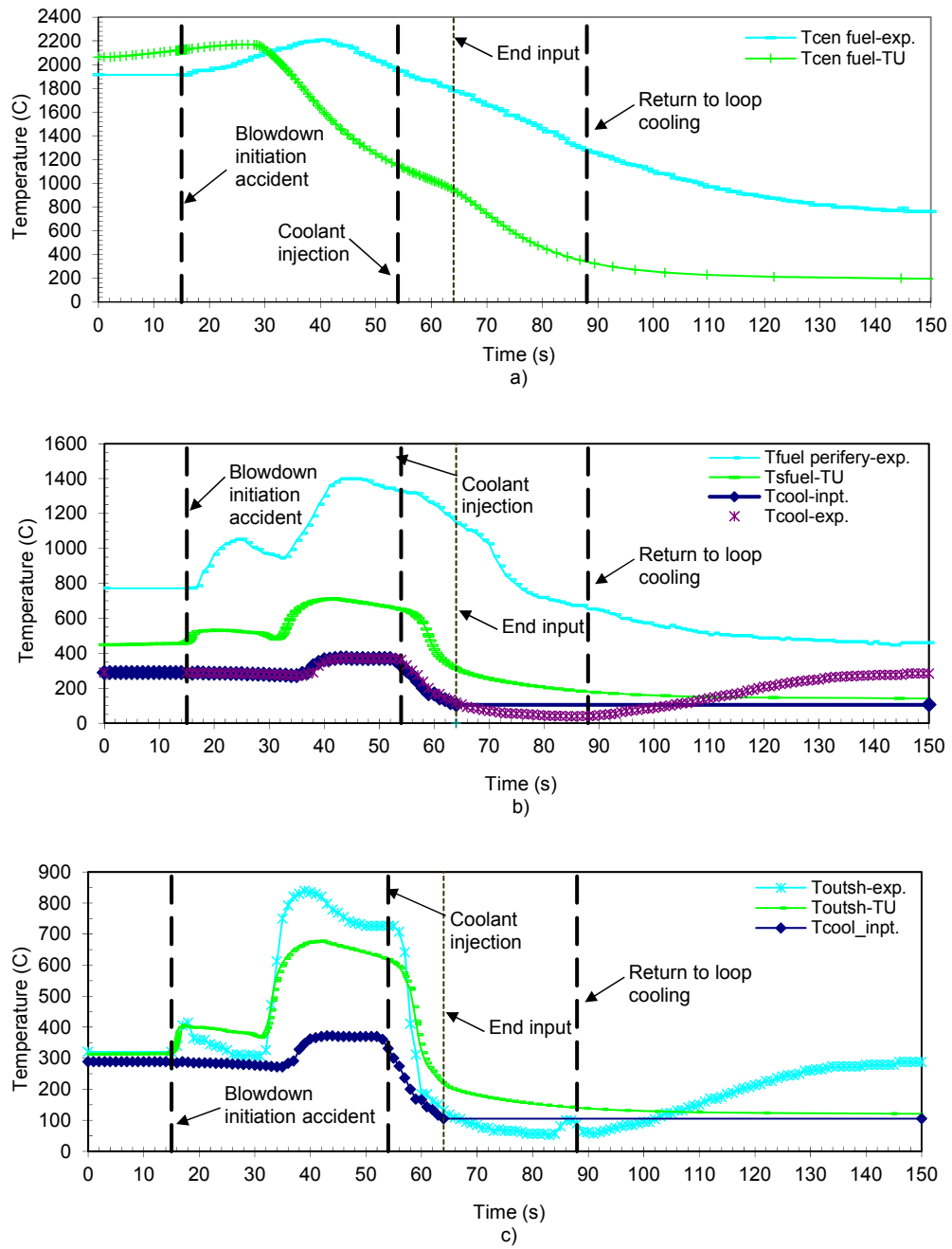
FIG.5. Temperatures evolution in the second blowdown in FIO-131 experiment: a) at fuel centre; b) at fuel perifery/outer surface; c) at cladding outer surface.
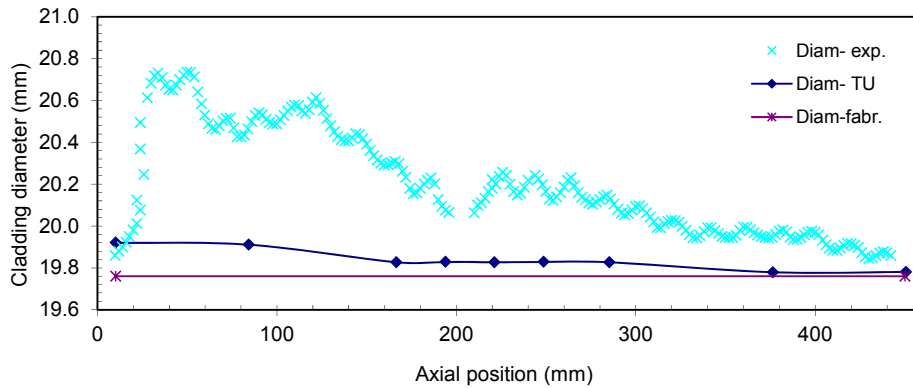
FIG.6. Axial profile of the cladding outer diameter in the second blowdown in FIO-131 experiment.

The evolution of the fuel central temperature (Fig. 5a) must be analysed taking into account all previous discussions. It observes that the maximum calculated value is around the maximum measured value but it is recorded to the smaller times.

Another parameter taken into discussion in the analysis of the fuel element performance is the axial profile of the outer diameter of cladding. As it observes form Fig. 6, there are great differences between the measured and calculated values, the code results being much under the post-irradiation measurements. However, a certain similarity of the two curve aspect can be observed.

To have a comparison term for the small calculated values of this parameter, in Fig. 6 is also drawn a line corresponding to the cladding diameter as fabrication. It is generally known that the cladding material properties are affected by the fast neutron flux during irradiation but these are implied in the cladding deformation calculus. Unfortunately the value of this parameter is not specified in the documentation of the FIO-131 irradiation experiment and a supposed value was used in the simulation.

In a LOCA analysis, the knowledge of the corrosion at the outside of cladding is an important issue. The corrosion degree of cladding can be expressed by either the thickness of the oxide layer, or the oxygen mass gain of the cladding material. In FIO-131 experiment, the oxide layer thickness in many axial points of the element cladding was post-irradiation measured.

In TRANSURANUS code are implemented three sets of parameters for the steam oxidation model applicable for zircaloy, and for steady-state irradiation the code offers the possibility to take or not into account the cladding oxidation. In this situation, the code was run for combinations of these model options as it is specified in Table 1. In this table it can be seen the code results along with the experimental measurements. All calculated values under estimate the measurements but they present a more accentuated tendency of corrosion at the bottom of the element as in experiment.

Concerning the under prediction both of cladding strain and of oxide layer thickness at cladding outside, by the TRANSURANUS code, some remarks must be done:

- the two performance parameters are measured post-irradiation while the calculation was performed only for the first 64 seconds from the blowdown onset, without the cooling recovery

period which range up to 150 seconds, so that the comparison measured-calculated values is not exactly correct but only qualitative;

- the two performance parameters are temperature dependent and the cladding temperature was under predicted as showed above.

TABLE 1. AXIAL PROFILE OF THE CLADDING OUTER SURFACE CORROSION IN FIO-131 IRRADIATION EXPERIMENT

| | ZrO$_2$ thickness (microns) | | | | | | | | | Corros. |
| | | | | | | | | | | * option |
	S1 (bott.)	S2	S3	S4	S5	S6	S7	S8	S9 (top)	SS+LOCA
Experiment	4 - 8	4 - 8	4	4	4	4	4	1 - 2	1 - 2	
	0.57	0.56	0.40	0.41	0.40	0.41	0.40	0.26	0.26	0+a
	0.71	0.70	0.57	0.57	0.57	0.57	0.57	0.45	0.45	1+a
TRANSURANUS	0.19	0.19	0.13	0.13	0.13	0.13	0.13	0.08	0.08	0+b
	0.47	0.47	0.42	0.42	0.42	0.42	0.42	0.37	0.37	1+b
	0.31	0.31	0.21	0.21	0.21	0.21	0.21	0.12	0.12	0+c
	0.53	0.53	0.45	0.45	0.45	0.45	0.45	0.38	0.38	1+c

* SS+LOCA - Steady-state and LOCA options for zircaloy cladding corrosion:
0 - SS corrosion is not considered,
1 - SS corrosion is considered (EPRI/C-E/KWU [8] model with thermal and mechanical effect),
a - Cathcart-Pawel [13] corrosion correlation with continuous thinning of cladding wall,
b - Leistikow [13] corrosion correlation with continuous thinning of cladding wall,
c - Baker-Just [14] corrosion correlation with continuous thinning of cladding wall

5. CONCLUSIONS

This work is a first attempt to use the TRANSURANUS code [8] to simulate a CANDU fuel element operating in normal conditions followed by high-temperature transient conditions associated with the onset of a LOCA. The experiment FIO-131 [7, 17] selected for simulation was performed at the Chalk River Laboratories, Canada in 1983, as part of an experimental program with the aim to provide quantitative code verification data.

To do this application some aspects regarding the consequences of a LOCA on the fuel element behaviour were summarized, followed by an outline of the LOCA modelling in TRANSURANUS code. A good simulation implies a detailed knowledge of the experiment as well as of the tool used for simulation. For that reason the FIO-131 experiment was also enough detailed presented based on the public information from ref. [7].

Comparisons between calculations and measurements can be resumed as follows:

- The fuel element survived the LOCA transient without experiencing cladding rupture and the TRANSURANUS code registered also no cladding failure message.

- Good agreement was found between measured maximum centreline temperature and the calculated by TRANSURANUS.
- Good qualitative results were obtained for the cladding outer surface temperature, fuel surface temperature, outer cladding diameter and thickness of the oxide layer outside cladding.
- Justifications for the quantitative differences registered versus the experimental measurements were discussed and corresponding remedies were suggested:
- Utilization of the TRANSURANUS code feature to support multiple restarts was found as solution to improve the calculation of the internal pressure and fuel temperatures.
- Avoidance the calculation of the cladding outer surface temperature when a valid value for the cladding-coolant heat transfer coefficient is not available is possible by supplying direct the temperature history for the cladding outer surface in the TRANSURANUS code input data.
- Finding either a valid evolution history for the fast neutron flux specific to the experimental irradiation conditions or an appropriate correlation for its calculation is recommended in order to obtain better results for cladding behaviour.
- Correction of the linear power history to take into calculation the lack of the material from all fuel pellets holes requested for element instrumentation, that are not exactly considered in evaluation with the code, can lead to an improvement of temperature prediction.
- Extension of the LOCA simulated history with the cooling recovery time period, i.e. up to 150 seconds total time of simulation must be done to obtain calculated values pertinent for comparison with post-irradiation measurements.

REFERENCES

[1] NUCLEAR REGULATORY COMMISSION, Acceptance criteria for emergency core cooling systems for light-water nuclear power reactors, 10 CFR 50.46, US Govt Printing Office, Washington, DC (1983).

[2] NAGASE, F., Fuel Safety Research at JAEA, paper presented at IAEA Technical Meeting on Fuel Behaviour and Modelling under Severe Transient and LOCA Conditions, Mito city, Ibaraki-ken, Japan, 18–21 October 2011.

[3] WIESENACK, W., KOLSTAD, E., Fuel Behaviour under Accident Conditions, IAEA Regional Workshop on Fuel Safety and Reliability, Kiev, Ukraine, 15–17 Nov. 2006.

[4] PETIT, M., GRANDJEAN, C., TREGOURES, N., BARE, F. and GIORDANO, P., IRSN R&D Studies on Fuel Behaviour under LOCA Conditions, paper presented at IAEA Technical Meeting on Fuel Behaviour and Modelling under Severe Transient and LOCA Conditions, Mito city, Ibaraki-ken, Japan, 18–21 October 2011.

[5] OECD NUCLEAR ENERGY AGENCY, Nuclear Fuel Behaviour in Loss-of-coolant Accident (LOCA) Conditions, State-of-the-art Report, Sect. 2.4 CANDU reactor LOCA, OECD/NEA No. 6846, 2009.

[6] F. J. DORIA, Atomic Energy of Canada Limited, CANDU Safety #12: Large Loss of Coolant Accident.ppt, Rev. 0, 24 May 2001.

[7] OECD/NEA-IFPE Database (IFPE/CANDU-FIO-131 NEA-1783/01).

[8] K. LASSMANN, J. VAN DE LAAR, TRANSURANUS Handbook, V1M1J03, European Commission, Joint Research Centre, Institute for Transuranium Elements, Karlsruhe, Germany, 2003.

[9]   A.PARASCHIV, INR-IR-7038 (2004), -7355 (2005), -7659 (2006), -7947 (2007), -8964 (2010).

[10] A.PARASCHIV, Applicability study of TRANSURANUS code to CANDU fuel, TRANSURANUS Workshop, Prague, Czech Republic, 23–24 June 2005.

[11] A.PARASCHIV, Recent results of the appliance of the TRANSURANUS code to CANDU fuel, TRANSURANUS Workshop, Karlsruhe, Germany, 25–26 June 2007.

[12] A.PARASCHIV, Application of the TRANSURANUS code to CANDU fuel behavior analyses, TRANSURANUS Workshop, Hannover, Germany, 12–13 April 2011.

[13] G. SCHANZ, Recommendations and Supporting Information on the Choice of Zirconium Oxidation Models in Severe Accident Codes; FZKA 6827, SAM-COLOSSP043, FZK Karlsruhe, 2003.

[14] L. BAKER, JR. AND L.C. JUST, Studies of Metal Water Reactions at High Temperature: III. Experimental and Theoretical Studies of Zirconium-Water Reaction, ANL 6548, Argonne National Laboratory, May 1962.

[15] T. FORGERON *et al.*, Experiment and Modeling of Advanced Fuel Rod Cladding Behavior Under LOCA Conditions: Aplha-Beta Phase Transformation Kinetics and EDGAR Methodology, Zirconium in the Nuclear Industry, 12th Symposium, ASTM STP 1354 (2000).

[16] F. J. ERBACHER *et al.*: Burst Criterion of Zircaloy Fuel Claddings in a Loss-of-Coolant Accident, Zirconium in the Nuclear Industry, 5th Symposium, ASTM STP 754 (1982).

[17] P.J. FEHRENBACH, J.A. WALSWORTH et al., In-Reactor Test of Zircaloy-Sheathed UO2 Fuel at Chalk River, Proceedings of the Canadian Nuclear Society 6th Annual Conference, June 1985.

MODELLING OF SEVERE ACCIDENTS AND EXPERIMENTAL SUPPORT

(Session 3)

Chairperson

J. Stuckert

Germany

INVESTIGATION OF VVER 1000 FUEL BEHAVIOR IN SEVERE ACCIDENT CONDITION

GROUDEV P., STEFANOVA A., GENCHEVA R.
Institute for Nuclear Research and Nuclear Energy,
Bulgarian Academy of Sciences,
Sofia, blvd.Tzarigradskoshaussee 72

Abstract. This paper presents the results obtained during a simulation of fuel behavior with the MELCOR computer code in case of severe accident for the VVER reactor core. The work is focused on investigating the influence of some important parameters, such as porosity, on fuel behavior starting from oxidation of the fuel cladding, fusion product release in the primary circuit after rupture of the fuel cladding, melting of the fuel and reactor core internals and its further relocation to the bottom of the reactor vessel. In the analyses are modeled options for blockage of melt and debris during its relocation. In the work is investigated the uncertainty margin of reactor vessel failure based on modeling of the reactor core and an investigation of its behavior. This is achieved by performing sensitivity analyses for VVER 1000 reactor core with gadolinium fuel type. The paper presents part of the work performed at the Institute for Nuclear Research and Nuclear Energy (INRNE) in the frame of severe accident research.

The performed work continues the effort in the modeling of fuel behavior during severe accidents such as Station Blackout sequence for VVER 1000 reactors based on parametric study. The work is oriented towards the investigation of fuel behavior during severe accident conditions starting from the initial phase of fuel damaging through melting and relocation of fuel elements and reactor internals until the late in-vessel phase, when melt and debris are relocated almost entirely on the bottom head of the reactor vessel. The received results can be used in support of PSA2 as well as in support of analytical validation of Sever Accident Management Guidance for VVER 1000 reactors. The main objectives of this work area better understanding of fuel behavior during severe accident conditions as well as plant response in such situations.

1. PURPOSE OF THE INVESTIGATION

The main purpose of this investigation is to analyze the influence of porosity on accident progression study of fuel behavior during a severe accident starting from core uncovering, fuel heat-up, hydrogen generation and rupture of fuel cladding, followed by core degradation, melted pool formation, relocation of fuel and other core materials to the reactor vessel lower head. The analyses are performed until failure of reactor vessel which causes corium injection to the cavity. The main attention during this study is focused on the influence of porosity on core degradation and the relocation of fuel and other internal materials.

In the report is also included a study of the influence of quenching on overheated reactor core at different core exit temperatures. For this purpose an SBO scenario was simulated with injection of cold water by high pressure pump in cold leg (quenching from the bottom of reactor core) at different core exit temperatures from 1200°C to 1500°C. In this way is investigated the response of the reactor core on quenching. The selected approach allows the observing of bigger damaging of reactor core during earlier quenching versus quenching at a higher temperature. In the presentation is given an explanation on the observed behavior of the reactor core.

The presented analysis of fuel behavior during severe accident conditions was performed with a MELCOR 1.8.5 computer code for severe accident analyses. The calculations were performed for "station blackout scenario with failure of pressurizer safety valve in open position". To investigate the severe accident management guidance were simulated also operator actions in some of the scenarios. The purpose of these analyses is to examine the possibility of keeping the

core from further damage during a severe accident and to assess the likelihood of additional generation of hydrogen by additional flooding of the heated core.

In the presented report are discussed the reactor core degradation with a subsequent relocation of debris on the bottom of a lower head, as well as the generated hydrogen.

2. BRIEF DESCRIPTION OF VVER 1000 NUCLEAR POWER PLANT

The nuclear reactor under consideration in this analysis is a typical VVER 1000 reactor, V-320 model with four primary coolant loops, each one including a main coolant pump (MCP) and a horizontal U-tube steam generator (SG). The thermal power of the reactor core is 3000 MW. The steam generators are fed by two different feed water systems. Each system consists of turbine-driven pumps and piping connecting to the feed water line at four different locations in each SG. All elements of the primary side are situated in a steel-lined, cylindrical, concrete containment building. The generated steam by all four SGs is transferred to one turbine with electrical power of 1000MW. All systems included in the plant are classified as follows:

Systems for normal operations in primary circuit are: reactor, main circulation pipes, steam generators, pressurizer system, makeup/letdown system, bypass purification system and others;

Systems for normal operations in secondary side are: steam lines, feed water system, and others.

Safety systems are divided in four groups - protection, localization, support and control systems presented below:

- protection systems: control rods, hydro accumulators, high pressure injection systems, low pressure injection systems, primary and secondary protection from over pressurization, emergency gas evacuation system;
- localization systems: containment, containment spray system, isolation valves.
- support systems: reliable electrical supply, service water systems and others;
- control systems: programs of ASSS, main and emergency control rooms, system of sensors and logic for safety systems control during reactor operation.

3. SHORT DESCRIPTION OF MELCOR 1.8.5 COMPUTER CODE

The MELCOR 1.8.5 computer code is a fully integrated, relatively fast running code that models the progression of severe accidents in the light water reactor nuclear power plants (NPP) and other NPPs. A huge spectrum of severe accident phenomena is modeled by MELCOR, based on the requirements of NPP safety. Some important characteristics of severe accident progression that can be treated with MELCOR are as follows:

- The thermal-hydraulic behaviour in the reactor coolant system, containment building, reactor cavity;
- The impact of engineered safety features on thermal-hydraulic;
- Core heat up and degradation; radionuclide release and transport;
- Hydrogen production, transport, and combustion;
- Core-concrete attack;
- Heat-structure behavior;
- Radionuclide behavior in containment.

The MELCOR code structure is built on separated packages. Most of them require a specific input because they model a specific part of the accident physical phenomena. The control volume hydrodynamics (CVH) package calculates the thermal/hydraulics of the control volume including one-phase or two-phase flow. The Heat Structure (HS) package models heat transfer structures such as walls, bottoms, ceilings. The flow path (FL) package models in conjunction with the CVH package. The FL package can simulate equipment as valves, check valves and pumps. The control function (CF) package evaluates user-specified system of functions that controls opening/closing valves; controlling plot writing, defining plot variables, etc.

The other packages can be divided into two groups. The first group represents phenomenological packages and the second group represents support packages.

The latest versions of the code are characterized by an increase in the internal arrays in order to calculate more detailed plant structures.

Further description of MELCOR is given in the presentation of VVER 1000 model for MELCOR.

4.   SHORT DESCRIPTION OF VVER 1000 MODEL FOR MELCOR 1.8.5

To assess the behavior of the investigated parameters of the "Station blackout" scenario is used a MELCOR 1.8.5 "input model" for Kozloduy NPP units 5 and 6 with VVER-1000 reactors. The model describing the VVER-1000 was developed and validated by the Institute for Nuclear Research and Nuclear Energy.

In the MELCOR "input model" of VVER-1000, the primary system (Fig. 1) has been modeled using two coolant loops representing the four reactor loops (unique loop and common loop, which includes three grouped loops) each one including an MCP and a horizontal SG. The reactor core has been presented by three radial rings and 10 axial levels for fuel part presented in detail below. The lower volume has five axial levels. COR package has been used to simulate the heat up, degradation and relocation of the reactor core.

The VVER 1000 model for MELCOR provides a detailed representation of the primary, secondary, and safety systems as well as containment. This model was defined to include all major systems of KNPP Units 5&6 namely reactor core, reactor vessel, PRz, main coolant pumps (MCP), steam generator (SG), steam lines and main steam header (MSH), emergency protection systems, pressure control system of the primary and secondary circuits, safety injection system low pressure pumps (LPP), high pressure pumps (HPP) and hydro-accumulators (HAs), steam dumping device to atmosphere (BRU-A), reactor cavity and main containment rooms. Also, the containment sprays system (CSS) and passive autocatalytic recombiners (PARs) have been modeled.

The hydrodynamic processes in the reactor vessel are modeled by means of tencontrol volumes (CVH). The geometry of the control volumes is taken into account by setting the elevation of change of free volume elements. Lower mixing chamber is modeled also by a CVH. Hydrodynamics of the reactor core is represented by 5 control volumes, which relate to the fuel part of the core. The upper mixing chamber of the reactor and the space under the upper cover head of the reactor vessel are modeled with two control volumes.

The total volume of coolant in the reactor vessel is 110 m^3. The coolant volume from inlet nozzles to the entrance in reactor core is 34 m^3. This section was modeled using control volumes CV 010, CV 020 and the first sub - volume of a control volume CV 030, (common for them is that there is no change in the density and the temperature of the coolant).

The lower mixing chamber is modeled by a control volume CV 020 and is subdivided into 5 sub volumes.

The thermal-hydraulic behavior in the reactor core area is modeled using the following control volumes: the sub-volumes of a control volume CV030, control volumes CV032, CV034, CV036 and CV038. The total volume of coolant in the active part of the reactor core with fuel is 14.8 m3. In the reactor core area there is an increase in temperature by 30 ˚C, which causes a decrease in the coolant density. The geometry of hydrodynamic elements is taken into account by setting the elevation of change of free volume elements.

FIG. 1. Discretization scheme of a primary circuit.

The space above the active part of the reactor core (including the head of assemblies) is modeled with control volume CV040.

The upper mixing chamber of the reactor and the space under the reactor cover head are modeled with two controlvolumesCV050 and CV060. The total volume of coolant above the active part of core is 61.2 m^3.

Fluid flow connections between the elements of the reactor are modeled by the actual geometry (diameter, length, etc.) and the adjacent components, and the respective coefficients of local resistance.

The four hydraulic accumulators are represented by two control volumes.

In the modeling of heat structures of the reactor vessel and the internals are taken into account the actual geometries, the composition of the structures, and also the relevant thermo physical properties of the materials of the structure according to the material temperature.

For the modeling of reactor core processes such as warming-up, melting, destruction and relocation of core materials is used COR package. The core is divided into 18 axial portions and 3 radial rings (Fig. 2). Core in this case has a wide meaning and includes additional elements positioned immediately below it: the supporting plate of the reactor core bottom and bottom of the reactor shaft. The numbering of the segments is from the bottom up. Each cell can contain one or more components. Possible components are: fuel tablets, cladding, "other structures" (control tube, grid, etc.).

First radial ring of the reactor core includes 37 fuel assemblies, 13 of them have control rods. Second core radial ring includes 54 fuel assemblies, 30 of which are assemblies control rods and third radial ring consists of 72 fuel assemblies, 18 of which are assemblies with control rods.

In the modeling of the core composition (qualitative and quantitative) are recorded all components (as well as the fact that , the fuel assembly comprises fuel rods of a zirconium shell , fuel tablets of uranium dioxide, spacer grids made of stainless steel , the central tube of alloy of zirconium , tails and heads of assemblies stainless steel , etc.). All the characteristics of the core components (geometry, thermo-physical characteristics, qualitative and quantitative composition of the components) are adopted on the basis of Kozloduy NPP data.
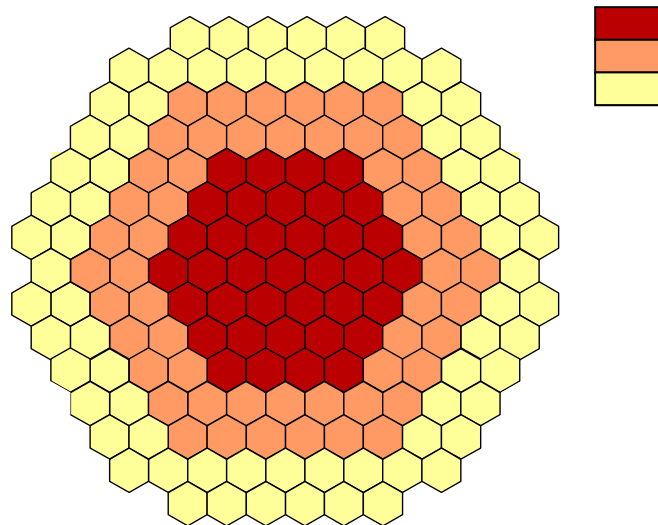
FIG. 2. Radial modeling of core.

The bottom head has been modeled using three radial rings and five axial layers. The first (internal) layer simulates stainless steel and the other four layers simulate carbon steel corresponding to the actual vessel bottom composition.

To represent the hexagonal fuel assemblies with triangulate grid using MELCOR's rectangular assemblies have been used sensitivity coefficients SC1151 (1÷4).

The radial distribution of energy release in the core is adopted in accordance with the data for the end of the fuel cycle.

The total mass of the fuel in the core 80 098.2 kg is distributed in proportion to the 10 axial levels from axial level 7 to axial level 16.The fuel is distributed in the radial rings as follows:

- Mass of fuel in one assembly = 312 x 1.575 = 491.4 kg;
- Mass of fuel in 37 assemblies = 37 x 491.4 = 18181.8kg- first ring;
- Mass of fuel in 54 assemblies = 54 x 491.4 = 26535.6kg- second ring;
- Mass of fuel in 72 assemblies = 72 x 491.4 = 353 80.8 kg- third ring.

4.1 Initial and boundary conditions

The main initial parameters used in the calculations versus KNPP design values are presented below in Table1.

TABLE 1. INITIAL CONDITIONS

Parameters	Design Value	MELCOR Value
Core power, MW	3000	3000
Primary pressure, MPa	15.7	15.8
Average coolant temperature at reactor outlet, °C	320.15	319
Maximum coolant temperature at reactor inlet, °C	290	289
Mass flow rate through one loop, kg/s	4400	4430
Pressure in SG, MPa	6.27	6.35
Pressure in MSH, MPa	6.08	6.10
Steam mass flow rate through SG, kg/s	408	410

The main assumptions are presented in Table 2.

TABLE 2. INITIAL AND BOUNDARY CONDITIONS

Initial and boundary conditions		
Parameters	**Value**	**Explanation**
Reactor power	100%	Nominal power
Steam generator water level	2400 mm	Nominal level at 100% reactor power
Decay power	End of life	maximal
Boundary Equipment Failure		
Failure of all DG	Loss of reactor core cooling;	
Failure of auxiliary DG		
Systems important for safety operation	Failure of ECCS HP and LP; Failure of Spray system; One HPP will be available after DG is available, for scenarios with operator action.	
	SVs of PRz are available and support primary side pressure; Gas removing system YR line is available.	
Failure of BRU-A	SVs of SG are available.	
After opening of Pressurizer SV (Sempell) at its set point starts to cycle and stuck in fully open position at 650 °C core exit temperature (for scenarios without operator actions).	Simulation of small break LOCA through Pressurizer - higher generation of hydrogen is expected.	
For scenarios with operator actions - operator open PRz SV at 650 °C and start to inject water with HPP at different core exit temperature.	Examination of SAMG strategy with primary depressurization.	
Failure of Emergency Feed Water (EFWP) pumps after DG is available.	Dry out of SGs at natural circulation and Loss of heat sink.	
Safety important system.	Hydro accumulators are available.	
MCPs seal leakages are not taken into account.	Loss of coolant is minimized, but removal of heat from primary side is also minimized.	

The following SBO Scenarios have been used:
- As a starting point (0.0 sec) is considered a complete loss of external power and a failure of the diesel generators in all three safety systems;
- Loss of MCPs;
- Reactor SCRAM;
- Loss of Makeup /Letdown system;
- Isolating of Turbo – Generator;
- Opening of SV of SGs;
- Dryout of SGs;
- Opening of PRz SV.

Based on this scenario have been calculated four cases using different values of porosity and the influence of this parameter on the progression of the accident has been analyzed. For one value of porosity have been conducted three additional calculations with operator actions. The observed phenomena and results have been discussed.

4.2 Discussion of results

The first set of analyses includes four calculations using different values of porosity (of debris bed):

PORDP = 0.1; 0.2; 0.3; 0.4;

After the initiation of Station Blackout the main coolant pumps stop and it causes the initiation of reactor SCRAM. Decay heat is removed from the core by natural circulation. Decay heat is transferred to the secondary side and removed via "steam dump" to the atmosphere by Steam Generator (SG) Safety Valves (SV). The secondary pressure oscillates between the opening and closing pressure thresholds of the Steam Dump to Atmosphere (SDA). As a consequence, the primary pressure is also oscillating according to the secondary pressure. The primary pressure essentially increases after SGs are not effective and Pressurizer safety valve opens at its set point and is stuck in fully open position at 650 oC core exit temperature. The primary pressure starts to decrease rapidly due to loss of coolant through the safety valve. Losing of coolant and flashing due to the decrease in primary pressure cause an uncovering of the reactor core. Heat up of the reactor core initiates a steam zirconium reaction with production of a huge volume of hydrogen and additional heat, which causes a failure of the fuel cladding and radionuclide release.

After reaching a set point of the hydro accumulator's initiation, they start to inject water in down comer and the upper volume of the reactor vessel.

There are two processes that contradict each other: on one side there is a heat up of reactor core and cool down of core by injection of water from HA. If the injected water is not enough for a successful cooling there is an observed flashing of injected water and this way increases the primary pressure and not allowing further injection of water for some period of time. So, if depressurization is not enough to allow successful cooling there will be damaging of the reactor core, melting, relocation and failure of the reactor pressure vessel, before depletion of HA water.

The list with main events is presented in Tables 3.

TABLE 3. MAIN EVENTS

No	Events	POR 0.1	POR 0.2	POR 0.3	POR 0.4
		Time, s			
1	Loss of all AC and DC power sources	0.0	0.0	0.0	0.0
2	MCPs are switched off	0.0	0.0	0.0	0.0
3	Makeup/Letdown switch off	0.0	0.0	0.0	0.0
4	Actuation of Reactor SCRAM	1.6	1.6	1.6	1.6
5	The TG valves are closed	11.6	11.6	11.6	11.6
6	First opening PRz SV and stay in open position	6899.0	6899.0	6899.0	6899.0
7	Beginning of hydrogen generation	10 715	10 715	10 715	10 715
8	Beginning of total core uncovering	11 220	11 220	11 220	11 220
9	First cladding rupture	11 507	11 507	11 507	11 507
10	First slump of corium in lower plenum	11 495	11 757	11 736	11 700
11	Start of HA water injection	12 016	12 016	12 016	12 016
12	End of HA injection	20 829	26 998	27 396	26 579
13	Failure of reactor vessel	43 848	68 212	77 498	85 960
14	End of calculation	100 000	100 000	100 000	100 000

The behavior of the main parameters is presented in Fig. 3 to Fig. 6. The behavior of the primary circuit pressure is presented in Fig. 3. As it is seen after reaching the set points of opening of PRz SV, in all cases is observed a rapid decrease in pressure. The observed fluctuations between 18 000 sec and 30 000 sec are explained with slumps of corium on the bottom head and the work of HA.

In the case with porosity = 0.1 is observed a significantly earlier failure of the reactor vessel. It can be explained using the results in Fig. 6, where the behavior of total mass of corium on the bottom head is presented. As it is seen in the first case of the calculations there is a smaller mass of corium compared to the other three cases. In all cases was observed almost simultaneously the beginning of relocation of debris on the bottom head. The main difference is that in the calculations with porosity of 0.2 and higher is observed a relocation of more mass of corium, which causes a production of significantly more steam. The produced steam from the bottom head goes up and cools down the core not allowing the melting of the core for a while.
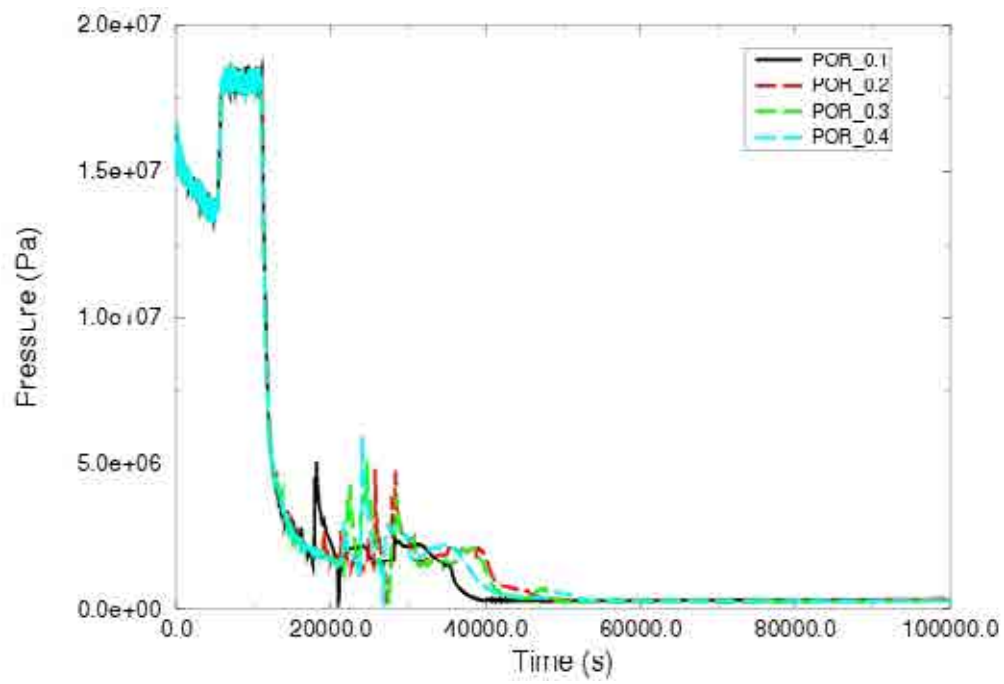
FIG. 3. Primary pressure.
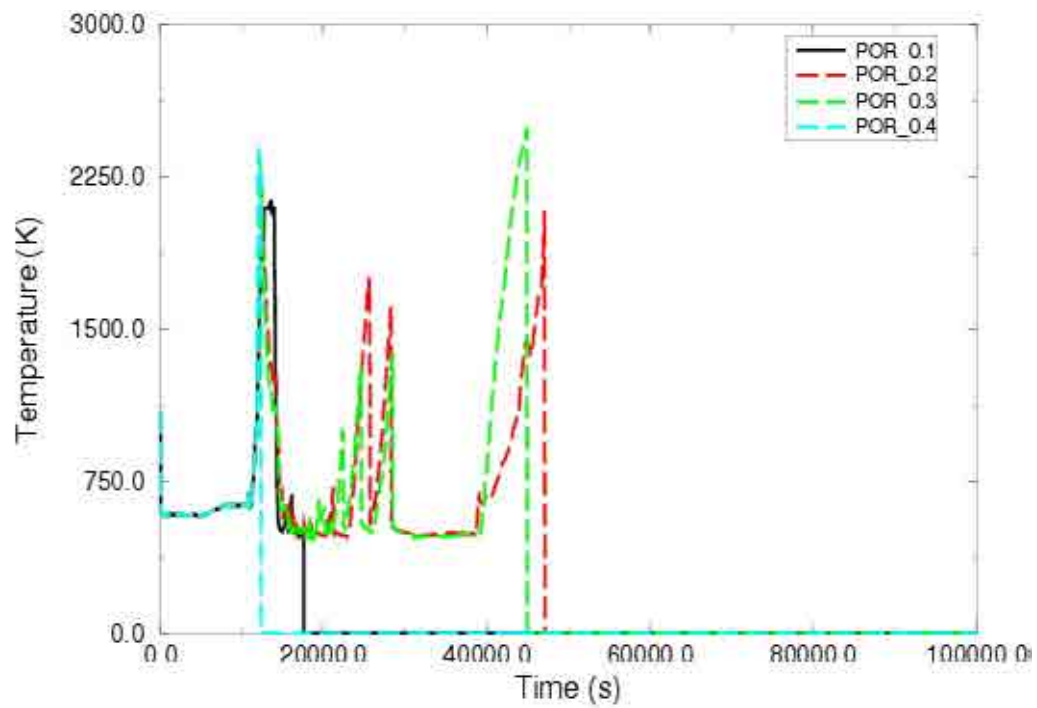
FIG. 4. Fuel Temperature at ring 1 – axial level 08.
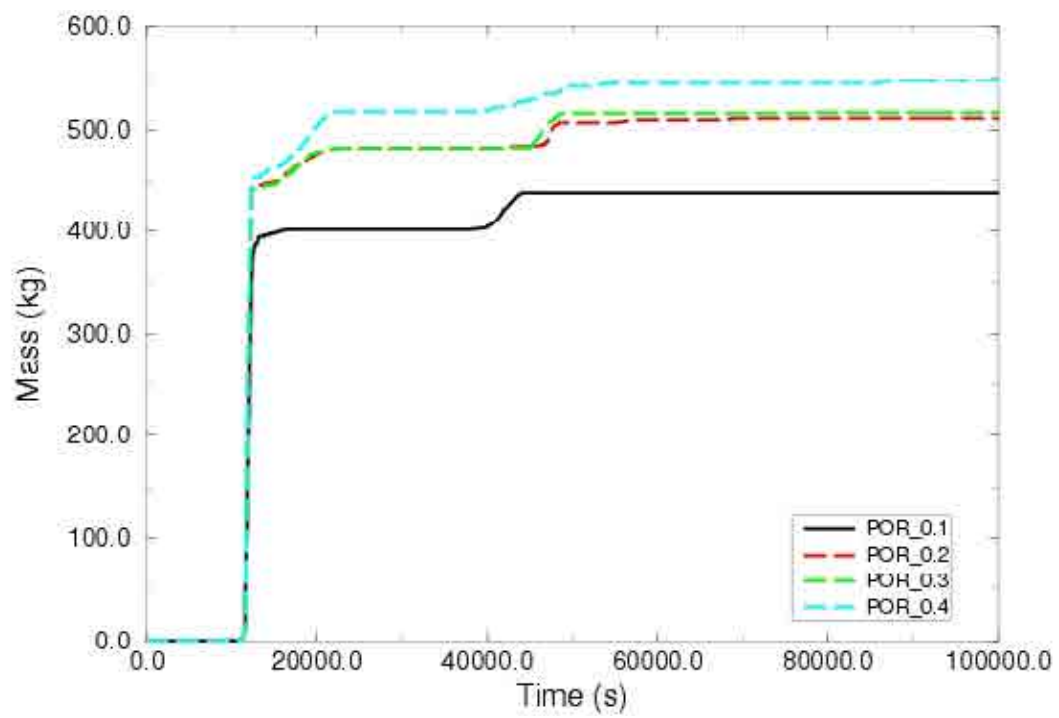
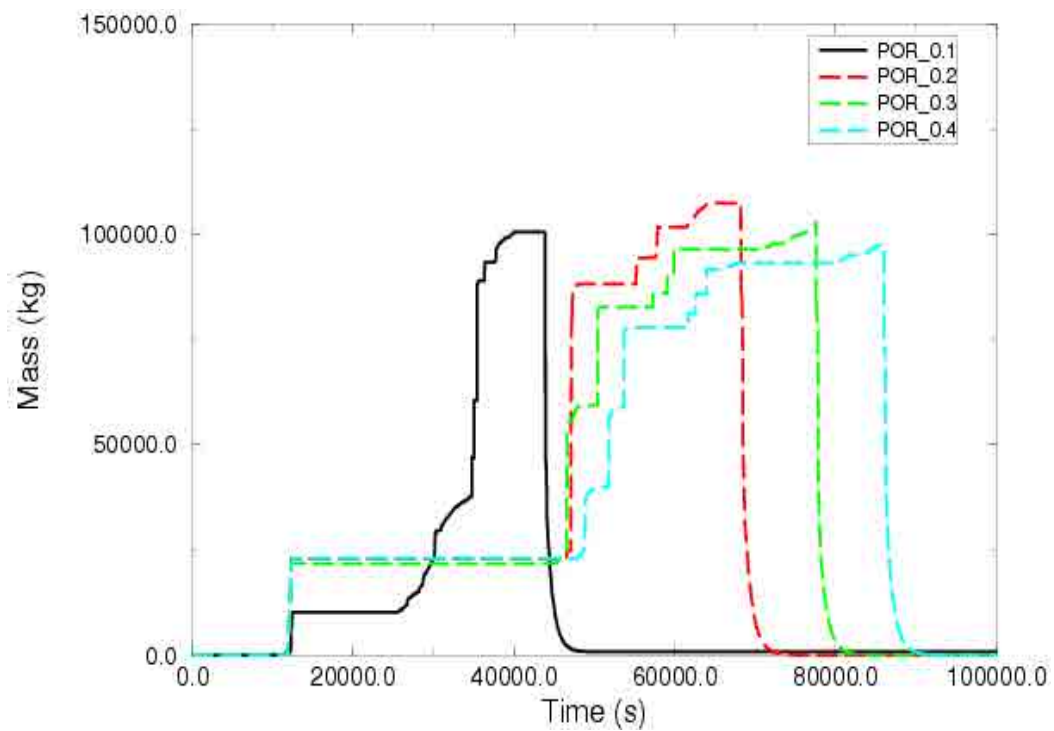*FIG. 5.Total hydrogen generation during in vessel phase.*

FIG. 6. Total mass of corium on the bottom head.

Using the same scenario and involving operator actions based on the severe accident management guidance, has also been studied the influence of injection of cold water on overheated reactor core at different core exit temperatures. For this purpose was simulated an SBO scenario with injection of cold water by high pressure pump in cold leg (quenching from the bottom of reactor core) at different core exit temperatures from 1200 °C to 1500 °C. The aim of the analysis is to track the evolution of the main parameters of the simulated accident. Particular attention is given to the validation of the operator strategy in the reduction of primary pressure and the injection of water in the overheated core. Because of that, was taken a decision to investigate the strategy from the moment of entrance in Severe Accident Management Guidance (SAMG), which will happen at 650°C (923°K). After that moment are investigated different options for quenching of reactor core using HPP at different core exit temperatures. Three analyses have been performed with injection of water at 1200°C, 1300°C and 1500°C. The same model with porosity PORDP = 0.1 has been used.

The calculated results are presented in Table 4, where progressions of the accident for three cases are compared.

TABLE 4. COMPARISON OF CORE QUENCHING

List of events	Reactor core quenching		
	at 1200 °C	at 1300 °C	at 1500 °C
	Time, sec		
Loss of all AC and DC power	0.0	0.0	0.0
MCPs are switched off	0.0	0.0	0.0
Pressurizer heaters are switched off	0.0	0.0	0.0
Actuation of Reactor SCRAM	1.6	1.6	1.6
Makeup/Letdown system is switched off	2.0	2.0	2.0
Stop of FWP	5.0	5.0	5.0
Closing of TSV	11.6	11.6	11.6
First opening of SG SV.	20.0	20.0	20.0
First opening of Pressurizer SV	6899	6899	6899
Beginning of hydrogen generation	10 735	10 735	10 735
Opening of YR line of PRz upon reaching 923 K (650 °C) – operator action	11 010	11 010	110 101
Starting of HPP	11 530	11 742	11 840
First slump of corium in lower plenum.	11 770	11 770	11 770
Beginning of HA injection	11 930	11 930	11 840
End of work of HA	N/A	N/A	N/A

List of events	Reactor core quenching		
	at 1200 °C	at 1300 °C	at 1500 °C
	Time, sec		
Reactor vessel failure.	N/A	N/A	N/A
End of calculation	≈24 400	≈19 500	≈24 700

The results of the calculations for the "station blackout "accident with operator actions are presented in Fig. 7–15. The behavior of the pressure in the primary circuit is shown in Fig. 7. Reliable cooling of the reactor core at the beginning of the accident is provided by the inertial rotation of the main circulation pumps (MCP) and after their final stop from the natural circulation of the coolant, which is observed to about 8500 sec. The energy generated in the core is removed from the steam generators SVs reliably so far as they lose much of the coolant in the secondary circuit and become ineffective up to 5 300 sec. This leads to primary pressure increase and reaching the value for PRz safety valve opening. So, the SV begins to open and close after 6899 sec, thereby maintaining the pressure in the primary circuit and bringing decay. As a result of the loss of coolant from the primary circuit, the core is partially uncovered and begins warming the core. The operator decides to reduce the pressure in the primary circuit by means of the YR line by opening its valve, resulting in a sharp pressure drop around 11 010 sec. As a result of pressure reduction the SV of PRz is closed. After reaching 5.88 MPa at 12 060 sec the hydro accumulators (HA) start and begin to flood the core. As a result of the fact that the core at that time is overheated, the injected water from HA is evaporated immediately and causes the increase in pressure and stops the injection by the HAs and in this way the efficient core cooling is lost.

The choice of a high pressure pump is made because the high pressure pump might be used in a much wider range starting at 110 kg/cm2, and also has a smaller flow rate compared to the low pressure pump. It could cause a higher production of hydrogen.

These results clearly demonstrate that due to the relatively high flow rate, the injection of the core does not result in further hydrogen generation, which would endanger the environment in the containment of flammability. Moreover, analyses with injection at 1500°C show that it is possible to save the core from significant damage. The behaviour of fuel temperature at rings 2 and 3 in case of HPP injection at 1200°C, 1300°C and 1500°C is presented in Figures 10 to 15. The temperature of the gas is used at the outlet of the core, which means that the value of the fuel temperature is higher. A partial relocalization of fuel flooding at 1300 °C, which is missing in the flooding at 1500°C could be explained by the sharp reduction in the pressure and then begins the injection of water from the HAs, which saves fuel. But in all three analyses there is only partial destruction, avoiding significant relocation of the fuel at the bottom of the reactor vessel.

When comparing the results it was observed that the flooding at 1300 °C has generated less hydrogen than the other two cases. This is precisely due to the reduction in relocation of the fuel that can be observed for a short time, after which the fuel temperature is lowered as a result of the filling of the reactor vessel and the restoration of the water level in the core, which does not allow for further destruction or relocation of the fuel.

Raising the temperature at the core exit over 1200 °C is an exponent, which leads to slight differences in the times of pump switching in the range of about 5 min from 11530 to 11870 sec. It is this proximity that makes the analysis difficult, although the core exit temperature is changed by 300°C.

It should be noted that the question of the destruction of the core and the relocation of the fuel is not sufficiently well known and there is a significant uncertainty. Despite the existing uncertainties it can be considered that the injection of water into the core of a VVER-1000 reactor with high pressure pump at temperatures exceeding 1200°C to 1500°C, will not result in the generation of additional amounts of hydrogen and even a partially damaged reactor core as a whole can be saved and a breakthrough the reactor vessel can be prevented.
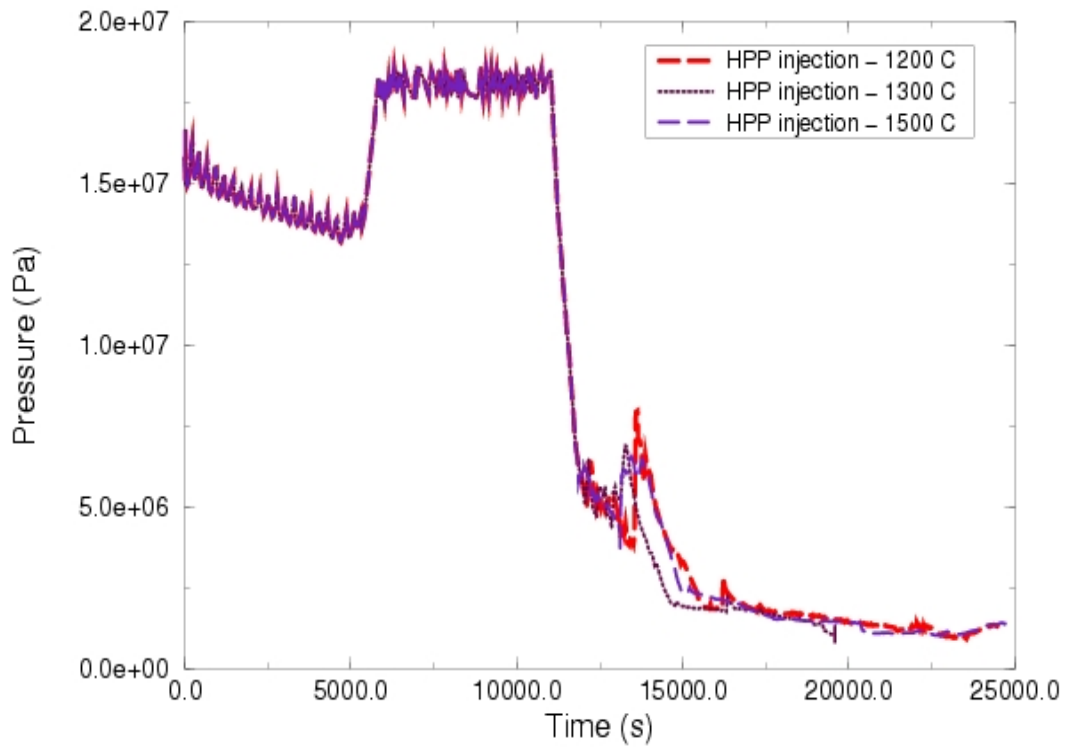
FIG. 7. Behavior of primary side pressure.
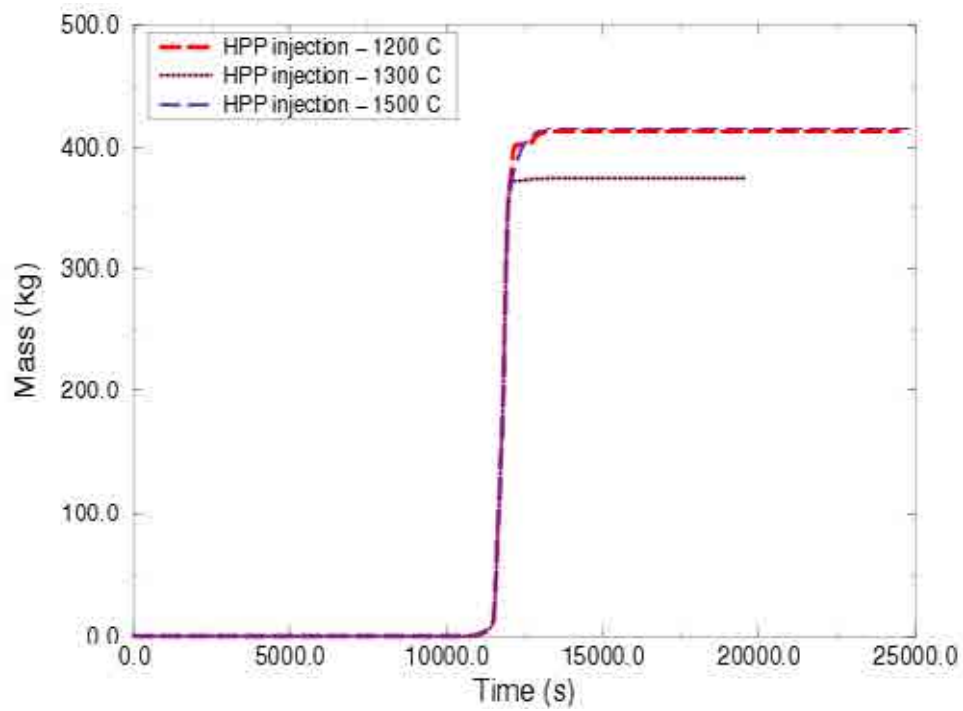
FIG. 8.Total hydrogen generation during in vessel phase.
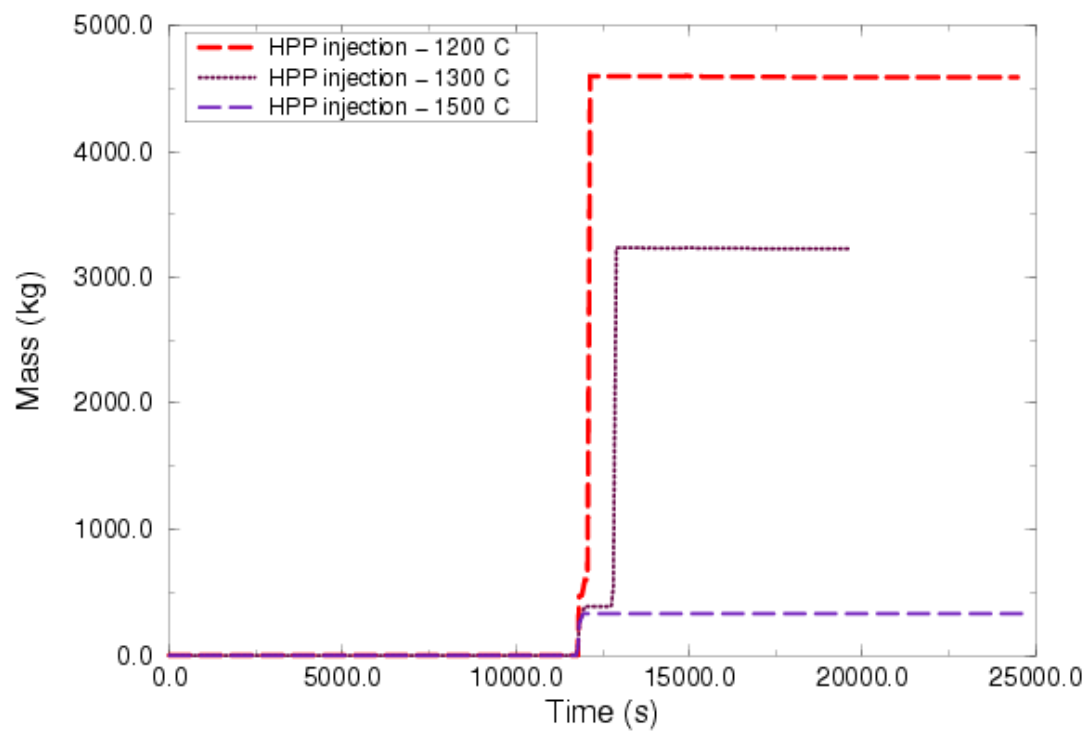
FIG. 9. Total mass of corium on the bottom.
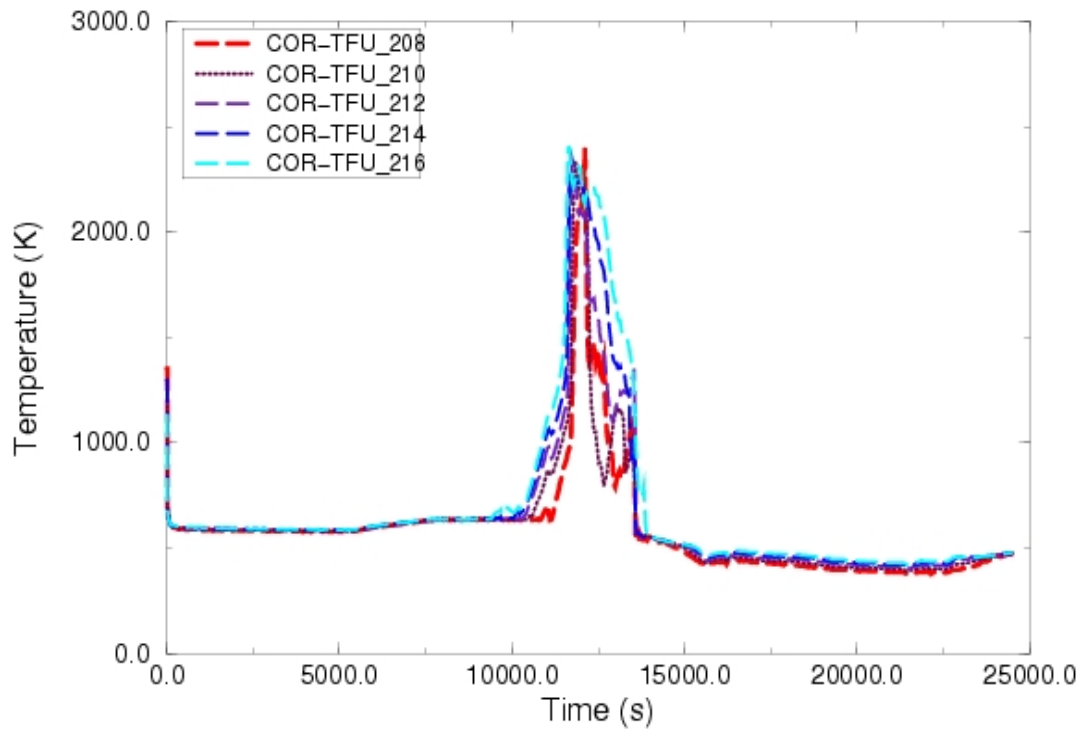
FIG. 10. Fuel temperature at ring 2 in case of HPP injection at 1200°C.
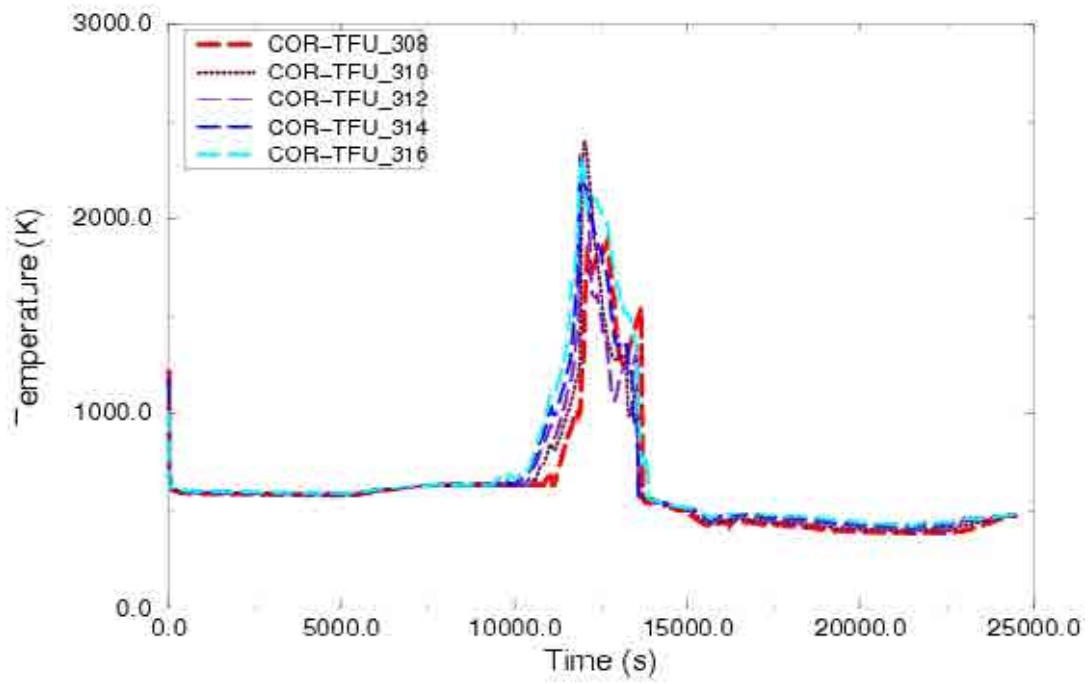
FIG. 11. Fuel temperature at ring 3 in case of HPP injection at 1200°C
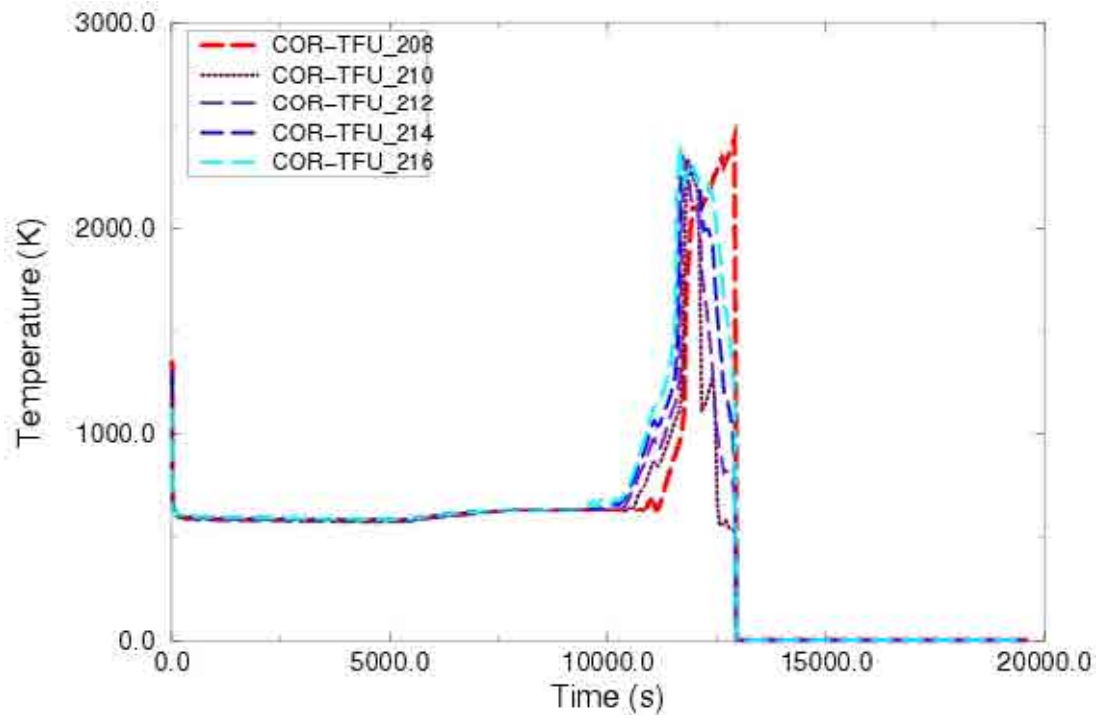
FIG. 12. Fuel temperature at ring 2 in case of HPP injection at 1300°C.
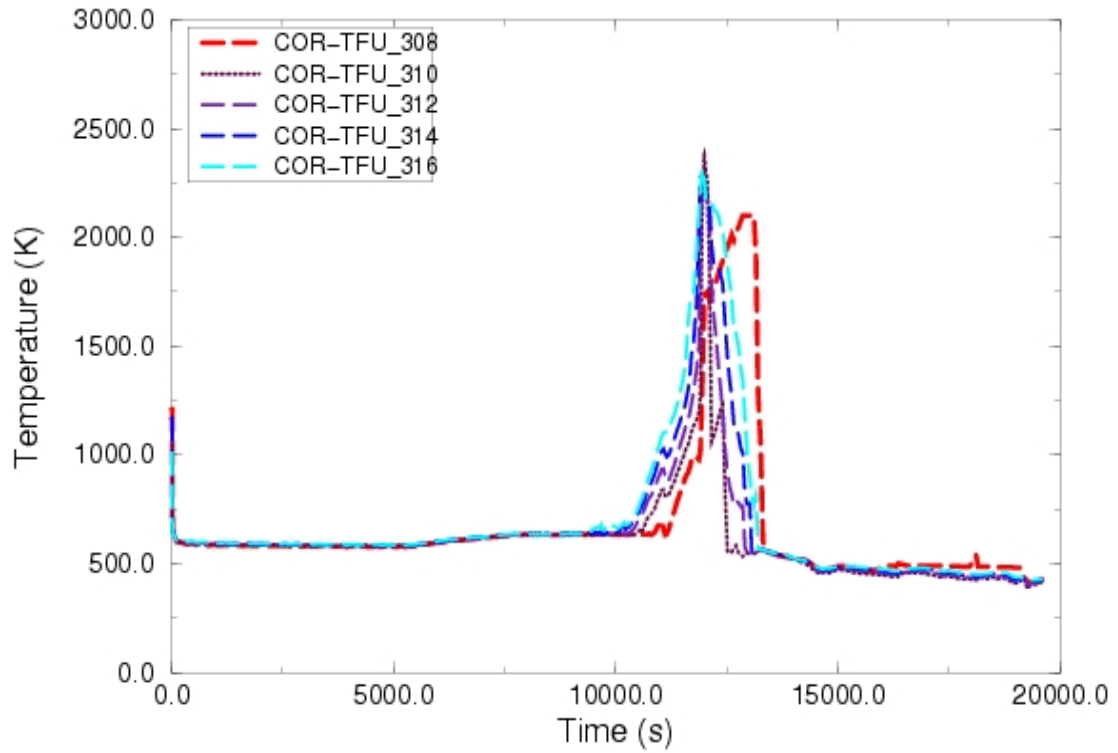
FIG. 13. Fuel temperature at ring 3 in case of HPP injection at 1300°C.
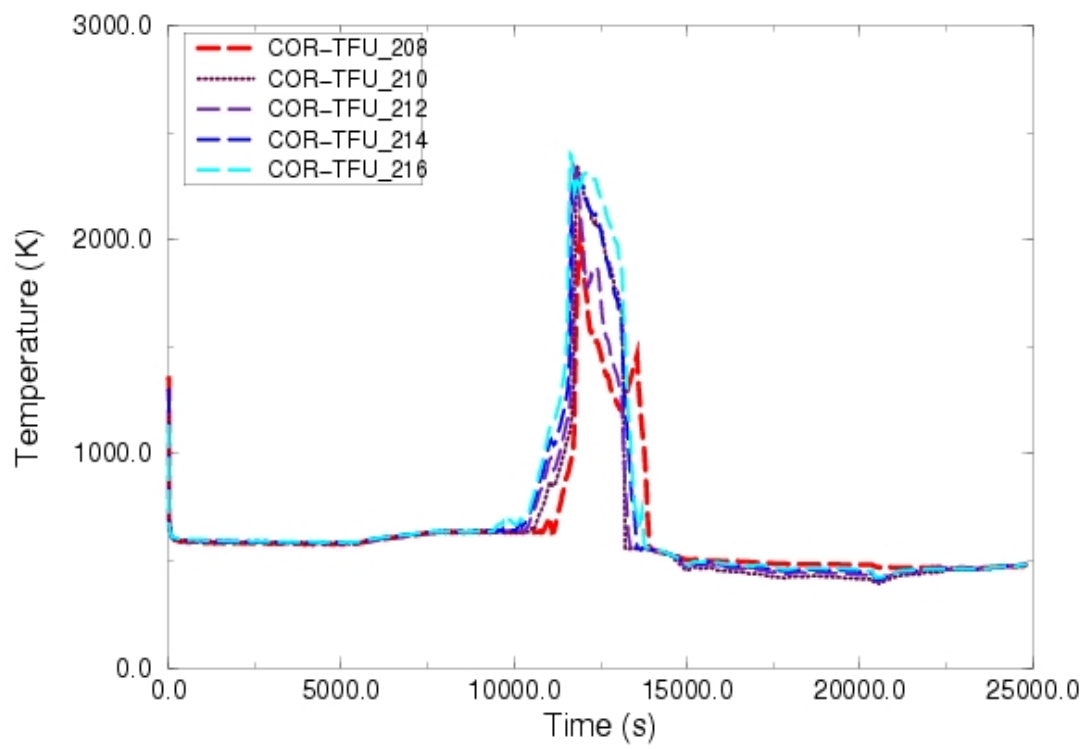
FIG. 14. Fuel temperature at ring 2 in case of HPP injection at 1500°C.
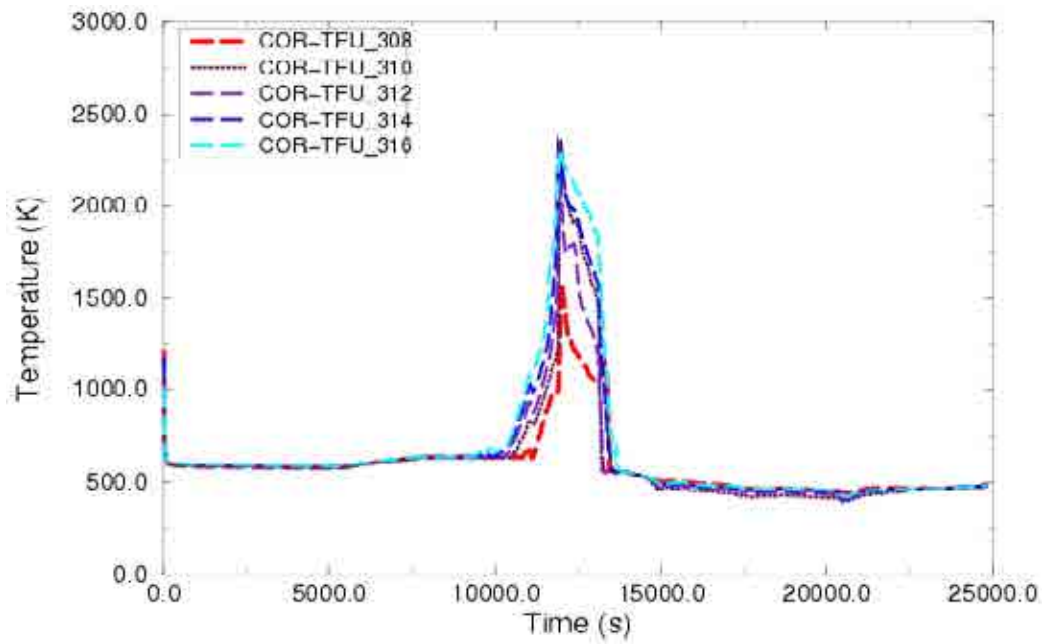
FIG. 15. Fuel temperature at ring 3 in case of HPP injection at 1500°C.

5. CONCLUSIONS

As seen in the first set of calculations, the results shown of the destruction of the core and the relocation of the fuel depend on the value of porosity. By increasing the value of porosity is observed initial bigger relocation of corium on the bottom head and a later failure of the reactor vessel.

The significant uncertainty in relocation of debris requests a further investigation for selecting the proper value for porosity.

The results obtained in the second group of calculations show that the overall strategy for saving the core with additional water injections with the high pressure pump is efficient and does not lead to additional generation of hydrogen, which would jeopardize the construction of containment.

Based on the analysis, it could be accepted reliably that the injection of water into the reactor core by the high pressure pump does not result in further generation of hydrogen and avoids significant destruction of the core at core exit temperatures above 1200°C to about 1500°C, and thus would prevent failure of the reactor vessel.

STUDY ON THE HIGH TEMPERATURE OXIDATION BEHAVIOR FOR N18 ZIRCONIUM ALLOY IN STEAM

JUN QIU, WENJIN ZHAO
Science and Technology Laboratory on Reactor Fuel and Materials,
Nuclear Power Institute of China (NPIC)
P. O. Box 436 (4)
Chengdu, 610041, P. R. China

Abstract. It is very important to study the oxidation behavior of zirconium cladding materials under postulated Loss-of-coolant accident condition in light water reactors. For this purpose, isothermal oxidation experiment were conducted at 700~1200℃ in steam with N18 zirconium alloy. The results show that the kinetics curves for N18 zirconium alloy oxidized in steam is similar to that of Zry-4 in the temperature range from 700℃ to 1000℃, which is parabolic rate to linear rate. At the temperature above 1100℃, the oxidation kinetics is parabolic rate and there is not transition for the kinetics curves. The cross-section morphologies of oxide layer corresponded with kinetics curves. The hydrogen pickup for N18 alloy was increased with the increasing of exposure time and temperature. The effect of the oxidation temperature on the hydrogen pickup of N18 alloy is especially important. The oxidation resistance of N18 alloy oxidized in steam is superior to that of Zircaloy-4 in steam.

1. INTRODUCTION

Fuel element, which mainly contains fuel pellets and cladding, is the key part of the nuclear reactor. The fuel cladding plays an important role of preventing leakage of radioactive materials into the coolant. Nowadays, the trend of developing nuclear fuel cladding is to increase the fuel discharge burn-up and prolong its cycle length. Many countries have developed advanced claddings, such as ZIRLO, M5, MDA, and NDA, for the high burn-up fuel to improve their safety and economical efficiency [1~4]. China is also developing advanced claddings to meet the demand of the high burn-up and long lifetime nuclear reactor core, which is named N18. Because of the different composition of the N18 zirconium alloy in comparison to the conventional Zircaloy-4, their properties of high temperature oxidation should be evaluated.

The paper describes the oxidation behaviour of zirconium alloy N18 oxidized in steam at temperature from 700 °C to 1200°C, including oxidation kinetics, evolution of matrix microstructure and hydrogen pick up.

2. SAMPLE PREPARATION AND EXPERIMENTAL PROCEDURE

The materials used in these experiments are recrystallized thin sheets of N18 and Zircaloy-4. Composition of the zirconium alloys used in this program is given in Table 1. The size of the specimens is 30 mm in length, 20 mm in width and 2 mm in thickness. All the specimens are finally picked in a solution of 5% HF, 45% HNO_3, and 50% H_2O. After the oxidation test, the microstructures of all the specimens are observed by an optical microscope.

TABLE 1. CHEMICAL COMPOSITION OF THE INVESTIGATED ALLOYS

	Sn (wt%)	Nb (wt%)	Fe (wt%)	C r(wt%)	O (wt%)	Zr (wt%)
Zry-4	1.30	<50Pppm	0.21	0.10	0.10	Balanced
N18	1.0	0.27	0.38	0.07	0.07	Balanced

The high-temperature oxidation testing is performed by the apparatus made by ourselves. The specimens are hung in the quartz tube, oxidized in steam at setted time and temperature, and then were dropped into the water under the quartz tube and were quenched.

3.   RESULTS AND DISCUSSION

3.1   Oxidation kinetics

The kinetics curves of the weight gain versus time for Zircaloy-4 and N18 in the temperature of 700~800°C are presented in Figure 1. From Fig. 1, we can see that the weight gains of all the alloys increase with the exposure time increasing. The weight gains of Zircaloy-4 are higher than that of N18 alloy. In the case of 700°C, the oxidation kinetics of all the alloys at early stage follows the parabolic rate law, and then with the proceeding of oxidation, the transition of oxidation rate for N18 and Zircaloy-4 alloys reveals after 90min. and 80min., respectively. The cases of 800°C are different. The weight gains of N18 alloy are higher than that of Zircaloy-4, which is due to the phase transformation for N18 begins at 775°C and the matrix phase transformation for N18 effect the stress relaxation inside oxide.

Fig. 2 shows the kinetics curves for for Zircaloy-4 and N18 at the temperature of 900°C and 1000°C. The case of 900°C is similar to that of 700°C. At the temperature of 1000°C, the transition from parabolic to linear kinetics takes place earlier. This transition is caused by breakaway oxidation [5]. Phase diagram of Zr-O shows that zirconium dioxide exhibits phase.

At 1000℃, because of the breakaway of oxide, the weight gains replaced by the thickness of oxide transformation from a monoclinic to a tetragonal at about 1000°C [6]. Phase transformation of ZrO_2 destroys the integrity of oxide, which results in the phenomenon of breakaway oxidation.

Fig. 3 shows the kinetics curves for Zircaloy-4 and N18 at the temperature of 1100~1200°C. Form 1100°C to 1200°C, The weight gains and the oxidation behaviour are similar for both of the alloys. Samples appear homogeneously oxidized, and the reaction follows parabolic kinetics during the whole test, in other words, there are no transition phenomenons at temperature above 1100°C.
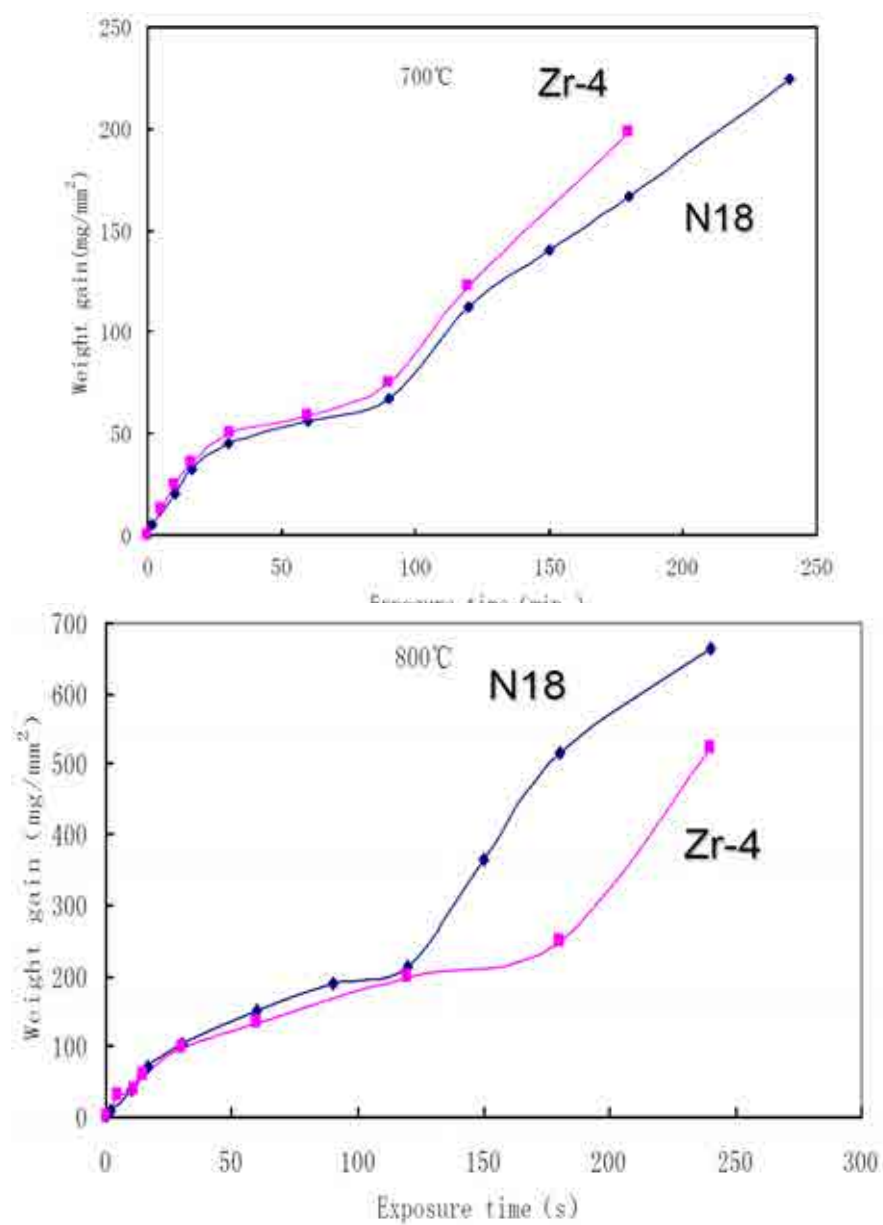
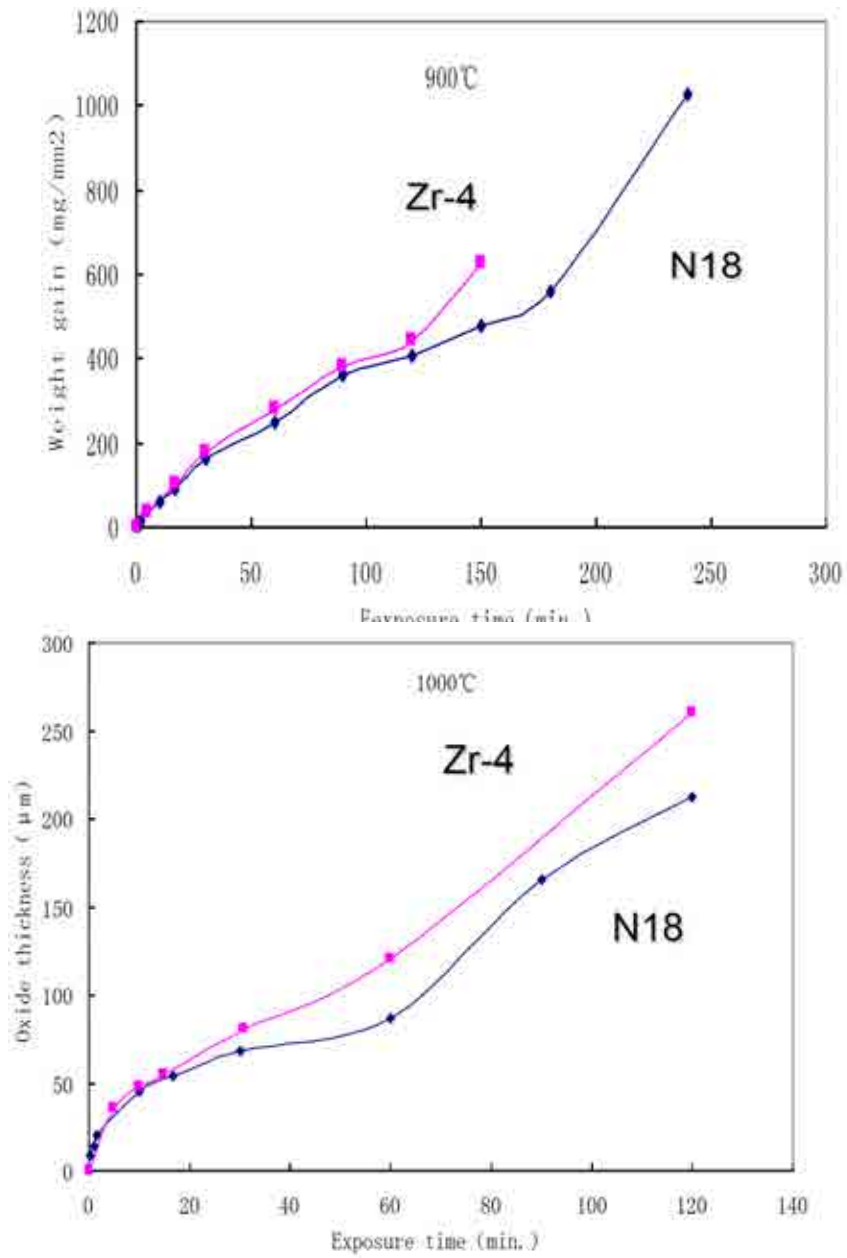*FIG. 1. Oxidation kinetics curves of N18 and Zircaloy-4 at the temperature of 700 ℃, 800 ℃.*

FIG. 2. Oxidation kinetics curves of N18 and Zircaloy-4 at the temperature of 900 ℃, 1000 ℃.

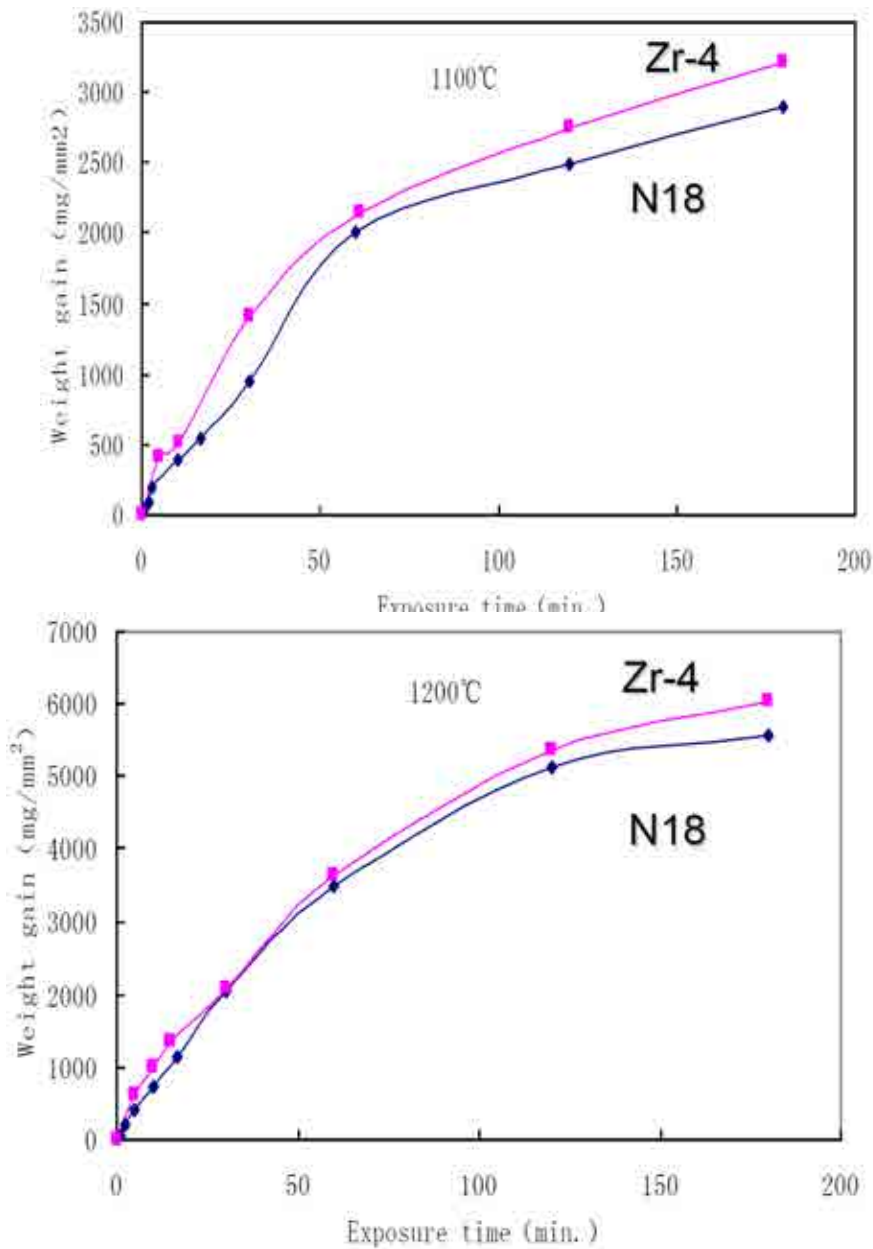*FIG. 3. Oxidation kinetics curves of N18 and Zircaloy-4at the temperature of 1100℃, 1200℃.*
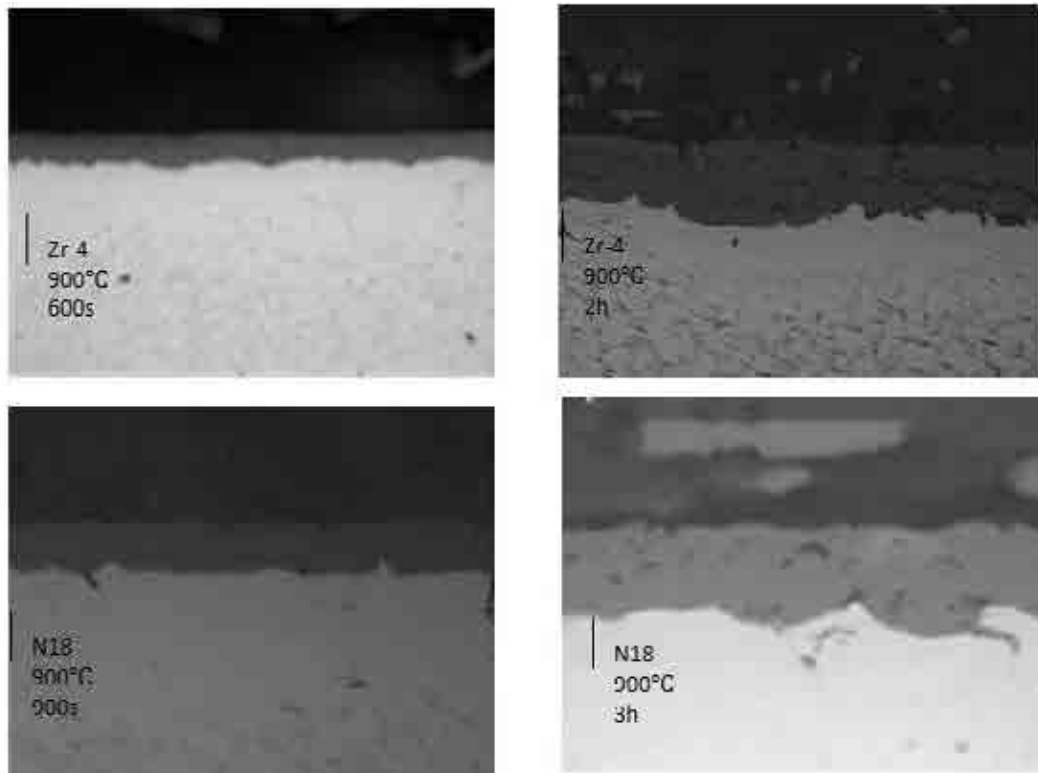
3.2 Oxide morphology

Figs 4–7 show the cross-section morphology of oxide layer for Zircaloy-4 and N18. At 700°C and 900°C, the oxide layer boundary keep flat before the rate transition, and there are some lateral cracks after the rate transition. At 1000 °C, lateral cracks appear in oxide layer soon. The boundary between oxide layer and matrix is undulate, and the oxide is rather porous. Above 1100°C, the oxide morphologies are revealed with columnar–like structure and the boundary keeps clear and straight, which is also corresponded with the trends of kinetics

curves at that temperature.
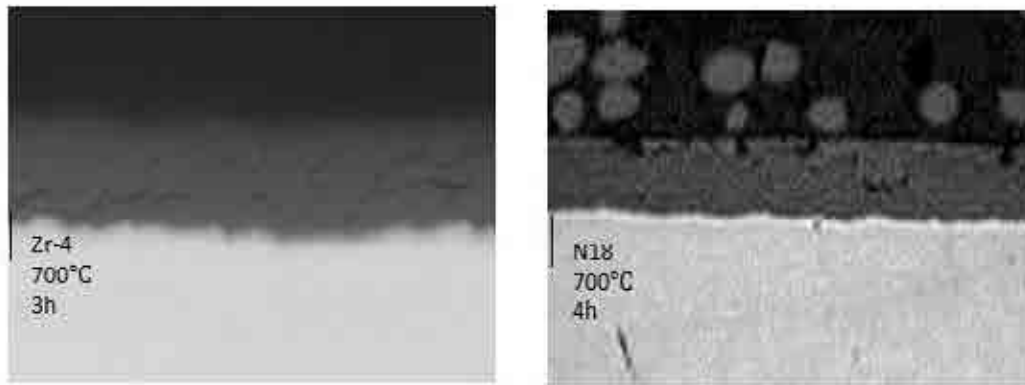
FIG. 4. Cross-section morphology of oxide layer of Zircaloy-4 and N18 at 700 ℃.

FIG. 5. Cross-section morphology of oxide layer of Zircaloy-4 and N18 at 900 ℃.
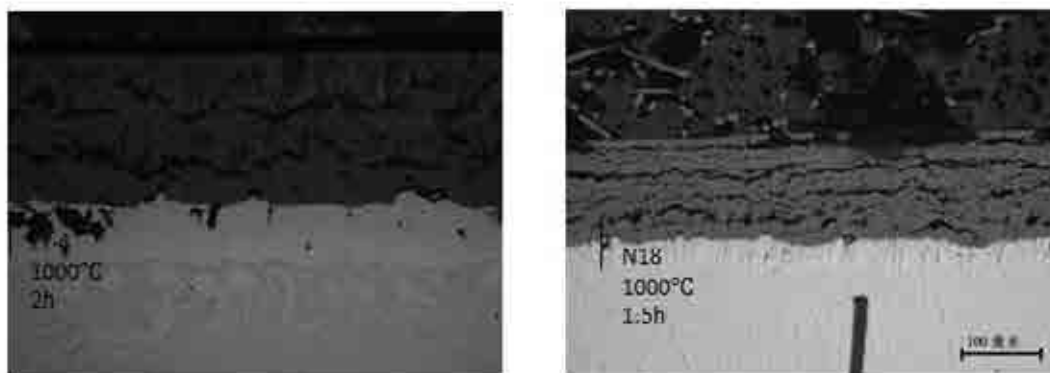
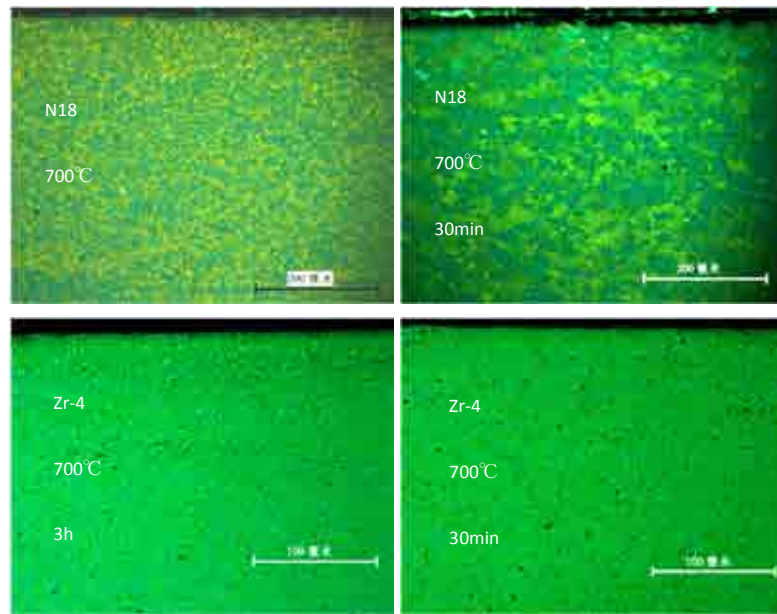*FIG. 6. Cross-section morphology of oxide layer of Zircaloy-4 and N18 at 1000 °C.*
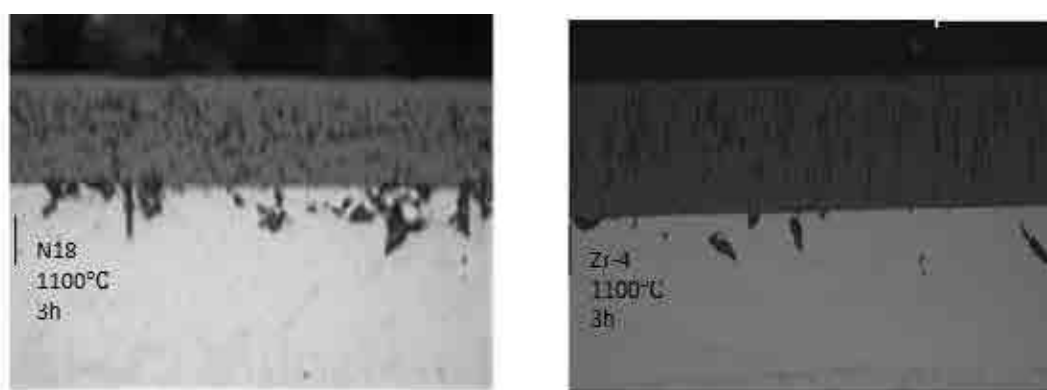
FIG. 7. Cross-section morphology of oxide layer of Zircaloy-4 and N18 at 1100 °C.

3.3 Evolution of matrix microstructure

Figs 8 and 9 show the changes of matrix microstructure for N18 and Zr after oxidized in steam at temperature form 700°C to 800°C. At 700°C, matrix for N18 and Zry-4 are single phase and consist of α phase. The grains coarsen with the oxidation time increasing (Fig. 8). The phase transformation temperature for N18 begins at the temperature of 775°C, so the matrix microstructure for N18 will go into double phase region when it oxidizes at the temperature of 800°C. At first, the microstructure is still single phase, but the phase transformation takes place after oxidized for 4 hours, and the microstructure consist of two phases —α phase in the region near the oxide film and the lath-shaped "ex-β" phase in the center region. The matrix for Zry-4 is still single phase and consists of α phase at 800°C.

264

FIG. 8 Cross-section morphology of oxide layer of Zircaloy-4 and N18 at 700°C.
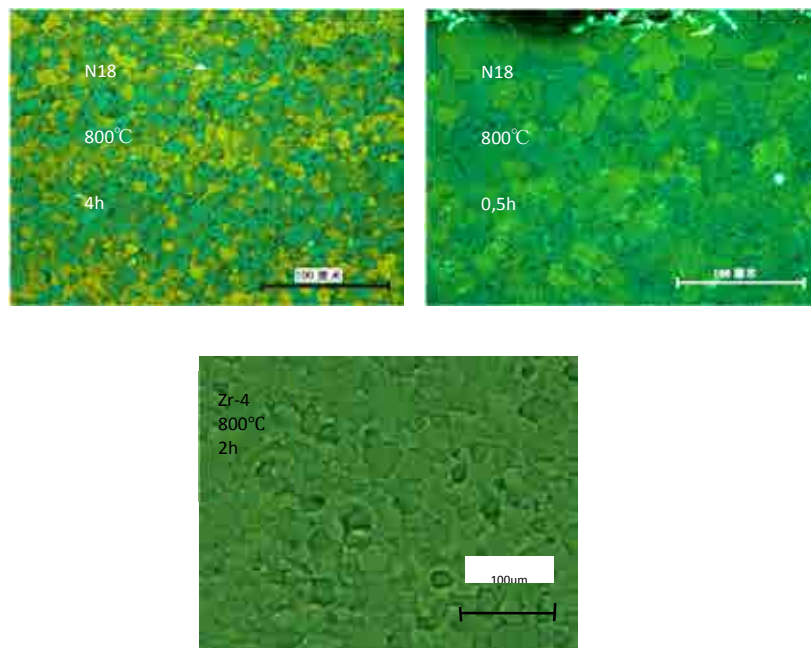

FIG. 9. Cross-section morphology of oxide layer of Zircaloy-4 and N18 at 800 ℃.

Figs 10 and 11 show the changes of matrix microstructure for N18 after oxidized in steam at temperature form 900°C to 1200°C. At 900°C, the microstructures of the matrix consisted of two phases of a-Zr and β -Zr. The end of phase transformation temperature for N18 alloy is 938°C, therefor the phase transformation for N18 alloy is completed at 1000°C. The specimens oxidized

at the temperatures above 1000°C had developed three layers: a zirconia phase, oxygen enriched α phase and "ex-β" phase with the depth from the outer surface. As the temperatures increased, the thickness of the oxygen-stabilized α -Zr layer was drastically increased and most of the prior β -Zr layer disappeared at 1200°C. This is the reason why the diffusion depth of the oxygen was expanded with the increasing temperatures.
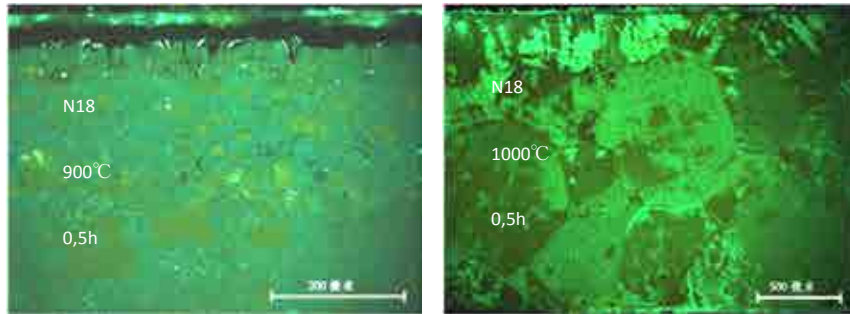

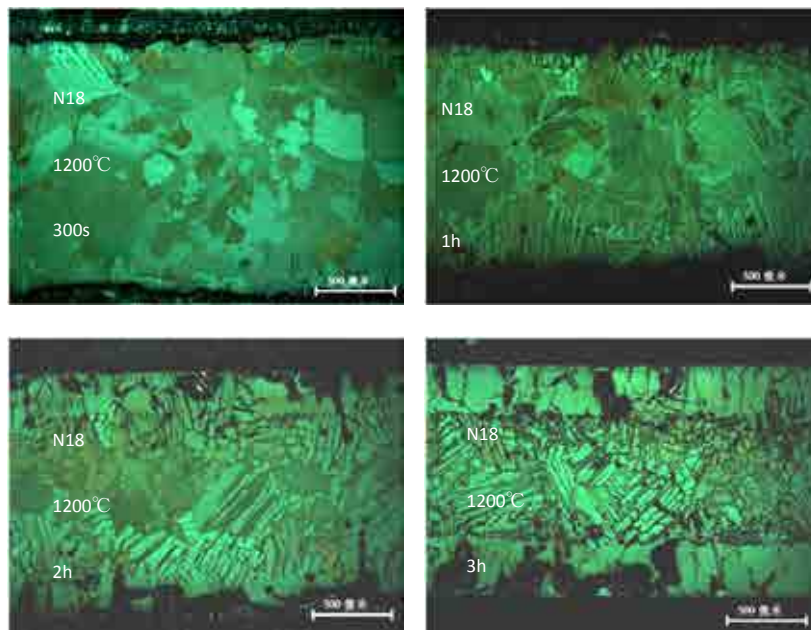FIG. 10. Changes of matrix microstructure of N18 at the temperature of 900 ℃, 1000 ℃.

FIG. 11. Changes of matrix microstructure of N18 at the temperature of 1200 ℃.

3.4 Behavior of hydrogen uptake

Zirconium alloys absorb hydrogen during its oxidation in steam. Hydrides dissolve in matrix in the form of supersaturation or precipitate rapidly during samples quenched. The size of the hydride is often very small, so the hydrides usually cannot be observed under optical microscope when the uptake of hydrogen is not high. At 700°C, small hydrides can be observed near the

grain boundary after oxidized in steam for 3 hour (Fig. 12). But at 900°C, the amount of hydrides increased with the time increasing (Fig. 13). At temperature of 1100°C, after rapidly quenched, dense and thin hydrides precipitates, numerous hydrides can be observed precipitated along the direction parallel to the grain boundary (Fig. 14). This phenomenon is attributed to the reaction between zirconium and water and the reaction rate between zirconium and water accelerate with the reaction temperature going up. At the same time, the increase of hydrogen partial pressure in the atmosphere accelerates the hydrogen absorption of zirconium.
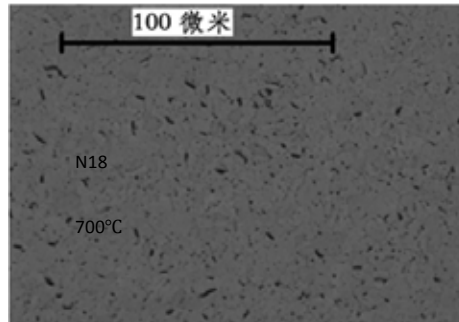

FIG. 12. Hydride morphology of N18 at the temperature of 700 ℃.
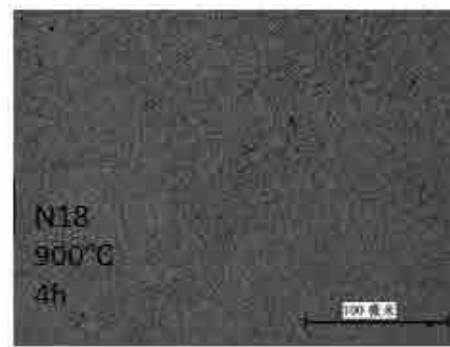

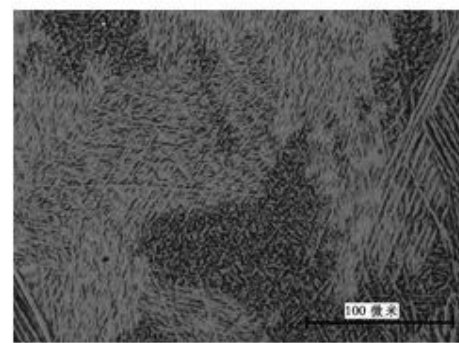*FIG. 13. Hydride morphology of N18 at the temperature of 900 ℃.*

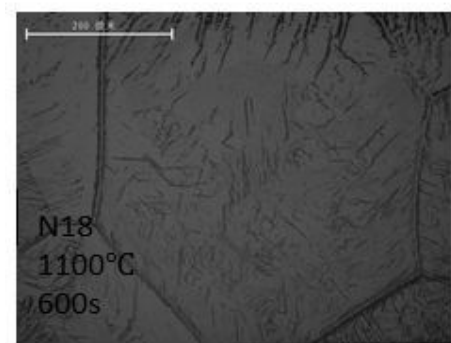*FIG. 14. Hydride morphology of N18 at the temperature of 1100 ℃.*

4. CONCLUSION

So, according to the previous discussion, it can be concluded that:

1) The kinetics curves for N18 zirconium alloy oxidized in steam is similar to that of Zry-4. There is not transition for the kinetics curves at the temperature above 1100°C;
2) The oxidation resistance of N18 alloy oxidized in steam is superior to that of Zircaloy-4 in steam;
3) The cross-section morphologies of oxide correspond with kinetics curves;
4) The hydrogen pickup for N18 alloy is increasing with the increasing of exposure time and temperature. The effect of the oxidation temperature on the hydrogen uptake for N18 is especially important.

REFERENCES

[1]   USNRC-SRP (Standard Review Plan), Sec. 4.2, NUREG-0800.
[2]   HOZER, Z., GYORI, CS., HORVATH, M., NAGY, I., MAROTI, L., MATUS, L., WINDBERG, P., FRECSKA, Ballooning Experiments with VVER Cladding, J., Nucl. Technology, **152** 3 (2005) 273-285.
[3]   ERBACHER, F.J., Cladding Tube Deformation and Core Emergency Cooling in a Loss Of Coolant Accident of a Pressurized Water Reactor, Nucl. Eng. Des. **103** 1 (1987) 55-64.
[4]   BILLONE, M., YAN, C., BURTSEVA, Y., CHUNG, H.M., 2005. ANL LOCA Research Results for Cladding Alloys: Zircaloy-2, Zircaloy-4, ZIRLO, and M5, Fuel Safety Research Meeting, Tokyo, March 2–3, 2005.
[5]   BAEK, Y.H., PARK, K.B., JEONG Y.H., Oxidation Kinetics of Zircaloy-4 and Zr–1Nb–1Sn–0.1Fe at Temperatures of 700–1200°C, Journal of Nuclear Materials **335** (2004) 443–456.
[6]   HAWKINS, D.T., HULTGREN, R. Metals Handbook. 8th, American Society for Metals, USA, Vol **8**:327.

RADIONUCLIDE RELEASE FROM HIGH BURNUP FUEL

V. TULKKI, A. NIEMINEN, A. RÄTY
VTT Technical Research Centre of Finland
P.O. Box 1000 02044 VTT Finland
Email: ville.tulkki@vtt.fi

Abstract. In this paper we investigate the production, evolution and release of radioactive fission products in a light water reactor. The production of the nuclides is determined by the neutronics, their evolution in the fuel by local temperature and by the fuel microstructure and the rate of release is governed by the scenario and the properties of the microstructure where the nuclides reside. The problem combines fields of reactor physics, fuel behaviour analysis and accident analysis. Radionuclide evolution during fuel reactor life is also important for determination of instant release fraction of final repository analysis.

The source term problem is investigated by literature study and simulations with reactor physics code Serpent as well as fuel performance code ENIGMA. The capabilities of severe accident management codes MELCOR and ASTEC for describing high burnup structure effects are reviewed. As the problem is multidisciplinary in nature the transfer of information between the codes is studied.

While the combining of the different fields as they currently are is challenging, there are some possibilities to synergy. Using reactor physics tools capable of spatial discretization is necessary for determining the HBS inventory. Fuel performance studies can provide insight how the HBS should be modelled in severe accident codes, however the end effect is probably very small considering the energetic nature of the postulated accidents in these scenarios. Nuclide release in severe accidents is affected by fuel oxidation, which is not taken into account by ANSI/ANS-5.4 but could be important in some cases, and as such, following the example of severe accident models would benefit the development of fuel performance code models.

1. INTRODUCTION

Nuclear fuel accumulates all kinds of radioactive nuclides during the irradiation. While the actinides can be claimed to be unwanted side product of the process, without the fission products there would be no power produced in the reactor. The downside are the dangers these radioactive nuclides pose to people and environment should they ever be released, whether it would happen during a reactor accident or after years of interim storage or millennia of repository life. For safety analysis knowing and understanding the source term is important, and while different disciplines do address nuclear fuel in various forms and scale, the approaches are by necessity often very different. In this paper the tools of reactor physics, fuel behaviour and severe accident analysis are investigated in order to find synergy between the strengths of different disciplines. Individual investigations are described also to serve as a reference of the use of the tools and the viewpoint utilized by different disciplines. This is important as it is well recognized that the first obstacle to fruitful co-operation is the one's inability to understand the mental framework and assumptions of the experts of other fields.

Long-term activity inventory calculations have been performed extensively with code ORIGEN-S both internationally and in the VTT. The calculated inventories from ORIGEN can be used as input for various accident analysis tools which make assumptions regarding distribution and behaviour of different radionuclides. The development of Monte Carlo based reactor physics calculation tool Serpent has given a tool to do these calculations with more spatial precision, thus enabling investigations in the scale of the fuel rod.

Fuel behaviour codes traditionally track only fission products that may affect rod integrity, in other words stable noble gases and in some cases iodine. The focus of the analysis has been the failure of the rod, not the subsequent release. Especially in the final repository assessments the similarity and differences between the behaviour of noble gases and the radionuclides have been investigated, but so far very little actual modelling has been performed.

The research of severe accident in-vessel phenomena have recently focused at VTT on core degradation and coolability. This approach has not enabled detailed analysis on radionuclide release. The integral codes only assume, that the radionuclide source term is initiated by diffusion from fuel grains, which does not take pre-existing radionuclide deposits or radically modified fuel structure into account. This model is assumed to give incorrect estimations in the case of slowly progressing accidents.

One of the focus areas of this work is the effect of increasing burnup, subsequent formation of high burnup structure (HBS) and its effect on the radionuclide release. As the Finnish utilities have gained permission to increase discharge burnup from the old 45 MWd/kgU, the highest power rods are well within the burnup region where HBS begins to form and its effect should be determined.

2. LITERATURE

2.1 Nuclide inventory

The nuclide inventory of the fuel is generated by the nuclear fission. The fission density across the fuel pellet varies due to the shelf-shielding effect, creating power and burnup distributions that peak on the surface of the fuel pellet. The various nuclides react to their environment, UO_2 matrix, depending on their chemical properties. Several categories of behaviour have been found, and [1] is the referenced source for these categories. Chemical state of the fission products can be divided into four categories:
  - Noble gases and volatile fission products: Kr, Xe, Br, I.
  - Fission products forming metallic precipitates: Mo, Tc, Ru, Rh, Pd, Ag, Cd, In, Sn, Sb, Tc.
  - Forming oxide precipitates: Rb, Cs, Ba, Zr, Nb, Te.
  - Dissolved as oxides in the fuel matrix: Sr, Zr, Nb and the rare earths.

There is overlap in the groups, depending on the surrounding as the chemical potentials of composites are close to each other.

The stable noble gases are most studied, as they stay in gaseous form in the rod free volume during the irradiation and thus increase the rod internal pressure and lower the gas gap thermal conductivity. Both of these effects have safety implications. The stable noble gases in the rod free volume are also easily measure during PIE, as they stay in their elemental forms. Other fission products such as iodine and caesium do move in the rod and deposit to cool surfaces. These nuclides are also chemically active and contribute to phenomena such as stress corrosion cracking that may cause rod failures during power ramps performed as a part of reactor operation.

Volatile nuclides diffuse to grain boundaries and some ultimately move to the gas gap. This in turn depends on their interaction with each other, as the fission products are concentrated in the

grain boundaries and cannot be treated as just being in contact with UO_2. Some products form stable precipitations of metallic or oxide particles, other may stay gaseous until being deposited to the (relatively) cool outer parts of the fuel and the cladding wall. The various structures in nuclear fuel are 1) UO_2 matrix, 2) intergranular gas bubbles and 3) rod free volume. With the rising burnup the formation of high burnup structure in the pellet rim becomes also relevant.

The reason to study the nuclide distribution in the fuel microstructure is the fact that the nuclide release rates may depend on their location. Traditionally, the gap activity is assumed to be released instantaneously after the cladding tube fails during an accident or the repository life. Other structures in fuel may or may not retain their nuclide inventory for a longer period. The nuclide distribution is determined by the fuel irradiation history as most of the diffusion processes are driven either by thermal movement or irradiation damage. As out of pile there is no on-going irradiation and the temperatures are fairly low, the nuclides tend to stay in the parts of fuel they were at the end of the irradiation.

The nuclide inventory is relevant to accidents, severe accidents and the final repository analysis, and the specialists of these different fields have developed their own methodologies. The high temperatures associated with severe accidents give rise to particular dynamic phenomena, which is discussed separately. The starting point in instant release during handling or low power accident, as well as instant release fraction (IRF) of repository analysis depend on the nuclide distribution, and they are discussed in this Section.

The American Nuclear Society's ANSI/ANS-5.4-2011 [2] standard represents the industry "best practices" in calculating the fractional release of volatile fission products. The standard provides guidelines for calculating fractional releases for short-lived (half-life less than 6 hours), intermediate (half-lives between 6 hours and 60 days) and long-lived (half-life longer than a year) isotopes. The standard is mostly based on published measurements performed at Halden Reactor.

The repository analysis deals mostly with the isotopes with long half-lives. However, as the nuclides of interest are often just longer-lived isotopes of the same chemical substances, such as iodine and caesium, their behaviour up to the accident or reactor shut-down should be identical. Much of the work done on the instant release fraction analysis is based on the work of L. Johnson [3, 4, 5], and coordinated research programmes are common.

2.2 Accident conditions

The ANS/ANSI-5.4-2011 standard provides an analytical method for calculation of so-called gap release, which is the inventory of volatile fission products that are available for fast release in case the cladding tube fails. Both short- and long-lived fission products are considered, the temperature range covers the normal irradiation conditions, and the data range covers burnups up to 95 MWd/kgU. The assumption is that the temperature rise during the accident is moderate (<300 K), as burst release is not taken into account, which excludes RIA conditions. Also, no fuel oxidation is allowed. Fuel oxidation enhances the nuclide release rate [6], and analysis of situations allowing for the oxidation would need a diffusion enhancement term in the model. A detailed description of the theory and the experiments behind the standard are publicly available in the background document prepared by PNNL [7].

The theoretical model is an adaptation of the model proposed by Booth [8]. Spherical grains are assumed, and the nuclides of interest diffuse to the grain boundary as per idealized diffusion. A fractional ratio between release and birth (*R/B*) for radial node *i* of axial node *m* is gained after several simplifications:

$$\left(\frac{R}{B}\right)_{i,m} = \left(\frac{S}{V}\right)_{i,m} \sqrt{\frac{\alpha_{nuclide}D_{i,m}}{\lambda_{nuclide}}} \ , \tag{1}$$

where α is a nuclide-dependent factor denoting the effect the nuclide's precursors have on its apparent diffusion rate and λ is the decay constant. The diffusion coefficient D depends on several factors:

$$D_{i,m} = 7.6 \times 10^{-7}e^{-35000/T_{i,m}} + 1.41 \times 10^{-18}\dot{F}_m^{0.5}e^{-13800/T_{i,m}} + 2 \times 10^{-30}\dot{F}_m \tag{2}$$

where $T_{i,m}$ is the local temperature and F_m is the fission density of the axial node *m*. And finally, the temperature and burnup dependent surface-to-volume ratio (*S/V*) represents the grain boundary gas bubble interlinkage. In a simplified form this essentially what is referred to as the Vitanza limit. While the grain boundary inventory and intergranular bubble interlinkage are not directly modelled, they are taken into account empirically by adjusting the *S/V* ratio depending on temperature, thus in a way modifying the size of the perceived fuel grain. The R/B ratio is calculated over all the axial and radial simulation nodes, and the weighted local ratio is integrated into a single R/B value. The resulting R/B ratio represents the inventory in the gap. Such a formulation is then used for ^{85m}Kr from Halden tests, and precursor effects are either taken directly into account, or a scaling factor is used to account for the difference in half-lives between ^{85m}Kr and the target nuclide. Precursor effects are used to account for high diffusion coefficients of nuclides such as bromine (20 times that of noble gases). Discrepancies in short-lived nuclide releases are reported by the background document, and the core cause remains unresolved. A concept of fractal surfaces has been proposed [9]. The fractal nature of the grain surface would strongly affect the diffusion distance experienced by short-lived fission products, and thus explain some of the observed discrepancy. This theory, however, is not unanimously accepted even by the group formulating the ANSI-5.4 standard.

The release of longer-lived nuclides (half-life > a year) is correlated with fuel performance code's FGR modelling. For Cs isotopes, a diffusion coefficient twice as high as that for noble gases is assumed.

The high burnup structure effect is not included in the model. While the dataset does go to high burnups, the data above 40 MWd/kgU is based only on four IFA-504 rods, and above 65 MWd/kgU on only a single rod. Also, as most of the release is coming from the high temperature central areas, the HBS does not contribute to the analysis. It could be claimed, therefore, that the HBS is not included in the ANS/ANSI-5.4-2011 standard, and any effect from the HBS should be considered separately.

2.3 Geological repository analysis

Several Euratom Framework Programs have been conducted related to geological disposal of spent nuclear fuel, such as Spent Fuel Stability, NF-PRO, MICADO and FIRST-Nuclides. Also repository feasibility analyses have been performed in many countries, such as Switzerland

[4], Sweden [10] and Finland [11]. Experimental work is on-going outside these programmes, and a recent publication [5] has provided much-needed data on IRF from high burnup fuel.

IRF of various fission products is often said to correlate with the release fraction of stable noble gases. This is due the analogy of radionuclide diffusion in the grain, and as the grain boundary inventory is considered to be part of the IRF, the release from grain boundary to the free volume is theoretically a non-issue. In practice the measurement of grain boundary inventory is problematic in itself. However, several leaching studies are claimed to show that the IRF of Cs isotopes is one third of the FGR and that the iodine IRF is tentatively the same as the FGR of the fuel rod. This would indicate that the iodine diffuses in the UO_2 matrix at roughly the same rate as noble gases, and caesium at 1/sqrt(3) times the speed of noble gases. Other elements are claimed to be diffusing at lower rates [12].

According to MICADO project, uncertainties related to IRF still remain. Straightforward limiting FGR values are difficult to ascertain, the relationship of fission product IRFs to FGR are still somewhat uncertain, especially for iodine, and the data for activation products are sparse. The dissolution rate at grain boundaries, which determines whether their inventories are part of the IRF or not, is uncertain, as is the long-term stability of the high burnup structure. For MOX fuel the issue is even worse, as to HBS-like structure surrounding Pu agglomerates houses a large part of the radioactive inventory.

2.4 High burnup structure

High burnup structure (HBS), also called rim formation as it is usually seen in the pellet periphery in UO_2 fuels, is a structure formed at high local burnup. While the actual mechanism of HBS formation is still under debate (see e.g. [13]), its properties during steady state irradiation are relatively well understood. The UO_2 grains break into sub-micrometre-scale grains and most of the gaseous fission products reside in highly pressurized bubbles which are much larger than the grains. There is both a threshold burnup (radially local burnup approximately 70 MW/kgU) and a limit temperature at which the structure forms (below 1100°C) [14, 15] for UO_2 fuel. As such, both the low temperature and peaking power at the pellet periphery facilitate the HBS formation at the pellet rim region. In MOX fuels the HBS forms also near the Pu agglomerates. Exceptions to this general formation behaviour have been reported (e.g. [13]), but are usually explained by irradiation conditions deviating from the norm.

High burnup structure is assumed to keep most of its fission gas inventory trapped inside the pores [13], and as such it does not overly contribute to the FGR in normal operating conditions. Also it has been shown that the HBS does not contribute to the instant release in leaching studies (e.g. [16]). Therefore, linear assumptions between noble gas FGR and rapid release fraction of volatile radionuclides do not take HBS into account.

The behaviour of HSB in accident conditions and its evolution over thousands of years of repository life are not certain. According to several authors [17, 18] the high burnup structure fractures after a sudden increase of temperature. A two-step threshold would appear to be approximately 20% FGR at 900 K and a total release of the gases at 1500 K. Also other fission products, such as tellurium, are released at the 1500 K mark [17]. These conditions would be encountered during LOCA accident prior to fuel melting. The fuel relocation and dispersion of the high burnup fuel during LOCA have become a pressing concern of late [19], and the role of

HBS rim is integral in it. According to CEA studies [20] HBS does not contribute to fission gas release during the RIA accidents.

HBS stability during the repository period has been investigated with numerical studies by C. Ferry [21] as the experimental studies over such time scales are hardly practical. While the numerical studies would indicate that the HBS would retain its integrity during the disposal, no certainty in this regard can be guaranteed.

2.5 Release models

While the accident analysis and repository assessments obviously deal with very different time scales both do base their fast release analysis on nuclide location in fuel microstructure and in parallel on noble fission gas release. The FGR has been extensively studied over the decades, as it is of safety significance in operating reactors, and as such serves as a useful proxy for other fission products.

Table 1 collects the various assumptions made at accident source term and repository analysis as relates to various nuclides. The notable difference is the assumption on the diffusion rate of caesium, which should be the same if the phenomena were well understood.

TABLE 1. ASSUMPTIONS MADE IN VARIOUS MODELS ON NUCLIDE RELEASE

| | Half-life | Grain release model | Diffusion in matrix | | | | Inventory includes | | |
			Diffusion rate based on	Diffusion rate I/Xe	Diffusion rate Cs/Xe	Grain boundary release	gap	grain boundary	HBS
	short	Model developed from Booth	Noble gases	Precursor effect	Precursor effect	Experimental interlinkage threshold	Yes	No	No
ANS/ANSI-5.4	long	Correlated to FGR	Noble gases	1	2	As per FGR	Yes	No	No
Repository	long	Correlated to FGR	Noble gases	1	1/3	GB included in IRF	Yes	Yes	Varies

Other opinions as to the relative diffusion rates of iodine and noble gases exist (e.g. [22 – 24]. It should be noted that many of these studies appear to use MOX or experimental fuel, and use doping, out-of-pile sintering or other means to simulate some part of irradiation.

3. MODELLING CONSIDERATIONS

Most of the fuel performance codes feature modules calculating the release of noble gases from the fuel grains to the rod free volume. The models in general feature a two-stage process, first the diffusion from UO_2 grain to the grain boundary and then evolution of the grain boundary gas inventory ultimately to the rod free volume. Differences in models do exist on the exact mechanisms and the detail of modelling.

3.1 Fast release fraction

Figure 1 depicts a VVER440 fuel bundle calculation with ENIGMA, showing maximum fuel temperature, calculated fission gas release (to which release of long-lived nuclides is relative to) and the release of quickly decaying iodine-131 calculated as per ANSI-5.4 [27]. It can be seen that while the fraction of released long-lived nuclides increases with burn-up, the fraction of short-lived nuclides is mostly related to fuel temperatures. At least in moderate temperature range achieved with VVER440 fuel featuring annular pellets.
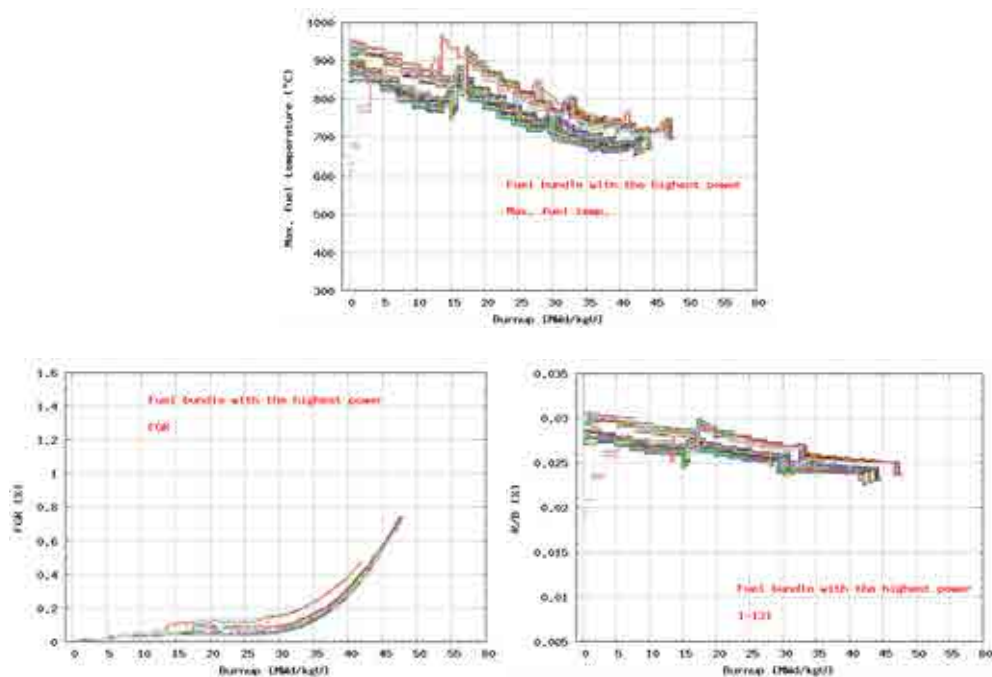
FIG. 1. Fuel maximum temperatures of a highest power bundle of a VVER440 reactor (top) along with release of long-lived (left) and short-lived (right) radionuclides. Figures originally from [27].

It should be noted that the previous analysis did not take fission product release from high burnup structure nor their radial distribution into account. Whether the HBS inventory is relevant or not creates a large difference in the resulting analysis, especially for severe accidents.

3.1 Effect of local temperature

Local fuel temperature affects fission gas release in at least two ways, by facilitating the diffusion of fission products to the grain boundaries and by triggering the release from the grain boundaries to the rod free volume. The fission product diffusion is usually considered to be a regular thermally driven diffusion along the concentration gradient, but the grain boundary release is a bit more complex phenomenon. One description is given by the Vitanza threshold, or Halden 1% release threshold, which is burnup-dependent fuel centreline temperature threshold whose crossing causes a fission gas release above 1% of the total inventory.

In normal operation the fuel pellet temperature ranges from approximately 500°C at the pellet periphery to over 1000 °C at the centreline. This affects the local diffusion rate of nuclides, as illustrated in Fig. 2, where a representative radial temperature distribution as well as

accompanying diffusion rates from Eq. 2 are plotted. From the figure it should be clear that the diffusion is pronounced in the central region of the fuel pellet, assuming the thermally driven diffusion is the dominating factor.
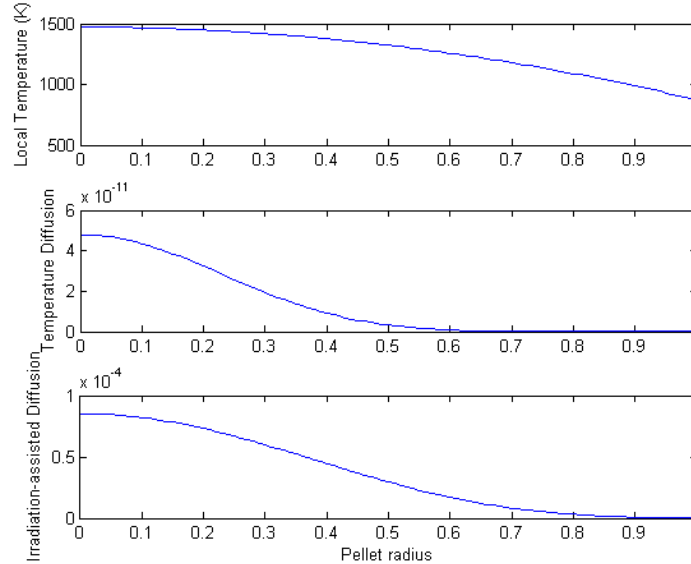

FIG. 2. *Typical temperature gradient across pellet radius (top, in kelvin) and resulting diffusion rate in arbitrary units for temperature-driven (middle) and irradiation assisted (bottom) diffusion.*

The noble gas release from the central pellet where the temperature is highest is verified by EPMA measurements of spent fuel [25]. Xenon depletes from the central part of the pellet, where the temperature has been sufficient for the thermal diffusion to activate. In the middle parts the grains still retain their xenon inventory, whereas most of the volatile gases in HBS are in the high pressure pores, which are not detected by EPMA. These gases are still retained by the fuel microstructure and should not be counted towards the gases in the free volume.

The diffusion rate is affected by the fuel oxidation state [26]. In general, the oxidation of UO_2 into U_3O_9 or similar makes it easier for various nuclides to diffuse, increasing the diffusion rates. This is the reason the oxidated fuel is ruled out of the ANSI-5.4 standard. Oxidation of the fuel would happen in cases where defective fuel stays inside the reactor, as well as in severe accident situations.

3.2 Nuclide concentrations

Radionuclides are born at the locations where fissions happen. Due to their mass the recoil energies are quickly dissipated into heat, and considering the scale of interest in this report, the nuclides can be assumed to start their diffusion from the region of the fission reaction. The more coarse neutronics codes such as ORIGEN-S do not take radial evolution of the fuel into account. As the HBS inventory is of interest, it would first be useful to find out whether the radial distribution of the nuclides could be determined in ways other than direct simulation by MC codes such as Serpent. ENIGMA power depression routine has been previously shown to be fairly good at replicating the exact power depression as given by Serpent [28]. The assumption

would be that the distribution of short-lived nuclides would correspond to current power distribution, as there is very little old inventory left, and long-lived nuclide distribution would be mostly dominated by long-term inventory, which would closely resemble the burnup distribution. The radial distribution of selected short- and long-lived nuclides from Serpent runs are shown in Fig. 3 and burnup and radial power deposition from ENIGMA at similar burnup in F.4. While the relative radial distribution is not exactly the same, some resemblance of such behaviour can be seen from the plots.
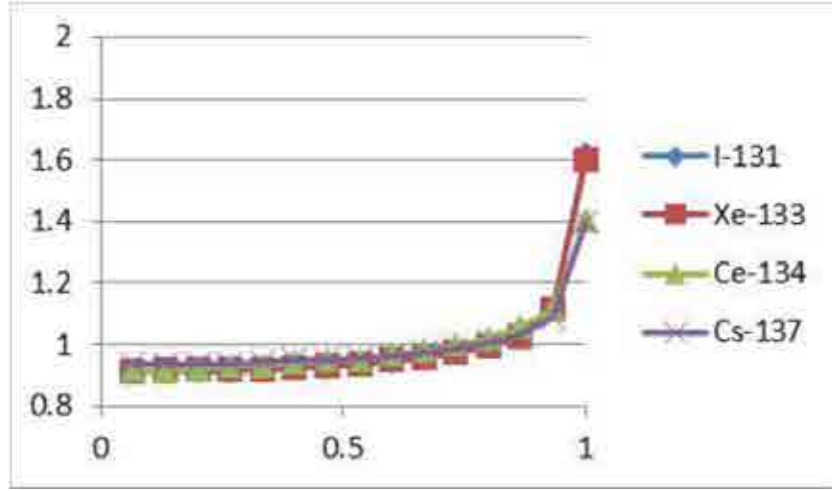
FIG. 3. *Relative radial distribution of I-131, Xe-133, Ce-134 and Cs-137 according to Serpent calculations.*
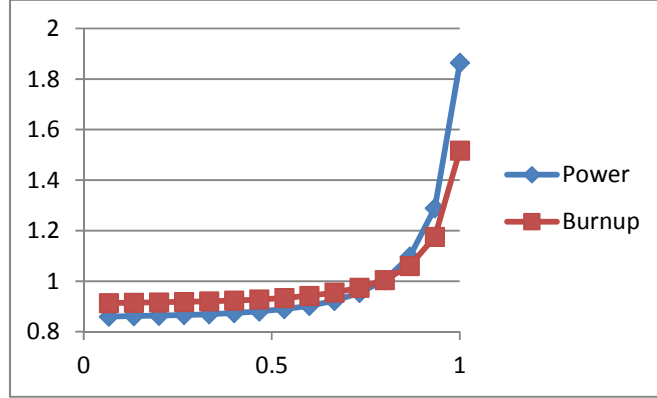

FIG. 4. *Relative radial distribution of burnup and power deposition at the end of ENIGMA simulation using similar power history as Serpent calculations of Figure 3.*

3.3 Effect of high burnup structure

Determining the width of the HBS rim is not entirely straightforward, but estimations have been made. A conservative width of HBS has been proposed [29] as:

$$w_{\text{HBS}} = 13.3(bu_{ave} - 30), \text{ if } bu_{ave} < 60 \text{ MWd/kgU} \tag{3}$$

$$w_{\text{HBS}} = 2.02e^{(bu_{ave}/11.35)}, \text{ if } 60 \text{ MWd/kgU} < bu_{ave} < 75 \text{ MWd/kgU} \tag{4}$$

$$w_{\text{HBS}} = 1500, \text{if } bu_{ave} > 75 \text{ MWd/kgU} \qquad\qquad (5)$$

Taking Eq (3) as a guide, the rim width for a pellet with pellet average burnup of 55 MWd/kgU could be conservatively estimated to be 330 μm, taking a bit over 10% of the pellet total volume, assuming pellet diameter of 1 cm. Should HBS lose its integrity in a high-temperature accident or during long-term storage, its radionuclide inventory would be released. Following [29] the average burnup of the rim would be 1.33 times the pellet average, thus harbouring 13% of the total long-lived nuclides and even larger fraction of short-lived radionuclides. These inventory fractions are in addition to those calculated in the FGR measurements/simulations, as the HBS does not contribute to the usual fission gas release and leaching results.

It should be noted that the assumption of the rim thickness is conservative, and taken as it is indicates large rim inventories. The HBS width given by equations 3–5 is determined mostly by a few outlier cases, with most of the measured HBS widths well below the values given by the equations. When a fuel performance code with a good radial power deposition model (or a link to neutronics code with the capability to spatial resolution) is available, a better way of determining the HBS rim width would be to use fine enough radial mesh and rules to local burnup and temperature as enumerated by Lassman in [14].

Further reduction of conservatism can be made by taking into account that not all of the nuclides reside in the pressurized pores, but some are still located in the grains. As the grains are very small, their retention capability is still less than that of the original sized fuel grains.

4. CONCLUSIONS

In this work the release of radioactive nuclides was investigated with a focus on radial heterogeneity of the fuel pellet. Taking account the radial production of nuclides would not affect the estimated amount of nuclides in the gap for normal operating scenarios as the fitting of the correlations is based on experiments at relatively low temperatures. However, the ratio of nuclides residing inside HBS grows with increasing burnup, which may increase the initial dose during an energetic accident.

The application of this review would be to include the increased rim inventory into models of severe accident management codes as well as an implementation of a fast release model describing the shattering rim inventory. As it currently stands, for instance ASTEC does contain a fuel model but not a dedicated rim description. However, it should be noted that the fast development in what is traditionally considered a severe accident make the detailed fuel modelling mostly irrelevant. As it is, the possible application of these analyses would concentrate more on less energetic scenarios, such as accident scenarios of spent fuel pools.

It should also be noted that even the basic understanding of evolution of radionuclides is still relatively uncertain. For instance there is a factor of 6 difference in the effective diffusion rate of caesium used in ANSI-5.4 standard and the current state of the art final repository analysis. Also fuel oxidation is more studied in the severe accident field than in the traditional fuel behaviour studies. While the analyses have traditionally been separated into different fields, improving the understanding of the common basic phenomena should benefit everyone.

REFERENCES

1. KLEYKAMP, H., The chemical state of the fission products in oxide fuels, Journal of Nuclear Materials, **131** (1985) 221.
2. American National Standard Method for Calculating the Fractional Release of Volatile Fission Products from Oxide Fuel, ANSI/ANS-5.4-2011, American Nuclear Society, 2011.
3. JOHNSON, L.H., TAIT, J.C., Release of segregated nuclides from spent fuel, SKB Technical Report 97–18, 1997.
4. JOHNSON, L. and MCGINNES, D., Partitioning of Radionuclides, in Swiss Power Reactors, Nagra Technical Report 02-07, 2007.
5. JOHNSON, L., GÜNTHER-LEOPOLD, I., WALDIS, J.K., LINDER H.P., LOW J., CUI D., EKEROTH, E., SPAHIU, K., EVINS, L.Z., Rapid aqueous release of fission products from high burn-up LWR fuel: Experimental results and correlations with fission gas release, Journal of Nuclear Materials **420** (2012) 54–62.
6. IGLESIAS, F.C., B.J. LEWIS, P.J. REID, P. ELDER, "Fission product release mechanisms during reactor accident conditions", Journal of Nuclear Materials **270** (1999) pp. 21–38.
7. NUREG/CR-7003 Background and Derivation of ANS-5.4 Standard Fission Product Release Model, Office of Nuclear Regulatory Research.
8. BOOTH, A.H., A suggested method for calculating the diffusion of radioactive rare gas fission products from UO_2 fuel elements and a discussion of proposed in reactor experiments that may be used to test its validity, Atomic Energy of Canada Limited Report, AECL-700. (1957).
9. WHITE, Fission gas release, swelling & grain growth in UO_2, OECD Halden Reactor Project, HPR-368.
10. Data report for the safety assessment SR-Site, SKB Technical Report TR-10-52, 2010.
11. Interim Summary Report of the Safety Case 2009, Posiva 2010-02, 2010.
12. JOHNSON, L., FERRY, C., POINSSOT, C., LOVERA, P., Spent fuel radionuclide source-term model for assessing spent fuel performance in geological disposal. Part I: Assessment of the instant release fraction, Journal of Nuclear Materials **346** (2005) 56–65.
13. NOIROT, J., DESGRANGES, L., LAMONTAGNE, J., Detailed characterisations of high burn-up structures in oxide fuels, Journal of Nuclear Materials **372** (2008) 318–339.
14. LASSMANN, K., WALKER, C.T., VAN DE LAAR, J., LINDSTRÖM, F., Modelling the high burnup UO 2 structure in LWR fuel, Journal of Nuclear Materials **226** (1995) 1–8.
15. BARON, D., M. KINOSHITA, P. THEVENIN, R. LARGENTON, Discussion about HBS transformation in high burn-up fuels, Nuclear Engineering and Technology, Vol. **41** No. 2 (2009) pp. 199–214.
16. ROUDIL, D., JEGOU, C., BROUDIC, V., TRIBET, M., Rim Instant Release Radionuclide Inventory from French High Burnup Spent UOX Fuel, Mater. Res. Soc. Symp. Proc. Vol. **1193** (2009).
17. HIERNAUT J.-P., T. WISS, J.-Y. COLLE, H. THIELE, C.T. WALKER, W. GOLL, R.J.M. KONINGS, Fission product release and microstructure changes during laboratory annealing of a very high burn-up fuel specimen, Journal of Nuclear Materials **377** (2008) 313–324.

18. MARCET, M., DESGRANGES, L., FELINES, I. and PONTILLON, Y., 2010. Correlation between Microstructure Changes and Fission Gas Release Mechanism during a LOCA Type Experiment: An E.S.E.M. investigation, Proceedings of 2010 LWR Fuel Performance /TopFuel/ WRFPM Orlando, Florida, USA, September 26–29, 2010, Paper 037.

19. Fuel Fragmentation, Relocation, and Dispersal During the Loss-of-Coolant Accident, NUREG-2121, Office of Nuclear Regulatory Research (2012).

20. NOIROT, J., DESGRANGES, L., MARIMBEAU, P., Contribution of the rim to the overall fission gas release: What do isotopic analyses reveal in: Fission Gas Behaviour in Water Reactor Fuels, Seminar Proceedings, Cadarache, France, 26–29 September 2000, NEA/OECD.

21. FERRY, C., J-P PIRON, A. AMBARD, Effect of helium on the microstructure of spent fuel in a repository: An operational approach, Journal of Nuclear Materials, **407** (2010) pp. 100–109.

22. LEWIS, B. J. and THOMPSON, W.T., IGLESIAS, F.C., Fission Product Chemistry in Oxide Fuels in Comprehensive Nuclear Materials, R. KONINGS (Ed.), Elsevier Ltd 2012.

23. HIERNAUT, J.-P., WISS, T., RONDINELLA, V.V., COLLE, J.-Y., SASAHARA, A., SONODA, T., KONINGS, R.J.M., 2009, Specific low temperature release of 131Xe from irradiated MOX fuel, Journal of Nuclear Materials **392** (2009) 434–438.

24. SHIRSAT, A.N., M. ALI (BASU), S. KOLAY, A. DATTA, D. DAS, "Transport properties of I, Te and Xe in thoria–urania SIMFUEL", Journal of Nuclear Materials, **392**, Issue 1, 1 July 2009, Pages 16–21.

25. SERNA, J., P. TOLONEN, S. ABETA, S. WATANABE, Y. KOSAKA, T. SENDO AND P. GONZALE, Experimental Observations on Fuel Pellet Performance at High Burnup, Journal of NUCLEAR SCIENCE and TECHNOLOGY, Vol. **43**, No. 9, (2006) pp. 1–9.

26. KONINGS, R. (Ed.), 2012. "Fission Product Chemistry in Oxide Fuels" in Comprehensive Nuclear Materials, Elsevier Ltd 2012.

27. ARKOMA, A., TULKKI, V., Release of radioactive nuclides from spent WWER fuel, 10th International Conference on WWER Fuel Performance, Modelling and Experimental Support, Bulgaria, September 2013.

28. VIITANEN, T., Serpent-ENIGMA – Combining Monte Carlo Reactor Physics with Fuel Performance, VTT-R-06265-11, VTT Technical Research Centre of Finland, 2011.

29. KOO, Y.-H., B-H. LEE, J.-Y. OH, K.-W. SONG, Conservative width of high-burnup structure in light water reactor UO2 fuel as a function of pellet average burnup, Nuclear Technology, Vol **164** (2008) pp. 337–347.

EXPERIMENTAL PROGRAM QUENCH AT KIT ON CORE DEGRADATION DURING REFLOODING UNDER LOCA CONDITIONS AND IN THE EARLY PHASE OF A SEVERE ACCIDENT

J. STUCKERT, M. STEINBRUECK, M. GROSSE
Karlsruhe Institute of Technology (KIT)
Hermann-von-Helmholtz-Platz 1, 76344 Eggenstein-Leopoldshafen
Germany
juri.stuckert@kit.edu, martin.steinbrueck@kit.edu, mirco.grosse@kit.edu

Abstract. The most important accident management measure to terminate a severe accident transient in LWR is the injection of water to cool the uncovered degraded core. In order to detailed investigation of the reflood effect on bundle degradation the QUENCH program was initiated in 1996 followed-up the CORA bundle tests and is still on-going. So far, 17 integral bundle QUENCH experiments with 21–31 electrically heated fuel rod simulators of 2.5 m length using zirconia as fuel substitute have been conducted. Influence of following parameters on bundle degradation were investigated: degree of pre-oxidation, temperature at reflood initiation, flooding rate, effect of neutron absorber materials (B_4C, Ag-In-Cd), air ingress, influence of the type of cladding alloy, formation of a debris bed in the core. Integral bundle experiments are supported by separate-effects tests. The program provides experimental data for the development of quench-related models and for the validation of SFD code systems. In seven tests, reflooding of the bundle led to a temporary temperature excursion. Considerable formation, relocation, and oxidation of melt were observed in all tests with escalation. The temperature boundary between rapid cool down and temperature escalation was typically 2100–2200 K in tests without absorber. Tests with absorber led to temperature escalations at lower temperatures. Although separate-effects tests have shown some differences in oxidation kinetics of advanced cladding materials, the influence of the various cladding alloys on the integral bundle behaviour during oxidation and reflooding was only limited. The two bundle tests with air ingress phase confirmed the strong effect of air on core degradation especially when pre-oxidation in steam is limited and oxygen starvation occurs during the air ingress phase. Oxidation in a nitrogen-containing atmosphere accelerates the kinetics by the temporary formation of zirconium nitride and causes strongly degraded and non-protective oxide scales. The latest QUENCH-LOCA tests investigated influence of secondary hydriding of ruptured cladding on mechanical properties of cladding tubes.

1. INTRODUCTION

The most important accident management measure to terminate a severe accident transient in a Light Water Reactor (LWR) is the injection of water to cool the uncovered degraded core. Since the TMI-2 accident in 1979 [1] fuel degradation under severe accident conditions has been studied extensively in integral and separate-effects experiments. Results of various integral in-pile and out-of-pile experiments like CORA [2], [3], LOFT [4], PHEBUS [5], and PBF [6] have shown that before the water succeeds in cooling the fuel pins there could be an enhanced oxidation of the Zircaloy cladding and other core components that, in turn, causes a sharp increase in temperature, hydrogen production, and fission product release.

The main objective of the QUENCH program at the Karlsruhe Institute of Technology (KIT, formerly FZK) is investigation of hydrogen production that results from the water or steam interaction with overheated elements of fuel assembly. Other ultimate goals of program are to identify the limits (temperature, injection rate, etc.) for which successful reflood and quench can be achieved [7], [8], [9] and to compare recently used cladding materials. Integral bundle experiments are supported by separate-effect tests (SET) and code analyses. The program provides experimental and analytical data for the development of quench and quench-related models and for the validation of severe fuel damage (SFD) code systems such as ASTEC [10].

The last status report on experiments and modelling related to quenching of degraded cores were issued by CSNI in 2000 [11]. Core coolability during reflooding was confirmed to be a high priority issue by the SARNET-SARP group [12]. The database on reflooding has been extended during the last decade especially by the KIT QUENCH program. In Hungary, the CODEX facility was used to investigation the reflood behaviour of oxidised and hydrogenated VVER small test bundles [13], [14]. In Russia, the PARAMETER test series at LUCH has been devoted to studying top flooding and combined top and bottom flooding [15]. This paper summarizes the essential experimental results of the QUENCH bundle and separate-effect tests obtained so far and then discusses the possible influence of various effects on hydrogen release and coolability of the core.

2. CORA PROGRAM ON THE EARLY PHASE OF SEVERE ACCIDENT

The CORA program at KIT [2], [3], preceding the QUENCH program, investigated out-of-pile the integral material behaviour of PWR (11 tests), BWR (6 tests) and VVER (2 tests) bundles up to about 2700 K (Table 1). The decay heat was simulated by electrical heating. Great emphasis was given to the fact that the test bundles contain all materials used in LWR fuel elements to investigate the different material interactions. Pellets, cladding, grid spacers, absorber rods and the pertinent guide tubes were typical to those of commercial LWRs with respect to their compositions and radial dimensions. The PWR-typical bundle consisted of 16 heated, 7 unheated and two absorber rods (Fig. 1). The (Ag 80%, In 15%, Cd 5%) absorber material was sheathed in stainless steel and this rod was surrounded by a Zry-guide tube. The BWR bundle simulated the arrangement of the B_4C absorber-cross placed between two bundles each with 6 heated and 3 unheated rods. VVER-1000 aspects were simulated by use of a 19-rod bundle with a hexagonal arrangement of 13 heated, one B_4C absorber and 5 unheated rods. Three phases can be recognised for each test: 1) gas preheat phase: 0–3000 s; 2) transient phase in steam: 3000–4900 s; 3) quench from bottom (3 tests) or cooling phase.

TABLE 1. MATRIX OF CORA EXPERIMENTS WITH PWR AND BWR TEST BUNDLES

Test No.	Date of Test	Max Cladding Temperature	Absorber Material	Other Test Conditions
2	Aug. 6,1987	≈ 2000°C	-	UO_2 refer. Inconel spacer
3	Dec. 3,1987	≈ 2400°C	-	UO_2 refer. high temperature
5	Feb. 26,1988	≈ 2000°C	AgInCd	PWR-absorber
12	June 9,1988	≈ 2000°C	AgInCd	quenching
16	Nov. 14,1988	≈ 2000°C	*BWR* B_4C	BWR-absorber
15	March 2, 1989	≈ 2000°C	AgInCd	rods with internal pressure
17	June 29,1989	≈ 2000°C	*BWR* B_4C	quenching
9	Nov. 9,1989	≈ 2000°C	AgInCd	10 bar system pressure
7	Feb. 22, 1990	< 2000°C	AgInCd	57-rod bundle, slow cooling

18	June 21, 1990	< 2000°C	*BWR* B$_4$C	59-rod bundle, slow cooling
13	Nov. 15, 1990	≈ 2200°C	AgInCd	quench initiation at higher temperature; OECD/ISP
29	Apr. 11, 1991	≈ 2000°C	AgInCd	pre-oxidized
31	July 25, 1991	≈ 2000°C	*BWR* B$_4$C	slow initial heat-up (≈ 0.3 K/s)
30	Oct. 30, 1991	≈ 2000°C	AgInCd	slow initial heat-up (≈ 0.2 K/s)
28	Feb. 25, 1992	≈ 2000°C	*BWR* B$_4$C	pre-oxidized
10	July 16, 1992	≈ 2000°C	AgInCd	cold lower end; 2 g/s steam flow rate
33	Oct. 1, 1992	≈ 2000°C	*BWR* B$_4$C	dry core conditions, no extra steam input
W1	Feb. 18, 1993	≈ 2000°C		WWER-test
W2	Apr. 21, 1993	≈ 2000°C	*WWER* B$_4$C	WWER-test with absorber
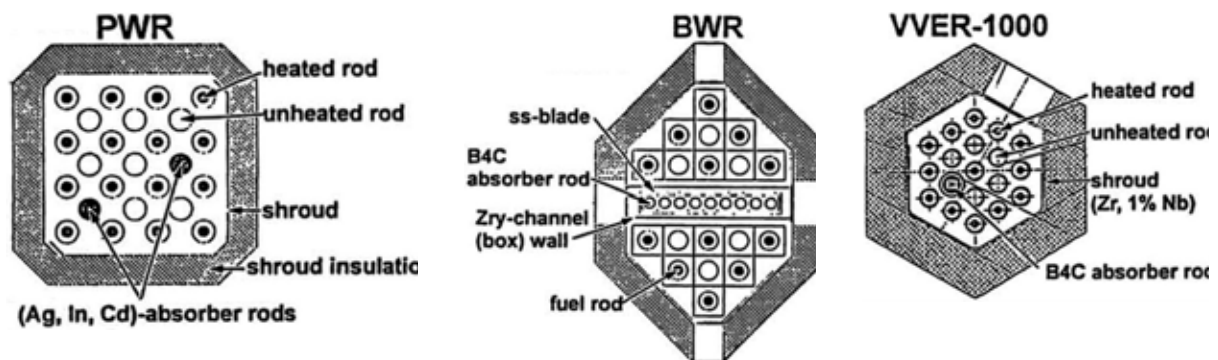
FIG. 1. Types of CORA test bundles.

The results of the integral CORA tests allow the definition of three temperature regimes in which large quantities of liquid phases form which cause extended fuel rod bundle damage and accelerate damage progression: 1) 1500–1700 K: localised core damage; 2) 2100–2300 K: extended core damage; 3) 2900–3150 K: total core destruction. A temperature escalation due to the zirconium-steam reaction started in the upper, i.e. hotter bundle half at about 1400 K and propagated from there downwards and upwards. The maximum heat-up rates and maximum temperatures measured were approx. 20 K/s and 2300 K, respectively. The cladding integrity can be lost far below the melting point of Zircaloy by eutectic interactions with stainless steel of absorber claddings or absorber materials themselves, resulting in formation of liquid phases at temperatures as low as 1550 K (Fig. 2). Significant molten UO$_2$ relocation can begin at the Zircaloy melting temperature of about 2025 K, about 1000 K below the melting point of UO$_2$. The low-temperature early fuel relocation is important for the increased release of volatile fission products and the redistribution of decay heat sources in damaged cores.
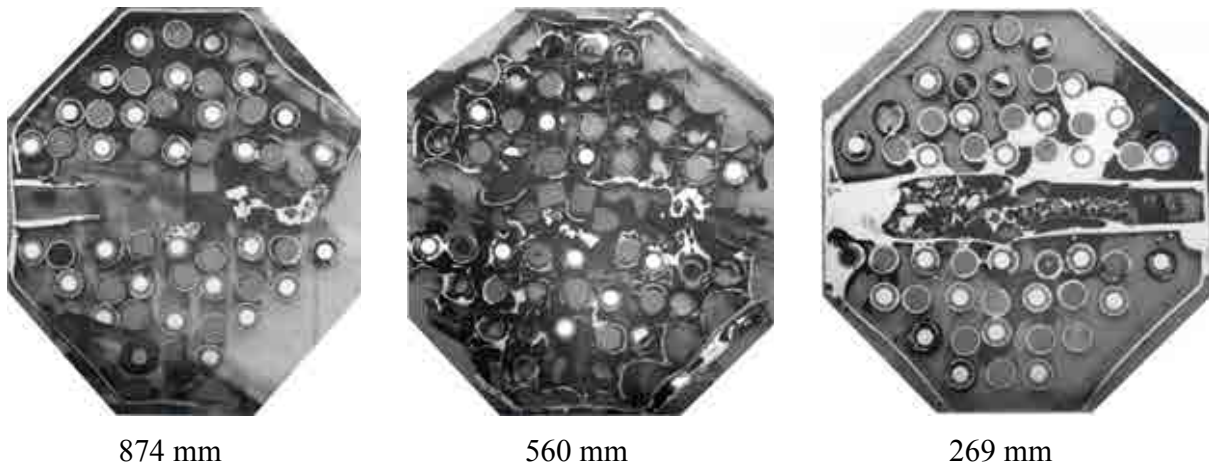
874 mm   560 mm   269 mm

FIG. 2. Melt formation and relocation for the BWR large test bundle CORA-18.

The CORA quench tests have demonstrated that quench did not result in an immediate decrease of the bundle temperature. Instead a preliminary temperature increase connected with additional oxidation with a concomitant rise in hydrogen production was seen in all tests (Fig. 3). In the BWR bundle, temperature and H_2 increases are larger and start also earlier after quench initiation due to 1) interaction of steam with large amounts of melt formed before quench as result of intensive reaction of B_4C with metal; 2) oxidation of B_4C remnants in steam. The last reaction is more exothermic and produces more hydrogen per gram of material than does Zircaloy, however the dominant process for the temperature escalation and increased hydrogen production during reflood should be the melt oxidation.

without quenh   with quench
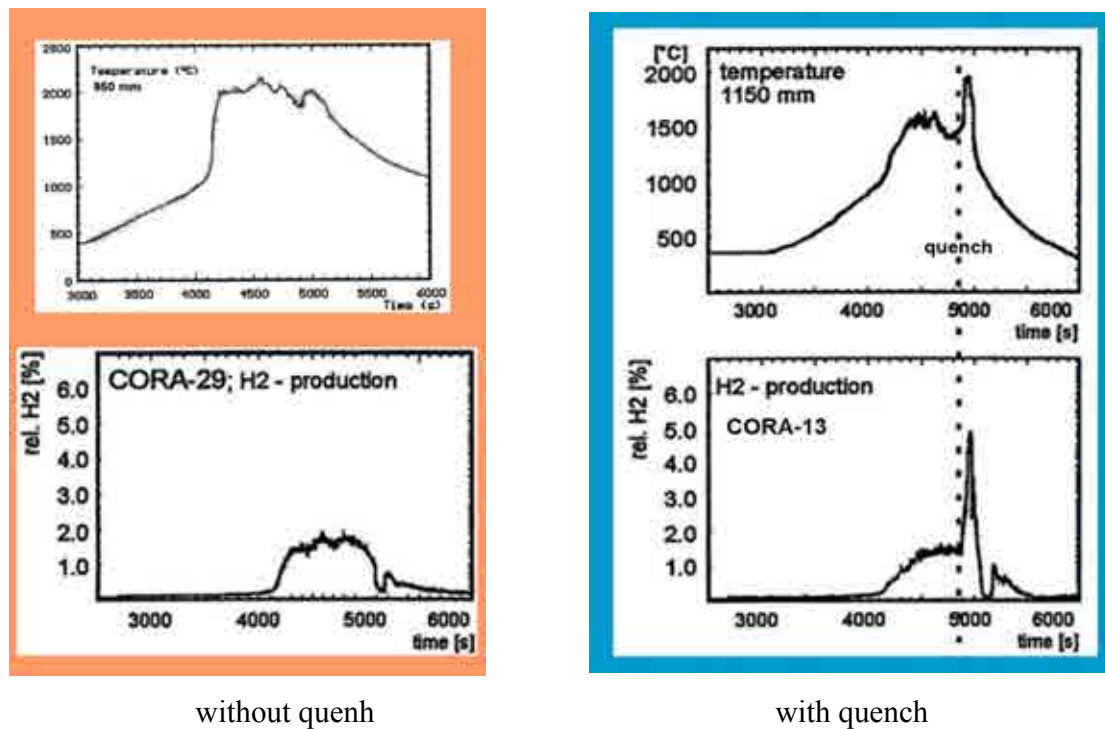
FIG. 3. Hydrogen production during CORA tests without/with reflood (quenching).

3. QUENCH PROGRAM ON THE EARLY PHASE OF SEVERE ACCIDENT

In order to explicitly investigate the effect of reflood on bundle degradation the QUENCH program was initiated in Karlsruhe in 1996 and is still on-going [9], [16] – [18]. This comprises bundle experiments as well as complementary separate-effects tests. So far, 17 integral bundle QUENCH experiments with 21–31 (Fig. 4) electrically heated fuel rod simulators of 2.5 m length using zirconia as fuel substitute have been conducted (Table 2). Following parameters and their influence on bundle degradation and reflood were investigated: degree of pre-oxidation, temperature at reflood initiation, flooding rate, effect of neutron absorber materials (B_4C, AIC), air ingress, and influence of the type of cladding alloy. Typical test scenario includes three phases: preoxidation, transient, quench (Fig. 5). The latest test QUENCH-Debris investigated the formation and coolability of a debris bed in the core.

QUENCH-12 VVER   QUENCH-14 (typical geometry)   QUENCH-15 ZIRLO™
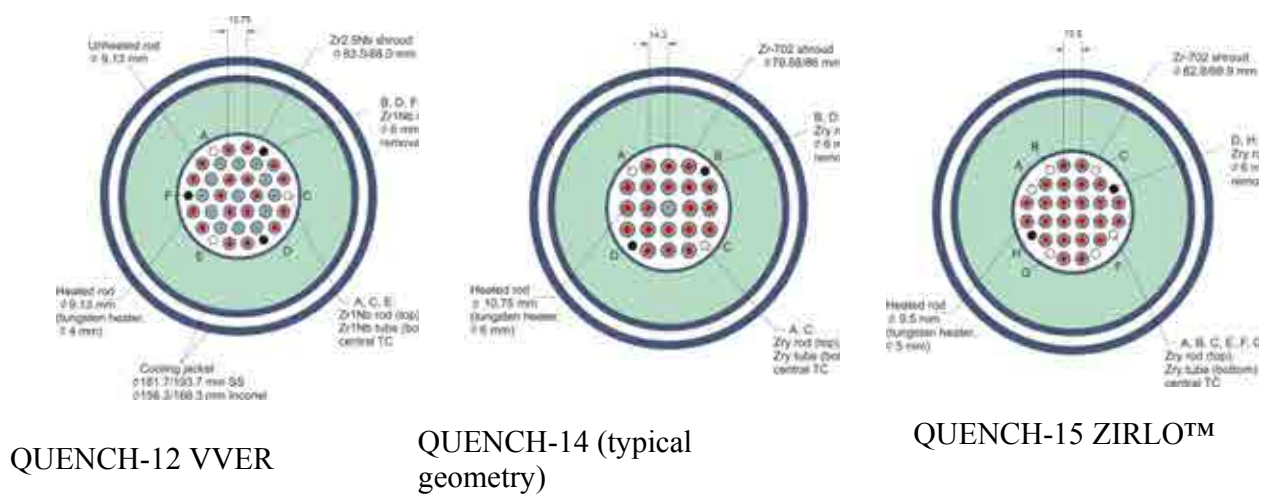
FIG. 4. Composition of different QUENCH bundles.

TABLE 2. MATRIX OF QUENCH EXPERIMENTS

Test	Quench medium / Injection rate	H$_2$ production before / during cooldown	Remarks, objectives
QUENCH-00 Oct. 9 - 16, 97	Water 80 g/s		commissioning test
QUENCH-01 February 26, 98	Water 52 g/s	**36 / 3**	pre-oxidized cladding
QUENCH-02 July 7, 98	Water 47 g/s	**20 / 140**	no additional pre-oxidation, **melt**
QUENCH-03 January 20, 99	Water 40 g/s	**18 / 120**	no additional pre-oxidation, **melt**
QUENCH-04 June 30, 99	Steam 50 g/s	**10 / 2**	slightly pre-oxidized cladding

| (Table 2 continued) Test	Quench medium / Injection rate	H2 production before / during cooldown	Remarks, objectives
QUENCH-05 March 29, 2000	Steam 48 g/s	**25 / 2**	pre-oxidized cladding
QUENCH-07 July 25, 2001	Steam 15 g/s	**66 / 120**	B_4C, **eutectic melt**
QUENCH-09 July 3, 2002	Steam 49 g/s	**60 / 400**	B_4C, **eutectic melt**
QUENCH-08 July 24, 2003	Steam 15 g/s	**46 / 38**	reference for QUENCH-07, **melt**
QUENCH-10 July 21, 2004	Water 50 g/s	**48 / 5**	air ingress
QUENCH-11 Dec 08, 2005	Water 18 g/s	**9 / 132**	boil-off, **melt**; *benchmark*
QUENCH-12 Sept 27, 2006	Water 48 g/s	**34 / 24**	VVER, **melt**
QUENCH-13 Nov. 7, 2007	Water 52 g/s	**42 / 1**	Ag/In/Cd (aerosol)
QUENCH-14 Sept 27, 2006	Water 41 g/s	**34 / 6**	M5® cladding
QUENCH-15 Nov. 7, 2007	Water 41 g/s	**41 / 7**	ZIRLO™ cladding
QUENCH-16 July 27, 2012	Water 50 g/s	**16 / 128**	air ingress, **melt**; *benchmark*
QUENCH-17 Jan. 31, 2013	Water 10 g/s	**110 / 1**	*DEBRIS formation*
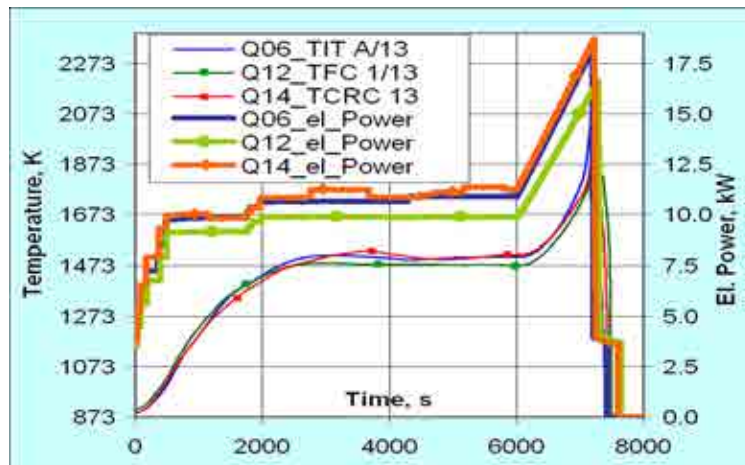
FIG. 4. Typical peak cladding temperatures and power histories during 3 test phases.

In seven tests, reflooding of the bundle led to a temporary temperature excursion driven by runaway oxidation of Zr-alloy components and resulting in release of a significant amount of hydrogen, typically two orders of magnitude greater than in those tests with "successful" quenching in which cool-down was rapidly achieved (Fig. 5). Considerable formation, relocation, and oxidation of melt were observed in all tests with escalation. The temperature boundary between rapid cool down and temperature escalation was typically 2100–2200 K in the "normal" quench tests, i.e. in tests without absorber and/or steam starvation. Tests with absorber and/or steam starvation led to temperature escalations at lower temperatures.
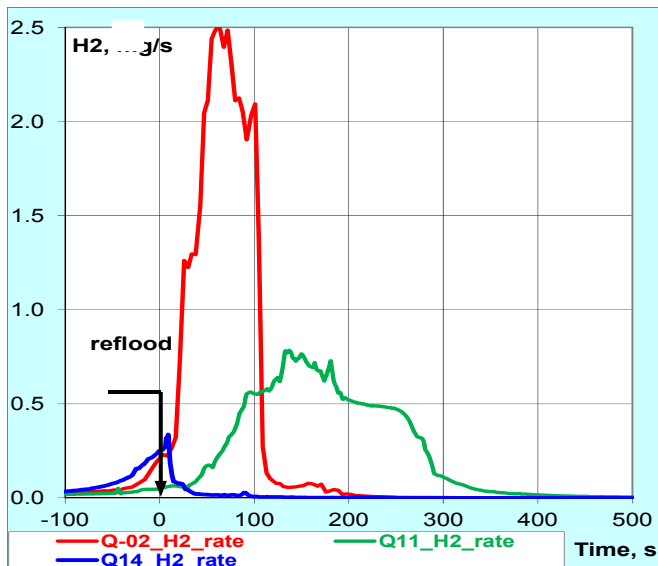
hydrogen production
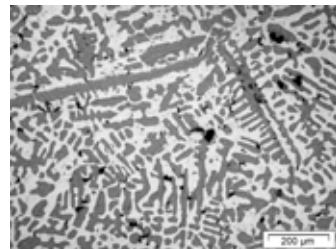
Q11: oxidation of melt released into the space between rods

FIG. 5. Hydrogen production during reflood of bundles with (Q02, Q11) and without (Q14) melt release.

Concerning control rod effects, B_4C neutron absorber has more effect than silver-indium-cadmium (AIC) due to eutectic interaction between B_4C and surrounded stainless steel (Fig. 6). Oxidation of melt formed during this interaction can contribute significantly to hydrogen production (Fig. 7).
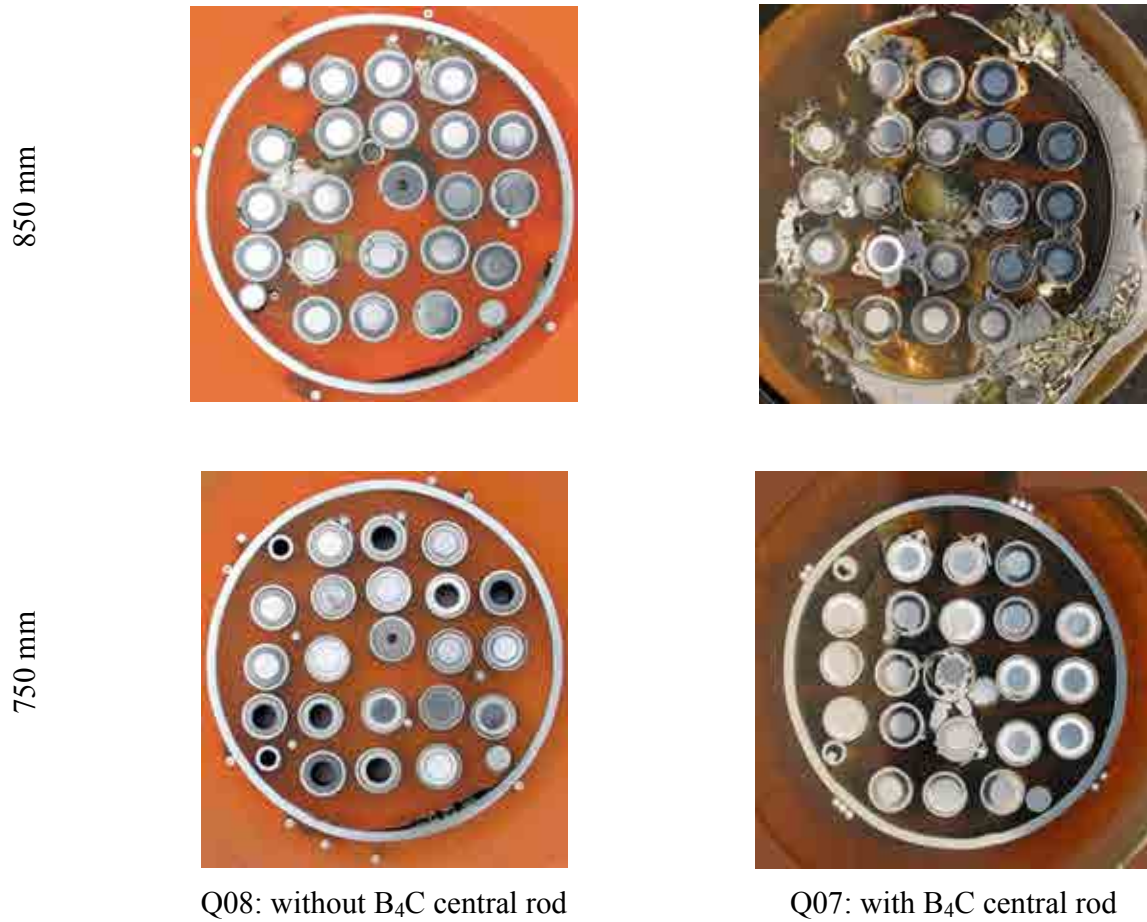

850 mm

750 mm

Q08: without B_4C central rod   Q07: with B_4C central rod

FIG. 6. Intensive melt formation for bundles with B_4C absorber rod.
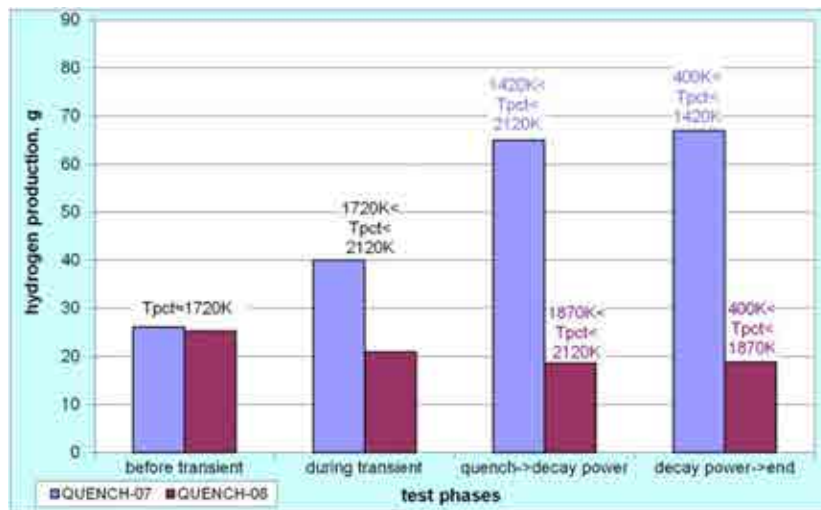
FIG. 7. Comparison of hydrogen release during different test phases for bundle without B₄C rod (QUENCH-08) and with B₄C rod (QUENCH-07).

Several bundle tests were devoted to the investigation of the behaviour of advanced cladding materials (ACM) M5® and ZIRLO™ in comparison with classical Zircaloy-4. Although separate-effects tests have shown some differences in oxidation kinetics, the influence of the various cladding alloys on the integral bundle behaviour during oxidation and reflooding was only limited. For all three alloys was observed formation of crack going through cladding. As result, the steam penetrated through these cracks has oxidised the inner cladding surface with formation of relative thick internal oxide layer (Fig. 8).
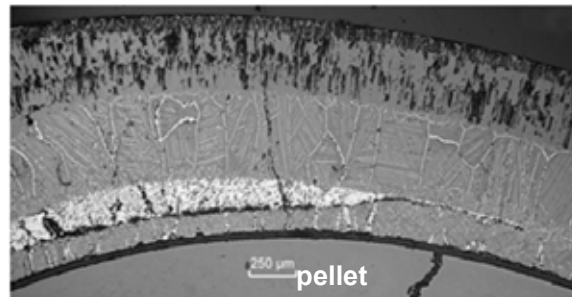

FIG. 8. Typical structure of the cladding at hot elevations: outer and inner oxide layers with interjacent localised melt.

In the case of steam starvation conditions at higher bundle elevations (consuming of steam at lower bundle part) the oxide layer will be degraded until full it dissolution due to oxygen diffusion from oxide to the metal layer (Fig. 9). Reflood of such metallic surfaces induces intensive hydrogen release.
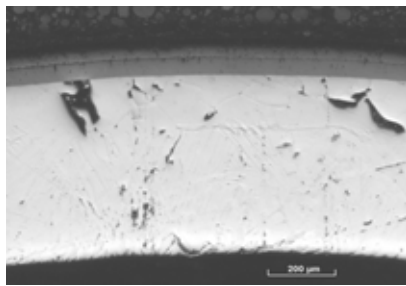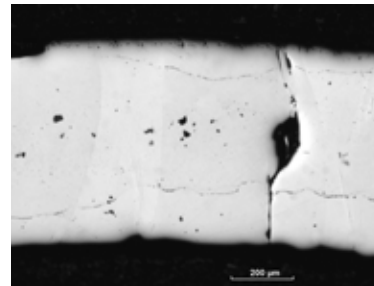
| oxidised cladding | annealing of oxidised cladding in Ar |

FIG. 9. Complete decomposition of oxide layer under steam starvation conditions

Air ingress may have diverse effects on bundle degradation and coolability. On the one hand, energy release by air oxidation is higher, and the cooling effect is lower in comparison with steam. Furthermore, oxidation in a nitrogen-containing atmosphere accelerates the kinetics by the temporary formation of zirconium nitride and causes strongly degraded and non-protective oxide scales. On the other hand, no hydrogen is directly produced by oxidation of metals in air. The two bundle tests with an air ingress phase performed so far confirmed the strong effect of air on core degradation especially when pre-oxidation in steam is limited and oxygen starvation occurs during the air ingress phase (Fig. 10).

| nitriding under steam starvation | re-oxidation of nitrides during reflood and formation of thick oxide underlayer |

FIG. 10. Complete decomposition of oxide layer under steam starvation conditions.

All phenomena occurring in the bundle tests have been further investigated in parametric and more systematic separate-effects tests [19], [20]. Oxidation kinetics of various cladding alloys, including advanced ones, have been determined over a wide temperature range (873–1773 K) in different atmospheres (steam, oxygen, air, and their mixtures). Hydrogen absorption by different Zr-alloys was investigated in detail, recently also using neutron radiography as non-destructive method for determination of hydrogen distribution in clad. Also, degradation mechanisms of absorber rods including B_4C and AIC as well as the oxidation of the resulting low-temperature melts have been studied. Steam starvation was found to cause deterioration of the protective oxide scale by thinning and chemical reduction.

A general outcome of the QUENCH experiments is, that a nuclear reactor core is coolable as long as the core is still intact and no or only local melt formation has already taken place. This is a realistic boundary condition up to 2200 K provided that the reflood water flow rate is >1 g/s

per rod, no strong eutectic melt formation occurred, and extended steam starvation phases before reflooding could be avoided.

4. SUMMARY OUTCOMES OF CORA AND QUENCH PROGRAMS

Together with results of former REBEKA program at KIT on the LOCA phenomena [21], [22] following main stages of the early phase of severe accident of are identified:

- 720–820°C: creep deformation (ballooning) and failure of the Zr-alloy clad in low pressure sequences, and melting in-situ of AIC absorber alloy

- 1200–1400°C: start of rapid Zr oxidation by steam leading to uncontrolled temperature excursion and extensive hydrogen production; liquefaction of Inconel grid spacers and absorber rod materials due to eutectic interactions, giving metallic melts which initiate core melt progression

- 1750–2400°C: melting of the remaining metallic Zr-alloy and/or alpha-Zr(O) with subsequent chemical dissolution of fuel, leading to formation of partially oxidised molten pools which relocate and form blockages on solidification

Additionally, air ingress into the overheated bundle accelerates oxidation and degradation of fuel rod claddings.

Injection of water into the overheated bundle can accelerate temperature excursion and hydrogen release due to following mechanisms:

- Low reflood flow rates < 1 g/s/rod (QUENCH-07, -08, -11);

- Breakaway effect with weakness and spallation of protective oxide layer (QUENCH-12);

- Steam starvation (QUENCH-09);

- Nitride formation by air ingress with formation of very porous oxide layer during following reflood (QUENCH-10, -16);

- High temperatures with melt relocation outside claddings and intensive melt oxidation (QUENCH-02, -03, -11);

- Eutectic interactions between B_4C, stainless steel and Zircaloy-4 leading to low melting point (QUENCH-07, -09).

5. QUENCH-LOCA PROGRAM AT KIT

Due to different advantages the current trend in the nuclear industry is to increase fuel burn-up. At high burn-up, fuel rods fabricated from conventional Zry-4 often exhibit significant oxidation, hydriding, and oxide spallation. Thus, many fuel vendors have proposed the use of recently developed advanced cladding alloys, such as Duplex DX-D4, M5[®], ZIRLO™ and other. Therefore, it is important to verify the safety margins for high burn-up fuel and fuel claddings with the new alloys. In recognition of this, LOCA-related behaviour of new types of cladding is being actively investigated in several countries [23], [24]. Due to long cladding hydriding period for the high fuel burn-up, post-quench ductility is strongly influenced not only by oxidation but also hydrogen uptake [25]. The 17% ECR limit is inadequate to ensure post-quench ductility at

hydrogen concentrations higher than ≈500 wppm [26]. Due to so called secondary hydriding (during oxidation of inner cladding surface after burst), which was firstly observed in JAEA [27], the hydrogen content can reach 4000 wppm in Zircaloy cladding regions around the burst [28].

To investigate the influence of these phenomena on the applicability of the embrittlement criteria for the German nuclear reactors it was decided to perform the QUENCH-LOCA bundle test series at the Karlsruhe Institute of Technology (KIT) in the QUENCH facility [29]. Compared to single-rod experiments, bundle tests have the advantage of studying the mutual interference of rod ballooning among fuel rod simulators as well as the local coolant channel blockages in a more realistic arrangement. The first experiment QUENCH-L0 was performed in July 2010 as commissioning test with not pre-oxidised Zry-4 cladding tubes. The heating rate during transient was 2.5 K/s. The second test QUENCH-L1 with the same claddings but with higher transient rate of about 6 K/s was performed recently in February 2012, the recent test QUENCH-L2 with the M5® cladding tubes was performed in July 203.

For QUENCH-L0 each rod was separately pressurized with krypton with initial pressures of 35, 40, 45, 50, and 55 bar. The duration of transient from 520 to 1070°C was 185 s. The increased ductility of the heated cladding resulted in a progressive ballooning and consequent burst of all of the pressurized rods (Fig. 11). The first burst occurred on 110 s after transient initiation. All pressurized rods failed within the next 60 s. The experiment was terminated by rapid cooling to 130°C.
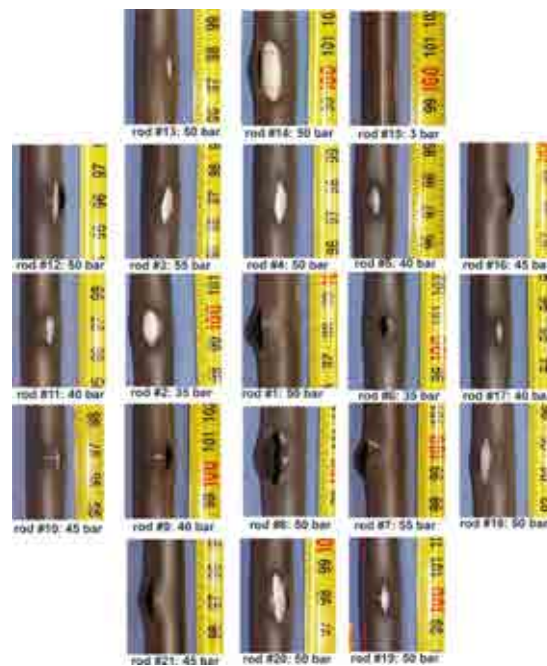

FIG. 11. Form and axial burst positions of burst openings for the QUENCH-L0 test.

The inner cladding surface was oxidized due to steam penetration through the rupture and axial and circumferential propagation in the gap between pellet and cladding. Thereby the inner surface was oxidized only in vicinity of the burst opening. Indeed, the oxidation grade of the inner cladding side, which was opposite to the burst opening, is comparable with oxidation of outer cladding surface at this elevation (Fig. 12). In contrast, the inner cladding surface at elevations located more than 20 mm away from the burst evident negligible or absent oxide layer.
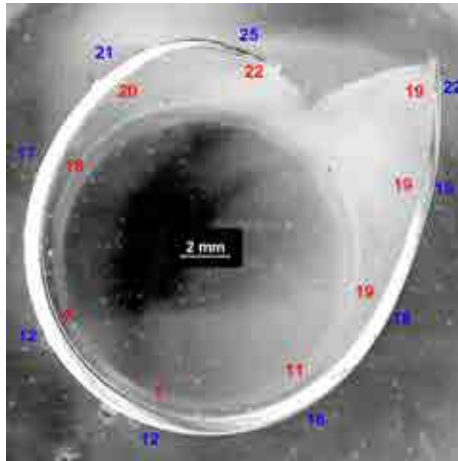
FIG. 12. Oxide layer thicknesses for inner and outer oxide layers at the burst position.

It can be assumed that hydrogen, released during the oxidation of the inner cladding surface, was absorbed by the cladding metal at the boundary of the oxide layer formed around the burst opening. Figure 13 shows neutron radiographs of the investigated rods. Different burst sizes are obvious. On both sides of the burst positions sloping and bended hydrogen containing darker bands can clearly be seen. Evaluation of tomography data showed that central rod #1 has maximal hydrogenation degree with hydrogen concentration of about 2500 wppm.
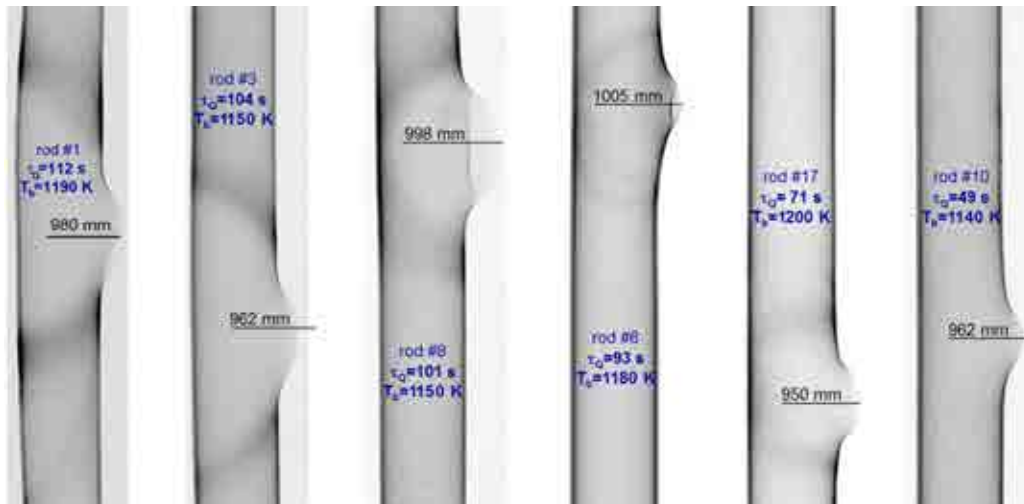

FIG. 13. Hydrogen bands around burst location.

Since usual ring-compression tests can be used only for cylindrical specimens (not for cone-shaped as in the burst region of cladding) and do not deliver quantitative stress-strain data, special tensile tests were performed. These experiments were carried out on longer cladding sections (length $L_0 \sim 0.5$ m) using an Instron testing machine (type 4505), equipped with special grip holders with chain link and an optical measurement system (CCD-cameras system). The optical device was used during tensile tests to measure the global axial deformation, as well as local axial deformations from defined cladding sections.

With the global deformation, the deformation and failure behaviour of the entire cladding can be determined. In Figure 14, a diagram with selected examples of deformation curves is presented, including a picture with corresponding points of rupture.
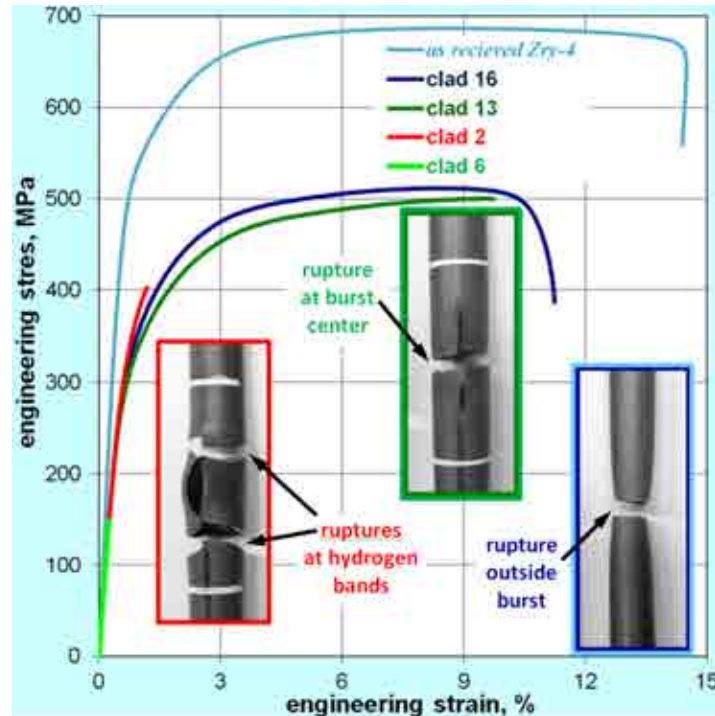

FIG. 14. Results of tensile testing for four rods.

In general it was observed, that failure is mainly influenced by the shape of the burst opening. If an opening edge shows a discontinuity like a buckle or a small cross crack, failure occurs independent of the tubes position in the bundle, within the burst region, based on local stress concentrations. If both crack edges exhibit geometry free from discontinuities, failure depends on the radial position of a cladding within the bundle. Based on a higher degree of oxidation/hydrogenation, tubes close to the bundle centre fail brittle near to burst opening along the hydrogen bands. Specimens from the bundle periphery show a distinctive ductile behaviour and rupture occurs after necking beyond the region of considerable ballooning.

6. PRELIMINARY RESULTS OF FIRST QUENCH-LOCA BUNDLE TESTS

- Typical ballooning and burst processes were observed for all pressurised rods. All burst cases took place during the transient heating phase at temperatures between 1073 und 1173 K. Burst opening lengths between 8 and 20 mm were measured.

- Measured circumferential strains are between 20 und 40%. Maximal blockage of cooling channel is 21%.

- Oxide layers formed on outer and inner cladding surfaces near to burst elevations. The axial expansion of inner oxidized area is between 10 and 20 mm from the burst centre. Only external oxide layer was observed farther from burst positions. Maximal oxide layer thickness of about 20 μm (ECR ~ 2%) was measured.

- Neutron radiography showed formation of hydrogen bands with a width of about 10 mm at the boundary of cladding inner oxidized area. Formation of this hydrogen bands was observed for rods with time interval between burst and quench initiation of more than 70 s. Hydrogen contents up to 2500 wppm at band locations were measured by means of neutron tomography.

- An increased micro hardness up to 360 HV was measured inside hydrogen bands. The micro hardness outside bands was close to values of as-received Zircaloy-4 (210 HV).

- No hydrides were detected by means of optical microscopy, XRD and TEM. Hydrogen is at least partially dissolved in the α-Zr lattice.

- Tension tests with cladding segments showed different rupture positions: 1) double brittle rupture along hydrogen bands with hydrogen concentration of more than 1500 wppm; 2) at burst centre due to stress concentration at burst discontinuities; 3) necking rupture at a distance of about 200 mm from the burst position.

ACKNOWLEDGMENTS

REFERENCES

[1]   Nuclear Technology 87, issues no.1–4, August-December 1989.

[2]   SCHANZ, G., HAGEN, S., HOFMANN, P., SCHUMACHER, G., SEPOLD, L., Information on the evolution of severe LWR fuel element damage obtained in the CORA program, J. Nucl. Mater. **18**8 (1992), pp. 131–145.

[3]   HOFMANN, P. et al., Chemical–physical behaviour of light water reactor core components tested under severe reactor accident conditions in the CORA facility, Nucl. Tech. **118**, 1997, pp. 200–224.

[4]   MODRO, S.M., CARBONEAU, M.L., The LP-FP-2 Severe Fuel Damage Scenario; Discussion of the Relative Influence of the Transient and the Reflood Phase in Affecting the Final Conditions of the Bundle., ISBN 92-64-03339-4, Report OECD/LOFT Final Event.

[5]   LUZE, O., HASTE, T., BARRACHIN, M., REPETTO, G., Early phase fuel degradation in Phébus FP: Initiating phenomena of degradation in fuel bundle tests. Ann. Nucl. Energy **61**, 2013, pp. 23–35

[6]   PETTI, D.A. et al, Power Burst Facility (PBF) Severe Fuel Damage Test 1–4, Test Results. U.S. Nuclear Regulatory Commission, Report NUREG/CR-5163, EGG-2541.

[7] HERING, W., HOMANN, C., Degraded core reflood: Present understanding and impact on LWRs. Nuclear Engineering and Design 237, 2007, pp. 2315–2321.

[8] HERING, W., HOMANN, C., TROMM, W., STATUs of experimental and analytical investigations on degraded core reflood. In: NEA/SARNET2 Workshop on In-Vessel Coolability, Issy-les-Moulineaux, France, October 12–14, 2009.

[9] STEINBRÜCK, M., GROSSE, M., SEPOLD, L., STUCKERT, J., Synopsis and outcome of the QUENCH experimental program, Nucl. Eng. Des. 240, 2010, pp. 1714–1727.

[10] VAN DORSSELAERE, J.P. et al., The ASTEC integral code for severe accident simulation, Nucl. Tech. 165, 2009, pp. 293–307.

[11] HASTE, T., Trambauer, K., Degraded Core Quench: Summary of Progress 1996–1999, Report NEA/CSNI/R(99)23, 2000. http://www.oecd-nea.org/nsd/docs/1999/csni-r99-23.pdf.

[12] SCHWINGES, B., JOURNEAU, C., HASTE, T., MEYER, L., TROMM, W., TRAMBAUER, K., Ranking of severe accident research priorities. Progr. Nucl. Energy 52, 2010, pp. 11–18.

[13] HÓZER, Z., Summary of the Core Degradation Experiments CODEX. Forum for nuclear safety EUROSAFE-2002. Berlin, 4–5 November, 2002. http://www.eurosafe-forum.org/files/euro02_2_3_core_degradation_codex.pdf.

[14] HÓZER, Z., BALASKÓ, M., HORVÁTH, M., KUNSTÁR, M., MATUS, L., NAGY, I, NOVOTNY, T, PEREZ-FERÓ, T., PINTÉR, A., VÉR, N, VIMI, A., WINDBERG, P., Quenching of high temperature VVER fuel after long term oxidationin hydrogen rich steam. Annals of Nuclear Energy 37 (2010), pp. 71–82.

[15] KISELEV, A., IGNATIEV, D., KONSTANTINOV, V., SOLDATKIN, D., NALIVAEV, V., SEMISHKIN, V., Main results and conclusions of the VVER fuel assemblies tests under severe accident conditions in the large-scale PARAMETER test facility. 16th International QUENCH Workshop, Karlsruhe, 16–18 November, 2010, ISBN 978-3-923704-74-3

[16] STUCKERT, J. et al., Experimental and calculation results of the integral reflood test QUENCH-14 with M5® cladding tubes, Ann. Nucl. En. 37, 2010, pp. 1036–1047.

[17] STUCKERT, J. et al., Experimental and calculation results of the integral reflood test QUENCH-15 with ZIRLOTM cladding tubes in comparison with results of previous QUENCH tests, Nucl. Eng. Des. 241, 2011, pp. 3224-3233.

[18] STUCKERT, J., STEINBRÜCK, M., Experimental results of the QUENCH-16 bundle test on air ingress, submitted to Prog. Nucl. En., May 2013.

[19] STEINBRÜCK, M., Prototypical experiments relating to air oxidation of Zircaloy-4 at high temperatures, J. Nucl. Mater. 392, 2009, pp. 531–544.

[20] STEINBRÜCK, M., Degradation and oxidation of B4C control rod segments at high temperatures, J. Nucl. Mater. 400, 2010, pp. 138–150.

[21] ERBACHER, F.J., Cladding Tube Deformation and Core Emergency Cooling in a Loss of Coolant Accident of a Pressurized Water Reactor, Nuclear Engineering and Design, 103 (1987), pp. 55-64.

[22] ERBACHER, F.J., NEITZEL, H.J., WIEHR, K., Cladding Deformation and Emergency Core Cooling of a Pressurized Water Reactor in a LOCA. Summary Description of the REBEKA Program, Scientific Report KfK 4781, Karlsruhe (August 1990), http://bibliothek.fzk.de/zb/kfk-berichte/KFK4781.pdf.

[23] BRACHET, J.-C., VANDENBERGHE-MAILLOT, V., PORTIER, L., GILBON, D., LESBROS, A., WAECKEL, N., and MARDON, J.-P., Hydrogen Content, Preoxidation,

and Cooling Scenario Effects on Post-Quench Microstructure and Mechanical Properties of Zircaloy-4 and M5® Alloys in LOCA Conditions. Journal of ASTM International, 5, Issue 5 (May 2008), Paper ID JAI 101116.

[24] CHUTO, T., NAGASE, F. and FUKETA, T., High Temperature Oxidation of Nb-containing Zr Alloy Cladding in LOCA Conditions. Nuclear Engineering and Technology, **41**, Issue 2 (March 2009), pp. 163–170.

[25] GRANDJEAN, C. and HACHE G., A state of the art review of past programs devoted to fuel behaviour under LOCA conditions - part 3; cladding oxidation, resistance to quench and post quench loads. Technical Report IRSN/DPAM/SEMCA 2008–093. http://www.irsn.fr/EN/Research/publications-documentation/Publications/DPAM/SEMCA/Documents/IRSN_review-LOCA-Part3.pdf.

[26] CHUNG, H.M., Fuel Behavior under Loss-of-Coolant Accident Situations. Nuclear Engineering and Technology, **37**, Issue 4 (August 2005), pp. 327–362.

[27] UETSUKA, H., FURUTA, T. and KAWASAKI, S., Zircaloy-4 Cladding Embrittlement due to Inner Surface Oxidation under Simulated Loss-of-Coolant Condition. Journal of Nuclear Science and Technology, **18,** Issue 9 (September 1981), pp. 705–717.

[28] BILLONE M., YAN Y., BURTSEVA T., DAUM R., Cladding Embrittlement During Postulated Loss-of-Coolant Accidents. NUREG/CR-6967 (July 2008). http://www.ipd.anl.gov/anlpubs/2008/08/62254.pdf.

[29] Stuckert, J., Große, M., Rössger, C., Klimenkov, M., Steinbrück, M., Walter, M., QUENCH-LOCA program at KIT on secondary hydriding and results of the commissioning bundle test QUENCH-L0. Nuclear Engineering and Design, **255** (2013), pp. 185– 201.

MODELLING OF CORE DEGRADATION AND PROGRESSION OF SEVERE ACCIDENT BY USING MELCOR CODE

C. MUGICA, V. GODINEZ
National Commission of Nuclear Safety and Safeguards,
Department of Energy,
Mexico City, Mexico
Email: cesar.mugica@cnsns.gob.mx

Abstract. After Fukushima Daiichi Nuclear Accident, every single nuclear-field organization in the world focused in the analysis and study of scenarios that leads to core damage and hydrogen releases, in this way the integrated code MELCOR is used by the Mexican Regulatory Body as a tool in the analysis of severe accident progression, core melting and degradation. Scenarios related to core melting could provide information that show important parameters such as: time to reach the core damage, time window for level recovery, etc. This information is useful in the analysis of progression for this kind of events. In this work, Mexican Regulatory Body presents two simulations for different scenarios: a) Station Blackout with no cooling water injection and b) Station Blackout with late cooling water injection. Those two scenarios enclose the response of the fuel under Severe Accident conditions (progression of melting, relocation, temperature profile), plots in this document are qualitative items that allow to analyze the behavior for fuel/core elements.

1. INTRODUCTION

MELCOR code is software with capabilities to simulate the progression of a severe accident as well as core degradation and thermal response. Core relocation during melting and phenomena earlier specified are modelled by COR Package [1].

MELCOR as a "simulation tool" is widely used by National Commission of Nuclear Safety and Safeguards (CNSNS - Mexican Nuclear Regulatory Body) to simulate scenarios that leads to core damage with leakages and releases as consequences of accident progression. Nowadays CNSNS has a model "enough tuned" to simulate scenarios for BWR – MARK II Containment Type (Mexican type - Nuclear Power Plan Laguna Verde). This model is used to evaluate the behaviour of BWR – MARK II Containment in severe accident conditions (Core Degradation, Relocation, Time of…, Releases, Hydrogen Generation, Venting Actions, among others).

This allow to CNSNS evaluate the analysis that supports the utility's response to request or requirements of changes, implementations, modifications for equipment or systems, as well as supporting to analyses that leads to Core Damage in Probabilistic Safety Analysis (PSA I and PSA II) developed in this institution (CNSNS – MEXICO) [2].

Scenarios follow the directions stated in Emergency Procedures (Currently CFE as NPP Operator is working on Severe Accident Management Guidelines (SAMG's) because of a requirement of Regulator Body - CNSNS) for events postulated to reach a severe condition / core damage / vessel or containment failure, (at this time is what CNSNS can evaluate directly documents, analyses, results or conclusions from utility, in near future, SAMG's will be the study case object).

In a more detailed and specific situation, core degradation is important to CNSNS, because the analyses related to core re-flooding to mitigate or delay the failure of fuel bundles, internal structures or peripherical elements represent an opportunity to evaluate the impact and reliability of usage of injection systems (ECCS) in early or late time term after core is going to be melted. High and low pressure scenarios leads to different time at when the core starts to be damaged, it

depends of many variables including the capacity of systems, consideration of strategies, core and fuel parameters.

Laguna Verde Nuclear Power Plant is a BWR (444 Fuel Assemblies Core Arrangement), Mark II Containment, 2317 MWth Utility, located in Alto Lucero City in State of Veracruz, México. CNSNS Melcor model is based in those features and includes characteristics plant parameters [3]. In this way trends and results of simulations performed for analysis are quite close to expected for a real case in an event of severe accident. It is important to know that a severe accident for a specific nuclear power plant is a hypothetical scenario, experiments related to ceramic and other internal elements are performed in several research facilities and compared against results provided by codes.

2.   SCENARIOS DETAILS

Features for each scenario are shown below, both of them are Station Blackout (SBO) type with an initial water injection during 4 hours by Reactor Core Isolation Cooling System (RCIC) (Mass Flow Injection = 25 kg/s), actions are performed in accordance with emergency procedures (most actions are related with Safety Relief Valves – SRVs to depressurisation of vessel reactor while power and pneumatic supply are available). Table I shows features for the first case: no cooling / no re-flooding (no water source recovered) and Table II shows the features for second case: cooling / re-flooding (water source recovered).

TABLE 1. SBO WITH NO COOLING WATER INJECTION (48 HRS TOTAL)

Scenario:	SBO (Diesel Generator Div I, II and III lost)
Available Systems	RCIC
Survival Time:	4 hours
Power Supply/Batteries Recovery:	NO
Core Re-Flooding:	NO
Systems Recovered:	NO
Uncovered Core Time Window (TAF Reached):	INFINITE
Actions performed (EP's):	Keep SRV open until reach 13 kg/cm^2 (Reactor Pressure) Close SRV to setpoint for automatic opening Re-open manually until reach again 13 kg/cm2 Close again until setpoint for automatic opening Repeat until batteries available RCIC will start automatically inject water during approximately 4 hours (batteries life) No Systems for injection will be recovered Progressive Core Damage is expected

TABLE 2. SBO WITH LATE COOLING WATER INJECTION (48 HRS TOTAL)

Scenario:	SBO (DG Div I, II and III lost)
Available Systems	RCIC
Survival Time:	4 hours
Power Supply/Batteries Recovery:	YES
Core Re-Flooding:	YES
Systems Recovered:	High and Low Pressure Systems
Uncovered Core Time Window (TAF Reached):	4 hrs approximately
Actions performed (EP's):	Keep SRV open until reach 13 kg/cm2 (Reactor Pressure) Close SRV to setpoint for automatic opening Re-open manually until reach again 13 kg/cm2 Close again until setpoint for automatic opening Repeat until batteries available RCIC will start automatically inject water during approximately 4 hours (batteries life) Systems for injection are recovered after 10 hrs of IE Core Damage is expected during uncovered stage, however mitigation after re-flooding could be considered

3. LAGUNA VERDE NPP MELCOR-CNSNS MODEL

LVNPP MELCOR-CNSNS Model is based on a BWR Mark II Reactor Type, Hardened Venting System is implemented (Utility is going to migrate to this in 2014) and other specific plant parameters are used to characterize this model, 10 uncollapsed SRVs modelled, 2 recirculation loops collapsed, and 7 control volumes to represent the entire vessel, other volumes arrangements are used to represent the primary containment, cavities, reactor building, among others. Figure 1 shows the model material arrangement that includes a 4-ring CORE with 9 axial levels (which only 6 are active fuel). Figure 2 shows the spatial nodalisation, radial rings are specified in lower section, notation for nodes are in format XZZ, where X is the radial location and ZZ the axial sector.

Options for core failure melting modeling in code were mostly used as default values and those suggested by specialized references and expert criteria [4]. A Technical Meeting with Sandia National Laboratories (SNL) MELCOR Team last year, resulted in a pool of comments, suggestions and notes to improve and perform changes to LVNPP MELCOR-CNSNS Model [5].

PLATE (SS)	PLATE (SS)	PLATE (SS)	PLATE (SS)	
COLUMN (SS) BLADE (NS)	COLUMN (SS) BLADE (NS)	COLUMN (SS) BLADE (NS)	COLUMN (SS) BLADE (NS)	
COLUMN (SS) BLADE (NS)	COLUMN (SS) BLADE (NS)	COLUMN (SS) BLADE (NS)	COLUMN (SS) BLADE (NS)	
COLUMN (SS) BLADE (NS)	COLUMN (SS) BLADE (NS)	COLUMN (SS) BLADE (NS)	COLUMN (SS) BLADE (NS)	
COLUMN (SS) BLADE (NS)	COLUMN (SS) BLADE (NS)	COLUMN (SS) BLADE (NS)	COLUMN (SS) BLADE (NS)	
COLUMN (SS) BLADE (NS)	COLUMN (SS) BLADE (NS)	COLUMN (SS) BLADE (NS)	COLUMN (SS) BLADE (NS)	
COLUMN (SS) BLADE (NS)	COLUMN (SS) BLADE (NS)	COLUMN (SS) BLADE (NS)	COLUMN (SS) BLADE (NS)	
COLUMN (SS) BLADE (NS)	COLUMN (SS) BLADE (NS)	COLUMN (SS) BLADE (NS)	COLUMN (SS) BLADE (NS)	
PLATEB (SS)	PLATEB (SS)	PLATEB (SS)	PLATEB (SS)	
COLUMN (SS)	COLUMN (SS)	COLUMN (SS)	COLUMN (SS)	
COLSPP (SS)	COLSPP (SS)	COLSPP (SS)	COLSPP (SS)	COLSPP (SS)
COLUMN (SS)	COLUMN (SS)	COLUMN (SS)	ENDCOL (SS)	PLATEG (SS)
ENDCOL (SS)	ENDCOL (SS)	ENCOL (SS)		
1.35 (52.7")	.233 (9.1")	.233 (9.1")	.233 (9.1")	.50273 (19.80")
60	26	16	7	0

FIG. 1. Control Blades and Supporting Structures Arrangement in CORE.

113	213	313	413	513
112	212	312	412	512
111	211	311	411	511
110	210	310	410	510
109	209	309	409	509
108	208	308	408	508
107	207	307	407	507
106	206	306	406	506
105	205	305	405	505
104	204	304	404	504
103	203	303	403	503
102	202	302	402	502
101	201	301	401	501

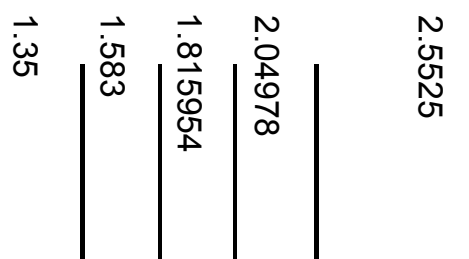Rings(m):

1.35   1.583   1.815954   2.04978   2.5525

FIG. 2. Radial/Axial Mapping of CORE for LVNPP MELCOR-CNSNS Model.

4. ANALYSIS, RESULTS AND PLOTS FOR SCENARIOS

4.1 SBO with no injection (no re-flooding)

Figures 3–6 (Power, Pressure, RCIC Injection and Level) show the trends of vessel parameters related with behaviour against features described in table 1 for scenario 1 (first case). Pressure is mitigated by RCIC injection (from top of vessel), once RCIC is tripped to inject water, pressure increases rapidly.

Because of RCIC provide enough water to recover level, TAF core limit is never reached (while RCIC is available), RCIC stops to inject water once it reaches the upper limit (RCIC had two actuations as showed in Figure 5), this injection allow to delay the core damage progression for some hours. (6 hrs approximately – compared against a boiloff scenario with no injection / no water sources)

Once injection is absent, level starts to decrease gradually as well as fuel temperature increases in core, Figs. 6–7 show those trends, fuel elements still heating and damage to structures appears at the time of heat is enough to melt the materials in core, figure 8 shows the total hydrogen generated for this process.

Figures 9–14 show that melting profile is in accordance with expected (from top to bottom nodes) and that failure of core elements and consequent fall to bottom sections for ring 1 occurs at approximately 11 hours from Initiator Event (Station Blackout).

Core damage is gradually increased as much as cell temperature in uncovered nodes, partial melting occurs firstly in top nodes for central ring in radial nodalisation which is expected for LVNPP MELCOR Model.

Central ring completely fails and collapses to bottom section, debris now is in contact with structures in there, and the heat in corium is transferred to lower wall structures, it causes the vessel failure at approximately 12 hours after initiator event.

Core temperature increases rapidly once core is uncovered, and time to reach the failure point (vessel) is approximately 2 hours after water level is below BAF. Corium in the bottom section is in contact with vessel lower wall and penetration (for LVNPP MELCOR Model there are 4 defined – one per ring) fails with an initial diameter of 0.1 meter.

Vessel failure occurs at high pressure, vessel is not depressurised because of there is not power to operate (to keep open) the safety relief valves (SRV's) in according to scenario features. (Depressurisation is preferred under those conditions in accordance with Emergency Procedures of Laguna Verde Nuclear Power Plant).

Corium is ejected to reactor cavity (interactions between corium and reactor pedestal are not considered neither simulated, so reactor supporting structure is not considered to fail or collapse) increasing the pressure drywell as well as temperature, venting option is not considered because of lack of power to operate valves related to venting system.
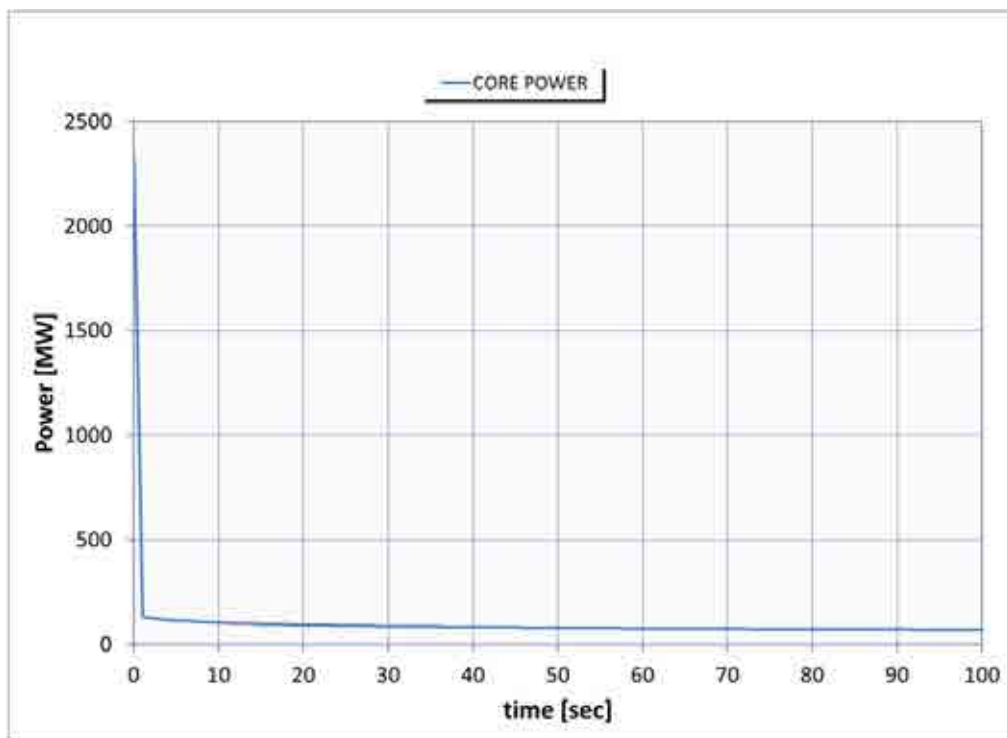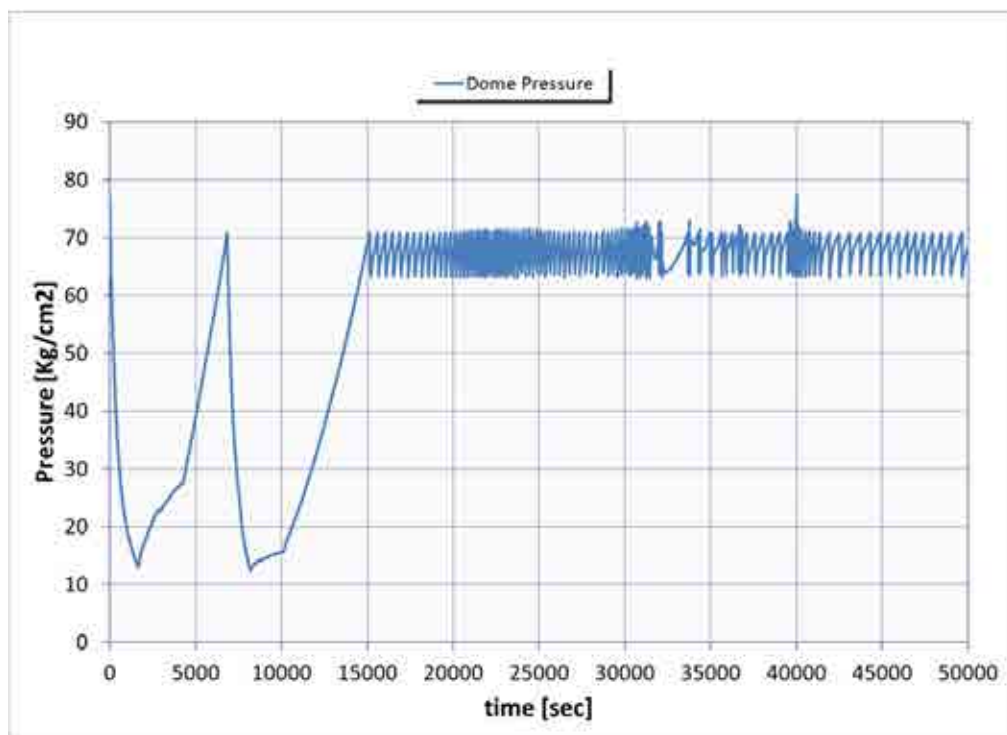
FIG. 3. Core Power after SCRAM.

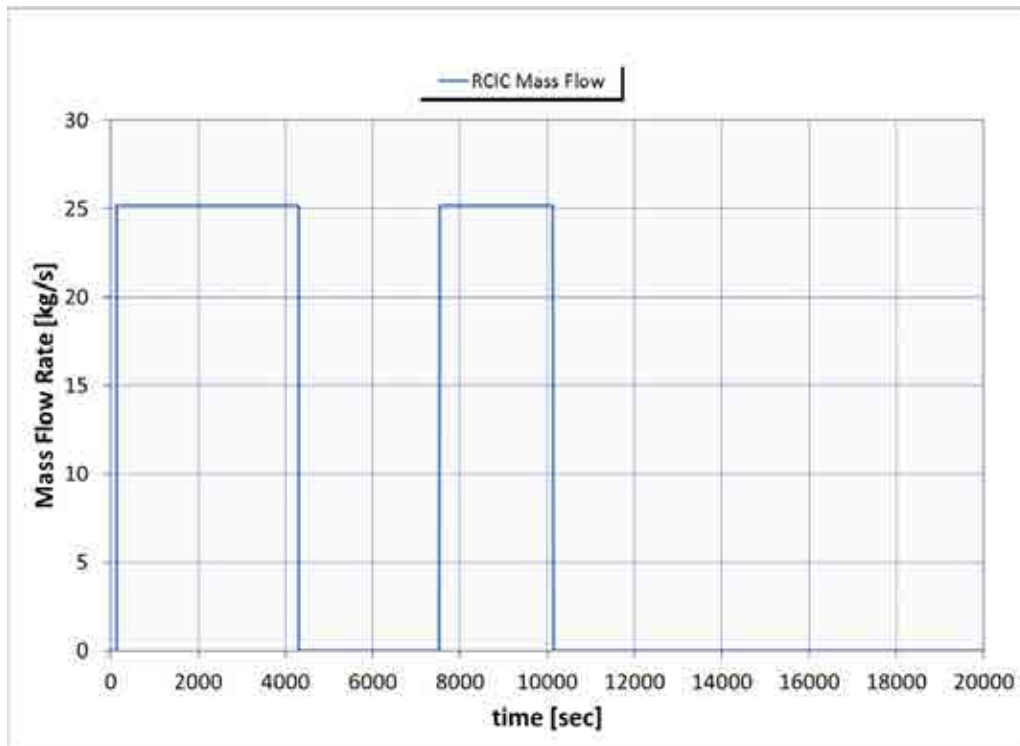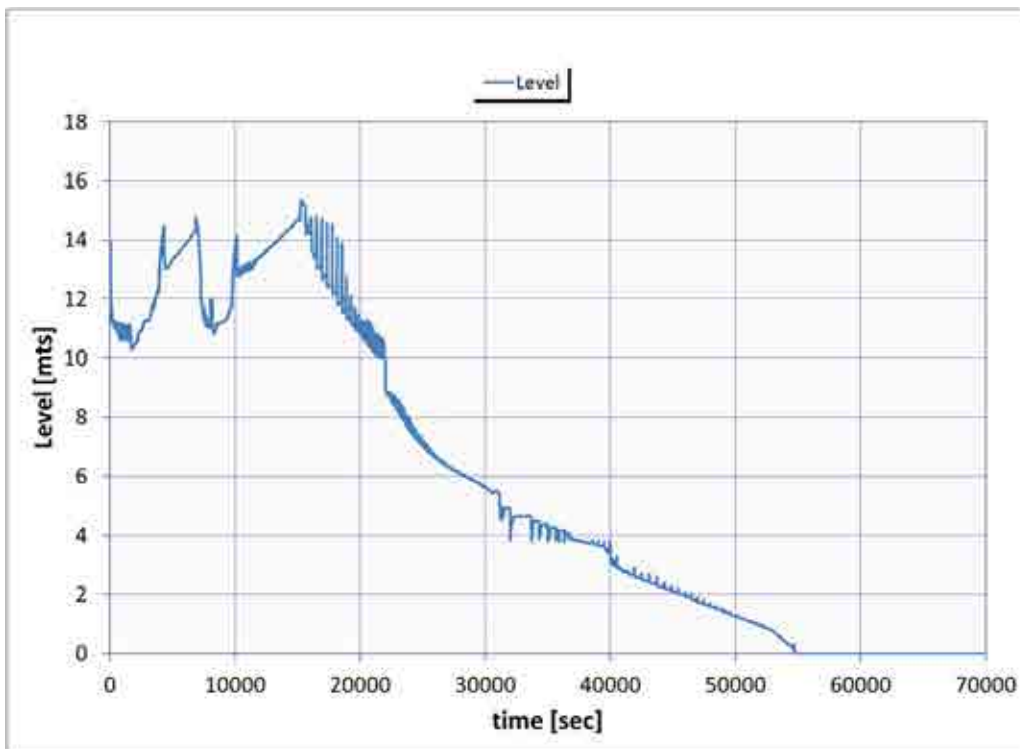*FIG. 4. Vessel Pressure for SBO.*

FIG. 5. RCIC Water Injection for SBO.

FIG. 6. Reactor Level for SBO.
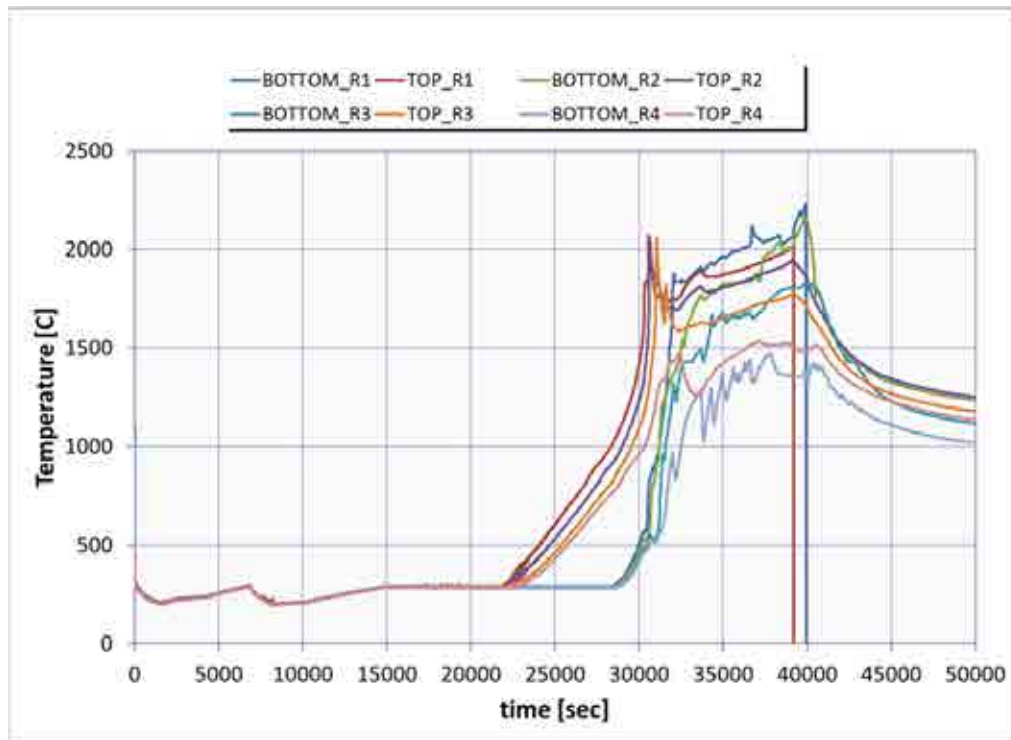
FIG. 7. Temperature Profile for Fuel Cells Elements (only TOP and BOTTOM.)

FIG. 8. Total Hydrogen Generated by All Process in Core.

306
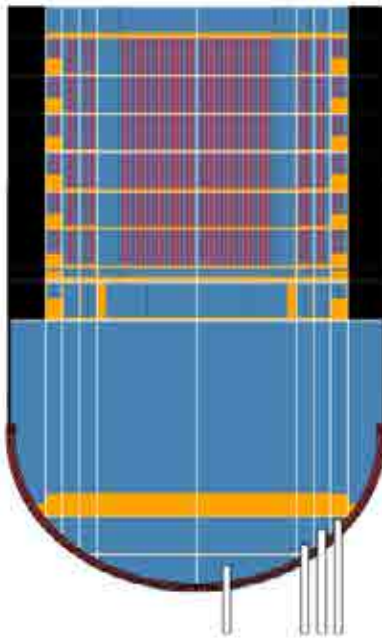
FIG. 9. Core Status at the Very Beginning of Scenario.

FIG. 10. Initial Hydrogen Generation (7.5 hrs approximately after IE), Core Uncovered 75%.

FIG. 11. Internal Structures Melting (9.5 hrs approximately after IE.
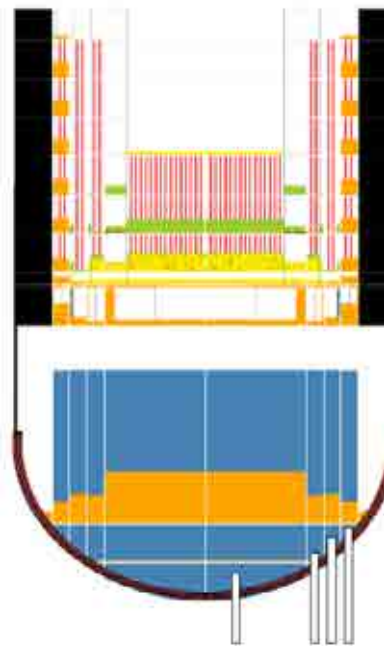
FIG. 12. Core Fuel Elements Melting (10.5 hrs approximately after IE).
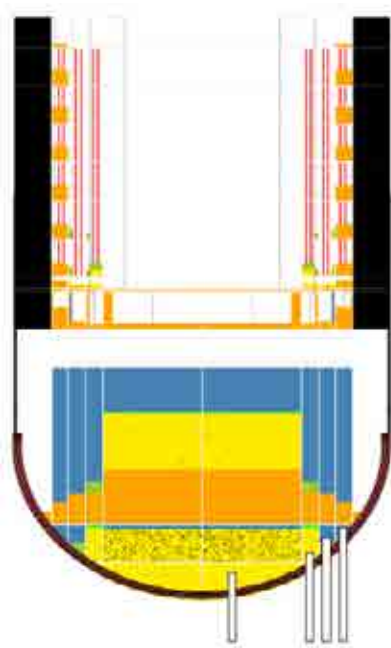
FIG. 13. Core Fuel Elements Melting (11 hrs approximately after IE).
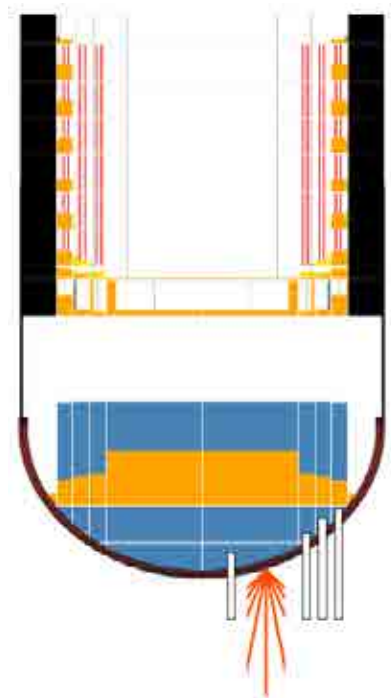
FIG. 14. Vessel Failure (12 hrs approximately after IE).

309

4.2   SBO with injection (Re-flooding)

All charts and thermo-hydraulics phenomena are the same for both scenarios in the time window 0–10 hrs, at approximately 36000 seconds from IE the assumption of "Water Source Recovery" allows injecting water to reactor vessel in order to recover level and keep covered the core above TAF.

Figure 15 shows vessel pressure profile, and depressurisation action by using one SRV once power is available, this allow to use either high pressure or low pressure emergency systems. Figure 16 shows the level inside reactor vessel, systems used are injecting water to keep the level in the vessel in the range 12.08 – 14.4 m (3 – 5 meters above TAF), however during the time that core was uncovered some structures melted at 9.5 hrs after IE, re-flooding helps to mitigate the increasing of temperature for fuel core elements even though the debris in the bottom section causes damage to the lower nodes.

Figure 17 shows the temperature profile for fuel elements, high temperature in lower nodes lead to collapsing of central ring assemblies to bottom section and corium presence that in contact with elements in lower nodes induces melting as well hydrogen is generated in core, figure 18 shows the total hydrogen generated in core.

Corium goes down to bottom head and enter in contact with vessel lower wall, this mass losses coolability because of loss of geometry, water in vessel cools the upper section of this mass, but with no cooling to the lower and middle section of this corium mass, the vessel lower wall starts to heat up by the heat transferred by melted elements in there. Figs 19–25 show the melting progression for core in case 2 specified by table II.

Vessel failure is present at approximately 19 hrs after IE, water level is considered above TAF always (after re-flooding) but core damage to some structures is present from early stage of accident (at 9.5 hrs from IE), this structures damage (melted in some cases) causes the failure of other structures as such as fuel, supporting and other elements.

Late injection (when some section of core either fuel of other material is melted) will causes with a high probability the failure of close structures, this leads to a vessel failure (if there does not exist a cooling source for vessel bottom outside wall), vessel failure is postulated (in model) as a penetration failure with an initial diameter of 0.1 meters.

This scenario shows that if water injection is available again once some part of core is melted, probably this leads to a failure of other structures with consequences in failure of penetrations (CRDs mostly).

Drywell spray and flooding to cool the outside of vessel wall must be a great help to mitigate the temperature increasing (because of heat up of vessel wall by corium heat transferred from lower section surface of corium mass) however this option was not simulated because the main objective of those simulations was focused on core damage progression for different situations.
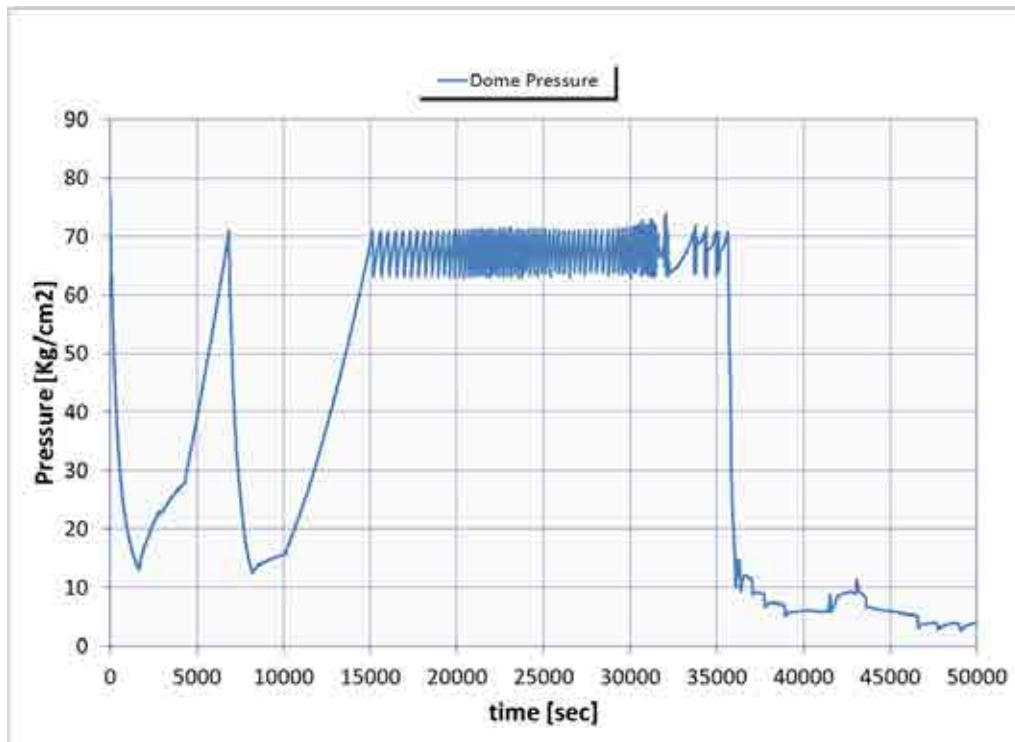
FIG. 15. Dome Pressure (Power Recovery).
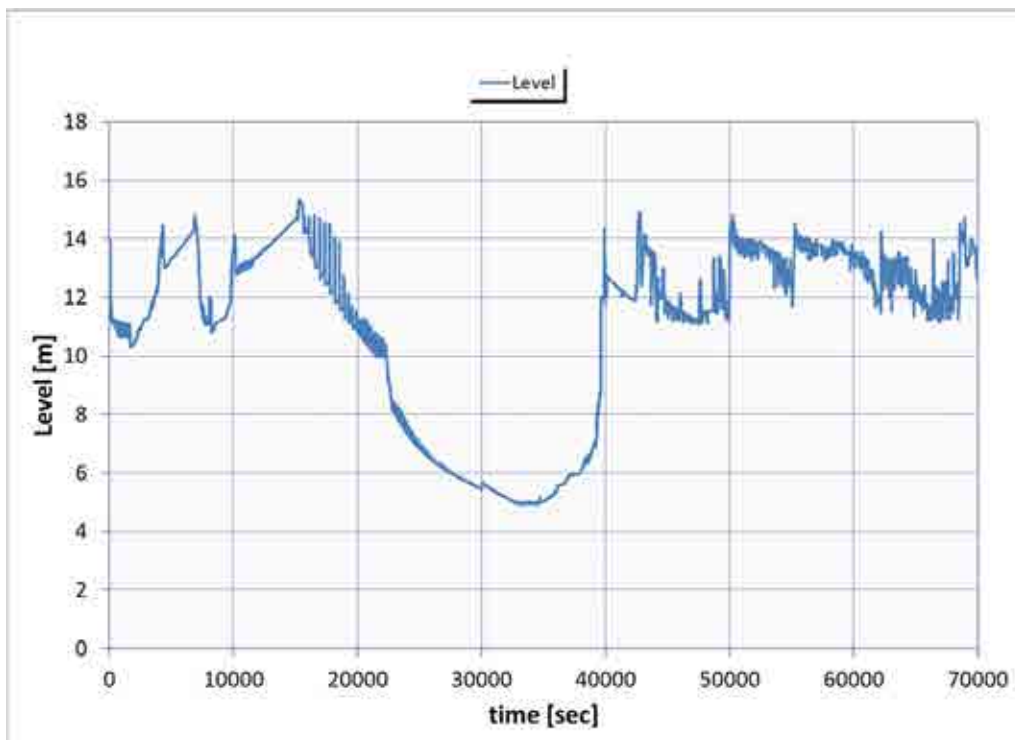
FIG. 16. Reactor Water Level (Water Source Recovery).

311
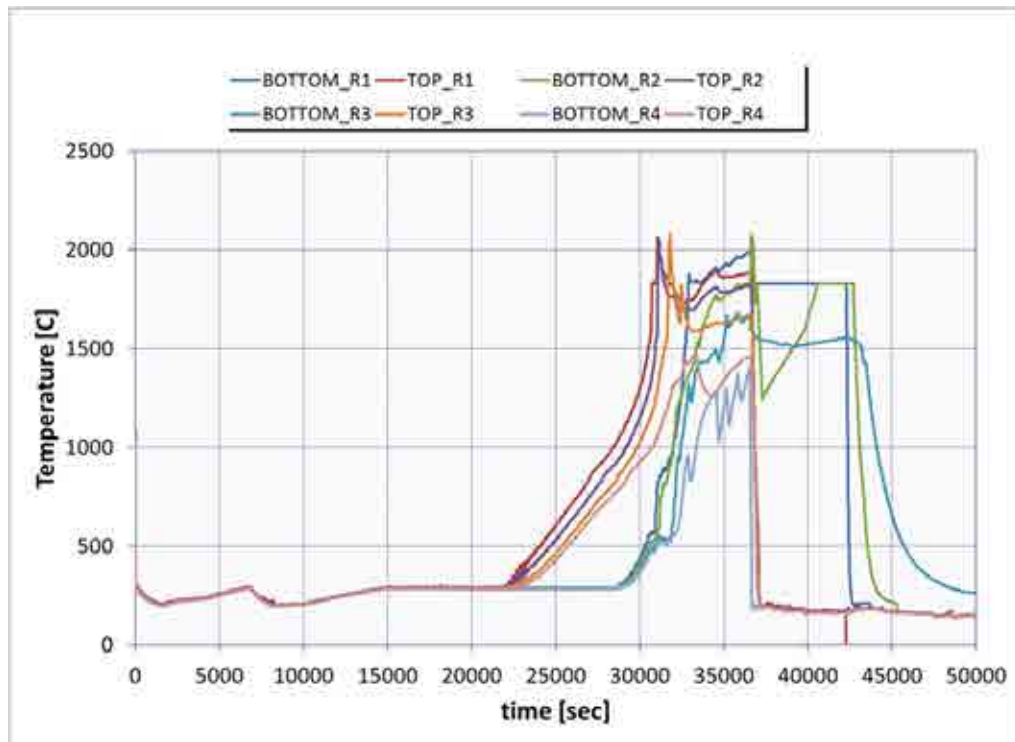
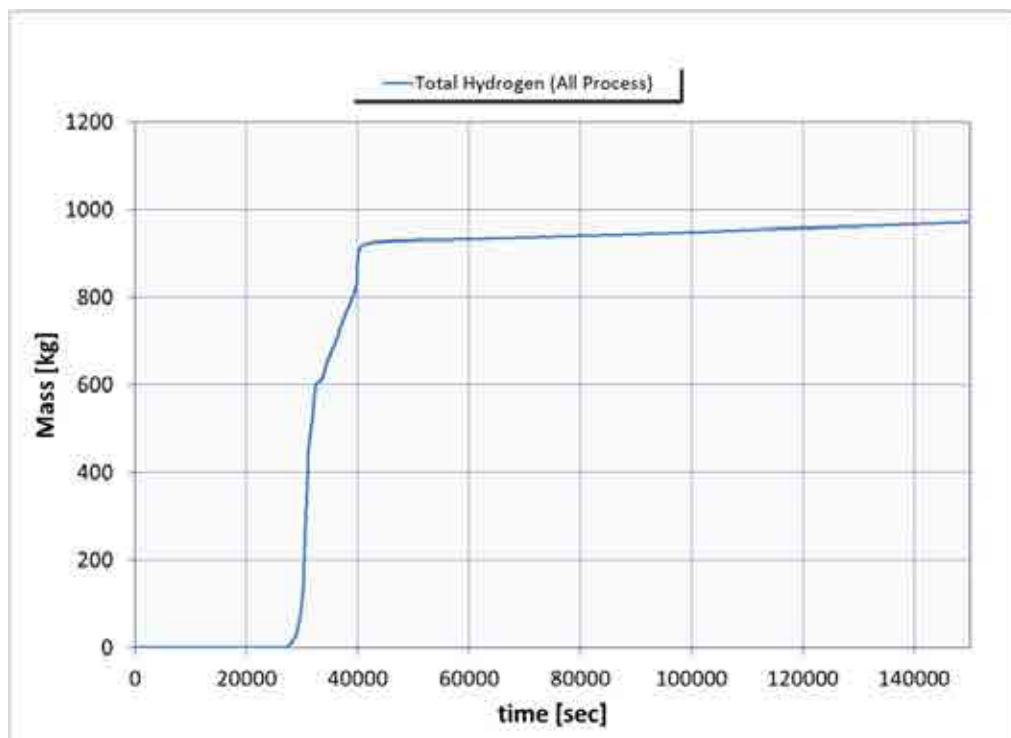*FIG. 17. Temperature Profile for Fuel Cells Elements (only TOP and BOTTOM).*
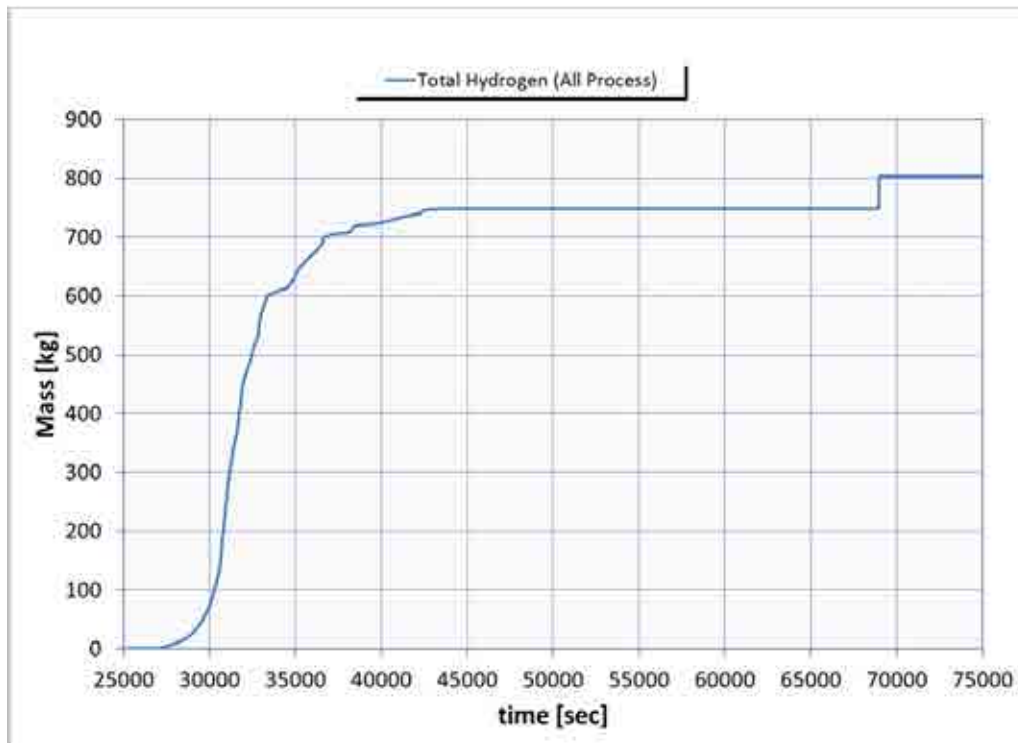
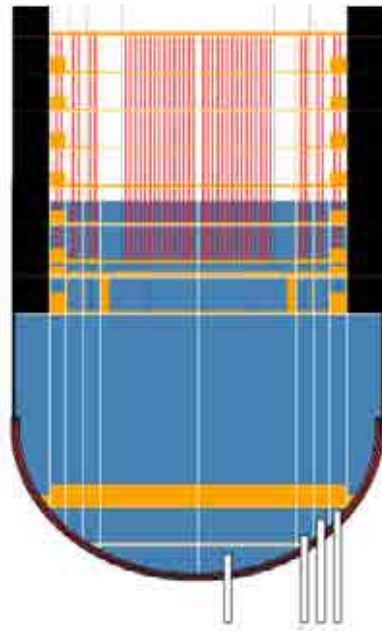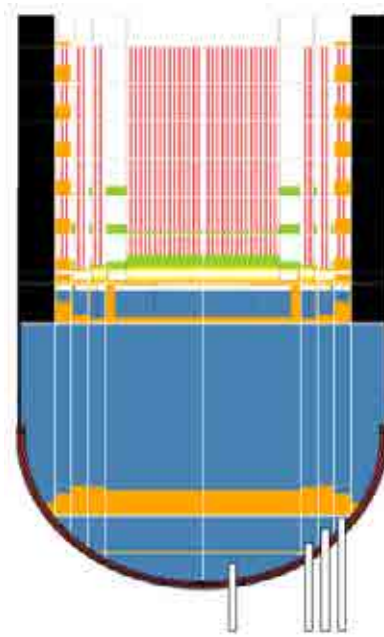*FIG. 18. Total Hydrogen Generated by All Process in Core.*
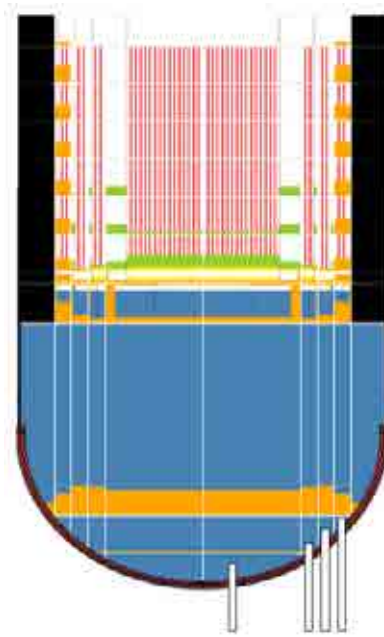
FIG. 19. Internal Structures Melting (9.5 hrs approximately after IE).
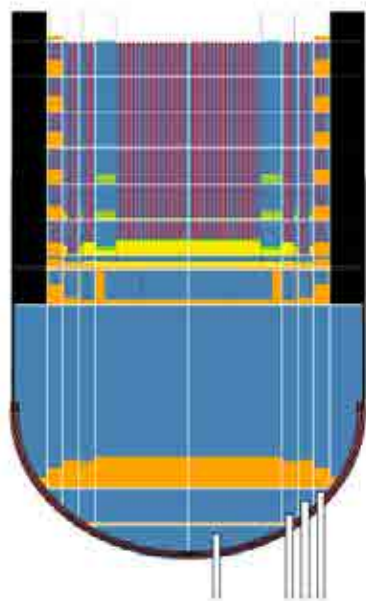
FIG. 20. Core Fuel Elements Melting (10.5 hrs approximately after IE).

313
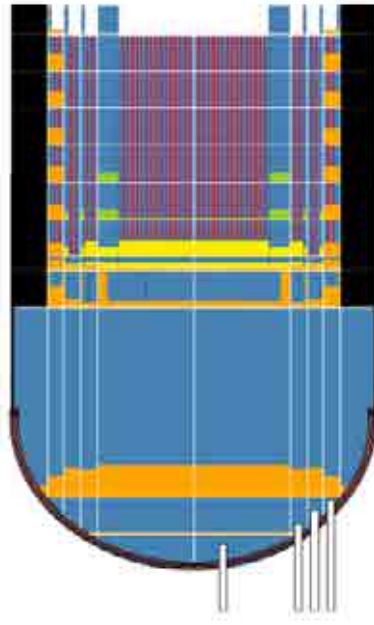
FIG. 21. Core Fuel Elements Melting (11 hrs approximately after IE).
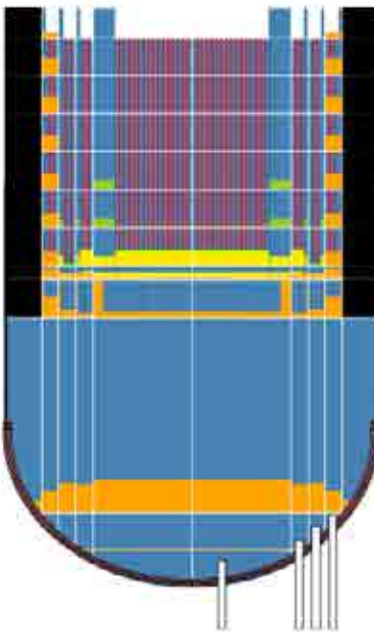
FIG. 22. Core Fuel Elements Melting (11.5 hrs approximately after IE).

314
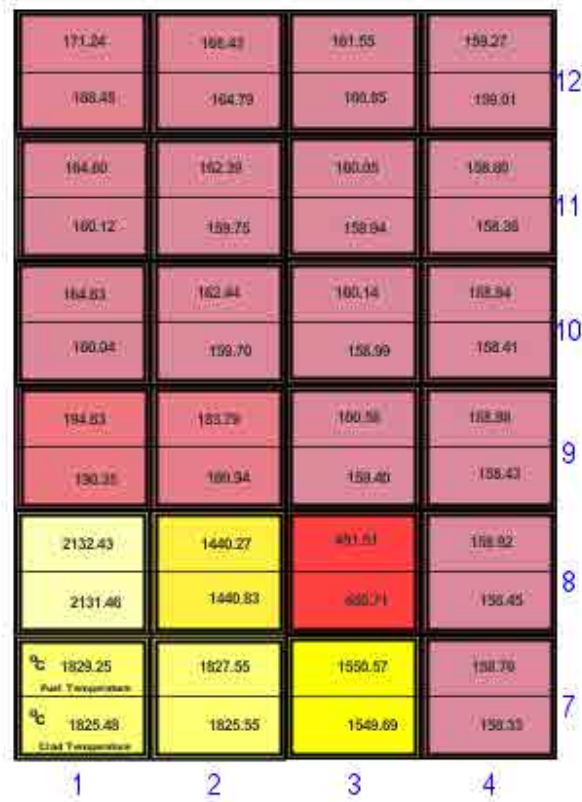
FIG. 23. Core Fuel Elements Temperature (11.5 hrs approximately after IE).
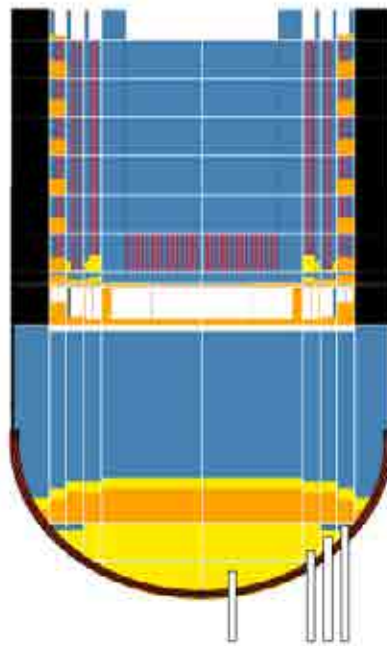
FIG. 24. Core Fuel Elements Melting (15.5 hrs approximately after IE).
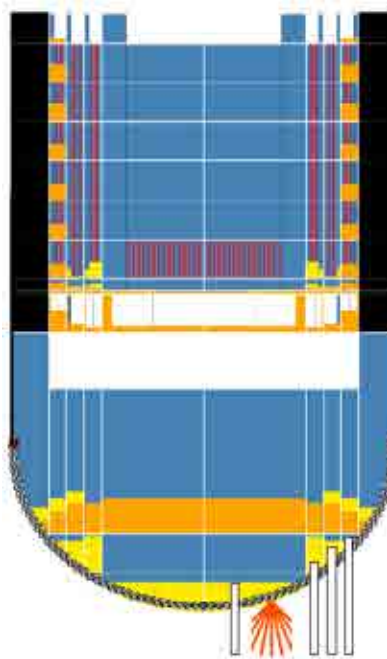
FIG. 25. Vessel Failure (19 hrs approximately after IE).

316

5.   CONCLUSIONS

Scenarios simulated were focused on core degradation after loss of cooling and uncovered core with a) no level recovery (no injection / no reflooding) and b) level recovery (injection / reflooding). Results show behaviour of core under specific conditions, once core is degradated and proportional damaged, injection could be either effective or not depending of what level of damage is present in core at the time of injection.

Case 1 results shows expected trends:

- Core damage and melting of structures at some point of time
- Collapsing of structures and fuel elements if lower nodes fail
- Heating up of bottom head (Vessel Reactor) and consequently penetration failure
- Core melting pattern in according with definition and geometry of core for model

Case 2 results shows following:

- Under partial uncovered core (about 4 hours) core damage and melting of structures is present partially
- Approximately 25% - 30% of core is damaged because of loss of cooling (water source is recovered, reflooding is considered)
- By injecting water in reactor with a damaged core in 25% - 30%, level is recovered and water cools intact elements, however this cooling is only effective in melted elements for surfaces in contact with water, isolated masses or masses surfaces in contact with vessel reactor walls will transfer heat to them causing failure firstly of penetrations
- Failure of penetration is function of how much material is in contact with walls, temperature of material and coolability of melted structures.

For case 1 core melting (structures) start at 9/9.5 hrs after initiator event, one hour later (10.5 hrs) central ring of fuel elements (upper nodes) melts and collapses through core to bottom section which causes melting of lower structures and fuel elements with collapsing of all this material to bottom of vessel reactor (11 hrs), once this mass is in contact with the vessel lower wall, heat is transferred to vessel which rapidly leads to failure of penetrations (vessel failure).

Case 2 shows that with core reflooding (water source recovery), vessel failure is delayed 10 hours against no reflooding case, failure is present because the melted masses in the lower section of core melt the structures in the lower nodes which causes the collapsing of fuel elements and transferring of debris/corium to vessel reactor bottom head.

With a drywell spray to cool the outside wall of vessel reactor, the probability of failure is lower, for those simulations we don't consider spray cooling to drywell.

REFERENCES

[1]   SANDIA NATIONAL LABORATORIES, MELCOR Reference Manual, NUREG/CR-6119, Vol. 2, Rev. 3194, September 2011.

[2]   NATIONAL COMMISSION OF NUCLEAR SAFETY AND SAFEGUARDS, LVNPP – MELCOR Model, 2013 Version 3.165a.

[3]   LAGUNA VERDE NUCLEAR POWER PLANT – Final Safety Analysis Report Amendment 65, 2012.

[4]   SANDIA NATIONAL LABORATORIES, MELCOR User Guide, NUREG/CR-6119, Vol. 1, Rev. 3179, September 2011.

[5]   LAGUNA VERDE NUCLEAR POWER PLANT – C97 Electronic Document Repository System.

MECHANISTIC CODE SFPR FOR MODELLING SINGLE FUEL ROD PERFORMANCE UNDER VARIOUS REGIMES OF LWR OPERATION, INCLUDING DESIGN-BASIS AND SEVERE ACCIDENTS

M.S. VESHCHUNOV[*], A.V. BOLDYREV, V.D. OZRIN, V.E. SHESTAK, V.I. TARASOV

Nuclear Safety Institute of Russian Academy of Sciences (IBRAE)

51, B. Tul'skaya, 115191, Moscow, Russian Federation

E-mail: vms@ibrae.ac.ru

Abstract. The SFPR code for mechanistic modelling of single fuel rod behaviour under various regimes of LWR reactor operation (normal and off-normal, including severe accidents) is under development at IBRAE. The code is designed by coupling of the two stand-alone mechanistic codes MFPR and SVECHA/QUENCH, or S/Q, intensively developed during the last two decades.

The code SVECHA/QUENCH (S/Q), currently the sub-module of SFPR, was initially developed for detailed modelling of re-flooding phenomena observed in the FZK (Karlsruhe) single-rod QUENCH rig test in collaboration with German experimentalists. In the S/Q code, the main physical phenomena occurring during the degradation of fuel rods are mechanistically considered: cladding oxidation, oxidized cladding mechanical deformation, hydrogen uptake and release by oxidized cladding, fuel rod liquefaction and download relocation (under SA conditions), etc. In application to secure accidents (SA), the code was intensively developed within several ISTC Projects; besides, it was successfully applied in collaboration with JRC/IE to interpretation of the molten corium pool formation, relocation and oxidation in the Phebus FP tests. The advanced mechanistic model for the so called secondary hydriding of ballooned under LOCA conditions Zr cladding, observed in the KIT bundle QUENCH L0 test, was recently developed and implemented in S/Q.

The code MFPR (Module for Fission Products Release), the other sub-module of SFPR, was developed for analysis of fission products (FP) release from irradiated UO2 fuel, in collaboration between IBRAE and IRSN (Cadarache), where the code is used to better understand the results of the experiments performed in the context of radiological consequences of accidents. MFPR gives the advantages of mechanistic, theory-based modelling, first of all, concerning the realistic consideration of FP behaviour based on physical-grounded parameters and self-consistently describes evolution of fuel micro-structure and FP release. The thermochemical module of MFPR includes detailed modelling of chemistry effects on the behaviour of FPs within irradiated oxide fuel at high temperatures in the interval 500-3000 K and various atmospheres typical for SA conditions.

1. INTRODUCTION

Nuclear fuel materials are exposed to complex thermo-mechanical and physico-chemical processes during manufacturing, operation and storage. The physics, chemistry and materials science of such materials are tremendously complicated by irradiation effects. That is why many commercial fuel performance codes incorporate empirical correlations to describe materials properties. The applicability of such correlations is limited to a regime where experimental data are available. Past attempts to extrapolate outside this regime have sometimes led to faulty predictions and costly engineering decisions.

To address these issues, a large number of models and codes have been developed all over the world to assess the properties of nuclear fuel materials. However, most assessments involve fitting of known data followed by extrapolations or interpolations into new temperature or pressure regimes. There is an obvious need for a more theory based approach to develop a fundamental understanding of properties of nuclear fuel materials, leading to improved tools for predicting phenomena such as phase stability, heat transfer, species diffusion, and fission

products (FP) retention. Development of such an approach was recently launched in various national and international projects (e.g. International Project MMSNF (Materials Models and Simulations for Nuclear Fuels) [1]) and is also attempted in the Nuclear Safety Institute (IBRAE) of the Russian Academy of Sciences.

2. CODE SINGLE FUEL ROD PERFORMANCE

A new mechanistic SFPR (Single Fuel Rod Performance) code for modeling of single fuel rod behavior under various regimes of LWR reactor operation (normal and off-normal, including severe accidents) is under development at IBRAE. The code is designed by coupling of two stand-alone mechanistic codes MFPR (for modeling of irradiated UO2 fuel behaviour and fission products release) and SVECHA/QUENCH, or S/Q (for modeling of Zr cladding thermo-mechanical and physico-chemical behavior). Both codes were initially designed for accident conditions (and for this reason, are rather mechanistic) and later extended to various normal operation conditions. The main physical models of the two codes were adapted and used in the Russian best-estimate integral code SOCRAT [2] designed for mechanistic analysis of severe accidents, which was applied to the safety justification of NPP with the new generation of VVER type reactor such as Tyanvan NPP in China and Kudamkulam NPP in India.

Coupling of the two codes allows mechanistic modeling of LWR fuel element behavior in steady, transient and abnormal modes under conditions of high fuel burnup, which implies self-consistent description of the following processes:

- Diffusion in and release from UO_2 fuel of gaseous fission products and their accumulation in the fuel pellet – cladding gap, resulting in change in thermo-physical properties of the gas gap;

- Fuel pellet densification at the initial stages of irradiation and subsequent swelling, resulting particularly in decrease of thermal conductivity of porous fuel pellet and reduction or disappearance of gas gap;

- Thermo-mechanical behavior of the fuel rod and physico-chemical interactions at high temperatures;

- Thermal conductivity of the "fuel – gas gap – cladding" system, taking into account microstructural changes in oxide fuel under higher burnup conditions and changes of its properties;

- Radial diffusion of oxygen in temperature gradient in a fuel pellet resulting in significant changes in local oxygen potential and, consequently, in the thermophysical properties of fuel.

The code SFPR has a modular structure that makes suitable implementation of new models or replacement of simplified models by more advanced ones.

2.1 Code SVECHA/QUENCH

The code SVECHA/QUENCH (S/Q), currently the sub-module of SFPR, was initially developed at IBRAE [3], [4] for detailed modeling of re-flooding phenomena observed in the FZK (Germany) single-rod QUENCH rig tests in close cooperation with FZK experimentalists [5–7], and also supported by various European organizations (IRSN, JRC/IE) within 4th–6th Framework Programs of EC in application to modeling of fuel rod degradation phenomena [8–

10]. In the S/Q code, the main physical phenomena occurring during degradation of fuel rods are mechanistically considered: cladding oxidation, cladding mechanical deformation, hydrogen uptake and release by oxidised cladding, fuel rod liquefaction and downward relocation, heat conduction inside the fuel rod, heat and mass exchange with the surrounding two-phase media, etc. [11].

Further development of the code in application to normal regimes of reactor operation, in particular, for the cladding material E110 (Zr1%Nb) in VVER nuclear reactors, was performed on the base of available data (e.g., [12]).

In the numerical scheme of S/Q, an intact fuel rod is divided into meshes along the axial direction. Each mesh comprises the fuel pellet and Zr alloy cladding, Fig. 1. For each mesh the cladding is considered as a cylindrical shell consisting of three layers: external oxide layer, α-Zr(O) and β-Zr layers. The three layers are assumed to have different visco-elastic properties up to the melting temperature. Mechanical properties and phase composition of the cladding layers depend on the oxygen content, which can change due to oxidation. The layers growth is calculated by the oxidation model which is based on the solution of the oxygen diffusion problem across the multilayered cladding structure and is tightly coupled with the hydrogen uptake and release model [13, 6]. In particular, the developed diffusion approach allows self-consistent consideration of internal cladding oxidation owing to interactions with the fuel after the gap collapse.

On the base of a thorough analysis of available isothermal oxidation kinetic results for Zry-4 alloy with respect to their reliability and statistical methods of evaluating the data sets, best-estimate diffusion coefficients for ZrO2, α-Zr(O) and β-Zr were deduced [6, 14]. Thus determined diffusion coefficients were successfully used for the oxidation model verification against temperature transient tests [15], Fig. 2. In these calculations influence of oxide cracking on the oxidation kinetics is self-consistently simulated by the mechanical deformation module tightly coupled with the oxidation module.
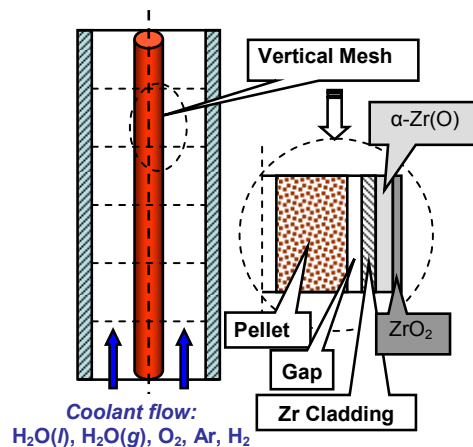
FIG. 1. Mesh structure of a single fuel rod considered in the S/Q numerical scheme.
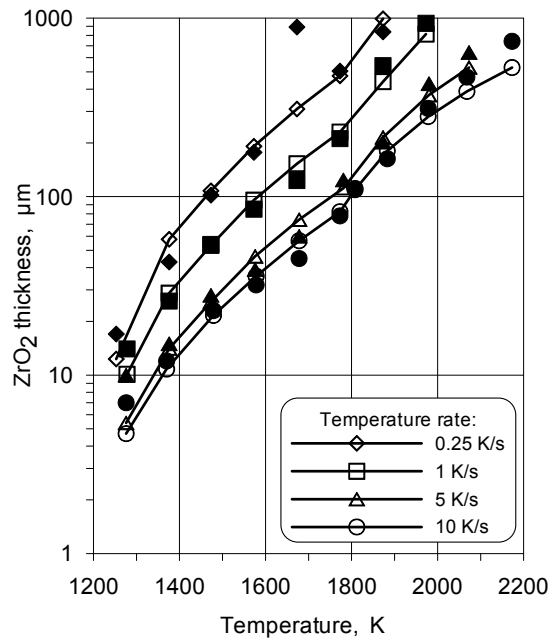
FIG. 2. Verification of the Zry-4 oxidation model against transient tests [15] with various heat-up rates: dependence of oxide scale thickness on maximum temperature (black markers represent the experimental data).

And vice versa, the strengthening effect of oxidation on deformation behavior of pressurized Zry fuel cladding in steam atmosphere can be demonstrated. In accordance with experimental observations [16], cladding oxidation can manifold increase time to rupture or even prevent it, owing to the substantial decrease of the creep rate of the oxygen-stabilized α-Zr(O) phase, Fig. 3.
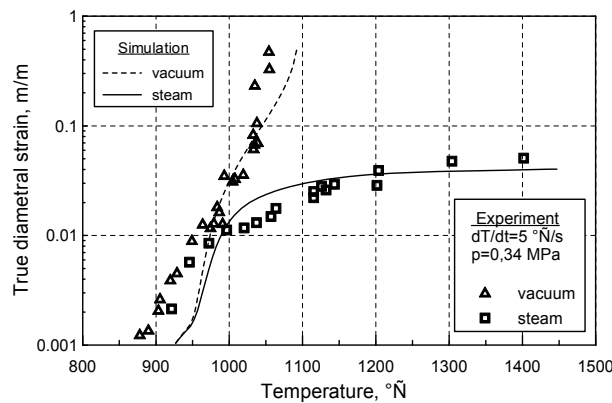
FIG. 3. Comparison of calculated and measured in [16] diametral strain data under heat-up conditions in neutral and oxidizing atmospheres.

In inert atmosphere the model correctly predicts the rupture temperature and time-to-rupture in the typical ballooning tests REBEKA [17] with various heat-up rates and internal overpressures, representing realistic conditions of loss of coolant accident (LOCA), Fig. 4.
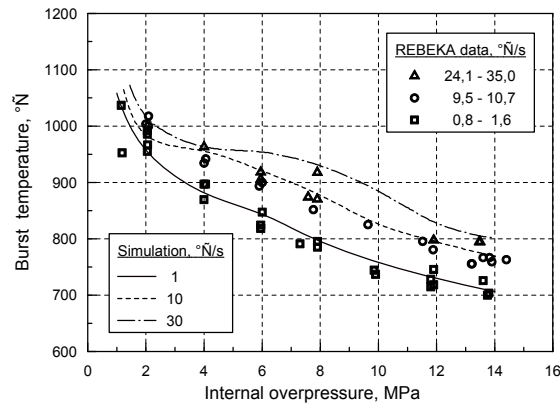
FIG. 4. Comparison of calculated and measured in [17] burst temperature versus internal overpressure in the fuel rod segment at different heat-up rates.

During quenching of the oxidized fuel cladding the tensile stress is generated in the oxide due to the radial temperature gradient and the difference in the thermal strains of the α-phase, β-phase and oxide layers. This tensile stress leads to the onset of microcracks in the oxide scale at temperatures above the tetragonal-to-monoclinic phase transition, Fig. 5 (left), whereas at temperatures below the transition (attained during quenching) the high level compressive stress in the oxide layer and the high level tensile stress in the alpha layer may induce the net of through-wall cracks, Fig. 5 (right), if the thickness of the β-Zr layer with low content of oxygen exceeds some critical value determined by the Chung-Kassner criterion. The developed approach to the through wall crack density evaluation furnishes a satisfactory agreement with experimental data [5,6] (see also [18]). This allows calculation of the hydrogen generation due to the through wall crack surface oxidation during quenching.
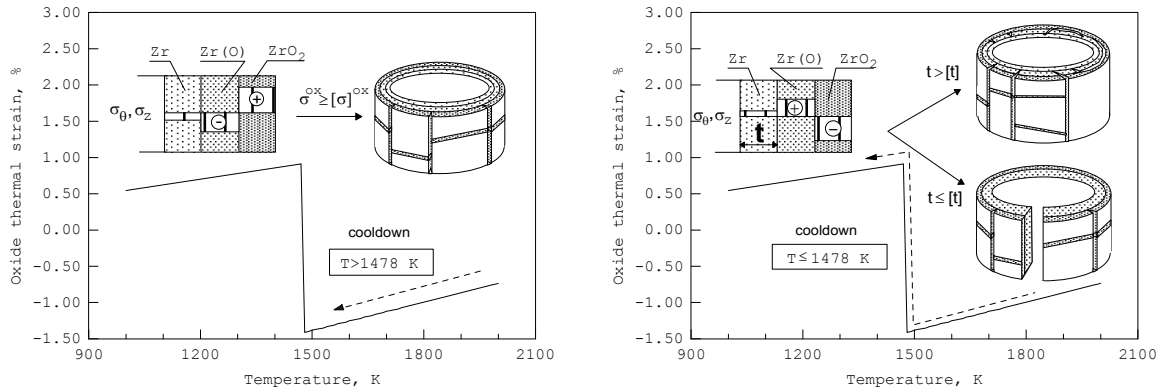
FIG. 5. Scheme of the stress state and failure modes of oxidized cladding on cool-down above (left) and below (right) the tetragonal-to-monoclinic phase transition temperature in oxide (σ^{ox} is the average stress in the oxide, $[\sigma]^{ox}$ is the oxide tensile strength, t is the β-layer thickness, [t] is its critical thickness).

In the course of the oxide film formation process in steam, a fraction of the hydrogen generated by decomposition of the steam enters the metal. The relationship between the amount of hydrogen generated during cladding oxidation and the amount of hydrogen absorbed by the

cladding is not a simple function, although it follows a characteristic pattern which seems to be general for all zirconium alloys.

The S/Q kinetic model for hydrogen absorption by Zr alloys during oxidation in steam in the temperature range typical for LOCA conditions, was developed in [13], basing on the experimental results of the KFKI (Hungary) tests [19] in the temperature range from 1173 to 1473 K for Zr1%Nb cladding, Fig. 6. Currently the model is further verified and refined [20] basing on analysis of new FZK tests [21] in the temperature range from 1273 to 1673 K for Zry-4 alloy, Fig. 7.
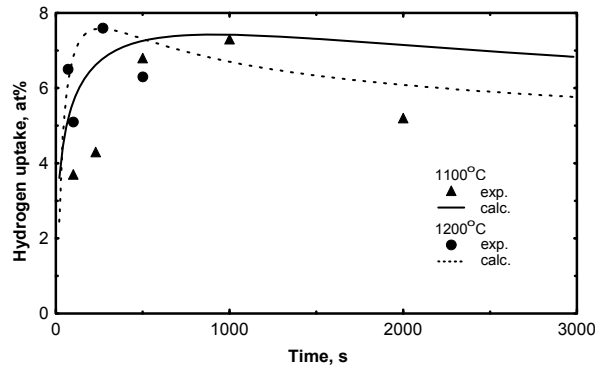
FIG. 6. Simulation of hydrogen uptake kinetics during Zry1%Nb (E110 alloy) oxidation in steam at 1373 and 1473 K measured in [19].
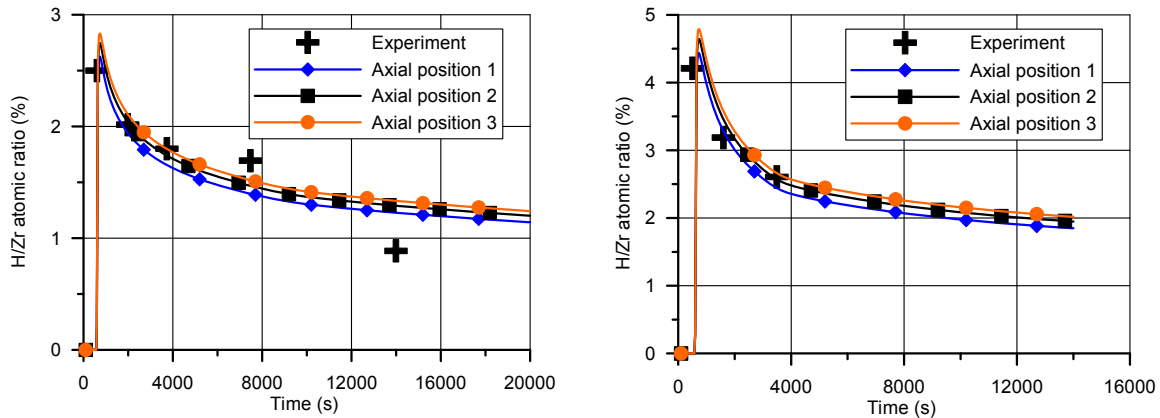
FIG. 7. Simulation of hydrogen uptake kinetics during Zry-4 oxidation in steam at 1373 K (left) and 1473 K (right) measured in [21].

The S/Q code with the implemented hydriding model was applied to simulations of ANL [22] and KIT [23] on "secondary hydriding" of bursted cladding under LOCA conditions, Fig. 8.
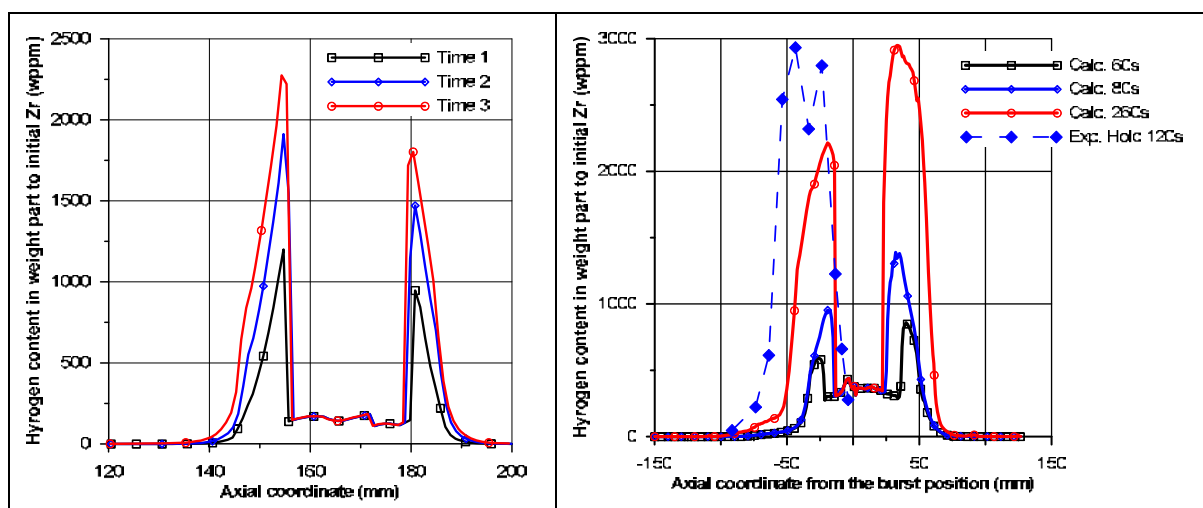
FIG. 8. Simulation of KIT [23] (left) and ANL [22] (right) tests on secondary hydriding of bursted cladding under LOCA conditions.

The S/Q code was further applied to analysis of fuel rod degradation phenomena – cladding oxide shell failure [10], fuel dissolution by molten Zry [24], corium melt oxidation [25] and relocation [26], observed under severe accident conditions in the bundle tests CORA [27], PHEBUS FP [28], QUENCH [29].

2.2 Code Module for Fission Products Release

The code MFPR (Module for Fission Products Release) [30, 31], currently the sub-module of SFPR, was developed for analysis of fission products (FP) release from irradiated UO_2 fuel in collaboration between IBRAE and IRSN (Cadarache, France), where the code is used to better understand the results of the experiments performed in the context of radiological consequences of accidents (e. g. [32]).

MFPR originated from critical analysis of the VICTORIA code [33] and gives the usual advantages of mechanistic modelling, first of all, concerning the realistic consideration of FP behaviour based on physically-grounded parameters. The main outputs of the code are gas-bubble size and concentration (including intra- and intergranular bubbles and pores), chemical speciation of solid-phase FPs, point- and extended-defect characteristics, fuel oxygen potential, densification, swelling and FP release.

The MFPR code self-consistently describes evolution of fuel micro-structure (point defects, such as vacancies and interstitials, and extended defects, such as gas bubbles, sintering pores and dislocations), which strongly influences the intra- and intergranular diffusion transport of gas atoms in irradiated UO_2 (see [34]). New microscopic parameters characterizing the crystal defect structure naturally arise, however, being physically grounded, these can be fixed from the analysis of available experimental data (and/or from atomic scale investigations, DFT, classical MD, KMC) and then used without any artificial tuning in further calculations. This is the main goal of the mechanistic approach realized in MFPR.

In particular, this approach allows mechanistic description of microstructure evolution under normal irradiation conditions up to very high burnups [35]. At high burn-ups the dislocation density significantly increases and influences the intra-granular bubbles evolution. Namely, predicted considerable suppression of the intra-granular bubbles generation leading to stabilisation of their concentration in the late stage of irradiation accompanied with a noticeable increase of the mean bubble size, was observed in high burn-up UO_2 fuel [36, 37], Fig. 9. On the other hand, the calculated by MFPR dislocation density behaviour dramatically changes in the temperature interval from 1300 to 1400 K, providing a reasonable interpretation of the temperature threshold detected in recent observations [37], above which no restructuring occurs, Fig. 10.
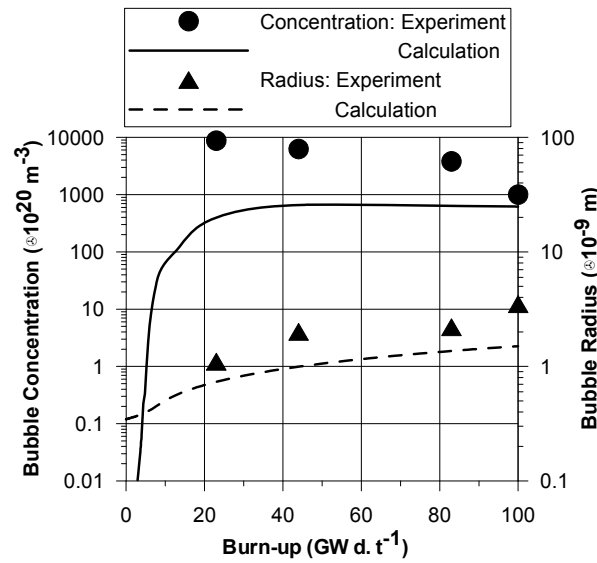
FIG. 9. *Intra-granular bubbles concentration and mean bubble radius as a function of burn-up at irradiation temperature ≈ 1000 K in comparison with experimental data [36].*
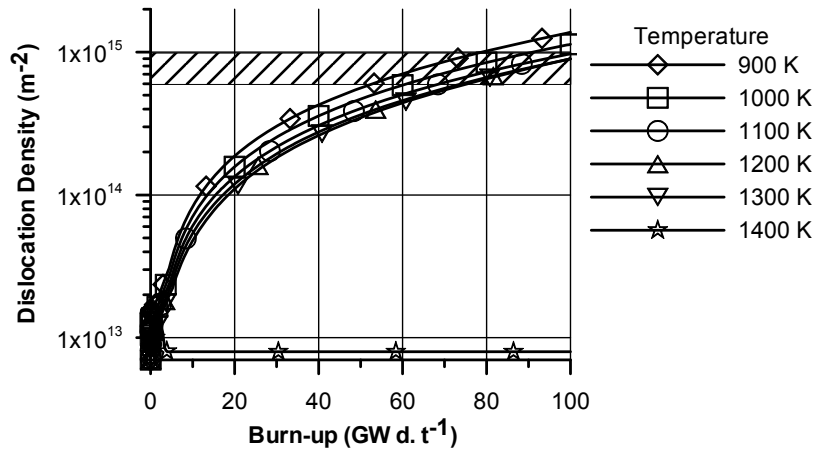
FIG. 10. *Dislocation density as a function of burn-up, calculated in steady state irradiation conditions at different temperatures, against the threshold interval (dashed band) where grain subdivision and restructuring occur [37].*

Furthermore, self-consistent consideration of intragranular bubbles biased migration in a vacancy gradient and their entrainment by climbing dislocations [30] allows an adequate description (within uncertainty of experimental data) of fission gas burst release from irradiated fuel (along with microstructure evolution) under annealing conditions in various tests with various burn-ups and temperatures [39, 40], Fig. 11 and Fig. 12.
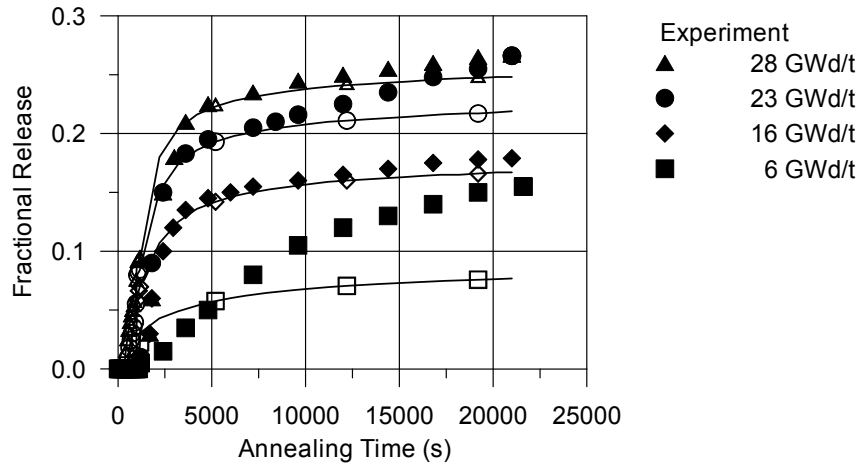
FIG. 11. Experimental data [39] (points) and MFPR calculation results (lines) for Kr release as a function of annealing time at temperature 2073 K for different burn-ups.
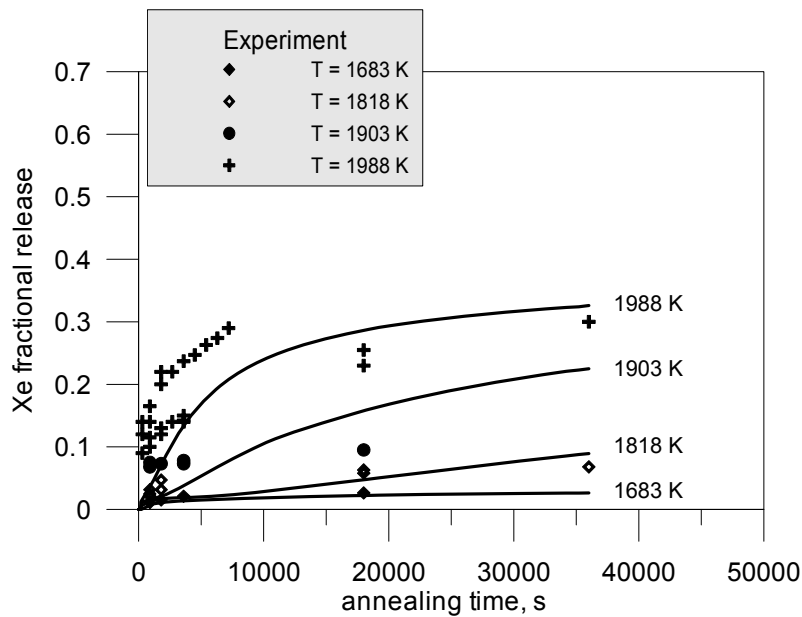
FIG. 12. Experimental data [40] (points) and MFPR calculation results (lines) for Xe release from irradiated fuel (25 GW·d·t-1) as a function of annealing time at different temperatures.

These calculations are performed simultaneously with consideration of intergranular bubbles growth and coalescence kinetics [41] under annealing conditions of the tests [40], presented in Fig. 13.

327
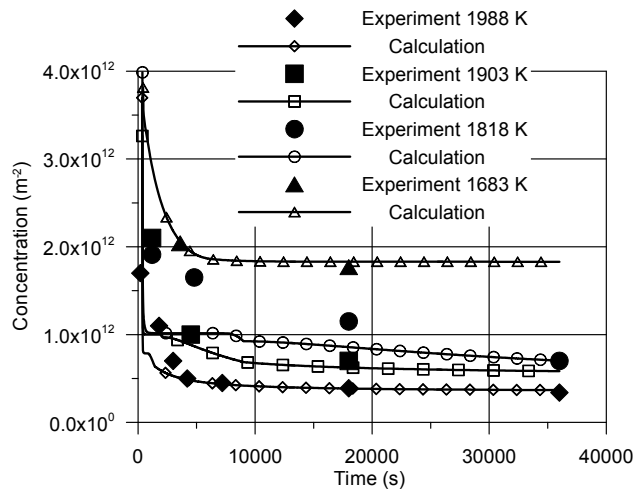
FIG. 13. Calculated (lines) surface concentration of intergranular bubbles as a function of annealing time at different temperatures in comparison with the experimental data (symbols) [40] for irradiated fuel (25 GW·d·t-1).

Following the general approach to consideration of FP release from irradiated UO_2 fuel, it is assumed in MFPR that the gas arriving at grain boundaries eventually saturates the grain boundaries through a network of interconnected bubbles. However, on the base of self-consistent consideration of the effects of atom diffusion over the grain surface, their trapping by and irradiation-induced re-solution from intergranular bubbles, the MFPR model [42, 43] allows prediction of a noticeable gas release from UO2 fuel without visible interlinkage of grain face bubbles, i.e. at a very low grain-face coverage, below the saturation threshold, in accordance with experimental observations of UO_2 and MOX fuel behavior under various irradiation conditions [39, 44], see Table 1.

TABLE 1. COMPARISON OF MFPR PREDICTIONS FOR EARLY GAS RELEASE WITH OBSERVATIONS [39] FOR UO2FUEL IRRADIATED IN COMMERCIAL BWR (LOCAL TEMPERATURE: ≈ 1000°C; BURN-UP: ≈ 28 GW·D·T^{-1})

	Face bubble diameter, nm	Fractional coverage, %	Kr release, %
MFPR calculations	216	5.9	10
Experiment	229	10.1	10–20

In the hot central zone of fuel pellets the release is enhanced by sweeping of gas atoms by moving grain boundaries. The corresponding mechanistic MFPR model for the grain growth kinetics retarded by growing intergranular bubbles was developed [25, 45] and thoroughly

validated against various tests under reactor irradiation conditions [46, 47], Fig. 14 (additionally demonstrating dependence of gas release on grain size).
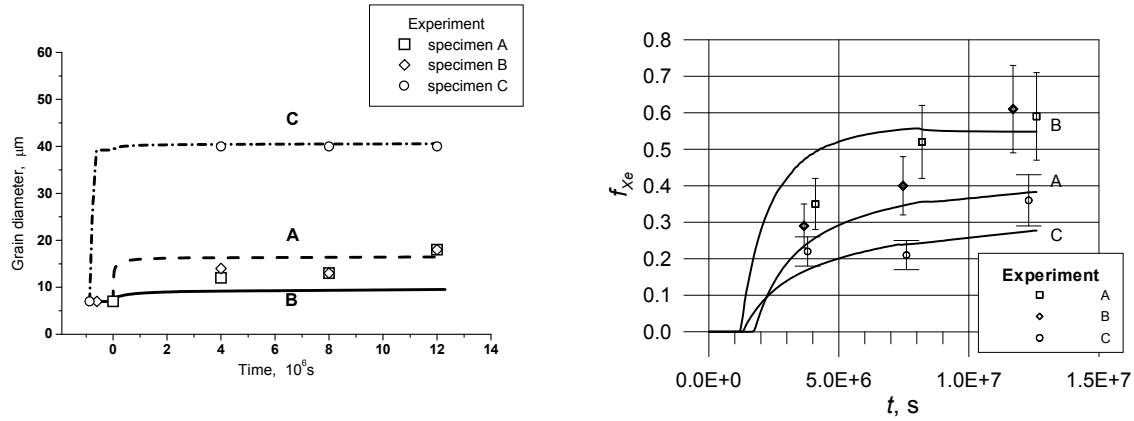
FIG. 14. MFPR simulations of the Turnbull's tests [46] with different pre-test annealing (C) and pre-irradiation (A, B) history for grain growth (left) and fractional gas release (right) in UO₂ fuel under reactor irradiation conditions.

Radial discretization of the fuel pellet is performed in MFPR that provides opportunity to consider inhomogeneous radial distribution of temperature and fission rate and to calculate oxygen diffusion and corresponding physicochemical effects along the pellet radius.

The thermochemical module of MFPR includes detailed modeling of chemistry effects on the behavior of FPs within irradiated oxide fuel at high temperatures in the interval 500–3000 K. The "U – FP – O" system is considered as a multi-phase system consisting of multi-component phases. Within the fuel matrix, fission products migrate to grain faces where they form gas bubbles and solid phase precipitates, and their mobility depends in particular on the extent of fuel oxidation characterized by the stoichiometry deviation. The release rate is thus proportional to partial pressures of FP vapors determined by chemical states of condensed FP species, and the major mechanism for release of the fission products is their vaporization into the open porosity. In connection with that description, a model for fuel oxidation in steam/air mixtures was also developed [34].

There is a strong evidence that the oxidation state of fuel during irradiation, characterized by the oxygen potential, and the fuel stoichiometry affect significantly such processes as thermal conductivity of the fuel and fission product release [48– 50]. Under normal reactor operation regimes, due to presence of strong temperature inhomogeneity, oxygen is diffusively redistributed in radial direction of a fuel pellet [51], whereas the average oxygen potential and stoichiometry increase with growth of fuel burn-up.

The oxidation state of fuel during irradiation is calculated in MFPR with a new model for the oxygen radial diffusion in the fuel pellet in the temperature (and fission rate) gradients that is formulated as a two scale problem [52]. On the local scale of the grain size, the problem of FP diffusion and local partial thermochemical equilibrium is solved that yields decomposition of

total oxygen to the "bond" and "free" components where the first one participates in formation of solid precipitates or strongly correlates to FP elements (as La, Zr, Ce, Nd) in solid solution. On the large scale of the pellet size, the problem of the thermal diffusion of "free" oxygen is considered with the boundary conditions imposed on the fuel pellet surface. For LWR fuel with burnup from 20 to 100 MWd/kgHM and typical temperature profile from ~750 to ~1400 K the MFPR model predicts the oxygen potential variations in the range of -440 – -380 kJ/mol that is in satisfactory agreement with experimental data [53] and [54] and somewhat underestimates (by about 50–100 kJ/mol) measurements [55], however, qualitatively correctly predicts the main trends of these observations (increase of oxygen potential with temperature and with a distance from the pellet center), Fig. 15.
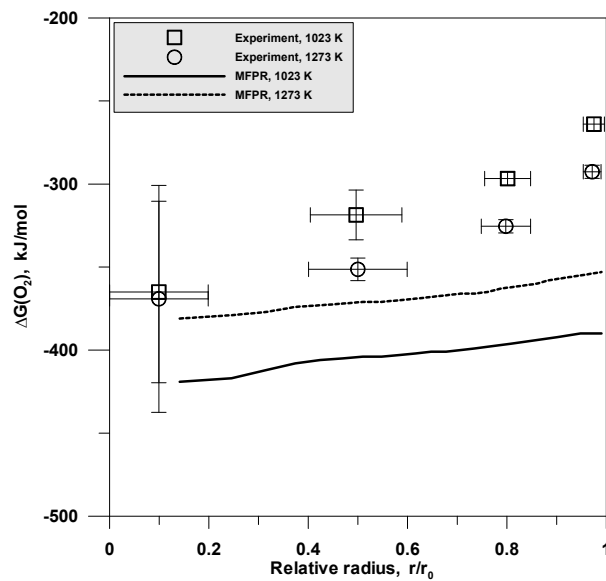
FIG. 15. Comparison of measured in [55] and calculated oxygen potentials at different distances from the pellet center for fuel burnup 102 MWd/kg HM.

MFPR was thoroughly validated against an extended matrix of out-of-pile analytical tests, including normal LWR reactor operation, high temperature annealing, loss of coolant accident (LOCA) and severe accidents conditions. An example of simulation of VERCORS-4 test, where high temperature (2573 K) annealing in pure hydrogen atmosphere followed the clad pre-oxidizing phase in steam/hydrogen mixture [56], is presented in Fig. 16 and Fig. 17-from [34].
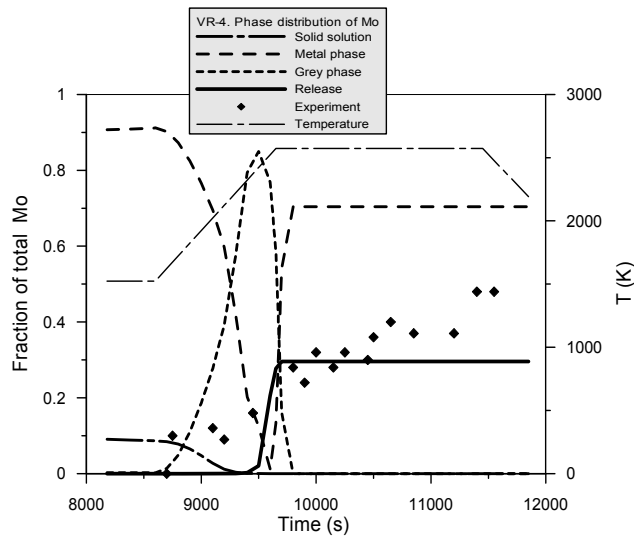
FIG. 16. Calculated phase distribution and release kinetics of Mo in comparison with that measured in VERCORS-4 test [56].
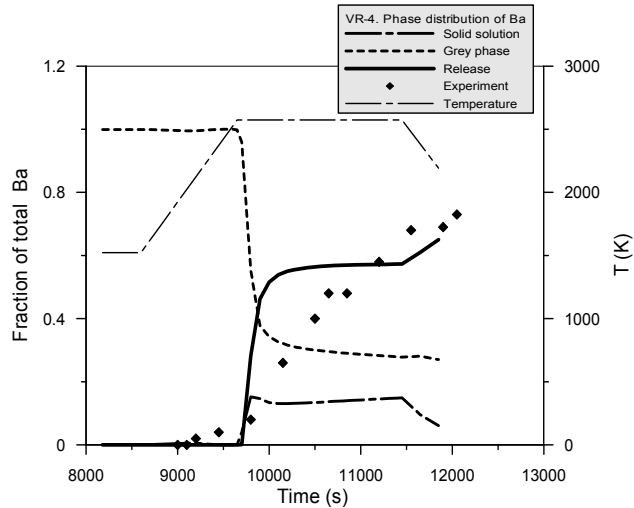
FIG. 17. Calculated phase distribution and release kinetics of Ba in comparison with that measured in VERCORS-4 test [56].

Starting from MFPR ver. 2.0, the model was extended to simulation of the yields and radioactive transmutations of fission products and their transport in the fuel [57, 58]. The corresponding numerical module was designed on the base of the code BONUS that has been elaborated at IBRAE for the express-evaluation of temporal evolution of the actinide and fission product composition, activity and decay heat rate both during nuclear regular reactor campaign and after the reactor shutdown. The model has been shown to provide a satisfactory accuracy (~10%) for activity and masses of FP chemical classes [59]. The developed model coupled with the MFPR thermochemistry module allows systematic and comprehensive description of FP diffusion (more than 200 isotopes) within and out of the fuel matrix applying realistic boundary conditions and taking into account their radioactive and thermochemistry transformations. This is illustrated by Fig. 18 [60] where the relative out-of-grain concentrations versus the half-life periods are plotted for 224 FPs. For illustrative reason, in particular to clearly demonstrate so-

called precursor effect, the calculations were performed with the artificial diffusivity $D = 10$–$20 \, m2/s$ and zero boundary conditions for all FPs.
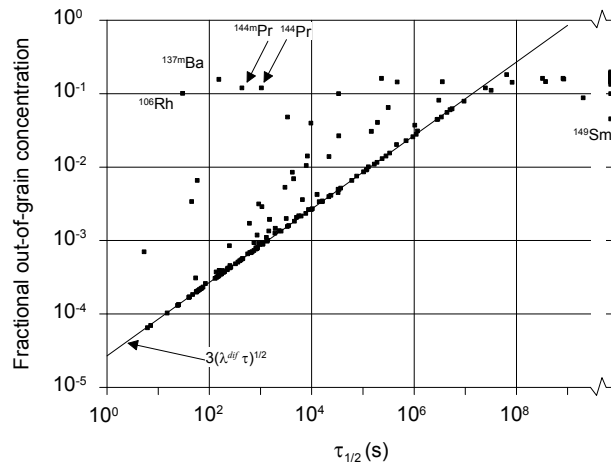
FIG. 18. Fractional releases from fuel grains of various radionuclides for typical reactor campaign calculated with simplified boundary conditions for intragranular diffusion transport (the lifetimes of the stable FPs were formally assigned to 1010 s) [60].

The code validation against tests [60] where release rates for the unstable rare gases were measured for samples of mono- and polycrystalline uranium dioxide in the temperature range 200–1500°C and interpreted in terms of diffusion of gas atoms and of their halogen precursors, is presented in Fig. 19.
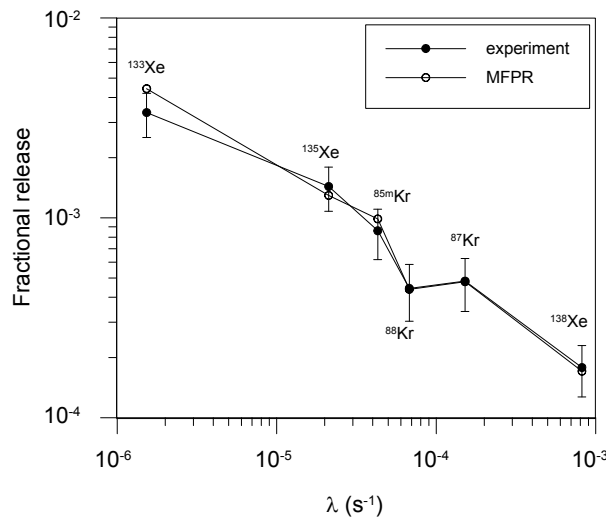
FIG. 19. MFPR calculations of the releases of the unstable rare gases, measured in [60] and interpreted in terms of diffusion of gas atoms and of their halogen precursors [60].

3. RESULTS OF SFPR VERIFICATION AGAINST IN-PILE TESTS

The principal function of a fuel performance code is to describe the behavior of reactor fuel in the most accurate way possible under whatever conditions – both normal and off-normal – that

are required by the licensing authority. In this way, all aspects of fuel performance are treated simultaneously and in a self-consistent manner, and it is therefore of importance to include data obtained from dedicated experiments in test reactors.

Coupling of the above described codes S/Q and MFPR allows new applications of SFPR to reactor tests with instrumented fuel rods pre-irradiated in commercial reactors. The first example of SFPR verification in this area is the CONTACT 1 test. The experiment is unique in that the rods operated for the majority of their lives under near constant and relatively high power, when diffusion of fission gases is the dominant release mechanism. Therefore, simulation of such a test is a good challenge for a fuel code to demonstrate its capability to predict diffusion release in a simple temperature scenario (that allows avoiding artificial tuning of code parameters typical for simulation of more complicated transient regimes).

The CONTACT series of experiments was a program of in-pile tests conducted in the SILOE reactor in Grenoble, France, funded jointly between CEA and Framatome [61]. Short rods with Zry-4 clad UO_2 pellets of typical PWR 17×17 design were irradiated under conditions designed to simulate those of commercial PWRs. Each rod was equipped with a fuel centerline thermocouple, diameter gauge, gas lines providing a flow of gas through the rod and internal pressure gauges to measure pressure drop along the fuel stack. The gas flow entrained released fission gases which were measured by a gamma detector installed in the out-of-reactor gas handling system.

CONTACT 1 operated at a constant 40 kW/m up to a burn-up of ~22 MWd/kgU. The data include temperatures as a function of burn-up, clad diameter changes as a function of power and burn-up, stable (85Kr) and radioactive fission gas release as a function of center temperature and burn-up.

In calculations, the initial grain size, fission rate and internal pressure were set equal, respectively, to 10 μm, 2.4·1019 fissions/m3·s and 1 MPa, in accordance with the experimental data. The centerline temperatures were measured to be rather stable (within ±4%) near 1747 K during all irradiation period. Using these data, dependence of gas fractional release on burnup (along with the temperature profile in the pellet) is calculated by SFPR and compared with the experiment in Fig. 20.
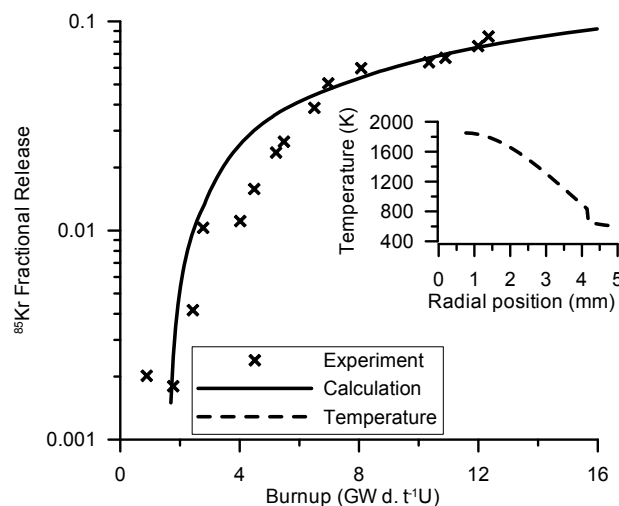
FIG. 20. SFPR simulations of cumulative fractional gas release in the CONTACT 1 test, markers representing the experimental data [61].

4. CONCLUSIONS

The new mechanistic code SFPR for modeling of single fuel rod behavior under various regimes of LWR reactor operation (normal and off-normal, including severe accidents) is under development at IBRAE. The code is designed by coupling of the two stand-alone mechanistic codes MFPR (for modeling of irradiated UO2 fuel behavior and fission product release) and SVECHA/QUENCH, or S/Q (for modeling of Zr cladding thermo-mechanical and physico-chemical behavior). Coupling of the two codes allows mechanistic modeling and self-consistent description of LWR fuel element behavior in steady, transient and abnormal modes under conditions of high fuel burnup. The first results of the code verification against the in-pile CONTACT1 experiment in the SILOE reactor demonstrate reasonable code predictions for gas release under steady irradiation conditions.

Further validation against various in-pile experiments (HALDEN, SILOE, MIR) and comparison with other fuel performance codes are foreseen in the close future. In parallel, further development of the SFPR models is in progress related to fuel restructuring and porosity evolution under high temperature conditions of fast reactors. Extension of the code to description of fuel rods with advanced fuels is an important part of the development plan (see, e.g., application of MFPR to TRISO fuel in [62]).

As a result of SFPR development in the form of a stand-alone fuel performance code, it is additionally anticipated to use this single-rod code as a constituent module of the Russian best estimate integral code SOCRAT [2] in application to analysis and safety justification of the new-generation nuclear reactors.

REFERENCES

[1]   M. Stan, Materials Models and Simulations in Support of Nuclear Fuels Development, Los Alamos National Laboratory Report, LA-UR-05-5652, 2005.

[2]   Bolshov. L., Strizhov. V., SOCRAT: The System of Codes for Realistic Analysis of Severe Accidents. – American Nuclear Society, 555 North Kensington Avenue, La Grange Park, IL 60526 (United States), 2006.

[3]   M.S. Veshchunov, A.V. Palagin, A.M. Volchek, N.V. Yamshchikov, A.V. Boldyrev, R.R. Galimov, S.Yu. Kurchatov, Code package SVECHA: Modeling of core degradation phenomena at severe accidents, Transactions of SMiRT-13 Conference, 1995, **1**, p.159-163.

[4]   V. Berdyshev, A.V. Boldyrev, A.V. Palagin, V.E. Shestak, M.S. Veshchunov, SVECHA/QUENCH Code for The Modeling of Reflooding Phenomena in Severe Accidents Conditions, Proceedings of the Ninth International Topical Meeting on Nuclear Reactor Thermal Hydraulics (NURETH-9), paper Log-19 (CD-ROM edition), San Francisco, California, USA 1999.

[5]   P. Hofmann, V. Noack, M.S. Veshchunov, A.V. Berdyshev, A.V. Boldyrev, L.V. Matweev, A.V. Palagin, V.E. Shestak, Physico-Chemical Behavior of Zircaloy Fuel Rod Cladding Tubes During LWR Severe Accident Reflood, Report FZKA 5846, Karlsruhe, Germany, 1997.

[6]   P. Hofmann, A. Miassoedov, L. Steinbock, M. Steinbrueck, A.V. Berdyshev, A.V. Boldyrev, A.V. Palagin, V.E. Shestak, M.S. Veshchunov, Quench Behavior of Zircaloy Fuel Rod Cladding Tubes. Small-Scale Experiments and Modeling of the Quench Phenomena, Report FZKA 6208, INV-COBE (98)-D018, Karlsruhe, Germany, 1999.

[7]   L. Sepold, G. Schanz, M. Steinbruck, J. Stuckert, A. Miassoedov, A. Palagin, M. Veshchunov, Results of the QUENCH-09 Experiment Compared to QUENCH-07 with Incorporation of B_4C Absorbe, Nucl. Technol. **154** (2006) 107.

[8]   B. Adroguer, F. Bertrand, P. Chatelard, N. Cocuaud, J.P. Van Dorsselaere, L. Bellenfant, D. Knocke, D. Bottomley, V. Vrtilkova, L. Belovsky, K. Mueller, W. Hering, C. Homann, W. Krauss, A. Miassoedov, G. Schanz, M. Steinbrück, J. Stuckert, Z. Hozer, G. Bandini, J. Birchley, T.V. Berlepsch, I. Kleinhietpass, M. Buck, J.A.F. Benitez, E. Virtanen, S. Marguet, G. Azarian, A. Caillaux, H. Plank, A. Boldyrev, M. Veshchunov, V. Kobzar, Y. Zvonarev, A. Goryachev, Core loss during a severe accident (COLOSS), Nucl. Eng. Des. **235** (2005) 173.

[9]   M.S. Veshchunov, A. V. Boldyrev, V.E. Shestak, K. Mueller, Analysis of Molten Pool Physico-Chemical Interactions in PHEBUS FP tests . Nucl. Eng. Des. **238**/7 (2008) 1728.

[10]   M.S. Veshchunov, A.V. Boldyrev, B. Toth, Application of mechanistic criteria of cladding oxide shell failure to the analysis of core degradation simulated in bundle meltdown tests. Nucl. Eng. Des. **238**/9 (2008) 2219-2229.

[11]   Models for the Fuel Rod Materials Interactions during Reactor Core Degradation under Sever Accident Conditions at NPP, Ed. by V.F. Strizhov. – Proceedings of Nuclear Safety Institute Ras (IBRAE RAS). Ed. by L.A. Bolshov, Nuclear Safety Institute (IBRAE) RAS.– Issue 1. – Moscow: Nauka, 2007. – 127 p.: ill. – ISBN 978-5-02-036139-3.

[12]   L. Yegorova, K. Lioutov, N. Jouravkova, A. Konobeev, V. Smirnov, V. Chesanov, A. Goryachev, "Experimental Study of Embrittlement of Zr-1%Nb VVER Cladding under LOCA-Relevant Conditions". Report NUREG/IA-021, IRSN 2005-194, NSI RRC KI 3188, NRC Washington, DC 20555-0001, March 2005.

[13] M.S. Veshchunov, A.V. Berdyshev, J. Nucl. Mater. Modelling of Hydrogen Absorption by Zirconium Alloys during High Temperature Oxidation in Steam, **255** (1998) 250-262.

[14] A.V. Berdyshev, L.V. Matveev, M.S. Veshchunov, "Development of the data base for the kinetic model of the Zircaloy4/steam oxidation at high temperatures (1000°C≤T≤1825°C)". Russian Academy of Sciences, Nuclear Safety Institute, IBRAE-97-05, Moscow, 1997.

[15] P. Hofmann, "Chemical Interactions of Zircaloy-4 Tubing with UO_2 Fuel and Oxygen at temperatures between 900 and 2000°C, Part1: Experimental results". KfK 4422, Kernforschungszentrum Karlsruhe, 1988.

[16] S. Sagat, H.E. Sills, J.A. Wolsworth, Failure criteria for Zircaloy-sheathed fuel elements under LOCA conditions. in: Zirconium in the Nuclear Industry: Sixth International Symposium, ASTM STP 824; D. G. Franklin, R. B. Adamson, Eds., American Society for Testing and Materials, 1984, pages 709-733.

[17] F.J. Erbacher, H.J. Neitzel, H. Rosinger and K. Wiehr, "Burst Criterion of Zircaloy Fuel Claddings in a Loss-of-Coolant Accident", in: Zirconium in the Nuclear Industry; Fifth Conference, ASTM STP 754, D.G.Franklin, Ed., American Society for Testing and Materials, 1982, pp. 271-283.

[18] M. Steinbrueck, J. Birchley, A.V. Boldyrev, A.V. Goryachev, M. Grosse, T.J. Haste, Z. Hozer, A.E. Kisselev, V.I. Nalivaev, V.P. Semishkin, L. Sepold, J. Stuckert, N. Ver, M.S. Veshchunov, "High-temperature oxidation and quench behaviour of Zircaloy-4 and E110 cladding alloys". Progress in Nuclear Energy, **52** (2010) 19–36.

[19] J. Freska, G. Konczos, L. Maroti, L. Matus, Oxidation and Hydrating of Zr1%Nb Alloys by Steam. Report KFKI-1995-17/G, 1995.

[20] M.S. Veshchunov, V.E. Shestak. Models for Hydrogen Uptake and Release Kinetics by Zirconium Alloys at High Temperatures. Nucl. Eng. Des. **252** (2012) 96–107.

[21] M. Grosse, M. Steinbrueck, E. Lehmann and P. Vontobel, Kinetics of hydrogen absorption and release in zirconium alloys during steam oxidation. Oxidation of Metals, **70** (2008) 149-162.

[22] M. Billone, Yong Yan, Tatiana Burtseva, Robert Daum, Cladding Embrittlement during Postulated Loss-of-Coolant Accidents, NUREG/CR–6967, ANL–07/04, June 30, 2008.

[23] J. Stuckert, M. Große, C. Rössger, M. Klimenkov, M. Steinbrück, M. Walter, QUENCH-LOCA program at KIT on secondary hydriding and results of the commissioning bundle test QUENCH-L0. Nuclear Engineering and Design **255** (2013) 185– 201.

[24] [24] M.S. Veshchunov, A.V. Berdyshev, Modeling of chemical interactions of fuel rod materials at high temperatures. Part 1: Simultaneous dissolution of UO_2 and ZrO_2 by molten Zircaloy in an oxidizing atmosphere, J. Nucl. Mater. **252** (1997) 98-109.

[25] M.S. Veshchunov, A New Model of Grain Growth Kinetics in UO_2 Fuel Pellets, J. Nucl. Mater. **346** (2005) 208 (part I), 220 (part II).

[26] M.S. Veshchunov and V.E. Shestak, "Model for Melt Blockage (Slug) Relocation and Physico-Chemical Interactions during Core Degradation under Severe Accident Conditions". Nucl. Eng. Des., **238** (2008) 3500–3507.

[27] V. Noack, S. Hagen, P. Hofmann, G. Schanz, L. Sepold, hemical-physical behavior of light water reactor core components tested under severe reactor accident conditions in the CORA facility. Nucl. Technol. **117** (1997) 158–170.

[28] M. Schwarz, B. Clement, A.V. Jones, Applicability of Phebus FP results to severe accident safety evaluations and management measures. Nucl. Eng. Des. **209** (2001) 173–181.

[29] M. Steinbrueck, M. Grosse, L. Sepold, J. Stuckert, Synopsis and outcome of the QUENCH experimental program. Nucl. Eng. Des. **240** (2010) 1714–1727.

[30] M.S. Veshchunov, V.D. Ozrin, V.E. Shestak, V.I. Tarasov, R. Dubourg, G. Nicaise, Development of the mechanistic code MFPR for modelling fission products release from irradiated UO2 fuel. Nucl. Eng. Des. **236** (2006) 179.

[31] M.S. Veshchunov, R. Dubourg, V.D. Ozrin, V.E. Shestak, V.I. Tarasov, Mechanistic modelling of urania fuel evolution and fission product migration during irradiation and heating. J. Nucl. Mater. **362** (2007) 327.

[32] R. Dubourg, H. Faure-Geors, G. Nicaise, M. Barachin, Fission product release in the first two PHEBUS tests FPT0 and FPT1. Nucl. Eng. Des. **235** (2005) 2183.

[33] T.J. Heames et al. "VICTORIA : A Mechanistic Model of Radionuclide Behavior in the Reactor Coolant System Under Severe Accident Conditions". NUREG/CR-5545 SAND90-0756 Rev 1 R3, R4, 1992.

[34] Models for Fission Products Release from Irradiated UO$_2$ Fuel. Ed. by R.V. Arutyunyan. – Proceedings of IBRAE RAS. Ed. by L.A. Bolshov, Nuclear Safety Institute (IBRAE) RAS. – Issue 5. – Moscow: Nauka, – 2008. – 157 p.: ill. – ISBN 978-5-02-036951-1.

[35] M.S. Veshchunov, V.E. Shestak, Model for Evolution of Crystal Defects in UO$_2$ under Irradiation up to High Burnups. J. Nucl. Mater. **384** (2009) 12.

[36] S. Kashibe, K. Une, K. Nogita, Formation and growth of intragranular fission gas bubbles in UO 2 fuels with burnup of 6–83 GWd/t . J. Nucl. Mater. **206** (1993) 22.

[37] K. Nogita, K. Une, Radiation-induced microstructural change in high burnup UO2 fuel pellets. Nucl. Instrum. Meth. Phys. Res. **B91** (1994) 301.

[38] M. Kinoshita, T. Sonoda, S. Kitajima, A. Sasahara, T. Kameyama, T. Matsumura, E. Kolstad, V.V. Rondinella, C. Ronchi, J.-P. Hiernaut, **T**. Wiss, F. Kinnart, J. Ejton, D., Papaioannou, Hj. Matzke, "HIGH BURNUP RIM PROJECT: (III) Properties of Rim-Structured Fuel", in: Proceedings of the 2004 International Meeting on LWR Fuel Performance, Orlando, Florida, Sep. 19-22, 2004.

[39] K. Une, S. Kashibe, Fission gas release during post irradiation annealing of BWR fuels. J. Nucl. Sci. Techn. **27** (1990) 1002.

[40] I. Zacharie, S. Lansiart, P. Combette, M. Trotabas, M. Coster, M. Groos, Thermal treatment of uranium oxide irradiated in pressurized water reactor: Swelling and release of fission gases. J. Nucl. Mater. **255** (1998) 85.

[41] M.S. Veshchunov, On the theory of fission gas bubble evolution in irradiated UO$_2$ fuel. J. Nucl. Mater. **277** (2000) 67.

[42] M. S. Veshchunov, V. I. Tarasov, An Advanced Model for Grain Face Diffusion Transport in Irradiated UO$_2$ Fuel. Part 1. Model Formulation. J. Nucl. Mater. **392** (2009) 78.

[43] V. I. Tarasov, M. S. Veshchunov, An Advanced Model for Grain Face Diffusion Transport in Irradiated UO$_2$ Fuel. Part 2. Model Implementation and Validation. J. Nucl. Mater. **392** (2009) 85.

[44] S. Ukai, T. Hosokawa, I. Shibahara and Y. Enokido, Evaluation of the fission gas release behavior from fast reactor mixed oxide fuel based on local concentration measurement of retained xenon. J. Nucl. Mater. **151** (1988) 209.

[45] M.S. Veshchunov, Modelling of Grain Growth Kinetics in Porous Ceramic Materials under Normal and Irradiation Conditions, Materials, **2** (2009) 1252-1287.

[46] J.A. Turnbull, The effect of grain size on the swelling and gas release properties of U02 during irradiation. J. Nucl. Mater. **50** (1974) 62.

[47] J.R. MacEwan and J. Hayashi, Grain growth in sintered uranium dioxide: I, Equiaxed grain growth. J. Am. Ceram. Soc. 4 (1962) 37.

[48] M.A. Mansouri, D.R. Olander, Fission product release from trace irradiated UO_{2+x}. J. Nucl. Mater. **254** (1998) 22.

[49] P.G. Lucuta, Hj. Matzke, R.A. Verrall, Thermal conductivity of hyperstoichiometric SIMFUEL, Journal of Nucl. Mater. J. Nucl. Mater. **223** (1995) 51.

[50] Hj. Matzke, Gas release mechanisms in UO2—a critical review. Radiat. Eff. **53** (1980) 219.

[51] K. Lassmann, The oxired model for redistribution of oxygen in nonstoichiometric uranium-plutonium oxides. J. Nucl. Mater. **150** (1987) 10.

[52] V.D. Ozrin, A model for evolution of oxygen potential and stoichiometry deviation in irradiated UO 2 fuel. J. Nucl. Mater. **419** (2011) 371.

[53] K. Une, Y. Tominaga, S. Kashibe, Oxygen Potentials and Lattice Parameter of Irradiated BWR Fuel, J. Nucl. Sci. Technol. 28 (1991) 409.

[54] Hj. Matzke, Oxygen potential measurements in high burnup LWR UO_2 fuel. J. Nucl. Mater. 223 (1995) 1.

[55] C.T. Walker, V.V. Rondinella, D. Papaioanou, S. Van Winckel, W. Goll, R. Manzel, On the oxidation state of UO_2 nuclear fuel at a burn-up of around 100MWd/kgHM. J. Nucl. Mater. **345** (2005) 192.

[56] G. Ducros, P.P. Malgouyres, M. Kissane, D. Boulaud, M. Durin, Fission product release under severe accidental conditions: general presentation of the program and synthesis of VERCORS 1–6 results. Nucl. Eng. Des. **208**/2 (2001) 191.

[57] V.I. Tarasov, Modeling of Diffusive Release of Radioactive Fission Products from UO2 Fuel. Atomic Energy, 106 (2009) 395-408V. I. Tarasov, V. D. Ozrin, M. S. Veshchunov, Modeling of Diffusive Release of Radioactive Fission Products from Nuclear Fuel in the Framework of SFPR Code**.** in: Proceedings of Top Fuel 2009, Paris, France, September 6–10, 2009, paper 2017.

[58] A.V. Avvakumov, A.E. Kiselev, E.F. Mitenkova, V.F. Strizhov, V.I. Tarasov, S.V. Tsaun, V.V. Bezlepkin, I.A. Potapov, A.S. Frolov, Verification of module BONUS in the framework of integral code SOCRAT. Atomic Energy, **106** (2009) 250.

[59] J.A. Turnbull, C.A. Friskney, J.R. Findlay, F.A. Johnson, A.J. Walter, The diffusion coefficients of gaseous and volatile species during the irradiation of uranium dioxide. J. Nucl. Mater. **107** (1982) 168.

[60] M. Bruet, J. Dodelier, P. Melin, M. L. Pointud, Contact 1 and 2 experiments: behaviour of PWR fuel rod up to 15000 MWd. t. in: IAEA Specialists'Meeting on Water Reactor Fuel Element Performance Computer Modelling, Blackpool, 17-21 March, 1980.

[61] M. Barrachin, R. Dubourg, M.P. Kissane, V. Ozrin, Progress in understanding fission-product behaviour in coated uranium-dioxide fuel particles. J. Nucl. Mater. **385** (2009) 372.

PRELIMINARY ASSESSMENT OF ACCIDENT TOLERANT FUEL PERFORMANCE AT NORMAL AND ACCIDENT CONDITIONS

PENG XU, PAOLO FERRONI, DAVE MITCHELL, LARS HALLSTADIUS
Westinghouse Electric Company

Abstract. The interest for improving the safety of light water reactors (LWRs) fuel designs, which has significantly grown after the Fukushima Daiichi Accident, has driven the U.S. Department of Energy (DOE) to fund three industry-led programs to facilitate the development of accident tolerant fuels (ATF) for LWRs. Westinghouse is leading one of them and engaged in developing a combined accident resistant cladding and high density fuel pellet. It is important to develop and apply fuel performance codes and other computational methods to model the novel fuel forms to better understand the in-core performance and to guide new fuel designs. In this paper, a preliminary assessment on the performance of various ATF concepts during normal and accident conditions is presented. These concepts include various combinations of accident tolerant fuel and cladding materials: UN/SiC, U_3Si_2/SiC, UN/Coated Zircaloy, and U_3Si_2/Coated Zircaloy. The properties of the new materials were collected from literature and their irradiation data will be selected from various test reactor experiments. The impact of ATF properties on design basis accidents and beyond design basis accident is also discussed.

1. INTRODUCTION

The occurrence of severe nuclear accidents, at Fukushima Daiichi in March 2011 and at Three Mile Island in 1979, is an indication that the frequency of these severe accidents may be higher than previously predicted, and therefore that plant owners are more likely at risk of the financial liabilities capable of severely damage them. These accidents stimulated the fuel vendors to pursue new fuel materials that provide a significant increase in the time for the reactor operator to respond to unforeseen events before significant releases of fuel materials occur. In addition to a safety improvement, any accident tolerant fuel (ATF) product that is developed must provide an operating cost improvement as well, in order to be commercially successful. The advanced fuel and cladding architecture offered by Westinghouse is summarized in Table 1. Table 2 and Table 3 show the key properties of the proposed fuel and cladding materials, respectively. A coloring scheme is used to indicate properties that are definitely better than those for the baseline materials (green), versus those that are definitely worse (orange). Properties for which the difference from the baseline materials is either not significant or not yet well understood are left uncolored.

TABLE 1. SUMMARY OF WESTINGHOUSE ADVANCED FUEL AND CLADDING ARCHITECTURE

ATF Fuel Architecture Parameter	Description
Assembly Geometry	Square assembly lattice and pitch composed of solid cylindrical fuel pellets in thin walled cladding tubes
Fuel	Solid cylindrical pellets of U_3Si_2 or treated $U^{15}N$ that is waterproof when cladding breach occurs
Cladding	SiC_f/SiC (SiC fiber in SiC matrix) Ceramic Matrix Composite (CMC) thin walled tubes or coated Zr base alloy tubes
Fuel Assembly Components other than Fuel and Cladding	SiC_f/SiC CMC or coated Zr base alloys

TABLE 2. COMPARISON OF KEY PROPERTIES OF THE PROPOSED FUEL MATERIALS TO UO2

Property	UO_2	U_3Si_2	UN
Theoretical/HM densities (g/cm^3)	10.98 / 9.68	12.2 / 11.3	14.3 / 13.5
Thermal conductivity, k (W/m K)	5–2 (300–2000°C)	9–20 (300–1200°C)	18–23 (300–1200°C)
Specific heat (J/kg K)	280–440 (300–2000°C)	230–320 (300–1200°C)	220–260 (300–1200°C)
Melting point, T_m (°C)	2840	1665	2760
Thermal margin: $k \times (T_m - 400°C)/100$	50–90	>100	>400
Irradiation-induced swelling	Low	Likely high. Assumed in this analysis: 12% dV/V at an assumed EOL burnup of 75 GWD/MTU	Likely medium-high. Assumed in this analysis: 8% dV/V at an assumed EOL burnup of 75 GWD/MTU
Reaction with water: negligible?	Yes	Likely yes	No, but may be reduced
Experience in nuclear applications	Large	Some	Some
Easy to manufacture	Yes	Less than UO_2	Much less than UO_2 (it requires ^{15}N enrichment)

TABLE 3. COMPARISON OF KEY PROPERTIES OF THE PROPOSED CLADDING MATERIALS TO UNCOATED ZIRCALOY

Property	Uncoated Zircaloy	Coated Zircaloy	SiC$_f$/SiC CMC
Thermal conductivity (W/m K)	16 (at 370°C, irradiated)	Assumed same as uncoated Zircaloy	4-5 (irradiated, ~independent on T)
Melting point (°C)	1825	Same as uncoated Zircaloy	>2500
High-temperature (≥1200 °C) oxidation rate in steam	X	<X	~X/100
Mechanical properties	Good	Same as uncoated Zircaloy	Worse than Zircaloy
Neutronic penalty with respect to uncoated Zr	-	Very minor for the coating types and thickness considered	None to some, in the range of cladding thicknesses under consideration
Experience in nuclear applications	Large	Base material: same as uncoated Zircaloy; Coating: none	No
Easy to manufacture	Yes	Same as uncoated Zircaloy	Somewhat
Other info			Assuring rod cap sealing is challenging
			Some properties are anisotropic and manufacture-dependent

2. PERFORMANCE ASSESSMENT FOR NORMAL OPERATION

A preliminary evaluation was performed to assess the impact of some basic fuel rod performance constraints on the geometry of an advanced fuel assembly. In this preliminary study it was decided to consider the reference robust fuel assembly (RFA) design and to estimate whether the adoption of various fuel-cladding material combinations would require the need to change this geometry in order to meet these constraints. The performance constraints used in this study are:

- Fuel centerline temperature should remain below melting at a conservatively high linear power of 20 kW/ft;

- To prevent strain-induced cladding failure, cladding tensile strain at end-of-life[2] (EOL) should remain below 2% for coated Zr and below 0.1% for SiC cladding;
- For SiC cladding, the proposed multilayer structure of the composite requires the cladding to be thicker than for conventional Zr alloy. Although, to preserve current enrichment levels, the SiC cladding is targeted to be approximately 0.030 in thick, in this preliminary analysis a very conservative approach has been used to account for manufacturing constraints, leading to a cladding thickness of 0.041 in. A typical thickness of 0.022 inches was instead used for conventional Zircaloy and coated Zr base alloy claddings.

The rationales behind the choice of the strain limits are different for the two cladding materials. For coated Zr, the 2% strain limit results from the following three considerations.

- Conventional Zircaloy has been demonstrated to resist short term strain (i.e. that experienced during hot cell tests) above 2%;
- Conventional Zircaloy's resistance to long term strain typical of reactor operation is higher than that to short term strain experienced during hot cell testing;
- Due to the relatively small coating thickness, the presence of a coating is not expected to affect the capability of coated Zr to resist strain.

For SiC cladding a 0.1% strain limit was chosen. Due to uncertainty in the irradiation effect on mechanical properties, the dependence of mechanical properties on the SiC composite and manufacture process, this relatively conservative low value was selected. This preliminary strain limit value will be evaluated later in the project.

2.1 Fuel Rod Sizing Results

Table 4 shows the fuel rod geometries, as well as the fuel loading, resulting from the application of the above mentioned constraints. The fuel loading is an indicator of the economic performance of the proposed fuel designs. Higher fuel loading results in longer fuel cycles and/or lower required fuel enrichment.

From Table 4 it can be seen that, depending on the materials considered, their implementation may or may not lead to a deviation in fuel rod geometry with respect to the reference design. UN-fueled geometries are more similar to current fuel design geometries than U_3Si_2-fueled ones. Specifically, the UN-fueled geometry using coated Zr has the same dimensions as the reference design. The fuel geometry using SiC cladding requires instead a thicker cladding, due to the limits of SiC CMC fabrication, and a larger pellet-clad gap due to the conservative clad strain limit value applied. In both cases, the use of UN fuel results in a

---

[2] This tensile strain is defined as 100(EOL diameter-minimum OD)/minimum OD, where the minimum diameter is over the rod life, and a burnup of 75 GWD/mtU is assumed for EOL.

significant increase in fuel loading, i.e. a 41% increase with coated Zr cladding and a 15% increase with SiC cladding, both relative to the Zr alloy clad/UO_2 fuel reference case. This results from the high HM density of UN.

U_3Si_2-fueled geometries may require a wider pellet-clad gap to accommodate the assumed higher swelling of this fuel and avoid exceeding the clad strain limit. However, if not properly sized, this larger pellet-cladding gap could result in an insufficient margin from fuel melting during anticipated transients. Although both UN and U_3Si_2 are expected to swell more than UO_2, protection against fuel melting is more of a concern for U_3Si_2 due to its low melting point, and should be carefully considered particularly in the case of SiC cladding, since its low thermal conductivity with respect to Zr penalizes the fuel temperature. For this reason, in this preliminary study, the U_3Si_2-SiC design is analyzed assuming a Liquid Metal (LM), such as Pb-Sn-Bi eutectic, as bonding material, in place of the conventional helium. This fuel bonding design option has been investigated and experimentally tested for UO_2 fuel, with good results, as discussed in Ref. [1] through [3]. However, it is much less preferable than helium from the fuel rod manufacture and operation viewpoints, and other design alternatives are under investigation to eliminate the need for such a high-conductive bonding material. In addition to a reduction in the thickness of the SiC cladding to 0.030 inches, there is also the option of providing the pellet with a small, internal void, which would allow reducing the width of the pellet-clad gap, with respect to a solid pellet, thus benefitting both fuel temperature and cladding strain. Also, testing will be required to determine if the irradiation-induced swelling assumed for U_3Si_2 is indeed valid. In fact a literature review revealed that the available experimental data on U_3Si_2 swelling refer to samples irradiated either at representative temperatures (~1000°C) but low burnup (~7 MWD/MTU) ([4]), or at high burnup (60–200 MWD/MTU) but low, unrepresentative, temperature (~100°C) ([5], [6]).

As a consequence of the analysis assumptions adopted for U_3Si_2, its implementation results in a reduction in fuel loading of approximately -13% for coated Zr cladding and approximately -30% for SiC cladding. These numbers imply a significant penalty on fuel cycle economics, which clearly indicates that gaining a better confidence in the swelling behavior of U_3Si_2, as well as in the strain resistance and required thickness for SiC cladding, is of paramount importance for the development of this fuel.

The thermal hydraulic performance of the geometries shown in Table4 are presented and discussed in Section 2.2.

TABLE 4. ASSEMBLY GEOMETRIES RESULTING FROM APPLICATION OF FUEL ROD
PERFORMANCE CONSTRAINTS

		Cladding/Fuel Material Combinations				
		Reference (UO₂/Zircaloy)	Coated Zr		SiC	
			UN	U₃Si₂	UN	U₃Si₂
Geometry	Clad OD, in.	0.374	0.374	0.374	0.382	0.382
	Clad ID, in.	0.329	0.329	0.329	0.300	0.300
	Clad Thickness, in.	0.0225	0.0225	0.0225	0.041	0.041
	Pellet OD, in.	0.3225	0.3225	0.2770	0.2910	0.2460
	Pellet-clad gap, in. (filling material)	0.00325 (He)	0.00325 (He)	0.026 (He)	0.0045 (He)	0.027 (LM*)
	Performance indicator: fuel loading					
Fuel loading per assembly (95% TD)	Total, kg	530	692	435	562	343
	HM, kg	464	653	403	531	318
	HM variation, %	0	+41	-13	+15	-31

*LM: Liquid Metal

2.2 Thermal Hydraulics Analysis

A preliminary evaluation was performed on the effect of the proposed fuel/cladding material combinations on fuel assembly thermal hydraulic (TH) performance. This evaluation includes the following sections.

2.2.1 Analysis Approach and Constraints Used

The preliminary evaluation of the steady-state TH performance of various fuel/cladding combinations was performed by modeling PWR cores operating with these new materials. Typically, the best practice in designing a high performance core involves performing a geometry optimization over wide ranges of assembly lattice parameters, i.e. fuel rod diameter and rod-to-rod distance, for both square and triangular lattices. Instead, for simplicity, this preliminary evaluation first considered a fixed fuel assembly geometry used for modeling all the fuel-cladding combinations, i.e. the 17×17 robust fuel assembly (RFA) design (Case 1), and then applied the same analysis methodology but to 17×17 lattices of rods whose geometry resulted

from the application of the fuel rod performance constraints listed previously (Case 2). The purpose of analyzing Case 1 was clearly to "isolate" the effect of the different material properties.

The reactor operating conditions selected are summarized in Table 5. These conditions are representative of design values typically used for Zr/UO_2 fuel system cores and therefore are not best estimates for nominal operation. In addition to the reference power distribution presented in Table 5, the alternative fuel/cladding combinations were also analyzed using an enthalpy rise hot channel factor (FdH) increased by 15% in order to account for the possibility of not being able to achieve the same low peaking of typical UO_2 fuel.

TABLE 5. OPERATING CONDITIONS SELECTED FOR PRELIMINARY THERMAL HYDRAULIC ASSESSMENT

Parameter	Value
Plant type	Typical Westinghouse 4-loop
Core power, MWt	3459
Core operating pressure, psi	2240
Core inlet temperature, °C	287.9
Core flow rate excluding bypass, kg/s	16395
Hot assembly flow distribution factor	0.95
Hot assembly peaking factor	1.55
Enthalpy rise hot channel factor (FdH)	1.62
Axial peaking factor (Fz) & axial power shape	1.55, cosine
Peak heat flux hot channel factor (Fq)	2.51
Pellet-clad gap conductance, $W/m^2 K$	$5682 \times t_{ref}/t$ (He-bonded); $35/t$ (LM bonded)*

*t is the pellet-cladding gap width, expressed in meters. t_{ref} is the value for the reference rod design

2.2.2 *Performance Indicators*

To assess the TH performance modeling results, the following six performance indicators are applied to all modeling in this subtask.

- Heavy metal (HM) loading per fuel assembly,
- Maximum fuel temperature,
- Maximum fuel average temperature across the pellet radius,
- Maximum temperatures on the inner and outer surfaces of the cladding,

- Minimum Departure from Nucleate Boiling Ratio (MDNBR), and
- Core pressure drop.

The heavy metal loading indicator has primarily economic implications in that higher HM loading can result in a longer fuel cycle and/or lower required enrichment. The other five performance indicators have primarily safety implications. The maximum fuel temperature needs to guarantee a margin from melting sufficient to allow operational flexibility and to accommodate transients. The maximum fuel average temperature affects the amount of fission gas released during operation as well as irradiation-induced swelling of the fuel pellet. The maximum cladding temperatures will affect the mechanical properties of the cladding material as well as the oxidation kinetics. MDNBR is monitored to allow for sufficient margin from critical heat flux (CHF) conditions and, in this analysis, evaluated to only have an indication of the relative DNB performance of the geometries considered with respect to the reference one. Key aspects of MDNBR as a performance indicator are as follows.

Due to the degradation in mechanical properties with increasing temperature of Zr base alloys, operation with rods in DNB is unacceptable using Zr alloy and coated Zr alloy cladding since clad failure will occur. However, the high temperature capabilities of SiC (high melting point and limited degradation of mechanical properties with temperature) make reaching CHF conditions less of a concern and operation of fuel in DNB may be possible without resulting in cladding failure. Thus it is possible that, from the DNB viewpoint, SiC may have significant safety and performance advantages compared to conventional Zr alloy cladding, thus deserving further investigation.

The surface wettability of the cladding material is known to affect CHF and is different for Zr alloy, coated Zr alloy, and SiC cladding. For this preliminary effort, the effect of surface wettability on CHF is conservatively[3] neglected. Due to this, and the fact that constant operating conditions and fuel assembly geometry are used for all fuel/cladding combinations examined in Case 1, the calculated MDNBR is the same for all fuel/cladding combinations. Thus, MDNBR is not a useful performance indicator for the fuel designs modeled in Case 1.

Finally, core pressure drop provides an indication of the effect that variations in assembly lattice geometry (fuel rod diameter in this analysis) would have on the coolant flow rate, since the flow provided by the reactor coolant pumps (RCPs) decreases as the hydraulic resistance increases.

2.2.3 Analysis Results and Observations

---

[3] Coated Zr and composite SiC are expected to have a CHF at least equal to that of conventional (uncoated) Zr, if not higher. The higher porosity characterizing both the protective layer deposited on Zr and, eventually, the SiC composite structure, are expected to yield a higher nucleation site density, whose enhancement is known to benefit CHF.

Results for Case 1 modeling are summarized in Table 6. Here, modeled cases 1a, 1b, and 1c use progressively higher peak linear power (q'_{max}). The calculated results are highlighted compared to the reference design (Zr/UO_2) using the following cell coloration scheme.

- no highlight – similar performance to Zr/UO_2
- green highlight – significantly better performance than Zr/UO_2
- yellow highlight – slightly worse performance than Zr/UO_2
- red highlight – significantly worse performance than Zr/UO_2

Results of Case 1 modeling shown in Table 6 can be summarized as follows:

- Use of U_3Si_2 and UN results in significantly higher HM loadings compared to the Zr/UO_2 reference design. U_3Si_2 increases HM content by 18% and UN by 41%. These values result from the high HM density of these fuels, as shown in Table 2, and are determined assuming 95% of theoretical density for all fuels.

- U_3Si_2 has a similar margin to melting compared to UO_2, whereas UN has a much higher margin. For U_3Si_2, this is due to the lower melting point but higher thermal conductivity of this fuel compared to UO_2 (see Table 7). Additionally, because the thermal conductivity of U_3Si_2 increases with temperature, the margin to melting of U_3Si_2 becomes larger than UO_2 as peak linear power and fuel temperature increase from Case 1a to Case 1c. For UN, the higher margin to melt in all cases is due to the high melting temperature and higher thermal conductivity of UN compared to UO_2.

- The temperature of the cladding is independent of the type of fuel used and dependent on the thermal conductivity of the cladding material. For this reason, this temperature is about 200°C higher than the reference design only when using SiC, 0.041 inches thick, as cladding material. The thermal conductivity of irradiated SiC is much lower than Zr and, after an irradiation equivalent to about 1 dpa, is almost independent of temperature, as shown in Fig. 1. This level of radiation damage is expected to be reached after 4-5 months of operation in a typical LWR [7].

- Core pressure drop is effectively equivalent for all designs due to the fixed assembly geometry and coolant flow assumed for Case 1.

347
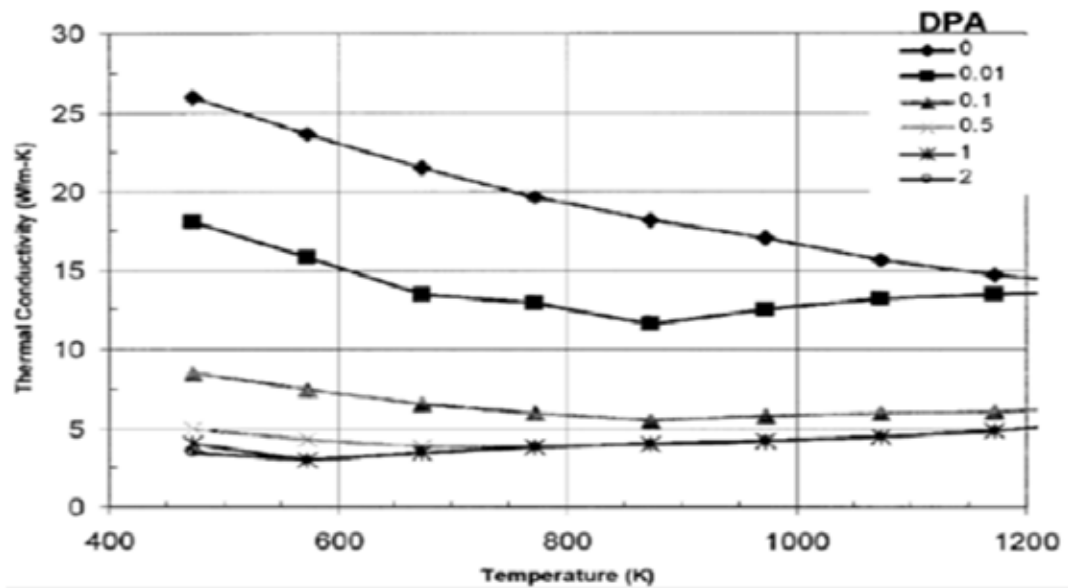
FIG. 1. Variation of thermal conductivity with temperature and irradiation for SiC composite (High-Nicalon Type S with CVI SiC from [8] and originally in [9].

Results for Case 2 modeling are presented in Table 7 and again Case 2a, 2b, and 2c only differ in the peak linear power used in the analysis. These results can be summarized as follows:

- With the exception of the Zr/UN design, application of fuel performance constraints results in a reduction of HM loading with respect to Case 1. This is due to the need for a larger pellet-clad gap, with respect to UO_2, when U_3Si_2 is adopted, and for a larger cladding thickness, with respect to Zircaloy, for SiC. Due to the lack of experimental data at LWR operating conditions and burnups, a very conservative swelling behavior for U_3Si_2 was used. As a consequence of this, the HM loadings for the silicide options decreased to -31% for SiC cladding and -13% for coated Zr alloy cladding, both compared to the Zr/UO_2 design. If swelling was found to be comparable to UO_2, the HM loading would increase about 8%. For UN, HM loading decreases to 15% for SiC cladding and remains the same at 41% for coated Zr alloy cladding, again both compared to the Zr/UO_2 design. This reduction in HM loading penalizes fuel cycle economics particularly for U_3Si_2 fuel.
- Because of the conservatively high swelling assumed for U_3Si_2 (see Table 7), and the subsequently large pellet-to-cladding gap, if helium was used as bonding material for this fuel the thermal resistance across the gap could challenge the fuel melting criterion. This is the case of the design option using SiC as cladding material: as discussed in Section 2.1, for this design a highly conductive Liquid Metal bond is proposed to replace He, which allows a sufficient margin from melting to be maintained. Instead, for the U_3Si_2-

fueled design but Zircaloy-clad, the better thermal conductivity of the latter with respect to SiC does not result in challenging the fuel melting criterion even with Helium as bonding material. Because of the preference for He vs a Liquid Metal to bond the rods[4], He is indicated in Table 7 for the U_3Si_2/coated Zircaloy design.

- UN shows significant margin to melting ranging from approximately 600 to 1500°C greater than that for UO_2. For UN, He was used as the bonding material due to the higher melting point and relatively smaller pellet-clad gap calculated for this fuel, with respect to U_3Si_2.

- Due to the increase in fuel rod outer diameter when using SiC cladding, the heat transfer area and the coolant velocity both increase, resulting in a ~3% higher MDNBR. However, core pressure drop increased approximately 7% in designs employing SiC, due to the tighter lattice resulting from the larger fuel rod diameter.

---

[4] See discussion in Section 2.1.

TABLE 6. PERFORMANCE OF VARIOUS FUEL-CLAD COMBINATIONS WHEN LOADED IN A
REFERENCE ASSEMBLY GEOMETRY (ROD OD=0.374", CLAD THICKNESS= 0.0225"; PELLET
OD=0.3225", HE-BONDED RODS)

| | | | Cladding and Fuel Materials | | | |
| | | Reference (Zr/ UO_2) | SiC | | Coated Zr | |
			U_3Si_2	UN	U_3Si_2	UN
Fuel loading per assembly	total, kg	530	590	692	590	692
	HM, kg	464	546	653	546	653
	HM variation (% compared to reference)	0	+18	+41	+18	+41
Case 1a: **design conditions** (q'_{max}=14.2 kW/ft)	maximum fuel centerline T, °C	2058	1066	1041	908	872
	margin from fuel melting T, °C	782	599	1722	757	1890
	maximum fuel average T, °C	1342	979	966	812	793
	hot spot cladding T (inside/outside), °C	402/348	579/348	579/348	402/348	402/348
	MDNBR[a]	2.769	2.769	2.769	2.769	2.769
	core pressure drop, psi	29.1	29.1	29.1	29.1	29.1
Case 1b: **+15% in FdH for ATF fuel-clad combinations** (q'_{max}=16.3 kW/ft)	maximum fuel centerline T, °C	-	1155	1127	973	937
	margin from fuel melting T, °C	-	510	1635	692	1825
	maximum fuel average T, °C	-	1058	1045	869	850
	hot spot cladding T (inside/outside), °C	-	610/348	610/348	409/348	409/348
	MDNBR[a]	-	2.307	2.307	2.307	2.307
	core pressure drop, psi		29.2	29.2	29.2	29.2
Case 1c: (q'_{max}=20 kW/ft)	maximum fuel centerline T, °C	2720	1374	1329	1125	1088
	margin from fuel melting T, °C	120	291	1433	540	1674
	maximum fuel average T, °C	1832	1251	1230	1001	982
	hot spot cladding T (inside/outside), °C	427/350	682/350	682/350	427/350	427/350
	MDNBR[a]	1.385	1.385	1.385	1.385	1.385
	core pressure drop, psi	29.6	29.6	29.6	29.6	29.6

[a] The Westinghouse WRB-2M correlation is used to compute CHF.

350

TABLE 7. PERFORMANCE OF ASSEMBLY DESIGNS SATISFYING FUEL ROD DESIGN CONSTRAINTS

		Cladding and Fuel Materials				
		Reference (Zr/ UO$_2$)	SiC		Coated Zr	
			U$_3$Si$_2$	UN	U$_3$Si$_2$	UN
Geometry	Cladding OD, in	0.374	0.382	0.382	0.374	0.374
	Cladding ID, in	0.329	0.300	0.300	0.329	0.329
	Clad thickness, in	0.0225	0.041	0.041	0.0225	0.0225
	Pellet OD, in	0.3225	0.246	0.291	0.277	0.3225
	Pellet-clad gap, in. (filling material)	0.00325 (He)	0.027 (LM)	0.0045 (He)	0.026 (He)	0.00325 (He)
Performance Indicator: fuel loading						
Fuel loading per assembly	total, kg	530	343	562	435	692
	HM, kg	464	318	531	403	653
	HM variation (%)	0	-31	+15	-13	+41
Performance Indicator: temperature and MDNBR						
Case 2a: **design conditions** **(q'$_{max}$=14.2 kW/ft)**	maximum fuel centerline T, °C	2058	1010	1396	1109	872
	margin from fuel melting T,°C	782	655	1366	556	1890
	maximum fuel average T,°C	1342	920	1328	562	793
	hot spot clad T (in./out.), °C	402/348	783/348	783/348	402/348	402/348
	MDNBR[a]	2.769	2.858	2.858	2.769	2.769
	core pressure drop, psi	29.1	31.2	31.2	29.1	29.1
Case 2b: **+15% in FdH for ATF** **fuel-clad combinations** **(q'$_{max}$=16.3 kW/ft)**	maximum fuel centerline T,°C	-	1089	1529	1205	937
	margin from fuel melting T,°C	-	576	1233	460	1825
	maximum fuel average T,°C	-	991	1454	1109	850
	hot spot clad T (in./out.), °C	-	840/348	840/348	409/348	409/348
	MDNBR[a]	-	2.385	2.385	2.307	2.307
	core pressure drop, psi	-	31.3	31.3	29.2	29.2
Case 2c: (q'$_{max}$=20 kW/ft)	maximum fuel centerline T,°C	2720	1284	1851	1438	1088
	margin from fuel melting T,°C	120	381	911	227	1674
	maximum fuel average T, °C	1832	1162	1755	1316	982

	hot spot clad T (in./out.), °C	427/350	975/350	975/350	427/350	427/350
	MDNBR[a]	1.385	1.431	1.431	1.385	1.385
	core pressure drop, psi	29.6	31.8	31.8	29.6	29.6

[a] The Westinghouse WRB-2M correlation is used to compute CHF.

3. SAFETY ASSESSMENT FOR OPERATIONAL TRANSIENTS AND ACCIDENTS

The safety-related performance of a PWR core during normal operation, anticipated transients, and design basis accidents (DBAs) is typically assessed through extensive analysis requiring comprehensive knowledge of all in-core components. Presently, this level of knowledge of cladding and fuel components is incomplete because information such as in-core material performance is unknown. However, a preliminary study of the safety performance of an advanced fuel design can be performed by using currently available material properties and making a relative comparison to current materials and components. Through this approach, engineering judgment can be used to perform this analysis and draw preliminary conclusions about materials and reactor response during transients. This engineering judgment analysis can be performed using two bases for the analysis: the type of fuel rod damage mechanism, discussed in section 3.1, and the type of transient, discussed in section 3.2.

3.1 Preliminary Advanced Fuel Safety Analysis based on Fuel Rod Damage Mechanism

This analysis is performed by surveying typical damage mechanisms considered in reactor analysis and determining if the properties of the new cladding and fuel materials will protect against these mechanisms. Damage mechanisms considered in reactor analysis can be classified into three major categories [10]:

Category I: Mechanisms potentially resulting from "fuel system damage", i.e. either fuel failure, deviation of fuel rod dimensions beyond tolerance margins, or reduction of functional capabilities below those assumed in safety analyses. These mechanisms apply to normal operation and anticipated operational occurrences (AOOs).

Category II: Mechanisms potentially resulting in fuel rod failure which apply to normal operation, AOOs, and postulated accidents.

Category III: Mechanisms resulting in loss of coolability, i.e. the fuel assembly does not retain its rod bundle geometric configuration with adequate coolant channels to permit heat removal. These mechanisms apply to postulated accidents.

Specfic fuel rod damage mechanisms belonging to each of these three categories are presented in column two of Table 8 for each failure mechanism category and fuel rod damage mechanism, Table 8 presents an engineering judgment on the relative performance of the selected fuel and cladding materials with respect to the current Zr/UO_2 fuel system. A coloring scheme is used to identify the damage mechanisms in which the new materials are expected to perform definitely better (green) or definitely worse (red) than current materials. Light blue is used to identify fuel rod damage mechanisms requiring further experimental or computational investigation. For some fuel rod damage mechanisms, Table 8 is supplemented with additional information identified by capital letters inside the table cells and correlated to the lettered paragraphs following the table.

TABLE 8. EXPECTED RELATIVE PERFORMANCE OF ADVANCED FUEL AND CLADDING

Failure Mechanism Categories	Fuel Rod Damage Mechanisms	Fuel Rod & Fuel Materials			
		SiC CMC (to Zr)	Coated Zr (to Zr)	U₃Si₂ (to UO₂)	UN (to UO₂)
Category I: *fuel system damage* (normal operation & AOOs)	clad design stress	BETTER at high T, TBD at normal operation (F)	SAME	WORSE Higher fuel swelling	WORSE Higher fuel swelling
	clad design strain		SAME	WORSE Higher fuel swelling	WORSE Higher fuel swelling
	clad fatigue		SAME	WORSE Higher fuel swelling	WORSE Higher fuel swelling
	clad fretting wear	SIGNIFICANTLY BETTER (C)	Probably WORSE	No effect	No effect
	oxidation & crud buildup	BETTER (E)	BETTER	No effect	No effect
	rod bow	BETTER (D)	Same	No effect	No effect
	axial growth	BETTER (D)	Same	No effect	No effect
	internal pressure	BETTER at high T, TBD at normal operation (F)	No effect	Unknown wider gap for swelling reduces pressure, burnable poisons still unknown	
	assembly liftoff	WORSE, but not a concern	Same	BETTER heavier fuel	
	clad hydriding	SIGNIFICANTLY BETTER	SIGNIFICANTLY BETTER	No effect	
	clad collapse - fuel densification	Somewhat BETTER (A)	Same	Somewhat BETTER due to higher fuel swelling	
	clad overheat by CHF	SIGNIFICANTLY BETTER (F)	Same	No effect	No effect
Category II: *fuel rod failure* (normal operation, AOOs, postulated accidents)	fuel overheat	WORSE due to low clad thermal conductivity and low creep (B)	Same	Somewhat BETTER due to higher thermal conductivity BUT lower melting T	BETTER due to higher thermal conductivity and similar melting T
	pellet-clad interaction	BETTER (A)	Same	WORSE due to higher fuel swelling	WORSE due to higher fuel swelling
	fuel rod fracturing by external loads - core/plate motion	BETTER at high T, undetermined during normal operation (F)	Same	No effect	No effect
	LOCA Clad Fragmentation	SIGNIFICANTLY BETTER (F)	BETTER	No effect	No effect
	expulsion of fuel upon RIA	BETTER (F)	Same	Probably WORSE	
Category III: fuel rod failure and loss of *fuel coolability* (postulated accidents)	Clad ballooning and flow blockage during LOCA	SIGNIFICANTLY BETTER (F)	Same	BETTER: lower fuel stored energy due to lower initial T	BETTER: lower fuel stored energy due to lower initial T
	fuel assembly structural damage from external forces	BETTER due to low degradation of mechanical properties with T (F)	Same	No effect	No effect

The letter scheme indicated in Table 8 refers to the following additional information:

A. Unlike Zircaloy, SiC does not creep up to 1300°C making PCMI less likely to occur under similar conditions of fuel geometry, fuel type, and irradiation level [11]. This is an advantage because it results in reduced stress in the cladding, but also a disadvantage because lack of creep defers the reduction in thermal resistance that occurs from gap closure. The combination of low thermal conductivity of irradiated SiC and lack of gap closure results in higher fuel temperatures when using SiC based cladding. Additionally, the lack of creep in SiC requires an increased pellet-clad gap in the as fabricated condition, to prevent excessive cladding strain upon gap closure.

B. Carpenter states that "SiC cladding performance may be limited unless cladding/fuel conductivity or gap conductance is improved" [11]. This is due to two factors:
   1. SiC experiences a significant degradation in thermal conductivity upon irradiation;
   2. SiC does not creep at temperatures below 1300°C.
   The reduction in thermal resistance that normally accompanies pellet-clad gap closure is deferred when using SiC base cladding. According to data from Youngblood (and reported by Carpenter), Hi-Nicalon Type-S SiC composite experiences a reduction in thermal conductivity to a saturation value of approximately 4 W/m K after 0.5 to 1 dpa of irradiation from an unirradiated value of 23 W/m K [8], [9]]. For a typical PWR or BWR, the time required to accumulate 1 dpa of radiation damage is approximately 4 to 5 months of operation at full power 12]

C. The degree of cladding fretting is expected to be much smaller for SiC than for Zircaloy, due to its hardness.

D. SiC CMC tubes have been experimentally verified to grow axially under irradiation to saturation values of 0.2 to 0.7% ($\Delta L/L$) after 240 EFPD of operation [12]. These values are consistent with data for solid SiC of 1.7% volume increase corresponding to 0.57% length increase [12]. Radial growth data for SiC ranges from 0.5 to 3% ($\Delta D/D$). Significant data scatter exists for both axial and radial growth of SiC.

E. Monolithic and composite SiC exposed to steam up to 1200°C exhibits oxidation kinetics 2 to 3 orders of magnitude slower than Zircaloy-2 and Zircaloy-4 [13], [14]. Carpenter also exposed SiC to steam under irradiation [11]. These tests showed that monolithic SiC exposed to steam at 300°C exhibited similar low oxidation kinetics, regardless of irradiation. Instead, SiC composites showed a reduction in oxidation resistance upon irradiation and specifically an increase in oxidation-induced weight change by 5–15 times with respect to that of unirradiated samples when provided with the so-called Environmental Barrier Coating (EBC), and by 10–25 times for those without this coating. In spite of this, the recession rates of the best performing composite tubes were below 3 μm/month which, for a 150–200 μm EBC layer, would guarantee protection throughout the assembly expected residence time in the reactor. Lastly, the oxidation rates of uncoated and coated SiC composites showed no dependence on exposure duration from 100 to 500 days exposure, as a demonstration of the saturation effect already noticed for other properties of SiC (e.g. thermal conductivity). This would advantage SiC over Zr based alloys for extended burnup applications since the property degradation for the latter

does not reach saturation but monotonically increases with fluence. These preliminary results strongly imply that SiC composite both with and without EBC's offer significant advantage over currently used Zr alloys in high temperature steam oxidation.

F. SiC melting point is very high (>2500°C). Also, this material is capable of maintaining room temperature mechanical properties to very high temperatures. For example, the tensile fracture stress of SiC is 300 MPa at 300 and 1000°C [12]. However, the mechanical properties of SiC composites are dependent on the composite architecture and construction. Even though the composite architecture for fuel cladding tubes has not been finalized, it can be stated that SiC CMC fuel cladding will have greater mechanical stability at elevated temperatures than currently used Zr base alloys.

3.2 Preliminary Advanced Fuel Safety Analysis Based on Event Type

For a safety analysis based on event type, events are divided into two categories which are subdivided into specific event groups as presented in Table 9.

TABLE 9. EVENT CATEGORIES AND GROUPS FOR PRELIMINARY SAFETY ANALYSIS BASED ON EVENT TYPE

Event Category	Event Group
Anticipated Transients	Reactor Cooling System (RCS) overcooling events
	RCS overheating events
	Reactivity insertion events
	Increase in RCS inventory events
	Decrease in RCS inventory events
	Fuel handling accident
Beyond Design Basis Accidents (BDBAs)	Anticipated Transients Without Scram (ATWSs)
	Station blackout event

Each event group comprises several specific events, which are typically analyzed for licensing purposes and whose results are presented in the Safety Analysis Report of any PWR plant in the US. These specific events are listed in the second column of Table 10. The analysis of each event requires input parameters, such as fuel and cladding thermophysical properties,

reactivity coefficients, or geometric characteristics of RCS components and has the ultimate goal to determine if specific safety acceptance criteria are met. Many of these input parameters are directly or indirectly dependent on the fuel and cladding materials. The effect that advanced fuel and cladding materials have on the reactor safety analysis can therefore be estimated by determining whether changes in those input parameters are beneficial or detrimental in meeting the acceptance criteria. This assessment is presented in Table 10 which for each event presents the following information:

- Category of event consistent with the frequency based classification developed by the American Nuclear Society in 1973 [15].
  - Condition I: Normal operation and AOOs;
  - Condition II: Faults of moderate frequency;
  - Condition III: Infrequent faults;
  - Condition IV: Limiting faults.

- Expected Impact of ATF was analyzed, specifically the fuel and cladding materials of ATF with impact ranked as Significant, Moderate, Minor, or None.
- Current Acceptance Criteria for each event.
- Expected Performance in meeting current Acceptance Criteria of each proposed cladding and fuel material. The performance of these materials is rated as Better, Worse, or unknown with respect to the currently used $Zr/UO2$ fuel system and the same coloring scheme as in Table 6 is used.
- Notes for discussion of the performance rating of the cladding and fuel materials for each event group analyzed. These notes are identified by capital letters inserted, in parenthesis, in the first or second column of the table, and coincide to descriptive paragraphs following the table.

The acceptance criteria presented in Table 10 are those used in the analysis of the current UO_2/Zr fuel system. Implementation of new cladding and fuel materials may not only change these criteria, but may also introduce new safety acceptance criteria. Therefore, some level of uncertainty exists in the performance rating presented in the table.

TABLE 10. EXPECTED PERFORMANCE IN MEETING ACCEPTED CRITERIA OF ADVANCED FUEL MATERIALS IN EVENT BASED SAFETY ANALYSIS

	Transient	Category	Expected impact of ATF on analysis	Current acceptance criteria (for conventional PWR)	Expected performance in meeting current acceptance criteria			
					SiC CMC (to Zr)	Coated Zr (to Zr)	U_3Si_2 (to UO_2)	UN (to UO_2)
RCS overcooling events (A)	HZP steamline break & HFP steamline break	IV	Moderate/Significant	MDNBR & no fuel melting	BETTER	~SAME	WORSE	WORSE
	increase in FW flow/decrease in FW enthalpy	II	Minor/Moderate	MDNBR & no fuel melting	BETTER	~SAME	WORSE	WORSE
	increase in steam flow/excessive load increase	II	Minor	MDNBR	BETTER	~SAME	WORSE	WORSE
	inadvertent opening of SG relief/safety valve	II	Minor	MDNBR	BETTER	~SAME	WORSE	WORSE
	RCP shaft seizure or RCP shaft break	IV	Moderate/Significant	RCS overpressure, PCT, fraction of rods in DNB	BETTER	~SAME	Unknown	Unknown
	complete loss of forced reactor coolant flow	III	Minor/Moderate	MDNBR	BETTER	~SAME	Unknown	Unknown
	partial loss of forced reactor coolant flow	II	Minor/Moderate	MDNBR	BETTER	~SAME	Unknown	Unknown
RCS overheating events (B)	loss of external electrical load, condenser vacuum, and turbine trip	II	Minor	MDNBR, RCS overpressure, MSS overpressure	BETTER	~SAME	BETTER	BETTER
	loss of normal FW flow	II	Minor	preclude PRZ overfill	~SAME	~SAME	BETTER but likely unchanged	BETTER but likely unchanged
	loss of non-emergency AC power to station auxiliaries	II	Minor	preclude PRZ overfill	~SAME	~SAME	BETTER but likely unchanged	BETTER but likely unchanged
	FW system pipe break	IV	Minor	prevent hot leg saturation	~SAME	~SAME	BETTER	BETTER
Reactivity insertion events	spectrum of RCCA ejection accidents (C)	IV	Significant	Fuel enthalpy <200 cal/gm; fuel melting <10% of pellet cross section; $Zr-H_2O$ reaction < 16%	BETTER	~SAME	WORSE	WORSE
	uncontrolled RCCA bank withdrawal from subcritical or low power startup (C)	II	Moderate/Significant	MDNBR & no fuel melting	BETTER	~SAME	WORSE	WORSE
	dropped RCCA (D)	III	Moderate	MDNBR & no fuel melting	BETTER	~SAME	Unknown	Unknown
	uncontrolled RCCA bank withdrawal at power (C)	II	Minor	MDNBR, no fuel melting, RCS overpressure	BETTER	~SAME	WORSE	WORSE
	CVCS malfunction resulting in B dilution (E)	II	Minor	action time to preclude criticality	~SAME	~SAME	~SAME	~SAME
RCS inventory increase (F)	inadvertent operation of ECCS at power	II	Minor	action time to preclude pressurizer overfill	~SAME	~SAME	~SAME	~SAME
	CVCS malfunction increasing RCS inventory	II	Minor	action time to preclude pressurizer overfill	~SAME	~SAME	~SAME	~SAME
RCS inventory decrease	large break LOCA (G)	IV	Significant	cladding oxidation	BETTER	BETTER	Unknown	Unknown
	steam generator tube rupture (H)	IV	Minor	Dose to the secondary side	~SAME	~SAME	~SAME	~SAME
	inadvertent opening of a PRZ relief valve (I)	II	Minor	MDNBR and pressurizer overfill	BETTER	~SAME	~SAME	~SAME
Misc (J)	fuel handling accident	IV	Minor/Moderate	dose	no effect		WORSE	WORSE
BDBAs (K)	station blackout	N/A	Moderate/Significant		BETTER	BETTER	BETTER	BETTER
	anticipated transients without scrams (ATWS)	N/A	Minor/Moderate	RCS overpressure	BETTER	BETTER	BETTER	BETTER

A. These events, typically bounded by the steam-line break, cause an overcooling of the RCS. Because of the negative MTC, these events result in an insertion of positive reactivity which, depending on the initial reactor condition, causes an increase in nuclear power or a return to power. In both cases, negative reactivity is subsequently inserted through the Doppler feedback integrated over the fuel temperature rise, which is lower for fuels having high thermal conductivity. For these events, the performance of U_3Si_2 and UN are expected to be worse than for UO_2 for three reasons:

    1.   an expected smaller Doppler integrated feedback,
    2.   the more negative Moderator Temperature Coefficient (MTC), and
    3.   the lower initial stored energy in the fuel for events starting at power.

These events are analyzed using a minimum fuel temperature to reduce the fuel stored energy (and consequently the heat transferred to the coolant) and thus maximize the RCS cool-down and resultant positive reactivity insertion.

For events starting at power, the temperature of U_3Si_2 and UN will be lower due to higher thermal conductivity, resulting in less heat transferred to the RCS and a more severe overcooling of the RCS. Combined with the more negative MTC and smaller Doppler integrated feedback for U_3Si_2 and UN, these fuels will be penalized compared to UO_2 because of a larger cool-down reactivity insertion and lower Doppler-induced power reduction. For events starting at zero power, the performance of U_3Si_2 and UN is expected to improve slightly since the penalty associated with the lower stored energy is not applicable. However, performance is expected to still be worse than UO_2 since the more negative MTC and the lower integrated Doppler feedback still apply.

B. For RCS overheating events, the RCS overheats due to a reduction in primary coolant flow or a reduction in heat removal capability by the secondary side. Depending on the specific event transient, the safety acceptance criteria are related to RCS expansion through heating of the coolant, DNB, and peak cladding temperature. The performance of U_3Si_2 and UN compared to UO_2 depends primarily on a tradeoff between three aspects:

    1. lower initial fuel stored energy for U_3Si_2 and UN,
    2. more negative MTC for U_3Si_2 and UN, and
    3. higher thermal conductivity for U_3Si_2 and UN.

The first two aspects help satisfy the safety criteria used for RCS overheating events, while the higher thermal conductivity is detrimental since it results in a faster heat transfer to the coolant (and therefore a faster RCS expansion) and, to a lesser extent for these events, in a smaller Doppler feedback due to the smaller fuel temperature rise. For rapid event transients such as RCP shaft seizure or complete loss of forced reactor coolant flow, these three aspects are equivalent and it is not possible to estimate whether U_3Si_2 or UN will perform better or worse than UO_2. For slower event transients such as the loss of normal feedwater flow, the lower stored energy in U_3Si_2 and UN will dominate compared to faster heat transfer to the RCS and the performance of U_3Si_2 and UN are expected to be better than UO_2.

C. For RIAs, the integrated Doppler feedback functions to terminate the event by inserting negative reactivity. For these events, U_3Si_2 and UN are penalized compared to UO_2 due to their slightly less negative Doppler temperature coefficient and their much higher thermal

conductivity. These fuel properties result in lower fuel temperature increase due to the initial reactivity insertion and therefore less negative Doppler integrated effect to terminate the event. Because the melting temperature of U_3Si_2 is more than 1000°C lower than UO_2 and UN, fuel pellet centerline melting could be a problem for U_3Si_2 during reactivity insertion events. Additionally, for events such as rod ejection accidents, the mechanical behavior of the proposed fuel rod and fuel materials will need to be experimentally verified to determine the impact on fuel assembly coolability.

D. In the analysis of an RCCA drop event, a power overshoot is postulated to occur as a consequence of the reactor control system trying to rebalance core power. The nuclear power evolution in the fuel assemblies subjected to this overshoot depends on the Doppler feedback, as well as on rod shadowing factors that must be considered due to the dropped rod interfering with the ability of the detectors to correctly measure the power response as the control system pulls some rods out. For U_3Si_2 and UN, they begin the transient at a lower temperature and their integrated Doppler feedback will be lower due to their higher thermal conductivity. Due to these two properties and the uncertainty in power redistribution during this transient, it is not possible to estimate whether U_3Si_2 or UN will perform better or worse than UO_2.

E. Because the neutron spectrum of U_3Si_2 and UN is likely to be harder, the B worth is expected to be lower compared to UO_2. Additionally for U_3Si_2 and UN, the degree of B dilution resulting from injecting the same amount of CVCS coolant into the RCS should also be lower due to the higher B concentration needed to compensate for the lower B worth. However, the difference in B worth is generally small and the overall performance of U_3Si_2 and UN compared to UO_2 for B dilution events is expected to be the same.

F. For RCS inventory increase events, fuel has little impact on the event progressions.

G. Large break (LB) LOCA considerations for the proposed cladding and fuel materials are presented below.

- SiC cladding: Compared to currently used Zr base alloy cladding, SiC cladding exhibits far superior high temperature steam oxidation resistance with minimal generation of H_2 from the oxidation reaction. This property alone should allow SiC cladding to exhibit superior performance compared to Zr cladding during LB LOCA conditions. However, the high stiffness and low fracture toughness of SiC could also reduce this materials durability during LB LOCA conditions. Further investigation is required to more accurately determine the relative behavior of SiC cladding compared to Zr cladding during LOCA conditions.
- Coated Zr cladding: A coating applied to the outer diameter of currently used Zr alloy cladding tubes should offer significant improvement of cladding corrosion resistance during LOCA events. However experimental data is needed to better quantify the corrosion behavior of a coated cladding as well as the adhesion of the protective layer during LOCA events.
- U_3Si_2 and UN: The maximum cladding temperature reached during the blowdown phase of a LB LOCA is likely to be lower with U_3Si_2 and UN with respect to UO_2. This is because during this initial phase of the LB LOCA transient, a very rapid and almost adiabatic heat redistribution inside the fuel rod occurs, which results in

cladding overheating proportional to the energy stored in the fuel during normal operation, which is lower for U_3Si_2 and UN due to their higher thermal conductivity. However, for U_3Si_2 potentially higher fuel swelling could require a large pellet-cladding gap resulting in an increase in fuel stored energy. The margin in blowdown cladding temperature from the UO_2 case could therefore be lower for U_3Si_2 than for UN.

H. In a steam generator tube rupture event, radioactive primary coolant enters the secondary side resulting in contamination. Although U_3Si_2 and UN are expected to be operated up to a higher burnup than UO_2, thus resulting in larger gaseous fission product inventory inside the assemblies, the nominal level of contamination of the primary coolant is not expected to differ significantly.

I. An event involving the opening of a pressurizer valve is typically non-limiting for DNBR, i.e. it does not result in DNBR values close to the limit imposed on this parameter, and would be expected to be non-limiting for whatever fuel integrity criterion replaces DNBR, if any. Also, the time to pressurizer overfill, which needs to be long enough to allow sufficient steam condensation by the pressurizer spray system and therefore to limit RCS pressure, in this event has a weak dependence on the fuel characteristics, and would not be expected to change significantly upon transition to the new fuels.

J. For a fuel handling accident, the amount and type of gaseous radionuclides released determine the dose-related consequences of such an event. Even if the type of radionuclides generated and released are the same, U_3Si_2 and UN are expected to be discharged at higher burnup compared to the current UO_2/Zr fuel system. Thus for a given fuel assembly geometry, the amount of gaseous radionuclides contained in the assembly and potentially released during this event should be greater.

K. ATWS could be any event in the table, however analyzed assuming no reactor scram. ATWS events are generally analyzed near beginning of cycle (BOC) conditions since the most limiting conditions occur with the least negative MTC. Preliminary assessment of the effect of ATF on reactivity coefficients indicates the MTC will be more negative than the value for UO_2/Zr fuel system, which is therefore expected to benefit the safety performance of the advanced materials for ATWS events. Also, due to the higher temperature capabilities and significantly reduced steam oxidation kinetics of SiC and coated Zr cladding, the proposed cladding should perform much better than the current UO_2/Zr fuel system during a station blackout event. However the timing of various events during a BDBA will be important and could dictate the performance improvement of the proposed cladding and fuel during such a transient.

4.   SAFETY ASSESSMENT FOR BEYOND DESIGN BASED ACCIDENTS

To better understand the response of advanced cladding to core uncovery accidents, Westinghouse in collaboration with Fauske & Associates (FAI) performed modeling using the Modular Accident and Analysis Program (MAAP) software [16]. As a base case model, the Three Mile Island Unit 2 (TMI-2) core uncovery accident was modeled with both a Zr base alloy and SiC as cladding materials. Fig. 2 below presents a result of this modeling showing that, for the TMI-2 accident, a SiC clad core could have survived as a coolable geometry reaching a peak temperature of approximately 1200°C.
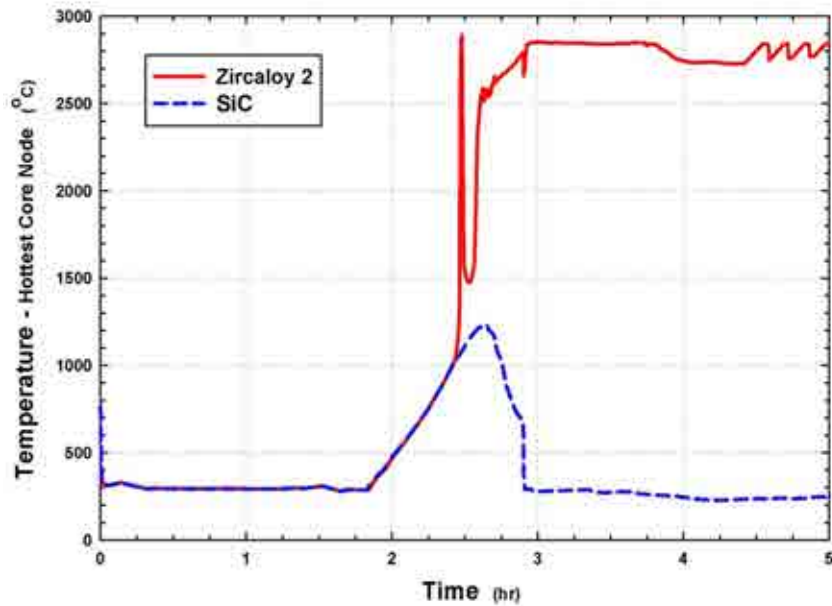
FIG. 2. Temperature of Zr and SiC cladding in the hottest core node during a modeled TMI-2 accident scenario.

Additionally, modeling of an extended station blackout event (SBO) was performed as an approach to determine how an advanced cladding would respond to an accident similar to what occurred at the Fukushima Daiichi nuclear power plant in Japan in March 2011. An extended SBO does not allow the hot leg creep rupture and therefore breach of the reactor cooling system (RCS) to occur during the accident. In this modeling approach, the materials of the fuel assemblies are exposed to core uncovery conditions for an extended period of time without allowing failure of other reactor systems. Fig. 3 presents results of the extended SBO model showing that SiC cladding could have survived a SBO accident in a coolable geometry reaching a peak temperature of approximately 1727°C. Clearly these modeling results indicate the potential of advanced cladding such as SiC_f/SiC CMC to survive both design basis and beyond design basis core uncovery accidents compared to currently used Zr base alloy cladding.
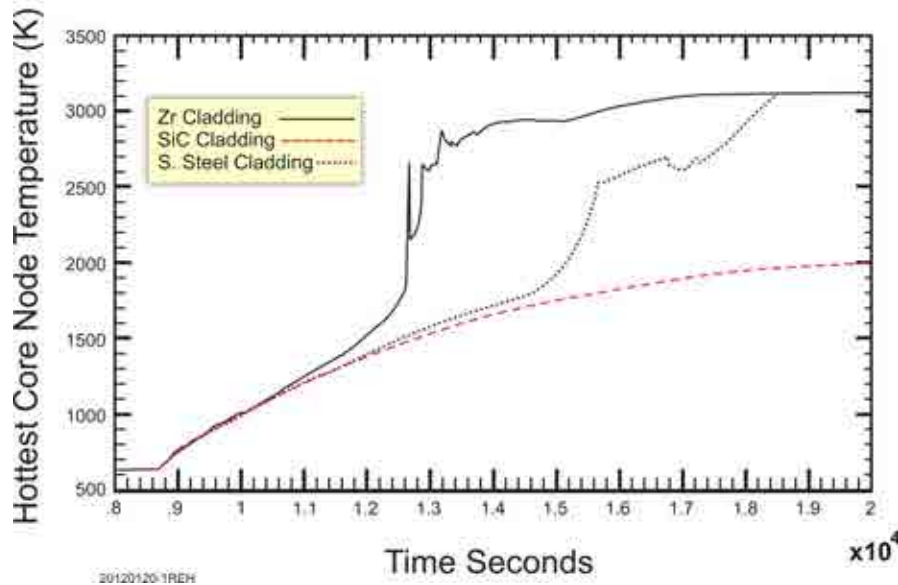
FIG. 3 Temperature of Zr, SiC, and stainless steel 316 cladding in the hottest core node during a modeled station blackout accident scenario.

While coated zr base alloy tubes would still not likely survive a sbo accident, they could provide additional reactor operator reaction time to perform ameliorative efforts. for shorter-timed events such as at tmi, treated zr tubes may have been sufficient to prevent the large scale damage that tmi suffered.

5.   CONCLUSIONS

Absent U235 enrichments greater than 5%, the use of higher density pellets for higher U235 loadings increases the economic attractiveness of ATF. U_3Si_2 offers ~17% gain in U235 density, reduced core stored energy due to an increased thermal conductivity, and minimal increases in production equipment. UN offers ~40% gain in U235 content, high melting point and a very high thermal conductivity which provide a large increase in the margin to centerline melting during transients and a low stored energy in the core. However, it requires N15 enrichment, to achieve an acceptable neutron economy, and a treatment to be oxidation resistant to reactor coolant. Additional effort is required for UN and, especially, U_3Si_2 to assess the degree of irradiation-induced swelling since the current data is extrapolated from experimental results obtained at temperatures and burnups that are significantly different from those likely to be experienced in commercial fuel service. If testing indicates that the swelling is an issue, then additional work on pellet additives and/or fuel rod designs will be needed. Although irradiation of the fuels alone has the priority, irradiation of U_3Si_2 and UN with SiC and treated Zr cladding is also required to determine the performance aspects of the fuel and cladding individually as well as a fuel system. At present, priority should be given to the key issues of irradiation-induced swelling of the fuel and interaction between the fuel and the cladding, especially SiC.

Coated Zr cladding offers significant improvement in fuel reliability during normal operations and moderate safety improvement during accidents. It could be implemented faster in the current LWR fleet due to using the same cladding bulk material and geometry. In spite

of a large degradation in thermal conductivity upon irradiation, SiC cladding offers significant safety improvement during both design basis and beyond design basis accidents. Nevertheless, due to the variety of SiC composites and manufacture methods investigated so far, further research and development efforts are needed to identify the best SiC composite candidate for LWR cladding applications, to reduce the cost of production and to fully understand the performance under irradiation.

REFERENCES

[1]   WONGSAWAENG, D., OLANDER, D., Liquid-metal bond for LWR fuel rods. Nuclear Technology, **159 3** (2007) 279-291.

[2]   WONGSAWAENG, D., OLANDER, D., Effect of replacing helium with a liquid metal in the fuel cladding gap on fission gas release. Nuclear Technology, **146**, (2004) 211–220.

[3]   WRIGHT, R.F., TULENKO, J.S., SCHOESSOW, G.J., Thermal bonding of Light Water Reactor fuel using non alkaline liquid-metal alloy. Nuclear Technology, **115**, (1996) 281–292.

[4]   SHIMIZU, H., The properties and irradiation behavior of U_3Si_2. NAA-SR-10621, Atomics International. July 25, 1965.

[5]   INERNATIONAL ATOMIC ENERGY AGENCY, IAEA-TECDOC-643, Research reactor core conversion guidebook – Volume 4: Fuels (Appendices IK), Vienna (1992).

[6]   FINLAY, M.R., HOFMAN, G.L., SNELGROVE, J.L., Irradiation behavior of uranium silicide compounds. Journal of Nuclear Materials **325** (2004) 118–128.

[7]   HEINISCH, H.L., et al., Displacement damage in silicon carbide irradiated in fission reactors Journal of Nuclear Materials, **327** (2004) 175–181.

[8]   CARPENTER, D.M., Assessment of innovative fuel designs for high performance Light Water Reactors. B.S. and M.S. thesis. Massachusetts Institute of Technology, 2006.

[9]   YOUNGBLOOD, G.E., presented at the 6th IEA SiC/SiC workshop. Boston, June 10–11, 2004.

[10]   WCAP-12488-A, Westinghouse Fuel Criteria Evaluation Process. October 1994.

[11]   CARPENTER, D.M., An assessment of Silicon Carbide as a cladding material for Light Water Reactors. PhD thesis. Massachusetts Institute of Technology. October 2010.

[12]   SNEAD, L.L., et al., Handbook of SiC properties for fuel performance modeling. Journal of Nuclear Materials, **371** (2007) 329–377.

[13]   CHENG, T., et al., Oxidation of fuel cladding candidate materials in steam environments at high temperature and pressure. Journal of Nuclear Materials **427** (2012) 396–400.

[14]   TERRANI, K.A., et al., High temperature oxidation of silicon carbide and advanced iron-based alloys in steam-hydrogen environments. TopFuel 2012, Manchester, United Kingdom, 2012.

[15]   American Nuclear Society 18.2-1973, Nuclear Safety Criteria for the Design of Stationary Pressurized Water Reactor Plants.

[16]   JOHNSON, S.C. *et. al.*, Severe Accident Modeling of a PWR Core with Different Cladding Materials, paper 12175, Proceedings of ICAPP'12 (June 2012) pp. 1–9.

ABBREVIATIONS

ATF	accident tolerant fuel
ANC	Advanced Fuels Corporation
AGE	adaptive linked gap element
APDL	ANSYS parametric design language
AIC	silver-indium-cadmium
ACM	advanced cladding material
AOO	anticipated operational occurrence
ATWS	anticipated transient without scram
BAF	burnable absorber fuel
BDBA	beyond design basis accident
BDM	boron deposition model
BOL	beginning of life
BRU-A	steam dumping device to atmosphere
CASL	Consortium for Advanced Simulation (of LWRs)
CF	critical function
CHF	critical heat flux
CIPS	CRUD-induced power shift
Clad-Elong	cladding elongation
CRUD	Chalk River unidentified deposit
CSS	containment sprays system
CVH	control volume hydrodynamics
DBA	design basis accident
DNB	departure from nucleate boiling
EBC	environmental barrier coating
ECCS	emergency core cooling system
ECR	equivalent cladding reacted ratio

EFWP	emergency feed water pump
EOL	end of life
FEA	finite element analysis
FEM	finite element method
FGR	fission gas release
FL	flow path
FP	fission products
FUMAC	fuel modelling in accident conditions
FUMEX	fuel modelling at extended burnup
HRP	Halden Reactor Project
HBS	high burnup structure
HBRP	high burnup rim project
HS	heat structure
HPP	high pressure pumps
HA	hydro-accumulator
HA	hydro accumulators
HM	heavy metal
IE	Initiator event
IFPE	international fuel performance experiments
IFA	instrumented fuel assembly
IP	inter-pellet
IRF	instant release fraction
JFNK	jacobian-free newton krylov
JMTR	Japan Materials Testing Reactor
LOCA	loss of coolant accident
KIT	Karlsruhe Institute of Techbology
LWRs	light water reactors
LM	liquid metal
LB	large break
LPP	low pressure pumps

MPS	missing pellet surfaces
MPO	materials performance and optimization
MP	mid-pellet
MCP	main coolant pump
MFPR	module for fission products release
MMSNF	materials models and simulations for nuclear fuels
MDNBR	minimum departure from nucleate boiling ratio
MTC	moderator temperature coefficient
MAAP	modular accident and analysis program
NPP	nuclear power plant
NSRR	nuclear safety research reactor
ND	neutron detectors
NRX	national research experimental
PAR	passive autocatalytic recombiner
PBF	power burst facility
PCMI	pellet-cladding mechanical interaction
PCT	peak clad temperature
PDF	probabilistic distribution function
PHWR	pressurized heavy water reactor
PIRT	phenomena identification and ranking table
PPN	peak power node
PRZ	pressurizer
PSA	probabilistic safety analysis
PWR	pressurized water reactor
RCIC	reactor core isolation cooling system
RCS	reactor cooling system
RCP	reactor coolant pump
RFA	robust fuel assembly
RIA	reactivity initiated accidents
RPV	reactor pressure vessel

SBO	station black-out
SFPR	single fuel rod performance
SCC	stress corrosion cracking
SED	strain energy density
SG	steam generator
SV	safety valves
SAMG	severe accident management guidance
S/V	surface-to-volume ratio
SET	separate-effect tests
SFD	severe fuel damage
SRVs	safety relief valves
S/Q	SVECHA/QUENCH
SA	secure accidents
SDA	steam dump to atmosphere
TAF	time at failure (in ms)
TCC	thermal contact coefficient
TM	technical meeting
TL	throughout life
TE	Tractebel Engineering
TH	thermal hydraulic
TWGFPT	(IAEA) Technical Working Group on Fuel Performance and Technology
UQ	uncertainty quantification
VPSC	visco-plastic self-consistent
WGFS	(NEA/OECD) Working Group on Fuel Safety

LIST OF PARTICIPANTS

ARGENTINA

Marino, A.C.

Comisión Nacional de Energía Atómica
Centro Atómico Bariloche; 8400 Bariloche
Argentina
+54 294 4445256; marino@cab.cnea.gov.ar

ARMENIA

Bznuni, S.

Nuclear and Radiation Safety Centre of Armenian Nuclear
Regulatory Authority
4 Tigran Mets; 0010 Yerevan Armenia
0037493-315415; s.bznuni@nsrc.am; a.melkumyan@anra.am

ARGENTINA

Denis, A.

CNEA Av del Libertador 8250 1429 Ciudad De Buenos Aires,
Argentinien
+54 11 4704-1000; denis@cnea.gov.ar

BELGIUM

Zhang, J.

Tracetebel Engineering (GDF SUEZ) Avenue Ariane 7; 1200
Brussles Belgium
003227739843; Jinzhao.zhang@gdfsuez.com

BULGARIA

Grudev, P.

Institute for Nuclear Research and Nuclear Energy – Bulgarian
Academy of Sciences, INRNE-BAS; Blvd. Tzarigradsko shaussee,
72, 1; 1784 Sofia, Bulgaria
groudev@mail.bg; 00359-2-888-955-385

CHINA

Hongxing, Y.

Nuclear Power Institute of China; P.O.Box 436-500(25#,Section
3,2nd Ring Road South),Chengdu, Sichuan, China (610041)

Li, W.

Nuclear Power Institute of China, Full Adrress: No.25, South 3rd
Section, 2nd Ring Road, Chengdu, Sichuan, China
86-028-85907434, lwj280@gmail.com

Bing, C.

Design sub-institute, Nuclear Power Institute of China, 25#,
Section 3, 2nd Ring Road South, Chengdu, China, 610041, Tel:+86
28 85908845,:+86 28 85908995, E-mail: chenbin@npic.ac.cn

Yunkang, P.

Assistant Dean, Nuclear Power Institute of China, 28#, Section 3,
2nd Ring Road South, Chengdu, China,
Tel:+86 28 85903276, Fax:+86 28 85903122, E-
mail:ykpengsc@163.com

Changxing, L.

deputy chief of Department of international cooperation and
marketing, China National Nuclear Company, 1#, Sanlihe South 3rd

Street, Disctrict Xicheng, Beijing, China, 100822,
E-mail: lcx@cnnc.com.cn

Chen, X.   China Nuclear Power Technology Research Institute; 17F/A, Jiangsu Building, Yitian Road, Futian District Shenzhen 518026 CHINA
0086-755-82960576; chxing@cgnpc.com.cn

Gao, L.   Nuclear Power Institute of China; P.O. Box 622-500, 610041, Chengdu, China
+86-15108288295; lijungaothu@gmail.com

Wang, T.   17F/A, Jiangsu Buiding, Yitian Road 6013, Futian District,Shenzhen, Guangdong ; province,P.R.CHINA
86-755-82940565; wting@cgnpc.com.cn

CZECH REPUBLIC

Klouzal, J.   UJV Řež a.s; Hlavní 130, Řež, 250 68 Czech Republic
+420602359091; klj@ujv.cz

FINLAND

Tulkki, V.   VTT Technical Research Centre of Finland; Tietotie 3, PO Box 1000, 02044 VTT Finland
00358 20 722 6114 ville.tulkki@vtt.fi

FRANCE

Bouloré, A.   CEA, DEN, Fuel Research Department, Centre de Cadarache Bat. 151, 13108 Saint Paul lez Durance
+33 4 42 25 44 15; antoine.boulore@cea.fr

Petit, M.   IRSN/PSN/SEMIA
Cadarache, BP 3 13115 Saint-lez-Durance Cedex
+33 4 4219 9646; marc.petit@irsn.fr

GERMANY

Stuckert, J.   Karlsruhe Institute of Technology (KIT); Hermann-von-Helmholtz-Platz 1; 76344 Eggenstein-Leopoldshafen; Germany
+49 721 608 22558; juri.stuckert@kit.edu

HUNGARY

Kulacsy, K.   Hungarian Academy of Sciences Centre for Energy Research (MTA EK); Konkoly Thege Miklos ut 29-33., H-1121 Budapest, Hungary
+36 1 3922222 ext. 3818; katalin.kulacsy@energia.mta.hu

JAPAN

Udagawa, Y.   Japan Atomic Energy Agency; Shirakata-Shirane 2-4, Tokai-mura, Naka-gun, barak'hken, Japan

+81-29-282-6230; udagawa.yutaka@jaea.go.jp

REPUBLIC OF KOREA

Kim, H.C.   Korea Atomic Energy Research Institute; 1045 Daedeok-daero, Yuseong-gu DAEJEON REPUBLIC OF KOREA
0082 42 868 8689; hyochankim@kaeri.re.kr

MEXICO

Mugica, V.   Comision nacional de seguridad nuclear y salvaguardias (CNSNS); Dr. Barragan 779 Col. Narvarte, C.P. 03020, Mexico, D. F. Mexico
52 5550953243; cesar.mugica@cnsns.gob.mx

PAKISTAN

Rafique, M.   Directorate General Nucelar Power Fuel; Pakistan ATomic Energy Commission; PO Box 1114 Islamabad Pakistan
0092512612306; m_rafique_pk@yahoo.com

ROMANIA

Paraschiv, A.   Nuclear Research Institute; 1 Campului street RO115400 Mioveni, Arges, Romania
Adrieana.paraschiv@gmail.com;
0040 248 213 400 ext 341

RUSSIAN FEDERATION

Sokolov, E.   Scientific and Engineering Centre for Nuclear and Radiation Safety (SEC NRS); Malaya Krasnoselskaya 2/8, building 5; 107140 Moscow, Russia
007499 2640 508 sokolov@secnrs.ru

Veshchunov, M.   IBRA 52, B. Tulskaya Moscow 115191
+7(495) 9552210; vms@ibrae.ac.ru

SOUTH AFRICA

Naidoo, K.   South AFrican National Nuclear Regulator
14 Atlantic Road, Duynefontein, Melkbosstrand
knaidoo@nnr.co.za

UKRAINE

Ieremenko, M.   State Scientific and Technical Centre for Nuclear and Radiation Safety; 35-37, V. Stusa street; 03142 Kyiv-142 Ukraine
ml_eremenko@sstc.kiev.ua; 00380444224955

USA

Xu, P.   Senior Engineer, PWR Fuel Technology; Westinghouse Electric Company 5801 Bluff Road, Hopkins SC 29209
Tel: (803) 647-1819 Fax: (803) 695-3973

xup@westinghouse.com

Williamson, R.	Idaho National Laboratory; PO Box 1625, Idaho Falls, Idaho, 83415, USA 208-526-0576; Richard.Williamson@inl.gov
Stanek, C.R.	Los Alamos National Laboratory Materials Science and Technology Division MS G755 Los Alamos, NM 87545 USA 505 664 0361; stanek@lanl.gov
Montgomery, R.	Nuclear Energy Sector Manager Pacific Northwest National Laboratory P.O. Box 999, MS K9-69 Richland, WA 99352 Phone: 509-371-6231 Cell: 858-774-2013 Robert.Montgomery@pnnl.gov

EUROPEAN COMISSION

Uffelen, P.V.	European Commission; Materials Research Department Institute for Transuranium Elements; Postfach 2340; 76125 Karlsruhe Germany Tel: +49 7247 951 384; paul.van-uffelen@ec.europa.eu